

Advanced Structured Materials

K. Annapurna  
Atiar Rahaman Molla *Editors*

# Glasses and Glass-Ceramics

Advanced Processing and Applications

 Springer


# Advanced Structured Materials

Volume 178

## Series Editors

Andreas Öchsner, Faculty of Mechanical Engineering, Esslingen University of Applied Sciences, Esslingen, Germany

Lucas F. M. da Silva, Department of Mechanical Engineering, Faculty of Engineering, University of Porto, Porto, Portugal

Holm Altenbach , Faculty of Mechanical Engineering, Otto von Guericke University Magdeburg, Magdeburg, Sachsen-Anhalt, Germany

Common engineering materials are reaching their limits in many applications, and new developments are required to meet the increasing demands on engineering materials. The performance of materials can be improved by combining different materials to achieve better properties than with a single constituent, or by shaping the material or constituents into a specific structure. The interaction between material and structure can occur at different length scales, such as the micro, meso, or macro scale, and offers potential applications in very different fields.

This book series addresses the fundamental relationships between materials and their structure on overall properties (e.g., mechanical, thermal, chemical, electrical, or magnetic properties, etc.). Experimental data and procedures are presented, as well as methods for modeling structures and materials using numerical and analytical approaches. In addition, the series shows how these materials engineering and design processes are implemented and how new technologies can be used to optimize materials and processes.

Advanced Structured Materials is indexed in Google Scholar and Scopus.

K. Annapurna · Atiar Rahaman Molla  
Editors

# Glasses and Glass-Ceramics

Advanced Processing and Applications

 Springer



*Editors*

K. Annapurna  
Specialty Glass Division  
CSIR-Central Glass and Ceramic Research  
Kolkata, West Bengal, India

Atiar Rahaman Molla  
Specialty Glass Division  
CSIR-Central Glass and Ceramic Research  
Kolkata, West Bengal, India

ISSN 1869-8433

ISSN 1869-8441 (electronic)

Advanced Structured Materials

ISBN 978-981-19-5820-5

ISBN 978-981-19-5821-2 (eBook)

<https://doi.org/10.1007/978-981-19-5821-2>

© The Editor(s) (if applicable) and The Author(s), under exclusive license to Springer Nature Singapore Pte Ltd. 2022

This work is subject to copyright. All rights are solely and exclusively licensed by the Publisher, whether the whole or part of the material is concerned, specifically the rights of translation, reprinting, reuse of illustrations, recitation, broadcasting, reproduction on microfilms or in any other physical way, and transmission or information storage and retrieval, electronic adaptation, computer software, or by similar or dissimilar methodology now known or hereafter developed.

The use of general descriptive names, registered names, trademarks, service marks, etc. in this publication does not imply, even in the absence of a specific statement, that such names are exempt from the relevant protective laws and regulations and therefore free for general use.

The publisher, the authors, and the editors are safe to assume that the advice and information in this book are believed to be true and accurate at the date of publication. Neither the publisher nor the authors or the editors give a warranty, expressed or implied, with respect to the material contained herein or for any errors or omissions that may have been made. The publisher remains neutral with regard to jurisdictional claims in published maps and institutional affiliations.

This Springer imprint is published by the registered company Springer Nature Singapore Pte Ltd. The registered company address is: 152 Beach Road, #21-01/04 Gateway East, Singapore 189721, Singapore

# Foreword

Natural glasses “always” existed, whereas synthetic inorganic glasses were possibly discovered circa 5–6 millennia ago in Mesopotamia (Iraq). For many centuries, they were used as vessels and ornamental objects. In the seventeenth century, glasses made possible the invention of the microscope and the telescope, which revealed the micro—and macro—universes, from microstructures to planets and galaxies. Glasses of optical quality were developed in the 1880s, which boosted the optical instruments industry and science. For that accomplishment, glasses have been nicknamed by some authors the “*eyes of science*.”

Glass windows have protected us from harsh weather for the past four centuries; glass bottles allow us to store water and other precious liquids free of contaminants, viruses and bacteria, filter light and other potential causes of degradation. Multi-colored “crystal” glasses achieve intricate forms in the hands of artists that fill us with awe and enchant our lives. Today, due to their attractive aesthetics and excellent optical, mechanical, thermal, electrical, and chemical properties, glasses are being increasingly used in numerous practical domestic applications and even more fascinating ones, such as optical fibers, lasers, visible-UV-IR filters, color blindness correctors, electrochromic windows, optical memories, bioglasses, nuclear waste disposal, etc.

Furthermore, through controlled crystallization, a new family of advanced materials denominated glass-ceramics emerged, which are used, for example, in cooktop plates, giant telescopic mirrors, and state-of-the-art cell phone displays. Due to all these great uses, the comfort provided to our lives, and its growing economic importance, 2022 was deservedly chosen by the UN as the **International Year of Glass!**

With the continuous research pursuits on glass science and engineering, advancements in glass technology are continuously witnessed, allowing the development of smart glasses with an even more comprehensive range of functionalities and commercial applications. Knowledge dissemination in this field is desirable to fetch progress with sustainability. To this end, the CSIR-Central Glass and Ceramic Research Institute (CSIR-CGCRI, Kolkata, India), in a joint endeavor with the International Commission on Glass (ICG), organized the 2nd ICG-CGCRI international tutorial

in the period January 18–27, 2021, in this series of tutorials to propagate knowledge about glass science and technology.

To “crystallize” all the valuable information discussed and celebrate the tutorial, a CGCRI team has organized a book entitled *Glasses and Glass-Ceramics—Advanced Processing and Applications*, Edited by doctors K. Annapurna and Atiar Rahaman Molla. In this book, properties of *Glasses and Glass-Ceramics* are explained. It summarizes some of the tutorial lectures covering an introduction to glass, its main properties, thermodynamics, and heat transfer in glass-forming melts, color in glass, and advanced characterization techniques to analyze the structure and properties of functional glasses and glass-ceramics. The authors from India, Germany, the USA, Japan, England, and France are experienced and well-known within the glass-research community. In this context, this book will undoubtedly contribute to the knowledge dissemination across the readership from the student community, researchers, scientists, professors, and technologists working in this field. It comprises the following chapters:

1. [Thermodynamics of Glasses](#) (Reinhard Conradt)
2. [Chemical Durability of Glasses](#) (Reinhard Conradt)
3. [Radiation Heat Transfer in Glass Melts: Key Concepts and Phenomena](#) (Manoj Choudhary)
4. [Thermomechanical Behaviour During Forming of Silicate Glasses—Modelling and Characterization](#) (Rahul Kumar, Soupitak Pal, and Dipayan Sanyal)
5. [Coloured Glass](#) (J. M. Parker)
6. [Computer Modeling of Glass Structures and Properties](#) (Akira Takada)
7. [Atomic Structure of Glasses Investigated by Diffraction and Scattering of Radiations](#) (Bernard Hehlen and René Vacher)
8. [Melt-Derived Bioactive Glasses: Approaches to Improve Thermal Stability and Antibacterial Property by Structure–Property Correlation](#) (Sakthi Prasad, Anustup Chakraborty, Kaushik Biswas)
9. [Nuclear Waste Vitrification and Chemical Durability](#) (Russell J. Hand)
10. [Glass–ceramics: A Potential Material for Energy Storage and Photonic Applications](#) (Anirban Chakrabarti, Sreedevi Menon, Anal Tarafder, and Atiar Rahaman Molla)

I warmly congratulate doctors Annapurna and Molla for this excellent initiative, which will undoubtedly be a positive addition to the IYOG celebrations!

Prof. Edgar Dutra Zanotto  
Director  
Center for Research, Technology  
and Education in Vitreous Materials  
Federal University of São Carlos  
São Carlos, Brazil  
<http://www.certev.ufscar.br>

# Preface

The book on *Glasses and Glass-Ceramics—Advanced Processing and Applications* has been edited by Dr. K. Annapurna and Dr. Atiar Rahaman Molla to be published by Springer Nature. Given the rapid growth of the field of glassy materials, a wide range of synthesis techniques, properties, and applications for glassy materials are already available, but progress in this field continues to be made at a remarkable rate. This book will be a useful mine of state-of-the-art information for those engaged in research and education in this domain. This is an outcome of an ICG-CGCRI tutorial on glass conducted in January 2021 which was hosted by CSIR-Central Glass and Ceramic Research Institute, Kolkata, India, in association with the International Commission on Glass (ICG) where glass experts across the globe delivered their presentations on cutting-edge topics on glass, starting from the horizons of synthesis techniques, physics and chemistry of glasses, advanced characterization techniques and that has expanded to advanced applications. This was realized that if all these amazing lectures can be collated into a book that will most likely represent a valuable source of information not only for scientists working on glassy materials but also for many interdisciplinary scientists involved in chemistry, physics, ceramics, and other engineering disciplines. This book covers ten illuminating chapters covering almost all the aspects of glass materials.

David L. Morse and Jeffrey W. Evenson of Corning Incorporated, New York, rightly pointed out that “Glass is one of the world’s most transformative materials”. Featuring tremendous versatility and distinctive technical capabilities, glass has been responsible for numerous cultural and scientific advancements from windows to optical fiber. Today, the pace of glass innovation is accelerating, thanks to scientists’ deep understanding of glass physics and chemistry, combined with modern analytic and control technologies. We believe that the world has entered in the Glass Age. We have an unprecedented opportunity to harness the unique capabilities of glass to solve some of our world’s most urgent challenges, such as more effective health care, cleaner energy and water, and more efficient communication in an article titled “Welcome to the Glass Age” published in the *international journal of applied glass science* (2016). Glass has been recognized as an outstanding material for transformation of human lives and a befitting tribute to the material was bestowed by the

United Nations through their declaration of the year 2022 as an International Year of Glass.

Before entering the enchanting world of glassy materials, a brief introduction to glass may be useful to novice glass researchers or non-professionals.

Glass is an amorphous solid completely lacking in long-range, periodic atomic structure, and exhibiting a region of glass transformation behavior. Any material, inorganic, organic, or metallic, formed by any technique, which exhibits glass transformation behavior is a glass.

Although many definitions for glass have been proposed by many researchers time and again starting from the 1930s, however, the above definition covers all aspects of glass. Glass is one of the earth's most enduring engineering materials. Glass's impermeability makes it useful for hermetic containers, displays, substrates for ICs, and appealing architectural applications. The transparency of glass has been exploited for optical and RF transmission. Glass surfaces have been engineered to make mechanically much stronger and damage resistant. Some glasses can withstand temperatures as high as 1000 °C without any deformation, maintaining absolute structural integrity. Glass has ingrained an indelible footprint on the health care sector by supplying bio-active glasses, implants, and anti-bacterial coatings to the human race.

The glass has a tremendous impact on the transformation of modern civilization. The contribution of glass has been realized with the discovery of spectacles using glasses in the thirteenth century and the fourteenth century presented the world with crown glasses that has been used as transparent windows enabling humans to protect themselves from the harshest environments while allowing the light to enter in their houses. For example, the discovery of telescopes in the seventeenth century helps the scientists to unravel the mysteries of the universe. The glass contributed tremendously for the advancements of medical sciences by presenting with a microscope that enabled the discovery of viruses, bacteria, cells, etc., leading to discoveries of vaccines, antibiotics and anti-viral drugs to name a few. We cannot just imagine a life, without mirrors, car windshields lenses, picture tubes, etc., made out of glasses that created massive transformations in photography, motion pictures, and television. The invention low-loss optical fiber in 1970 created a revolution in the Internet-based communication technology.

Glass-ceramics are on the other hand polycrystalline materials derived from glasses by controlled crystallization. It contains both the glassy as well as crystalline phases and expands the possibilities of multi-functional applications by generating suitable crystals within glass matrices. By changing the compositions and crystallization heat-treatment parameters, volume fractions of crystals, its morphology, etc., can be controlled to tailor the properties of glass-ceramics, resulting in enormous possibilities for applications in cutting-edge technologies. Optical, thermal, chemical, biological, mechanical, electrical, and magnetic properties of glass-ceramics can be tailored and that finds many important applications. Glass-ceramics are used for many technical applications including in radomes, space, magnetic memory, liquid crystal display, consumer applications (cookware, tableware, stove-tops), telescope mirrors,

luminescent material, solar concentrators, white LED, medical and dental applications, electrical and electronic applications, architectural applications, coatings and solders, energy applications to name a few.

The book covers the tutorial lectures delivered at the 2nd ICG-CGCRI online tutorial organized by the CSIR-CGCRI, Kolkata. The book comprises of 10 chapters consisting of [Thermodynamics of Glasses](#) (Reinhard Conradt), [Chemical Durability of Glasses](#) (Reinhard Conradt), [Radiation Heat Transfer in Glass Melts: Key Concepts and Phenomena](#) (Manoj Choudhary), [Thermomechanical Behaviour During Forming of Silicate Glasses—Modelling and Characterization](#) (Dipayan Sanyal and Rahul Kumar), [Coloured Glass](#) (J. M. Parker), [Computer Modeling of Glass Structures and Properties](#) (Akira Takada), [Atomic Structure of Glasses Investigated by Diffraction and Scattering of Radiations](#) (Bernard Hehlen and René Vacher), [Melt-Derived Bioactive Glasses: Approaches to Improve Thermal Stability and Antibacterial Property by Structure–Property Correlation](#) (Sakthi Prasad, Anustup Chakraborty, Kaushik Biswas), [Nuclear Waste Vitrification and Chemical Durability](#) (Russell J. Hand) and [Glass–ceramics: A Potential Material for Energy Storage and Photonic Applications](#) (Anirban Chakrabarti, Sreedevi Menon, Anal Tarafder, and Atiar Rahaman Molla). We are grateful to all the authors for their fine contributions for this book. This book has been contributed by the stalwarts in the field of glass from across the globe from India, Germany, the USA, Japan, and France.

The editors are indebted to Prof. E. D. Zanotto, Federal University of Sao Carlos, Brazil, for giving two outstanding lectures in the tutorial and for his remarkable Foreword for this book.

We gratefully acknowledge the supports made by the colleagues of CSIR-CGCRI, Kolkata, for conducting the online tutorial successfully.

We are particularly grateful to Dr. (Mrs.) Suman Kumari Mishra, Director, CSIR-CGCRI, for her continuous support and encouragement for conducting the online ICG-CGCRI tutorial on glass. Mr. Sitendu Mandal, Chief Scientist, and Head, Specialty Glass Division, CSIR-CGCRI, has been instrumental for successfully conducting this event. We are indebted for the profound contributions made by our colleagues from the Specialty Glass Division, CSIR-CGCRI especially to Dr. Kaushik Biswas, Dr. Anal Tarafder, Dr. Ashis Kumar Mandal, Dr. Shirshendu Chakraborty, Dr. N. C. Pramanik, Dr. Sunirmal Jana, Dr. Himanshu Maharana.

The General Assembly of the United Nations deserves a special thank for their kind resolution to declare the year 2022 as the International Year of Glass considering immense contributions *the Glass* has made to the society.

K. Annapurna  
Chief Scientist  
CSIR-Central Glass and Ceramic Research  
Kolkata, India

Professor  
Faculty of Physical Science  
Academy of Scientific and Innovative Research (AcSIR)  
CSIR- Human Resource Development Centre  
(CSIR-HRDC) Campus  
Ghaziabad, Uttar Pradesh, India

Atiar Rahaman Molla  
Principal Scientist  
CSIR-Central Glass and Ceramic Research  
Kolkata, India

Associate Professor  
Faculty of Engineering Science  
Academy of Scientific and Innovative Research (AcSIR)  
CSIR- Human Resource Development Centre  
(CSIR-HRDC) Campus  
Ghaziabad, Uttar Pradesh, India

# Contents

<b>1</b>	<b>Thermodynamics of Glasses</b> .....	1
	Reinhard Conradt	
1.1	Introduction .....	1
1.2	The Language of Phenomenological Thermodynamics .....	3
1.3	The Glassy State .....	7
1.4	Multicomponent Glasses .....	13
1.5	Summary and Outlook .....	29
	Appendix 1 .....	30
	Appendix 2 .....	31
	Appendix 3 .....	32
	References .....	34
<b>2</b>	<b>Chemical Durability of Glasses</b> .....	37
	Reinhard Conradt	
2.1	Introduction .....	37
2.2	Design and Evaluation of Corrosion Tests .....	40
	2.2.1 Design of Corrosion Tests .....	40
	2.2.2 Evaluation of Corrosion Tests .....	43
2.3	Sub-surface Layers .....	45
2.4	Thermodynamic Approach to the Hydrolytic Stability .....	51
2.5	Rate Equation .....	61
2.6	Reaction Path Calculation, Corrosion Layers, Long-Term Behavior .....	65
2.7	Summary and Outlook .....	71
	References .....	73
<b>3</b>	<b>Radiation Heat Transfer in Glass Melts: Key Concepts and Phenomena</b> .....	77
	Manoj Choudhary	
3.1	Introduction .....	77
3.2	Review of Some Basic Concepts of Thermal Radiation .....	78



3.2.1	Planck’s Law (Spectral/Monochromatic Blackbody Emissive Power) . . . . .	79
3.2.2	Stefan–Boltzmann Law (Total Blackbody Emissive Power) . . . . .	79
3.2.3	Intensity of Radiation . . . . .	80
3.2.4	Radiation Properties of Surfaces . . . . .	82
3.3	Radiation in Absorbing, Emitting, and Scattering Media . . . . .	83
3.3.1	Attenuation of Radiative Intensity by Absorption and Scattering . . . . .	84
3.3.2	Augmentation of Radiative Intensity by Emission and Scattering . . . . .	85
3.3.3	The Radiative Transfer Equation . . . . .	87
3.4	Radiative Heat Flux and Its Divergence . . . . .	87
3.5	Approximate and Limiting Cases of RTE . . . . .	88
3.5.1	One-Dimensional RTE in a Non-scattering Medium . . . . .	89
3.5.2	Optically Thin Limit ( $\tau_{L\lambda} \ll 1$ ) . . . . .	93
3.5.3	Optically Thick Limit ( $\tau_{L\lambda} \gg 1$ ) . . . . .	94
3.5.4	An Approximate Solution for One-Dimensional Gray Medium . . . . .	96
3.6	Absorption Spectra of Glass Melts . . . . .	97
3.7	Modeling of Thermal Radiation in Glass Melts . . . . .	99
3.7.1	Discrete Ordinates Method (DOM) . . . . .	99
3.7.2	Diffusion Approximation: Radiative Conductivity of Glass Melts . . . . .	101
3.8	Illustrative Thermal Radiation Modeling Results . . . . .	102
3.9	Concluding Remarks . . . . .	107
	References . . . . .	108
<b>4</b>	<b>Thermomechanical Behaviour During Forming of Silicate Glasses—Modelling and Characterization</b> . . . . .	<b>109</b>
	Dipayan Sanyal and Rahul Kumar	
4.1	Introduction . . . . .	109
4.2	Rheological Behaviour of Silicate Glasses . . . . .	111
4.2.1	Viscous Behaviour of Glasses . . . . .	113
4.2.2	Viscoelastic Behaviour of Glasses . . . . .	115
4.2.3	Maxwell Model . . . . .	119
4.3	Relaxation Phenomena in Silicate Glasses . . . . .	120
4.3.1	Structural Relaxation . . . . .	120
4.3.2	Stress Relaxation . . . . .	122
4.4	Modelling and Characterizations . . . . .	126
4.4.1	Fictive Temperature and Glass Transition Temperature . . . . .	126
4.4.2	Stress Relaxation Behaviour . . . . .	128
4.4.3	Material Modelling . . . . .	129

4.4.4	Benchmark Simulation .....	130
4.5	Conclusion .....	133
	References .....	134
<b>5</b>	<b>Coloured Glass .....</b>	<b>137</b>
	J. M. Parker	
5.1	Summary .....	137
5.2	Introduction and History .....	137
5.3	Light Absorption .....	139
5.3.1	Measuring Absorption .....	140
5.3.2	De-Excitation Processes .....	142
5.3.3	Interpreting Absorption Spectra—Peak Positions .....	143
5.3.4	Interpreting Absorption Spectra—The Effect of Host Composition .....	144
5.3.5	Consequences of Different Iron Oxidation States for Applications .....	145
5.4	Perceived Colour—Colour Coordinates .....	145
5.4.1	Optimising Iron Colour .....	146
5.5	Kinetics and Cooling .....	147
5.5.1	Redox Reactions with Two or More Redox Ions .....	148
5.5.2	Kinetics of Redox Reactions .....	151
5.5.3	Redox Reactions as a Function of Temperature .....	151
5.6	Rare Earth Elements and Optical Properties .....	152
5.7	Defects .....	152
5.8	Colouring Glasses by Nanoparticles .....	153
5.9	Glass Ceramics for Optical Devices .....	154
5.10	Periodic Structures .....	154
	References .....	155
<b>6</b>	<b>Computer Modeling of Glass Structures and Properties .....</b>	<b>157</b>
	Akira Takada	
6.1	Introduction .....	157
6.2	Basics of Numerical Simulations .....	159
6.2.1	General Features .....	159
6.2.2	The Importance of Interatomic Potentials .....	161
6.2.3	Scheme of Molecular Dynamics Simulation .....	163
6.2.4	Practical Recipe for Numerical Simulation .....	164
6.3	Modeling of Glass Structures .....	165
6.3.1	Overall Structure and Short-Range Order .....	165
6.3.2	Ring Size Distribution and Geometrical Modeling for Medium-Range Order .....	169
6.4	Modeling of Glass Properties .....	170
6.5	Experimental and Computational Complementarity .....	173
6.6	Perspectives .....	173
	References .....	176

<b>7</b>	<b>Atomic Structure of Glasses Investigated by Diffraction and Scattering of Radiations</b> .....	177
	Bernard Hehlen and René Vacher	
7.1	Diffraction—Elastic Scattering .....	177
7.1.1	X-Ray and Neutron Diffraction Method .....	177
7.1.2	Description of Glass Structure .....	179
7.1.3	Amplitude of the Scattered Field: The Form Factor ....	182
7.1.4	Diffacted Intensity .....	184
7.1.5	Structure of Vitreous Silica and Some Silicate and Borate Glasses .....	187
7.1.6	Neutron Diffraction: Isotopic Substitution .....	189
7.2	Inelastic Scattering .....	192
7.2.1	Inelastic Scattering Spectroscopy .....	193
7.2.2	Origin of the Scattering .....	195
7.2.3	Raman Selection Rules .....	197
7.2.4	Raman Spectroscopy in Silicate Glasses .....	200
7.3	Conclusion .....	202
	References .....	203
<b>8</b>	<b>Melt-Derived Bioactive Glasses: Approaches to Improve Thermal Stability and Antibacterial Property by Structure–Property Correlation</b> .....	205
	Sakthi Prasad, Anustup Chakraborty, and Kaushik Biswas	
8.1	Introduction .....	205
8.2	General Composition of Melt-Derived Bioactive Glasses .....	208
8.3	Glass Thermal Stability .....	211
8.4	Improving the Thermal Stability and Bioactivity Using Compositional Modifications .....	213
8.4.1	Incorporation of $B_2O_3$ .....	214
8.4.2	Increment of CaO .....	215
8.4.3	Incorporation of $K_2O$ .....	217
8.4.4	Incorporation of $Li_2O$ .....	219
8.4.5	Incorporation of MgO .....	219
8.4.6	Incorporation of SrO .....	221
8.4.7	Incorporation of ZnO .....	222
8.4.8	Increment of $P_2O_5$ .....	224
8.4.9	Incorporation of Fluoride .....	226
8.5	Antibacterial Properties .....	229
8.6	Conclusions and Future Trends .....	231
	References .....	232
<b>9</b>	<b>Nuclear Waste Vitrification and Chemical Durability</b> .....	243
	Russell J. Hand	
9.1	Introduction .....	243
9.2	Waste Vitrification .....	245
9.2.1	Glasses for Waste Vitrification .....	246

9.2.2	Problem Species and Waste Loading	247
9.2.3	Vitrification Technologies	248
9.3	Durability	250
9.3.1	Thermal Durability	250
9.3.2	Mechanical Durability	251
9.3.3	Radiation Durability	251
9.3.4	Chemical Durability Testing	253
9.3.5	Durability Behaviour Under Low Flow Conditions	256
9.3.6	Durability of Natural and Anthropogenic Analogue Glasses	258
9.4	Summary	259
	References	260
<b>10</b>	<b>Glass–ceramics: A Potential Material for Energy Storage and Photonic Applications</b>	<b>265</b>
	Anirban Chakrabarti, Sreedevi Menon, Anal Tarafder, and Atiar Rahaman Molla	
10.1	Introduction	265
10.1.1	History	265
10.1.2	Definition of Glass–ceramics	266
10.1.3	Importance of Glass–ceramics	266
10.1.4	Crystallization of Glass	267
10.1.5	Fabrication Techniques	269
10.1.6	Properties	271
10.1.7	Applications	272
10.2	Glass–ceramics for Energy Storage	274
10.2.1	Introduction	274
10.2.2	Key Parameters for Evaluating Energy Storage Density and Efficiency	274
10.2.3	Value of Glass–ceramics for Energy Storage	277
10.2.4	Categorization of Glass–ceramics for Energy Storage Applications	279
10.2.5	Factors Affecting Energy Storage Properties of Glass–ceramics	290
10.2.6	Future Aspects	291
10.3	Glass–ceramics for Photonic Applications	291
10.3.1	Introduction	291
10.3.2	Classification of Glass–ceramics for Photonic Applications	292
10.3.3	Future Aspects	296
	References	297

## About the Editors

**Dr. K. Annapurna** is presently working as Chief Scientist at CSIR-CGCRI and also serving as Professor at Academy of Scientific and Innovative Research (AcSIR) an Institute of National Importance. She obtained her Ph.D. in 1993 followed by post-doctoral research at Sri Venkateswara University, India. She joined CSIR-Central Glass and Ceramic Research Institute, Kolkata, India, in 1996, and since then, she is actively involved in the research and development of specialty glasses like Nd-doped phosphate laser glass for high power laser systems, infrared absorbing and infrared transmitting filter glasses, non-oxide chalcogenide glasses for thermal imaging applications, space grade optical glasses, including their process technology. She has taken active role in establishing architectural research and testing facility at CGCRI. Her basic research includes structure and property studies of rare earth/transition metal-doped glasses and transparent glass ceramics for photonic and energy applications. She has around 140+ publications in international and national journals of repute and one Indian and six international patents to her credit. She has served as Lab Coordinator for the Academy of Scientific and Innovative Research (AcSIR) at CSIR-CGCRI. For notable contributions in field of materials science and technology, she has been conferred with R. L. Thakur Award for Young Scientists 1998.

**Dr. Atiar Rahaman Molla** is presently working as Principal Scientist at the CSIR-Central Glass and Ceramic Research Institute, Kolkata, where he started his research career as Junior Scientist in 2001. He is also currently serving as Associate Professor of the Academy of Scientific and Innovative Research, New Delhi. He obtained his B.Tech. in Ceramic Technology from University of Calcutta and M.Tech. in Materials Metallurgical Engineering from the Indian Institute of Technology (IIT) Kanpur prior to obtaining his Ph.D. in Engineering from Jadavpur University, Kolkata. He worked at Federal University of São Carlos, Brazil as Visiting Scientist. His major areas of research interests includes specialty glasses and glass-ceramics, particularly on high-strength glasses and glass-ceramics, glass-ceramics for energy storage and photonics applications, chalcogenide glasses for diamond processing and thermal

imaging applications and utilization of industrial wastes for synthesis of glasses and glass-ceramics. He has published more than 50 papers in international journals of repute, six granted patents in India, Germany, EU, Indonesia, Turkey and China, one Malaysian patent is pending, contributed two book chapters.

# Chapter 1

## Thermodynamics of Glasses



Reinhard Conradt

### 1.1 Introduction

#### *Scope of the chapter*

The present chapter is devoted to the thermodynamic description of glasses, with a focus on silicate glasses. This is done in the language of classical, i.e., phenomenological thermodynamics, which—in contrast to statistical thermodynamics—rests on macroscopic quantities only. It is true, that such an approach does not appeal to the sense of imagination. The reader may miss the typical images of glass structures found in many textbooks. However, this shortcoming is well compensated by the fact that the thermodynamic approach always yields quantitative results. Thus, it is a key to the assessment of the properties of glasses and glass melts. It serves as a powerful tool in the design of glasses with desired properties and allows one to analyze in a quantitative way chemical reactions involving glasses and their melts. Typical examples are: the batch-to-melt conversion, evaporation from glass melts, and the chemical durability of glasses. In Sect. 1.2, an introduction to the quantities used in phenomenological thermodynamics—so-to-speak, to the vocabulary of its language—is given. Section 1.3 presents a short review of the typical features of the glassy state. Ways are outlined how to describe glass-forming one-component systems in terms of thermodynamic quantities. Section 1.4 of the chapter is devoted to multicomponent glasses. After all, the majority of glasses produced worldwide belong to this class of systems. The part is supported by examples demonstrating how thermodynamic calculations on such systems are performed.

#### *Relation between structure and energetics*

According to traditional understanding, silicate glasses build a random network constituted by the nature of their atomic bonds. No unit cell of a glass can be given.

---

R. Conradt (✉)  
Nizzaallee, 75, 52072 Aachen, Germany  
e-mail: [reinhard.conradt@gmail.com](mailto:reinhard.conradt@gmail.com)

Glass structure is often described in categories of network forming versus network modifying bonds. This paradigm is based on the work by Zachariasen [1], later modified by Greaves [2]. Glasses have been termed amorphous materials. This is, in fact, a poor statement. The term “amorphous” means “absence of a defined structure”, thus expressing what we do not know about glass structure only. Therefore, let us consider the structural hierarchies in condensed phases, i.e., crystals X, glasses GL, liquids L, namely: short-range order (SRO), medium-range order (MRO), and long-range order (LRO). This approach is highly simplified and does not account for the formation of any defects, clusters, or phase boundaries. In oxide systems, the SRO primarily relates to the nature of the cation–anion polyhedra, while the MRO relates to how they are connected, for example via corners, edges, or surfaces. Ignoring fractals and quasicrystals for the sake of simplicity, the LRO relates to the translational symmetry of the structure. Only states X have translational symmetry. Table 1.1 compares the atomic ordering, interatomic interactions, and atomic displacement in the states of gas, crystal, liquid, and glass. Detailed theories have been developed for gases and crystals. This has not yet been achieved to the same extent for liquids and glasses. According to Landau [3], this is because gases and crystals both have a “negligibly small parameter”, i.e., the interaction or static displacement, respectively, can be neglected. This simplification is not possible in general for liquids and glasses. The diffusion coefficients in Table 1.1 reflect the order of magnitude of atomic mobility. For isochoric heat capacities  $c_V$  of solid condensed phases, Table 1.1 lists the uniform distribution or Dulong-Petit value  $c_V = 3N \cdot k$ , with  $N =$  Avogadro’s number,  $k =$  Boltzmann’s constant. It is the upper-temperature threshold reached in crystalline solid phases. For elements and simple compounds, this is a surprisingly accurate assessment. For more complex compounds like silicates, however, it only applies as a rough approximation. For the  $c_V(T)$  function of gases and solids, elaborate theories (kinetic gas theory, Debye-Einstein model, respectively) are available. For liquids, even the number  $f$  of atomic degrees of freedom is uncertain. A recent proposition for  $f$  reads  $f = 3 - (\omega_F/\omega_D)^3$  [4];  $\omega_F =$  Frenkel frequency of positional hopping of atoms,  $\omega_D =$  Debye frequency. But this proposition does not take into account any configurational degrees of freedom in  $c_V(T)$ . In glasses and liquids, the spatial degree of order is grasped by the categories of short-range order (SRO) and medium-range order (MRO) only. From the point of view of energetics, glasses of a given chemical composition differ from their isochemical crystalline counterpart by small enthalpy and entropy differences only. Frenkel [5] stated that, in view of these small differences, the structural disorder of glasses and even liquids cannot be dramatic. According to Planck, the kinetic energy  $E_{\text{kin}}$  of an individual atom vibrating around a fixed position is given (in each space direction) by  $E_{\text{kin}} = \hbar \cdot \omega$ , where  $\omega$  denotes the vibration frequency. The macroscopic effect, i.e., the thermal energy of a material, is determined by the density of vibrational states (DVS) in the material. At ambient temperature, glasses show nearly the same DVS as their crystalline counterparts. It is true, the similarity of DVS does not generally extend to the low-frequency part, but this becomes macroscopically relevant at very low temperatures only. The macroscopic quantity reflecting the DVS of oxide glasses is the heat capacity. In spite of lack of translational order in glasses, the vibrational states do



**Table 1.1** Comparison of structural and dynamic features of gases, crystals, liquids, and glasses;  $c_V$  = isochoric heat capacity,  $N$  = number of atoms in the formula,  $k$  = Boltzmann's constant;  $D_{25}$  = diffusion coefficient at 25 °C

State	Kind of order	Atomic interaction	Atomic* displacement	$\frac{c_V}{N \cdot k}$	$\log D_{25}$ , $D_{25}$ in $\text{cm}^2 \text{s}^{-1}$
Gas	Dynamic disorder	$\rightarrow 0$	Very large	3/2	-1.2 to 0.2
Crystal X	Static order; SRO, MRO, LRO	Large	$\rightarrow 0$	3	-15 to -6
Liquid L	Static and dynamic disorder; SRO, MRO	Large	Moderate	$f^{**}$	-6 to -3
Glass GL	static disorder; SRO, MRO	Large	Minor	3	-15 to -6

\*The displacement of individual atoms is characterized by the diffusion coefficient

\*\*After [4]  $f = 3 - (\omega_F/\omega_D)^3 < 3$  yielding a high-T limit of  $c_V = 2 N \cdot k$ ;  $\omega_F$  = Frenkel frequency (positional change of atoms);  $\omega_D$  = Debye frequency; for X and GL, the Dulong-Petit limit of  $c_V$  is given; the isobaric heat capacities  $c_P$  of liquids at  $T > T_{\text{liq}}$  reach values of  $f \approx 3.75 \pm 0.5$  as verified by a survey of > 100 pure substances: oxides, silicates, borates, phosphates, sulfates

not dissipate. The same applies to elastic waves (sound waves). As a consequence, glasses behave like elastic solids; they may be treated like low-density polymorphs of a given composition. The macroscopic quantities reflecting the response to elastic waves are the elastic moduli. As macroscopically isotropic materials, glasses possess two independent elastic moduli only.

## 1.2 The Language of Phenomenological Thermodynamics

As said before, phenomenological thermodynamics—in contrast to statistical thermodynamics—describes the world in terms of macroscopic quantities. It focuses on energy, in specific, on its amount, its transformation (e.g., heat to work), and its dissipation (e.g., through equilibration of thermal or chemical gradients). As a most basic concept of school physics, the energy  $E$  of a system is composed of two parts, i.e., a part related to its position termed potential energy  $E_{\text{pot}}$ , and a part related to its motion termed kinetic energy  $E_{\text{kin}}$ :  $E = E_{\text{pot}} + E_{\text{kin}}$ . The law of energy conservation (1st law of thermodynamics) is one of the most fundamental laws of nature. Energy cannot be defined in an absolute way, but as difference  $\Delta E$  to a given reference position  $L$  (e.g., sea level) and reference velocity  $v$  (e.g., the laboratory table) only. At reference position and velocity,  $\Delta E = 0$ . Thermodynamics extends this view proposing that such a system still contains “internal energy”  $U$ . Such an extension is suggested, e.g., by the experience that the system may feel warm or cold. If the system is isolated from the environment,  $U$  remains constant:  $dU = 0$ . Changes in the internal energy  $U$  are brought about by transferring heat  $Q$  or matter  $m$  to the system, or by performing work  $W$  on the system. If transfer of matter is excluded,

then

$$dU = \delta Q + \delta W. \quad (1.1)$$

The symbol  $\delta$  denotes that both work and heat describe energy in transformation between two different states, not energy attributed to a certain state. An isolated system does not “possess” work. The volume work reversibly performed is given by

$$\delta W = -P dV. \quad (1.2)$$

The amount of heat reversibly transferred to the system has been used by Clausius to define a function of state termed entropy,

$$S = Q_{\text{rev}}/T. \quad (1.3)$$

Thus, we obtain the well-known expression

$$dU = T dS - P dV. \quad (1.4)$$

Equation (1.4) shows that the internal energy is closely related to the volume as working coordinate, and hence, to the condition  $dV = 0$  in the absence of volume work. This is a convenient boundary condition for computer simulation. For condensed phases in the real world, however, conditions  $dV \approx 0$  can be maintained at extreme experimental effort only. On the other hand, an environment at constant pressure always imposes an energy contribution  $-P \cdot V$  on a material. Let us re-normalize the energy by subtracting this part from  $U$ . By this re-normalization, a quantity termed enthalpy  $H$  is obtained:  $H = U - (-P \cdot V)$ . The enthalpy change  $dH$  is given by

$$dH = T dS + V dP. \quad (1.5)$$

From a practical point of view,  $H$  is a much more suitable representation of the energy of a system in the real world than  $U$ . At constant pressure,

$$dH|_{P=\text{const}} = \delta Q_{\text{rev}}. \quad (1.6)$$

hence the letter  $H$  for “heat” chosen by Gibbs. As a large number of production processes run at constant environmental pressure, Eq. (1.6) is the basis of industrial heat balances. By the way, at  $P = 1$  bar and at  $V \approx 5\text{--}20 \cdot 10^{-6} \text{ m}^3/\text{g-atom}$  for condensed phases, the term  $P \cdot V$  amounts to  $0.5\text{--}2 \text{ J/g-atom}$  only while  $H$  is in the order of  $\text{kJ/g-atom}$ . Thus,  $H$  is almost identical to  $U$  under these conditions. For the sake of completeness: With such re-normalizations (termed Legendre transformations), further representations of energy are obtained, which are: the Helmholtz energy  $F = U - T \cdot S$  and the Gibbs energy  $G = U - T \cdot S + P \cdot V = H - T \cdot S$ .

What is the appropriate reference state for the enthalpy of a system equivalent to the reference states for  $E_{\text{pot}}$  and  $E_{\text{kin}}$ ? Let us first split up  $H$  into shares of internal potential and kinetic energy. The potential energy is determined by the positions of the atoms in the landscape of their superimposed interaction potentials; the enthalpies of the individual elements in their states at 298 K and 1 bar are chosen as the zero line (the earlier reference pressure 1 atm = 1.01325 bar has been replaced by 1 bar). Enthalpies of substances are expressed as differences to this line; the  $H$  values thus obtained are termed standard enthalpies and labeled  $H^\circ$ . By this definition, all elements at 298 K, 1 bar, have  $H^\circ = 0$ . Note that the actual state at 298 K, 1 bar has to be taken for the elements, e.g., Fe(fcc), Hg(liq), O<sub>2</sub>(g), etc. The kinetic energy term of  $H$  is related to the temperature,

$$\Delta H_T = \int_{298\text{K}}^T c_p \cdot dT, \quad (1.7)$$

where  $c_p$  is the isobaric heat capacity. The entire enthalpy function is given as the sum of potential and kinetic parts, reading

$$H(T) = H^\circ + \int_{298\text{K}}^T c_p \cdot dT. \quad (1.8)$$

An alternative reference line for  $H$  has been used in several books and tables, defining the enthalpies of the elements at 1 bar to zero at any temperature. These enthalpies are termed formation enthalpies  $H^f$ . The relation between  $H^\circ$  and  $H^f$  is given by Eq. (1.9) below (the user of thermodynamic tables is cautioned to carefully check the respective reference state used):

$$H^f(T) = H^\circ(T) - \sum \left( \nu_{\text{el}} \cdot \int_{298\text{K}}^T c_{p,\text{el}} \cdot dT \right). \quad (1.9)$$

The integral denotes the heat physically stored in element el at temperature  $T$  relative to 298 K;  $\nu_{\text{el}}$  is a stoichiometric coefficient; the sum is extended over all el contained in the substance. Let us again invoke the definition of Gibbs energy  $G$  and present it by Gibbs' main equation

$$G = H - T \cdot S. \quad (1.10)$$

With  $G$ ,  $H$ ,  $S$ , and  $T$ , we obtain a consistent description frame for all thermodynamic states of substances at  $P = 1$  bar.  $G$  is the key function for the treatment of heterogeneous phase equilibria and chemical equilibria. This is demonstrated in Fig. 1.1. Panel a shows the  $G$  curves for solid and liquid Al<sub>2</sub>O<sub>3</sub>; the condition

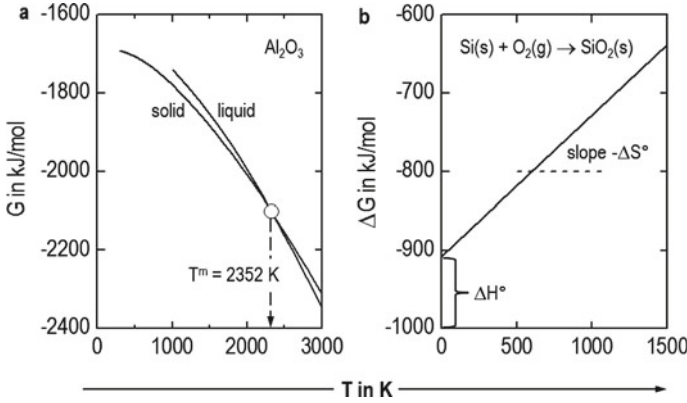


**Fig. 1.1** **a** Gibbs energy  $G$  of  $\text{Al}_2\text{O}_3$  in the solid and liquid state **b** Gibbs energy difference  $\Delta G$  of the formation reaction of  $\text{SiO}_2$  (cristobalite) from  $\text{Si}$  and  $\text{O}_2(\text{g})$

$G_{\text{liquid}} - G_{\text{solid}} = 0$  determines the melting point  $T^m$  of  $\text{Al}_2\text{O}_3$ . Panel **b** shows the formation reaction of  $\text{SiO}_2$  (cristobalite) from solid  $\text{Si}$  and  $\text{O}_2$ .

Let us come back to the definition of the entropy in Eq. (1.3). For natural (i.e., irreversible) processes, according to Clausius,  $S = Q_{\text{rev}}/T > Q/T$ . This imposes a severe constraint to such processes (2nd law of thermodynamics). The difference  $Q_{\text{rev}} - Q$  is termed “uncompensated heat”. It was de Donder [6] who linked the uncompensated heat to the concept of entropy generation. Based on this concept, his scholar Prigogine [7] explicitly pointed out that the entropy change in a natural process is composed of two contributions,

$$dS = dS^{\text{ext}} + dS^{\text{int}}, \quad (1.11)$$

where  $S^{\text{ext}}$  denotes the entropy exchange with the environment and  $S^{\text{int}}$  the internal entropy generation. The term  $dS^{\text{ext}}$  has no constraint for its sign; it may be positive or negative. It may be manipulated at will, and the entropy of a system may be lowered significantly at the expense of an entropy increase in the environment. This is the basis of all biological growth as well as all industrial processes (from crude raw materials to sophisticated products). By contrast, the term  $dS^{\text{int}}$  is  $\geq 0$  always;  $dS^{\text{int}} = 0$  corresponding to  $S^{\text{int}} = \text{maximum}$  denoting internal equilibrium—with one important exception. As a matter of fact, an isolated system with  $dU = 0$  may still undergo an internal entropy increase until internal equilibrium is reached. But this is not the only way for  $dS^{\text{int}}$  to reach zero. The so-called dissipation function  $T \cdot dS^{\text{int}}$  may be presented, in a most general way, by the product of an internal driving force  $f$  and a reaction path parameter  $\xi$  as

$$T \cdot dS^{\text{int}} = f \cdot d\xi, \quad (1.12)$$

Let us, for simplicity, imagine a spring stretched by a length  $d\xi$  from its equilibrium position. It is true if the internal driving force approaches zero, then  $dS^{\text{int}}$  also becomes zero, and internal equilibrium is reached. But  $dS^{\text{int}}$  may also approach zero at a finite value of  $f$  if  $\xi$  comes to an arrest at a non-equilibrium position, hence  $d\xi = 0$ , due to some internal constraint. Such a system would assume, in most general terms, a frozen-in non-equilibrium state. The reader will agree at once that this case is most relevant for the description of the glassy state.

### 1.3 The Glassy State

#### *Definition of the glassy state*

In literature, several definitions of the glassy state have been given. A historical review of such definitions by Richet is found in [8]. The author concludes: *It is thus tempting to define very simply a glass as a macroscopically homogeneous amorphous solid whose properties (physical, chemical, or structural) vary with its preparation conditions.* Below, some further definitions are quoted from memory. A glass is

- a material cooled down from a melt to a rigid condition without crystallization;
- a material characterized by the absence of long-range translational order at the atomic scale;
- a dense (non-fractal) isotropic and homogeneous non-crystalline solid without any internal phase boundaries.

The first definition does not reflect the fact that glasses may be formed via the pressure coordinate, or a composition coordinate (polymerization), or by precipitation from the gas phase. The second definition would also be valid for xerogels and aerogels with fractal structures and internal porosity. The third definition clarifies this issue. The definition reflecting best the situation discussed at the end of the previous section reads:

- A glass is an undercooled frozen-in liquid

This definition is rather abstract and may be misunderstood. The noun “liquid” led people to speculate on church windows to flow during the centuries rendering their lower parts thicker than their upper ones. The latter observation is true—it stems from handicraft practice to put the thicker part of a glass panel to the bottom—but the former interpretation is not true. Scientifically, this has been refuted, e.g., by Zanotto [9] who concluded *that medieval and contemporary window glasses cannot flow at room temperature in human time scales.* In fact, the frozen-in liquid state is rigid, brittle, highly elastic, and much less ductile than many crystalline solids. A glass is no liquid in the sense of fluid dynamics but a rigid body. In terms of thermodynamics, however, it still bears the energetic and structural signature of the liquid state. The sketch in Fig. 1.2, panel **a**, shows that the frozen-in state reached by cooling a melt is no unambiguous state. It depends on the cooling rate, i.e., it is

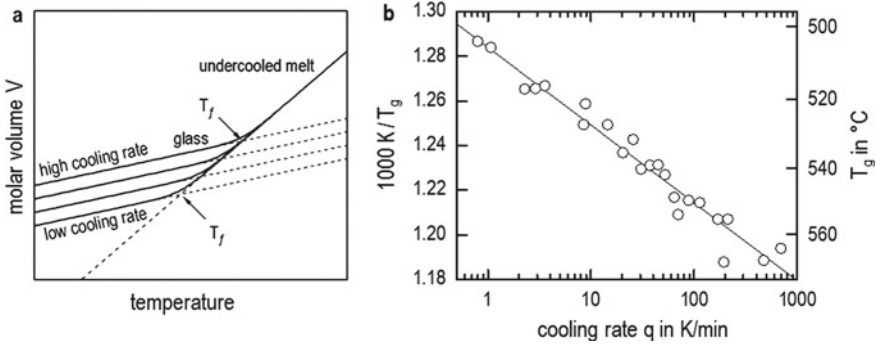


**Fig. 1.2** **a** Molar volume  $V$  of glasses cooled down from a melt at different cooling rates as a function of temperature;  $T_f$  = fictive temperature; principle sketch; **b** Glass transition temperature  $T_g$  of a simple silicate system [10] as a function of the cooling rate  $q$

path dependent. So, from a purist’s point of view, it should not be called a state at all. By experience, however, glasses in amounts of many 1000 t can be produced with densities  $\rho$  kept constant within a narrow range of  $\delta\rho < 10^{-3} \text{ g/cm}^3$ . So, from an operational point of view, the term “glassy state” is well justified. The temperature at which the system freezes in, i.e., drops out of internal equilibrium (with a finite residual driving force present), is termed fictive temperature  $T_f$ . The glassy state is a function of its composition, the temperature and pressure of the environment, and the fictive temperature  $T_f$ .  $T_f$  depends on the cooling rate  $q$  like

$$1/T_f \propto \ln q \quad (1.13)$$

with a negative slope. Within the scope of this article, no distinction is made between  $T_f$  and the glass transition temperature  $T_g$ ; both  $T_f$  and  $T_g$  are used as synonyms. Strictly speaking,  $T_g$  is linked to an experimental standard procedure performed on well-annealed samples at a well-defined heating rate; some authors prefer the definition that  $T_g$  denotes the temperature at which a viscosity of  $10^{13} \text{ dPas}$  is reached. So, the concept of  $T_f$  is broader than that of  $T_g$ . Panel **b** of Fig. 1.2 shows, in agreement with Eq. (1.13), that the  $T_g$  of a simple silicate glass varies with the cooling rate  $q$ . Under standard cooling conditions at  $q = 5 \text{ K/min}$ ,  $T_g = 520 \text{ }^{\circ}C$  for the given example.

### Heat capacity

A quote often attributed to Einstein reads: *If you can perform one type of experiment on a material only, then measure its heat capacity.* It could not be verified here whether or not this is a genuine Einstein quote. Yet, the statement is worthwhile being taken into consideration. Indeed, the function  $c_p(T)$  reveals a maximum of information on a material. We follow this recommendation and demonstrate the results for several one-component silicate systems. Figure 1.3 presents data for a sodium silicate

glass with composition of 27.6 Na<sub>2</sub>O, and 72.4 SiO<sub>2</sub>, which is the eutectic composition with the lowest liquidus,  $T_{\text{liq}} = 1073 \text{ K}$  (800 °C), of the whole Na<sub>2</sub>O–SiO<sub>2</sub> system. Within a narrow temperature range around the glass transition temperature  $T_g$ , the quantity  $c_P$  increases from the value  $c_{\text{GL}}$  of solid glass to the value  $c_L$  of undercooled liquid. The onset of the  $c_P$  jump satisfies the relation  $c_{\text{GL}}(T_g) \approx 3R$ , which may tentatively be described as a universal feature of glasses. The relationship between  $c_P$  and  $T_g$  tentatively described as universal has been observed to hold in many glass-forming systems [13]. This is shown in Fig. 1.4. The graph also shows that the heat capacities of liquids above  $T_g$  are often not constant. However, above  $T_{\text{liq}}$ , they lie within the range quoted below Table 1.1. Unfortunately, many thermodynamic tables list constant values for  $c_L$ . This is a blind spot that we must currently live with. The labels of Fig. 1.4 use the shorthand notation for oxide compounds. This avoids writing out the inconveniently lengthy stoichiometric formulas. The abbreviations used here and throughout the rest of these notes are as follows: S = SiO<sub>2</sub>, T = TiO<sub>2</sub>, P = P<sub>2</sub>O<sub>5</sub>, A = Al<sub>2</sub>O<sub>3</sub>, B = B<sub>2</sub>O<sub>3</sub>, F = Fe<sub>2</sub>O<sub>3</sub>, C = CaO, M = MgO, Z = ZnO, L = Li<sub>2</sub>O, N = Na<sub>2</sub>O, K = K<sub>2</sub>O. For instance, the compound CaMgSi<sub>2</sub>O<sub>6</sub> is abbreviated to CMS<sub>2</sub>, and NaAlSi<sub>3</sub>O<sub>8</sub> is shortened to ½·NAS<sub>6</sub>. Finally, Fig. 1.5 presents data for the system CaO·MgO·2SiO<sub>2</sub> in the crystalline (X), glassy (GL), and liquid (L) states for temperatures reaching from close to 0 K beyond the melting temperature  $T^m$ . In the following, let us denote the isobaric heat capacities of X, GL, and L by  $c_X$ ,  $c_{\text{GL}}$ , and  $c_L$ , respectively; the index GL and L denotes the states from solid glass to undercooled melt. Note how much work had to be invested to accomplish such a set of data. In panel **a**, the typical  $c_P$  jump at  $T_g$  is clearly seen. The overshoot peak of the glass at  $T_g$  has no effect on the integral values derived later. At melting temperature, both GL and X merge to an identical state, i.e., the liquid L. For  $T$  sufficiently below  $T_g$ ,  $c_X$  and  $c_{\text{GL}}$  are nearly identical. This is due to the fact that the short wavelengths  $\lambda$  of phononic vibrations probe the SRO of the structure only;  $\lambda = h \cdot u / (kT)$  (with an upper limit set by the interatomic distance);  $u$  = sound velocity;  $h$  = Planck's constant;  $k$  = Boltzmann's constant. Thus, we conclude that, on spatial average, the SRO of crystal and glass is nearly identical, too. Again, the  $c_P$  jump occurs at a temperature where  $c_X$  reaches the Dulong-Petit limit  $c_{\text{DP}} = 3N \cdot R$ ; for CaO·MgO·2SiO<sub>2</sub>, the atom number  $N$  per formula unit is 10;  $R$  = gas constant; hence,  $c_{\text{DP}} = 249.4 \text{ J}/(\text{mol} \cdot \text{K})$ . In panel **b**, the low-T range is shown. For  $T \rightarrow 0$ ,  $c_P \rightarrow 0$ . In agreement with Debye's law, the crystal approaches zero like  $c_X \propto T^3$ . The glass displays a heat capacity excess relative to the crystal. The maximum deviation from Debye's law occurs at a temperature corresponding to a phonon wavelength of  $\lambda \approx 2\text{--}3 \text{ nm}$ . This has been interpreted as a length scale of MRO. Indeed,  $c_P(T)$  reveals a lot of details on the glassy state.

### **Description of one-component systems**

The information provided by Fig. 1.5 is used for a comprehensive thermodynamic characterization of the entire system in its states X, GL, and L. The enthalpies and entropies can be given in terms of the integrals over  $c_P$  and  $c_P/T$ , respectively. Figure 1.6 summarizes the results.

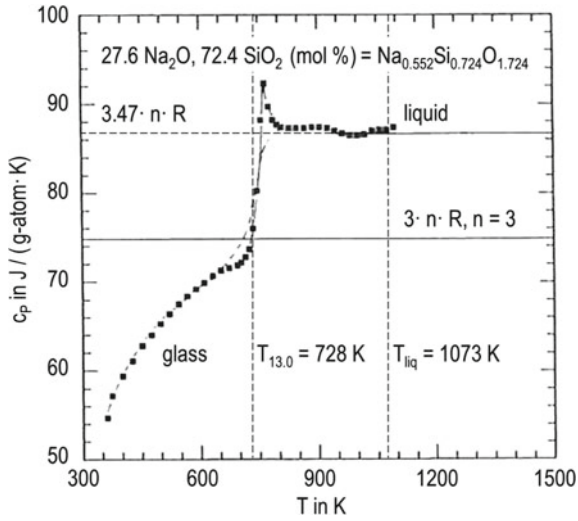


**Fig. 1.3** Heat capacity  $c_p$  of composition 27.6 Na<sub>2</sub>O, 72.4 SiO<sub>2</sub> (mol %) in the state's glass, metastable undercooled liquid, and stable liquid [11]; in the original paper, the stoichiometric coefficients are incorrect;  $T_{13.0}$  is the temperature at  $\eta = 10^{13}$  dPa·s as calculated after [12];  $T_{13.0}$  is practically identical with the calorimetric glass transition temperature

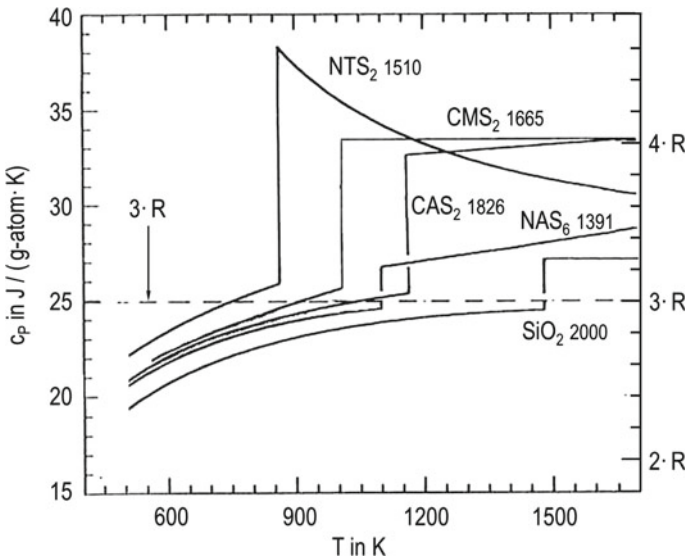


**Fig. 1.4** Heat capacities of different oxide compounds in their states GL and L [13]; oxide shorthand notation N = Na<sub>2</sub>O, C = CaO, M = MgO, T = TiO<sub>2</sub>, S = SiO<sub>2</sub>; small numbers beside the composition formulas denote the melting temperatures  $T^m$  in K



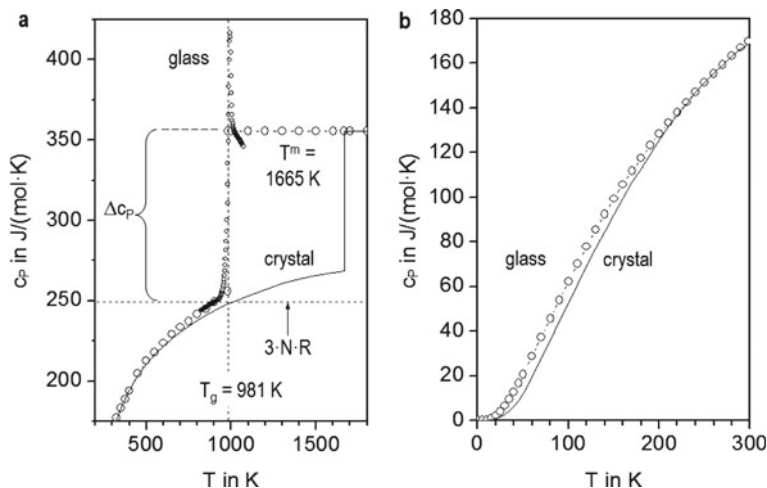


**Fig. 1.5** a Ambient to high-T range of heat capacity of  $\text{CaO}\cdot\text{MgO}\cdot 2\text{SiO}_2$  crystal, glass, and melt; **b** Low-T range of heat capacity of  $\text{CaO}\cdot\text{MgO}\cdot 2\text{SiO}_2$  crystal and glass; lines: crystal; symbols: glass; data from [14–18]

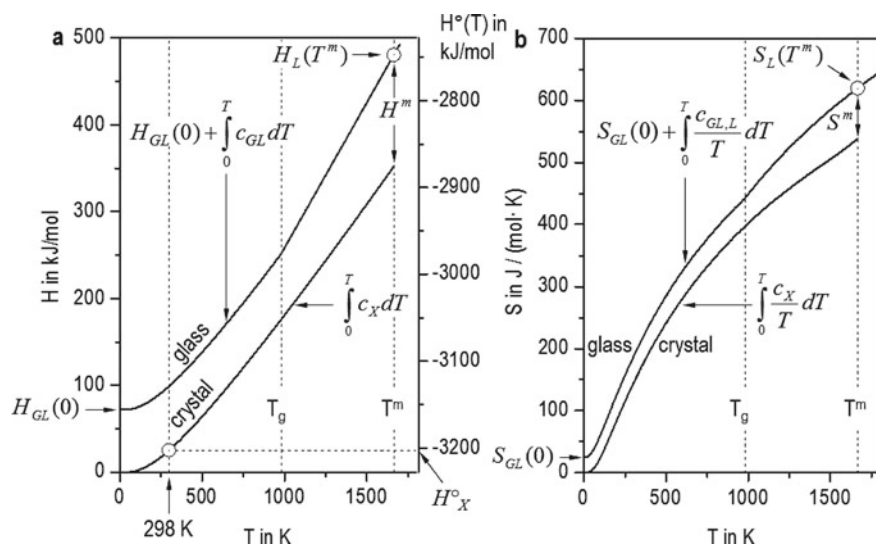


**Fig. 1.6** a Enthalpy of  $\text{CaO}\cdot\text{MgO}\cdot\text{SiO}_2$  crystal and glass; left ordinate: values of the integrals; right ordinate: normalization to the standard enthalpy  $H^\circ_X$  of  $\text{CaO}\cdot\text{MgO}\cdot\text{SiO}_2$  **b** Entropy of  $\text{CaO}\cdot\text{MgO}\cdot\text{SiO}_2$  crystal and glass

The branch in panel **a** representing the integral  $\int c_X \cdot dT$  starts at zero. The enthalpy value of the crystal at 298 K is normalized to the standard enthalpy of formation  $H^\circ_X$  of  $\text{CaO} \cdot \text{MgO} \cdot \text{SiO}_2$  (see Sect. 1.2). This yields the right-hand ordinate of panel **a**. The branch representing the integral  $\int c_{GL} \cdot dT$  also starts at zero. However, as identical states are reached for GL and X at melting temperature  $T^m$ , the unknown integration constant is determined by shifting the branch upwards in a way that it matches with the value  $H_L(T^m)$ . This yields, in turn, the zero Kelvin excess enthalpy of the glass,  $H_{GL}(0)$ .

In panel **b**, the very same procedure is performed on the integrals  $\int (c/T) \cdot dT$ . Yet, according to the 3rd law of thermodynamics, the entropy of the crystal—as a phase in internal equilibrium—becomes zero at zero Kelvin. Therefore, no additional right-hand ordinate is required for panel **b**. The finite value  $S_{GL}(0)$  of the zero Kelvin excess entropy of the glass is obtained, like before, by shifting the branch GL, L upwards in a way that it matches with the value  $S_L(T^m)$ .

In Fig. 1.7, the differences  $H_{GL} - H_X$ ,  $G_{GL} - G_X$ , and  $S_{GL} - S_X$  are plotted. For the range  $T < T_g$ , the temperature-dependent differences are approximated by constant values  $H^{\text{vit}}$  and  $S^{\text{vit}}$ , representing, on average, the residual enthalpy and entropy, respectively (Simon's approximation). This procedure significantly simplifies the thermodynamic treatment of glasses in the temperature range from ambient to high temperatures.

In conclusion, a one-component system is described as follows:

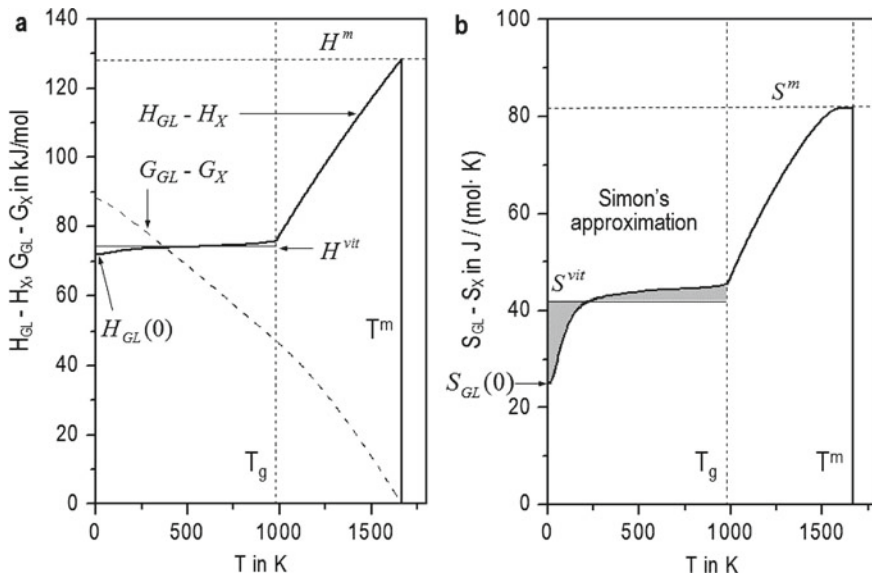


**Fig. 1.7** **a** Differences  $H_{GL} - H_X$  and  $G_{GL} - G_X$  of  $\text{CaO} \cdot \text{MgO} \cdot 2\text{SiO}_2$ ; **b** Difference  $S_{GL} - S_X$  of  $\text{CaO} \cdot \text{MgO} \cdot 2\text{SiO}_2$ ; the values  $H^{\text{vit}}$  (**a**) and  $S^{\text{vit}}$  (**b**) as obtained by Simon's approximation

in the crystalline state: by  $H^\circ_X$ ,  $S^\circ_X$ ,  $c_X(T)$ ;  $c_X(T)$  is typically represented by a polynomial.

the liquid state: by  $H^m$ ,  $T^m$ , and  $c_L$ ;  $S^m = H^m/T^m$ ; thermodynamic tables typically give constant values for  $c_L$  (which is an oversimplification);

the glassy state: by  $H^{\text{vit}}$  and  $S^{\text{vit}}$  (Simon's approximation) and  $c_{\text{GL}} = c_X$ ,  $X = \text{low-density polymorph at } 25^\circ\text{C}$ ; values of  $H^{\text{vit}}$  and  $S^{\text{vit}}$  are compiled in [20] for many systems; if data are not available,  $H^{\text{vit}} \approx 1/2 \cdot H^m$ ,  $S^{\text{vit}} \approx 1/3 \cdot S^m$ ,  $T_g/T^m \approx 2/3$ ,  $\Delta c_P/S^m \approx 3/2$  may serve as rules of thumb; integrating the difference  $c_L - c_X \approx \text{const.}$  Over the range from  $T_g$  to  $T^m$  and using the above rules yields  $H^{\text{vit}}/H^m \approx 1 - (\Delta c_P/S^m) \cdot (1 - T_g/T^m) = 1/2$  again but  $S^{\text{vit}}/S^m \approx 1 + (\Delta c_P/S^m) \cdot \ln(T_g/T^m) = 0.39$ ; in reality,  $S^{\text{vit}}/S^m \approx 1/3$  is obeyed quite well but  $T_g/T^m \approx 2/3$ ,  $\Delta c_P/S^m \approx 3/2$  are rough guidelines only. One should keep in mind that  $c_L - c_X \approx \text{const.}$  is an approximation, too.

The application of the above rules may be used to check data for consistency. The term  $T_g/T^m$  in the above formulas points to a relation between thermodynamics and rheology. In the following section, the ratio  $\Delta c_P/S^{\text{vit}} \approx 3 \cdot \Delta c_P/S^m$  will play a major role in this context. The above relations apply to constant pressure  $P = 1$  bar. Pressure dependence is not discussed here in detail. For pressures  $P$  negligible against the bulk modulus  $K$ , the effect of pressure is approximated by

$$G(T, P) \gg G(T, P^\circ) + V^\circ \cdot [1 + 3 \cdot \alpha \cdot (T - T^\circ)] \cdot (P - P^\circ); \quad (1.14)$$

$V^\circ = \text{molar volume at } T^\circ = 298 \text{ K}, P^\circ = 1 \text{ bar}$ ;  $\alpha = \text{linear thermal expansion coefficient as determined in a dilatometer.}$

## 1.4 Multicomponent Glasses

### *The concept of thermodynamic components*

As useful as the assessment of a comprehensive set of thermodynamic data for one-component glasses may be, a most essential question remains open: How can the principles from Sect. 1.3 be applied to multicomponent glasses of arbitrary composition? Before we enter the discussion, we have to do some homework: We have to clarify the term "component" used in thermodynamics.

- I. A component is a compositional entity of a system specified by a stoichiometric formula, such as  $\text{SiO}_2$ ,  $\text{Na}_2\text{O} \cdot \text{Al}_2\text{O}_3 \cdot 6\text{SiO}_2$ , etc. However, not any arbitrary grouping of such formulas qualifies as components. A component is a member of a distinguished set of compositional entities. The set must allow one to express the composition of a system in a *complete and irreducible* way. For example,

in an aqueous solution containing  $\text{Na}^+$  and  $\text{Cl}^-$  ions,  $\text{H}_2\text{O}$ ,  $\text{NaOH}$ , and  $\text{HCl}$  are such a set. By contrast, the set  $\text{H}_2\text{O}$ ,  $\text{NaOH}$ ,  $\text{HCl}$ , and  $\text{NaCl}$  do not qualify; it is redundant and reducible. If  $\text{NaCl}$  shall be chosen as a component, then the sets  $\text{H}_2\text{O}$ ,  $\text{HCl}$ ,  $\text{NaCl}$  or  $\text{H}_2\text{O}$ ,  $\text{NaOH}$ ,  $\text{NaCl}$ , or  $\text{HCl}$ ,  $\text{NaOH}$ ,  $\text{NaCl}$  would qualify. The set is irreducible if the number of components is three. As simple as this example may be, one should keep the principle in mind when moving to multicomponent systems.

- II. If the conditions of completeness and irreducibility are fulfilled, there is a lot of freedom. For example, in the system  $\text{CaMg}(\text{CO}_3)_2\text{-NaCl}$ , one may prefer to choose  $\text{Na}_4\text{Cl}_4$  instead of  $\text{NaCl}$ ; this would maintain the anion–cation balance along the compositional axis. As another example,  $\text{Na}_2\text{O}\cdot\text{Al}_2\text{O}_3\cdot 6\text{SiO}_2$  or  $\text{NaAlSi}_3\text{O}_8$  may be chosen alternatively. The number of possible choices is unlimited.
- III. Among all possible sets of components, there is always one set that stands out. This is the set representing, for a given composition, the equilibrium at 298 K. The members of this set are termed constitutional components. For example, the constitutional components of a glass with 70  $\text{SiO}_2$ , and 30  $\text{Na}_2\text{O}$  (by mol) are  $\text{Na}_2\text{O}\cdot 2\text{SiO}_2$  and  $\text{SiO}_2$ . In order to distinguish oxide components from constitutional ones, the following shorthand notation is introduced for the latter ones:  $\text{SiO}_2 = \text{S}$ ,  $\text{Al}_2\text{O}_3 = \text{A}$ ,  $\text{MgO} = \text{M}$ ,  $\text{CaO} = \text{C}$ ,  $\text{Na}_2\text{O} = \text{N}$ ,  $\text{K}_2\text{O} = \text{K}$ , etc.

### *Description of multicomponent glasses and liquids*

The Gibbs energy of a one-component glass at 298 K is given by

$$G_{\text{GL}} = H_{\text{X}}^{\circ} + H^{\text{vit}} - 298 \text{ K} \cdot (S_{\text{X}}^{\circ} + S^{\text{vit}}), \quad (1.15)$$

the Gibbs energy of a system containing many oxide components  $j$  is given by

$$G = \sum n_j \cdot G_j^{\bullet} + G^{\text{MIX}} \quad (1.16)$$

with an unknown contribution  $G^{\text{MIX}}$ ; the dot marks the value of the pure oxide  $j$ , and  $G^{\text{MIX}}$  is given as

$$G^{\text{MIX}} = H^{\text{MIX}} - T \cdot S^{\text{MIX}} = RT \cdot \sum n_j \cdot \ln a_j. \quad (17a)$$

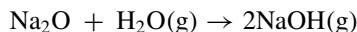
The chemical potentials of individual oxides  $j$  satisfy the relation

$$\mu_j = G_j^{\bullet} + RT \cdot \ln a_j. \quad (1.17b)$$

In Eq. 1.17a–b,  $a_j = x_j \cdot f_j$  denote the activities of oxides  $j$  in the mixture;  $f_j$  is the activity coefficients and  $x_j$  are the molar fractions. The  $a_j$  refers to the pure oxides with  $x_j = 1$  and  $f_j = 1$  taken in their states present at temperature  $T$ . The symbol

$n_j$  in Eq. 17a denotes the molar amounts of oxides  $j$  in the glass composition. Since chemical compositions of industrial glasses are typically communicated in terms of wt. % or  $m_j$  in units g/100 g, it is advisable to normalize  $n_j$  to a total mass of 100 g. Then,  $n_j$  is calculated as  $n_j = m_j / M_j$ .  $M_j$  in g/mol is the molar mass of oxide  $j$ ;  $n_j$  has the dimension mol/100 g. In an ideal mixture,  $H^{\text{MIX}} = 0$ ,  $a_j = x_j$ , hence,  $f_j = 1$ , and  $S^{\text{MIX}} = -R \cdot \sum \ln x_j$ . Then  $G^{\text{MIX}}$  becomes a small correction term to  $G$  only. Unfortunately, oxide systems are extremely non-ideal mixtures of their oxide components with  $a_j$  deviating from  $x_j$  by several orders of magnitude, resulting in high  $G^{\text{MIX}}$  (see Fig. 1.8). A comprehensive thermodynamic treatment of the binary mixtures shown in Fig. 1.8 in terms of empirical parameters derived from experimental data is given in Appendix 1.

An earlier observation by Turner [21] (see Fig. 1.9) points us into the right direction on how to treat non-ideal oxide mixtures with their strong tendency toward compound formation in an alternative way. Turner measured the evaporation losses from binary  $\text{Na}_2\text{O}-\text{SiO}_2$  melts at 1400 °C. The losses are chiefly brought about by the reaction.



with the equilibrium pressure  $P_{\text{NaOH}}$  being proportional to  $\sqrt{(P_{\text{H}_2\text{O}} \cdot a_{\text{Na}_2\text{O}})}$ . Figure 1.9 shows that the melt at 1400 °C maintains a memory of the constitutional relations in the system  $\text{Na}_2\text{O}-\text{SiO}_2$ . Obviously, an approx. constant value of  $a_{\text{Na}_2\text{O}}$  is valid in the range S-NS<sub>2</sub>, and another (higher) one in the range NS<sub>2</sub>-NS. The presence of

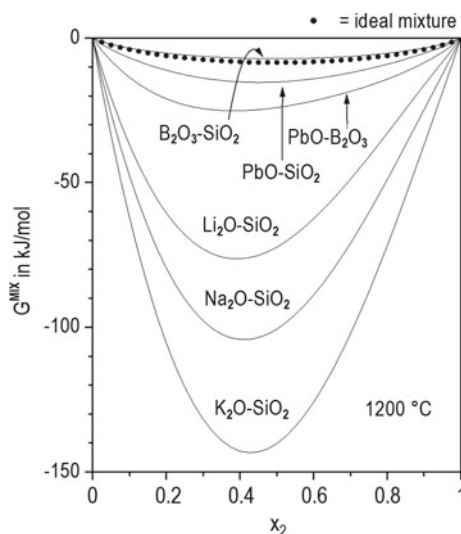


**Fig. 1.8** Gibbs energy of mixing  $G^{\text{MIX}}$  in binary oxide melts at 1200 °C as a function of the molar fraction of the second oxide component of the mixture; for further details see Appendix 1

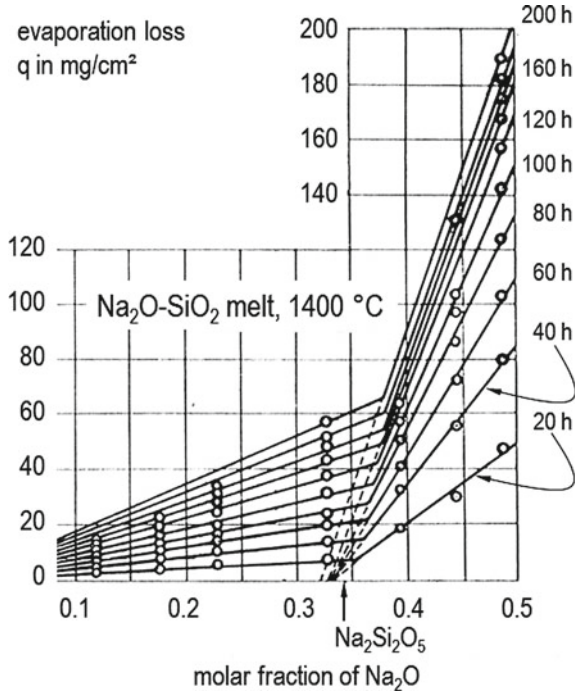


**Fig. 1.9** Evaporation losses from  $\text{Na}_2\text{O}-\text{SiO}_2$  melts at  $1400^\circ\text{C}$  [21]

quasi-constitutional entities in melts and glasses has been verified by many structural investigations (NMR, X-ray, and neutron scattering, see, e.g., [22]). This shows the close relation between thermodynamic and structural studies on glass melts and glasses.

Navrotsky et al. [23] measured the heats of mixing  $H^{\text{MIX}}$  in binary and ternary silicate glasses (Table 1.2). The compositions are expressed, not in terms of oxides  $j$ , but of constitutional compounds  $k$ . If compared to the weighted sums of the enthalpies of the pure compounds, the  $H^{\text{MIX}}$  is negligibly small. In conclusion, these systems are close-to-ideal mixtures, not of the oxides, but of the components  $k$ . When considering merely statistical mixing among the entities  $k$ , and in view of the number  $N_k$  of atoms contained in the individual  $k$ , then the entropy of mixing,

$$S^{\text{MIX}} = -R \cdot \sum \frac{n_k}{N_k} \cdot \ln x_j, \quad (1.18)$$

becomes negligibly small, too. This leads to the simple relation

$$G = \sum n_k \cdot G_k^\bullet, \quad (1.19)$$

**Table 1.2** Equimolar mixtures of binary and ternary glasses with components  $k = \text{CaAl}_2\text{Si}_2\text{O}_8$ ,  $\text{CaMgSi}_2\text{O}_6$ ,  $\text{NaAlSi}_3\text{O}_8$ , and  $4\text{SiO}_2 = \text{Si}_4\text{O}_8$ ; the sums of molar amounts  $n_k$  are  $n = \sum n_k = 1 \text{ mol}$ ;  $H^{\text{MIX}}$  was measured calorimetrically at  $T = 712 \text{ }^\circ\text{C}$  (this is below  $T_g$  in all cases) by dissolving the glasses in a  $2\text{PbO}\cdot\text{B}_2\text{O}_3$  melt [23];  $H_k$  and  $S_k$  of the pure components  $k$  in the undercooled liquid state are calculated from tabulated data [24];  $S^{\text{MIX}}$  is calculated from Eq. (1.18)

Molar composition	$\sum n_k \cdot H_k$	$H^{\text{MIX}-k}$	$\sum n_k \cdot S_k$	$S^{\text{MIX}-k}$
	kJ/mol		J/(mol·K)	
$\frac{1}{2}\cdot\text{CaAl}_2\text{Si}_2\text{O}_8 - \frac{1}{2}\cdot\text{CaMgSi}_2\text{O}_6$	-3434.3	-6.8	511.4	1.0
$\frac{1}{2}\cdot\text{CaAl}_2\text{Si}_2\text{O}_8 - \frac{1}{2}\cdot\text{NaAlSi}_3\text{O}_8$	-3774.4	-8.6	587.1	0.9
$\frac{1}{2}\cdot\text{NaAlSi}_3\text{O}_8 - \frac{1}{2}\cdot\text{CaMgSi}_2\text{O}_6$	-3318.0	+ 5.9	509.0	1.0
$\frac{1}{2}\cdot\text{Si}_4\text{O}_8 - \frac{1}{2}\cdot\text{CaAl}_2\text{Si}_2\text{O}_8$	-3683.4	-2.2	517.6	0.9
$\frac{1}{2}\cdot\text{Si}_4\text{O}_8 - \frac{1}{2}\cdot\text{NaAlSi}_3\text{O}_8$	-3567.2	$\pm 0.0$	515.2	0.9
$\frac{1}{3}\cdot\text{CaAl}_2\text{Si}_2\text{O}_8 - \frac{1}{3}\cdot\text{NaAlSi}_3\text{O}_8 - \frac{1}{3}\cdot\text{CaMgSi}_2\text{O}_6$	-3508.9	-5.2	535.8	2.3
$\frac{1}{3}\cdot\text{Si}_4\text{O}_8 - \frac{1}{3}\cdot\text{CaAl}_2\text{Si}_2\text{O}_8 - \frac{1}{3}\cdot\text{NaAlSi}_3\text{O}_8$	-3675.0	-6.2	539.9	2.2

hence,  $G$  may be expressed as a simple bilinear sum of molar amounts  $n_k$  and Gibbs energies  $G_k^\bullet$  of the pure constitutional components  $k$ . The following set of equations extends this result to the thermodynamic properties of glasses and glass melts from ambient to high temperatures.

$$H_{\text{GL}}^\circ = \sum_k n_k \cdot (H_k^\circ + H_k^{\text{vit}}), \quad (20a)$$

$$S_{\text{GL}}^\circ = \sum_k n_k \cdot (S_k^\circ + S_k^{\text{vit}}), \quad (20b)$$

$$S^{\text{vit}} = \sum_k n_k \cdot S_k^{\text{vit}}, \quad (20c)$$

$$c_{\text{GL}}(T) = \sum_k n_k \cdot c_{X,k}(T), \quad (20d)$$

$$H_{\text{L},1673} = \sum_k n_k \cdot H_{\text{L},k,1673}^\circ, \quad (20e)$$

$$S_{\text{L},1673} = \sum_k n_k \cdot S_{\text{L},k,1673}^\circ, \quad (20f)$$

$$G_{\text{GL}}^f = \sum_k n_k \cdot G_{\text{GL},k}^f, \quad (20g)$$

$$c_{\text{L}} = \sum_k n_k \cdot c_{\text{L},k}, \quad (20h)$$

$$H_{\text{L}}(T) = H_{\text{L},1673} + c_{\text{L}} \cdot (T - 1673), \quad (20i)$$

$$S_L(T) = S_{L,1673} + c_L \cdot \ln(T/1673), \quad (20j)$$

$$\Delta H_L(T) = H_L(T) - H_{GL}^o, \quad (20k)$$

$$c_{DP} = 3 \cdot R \cdot \sum_{el} n_{el}, \quad (20l)$$

$$\Delta c_P = c_L - c_{DP}, \quad (20m)$$

$$a_{AG} = \Delta c_P / S^{\text{vit}}, \quad (20n)$$

$$\rho = \frac{1}{\sum_k n_k \cdot M_k / \rho_k}, \quad (20o)$$

$$E = \sum_k m_k \cdot E_k \quad (20p)$$

Since the  $n_k$  have units of mol/100 g and the  $m_k$  are expressed in g/100 g, all results are stated per 100 g of glass or melt. Multiplying by 0.01 yields  $c$  in J/(g·K) and  $E$  in GPa; multiplying by 100 yields  $\rho$  in g/cm<sup>3</sup>. Equations (20a–p) give expressions for the standard enthalpies, entropies, and Gibbs energies of glasses (25 °C, 1 bar), the enthalpies, entropies, and heat content of melts at arbitrary temperatures down to the undercooled region. The glass transition temperature  $T_g$  is reached if the heat capacity of the glass  $c_{GL}(T)$  reaches the Dulong-Petit limit  $c_{DP}$ ; the heat capacity jump to the value  $c_L$  of the melt is  $\Delta c_P = c_L - c_{DP}$ ;  $a_{AG} = \Delta c_P / S^{\text{vit}}$  is the Adam-Gibbs parameter (see the discussion of viscosity models at the end of this section and in Appendix 3). If  $a_{AG}$  is deduced from viscosity measurements independently of Eq. (20n) (viscosity data are always available for industrial glasses), then we can determine the term  $S^{\text{vit}}$  from the jump in the heat capacity at  $T_g$  without needing calorimetric data at low temperatures. Table 1.3 lists data for a large number of substances that occur as components of industrial glasses. For substances that cannot form one-component glasses, hypothetical values of  $H^{\text{vit}}$  and  $S^{\text{vit}}$  are given; after all, in multicomponent glasses, these substances are present in a partial molar glassy state. To precisely calculate the heat capacities themselves, the values  $\langle c_{L,j} \rangle$  listed in Table 1.4 are recommended. The data  $c_{L,1673}$  in Table 1.3 are sufficiently precise to establish the heat balance of an industrial glass melt. Table 1.5 shows data for the elements involved. The data summarized in Table 1.6 allow the molar volumes, the densities, and Young's moduli to be calculated.

### ***Constitutional approach to multicomponent systems***

What is left to be done is the determination of the identity of the  $k$ , and their molar amounts  $n_k$ , for a given glass composition. By virtue of Gibbs' phase rule, the number



**Table 1.3** Thermodynamic data compounds, constituting potential components of industrial glasses;  $H$  = enthalpy,  $S$  = entropy,  $G$  = Gibbs energy,  $c$  = heat capacity at  $P = \text{const.}$ ; superscripts:  $^\circ$  = standard state (298.15 K, 1 bar),  $^{\text{vit}}$  = vitrification,  $^f$  = formation from the elements in the standard state; subscripts:  $X$  = crystal,  $_{\text{GL}}$  = glass,  $_{\text{L}}$  = liquid,  $_{1673}$  = 1673.15 K; data obtained by evaluating [18, 24–27]

compound	$-H^\circ_X$	$H^{\text{vit}}$	$-H_{\text{L},1673}$	$-G^f_{\text{GL}}$	$S^\circ_X$	$S^{\text{vit}}$	$S_{\text{L},1673}$	$c_{\text{L},1673}$
	kJ/mol				J/(mol·K)			
P <sub>2</sub> O <sub>5</sub> ·3CaO	4117.1	135.1	3417.1	3822.5	236.0	51.5	898.7	324.3
P <sub>2</sub> O <sub>5</sub>	1492.0	18.2	1138.5	1333.4	114.4	9.5	586.6	181.6
Fe <sub>2</sub> O <sub>3</sub>	823.4	45.2	550.2	701.4	87.4	17.2	370.3	142.3
FeO·Fe <sub>2</sub> O <sub>3</sub>	1108.8	82.8	677.8	933.7	151.0	31.4	579.9	213.4
FeO·SiO <sub>2</sub>	1196.2	36.7	962.3	1085.8	92.8	13.8	342.7	139.7
2FeO·SiO <sub>2</sub>	1471.1	55.2	1118.8	1321.1	145.2	20.5	512.1	240.6
MnO·SiO <sub>2</sub>	1320.9	40.2	1085.3	1208.9	102.5	15.1	345.2	151.5
2ZnO·SiO <sub>2</sub>	1643.1	82.4	1261.1	1456.5	131.4	31.4	494.5	174.5
ZrO <sub>2</sub> ·SiO <sub>2</sub>	2034.7	86.6	1686.2	1843.5	84.5	32.6	381.2	149.4
CaO·TiO <sub>2</sub>	1660.6	67.4	1365.7	1515.5	93.7	25.5	360.2	124.7
TiO <sub>2</sub>	903.7	40.2	741.0	854.3	185.4	19.7	335.6	87.9
BaO·Al <sub>2</sub> O <sub>3</sub> ·2SiO <sub>2</sub>	4222.1	130.5	3454.3	3899.4	236.8	95.4	1198.3	473.2
BaO·2SiO <sub>2</sub>	2553.1	81.6	2171.1	2342.7	154.0	26.8	533.5	241.4
BaO·SiO <sub>2</sub>	1618.0	56.5	1349.8	1489.0	104.6	41.0	361.1	146.4
Li <sub>2</sub> O·Al <sub>2</sub> O <sub>3</sub> ·4SiO <sub>2</sub>	6036.7	184.1	5235.4	5524.7	308.8	12.1	1173.2	498.7
Li <sub>2</sub> O·SiO <sub>2</sub>	1648.5	16.7	1416.7	1542.8	79.9	6.3	339.7	167.4
K <sub>2</sub> O·Al <sub>2</sub> O <sub>3</sub> ·6SiO <sub>2</sub>	7914.0	106.3	6924.9	7369.1	439.3	29.3	1559.4	765.7
K <sub>2</sub> O·Al <sub>2</sub> O <sub>3</sub> ·2SiO <sub>2</sub>	4217.1	80.4	3903.7	3911.4	266.1	22.1	666.5	517.6
K <sub>2</sub> O·4SiO <sub>2</sub>	4315.8	26.4	3697.8	4038.8	265.7	21.3	983.7	410.0
K <sub>2</sub> O·2SiO <sub>2</sub>	2508.7	12.6	2153.1	2357.4	190.6	23.9	595.4	275.3
Na <sub>2</sub> O·Al <sub>2</sub> O <sub>3</sub> ·6SiO <sub>2</sub>	7841.2	125.0	6870.1	7279.6	420.1	28.4	1512.5	648.1
Na <sub>2</sub> O·Al <sub>2</sub> O <sub>3</sub> ·2SiO <sub>2</sub>	4163.5	92.0	3614.1	3850.6	248.5	27.9	856.9	423.8
B <sub>2</sub> O <sub>3</sub>	1273.5	18.2	1088.7	1179.5	54.0	11.3	271.1	129.7
Na <sub>2</sub> O·B <sub>2</sub> O <sub>3</sub> ·4SiO <sub>2</sub>	5710.9	42.7	4988.0	5331.6	270.0	21.1	1090.2	637.6
Na <sub>2</sub> O·B <sub>2</sub> O <sub>3</sub> ·2SiO <sub>2</sub>	3834.5	43.2	3286.9	3569.7	208.6	20.3	814.5	465.3
Na <sub>2</sub> O·4B <sub>2</sub> O <sub>3</sub>	5900.7	59.9	4986.7	5498.3	297.1	37.0	1275.5	704.2
Na <sub>2</sub> O·2B <sub>2</sub> O <sub>3</sub>	3284.9	48.8	2735.9	3046.5	189.5	18.5	780.3	444.8
Na <sub>2</sub> O·B <sub>2</sub> O <sub>3</sub>	1958.1	43.6	1585.7	1807.8	147.1	19.5	538.7	292.9
CaO·2B <sub>2</sub> O <sub>3</sub>	3340.9	56.7	2795.8	3099.8	134.7	29.9	698.9	444.8
CaO·B <sub>2</sub> O <sub>3</sub>	2027.1	37.1	1712.6	1888.5	105.9	17.2	429.5	258.2
2MgO·2Al <sub>2</sub> O <sub>3</sub> ·5SiO <sub>2</sub>	9113.2	135.8	7994.8	8504.1	407.1	41.4	1606.2	1031.8

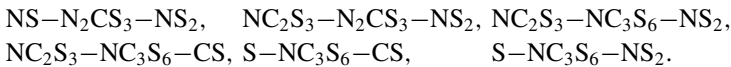
(continued)

**Table 1.3** (continued)

compound	$-H^\circ_X$	$H^{\text{vit}}$	$-H_{L,1673}$	$-G^f_{GL}$	$S^\circ_X$	$S^{\text{vit}}$	$S_{L, 1673}$	$c_{L, 1673}$
MgO·SiO <sub>2</sub>	1548.5	46.6	1318.0	1419.1	67.8	13.6	296.2	146.4
2MgO·SiO <sub>2</sub>	2176.9	61.4	1876.1	1999.8	95.4	11.0	402.9	205.0
CaO·MgO·2SiO <sub>2</sub>	3202.4	92.3	2733.4	2943.6	143.1	25.7	621.7	355.6
2CaO·MgO·2SiO <sub>2</sub>	3876.9	106.7	3319.2	3582.3	209.2	32.0	775.3	426.8
CaO·Al <sub>2</sub> O <sub>3</sub> ·2SiO <sub>2</sub>	4223.7	103.0	3628.8	3907.2	202.5	37.7	791.2	380.7
2CaO·Al <sub>2</sub> O <sub>3</sub> ·SiO <sub>2</sub>	3989.4	129.9	3374.0	3672.0	198.3	49.4	787.8	299.2
CaO·SiO <sub>2</sub>	1635.1	49.8	1382.0	1505.9	83.1	18.8	329.7	146.4
2CaO·SiO <sub>2</sub>	2328.4	101.3	1868.2	2121.8	120.5	38.5	509.2	174.5
Na <sub>2</sub> O·2SiO <sub>2</sub>	2473.6	29.3	2102.5	2302.6	164.4	13.2	588.7	261.1
Na <sub>2</sub> O·SiO <sub>2</sub>	1563.1	37.7	1288.3	1449.6	113.8	9.8	415.1	179.1
3Na <sub>2</sub> O·8SiO <sub>2</sub>	9173.0	103.9	7860.9	8589.5	597.0	47.0	1242.2	955.6
Na <sub>2</sub> O·CaO·5SiO <sub>2</sub>	5934.0	59.8	5130.9	5545.1	349.0	16.0	2100.8	579.9
Na <sub>2</sub> O·3CaO·6SiO <sub>2</sub>	8363.8	141.9	7068.2	7797.3	461.9	95.0	1745.5	785.7
Na <sub>2</sub> O·2CaO·3SiO <sub>2</sub>	4883.6	92.5	4240.9	4540.7	277.8	47.4	990.4	465.6
2Na <sub>2</sub> O·CaO·3SiO <sub>2</sub>	4763.0	92.5	4029.6	4408.7	309.6	38.4	1107.9	494.7
SiO <sub>2</sub> CR	908.3	6.9	809.6	848.8	43.5	4.0	157.3	86.2

of oxides and constitutional components is equal. For convenience, let us write the composition in vector form as line or column vectors  $\mathbf{n}_j^T$ ,  $\mathbf{n}_k^T$  or  $\mathbf{n}_j$ ,  $\mathbf{n}_k$ , respectively, and the thermodynamic functions  $Z = H, S, G$  in the analogous way as  $\mathbf{Z}_j^T$ ,  $\mathbf{Z}_k^T$  or  $\mathbf{Z}_j$ ,  $\mathbf{Z}_k$ . Then the sums of the form  $Z = \sum n_k \cdot Z_k$ , etc. may be written as scalar products  $\mathbf{n}_k^T \cdot \mathbf{Z}_k$ . Let ( $\mathbf{M}$ ) be the coefficient matrix linking the stoichiometries of the  $j$  and  $k$ .

In the remaining part of the present chapter, this shall be exercised with a glass (and its melt) of composition 75 SiO<sub>2</sub>, 10 CaO, and 15 Na<sub>2</sub>O (by mol). The example is simple, yet at the same time, sufficiently complex so that all steps involved in the procedure for multicomponent glasses can be addressed. In order to identify the identity of the set of components  $k$ , we need to inspect existing phase diagrams. For the given example, we need to evaluate the phase diagram in Fig. 1.10. It represents six different constitutional ranges, namely



The positions of compounds  $k$  are marked by open circles. The compounds with shaded circles are metastable at 25 °C; therefore, they are ignored in the constitution. 1:2:3 denotes NC<sub>2</sub>S<sub>3</sub>, etc. The constitutional ranges are triangular areas encompassed by the lines connecting the  $k$ . The position of glass 75 SiO<sub>2</sub>, 10 CaO, 15 Na<sub>2</sub>O (by

**Table 1.4** Thermodynamic data of selected oxides; same symbols as in Table 1.8;  $M$  = molar mass;  $G_{\text{ref}}$  refers to X if  $T^m > 1673$  K, and to L otherwise;  $(c_{L,j})$  = average partial molar heat capacities in oxide melts [28];  $M$  in g/mol;  $T$  in K;  $G$ ,  $H$  in kJ/mol;  $S$ ,  $c$  in J/(mol·K)

Oxide	$M$	$T^m$	$-G_{\text{ref},1673}$		$-H^\circ$	$-H_{L,1673}$	$S^\circ$	$S_{L,1673,L,1673}$	$c_{L,1673}$	$(c_{L,j})$
			X	L						
SiO <sub>2</sub> qtz	60.084	-	-	-	910.9	-	41.5	-	-	-82.6
SiO <sub>2</sub> CR	60.084	2000	1073.8	1072.8	908.3	809.6	43.5	157.3	86.2	82.6
TiO <sub>2</sub>	79.898	2143	1131.6	1132.7	944.0	853.9	50.6	166.7	100.4	109.2
ZrO <sub>2</sub>	123.218	2950	1289.3	1256.0	1100.8	924.3	50.4	198.3	87.9	-
Al <sub>2</sub> O <sub>3</sub>	101.961	2325	1924.6	1899.2	1675.7	1433.8	50.9	278.2	184.1	170.3
B <sub>2</sub> O <sub>3</sub>	69.619	723	-	1542.3	1273.5	1088.7	54.0	271.1	129.7	-
Fe <sub>2</sub> O <sub>3</sub>	159.691	1735	1182.3	1169.8	823.4	550.2	87.4	370.3	142.3	241.0
FeO	71.846	1650	-	456.8	272.0	167.3	60.8	173.0	68.2	78.8
P <sub>2</sub> O <sub>5</sub>	141.945	843	-	1945.0	1505.0	1250.9	114.4	418.8	185.0	-
MgO	40.311	3105	716.7	682.0	601.6	460.2	26.9	132.5	60.7	94.2
CaO	56.079	3100	773.4	758.4	634.9	539.2	38.1	131.0	83.7	89.8
BaO	153.339	2286	748.6	733.1	548.1	413.4	72.1	191.0	66.9	-
MnO	70.937	2058	560.5	550.3	384.9	256.3	59.8	175.7	60.7	-
ZnO	81.369	2248	496.5	482.0	350.5	222.2	43.6	155.3	60.7	-
Li <sub>2</sub> O	29.877	1726	771.4	770.0	597.9	439.9	37.7	197.3	97.1	-
Na <sub>2</sub> O	61.979	1243	-	681.5	415.1	226.1	75.1	272.2	104.6	97.6
K <sub>2</sub> O	94.203	1013	-	701.0	363.2	194.4	94.1	302.8	104.6	98.5

**Table 1.5** Thermodynamic data of selected elements [24]; same symbols as in Table 1.3;  $H^\circ$  of the elements is zero

Element	$M$	$S^\circ_{el}$
	g/mol	J/(mol·K)
O <sub>2</sub>	31.999	205.1
Si	28.086	18.8
Ti	47.900	30.7
Zr	91.220	39.0
Al	26.982	28.3
B	10.811	5.9
Fe	55.847	27.3
P	30.974	41.1
Mg	24.312	32.7
Ca	40.080	41.6
Ba	137.340	62.4
Mn	54.938	32.0
Zn	65.370	41.6
Li	6.939	29.1
Na	22.990	51.3
K	39.102	64.7

**Table 1.6** Macroscopic properties of compounds  $k$  in the glassy state at 25 °C;  $M$  = molar mass,  $\rho$  = density,  $E$  = Young's modulus; data for  $\rho_k$  and  $E_k$  are taken from [29]

compound $k$	$M_k$	$\rho_k$	$E_k$
	g/mol	g/cm <sup>3</sup>	GPa
Na <sub>2</sub> O·Al <sub>2</sub> O <sub>3</sub> ·6SiO <sub>2</sub>	524.444	2.369	70
Na <sub>2</sub> O·Al <sub>2</sub> O <sub>3</sub> ·2SiO <sub>2</sub>	284.108	2.490	74
2MgO·2Al <sub>2</sub> O <sub>3</sub> ·5SiO <sub>2</sub>	584.964	2.624	105
MgO·SiO <sub>2</sub>	100.395	2.761	107
2MgO·SiO <sub>2</sub>	140.706	2.90	113
CaO·MgO·2SiO <sub>2</sub>	216.558	2.863	102
2CaO·MgO·2SiO <sub>2</sub>	272.637	2.90	105
CaO·Al <sub>2</sub> O <sub>3</sub> ·2SiO <sub>2</sub>	278.208	2.693	94
2CaO·Al <sub>2</sub> O <sub>3</sub> ·SiO <sub>2</sub>	274.203	2.860	97
CaO·SiO <sub>2</sub>	116.163	2.880	93
Na <sub>2</sub> O·2SiO <sub>2</sub>	182.147	2.490	59
Na <sub>2</sub> O·3CaO·6SiO <sub>2</sub>	590.720	2.703	83
SiO <sub>2</sub>	60.084	2.204	72

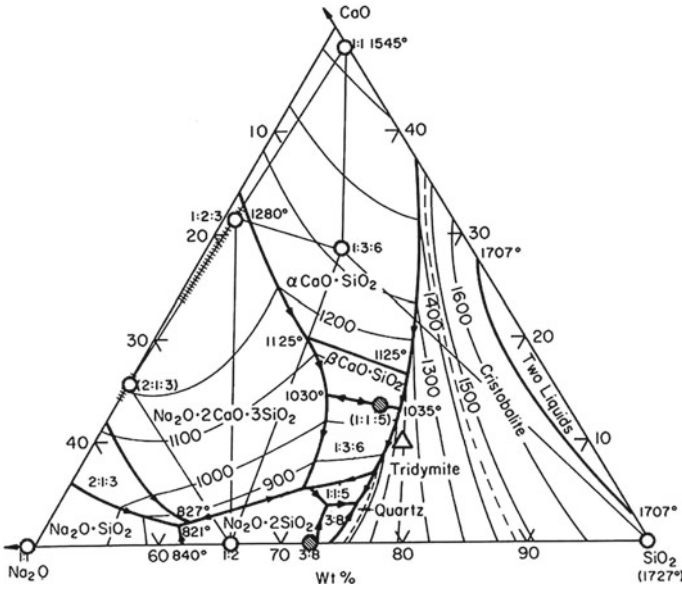


**Fig. 1.10** Phase diagram of the system  $\text{SiO}_2\text{--CaO--Na}_2\text{O}$ ; after [30]; open symbols: equilibrium phases at 25 °C, 1 bar; hatched symbols: phases metastable at 25 °C, 1 bar; open triangle: position of a glass with composition 75  $\text{SiO}_2$ , 10  $\text{CaO}$ , 15  $\text{Na}_2\text{O}$  (mol %)

mol) = 70.15  $\text{SiO}_2$ , 9.35  $\text{CaO}$ , 15.50  $\text{Na}_2\text{O}$  (by wt.) is marked by the open triangle. Its constitutional range is  $S\text{--NC}_3\text{S}_6\text{--NS}_2$ ;  $\mathbf{n}_j$  and  $(\mathbf{M})$  take the form

$$\mathbf{n}_j = \begin{pmatrix} n_{\text{SiO}_2} \\ n_{\text{CaO}} \\ n_{\text{Na}_2\text{O}} \end{pmatrix}, \quad \mathbf{n}_j^T = (n_{\text{SiO}_2} \ n_{\text{CaO}} \ n_{\text{Na}_2\text{O}}), \quad (1.21)$$

the coefficients aligned column-wise in  $(\mathbf{M})$  are obtained in a straight-forward way from  $S = N_0\text{C}_0\text{S}_1$ ,  $\text{NC}_3\text{S}_6 = N_1\text{C}_3\text{S}_6$ ,  $\text{NS}_2 = N_1\text{C}_0\text{S}_2$ .

$$\begin{aligned} (\mathbf{M}) &= \begin{pmatrix} 1 & 6 & 2 \\ 0 & 3 & 0 \\ 0 & 1 & 1 \end{pmatrix}, \quad (\mathbf{M}^{-1}) = \begin{pmatrix} 1 & -1.333 & -2 \\ 0 & 0.333 & 0 \\ 0 & -0.333 & 1 \end{pmatrix}, \\ (\mathbf{M}^{-1})^T &= \begin{pmatrix} 1 & 0 & 0 \\ -1.333 & 0.333 & -0.333 \\ -2 & 0 & 1 \end{pmatrix}; \end{aligned} \quad (1.22)$$

The composition in terms of compounds is calculated as  $\mathbf{n}_k = (\mathbf{M}^{-1}) \cdot \mathbf{n}_j$  or  $\mathbf{n}_k^T = \mathbf{n}_j^T \cdot (\mathbf{M}^{-1})^T$ , where  $(\mathbf{M}^{-1})$  and  $(\mathbf{M}^{-1})^T$  is the inverse and the transposed inverse

coefficient matrix, respectively. It may be inconvenient (and for systems with more than three components even impossible) to identify the position of a given glass within the many constitutional ranges graphically. So, in a generalized approach, we solve the above equations for all possible ranges (here six ranges) simultaneously. The range yielding a vector  $\mathbf{n}_k$  with non-negative members is the correct range; the rest is ignored. The results of the calculation is summarized in Table 1.7. Panel **a** shows how the  $n_j$  are calculated from the glass composition in oxide wt. % or  $m_j$  in units g/100 g. Then  $n_j = m_j/M_j$ . The 5th column of panel **a** shows the molar amounts of the elements, e.g., for  $\text{SiO}_2$ ,  $n_{\text{el}} = 3 \cdot n_{\text{SiO}_2}$  because  $\text{SiO}_2$  is composed of three atoms, and so on. The sum  $\sum n_{\text{el}}$  is the molar amount of atoms in the glass. So, the Dulong-Petit heat capacity  $c_{DP}$  in J/(100 g·K) is readily calculated as  $c_{DP} = 3 \cdot R \cdot \sum n_{\text{el}}$ . The 4th column of panel **b** shows the  $n_k$  calculated as  $\mathbf{n}_k = (\mathbf{M}^{-1}) \cdot \mathbf{n}_j$ ; the wt. % of  $k$  are calculated as  $m_k = n_k \cdot M_k$ . Table 1.8 summarizes thermodynamic data for the components  $k$  used in this specific example. The results for the composition are then as follows:

$$\begin{aligned}
 c_{DP} &= 1.2061 \text{ kJ}/(\text{g} \cdot \text{K}), \\
 c_L &= 1.3999 \text{ kJ}/(\text{g} \cdot \text{K}), \\
 \Delta c_P &= 0.1937 \text{ kJ}/(\text{g} \cdot \text{K}), \\
 S^{\text{vit}} &= 0.0996 \text{ kJ}/(\text{g} \cdot \text{K}), \\
 \Delta c_P/S^{\text{vit}} &= 1.945 \text{ (experimental value derived from viscosity data is 1.964)}, \\
 -G_{\text{GL}}^f &= 1332.7 \text{ kJ}/100 \text{ g}, \\
 -H^\circ &= 1408.6 \text{ kJ}/100 \text{ g} = 3912.7 \text{ kWh}/\text{t}, \\
 \Delta H_{1400} &= 162.2 \text{ kJ}/100 \text{ g} = 450.5 \text{ kWh}/\text{t}, \\
 \Delta H_{1300} &= 148.2 \text{ kJ}/100 \text{ g} = 411.6 \text{ kWh}/\text{t}; \\
 E &= 71.0 \pm 0.6 \text{ GPa (experimental value is } 69.8 \pm 0.6 \text{ GPa)}.
 \end{aligned}$$

This is a fully quantitative thermodynamic characterization of the given glass and its melt. The value  $G_{\text{GL}}^f$  will be used in the calculation of the chemical durability of the glass (see the respective chapter in this book).  $H^\circ$  is used in the calculation of the chemical heat demand of the batch-to-melt conversion: batch  $\rightarrow$  glass + batch gases.  $\Delta H_{1300}$  is equal to the amount of heat drawn from a glass furnace at technological melt exit temperature of 1300 °C. The option to calculate Young's modulus  $E$  opens

**Table 1.7** **a** Calculation of the molar amounts  $n_j$  and  $n_{\text{el}}$  of oxides  $j$  and elements el, respectively, from the glass composition 75.17  $\text{SiO}_2$ , 9.35  $\text{CaO}$ , 15.50  $\text{Na}_2\text{O}$  by wt. corresponding to 75  $\text{SiO}_2$ , 10  $\text{CaO}$ , and 15  $\text{Na}_2\text{O}$  by mol; **b** Molar amounts  $n_k$  as calculated via matrix calculation, and composition in terms of wt. % of components  $k$  for the same glass

<b>a</b>					<b>b</b>			
$j$	wt. % g/100 g	$M_j$ g/mol	$n_j$ mol/100 g	$n_{\text{el}}$ mol/100 g	$k$	wt. % g/100 g	$M_k$ g/mol	$n_k$ mol/100 g
$\text{SiO}_2$	75.15	60.084	1.2507	3.7522	S	31.74	60.084	0.5283
$\text{CaO}$	9.35	56.079	0.1667	0.3335	$\text{NC}_3\text{S}_6$	32.83	590.720	0.0556
$\text{Na}_2\text{O}$	15.50	61.979	0.2501	0.7503	$\text{NS}_2$	35.43	182.147	0.1945
sum	100.00			4.8360		100.00		

**Table 1.8** Thermodynamic data for the constitutional components  $k = \text{S}, \text{NC}_3\text{S}_6$ , and  $\text{NS}_2$  of the glass composition presented in Table 1.7

$k$	$-H^\circ_k$	$H^{\text{vit}}_k$	$-H_{\text{L}, 1673}$	$-G^f_k$	$S^\circ_k$	$S^{\text{vit}}_k$	$S_{\text{L}, 1673,k}$	$c_{\text{L}, 1673,k}$	$E_k$
	kJ/mol				J/(mol·K)				GPa
S	908.3	6.9	809.6	848.6	43.5	4.0	157.3	86.2	72
$\text{NC}_3\text{S}_6$	8363.8	141.9	7076.2	7797.3	461.9	95.0	1745.5	785.7	83
$\text{NS}_2$	2473.6	29.3	2102.5	2302.6	164.4	13.2	588.7	261.1	59

the possibility to explore phase diagrams for glass compositions with especially high  $E$ . The data for  $\text{NC}_3\text{S}_6$  in Table 1.3 have been re-assessed; so please use these data instead of the data compiled in [20].

The Gibbs energy can be expressed on the basis of either oxides  $j$  or compounds  $k$ :

$$G = \sum n_j \cdot (G_j^\bullet + G_j^{\text{MIX}}) = \mathbf{n}_j^T \cdot (\mathbf{G}_j^\bullet + \mathbf{G}_j^{\text{MIX}}), \quad (23a)$$

$$G = \sum n_j \cdot G_k^\bullet = \mathbf{n}_k^T \cdot \mathbf{G}_k^\bullet. \quad (23b)$$

Here,  $G_j^{\text{MIX}} = RT \cdot \ln a_j$ . Substituting the relation  $\mathbf{n}_k^T = \mathbf{n}_j^T \cdot (\mathbf{M}^{-1})^T$  into Eq. (23b) and comparing it with Eq. (23a) gives

$$\mathbf{n}_k^T \cdot \mathbf{G}_k^\bullet = \mathbf{n}_j^T \cdot (\mathbf{M}^{-1})^T \cdot \mathbf{G}_k^\bullet = \mathbf{n}_j^T \cdot (\mathbf{G}_j^\bullet + \mathbf{G}_j^{\text{MIX}}) \Rightarrow (\mathbf{M}^{-1})^T \cdot \mathbf{G}_k^\bullet = \mathbf{G}_j^\bullet + \mathbf{G}_j^{\text{MIX}} \quad (23c)$$

where  $(\mathbf{M}^{-1})^T \cdot \mathbf{G}_k^\bullet = \mathbf{J}_j$  is a vector relating to the oxides, i.e., with its members representing properties of the oxides  $j$ . It immediately follows that

$$\mathbf{G}_j^{\text{MIX}} = \mathbf{J}_j - \mathbf{G}_j^\bullet \quad (23d)$$

Writing out each oxide row of Eq. (23d) gives

$$G_j^{\text{MIX}} = RT \cdot \ln a_j = J_j - G_j^\bullet. \quad (23e)$$

Thus, we have also determined the activities of the oxides  $j$ . As stated above, the  $a_j$  are derived by equating  $G = \mathbf{n}_j^T \cdot (\mathbf{G}_j^\bullet + \mathbf{G}_j^{\text{MIX}}) = \mathbf{n}_k^T \cdot \mathbf{G}_k^\bullet$ , and further  $\mathbf{J}_j = (\mathbf{M}^{-1})^T \cdot \mathbf{G}_k^\bullet$ . For the example chosen, this yields

$$-\mathbf{G}_{j,1400}^\bullet = \begin{pmatrix} 1073.8 \\ 773.4 \\ 618.5 \end{pmatrix}, -\mathbf{G}_{k,1400}^\bullet = \begin{pmatrix} 1072.8 \\ 9988.7 \\ 3087.5 \end{pmatrix}, -\mathbf{J}_{j,1400} = \begin{pmatrix} 1072.8 \\ 870.0 \\ 941.9 \end{pmatrix}. \quad (1.24)$$

**Table 1.9** Calculation scheme after Eq. (23a–e) for oxide activities  $a_j$  in a melt of a composition as given in Table 1.7 at 1400 °C;  $x_j$  = molar fraction;  $f_j = a_j/x_j$  = activity coefficient;  $\mu_j$  = chemical potential;  $RT = 13.911$  kJ/mol

Oxide $j$	$x_j$	$G^*_j$	$G^*_k$	$J_j = \mu_j$	$\ln a_j$	$\log a_j$	$\log f_j$
		kJ/mol					
SiO <sub>2</sub>	0.75	−1073.8	−1072.8	−1072.8	0.072	0.031	0.156
CaO	0.10	−773.4	−9988.8	−870.0	−6.944	−3.016	−2.016
Na <sub>2</sub> O	0.15	−681.5	−3087.5	−941.9	−18.720	−8.130	−7.306

All entries are given in kJ/mol. Note that the members of vector  $\mathbf{J}_j$  refer to the oxides  $j$ . Thus, the individual oxide activities can be assessed, line by line, as

$$\ln a_j = \frac{1}{RT} \cdot (J_j - \mathbf{G}^*_j). \quad (1.25)$$

In fact, the member of vector  $\mathbf{J}_j$  are identical with the chemical potentials  $\mu_j$  of individual oxides,

$$J_j = \mu_j = G^*_j + RT \cdot \ln a_j. \quad (1.26)$$

Table 1.9 summarizes the result for the activities  $a(j)$ . With these data, chemical reactions involving individual oxides in the melt can be calculated, e.g., evaporation reactions like in Fig. 1.9, reactions between melt and refractory materials, etc. In Fig. 1.11, calculated activity data for the binary system Na<sub>2</sub>O–SiO<sub>2</sub> are compared to experimental results.<sup>1</sup>

For systems with a large number of oxides  $j$ , graphical versions of phase diagrams are usually not available. In these cases, the identity of the constitutional compounds  $k$  is assessed by computer-assisted calculations (the co-called CALPHAD method

<sup>1</sup> The reader may be discouraged by the concept of matrix calculation. In fact, nowadays, even simple spreadsheet calculators offer this option, with EXCEL probably being the most widespread version today. Here, the respective EXCEL commands are compiled. For matrix operations in a 3-component system, mark a 3×3 array for  $\mathbf{M}^{-1}$  or  $\mathbf{M}^T$ , respectively, and enter the following commands:

for matrix inversion  $\mathbf{M} \rightarrow; \mathbf{M}^{-1}$ : MINV(array of  $\mathbf{M}$ ),  
 for matrix transformation  $\mathbf{M} \rightarrow; \mathbf{M}^T$ : MTRANS(array of  $\mathbf{M}$ ),  
 for vector operations  $\mathbf{a} \rightarrow; \mathbf{a}^T$ , mark a 3-member line for  $\mathbf{a}^T$ , and do the above operation on the 3-member column array of vector  $\mathbf{a}$ ,  
 for multiplication  $\mathbf{b} = (\mathbf{M}^{-1}) \cdot \mathbf{a}$ , mark a 3-member column for  $\mathbf{b}$  and enter the command MMULT(array of  $\mathbf{M}^{-1}$ ; array of  $\mathbf{a}$ ),  
 for multiplication  $\mathbf{b}^T = \mathbf{a}^T (\mathbf{M}^{-1})^T$ , mark a 3-member line for  $\mathbf{b}^T$  and enter the command MMULT(array of  $\mathbf{b}^T$ ; array of  $(\mathbf{M}^{-1})^T$ ),  
 Always finalize the operation by the 3-key-stroke command *Control Shift Enter*. The procedure is extended easily to glasses with many components.



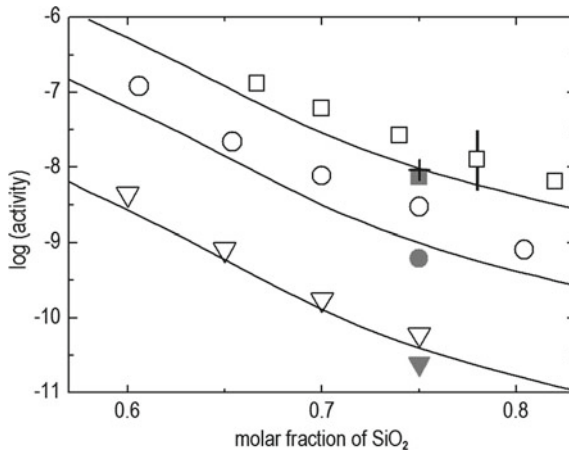


**Fig. 1.11** Activities of  $\text{Na}_2\text{O}$  in binary  $\text{Na}_2\text{O}$ - $\text{SiO}_2$  melts; lines: experimental values from multiple sources; upper, mid, and lower line: temperature  $T = 1400, 1200, 1000$  °C, respectively; open symbols: experimental values from [34, 35]; full symbols: calculated values; square (1400 °C), circle (1200 °C), triangle (1000 °C); cross: the data point calculated in Appendix 1 for 1200 °C is in poor agreement with the rest only

[31–33]) in a most general way. The disadvantage of this method lies in the high costs for commercially available software, hence, in its limited dissemination to students and glass technologists alike. Typically, however, individual families of industrial glasses cover narrow compositional ranges only. So within a given glass family, it is always the same type of linear equation system which has to be solved. In order to facilitate the determination of the amounts of components  $k$  for a given glass composition, a ready-made solution for soda lime silicate-based mass glasses is presented below. Oxide amounts are inserted in wt. % and the respective amounts of components  $k$  are obtained in wt. %, too. The component  $k = \text{SiO}_2$  is obtained from the mass difference to 100% in all cases. The compounds  $k$  are given as

$$\begin{aligned}
 k &= \text{Na}_2\text{O} \cdot \text{Al}_2\text{O}_3 \cdot 6\text{SiO}_2 = 5.1436 \text{Al}_2\text{O}_3 - 5.5672\text{K}_2\text{O}, \\
 k &= \text{K}_2\text{O} \cdot \text{Al}_2\text{O}_3 \cdot 6\text{SiO}_2 = 5.9092 \cdot \text{K}_2\text{O}, \\
 k &= \text{MgO} \cdot \text{SiO}_2 = 2.4905\text{MgO}, \\
 k &= \text{Na}_2\text{O} \cdot 3\text{CaO} \cdot 6\text{SiO}_2 = -1.7864\text{Al}_2\text{O}_3 - 1.0827\text{CaO} + 2.9389\text{Na}_2\text{O} \\
 &\quad + 1.9336 \cdot \text{K}_2\text{O};
 \end{aligned}$$

$\text{TiO}_2, \text{B}_2\text{O}_3$  are  $\text{Fe}_2\text{O}_3$  are approximated by letting  $j = k$ . Alternatively,  $\text{TiO}_2$  may be allotted to  $\text{CaO} \cdot \text{TiO}_2$ .

Figure 1.12 shows the heat capacity of the standard float glass DGG-1 [36]. Numerical results are compiled in Appendix 2.

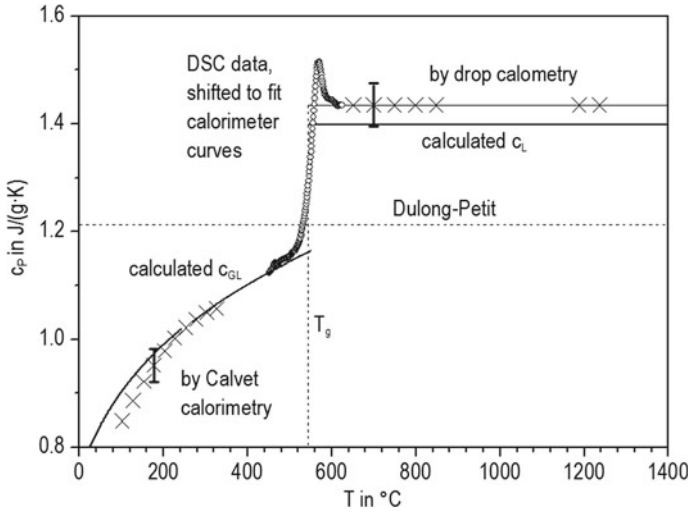


**Fig. 1.12** Heat capacity  $c_p$  of standard float glass DGG-1 [36]; bold lines: calculated from the constitutional phases  $k$ ; crosses: experimental data by Calvet calorimetry (low T) and by drop calorimetry (high T); open circles; experimental data by DSC

### Relation to viscosity

At the end of Sect. 1.3, the ratio  $\Delta c_p/S^{\text{vit}}$  was announced to play a significant role in the viscosity of a glass. Standard float glass DGG-1 [36] is taken as example here. Experimental viscosity data of glass DGG-1 were measured at 44 points within the temperature range between  $T_g = 543.1$  °C and  $T = 1397$  °C by the Federal Bureau of Standards, Braunschweig, Germany. The experimental data were fitted by a least-squares procedure to four prominent viscosity models, namely, the Vogel-Fulcher-Tammann (VFT), Adam-Gibbs (AG), Avramov, or Kohlrausch-Williams-Watts (KWW), and Mauro-Yue-Ellison-Gupta-Allan (MYEGA) model. Details of the models are given in the Appendix 3. The fit constants  $L_\infty = \log \eta(T \rightarrow \infty)$ , the non-Arrhenius parameters, and the statistical errors  $\pm \delta L = \pm \delta \log \eta$  of the fit are summarized in Table 1.10;  $\eta$  in dPa·s. Note that the  $\Delta c_p/S^{\text{vit}}$  received from the fits (AG and MYEGA) and its value calculated via thermodynamics agree very well. As for the parameter  $a_{\text{KWW}}$ , there is a relation between  $a_{\text{KKW}}$  and the molar fraction  $x_{\text{MOD}}$  of modifier oxides in the glass,  $a_{\text{KWW}} = 0.2 + 6 \cdot x_{\text{MOD}}$ , which holds well for binary glasses. For DGG-1 with  $x_{\text{MOD}} = x_{\text{MgO}} + x_{\text{CaO}} + x_{\text{Na}_2\text{O}} + x_{\text{K}_2\text{O}} = 0.28$ , the agreement is poor. One may, however, use the experimental viscosity data and use  $a_{\text{KKW}}$  to calculate an effective molar fraction  $x_{\text{MOD, eff}}$  of rheologically relevant modifier as  $x_{\text{MOD, eff}} = (a_{\text{KKW}} - 0.2)/6 = 0.30$ . From a practical point of view, the traditional VFT model yields the most accurate representation of the viscosity function between  $T_g$  and high temperatures while KWW yields the largest, albeit still very small, deviations. The above statements are not in conflict with the fact that the MYEGA model enfolds its specific strengths at temperatures below  $T_g$ .

**Table 1.10** Fit constants and statistical errors  $\pm \delta L$  of the viscosity-temperature function of standard float glass DGG-1 glass [36]; viscosity data were measured at 44 temperatures between  $T_g = 543.1$  °C and  $T = 1397$  °C by the Federal Bureau of Standards, Braunschweig, Germany; the non-Arrhenius parameters marked “external” are values derived by thermodynamic calculation (AG, MYEGA) and from molar fraction of modifier oxides  $x_{\text{MOD}} = x_{\text{MgO}} + x_{\text{CaO}} + x_{\text{Na}_2\text{O}} + x_{\text{K}_2\text{O}} = 0.28$  in the glass (KWW)

viscosity model	$L_\infty$	non-Arrhenius parameter		$\pm \delta L$
		From fit	External	
VFT	-1.601	$a_{\text{VFT}} = 1.7484^*$	—	0.0159
AG	-0.650	$\Delta c_p/S^{\text{vit}} = 1.8657$	1.82	0.0163
KWW	+ 0.899	$a_{\text{KWW}} = 2.0055$	1.88**	0.0519
MYEGA	-0.292	$\Delta c_p/S^{\text{vit}} = 1.8366$	1.82	0.0290

\*The familiar VFT constants are  $A = L_\infty$ ,  $B = \frac{(13-L_\infty)}{1+a_{\text{VFT}}} \cdot \frac{T_g}{K}$ ,  $\frac{T_0}{^\circ\text{C}} = \frac{a_{\text{VFT}}}{1+a_{\text{VFT}}} \cdot \frac{T_g}{K} - 273.15$ ;  
 $A = -1.601$ ,  $B = 4336.5$ ,  $T_0 = 246.1$ ;

\*\* $a_{\text{KWW}} = 0.2 + 6 \cdot x_{\text{MOD}}$ ; for multicomponent glasses, one may calculate an effective  $x_{\text{MOD, eff}} = (a_{\text{KWW}} - 0.2)/6 = 0.30$ .

The excellent agreement between the non-Arrhenius parameters  $a_{\text{AG}}$  and  $a_{\text{MYEGA}}$  on the one hand, and the ratio  $\Delta c_p/S^{\text{vit}}$  as calculated via thermodynamics, on the other hand, opens a most interesting option, i.e., the formulation of a generic viscosity model not requiring any empirical parameters. The missing link is the high-T limit  $L_\infty = \log \eta_\infty$ . Frenkel [5] pointed out that  $\eta_\infty = h/\lambda^3$  where  $\lambda$  is a length of a rheologically relevant positional change at the atomic scale. To date, however, no approach is available on how to assess  $\lambda$  in multicomponent glasses at an accuracy satisfying technological requirements.

## 1.5 Summary and Outlook

At this point, the journey through the world of thermodynamics comes to an end. The author sincerely hopes that the reader is now convinced of the power offered by the thermodynamic approach to glasses. More than this, he hopes that the tutorial will encourage the reader to apply the approach to his/her own research. This is the reason why calculation procedures were explained so broadly, and detailed examples for specific glasses were carried through, yielding a host of quantitative results useful for both glass science and technology.

The reader may miss a procedure allowing one to also calculate the liquidus temperatures of multicomponent glasses. In fact, in contrast to one-component systems, such glasses do not possess a melting point  $T^m$ , but a melting range extending from the solidus temperature  $T_{\text{sol}}$  (appearance of a first molten phase in the polycrystalline system) to the liquidus temperature  $T_{\text{liq}}$  (complete melting, state of a stable equilibrium melt). Knowing  $T_{\text{liq}}$  is of high importance in glass technology, e.g., in

the production of continuous fibers: The temperature of the fiber drawing nozzles  $T(3.0)$  corresponding to  $\eta = 10^{3.0}$  dPa·s must be kept above  $T_{\text{liq}}$  by at least 50–60 K. This condition cannot be optimized unless  $T_{\text{liq}}$  is known. In industry,  $T_{\text{liq}}$  is determined experimentally for each individual glass composition, which is a cumbersome procedure. Beyond this, it does not allow one to perform desktop development of new glass compositions. It is true,  $T_{\text{liq}}$  can be calculated via an extended thermodynamic approach, in specific, via the CALPHAD method [31–33]. But this is an issue reaching beyond the scope of the present tutorial.

## Appendix 1

The Gibbs energy of mixing  $G^{\text{MIX},j}$  in a binary mixture of oxides  $j = 1, 2$  is given by

$$G^{\text{MIX},j} = G^{\text{MIX},j,\text{id}} + G^{E,j}.$$

Here

$$G^{\text{MIX},j,\text{id}} = RT \cdot (x_1 \cdot \ln x_1 + x_2 \cdot \ln x_2)$$

Represents the contribution of ideal (i.e., merely statistical) mixing while  $G^{E,j}$  is the so-called excess Gibbs energy comprising all further contributions to  $G^{\text{MIX},j}$  in the real mixture;  $x$  = molar fraction,  $R$  = gas constant. The symbol  $j$  in the superscript indicates that the respective quantities refer to the component basis of oxides  $j$ . In fact, the values of  $G^{\text{MIX},j}$ ,  $G^{\text{MIX},j,\text{id}}$ , and  $G^{E,j}$  depend on the choice of the component basis. The excess Gibbs energy is determined experimentally. It may be modeled by a simple polynomial,

$$G^{E,j} = RT \cdot x_1 \cdot x_2 \cdot (a + b \cdot x_1 + c \cdot x_1^2 + \dots);$$

in many cases, three constants are sufficient to represent the experimental data. With the constants  $a$ ,  $b$ , and  $c$  known, the activity coefficients  $f_j$  are given by<sup>2</sup>

$$\ln f_1 = A_2 \cdot x_2^2 + A_3 \cdot x_2^3 + A_4 \cdot x_2^4,$$

$$\ln f_2 = B_2 \cdot x_1^2 + B_3 \cdot x_1^3 + B_4 \cdot x_1^4.$$

The constants  $A_2, A_3, A_4$ , and  $B_2, B_3, B_4$  are readily calculated from  $a, b$ , and  $c$  as

$$A_2 = a + 2b + 3c, \quad A_3 = -2b - 6c, \quad A_4 = 3c;$$

$$B_2 = a - b = A_2 + (3/2) \cdot A_3 + 2 \cdot A_4, \quad B_3 = 2b - 2c = -A_3 - (8/3) \cdot A_4, \quad B_4 = 3c = A_4.$$

<sup>2</sup> R. Haase: *Thermodynamik der Mischphasen* (Springer, Berlin 1956).

Thus, for the description of a mixture at constant T, three independent constants are required only. The above relations are a direct consequence of Gibbs-Duhem's relation. The so-called Henry coefficients  $f_1^\infty$  and  $f_2^\infty$  are the activity coefficients of oxide 1 or 2 infinitely diluted in oxide 2 and 1, respectively, i.e., at  $x_1 \rightarrow 0$  and  $x_2 \rightarrow 0$ , respectively:

$$\ln f_1^\infty = A_2 + A_3 + A_4,$$

$$\ln f_2^\infty = B_2 + B_3 + B_4.$$

The oxide activities are given by  $a_j = x_j \cdot f_j$ ,  $j = 1, 2$ , yielding

$$G^{\text{MIX},j} = RT \cdot (x_1 \cdot \ln a_1 + x_2 \cdot \ln a_2).$$

For the binary oxide systems shown in Fig. 1.8, the following data are obtained from experimental results compiled in.<sup>3</sup>  $G^{\text{MIX},j}_{\min}$  denotes the minimum value of  $G^{\text{MIX},j}$  and  $x_2(\min)$  denote the composition at the minimum.

$j = 1$	$j = 2$	$a$	$b$	$c$	$G^{\text{MIX},j}_{\min}$ in kJ/mol	$x_2(\min)$	$\log a_1$ at $x_2 =$ 0.75	$\log f_1^\infty$
Ideal mixture		0	0	0	-8.5	0.50	-1.204	0
Li <sub>2</sub> O	SiO <sub>2</sub>	-8.662	-25.182	1.651	-76.6	0.39	-5.718	-3.762
Na <sub>2</sub> O	“	-15.791	-31.172	5.122	-104.6	0.41	-8.033	-6.858
K <sub>2</sub> O	“	-26.070	-39.032	10.323	-143.8	0.43	-11.265	-11.322
PbO	“	-0.857	-3.549	1.760	-15.4	0.45	-1.164	-0.372
B <sub>2</sub> O <sub>3</sub>	“	0.465	-0.140	0.173	-7.2	0.48	-0.498	+ 0.202
PbO	B <sub>2</sub> O <sub>3</sub>	-4.328	2.878	-8.689	-25.2	0.38	-1.706	-1.880

## Appendix 2

Panel for the calculation of thermodynamic properties of standard float glass DGG-1 [36];  $m$  = mass,  $M$  = molar mass,  $n$  = molar amount,  $G$  = Gibbs energy,  $a$  = activity calculated relative to the pure oxides in their liquid state; subscripts  $j$  = oxides,  $k$  = compounds,  $el$  = elements,  $L$  = liquid at 1400 °C;  $G^{\text{MIX},j}$  = Gibbs energy of mixing of the oxides.

<sup>3</sup> R. Conradt, H. Scholze: On volatilization from glass melts. Glastechn. Ber. **59**, 34–52 (1986).

Oxides								
<i>j</i>	<i>m<sub>j</sub></i> g/100 g	<i>M<sub>j</sub></i> g/mol	<i>n<sub>j</sub></i> mol/100 g	<i>n<sub>el</sub></i> mol/100 g	$-G_{L,j}$ kJ/mol	$-n_j \cdot G_{L,j}$ kJ/100 g	$-G^{\text{MIX},j}$ kJ/100 g	$\log a_j$
SiO <sub>2</sub>	71.72	60.084	1.1937	3.5810	1072.8	1280.5	0.0	0.00
TiO <sub>2</sub>	0.14	79.898	0.0018	0.0053	1132.8	2.0	-0.1	1.58
Al <sub>2</sub> O <sub>3</sub>	1.23	101.961	0.0121	0.0603	1899.2	22.9	1.5	-3.84
Fe <sub>2</sub> O <sub>3</sub>	0.19	159.691	0.0012	0.0059	1169.8	1.4	0.0	n.d.0
MgO	4.18	40.311	0.1037	0.2074	682.0	70.7	6.1	-1.84
CaO	6.73	56.079	0.1200	0.2400	758.4	91.0	15.3	-3.99
Na <sub>2</sub> O	14.95	61.979	0.2412	0.7236	681.5	164.4	62.8	-8.13
K <sub>2</sub> O	0.38	94.203	0.0040	0.0121	701.0	2.8	1.5	-11.68
Sum	99.52			4.8356		1635.7	87.2	
Compounds								
K	<i>m<sub>k</sub></i> g/100 g	<i>M<sub>k</sub></i> g/mol	<i>n<sub>k</sub></i> mol/100 g	<i>n<sub>el</sub></i> mol/100 g	$-G_{L,k}$ kJ/mol	$-n_j \cdot G_{L,k}$ kJ/100 g		
S	23.65	60.084	0.3935	1.1806	1072.8	422.2		
CT	0.24	135.977	0.0018	0.0087	1968.4	3.4		
NAS <sub>6</sub>	4.21	524.444	0.0080	0.2088	9400.7	75.5		
Fe <sub>2</sub> O <sub>3</sub>	0.19	159.691	0.0012	0.0059	1169.8	1.4		
MS	10.41	100.395	0.1037	0.5185	1813.6	188.1		
NC <sub>3</sub> S <sub>6</sub>	23.29	590.720	0.0394	1.0643	10,037.4	395.7		
NS <sub>2</sub>	35.29	182.147	0.1938	1.7439	3087.5	598.2		
KAS <sub>6</sub>	2.25	556.668	0.0040	0.1049	9534.0	38.5		
sum	99.52			4.8356		1722.9		

The properties of the glass and its melt read as follows:

Dulong-Petit value	$c_{DP}$ 1.212 J/(g·K) (normalized to 100 wt. %).
heat capacity of the melt	$c_L$ 1.398 J/(g·k).
heat capacity jump at $T_g$	$\Delta c_P$ 0.186 J/(g·K).
entropy of vitrification	$S^{\text{vit}}$ 0.102 J/(g·K).
Adam-Gibbs parameter	$a_{AG}$ 1.82 (form viscosity data, (Table 1.10), 1.85 ± 0.02).
Gibbs energy of formation at 25°C	$G^f$ -1326.4 kJ/100 g.
standard enthalpy of the glass	$H^\circ$ -1401.4 kJ/100 g.
heat content of the melt at 1300°C	$\Delta H_{1300^\circ\text{C}}$ 157.7 kJ/100 g (relative to 25 °C).

## Appendix 3

Four viscosity models are depicted below. In this particularly short presentation, the respective physical background of the individual models is not explained. The compilation is chosen, in particular, to show how closely related the individual models actually are. All models can be presented in a unified way. Let us introduce the abbreviations

$$L = \log \eta, \quad \eta = \eta(T), \quad \eta \text{ in dPa} \cdot \text{s},$$

$L_0 = \log \eta(T \rightarrow \infty)$  as the intercept in a  $\log \eta$  versus  $T_g/T$  plot at  $T_g/T = 0$ ,

$$L_g = \log \eta(T_g) = 13.0,$$

$$y = T_g/T.$$

Then all models take the same form

$$\frac{L - L_\infty}{L_g - L_\infty} = f(y) = y \cdot g(y)$$

The different viscosity models differ by the type of the function  $g(y)$  only. This is shown for the four models presented below.

I. The **VFT** type <sup>(1)</sup> or free-volume **WLF** type <sup>(2)</sup> has

$$g(y) = \frac{1}{1 + a_{\text{VFT}} \cdot (1 - y)};$$

with  $a_{\text{VFT}} = T_0 / (T_g - T_0)$ ,  $f(y) = y g(y)$  assumes the familiar form  $f(y) \propto 1/(T - T_0)$ .

II. The **Adam-Gibbs** (AG) type <sup>(3)</sup> has

$$g(y) = \frac{1}{1 - a_{\text{AG}} \cdot \ln y}$$

where  $a_{\text{AG}}$  has a direct thermodynamic meaning, i.e.,

$$a_{\text{AG}} = \frac{c}{S^{\text{vit}}};$$

$\Delta c_p$  is the heat capacity jump in the glass transition and  $S^{\text{vit}}$  is the frozen-in configurational entropy of the glass in Simon's approximation. The Adam-Gibbs model formally merges with the VFT model if  $\ln y$  is approximated as  $\ln y \approx y - 1$ .

III. The **Avramow** or **KWW** type <sup>(4)</sup> has

$$g(y) = y^{a_{\text{KWW}}}.$$

This corresponds to a stretched exponential equation for the viscosity. For network forming glasses, the constant  $a_{\text{KWW}}$  is approximately given by the molar fraction  $x_{\text{MOD}}$  of network modifiers,

$$a_{\text{KWW}} = 0.2 + 6 \cdot x_{\text{MOD}}.$$

Let us write  $y^{a_{KWW}} = \exp(a_{KWW} \cdot \ln y)$  and use the approximation  $\ln y \approx y-1$  like before. Then, we arrive at  $g(y) = \exp(a_{KWW}(y-1))$ , which formally agrees with the MYEGA model.

IV. The **MYEGA** type <sup>(5)</sup> has

$$g(y) = \exp(a_{MYEGA} \cdot (y - 1))$$

In a numerical evaluation,  $a_{MYEGA}$  assumes values very close to  $a_{AG} = \frac{c}{S_{VFT}}$ . In all models, the viscosity-temperature function is a linear function of  $f(y)$ :

$$L = L_{\infty} + (L_g - L_{\infty}) \cdot f(y).$$

The constants  $a_{VFT}$ ,  $a_{AG}$ ,  $a_{KWW}$ , and  $a_{MYEGA}$ , respectively, describe the non-Arrhenius behavior of  $(T)$ . Let us call these constants non-Arrhenius parameters. For a given set of experimental data of  $(T)$ , the values of  $a$  and  $L_{\infty}$  are determined in the following way: A linear regression is performed on the data set  $X = f(y) = f(T_g/T)$  and  $Y = L = \log \eta(T)$  using an arbitrary initial value of  $a$ . Then,  $a$  is varied numerically until the mean deviation  $\pm \delta L$  from a straight line assumes a minimum. With the  $a$  thus determined,  $L_{\infty}$  is readily obtained as intercept at  $f(y) = 0$ .

(1) Vogel H (1921) Das Temperaturabhängigkeitsgesetz der Viskosität von Flüssigkeiten, Physik. Zeitschrift 22:645–646

Fulcher G (1925) Analysis of recent measurements of the viscosity of glasses. J Am Ceram Soc 8:339–355

Tammann G, Hesse W (1926) Die Abhängigkeit der Viskositäts von der Temperatur bei unterkühlten Flüssigkeiten. Z Anorg Chem 156:245–257

(2) Williams ML, Landel RF, Ferry JD (1955) The temperature dependence of relaxation mechanisms in amorphous polymers and other glass-forming liquids. J Am Chem Soc 77:3701–3703

(3) Adam G, Gibbs JH (1965) On the temperature dependence of cooperative relaxation properties in glass-forming liquids. J Chem Phys 43:139–146

(4) Avramov I (1998) Viscosity of glassforming melts. J Non-Cryst Solids 238:6–10

(5) Mauro JC, Yue Y, Ellison AJ, Gupta PK, Allan DC (2009) Viscosity of glass-forming liquids. Proc Natl Acad Sci U.S.A. 106:19780–19784

## References

1. Zachariasen WH (1932) The atomic arrangement in glass. J Chem Soc 54:3841–3851
2. Greaves GN (1985) EXAFS and the structure of glass. J Non-Cryst Solids 7:203–217
3. Landau LD, Lifshitz EM (1969) Statistical physics. Pergamon Press, Oxford
4. Brazhin VV, Trachenko K (2014) Collective excitations and thermodynamics of disordered states: new insights into an old problem. J Chem Phys B118:11417
5. Frenkel J (1946) Kinetic theory of liquids. Oxford Clarendon Press



6. de Donder T, van Rysselberghe P (1936) Thermodynamic theory of affinity. Stanford University Press
7. Prigogine I (1955) Thermodynamics of irreversible processes. Ch. Thomas Press, Springfield
8. Richet P (2021) A history of glass science. Ch. 10.11. In: Richet P (ed) Encyclopedia of glass science, technology, history, and culture. Wiley, Hoboken, New Jersey
9. Zanutto ED (1998) Do cathedral glasses flow? *Am J Phys* 66:392–395
10. Gutzow I, Pascova R, Schmelzer JWP (2010) Glass transition behavior: a generic phenomenological approach. *Int J Appl Glass Sci* 1:221–236
11. Yageman VD, Mateev GM (1982) Heat capacity of glasses in the system  $\text{SiO}_2\text{--Na}_2\text{O--SiO}_2$ . *Fiz Khim Stekla* 8:238–245
12. Fluegel A (2007) Glass viscosity calculation based on a global statistical modelling approach. *Glass Technol Eur J Glass Sci Technol A48*:13–30
13. Richet P, Bottinga Y (1995) Rheology and configurational entropy of silicate melts. 67–94. In: Stebbins JF, McMillan PF, Dingwell DB (eds) (1995) Structure, dynamics and properties of silicate melts. *Rev Mineralogy* 32. Mineral Soc Am, Washington D.C
14. Richet P, Bottinga Y (1984) Anorthite, andesine, wollastonite, diopside, cordierite and pyrope: thermodynamics of melting, glass transitions, and properties of the amorphous phases. *Earth Planet Sci Lett* 67:415–432
15. Martens RM, Rosenhauer M, Büttner H, Gehlen KV (1987) Heat capacity and kinetic parameters in the glass transition interval of diopside, anorthite, and albite glass. *Chem Geol* 62:49–70
16. Krupka KM, Robie RA, Hemingway BS, Ito J (1985) Low-temperature heat capacities and derived thermodynamic properties of anthophyllite, diopside, enstatite, bronzite, and wollastonite. *Am Mineralogist* 70:249–260
17. Krupka KM, Hemingway BS, Robie RA, Kerrick DM (1985) High-temperature heat capacities and derived thermodynamic properties of anthophyllite, diopside, dolomite, enstatite, bronzite, talc, and wollastonite. *Am Mineralogist* 70:261–271
18. Richet P, Robie RA, Hemingway BS (1986) Low-temperature heat capacity of diopside glass ( $\text{CaMgSi}_2\text{O}_6$ ): a calorimetric test of the configurational entropy theory applied to the viscosity of liquid silicates. *Geochim Cosmochim Acta* 96:1521–1533
19. Knacke O, Kubaschewski O, Hesselmann K (eds) (1991) Thermochemical properties of inorganic substances, vol I–III. Springer, Berlin
20. Conradt R (2008) The industrial glass melting process, 282–303. In: Hack K (ed) *The SGTE casebook. Thermodynamics at work*. CRC press, Boca Raton; *ibid* (2010) Thermodynamics of glass melting, 385–412. In: Wallenberger FT, Bingham PA (eds) *Fiberglass and glass technology, energy-friendly compositions and applications*. Springer, Berlin
21. Turner WES (1934) Studies on volatilization from glass melts. *Glastechn Ber* 12:409–413
22. Shakhmatkin BA, Vedishcheva NM, Wright AC (2001) Thermodynamic modeling of the structure of glasses and melts: Single-component, binary and ternary systems. *J Non-Cryst Solids* 293 & 295:312–317
23. Navrotsky A, Hon R, Weill DF, Henry DJ (1980) Thermochemistry of glasses and liquids in the system  $\text{CaMgSi}_2\text{O}_6\text{--CaAl}_2\text{Si}_3\text{O}_8\text{--NaAlSi}_3\text{O}_8$ ,  $\text{SiO}_2\text{--CaAl}_2\text{Si}_2\text{O}_8\text{--NaAlSi}_3\text{O}_8$  and  $\text{SiO}_2\text{--Al}_2\text{O}_3\text{--CaO--Na}_2\text{O}$ . *Geochim Cosmochim Acta* 44:1409–1423
24. Kubaschewski O, Alcock CB, Spencer PJ (1993) *Materials thermochemistry*. Pergamon Press, London
25. Gutzow I, Schmelzer J (1995, 2013) *The vitreous state*. Springer, Berlin
26. Schmelzer JWP, Gutzow IS (2011) *Glasses and the glass transition*. Wiley VCH, Weinheim
27. Mysen BO, Richet P (2005) *Silicate glasses and melts*. Elsevier, Amsterdam
28. Navrotsky A (1995) Energetics of silicate melts, 121–143. In: Stebbins JF, McMillan PF, Dingwell DB (eds) Structure, dynamics and properties of silicate melts. *Rev Mineralogy* 32. Mineral Soc Am, Washington D.C
29. Philipps K, Stoffel RP, Dronskowski R, Conradt R (2017) Experimental and theoretical investigation of the elastic moduli of silicate glasses and crystals. *Front Mater* 4(2)

30. Phase equilibria diagrams PC database ver. 2.1, ver. 4.2 (1998, 2017). The American Ceramic Society, Westerville, Ohio
31. Bale CW, Bélisle E, Chartrand P, Decterov SA, Eriksson G, Hack K, Jung I-H, Kang Y-B, Melançon J, Pelton AD, Robelin C, Petersen S (2009) FactSage thermochemical software and database—recent developments. *Calphad* 33:295–311
32. Eriksson G, Hack K (1990) ChemSage—a computer program for the calculation of complex chemical equilibria. *Met Trans B* 21B:1013
33. FACTSAGE software ver 5.2 (2004) Thermfact Montreal and GTT Technologies Aachen
34. Dorfeld WG (1988) Structural thermodynamics of alkali silicates. *Phys Chem Glasses* 29:179–186
35. Rego DN, Sigworth GK, Philbrook WO (1985) Thermodynamic study of Na<sub>2</sub>O–SiO<sub>2</sub> melts at 1300 and 1400 °C. *Metallurg Trans* 16B:313–323
36. Standard float glass DGG-1, Deutsche Glastechnische Gesellschaft, Offenbach

# Chapter 2

## Chemical Durability of Glasses



Reinhard Conradt

### 2.1 Introduction

Glass is widely used as packing material for beverages, food, and drugs, as tableware, lab ware, and components of chemical plants, in architectural and automotive applications, as cover glasses of solar panels, or touch screens of electronic devices. In all these uses, glass is exposed to aqueous solutions in some form, such as bulk liquid, rain, fingertip sweat, etc. This makes chemical durability one of the most important properties of a glass. By public perception, glass has the image of almost perfect chemical inertness. However, glass manufacturers are well aware of the fact that freshly produced glass surfaces are very sensitive to corrosion (see the example of a stemware glass in Fig. 2.1a). Therefore, as-produced float glass panels are never stacked in direct glass-to-glass contact. It is only after exposure to water in daily use that this sensitivity vanishes. Some years ago, the composition of household dishwasher agents was redesigned by replacing the very caustic sodium metasilicates by less caustic disilicates. This was done for safety reasons. It was at that time that a broader public awareness of the chemical vulnerability of glass arose (see Fig. 2.1b–d). Yet, as early as in the seventeenth century, Robert Boyle (1627–1692) reported an observation made during repeated distillation of water in a glass vessel. No matter how often he repeated the distillation procedure, there was always a “white earth” remaining at the bottom of the vessel. He reported that distillation was repeated many times “without the liquid’s tiring of producing white earth.” Within the frame of chemical understanding at that time, he attributed his observation to the reaction of *water + fire* → *earth*. It took about 100 years before Lavoisier correlated the amount of “white earth” to the mass loss of the glass vessel. To my knowledge, this is the first scientific account of glass corrosion.

---

R. Conradt (✉)  
Nizzaallee, 75, 52072 Aachen, Germany  
e-mail: [reinhard.conradt@gmail.com](mailto:reinhard.conradt@gmail.com)

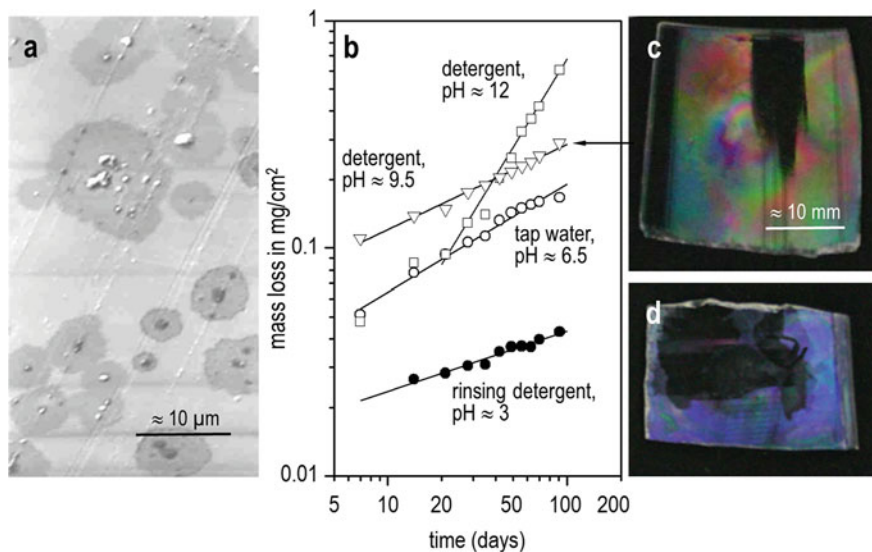


**Fig. 2.1** Corrosion phenomena observed on commercial glasses. **a** SEM image of the as-produced surface of a low-price stemware glass after storage in the warehouse in a humid tropical climate; **b** mass loss per surface area of a modern stemware glass composition exposed to different dish washer detergents and to tap water as a function of exposure time; appearance of the corrodes surface of the above stemware glass (**c**) and a lead crystal glass (**d**) after 100 days

An important milestone in understanding the chemical durability of glasses was the discovery of the glass electrode. Cremer [1] was the first to discover that the electrical potential measured across a glass membrane is proportional to the pH difference across the membrane. In fact, the scientific concept of pH was formulated by Sørensen three years later only. In the same year, Haber and Klemensiewicz [2] presented the first glass electrode. Since that time, proton transfer has been known to be the elementary mechanism of glass corrosion. The role of glass composition came into focus when glass electrodes were commercialized. A famous example of an early electrode glass is the MacInnes-Dole glass (Corning 1929) with 72 SiO<sub>2</sub>, 6CaO, and 20 Na<sub>2</sub>O by mol. Baucke [3–5] comprehensively described the function of glass electrodes, thereby refuting some long-standing misconceptions. Yet, the effect of glass composition on chemical durability, in general, remained unknown. Highly durable glasses (Jenaer Glas<sup>®</sup>, Duran<sup>®</sup>, Pyrex<sup>®</sup>), also displaying an excellent thermal shock resistance, were essentially developed on an empirical basis.

A new boost of research effort occurred in the late 70ies with the concept of underground radioactive waste storage in glass matrices. Soon, it became obvious that the scientific basis to systematically explore composition space for optimal chemical durability was extremely narrow. Beyond this, no scientific models were available to reliably predict the corrosion behavior of glasses over extended time scales. Similar questions arose with a health concern related to man-made mineral fibers (most of which are glasses), in specific, with the dwell time of inhaled fiber

fragments in human lung fluid. We may extend the issue to bioglasses and their behavior in human tissue, which constitutes a complex aqueous environment. All these cases call for a profound understanding of the chemical durability of glasses in relation to glass composition as well as to the nature of the aqueous solution. The present article is designed to give an introduction to this topic.

The chemical durability or hydrolytic resistance of a glass is not a material property like the density, the thermal expansion coefficient, or the modulus of elasticity. The concept of “hydrolytic resistance” encompasses complex behaviors of the glass material that depend on both its chemical composition and the type of corrosion medium. Glasses that turn out to be very resistant in dilute aqueous media even at extreme pH values may still fail dramatically in the presence of organic complexing agents. Conversely, glasses that tend to be unstable in dilute aqueous media may be surprisingly stable in certain highly concentrated media.

The literature on glass corrosion is extremely extensive. A few foundational works are listed below that are indispensable to anyone working with glass corrosion from the perspective of a developer (glass for general usage, cleaning agents, applications in the pharmaceutical and biotechnology sector). In 1972, the International Commission on Glass (ICG) summarized the state of knowledge at the time with almost 1000 citations [6]. The robustly established state of the art is summarized in the books by Scholze [7], Paul [8], Doremus [9], Clark et al. [10], Clark and Zaitos [11], and Bach and Krause [12], but this list is not exhaustive. There are also data sources that will not be directly found by searching for the keyword “glass corrosion”, despite being fundamentally important. The atlas by Pourbaix [13] gives a comprehensive presentation of the equilibria of many elements in aqueous solutions. “The Iler” [14] is an indispensable standard work that discusses the chemistry of  $\text{SiO}_2$ , primarily in aqueous solutions, with more than 2600 citations. The book by Butler [15] is a standard reference on water hardness. More recent works by Bergna [16] and Sposito [17] examine the chemistry of  $\text{SiO}_2$  and  $\text{Al}_2\text{O}_3$  in water. The thermodynamic and kinetic foundations of interactions between minerals and water can be found in the works of Bowers et al. [18], Baes and Mesmer [19], and Aargard and Helgeson [20]. Further important references are compiled in an own review [21]. The extensive recent work by Gin and colleagues [22, 23], just to quote some highlights, needs to be added to the list. Altogether, these references provide the foundations for thermodynamic-kinetic models of glass corrosion. The above compilation of references offers an introduction to an in-depth systematic treatment of glass corrosion based on a set of relevant sources.

All progress in understanding chemical durability rests on an accurate experimental assessment of chemical durability and the individual phenomena involved. Therefore, the article starts with addressing this issue (Sect. 2.2). In Sect. 2.3, the focus is directed toward the glass surface and the immediate sub-surface region. In Sect. 2.4, a thermodynamic approach to the driving forces of glass corrosion is presented. This approach opens the door for understanding the role of glass composition in a most general way. In Sect. 2.5, transition state theory is invoked with the purpose to derive general rate equations of glass corrosion. Finally, in Sect. 2.6, the case of long-term behavior is addressed in a scenario where large amounts of matter

released from the glass accumulate in the solution, and corrosion layers similar to rust on iron form on top of the glass. In the summary, a brief compilation of open questions is presented.

## 2.2 Design and Evaluation of Corrosion Tests

### 2.2.1 Design of Corrosion Tests

As a general observation, silicate glasses are most stable in slightly acid, neutral, and slightly caustic solutions ( $\text{pH} \approx 4\text{--}8$ ), less stable in strong acids, and very unstable in strong caustic solutions. In an empirical quantitative approach, stabilities are communicated in terms of so-called stability classes. The classes are determined by well-defined experimental norm procedures as outlined below:

*Stability in acids* (ISO 1776):

- monolithic samples  $\approx 300 \text{ cm}^2$ ;
- boiling in 1.5 L of 6 m HCl for 6 h;
- classes I–III: mass loss:  $<1.5/15/>15 \text{ mg/d m}^2$ .

*Hydrolytic stability* (ISO 719):

- granular samples, 315–500  $\mu\text{m}$ ,  $4 \times 2 \text{ g}$ ;
- exposition to 30 ml D.I. water at 98 °C in 50 ml volumetric flasks for 1 h;
- cooling and filling to 50 ml, titration of 25 ml aliquots with 0.01 m HCl;
- classes I–V: volume of HCl:  $<0.1/0.2/0.85/2/3.5 \text{ ml per g glass}; >3.5 \text{ ml: beyond range}$ .

*Hydrothermal stability* (ISO 720):

- granular samples, 300–420  $\mu\text{m}$  ( $4 \times 10 \text{ g}$ );
- exposition to 50 ml D.I. water at 121 °C (2 bar) in 100 ml volumetric flasks for 0.5 h;
- cooling and filling to 100 ml, titration with 0.02 m  $\text{H}_2\text{SO}_4$ ;
- classes I–III: volume of  $\text{H}_2\text{SO}_4$ :  $<0.1/0.85/1.5 \text{ ml H}_2\text{SO}_4 \text{ ml per g glass}; >1.5 \text{ ml: beyond range}$ .

*Stability in caustic solutions* (ISO 695):

- monolithic samples, 10 bis  $15 \text{ cm}^2$ ,
- boiling in 0.8 L of 1 m NaOH + 1 m  $\text{Na}_2\text{CO}$  solution for 3 h,
- classes according to mass loss:  $<75/175/>175 \text{ mg/d m}^2$ .

When expressing the results from the hydrolytic and isothermal tests in terms of mass losses, then the norm classification of chemical durability can be presented graphically (see Fig. 2.2). The graph supports common lab practice to store strong acids in thick-walled glass bottles. By contrast, concentrated NaOH or KOH solutions

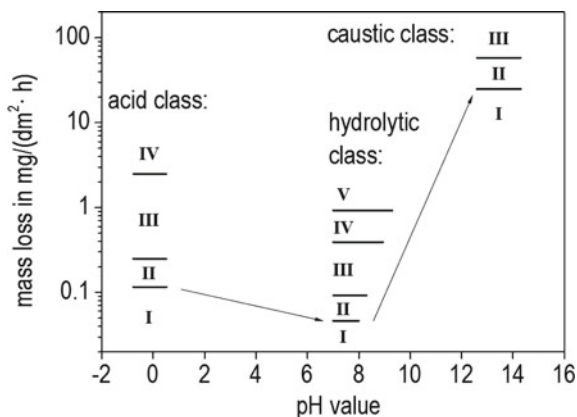


**Fig. 2.2** Graphical representation of the norm classes of chemical durability in terms of mass losses as a function of pH

must be kept in polymer containers. The best glasses commercially available are I-II glasses, e.g., FIOLAX<sup>®</sup> from Schott Co. Even pure silica glass does not reach caustic class I. This is the realm of alkali zirconia silicate glass fibers (CemFil<sup>®</sup>), a II–III–I glass. It reaches caustic class I, however, at the expense of a relatively high leachability in water and a poor performance in strong acids.

Beyond the above norms, there are several other ones adapted to specific glass products, such as ISO 4794 (lab ware), ISO 8424 and 10,629 (optical glass), DIN EN 12875-2 (glass in dish washers), DIN 52289 (automotive glass), ISO 20492 (architectural glass), etc.

Norm experiments as described above are useful to characterize commercial products. They do not reveal anything about the corrosion mechanisms involved, and nothing about the progress of glass corrosion with time. For scientific investigations, more appropriate tests have to be designed. The following compilation summarizes the main factors which have to be taken into account in the design of a corrosion experiment:

### *pH Value*

The important role of pH has already been addressed in Fig. 2.2. Unfortunately, there is no such thing like a standard reference aqueous system. Even pure water—de-ionized (D.I.) water prepared by an ion exchanger, or distilled water—does not qualify as reference system. First, due to omnipresent CO<sub>2</sub> in the atmosphere, D.I. and distilled water have a pH of 5.5–6.0. Preparing water with pH = 7 requires a lot of extra work. Second: During a corrosion test, the pH value of pure water may be shifted rapidly toward higher pH values. Independent of its exact composition, a typical soda-lime silicate glass reaches pH = 9.8 after a few hours (an explanation will follow in Sect. 2.4). The use of pH buffers and the problems going along with it are discussed below.

### *Temperature*

Temperature is a very sensitive parameter. The activation energy of the glass corrosion process is about 60–80 kJ/mol. Thus, an increase of 2, 5, 10 K results in an increase of reaction rates by a factor of 1.2, 1.5, and 2.3, respectively. In corrosion experiments, the temperature should be kept constant within  $\pm 1$  K. The good news reads: Corrosion experiments may be interrupted for intermediate manipulations by cooling to ambient temperature. The time counts for the exposure at target temperature only.

### *Surface Area to Solution Volume Ratio; Static Versus Dynamic Conditions*

In static experiments, this ratio is given by  $s = A/V_{\text{soln}}$ ;  $A$  in  $\text{cm}^2$  = surface of the glass sample,  $V_{\text{soln}}$  in  $\text{cm}^3$  = volume of the solution;  $s$  is given in units of  $\text{cm}^{-1}$ ;  $s = 0.01 \text{ cm}^{-1}$  is widely used as standard condition. Flow experiments offer the advantage to expose the glass to an almost unaltered solution; the exact value of the volume flow rate  $V'_{\text{soln}}$  in  $\text{cm}^3/\text{s}$  has to be balanced between the requirements to minimize the alteration of the solution and to still find detectable amounts of released glass constituents in the solution. With a sampling time  $\Delta t$  of the solution, the effective  $s$  parameter is given by  $s = A/(V'_{\text{soln}} \cdot \Delta t)$ . Under static conditions, the cumulative mass loss per surface area  $q$  in  $\text{mg}/(\text{cm}^2 \text{ s})$  scales with the time like  $q \propto s \cdot t$ . Thus, a series of experiments with  $s$  varied over a wide range may be used as time acceleration experiments. By contrast, temperature never should be taken into consideration as a time accelerating parameter, as temperature changes the thermochemical equilibria (solubilities) in the solution.

### *Sample Surface Condition*

Unless required otherwise, the use of monolithic glass chips is recommended. Experiments should be performed in PPA or Teflon containers, never in metal containers. ISO 695 (caustic test) using Ag vessels is an exception to this rule. Samples should be suspended in a way that the solution has access from all sides. The geometrical surface area is the most appropriate approach to surface area  $A$ . For monolithic glass chips, determining the real surface, e.g., by BET measurement does not yield any advantage. The issue of size distributed glass granules and fibers is not addressed here. It has been recommended to cut samples with a low-speed saw, using a 60 grid diamond cutting blade and petroleum (no water!) as cutting fluid. For long-term experiments, at least  $>7$  d, samples may be used in this condition right away. For shorter times, acid polishing of the cut surface by dilute hydrofluoric acid (0.5% HF + 1–2%  $\text{HNO}_3$ ) is recommended. Mechanical polishing may be used, but this procedure alters the glass surface significantly; after polishing, the same procedure of HF etching should be performed to a dissolution depth of at least  $1 \mu\text{m}$ . The dissolution depth  $L$  is determined gravimetrically as  $L = q/\rho$ ;  $\rho$  = density of the glass.

### *Ionic Strength*

As already known from the function of pH electrodes, the presence of ionic salts has a big influence on the elementary mechanisms of corrosion. Dissolution rates in 1 m NaCl at neutral pH are about equal to the dissolution rates in 1 m HCl.



Human body fluids contain 9 g/L NaCl. Therefore, tests mimicking in vivo behavior of glasses need to be adjusted accordingly.

### *Buffers, Complexing Agents, Organic Constituents*

As a general rule, a buffer system does not only keep the pH value of the bulk liquid at a constant level. It also interferes with the elementary corrosion mechanisms. Bicarbonate, biphosphate, TRIS, and HEPES buffers exert moderate interference only. Anyway, one should keep in mind that a constant pH value in the bulk liquid does not tell anything yet about the local pH at the glass surface. This is because the glass constituents, namely siliceous acid, act as buffer, too. Human body fluids also contain citric acid. This is a strong complexing agent. It destabilizes alumina and ferric oxide, two constituents known to render glasses very stable against water attack. Such glasses show very different behavior in body fluids as compared to simple aqueous systems.

### *Use of Isotopes*

Specific insights into the fundamental mechanisms of glass corrosion are obtained from experiments using isotopes [24–29]. Glasses have been exposed to  $^2\text{D}_2\text{O}$  or  $^2\text{D}_2^{18}\text{O}$  instead of  $\text{H}_2\text{O}$ . This allows one to trace the incorporation of  $^2\text{D}^+$  (as a place marker of  $\text{H}^+$ ) and oxygen from the solution into the sub-surface layer of a corroded glass. Radioactive isotopes  $^{22}\text{Na}$  have been used to monitor the sodium distribution and self-diffusion coefficient in the sub-surface layer.

## **2.2.2 Evaluation of Corrosion Tests**

The evaluation of corrosion experiments aims at determining the elemental release from the glass as well as the differentiation of the glass surface and the immediate sub-surface zone. The following methods have been applied with success:

### *Gravimetry*

Cumulative mass losses  $\Delta m$  are determined by a micro balance to the nearest  $\mu\text{g}$ . The specific mass loss  $q$  in  $\text{mg}/\text{cm}^2$  is  $q = \Delta m/A$ . With glass chips, a change of the surface area  $A$  with time need not be taken into account. The cumulative amount of matter released to the solution is  $c$  in  $\text{mg}/\text{cm}^3$ ,  $c = q \cdot s$ . It may be present in dissolved form or as solid precipitates. Especially upon longer exposure times, crusts of precipitates form on top of the glass surface. These crusts are removed by a rubber wiper prior to weighing. Removal is always possible in an unambiguous way, even if the layer adheres to the glass like ice on a car windshield.

### *Elemental Analysis of the Solution*

The concentrations  $c_e$  of elements  $e$  released from the glass to the solution are analyzed by standard analytical techniques (ICP, AAS, AES, etc.). The elemental mass losses per surface area are given by  $q_e = c_e/s$ . When dividing  $q_e$  by the mass

fraction  $y_e$  of element  $e$  in the glass, then the normalized specific elemental mass losses  $q_e^* = q_e/y_e$  are obtained. Upon congruent dissolution and in the absence of any precipitates, all  $q_e^*$  are identical to the gravimetric mass loss  $q$ . If  $q_e^* > q$ , then element  $e$  is preferentially released from the glass. If  $q_e^* < q$ , then element  $e$  is enriched in the glass surface or takes part in the formation of a precipitate. Elements known to not forming precipitates, like boron, may be used as indicator elements for the overall progress of glass dissolution. After a short initial phase, during which minor amounts of boron are preferentially released to a depth of a few 10 nm,  $q_B^* = q$ . This is an excellent cross-check of the gravimetric results. The method may be used, too, if a corrosion crust is left on top of the glass for further investigations.

### *Analysis of the Residual Glass*

SEM–EDX may be used to check the overall appearance of a corroded sample, and to analyze the nature of the crust on top of the glass, if any. The lateral differentiation of the surface at the nm scale may be investigated by AFM (atomic force microscopy) [30]. The major interest of investigation, however, lies on the concentration profiles of individual elements in the sub-surface zone of the glass. Depth profiles of the elemental distribution within sub-surface layers have been studied by instrumental analysis like XPS (X-ray photoelectron spectroscopy), SIMS (secondary ion mass spectroscopy) [31], SNMS (secondary neutral particles mass spectroscopy) [24], the latter three in combination with Ar ion sputtering, and NMP (nuclear microprobe) [32, 33], as well as by wet-chemical methods [34]. The depth resolution of the instrumental techniques is better than 5 nm. NMP has been used to trace hydrogen depth profiles in corrodes glasses in a fully quantitative way. This method requires the use of an accelerator directing a beam of  $^{15}\text{N}$  ions toward the glass surface. It is based on the nuclear reaction  $^{15}\text{N} + ^1\text{H} \rightarrow ^{12}\text{C} + ^4\text{He} + 2\gamma$ . The depth resolution stems from the extremely narrow resonance interval of  $6385 \pm 0.005$  meV of the reaction with the incoming  $^{15}\text{N}$  beam; the response energy of the  $\gamma$  quants is 4.43 meV. An example will be given in Sect. 2.3. Beyond this, NMP can be applied to very few kinds of atoms only. The other instrumental methods are much more versatile chemically. However, results are obtained in terms of relative intensities only. Elemental profiles in the sub-surface layer have been measured successfully by a sequential wet-chemical etching technique, too [34]. For this purpose, an etching solution composed of 5% of an aqueous system (containing 0.5% HF and 1%  $\text{HNO}_3$ ) plus 95% isopropanol, kept at a temperature of  $-10$  °C, is used. Etching steps of 20 s yield reproducible dissolution depths of 5–15 nm, depending on the glass composition. By consecutive chemical analysis of the solution after each step, elemental depth profiles are obtained. The depth resolution is about 5–10 nm; the results are obtained in terms of absolute amounts, not as relative intensities. In general, the shapes of the elemental depth profiles resemble complex diffusion profiles [9]. Starting from the interface solution/glass, they consist of a transition range (often with enhanced structural compaction), a range of approx. constant water content as well as constant OH– $\text{H}_2\text{O}$  ratio, and a transition range to the bulk [26]. Depending on glass composition, the relative extensions of these ranges may differ considerably.

The above compilation summarizes the most successful methods, but it is not complete. Many other methods, like IR reflection spectroscopy, Rutherford back-scattering, and small-angle X-ray scattering have been used in the characterization of corroded glass surfaces, however, with less success than the ones compiled above.

## 2.3 Sub-surface Layers

It is the primary focus of this section to highlight the state of the sub-surface zone and to clearly distinguish it from other phenomena. An emphasis is laid upon the discussion of the local equilibria involved rather than discussing the kinetics of the processes by which the zone is formed. This will be done in Sect. 2.5. Every glass exposed to an aqueous solution develops a sub-surface zone differing in its chemical composition from the bulk glass. In an earlier paper, Hench [35] had proposed a qualitative classification of sub-surface zones, which by and large reflects the different options expected from an incongruent dissolution process. As, e.g., suggested by Doremus [9, 36], the sub-surface zone should be clearly distinguished from other types of layers (often termed “reaction layers”, “precipitated layers”, “back precipitation layers”) developing at the glass surface. Moreover, the indiscriminate use of the term “gel layer” for any kind of layer observed at the glass surface should be avoided. It is true, in specific cases, e.g., for silica glass, the sub-surface zone is established solely by the penetration of water molecules into the bulk material. But in general, ion exchange between glass and solution is an important ingredient to the formation of the zone.

Much information is obtained from experiments performed in water labeled by isotopes  $^2\text{H} = \text{D}$ , or  $^{18}\text{O}$ , or both. In soda-lime glasses, the exchange ratio  $\text{D}:\text{Na}$  is found to assume values between 1 and 3. Thus it is concluded that in water neither a pure  $\text{Na}^+$  versus  $\text{H}_3\text{O}^+$  nor  $\text{Na}^+$  versus  $\text{H}^+$  exchange takes place. However, irrespective of this, it is always the mobility of the proton which determines the rate of ion exchange [25]. Bear et al. [27] found that considerably more labeled  $^{18}\text{O}$  in comparison to  $\text{D}$  was incorporated in soda-lime silicate and borosilicate glass, crystalline albite, and quartz exposed to  $\text{D}_2^{18}\text{O}$ , whereas the  $^{18}\text{O}:\text{D}$  ratios were consistent with the amount of incorporated water for fused silica and glassy albite. The former findings can be explained by a dynamic equilibrium between incorporated molecular water and siloxane bonds [37], and a relatively fast exchange of water molecules between the sub-surface zone and the solution, or even with atmospheric water [25]. The reconstruction of the networks of both silicate glasses and crystalline silicates by the condensation of initially formed silanol groups to siloxane bonds and interstitial water has been frequently addressed [26]. Reconstruction yields a network with an enhanced connectivity [38], eventually a structural compaction of the outermost range of the zone [39]. Although in the initial stage, the depleted zone may temporarily maintain its original network structure, it inevitably undergoes restructuring [40]. Tomozawa et al. [41] used small-angle X-ray scattering to demonstrate that the sub-surface zone may be phase separated. Summarizing the information

compiled above, we may draw a number of conclusions on the nature of the sub-surface zone: It is characterized by relatively high amounts of—mostly molecular—interstitial water which is highly mobile and forms a percolating structure within the glass network. It thus resembles what Liesegang termed a “gel” as early as 1897 [42]. Liesegang had shown that within gels, the same kind of chemistry takes place as within aqueous solutions; differences consist in the absence of buoyancy effects (e.g., in the case of precipitation), eventually in different rate constants of individual reactions. Liesegang’s conclusions comprise, in specific, the fundamental reactions of hydrolysis, protolysis, neutralization, and proton transfer, which are altogether based on the proton as the rate controlling entity. The reactions just mentioned are among the fastest chemical reactions found in condensed matter, with rate constants of the order of  $10^{11} \text{ s}^{-1}$  (for comparison: the Brownian frequency at room temperature is  $6 \times 10^{13} \text{ s}^{-1}$ ). Thus we may conclude that the sub-surface zone of a corroded glass is characterized by well-established local chemical equilibria. This goes together well with the findings that the depletion of elements from the zone does not follow the categories of network former versus network modifier, but rather the elemental solubilities in water.

Figure 2.3 shows a textbook example of the corrosion mechanisms of a simple sodium silicate glass, comprising two main mechanisms, i.e., matrix dissolution and leaching. Matrix dissolution proceeds at a constant dissolution velocity  $v$ . It is based on the dissolution of  $\text{SiO}_2$  in water. The second mechanism, leaching, is an exchange between the protons  $\text{H}^+$  from the solution and the  $\text{Na}^+$  ions in the glass matrix. Empirically, it proceeds like a diffusion process with an effective diffusion coefficient of the order of  $D \approx 1 \times 10^{-14} \text{ cm}^2/\text{s}$ . During the first stages of corrosion, leaching dominates, and an ion exchange zone is formed. The exchange depth  $L_D$  develops like  $L_D \approx \sqrt{(D \cdot t)}$ , i.e., it slows down with increasing exchange depth. When the shift velocity of the internal boundary between ion exchange zone and bulk glass approaches  $v$ , then the corrosion process becomes stationary and proceeds by a linear time law. Then, the depth of the exchange zone assumes a stationary value  $L_D = D/v$ , where  $v$  may be derived from the cumulative specific mass loss  $q$  and the glass density  $\rho$ ,  $v = q/\rho$ . As a consequence, the determination of  $L_D$  allows one to determine the effective diffusion coefficient.

From a mechanistic perspective, however, the view of an ionic exchange process  $\text{H}^+ \leftrightarrow \text{Na}^+$  or  $\text{H}_3\text{O}^+ \leftrightarrow \text{Na}^+$  is misleading. After all,  $\text{H}^+$  is not an ion, but an elementary particle. In aqueous media as well as in the matrix of oxide glasses, it allocates itself within the electron cloud of the oxygen. The sequence  $\text{O}^{2-}$ ,  $\text{OH}^-$ ,  $\text{H}_2\text{O}$ ,  $\text{H}_3\text{O}^+$  represents entities with decreasing size, very different from the situation with an entity  $\text{Na}^+$ . Proton transport over distances beyond the immediate atomic neighborhood does not require the transport of an individual  $\text{H}^+$  in the same way as electron transport through a Cu wire does not require the transfer of an individual  $e^-$  from one end to the other. It is merely the charge excess that is passed through (Grotthuss mechanism). This, again, is fundamentally different from the transport of  $\text{Na}^+$  ions which move as individual entities.

The leaching rates observed in  $\text{D}_2\text{O}$  as compared to  $\text{H}_2\text{O}$  slow down by a factor of 1.4. Since such isotope effects depend on  $\sqrt{m}$ ,  $m =$  mass of the transferred entity,

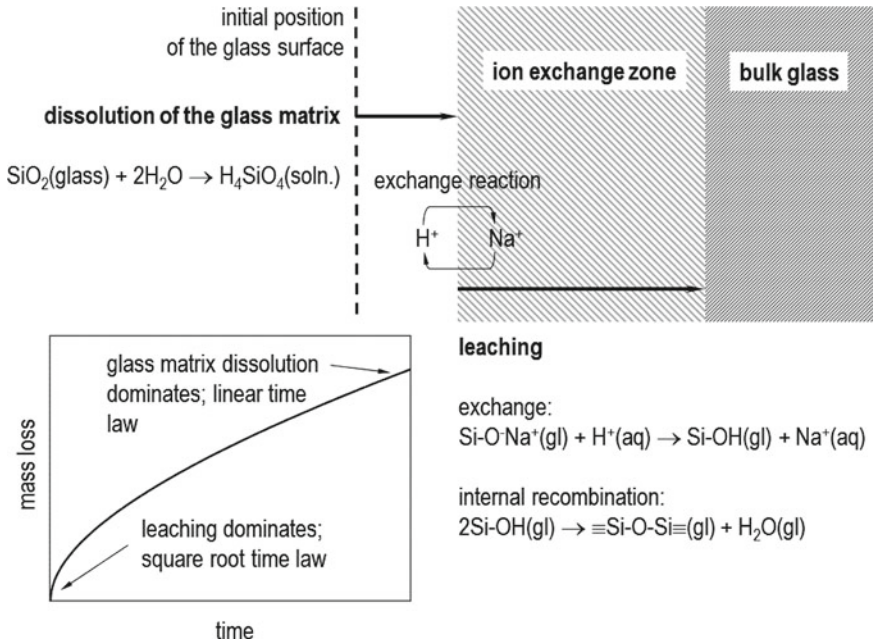


**Fig. 2.3** Illustration of the main corrosion mechanisms of a simple sodium silicate glass, comprising network dissolution and leaching; the lower left insert shows the mass loss as a function of time in arbitrary units

these experiments clearly show that it is the transfer of H<sup>+</sup>, not of H<sub>2</sub>O or H<sub>3</sub>O<sup>+</sup>, which governs the elementary mechanism. The amounts of H<sup>+</sup> exchanged per released Na<sup>+</sup> ion assume non-stoichiometric values 1 < ν < 3. Thus, the effective exchange balance reads H<sup>+</sup> + 1/2 · (ν - 1)H<sub>2</sub>O ↔ Na<sup>+</sup>. Moreover, as revealed by experiments in D<sup>18</sup>O, an about six times higher amount of oxygen than 1/2 (ξ - 1) is eventually found in the leached layer. This is a clear indication that the internal recombination reaction (Fig. 2.3) is a highly dynamic backward-forward reaction, and that the water molecules formed within the glass structure easily exchange with water molecules from the solution. In conclusion, we have to replace the simple textbook example in Fig. 2.3 by a more adequate concept. This is done in Fig. 2.4. This figure illustrated five mechanisms. They are compiled in the following list and complemented by further mechanisms:

- (1) *Surface charge balance*: This mechanism is equal to the fundamental reaction at the surface of a glass electrode. In condensed phases, it does not matter if we write <sup>-</sup>O-Si≡ or HO<sup>-</sup>HO-Si≡ in the case of negative charging, and H<sub>3</sub>O<sup>+</sup>HO-Si≡ or H<sup>+</sup>HO-Si≡ in the case of positive charging, respectively. It is the charge balance that counts. The surface charge balance is a true thermodynamic equilibrium. It is established within 1–10 ms and sustained by charge transfer rates of 1–10 μA/cm<sup>2</sup>.

- (2) *Mobilization of Na<sup>+</sup> ions*: The excess charge of a proton accidentally entering the electron cloud of an oxygen atom of the glass surface forms a ≡Si–OH group at once. The excess charge mobilizes the Na<sup>+</sup> ion and pushes it out of the glass matrix. By virtue of the Grotthuss mechanism, this process takes place across the entire sub-surface zone and continues at the boundary to the bulk glass.
- (3) *Matrix dissolution*: The dissolution of the glass matrix proceeds in the same way as already sketched in Fig. 2.3. The view will be extended in Sect. 2.5.
- (4) *Internal recombination*: The highly dynamic back and forth recombination reaction increases the connectivity in the sub-surface zone and generates interstitial water molecules. As compared to the bulk glass, very few non-bridging oxygens are present in the sub-surface zone. In fact, the zone is converted to a gel in the sense of physical chemistry, characterized by two percolating structures, i.e., the SiO<sub>2</sub> network and the H<sub>2</sub>O molecules. The gel is as rigid as the glass, but it is a zone where all reactions familiar from aqueous solutions (hydrolysis, protolysis, neutralization, precipitation) may take place, albeit at a much reduced rate. At the end of the nineteenth century, Liesegang [42] demonstrated this principle with acid–base and precipitation reactions in agar gels.
- (5) *Exchange with the solution*: Ions and water molecules continue to exchange between the gel zone and the solution. This proceeds at an effective diffusion coefficient of  $D \approx 1 \times 10^{11} \text{ cm}^2/\text{s}$ , significantly higher than the diffusion coefficient describing the shift of the boundary between sub-surface zone and bulk glass.
- (6) *Densification*: This mechanism is not sketched in Fig. 2.4. The outermost layer of the sub-surface zone condenses to a dense silica network. No glass technologist ever designed this, but in fact, this densification is a self-improvement mechanism rendering a glass, once exposed to water, much more durable than an as-produced glass. Float glass producers are very well aware of the sensitivity of the freshly produced glass, and special strategies of careful handling and stacking are applied.

Figure 2.5 presents elemental depth profiles in corroded glasses. Panel **a** shows the results for a glass with 74 SiO<sub>2</sub>, 10 CaO, and 14 Na<sub>2</sub>O (by mol) corroded in D<sub>2</sub>O at 85 °C,  $s = 0.028 \text{ cm}^{-1}$  for 15 min [24]. The depth of the exchange zone extends to 60 nm. At the very surface, the nature of the zone changes. This is the densified zone mentioned above. Panel **b** shows H profiles as determined by nuclear microprobe. The results refer to a simulated (inactive) nuclear waste glass corroded in high ionic strength solution under hydrothermal conditions at 200 °C and  $s = 0.034 \text{ cm}^{-1}$  for up to 1 year [43, 44]. The exchange layer reaches a stationary depth of only  $L_D = 200 \text{ nm}$ . With a specific mass loss after 360 days of  $q(360 \text{ d}) = 57 \text{ mg/cm}^2$  and a glass density of  $\rho = 2.8 \text{ g/cm}^3$ , the glass has dissolved to a depth of  $L = q/\rho = 200 \text{ }\mu\text{m}$ , corresponding to an average dissolution velocity of  $v = 6.6 \times 10^{-10} \text{ cm/s}$  and an effective diffusion coefficient  $D = L_d \cdot v = 1.3 \times 10^{-14} \text{ cm}^2/\text{s}$ .

In another test series [45], glasses of composition 72 SiO<sub>2</sub>, 14 M<sub>x</sub>O<sub>y</sub>, 14 Na<sub>2</sub>O (by mol) were exposed to D.I. water at 98 °C,  $s = 0.01 \text{ cm}^{-1}$ , for time intervals of 1, 2, 4, 8, 24, 48, and 96 h. Me<sub>x</sub>O<sub>y</sub> denotes CaO, ZnO, B<sub>2</sub>O<sub>3</sub>, or Al<sub>2</sub>O<sub>3</sub>, and the glasses are



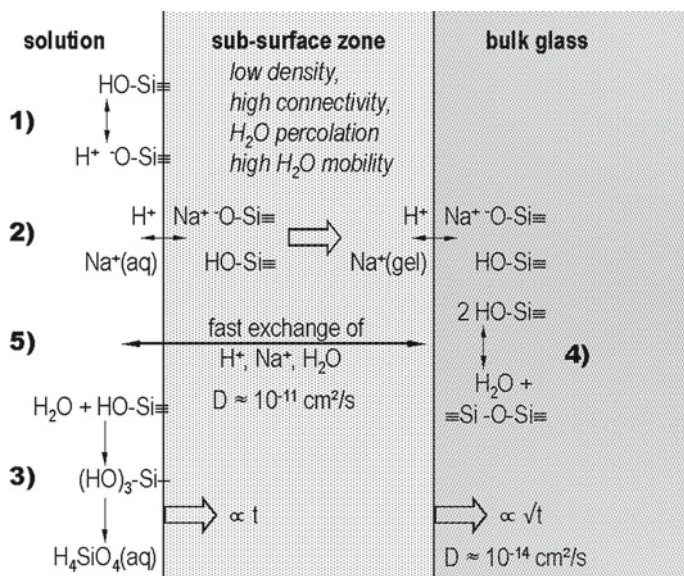


**Fig. 2.4** Illustration of five fundamental mechanisms taking place at the surface of a sodium containing silicate glass during exposure to water; (1) surface charge equilibrium, (2) ion exchange at the glass surface and further at the transition zone between sub-surface zone and bulk glass, (3) dissolution of the  $\text{SiO}_2$  matrix, (4) internal recondensation at the transition between sub-surface zone and bulk glass, (5) fast exchange of ions and molecular water between solution and sub-surface zone

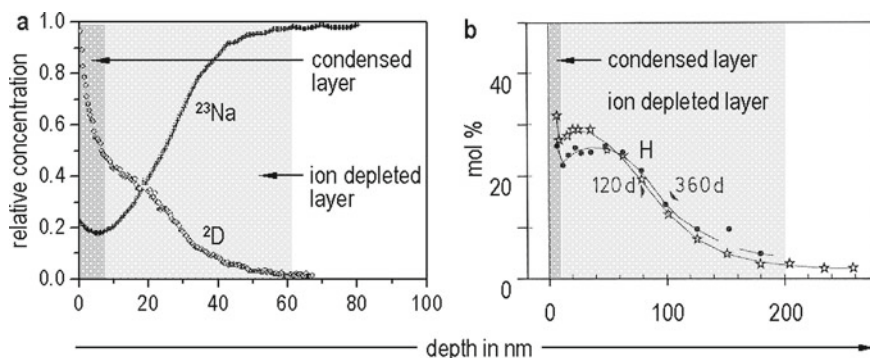


**Fig. 2.5** **a** Depth profiles of D and Na in the surface of glass 74  $\text{SiO}_2$ , 10  $\text{CaO}$ , 16  $\text{Na}_2\text{O}$  (by mol) exposed for 15 min to  $\text{D}_2\text{O}$  at 85 °C,  $s = 0.028 \text{ cm}^{-1}$  [24]. **b** Depth profiles of H in the surface of a simulated waste glass corroded for 120 and 360 d in a high ionic strength solution under hydrothermal conditions at 200 °C,  $s = 0.034 \text{ cm}^{-1}$  [44]

named NCS, NZS, NBS, and NAS, respectively. After 24 h already, NCS and NBS reached stationary conditions, with the normalized elemental releases  $q_{Si}^*$ ,  $q_{Ca}^*$ ,  $q_B^*$ , and  $q_{Na}^*$  running parallel to the cumulative mass loss  $q$ . During the initial 24 h, pH rose to 9.8 and 6.8, respectively, and maintained this value. By contrast, NZS and NAS did not reach stationary conditions. Although  $q_{Si}^*$ ,  $q_{Zn}^*$ ,  $q_{Al}^*$  ran parallel to  $q$  after 24 h, this was not the case with  $q_{Na}^*$ , which continued to increase far beyond  $q$ . The pH after 24 h reached 8 and 7, respectively, but kept increasing slightly. Figure 2.6 shows the elemental profiles and the local densities as obtained by HF etching after 96 h. The matrix dissolution depths  $L$  after 96 h are also given in Fig. 2.6. They differ significantly among the glasses; NCS is the most unstable glass (due to the shift to high pH), while NAS is the most stable one. For the stationary cases, effective diffusion coefficients were calculated from the depths  $L_D$  of the exchange zones. For NCS,  $D$  assumes a value in the order of  $10^{-14}$  cm<sup>2</sup>/s, while for NBS,  $D$  is about one order of magnitude smaller.

As a first observation, all glasses exhibit a pure and highly dense silica layer at the very surface. In NCS (panel a), this is followed by a SiO<sub>2</sub>-CaO layer. If CaO reaches the bulk concentration, Na<sub>2</sub>O starts to increase until bulk composition is

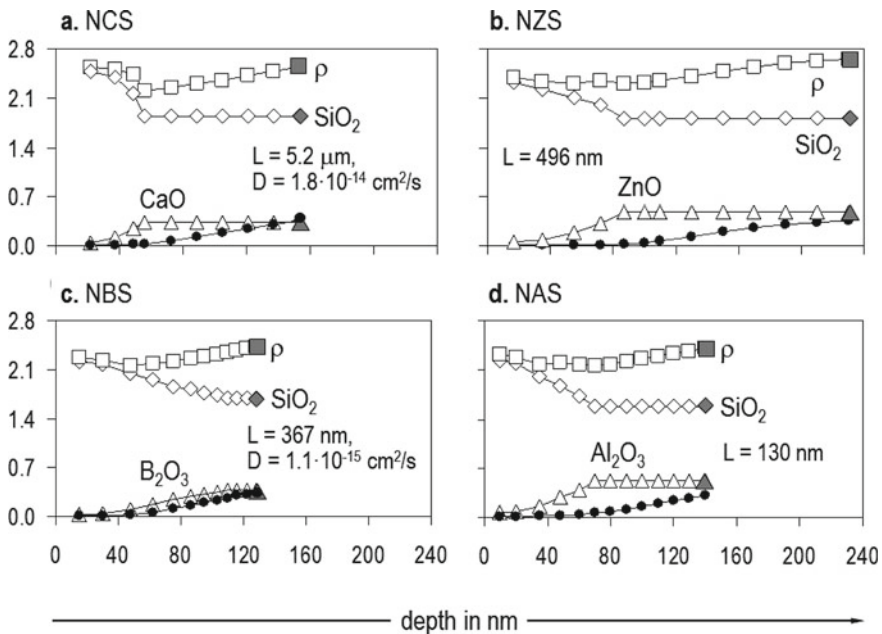


**Fig. 2.6** Local densities and elemental depth profiles [45] in glasses 72 SiO<sub>2</sub>, 14 M<sub>x</sub>O<sub>y</sub>, 14 Na<sub>2</sub>O (by mol) after 96 h of exposure to D.I. water at 98 °C,  $s = 0.01$ ; M<sub>x</sub>O<sub>y</sub> = CaO (glass NCS, panel a), ZnO (glass NZS, panel b), B<sub>2</sub>O<sub>3</sub> (glass NBS, panel c), and Al<sub>2</sub>O<sub>3</sub> (glass NAS, panel d); gray symbols = bulk values; Na<sub>2</sub>O reaches the bulk value in NCS and NBS, however, not in NZS and NAS;  $L$  = matrix dissolution depth, i.e. the positions at which the diffusion profiles start at depth = 0;  $D$  = effective coefficient of Na<sup>+</sup>



reached at 155 nm depth. A similar behavior is found with NZS (panel **b**), with the exception that Na does not reach the bulk value. Panel **c** provides an explanation of why a highly soluble oxide like  $B_2O_3$  is able to enhance the chemical durability. This is because Na and B are, so to speak, released *en pas de deux*. The low mobility of the highly charged  $B^{3+}$  ion thus slows down the mobility of  $Na^+$ . In glass NAS (panel **d**), the densified silica layer is followed by a  $SiO_2-Al_2O_3$  zone while  $Na_2O$  continues being leached out. This is a behavior well-known from the differentiation of feldspatic minerals to clay minerals. The question remains why  $Al^{3+}$  and  $Na^+$  are not released *en pas de deux*. This is attributed to the fact that protons may replace the position of  $Na^+$  in a  $Na^+[AlO_4]$  unit while this is not possible in a  $Na^+[BO_4]$  unit. So the mobilities of Na and B remain strictly correlated in the latter case while they are decoupled in the former one.

The issue of the fundamental mechanisms active in the glass surface will be resumed in Sect. 2.5 in connection with transition state theory. Meanwhile, we have to clarify the role of glass composition on chemical durability in a systematic way, which remained vague until here.

## 2.4 Thermodynamic Approach to the Hydrolytic Stability

In his book “Chemistry of Glasses” [8], Paul introduced a thermodynamic approach to the chemical durability of glasses. His approach was adopted [46, 47] and applied to radioactive waste glasses containing a large number of oxides. The innovation of the approach chiefly consisted in a stringent thermodynamic description of the solution containing the dissolved glass constituents. The foundation for this description had been laid before by Pourbaix [13]. In these early approaches, the glasses were described by the weighted sums of metasilicates and oxides, which is a crude approach at best. The idea to invoke a more concise description of glasses arose during the evaluation of a large number of experiments [43] and was developed to a general description frame [48, 49]. Panel **a** of Fig. 2.7 summarizes the details of the approach.  $G^f_x$  denotes the Gibbs energy of formation from the elements of the isochemical polycrystalline system corresponding to a given glass composition, and  $G^{vit}$  denotes the small energetic difference between the polycrystalline system and the glass. The energy level of the glass is  $G_{GL}$ , GL = glass. For the details of the thermodynamic description of multicomponent glasses, see Chap. 2 in this book. The quantity  $G^f_{aq}$  is the Gibbs energy of the aqueous system. The index aq denotes the thermodynamic state “dissolved in aqueous solution”.  $G^f_{aq}$  is given in the reference state “formation from elements”. Consequently, all other Gibbs energies are referred to as the reference “formation from the elements”, too, even if this is not highlighted by the superscript *f*. To complete the picture, panel **b** of Fig. 2.7 illustrates how time enters the scene. Silicon atoms released from a silicate glass to the solution have to pass through an energetically unfavorable state (termed: transition state, transient state, or activated complex) characterized by an activation energy  $E_A$ . The occupation density of this transient state is governed by an equilibrium with

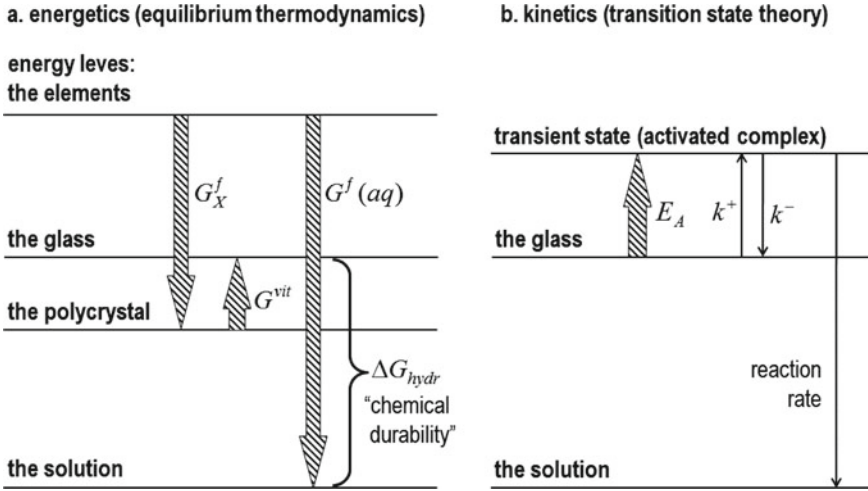


**Fig. 2.7** **a** Gibbs energy levels of glass, the isochemical polycrystalline system, and the aqueous solution formed by glass dissolution. **b** Kinetics of the glass dissolution process, passing through the transient state of an activated complex;  $E_A$  = activation energy;  $k^+$  and  $k^-$  = forward and backward reaction constant, respectively

equilibrium constant  $K^\# = k^+/k^-$ ;  $k^+$  and  $k^-$  denote a forward and backward reaction rate constant, respectively. This equilibrium may be described by a pH-dependent surface loading  $\theta$  of the glass with electric charges;  $0 < \theta < 1$ . The issue will be resumed in Sect. 2.5. What remains to be done with respect to the thermodynamic approach is to describe the state of the aqueous system containing the dissolved glass constituents. Its overall energy level is  $G_{aq,GL}$ . The driving force of glass corrosion is readily determined as

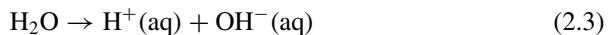
$$\Delta G_{hydr} = G_{aq,GL} - G_{GL}. \tag{2.1}$$

We may decide to adopt  $\Delta G_{hydr}$  as a quantitative representation of chemical durability.

For the description of aqueous solutions, a specific state of matter has been defined. It is the state “dissolved in water at high dilution” and is labeled by “aq”. Its description rests on two fundamental equilibria, i.e., the decomposition reaction of water



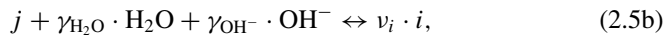
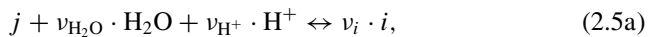
with  $\Delta G_{decomp} = 474.36$  kJ/mol, and the dissociation reaction



with  $\Delta G_W = 79.88$  kJ/mol, both at 25 °C, 1 bar. The corresponding equilibrium constants, calculated as  $K = \exp\left(-\frac{\Delta G}{RT}\right)$ , are  $\log K_{\text{decomp}} = -83.1$  and  $\log K_W = -14.0$ , respectively. Equations (2.2) and (2.3) constitute the stability plot of water (Fig. 2.8). The abscissa displays the pH value,  $\text{pH} = -\log [\text{H}^+]$ , while the ordinate displays the Gibbs energy in terms of a voltage  $\Phi$  (electromotive force) with  $G = z \cdot F \cdot \Phi$ ;  $F$  = Faraday's constant = 96,500 As/mol,  $z$  = number of transferred electrons = 4. Gibbs energies in the state aq are normalized to the potential of the normal hydrogen electrode ( $\text{pH} = 0$ ,  $P(\text{H}_2) = 1$  bar) representing the equilibrium



at 25 °C, 1 bar. Thus, the Gibbs energy of the proton is  $G_{\text{H}^+} = 0$ . All tabulated Gibbs energies of aqueous species are normalized to this state. From Fig. 2.8, one may read at which voltage, at a given pH value, water starts to decompose. Water is stable in-between the bold lines only. Water equilibrated with air (21% O<sub>2</sub>) has  $\log [\text{O}_2] = -0.67$ ; so it comes close to the upper bold line. The water stability diagram can be extended to the states of aqueous species of any element exposed to water (so-called Pourbaix diagram). This is shown in Fig. 2.9 for the example of Fe. In water, Fe may be present as ferric or ferrous ion, or as solid precipitates Fe(OH)<sub>3</sub> and Fe(OH)<sub>2</sub>, respectively. In the presence of metallic iron, water decomposes and releases H<sub>2</sub>(g), especially at low pH. Above pH = 6, the metal surface is partially passivated by a thin Fe(OH)<sub>2</sub> layer (partially only, because the layer is not dense). The H<sub>2</sub>(g) release rate is very small; the release is hardly noticed by the naked eye. With other metals, more dramatic effects are observed. The reader may remember from school that significant rates of hydrogen formation are reached when Zn granules are dropped in a test tube containing concentrated HCl. Figure 2.9 provides a solid reason that glass corrosion experiments should not be performed in metal vessels. We now leave the  $\Phi - \text{pH}$  plots and deal with the formation of aqueous systems in air-saturated water, i.e., in the vicinity of the upper stability limit of water. Then, the formation of species may be described as a function of pH alone. Let  $j$  be an oxide component and  $i$  an aqueous species formed from oxide  $j$ . The equilibrium between oxide  $j$  and species  $i$  is presented in an alternative way by two equations, depending on whether the oxide dissolves via protolysis or hydrolysis. The reaction equilibria for protolysis and hydrolysis, respectively, read:



with stoichiometric coefficients  $\nu$  and  $\gamma$ . Formally, Eq. (2.5b) may be converted to Eq. (2.5a) by putting  $\nu_{\text{H}_2\text{O}} = \gamma_{\text{H}_2\text{O}} + \gamma_{\text{OH}^-}$  and  $\nu_{\text{H}^+} = -\gamma_{\text{OH}^-}$ . In other words, Eq. (2.5a) comprises both protolysis and hydrolysis if we allow  $\nu_{\text{H}^+}$  to assume both positive and negative values. This yields a unified description easily presented as a function of pH. The Gibbs energy of the equilibrium is

$$\Delta G_{j \leftrightarrow i} = \nu_i \cdot G_i - G_j - \nu_{\text{H}_2\text{O}} \cdot G_{\text{H}_2\text{O}} - \nu_{\text{H}^+} \cdot G_{\text{H}^+}, \tag{2.6}$$

where  $G_{\text{H}^+} = 0$ . The equilibrium constant  $K_{j \leftrightarrow i}$  is given as

$$K_{j \leftrightarrow i} = \exp\left(-\frac{\Delta G_{j \leftrightarrow i}}{RT}\right) = \frac{[i]^{\nu_i}}{[j] \cdot [\text{H}_2\text{O}]^{\nu_{\text{H}_2\text{O}}} \cdot [\text{H}^+]^{\nu_{\text{H}^+}}} \tag{2.7}$$

Resolving Eq. (2.7) for  $[i]$  yields

$$\log[i] = \log a(i) = \frac{1}{\nu_i} \cdot \log K_{j \leftrightarrow i} - \frac{\nu_{\text{H}^+}}{\nu_i} \cdot pH, \tag{2.8}$$

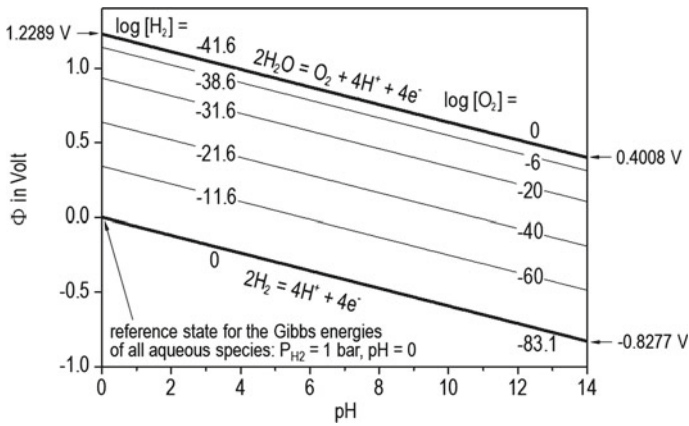


Fig. 2.8 Stability diagram of water

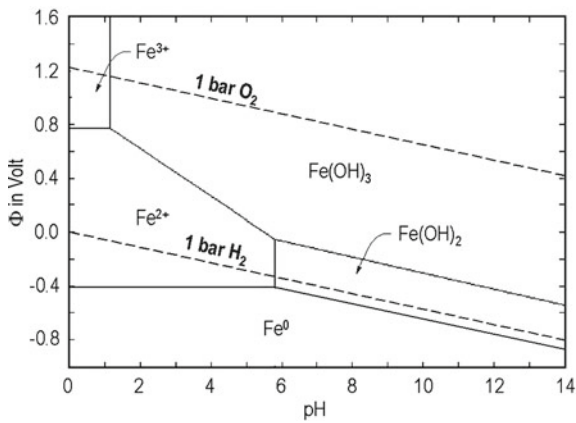


Fig. 2.9 Stability diagram (Pourbaix diagram) of the element Fe in aqueous solution

where  $[i]$  and  $a(i)$  denote the activity of  $i$  in the systems, which is approx. equal to the concentration at high dilution. With a complete set of different aqueous species  $i$  formed from oxide  $j$ , the relative distribution  $x(i)$  of any individual species  $i$ ,  $0 \leq x(i) \leq 1$ , is obtained by

$$x(i) = \frac{[i]}{\sum [i]} \quad (2.9)$$

The sum in the denominator extends over all species formed from oxide  $j$ . In Table 2.1, the procedure is demonstrated for the aqueous species formed by the dissolution of  $\text{SiO}_2$ . In the absence of  $\text{Na}^+$  ions, nine different species are formed. The calculation procedure is a little cumbersome, but not difficult.

Figure 2.10 summarizes the results. Panel **a** shows the activities of species  $a(i)$  in a logarithmic plot as function of pH. As complicated as the situation may appear from Table 2.1, the aqueous state of  $\text{SiO}_2$  is dominated by three species, namely, by  $\text{SiO}_2^0$  (undissociated siliceous acid comprising both  $\text{H}_4\text{SiO}_4^0$  and dimeric  $\text{H}_2\text{SiO}_3^0$ ), the univalent species  $\text{H}_3\text{SiO}_4^-$  and the tetravalent species  $[\text{H}_2(\text{H}_2\text{SiO}_4)]^{4-}$ . The latter species is an entity of approx. 2 nm size and may be perceived as a borderline case between an ionic species and a charged colloidal particle. Panel **b** illustrates the relative species distribution. At their equivalence points, the coexistence of two predominant species constitutes a buffer system. This is the reason why the pH value in experiments performed on commercial soda-lime silicate glasses always approaches  $\text{pH} = 9.8$ , essentially independent of the actual glass composition. When

**Table 2.1** Gibbs energies  $\Delta G_{j \leftrightarrow i}$  of the reaction of oxide  $j =$  vitreous silica to aqueous species at 25 °C,  $j + \nu_{\text{H}_2\text{O}} \cdot \text{H}_2\text{O} + \nu_{\text{H}^+} \cdot \text{H}^+ \leftrightarrow \nu_i \cdot i$ ;  $\nu =$  stoichiometric coefficients in the formation equilibrium;  $\log K_{j \leftrightarrow i} = -\Delta G_{j \leftrightarrow i}/(RT \cdot \ln 10)$ ;  $K_{j \leftrightarrow i} =$  equilibrium constant;  $RT \cdot \ln 10 = 5.70769$  kJ/mol

Reaction equation	$\Delta G_{j \leftrightarrow i}$ (kJ/mol)	$\log K_{j \leftrightarrow i}$	$\nu_i$	$\nu_{\text{H}_2\text{O}}$	$\nu_{\text{H}^+}$	
$\text{SiO}_2(\text{gl}) = \text{SiO}_2^0(\text{aq})$	15.600	-2.733	1	0	0	
$\text{SiO}_2(\text{gl}) + 2\text{H}_2\text{O}$	$= \text{H}_3\text{SiO}_4^- + \text{H}^+$	71.370	-12.504	1	2	-1
	$= \text{H}_2\text{SiO}_4^{2-} + 2 \text{H}^+$	137.900	-24.160	1	2	-2
	$= \text{HSiO}_4^{3-} + 3 \text{H}^+$	206.813	-36.234	1	2	-3
	$= \text{SiO}_4^{4-} + 4 \text{H}^+$	275.130	-48.203	1	2	-4
	$= 1/4 \cdot \text{H}_6[(\text{H}_2\text{SiO}_4)_4]^{2-} + \text{H}^+$	35.051	-6.141	1/4	2	-1/2
	$= 1/4 \cdot \text{H}_4[(\text{H}_2\text{SiO}_4)_4]^{4-} + \text{H}^+$	66.872	-11.716	1/4	2	-1
$\text{SiO}_2(\text{gl}) + \text{H}_2\text{O}$	$= \text{HSiO}_3^- + \text{H}^+$	80.724	-14.143	1	1	-1
	$= \text{SiO}_3^- + 2 \text{H}^+$	147.668	-25.872	1	1	-2
$\text{SiO}_2(\text{gl}) + \text{H}_2\text{O} + \text{Na}^+$	$= \text{NaHSiO}_3^0(\text{aq}) + \text{H}^+$	62.990	-11.036	1	1	-1

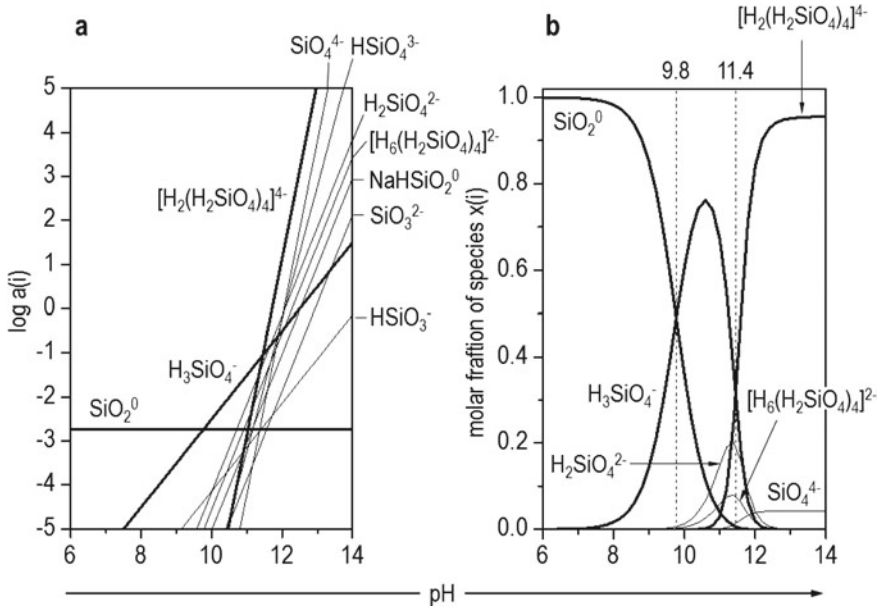


**Fig. 2.10** **a** Activity plot of species formed from SiO<sub>2</sub> in aqueous solutions. **b** Species plot: relative species distribution of SiO<sub>2</sub> dissolved in aqueous solution

fine granules of such glasses are exposed to water for extended times, pH approaches 11.4.

In Table 2.2, data of aqueous species are compiled for a large number of oxides, allowing one to specify the aqueous system of all kinds of glasses. The data are given with respect to the state of infinite dilution in water, or at a concentration of 1 mol/L for readily soluble substances. Since 1 L of H<sub>2</sub>O corresponds to a quantity of matter of 55.51 mol, distinguishing more precisely between the two cases is irrelevant here. The reader is cautioned to not expand the data sets of individual oxides by adding data of individual aqueous species found elsewhere in literature. Rather, a consistency check for the consistency of the entire set of species is required. For example, some sources comprise Gibbs energies of the species  $\text{H}_4\text{SiO}_4^0(\text{aq})$  as  $-1782.120$  kJ/mol which turns out to be identical with the value  $\text{SiO}_2^0(\text{aq}) + 2\text{H}_2\text{O}$ . Some data tables quote data for undissociated dimeric siliceous acid  $\text{H}_3\text{SiO}_3^0(\text{aq})$ ; data vary from  $-1062.8$  to  $-1079.5$  kJ/mol which, on average, is in fair agreement with  $\text{SiO}_2^0(\text{aq}) + \text{H}_2\text{O}$ . Therefore, undissociated siliceous acid is exclusively represented as  $\text{SiO}_2^0(\text{aq})$ , and no further data should be added. Likewise, some sources contain the species  $\text{AlO}_2^-(\text{aq})$  with a Gibbs energy of  $-823.411$  kJ/mol. Yet, this is identical with  $\text{Al}(\text{OH})_4^- - 2\text{H}_2\text{O}$ , hence, data for a new species  $\text{AlO}_2^-(\text{aq})$  must not be added to the set.

The calculation of aqueous species for a given oxide is performed in the way as demonstrated in Table 2.1 for SiO<sub>2</sub>: Write down Eq. (2.5a) for each species devolving

**Table 2.2** Gibbs energies  $G^f$  of formation from the elements in kJ/mol; **bold**: reference states of oxides, gases, and  $H_2O(l)$ ; **bold italic**: solid precipitates; *am* = amorphous; normal print: aqueous species

Species	$-G^f$	Species	$-G^f$	Species	$-G^f$	Species	$-G^f$
$CO_2(g)$	394.570	$P_2O_5(s)$	1349.570	$MgO(s)$	569.840	$Na_2O(s)$	376.740
$CO_2^0$	386.016	$H_3PO_4^0$	1142.650	<b><i>Mg(OH)_2</i></b>	833.746	$Na^+$	262.211
$HCO_3^-$	586.848	$H_2PO_4^-$	1130.391	$MgCO_3$	1012.110	<b><i>K_2O(s)</i></b>	322.200
$CO_3^{2-}$	527.895	$HPO_4^{2-}$	1089.263	$Mg^{2+}$	455.261	$K^+$	282.671
$SiO_2(s)$	854.910	$PO_4^{3-}$	1018.804	$MgOH^+$	638.064	<b><i>Rb_2O(s)</i></b>	299.960
<b><i>SiO_2(am)</i></b>	833.658	$H_4P_2O_7^0$	2032.160	$Mg(OH)_2^0$	769.438	$Rb^+$	283.270
$SiO_2^0$	1307.760	$H_3P_2O_7^-$	2026.830	$MgCO_3^0$	1002.486	<b><i>Cs_2O(s)</i></b>	308.300
$H_3SiO_4^-$	1251.990	$H_2P_2O_7^{2-}$	2003.410	$MgHCO_3^-$	1050.602	$Cs^+$	292.001
$H_2SiO_4^{2-}$	1185.460	$HP_2O_7^{3-}$	1961.710	<b><i>CaO(s)</i></b>	604.460	<b><i>Nd_2O_3(s)</i></b>	1721.700
$HSiO_4^{3-}$	1116.547	$P_2O_7^{4-}$	1919.200	<b><i>Ca(OH)_2</i></b>	897.008	<b><i>Nd(OH)_3</i></b>	1259.221
$SiO_4^{4-}$	1048.230	$H_5P_3O_{10}^0$	2921.670	<b><i>CaCO_3</i></b>	1128.760	$Nd^{3+}$	671.532
$H_6[H_2SiO_4]_4^{2-}$	5153.236	$H_4P_3O_{10}^-$	2923.190	$Ca^{2+}$	552.706	$Nd_2(OH)_2^{4+}$	1738.230
$H_4[H_2SiO_4]_4^{4-}$	5025.951	$H_3P_3O_{10}^{2-}$	2917.480	$CaOH^+$	716.970	$Nd(OH)^{2+}$	863.126
$HSiO_3^-$	1005.46	$H_2P_3O_{10}^{3-}$	2094.550	$Ca(OH)_2^0$	868.138	$Nd(OH)_4^-$	1407.096
$SiO_3^{2-}$	938.51	$HP_3O_{10}^{4-}$	2872.550	$CaCO_3^0$	1081.438	<b><i>MoO_3(s)</i></b>	655.778
<b><i>Al_2O_3(s)</i></b>	1583.150	$P_3O_{10}^{5-}$	2821.490	$CaHCO_3^-$	1145.035	$MoO_2^{2+}$	411.287
<b><i>Al(OH)_3(am)</i></b>	1137.630	<b><i>B_2O_3(s)</i></b>	1194.270	<b><i>SrO(s)</i></b>	562.680	$MoO_2(OH)^+$	645.884
$Al^{3+}$	492.000	$H_3BO_3^0$	968.638	<b><i>Sr(OH)_2</i></b>	881.987	$H_2MoO_4^0$	877.134
$Al(OH)^{2+}$	700.653	$H_2BO_3^-$	917.564	<b><i>SrCO_3</i></b>	1140.140	$HMoO_4^-$	866.632
$Al(OH)_2^+$	907.384	$HBO_3^{2-}$	845.695	$Sr^{2+}$	571.451	$MoO_4^{2-}$	838.055
$Al(OH)_3^0$	1111.061	$BO_3^{3-}$	769.182	$SrOH^+$	733.55	<b><i>Nb_2O_5(s)</i></b>	1765.82

(continued)

Table 2.2 (continued)

Species	$-G^f$	Species	$-G^f$	Species	$-G^f$	Species	$-G^f$
$\text{Al}(\text{OH})_4^-$	1305.410	$\text{TiO}_2(\text{s})$	889.940	$\text{Sr}(\text{OH})_2^0$	871.109	$\text{Nb}(\text{OH})_4^+$	1219.112
$\text{Fe}_2\text{O}_3(\text{s})$	739.960	$\text{TiO}(\text{OH})_2$	1058.552	$\text{SrCO}_2^0$	1087.338	$\text{Nb}(\text{OH})_5^0$	1459.692
$\text{Fe}(\text{OH})_3$	696.636	$\text{TiO}^{2+}$	577.392	$\text{BaO}(\text{s})$	528.690	$\text{Nb}(\text{OH})_6^-$	1714.614
$\text{Fe}^{3+}$	17.866	$\text{TiO}_2\text{OH}^-$	467.353	$\text{Ba}^{2+}$	547.518	$\text{HF}(\text{g})$	274.646
$\text{FeOH}^{2+}$	240.413	$\text{ZrO}_2(\text{s})$	1036.870	$\text{ZnO}(\text{s})$	318.470	$\text{F}_2(\text{g})$	0.000
$\text{Fe}(\text{OH})_2^+$	457.228	$\text{ZrO}(\text{OH})_2$	1303.316	$\text{Zn}^{2+}$	147.193	$\text{F}^-$	279.993
$\text{Fe}(\text{OH})_3^0$	670.695	$\text{Zr}^{4+}$	594.128	$\text{ZnOH}^+$	333.256	$\text{HF}^0$	298.110
$\text{Fe}(\text{OH})_4^-$	841.821	$\text{ZrO}^{2+}$	843.076	$\text{Zn}(\text{OH})_2^0$	535.385	$\text{HF}_2^-$	581.492
$\text{FeO}(\text{s})$	250.990	$\text{ZrO}_2\text{OH}^-$	1203.737	$\text{Zn}(\text{OH})_3^-$	704.711	$\text{HCl}(\text{g})$	95.312
$\text{Fe}(\text{OH})_2$	486.599	$\text{MnO}(\text{s})$	363.340	$\text{Zn}(\text{OH})_4^{2-}$	871.276	$\text{Cl}_2(\text{g})$	0.000
$\text{Fe}^{2+}$	92.257	$\text{Mn}(\text{OH})_2$	615.048	$\text{PbO}(\text{s})$	188.489	$\text{HCl}^0$	131.252
$\text{FeOH}^+$	279.951	$\text{Mn}^{2+}$	229.953	$\text{Pb}^{2+}$	24.393	$\text{Cl}^-$	131.252
$\text{Fe}(\text{OH})_2^0$	457.102	$\text{MnOH}^+$	406.685	$\text{PbOH}^+$	226.354	$\text{H}_2\text{O}(\text{l})$	237.180
$\text{Fe}(\text{OH})_3^-$	619.232	$\text{Mn}(\text{OH})_3^-$	746.426	$\text{Pb}(\text{OH})_2^0$	400.827	$\text{H}_2(\text{g})$	0.000
$\text{Na}_2\text{O} \cdot \text{Al}_2\text{O}_3 \cdot 4 \text{SiO}_2 \cdot 2 \text{H}_2\text{O}$			6183.750	$\text{Pb}(\text{OH})_3^-$	575.718	$\text{O}_2(\text{g})$	0.000
$5 \text{CaO} \cdot 6 \text{SiO}_2 \cdot 10.5 \text{H}_2\text{O}$			11,075.480	$\text{Li}_2\text{O}(\text{s})$	561.760	$\text{H}^+$	0.000
$\text{Al}_2\text{O}_3 \cdot 2 \text{SiO}_2 \cdot 2 \text{H}_2\text{O}$			3706.760	$\text{Li}^+$	292.629	$\text{OH}^-$	157.300
$4 \text{CaO} \cdot \text{Al}_2\text{O}_3 \cdot 13 \text{H}_2\text{O}$			7331.970			$\text{H}_2\text{O}-\text{OH}^-$	79.880



from a given oxide, then calculate  $\Delta G_{j \leftrightarrow i}$  and  $K_{j \leftrightarrow i}$  after Eqs. (2.6) and (2.7) using the data in Table 2.2; then calculate  $x(i)$  after Eqs. (2.8) and (2.9).

Now we are ready to determine the chemical durability of a glass with arbitrary composition in terms of its Gibbs energy of hydration  $\Delta G_{\text{hydr}}$  (see Fig. 2.7a). In contrast to the species equilibria, the dissolution reaction proceeds in one direction only. That is why we now have to distinguish between protolytic and hydrolytic dissolution. But like before, with Eq. (2.5a), we may use a single equation. The Gibbs energy of a species formation now reads

$$\Delta G_{\text{aq},i \rightarrow i} = \Delta G_{j \leftrightarrow i} + G_j - \nu_{\text{H}^+} \cdot G_{\text{H}^+}^*, \quad (2.10)$$

with  $\Delta G_{j \leftrightarrow i}$  given by Eq. (2.6),  $G_j$  = Gibbs energy of the pure oxide;  $G_{\text{H}^+}^* = 0$  for  $\nu_{\text{H}^+} \geq 0$ , (prolytic reaction), while  $G_{\text{H}^+}^* = G_{\text{H}_2\text{O}} - G_{\text{HO}^-} = -79.880$  kJ/mol for  $\nu_{\text{H}^+} < 0$ . As an intermediate result, the hydrolytic stabilities of individual pure oxides  $j$  are obtained as

$$G_{\text{aq},j} = \sum_i x_i \cdot \Delta G_{\text{aq},i \rightarrow i}, \quad (2.11a)$$

$$\Delta G_{\text{hydr},j} = G_{\text{aq},j} - G_j \quad (2.11b)$$

(see Fig. 2.11). This plot gives a most interesting insight in how individual oxides influence the stability of a glass in a specific pH range. Note that both  $\text{Al}_2\text{O}_3$  and  $\text{Fe}_2\text{O}_3$  have the potential to significantly enhance the chemical durability of a glass, however, not in strong acids or bases.  $\text{ZnO}$ ,  $\text{PbO}$ , and  $\text{FeO}$  enhance the stability in caustic solutions. By and large, the stabilities of the divalent oxides follow Dietzel's field strength rule. The alkali oxides are not shown in Fig. 2.11; they would exhibit straight lines (one species only) well above 300 kJ/mol.

According to Fig. 2.7a, the final steps toward the calculation of the Gibbs energy  $\Delta G_{\text{hydr}}$  of a glass are summarized by Eqs. (2.12a)–(2.12c) below:

$$G_{\text{aq,GL}} = \sum_j n_j \cdot G_{\text{aq},j}, \quad (2.12a)$$

$$G_{\text{GL}} = \sum_k n_k \cdot (G_{k,X} + G_k^{\text{vit}}), \quad (2.12b)$$

$$\Delta G_{\text{hydr}} = G_{\text{aq,GL}} - G_{\text{GL}}. \quad (2.12c)$$

In Eq. (2.12a), the  $n_j$  denotes the molar amounts of oxides  $j$  in units of mol/100 g glass. Thus, all left-hand quantities in Eqs. (2.12a)–(2.12c) bear the unit kJ/100 g. The energy level  $G_{\text{aq,GL}}$  of the entire aqueous system is given by the weighted sum of the  $G_{\text{aq},j}$ —see Eq. (2.11a).  $G_{\text{GL}}$  is determined from the Gibbs energies  $G_{k,X}$  of the constitutional phases  $k$  of the crystalline state isochemical to the glass composition and a vitrification term  $G_k^{\text{vit}}$ . For details, see the Chap. 2. The difference of  $G_{\text{aq,GL}}$

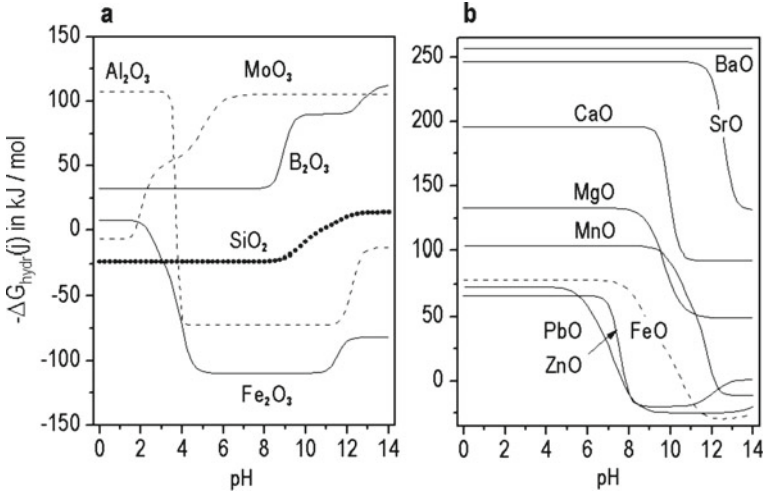


**Fig. 2.11** Hydrolytic stabilities of individual pure oxides  $j$  (panel **a**: tri- to hexavalent oxides, panel **b**: divalent oxides) in terms of their Gibbs energy of hydration  $\Delta G_{\text{hydr}}(j)$  as function of pH; stability decreases in vertical direction

and  $G_{\text{GL}}$  yields the desired result. This is the result valid for a situation at high water excess, i.e., at infinitely high dilution of species  $i$ .

During the corrosion of commercial glasses, very thin layers of certain precipitates form at quite early stages of the process already. Four typical candidates are compiled in the lower left part of Table 2.2, namely,  $p = \text{Na}_2\text{O} \cdot \text{Al}_2\text{O}_3 \cdot 4\text{SiO}_2 \cdot 2\text{H}_2\text{O}$  (analcime),  $5\text{CaO} \cdot 6\text{SiO}_2 \cdot 10.5\text{H}_2\text{O}$  (CSH phase),  $\text{Al}_2\text{O}_3 \cdot 2\text{SiO}_2 \cdot 2\text{H}_2\text{O}$  (a clay mineral), and  $4\text{CaO} \cdot \text{Al}_2\text{O}_3 \cdot 13\text{H}_2\text{O}$ . Let  $N = \text{Na}_2\text{O}$ ,  $C = \text{CaO}$ ,  $A = \text{Al}_2\text{O}_3$ ,  $S = \text{SiO}_2$ . Then the molar amounts  $n_N$ ,  $n_C$ ,  $n_A$ , and  $n_S$  of the glass are distributed to these precipitates first. This is done in consecutive order like:

$$\begin{aligned} n(\text{Na}_2\text{O} \cdot \text{Al}_2\text{O}_3 \cdot 4\text{SiO}_2 \cdot 2\text{H}_2\text{O}) &= \text{MIN}(n_N, n_A, 1/4 \cdot n_S), \\ n(5\text{CaO} \cdot 6\text{SiO}_2 \cdot 10.5\text{H}_2\text{O}) &= \text{MIN}(1/6 \cdot n_C, 1/5 \cdot n_S), \\ n(\text{Al}_2\text{O}_3 \cdot 2\text{SiO}_2 \cdot 2\text{H}_2\text{O}) &= \text{MIN}(n_A, 1/2 \cdot n_S), \\ n(4\text{CaO} \cdot \text{Al}_2\text{O}_3 \cdot 13\text{H}_2\text{O}) &= \text{MIN}(1/4 \cdot n_C, n_A), \end{aligned}$$

$\text{MIN}(\dots)$  = minimum of the values in parentheses; the assessment of the Gibbs energy of the solution, next step, is performed on the residual amounts of  $n_N$ ,  $n_C$ ,  $n_A$ ,  $n_S$  left from the previous one. The  $G_{\text{aq},p}$  of each of the above precipitates  $p$  is calculated as

$$G_{\text{aq},p} = G_p - \nu_{\text{H}_2\text{O}} \cdot G_{\text{H}_2\text{O}}, \quad (2.13)$$

where  $\nu_{\text{H}_2\text{O}}$  is the stoichiometric coefficient of  $\text{H}_2\text{O}$  in the respective formula. The contribution of all precipitates is

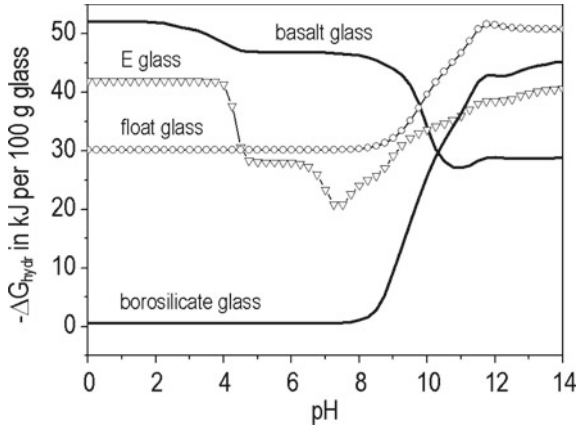


**Fig. 2.12** Chemical durability fingerprints of four commercial glasses in terms their Gibbs energy of hydration  $\Delta G_{\text{hydr}}$  as a function of pH; stability decreases in vertical direction

$$G_{\text{aq}}(\text{ppts}) = \sum n_p \cdot G_{\text{aq},p}. \quad (2.14)$$

The quantity  $G_{\text{aq,GL}}$ , Eq. (2.12a), is calculated by using the amounts  $n_j, j = \text{N, C, A, S}$ , left after the above procedure. The Gibbs energy  $\Delta G_{\text{hydr}}$  is obtained as

$$\Delta G_{\text{hydr}} = G_{\text{aq,GL}} + G_{\text{aq}}(\text{ppts}) - G_{\text{GL}}. \quad (2.15)$$

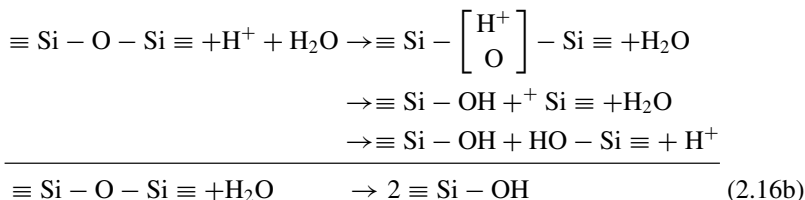
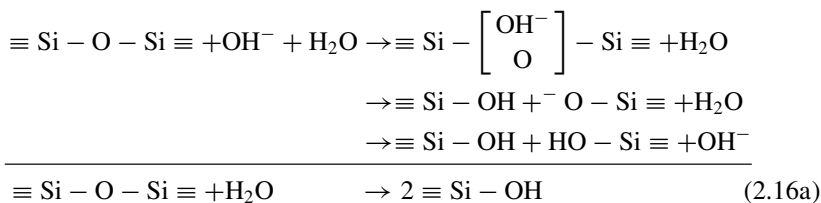
This is the result of stationary corrosion extending beyond the limit of infinite dilution. In any case,  $\Delta G_{\text{hydr}}$  plotted as a function of pH yields the hydrolytic stability fingerprint of a glass. This is shown in Fig. 2.12 for a number of commercial glasses. The procedure outlined above allows one to perform desktop development of glass compositions with a desired profile of chemical durability.

Finally, Table 2.2 may be expanded by compiling species with organic anions like acetates, oxalates, citrates, lactates, pyruvates, etc., which allows one to determine the chemical durability in a bio environment; in this case, physiological NaCl and CO<sub>2</sub> concentrations have to be taken into account, too. For bioglasses, hydroxyl apatite needs to be added to the list of early forming precipitates.

## 2.5 Rate Equation

As sketched in Fig. 2.7b, matter (in specific: Si atoms) released from a glass surface to an aqueous solution has to pass through an energetically unfavorable transient state. The nature of this state depends on the surface charge equilibrium (mechanism 1 in Fig. 2.4) and hence, on pH. In fact, there are two distinctly different types of transient states, one occurring in the presence of negative charges, to another one in

the presence of positive charges. This is summarized by the equations below:



Both mechanisms bring about the same final result, i.e., the split of a siloxane bond  $\equiv\text{Si}-\text{O}-\text{Si}\equiv$  into two silanol groups  $\equiv\text{Si}-\text{OH}$ . If all (max.) four bonds of a  $[\text{SiO}_4]$  tetrahedron are split in this way, silica is released to the solution as siliceous acid—of course in the respective speciation as shown in Fig. 2.10. Note that in both reaction paths, Eqs. (2.16a) and (2.16b), the initiating charge species  $\text{OH}^-$  or  $\text{H}^+$ , respectively, appear again at the end of the path. So, we may speak of a  $\text{OH}^-$  versus an  $\text{H}^+$  catalyzed split of the siloxane bonds. The nature of the activated complex, is shown in Eqs. (2.16a) and (2.16b) in square brackets, is different for each path. In both cases, however, the elementary step involved is proton transfer from the charged species to the oxygen in the silanol bond. It occurs, independent of pH, at the same fundamental rate. Thus, the amount of silica released to the solution per time unit depends on the number of surface sites at which the elementary process is active, i.e., it depends on the coverage of the glass surface by charges—and this definitely is a function of pH. Figure 2.13 shows the effective coverage  $\theta$ ,  $0 < \theta < 1$ , of a silica surface by positive and negative charges as derived from data compiled in [14]. Full occupation with  $\text{OH}^-$  is reached at  $\text{pH} \approx 11$  with 5.5–5.8  $\text{OH}^-$  groups per  $\text{nm}^2$ . At the point of zero charge (pzc), equal amounts of positive and negative charges are present. For tap water with natural water hardness, pzc occurs at  $\text{pH} \approx 4$  (bold line), in D.I. water at  $\text{pH} \approx 2$  (crosses). The presence of alkali ions shifts the branch  $\delta^+$ , and hence pzc, to the right, thus significantly increasing the number of surface charges in the weakly acid to neutral range. This is why (see Sect. 2.2) glass dissolution is enhanced in high ionic strength solutions. All these facts go together with the theory of the glass electrode. For comparison, Fig. 2.13 also shows the surface coverage of an alumina surface. This is relevant for silica-poor, alumina-rich glasses typical of some stone wool compositions. In a more general approach, the role of elements other than Si at the glass surface may be comprised by the surface coverage  $\theta$  in a cumulative way by a superposition of the  $\theta$  of pure oxide surfaces weighted by their presence in the glass surface. The qualitative classification of glass surfaces given

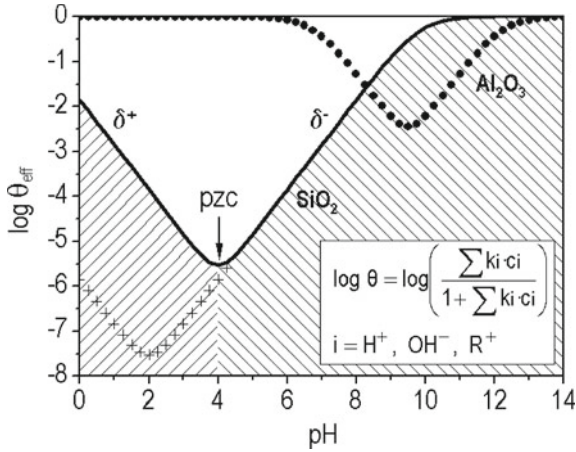


**Fig. 2.13** Logarithmic plot of the effective surface coverage  $\theta_{\text{eff}}$  of a silica glass surface; the branches  $\delta^+$  and  $\delta^-$  refer to positive and negative charges, respectively; pzc = point of zero charge; bold line: tap water; crosses: D.I. water; big dots: alumina surface; the insert shows a Langmuir type relation for  $\theta_{\text{eff}}$ ;  $k_i$  = reaction constant;  $c_i$  = concentration

by Hench [35] (see Fig. 2.14) may serve as a guideline as to which oxides have to be taken into account.

Based on the above facts, we may now formulate a rate equation for glass dissolution. In its most general form, the rate law reads

$$r = r_+ \cdot f(i) \cdot (1 - \text{IAP}/\text{IAP}_s) \tag{2.17a}$$

where  $r$  denotes the corrosion rate,  $r_+$  is a forward rate, and  $f(i)$  is a term summarizing the effects of dissolved species  $i$  on the dissolution rate. The affinity term  $(1 - \text{IAP}/\text{IAP}_s)$  describes the degree of saturation of the solution with respect to the dissolving phase in terms of an adequate ion activity product IAP; the index  $s$  denotes saturation. A first type of rate equation was given by Grambow [50]. An overview of different concepts is given in [21]. Now, the following assumptions are made:

- For silicate glasses, IAP can always be expressed in terms of the resulting concentration of dissolved silica.
- The effect of dissolved species  $i$  on the dissolution rate  $r$  is taken account for by the surface charge coverage  $\theta$  in a cumulative way.
- The proportionality between  $\log r$  and  $\Delta G_{\text{hydr}}$  is modified by a factor  $\varepsilon$  as proposed by Jantzen [47].

This results in a rate equation reading

$$\log r(\xi) = \log r_X + (1 - \beta) \cdot \log \theta - \varepsilon \cdot \frac{\Delta G_{\text{hydr}}(\xi)}{RT} + \log \left( 1 - \frac{c(\xi)}{c_S} \right). \tag{2.17b}$$

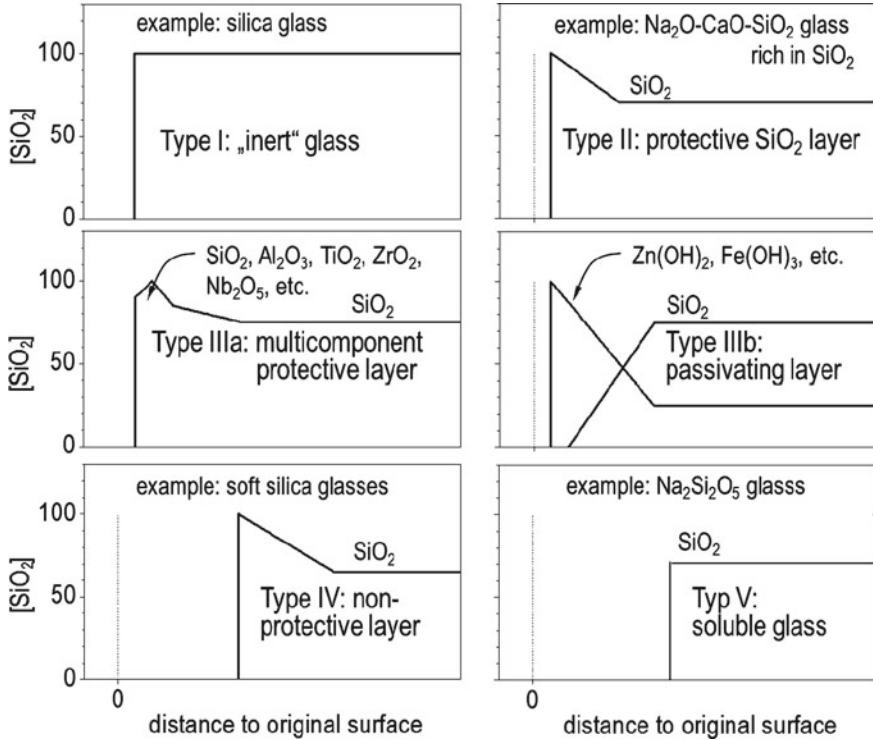


Fig. 2.14 Classification of corroded glass surfaces after Hench [xx]

where  $r_X$  is a fundamental forward rate that depends on temperature like

$$r_X = X \cdot \exp\left(-\frac{E_A}{RT}\right). \tag{2.17c}$$

$X$  is a fundamental rate constant for silicate glasses,  $X = 0.035 \frac{\text{mol Si}}{\text{cm}^2 \text{s}}$  [50]. The activation energy is  $E_A \approx 70 \text{ kJ/mol}$  (it may vary from 65 to 75 kJ/mol, decreasing with the basicity of the glass). Thus, at 90 °C,  $r_X = 3 \times 10^{-12} \frac{\text{mol Si}}{\text{cm}^2 \text{s}} = 6 \times 10^{-5} \frac{\text{g}}{\text{cm}^2 \text{d}}$ . The constant  $\beta = 0.78$  is the transference number of  $\text{H}^+$  [51]. The parameter  $\xi$  is a reaction variable, most conveniently expressed by the turnover of Si. Thus  $c(\xi)$  denotes the actual concentration of silica in the solution and  $c_S$  the saturation concentration of amorphous SiO<sub>2</sub>. The factor  $\varepsilon$  may be approximated as

$$\varepsilon = \frac{\beta}{4x_{\text{SiO}_2} \cdot \langle M \rangle} \tag{2.18}$$

where  $\langle M \rangle = 0.01 \cdot \sum x_j \cdot M_j$  is the mean molar weight of the glass in units 100 g per mol;  $x_j$  and  $M_j$  in g/mol is the molar fraction and molar weight, respectively, of

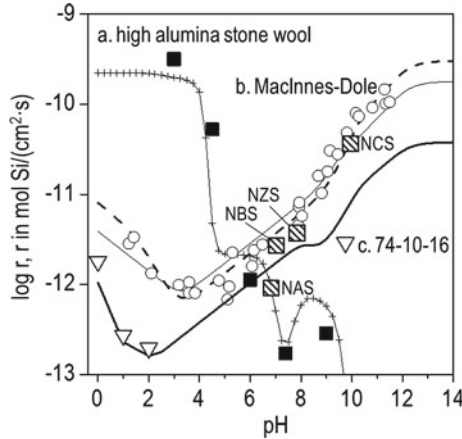


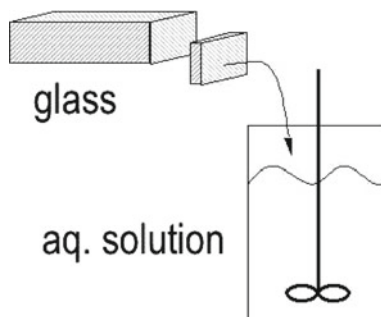
**Fig. 2.15** Dissolution rates, experimental values and calculations; closed squares and line with crosses: high alumina stone wool glass; 90 °C,  $s = 0.01 \text{ cm}^{-1}$ ; open circles: MacInnes-Dole glass, 75 °C,  $s = 0.76 \text{ cm}^{-1}$ ,  $[\text{Na}] = 0.2 \text{ mol/L}$  [24]; thin line: no ppt., bold dashed line: C–S–H ppt. [9]; open triangles: granules of glass 74 SiO<sub>2</sub>, 10 CaO, 16 Na<sub>2</sub>O mol %, 100 °C,  $s = 10 \text{ cm}^{-1}$ , after 16 h; the point at pH = 9.8 belongs to a sample originally exposed to pH = 4; bold line: ppt C–S–H taken into account; hatches squares: experimental results for the glasses shown in Fig. 2.6, 90 °C,  $s = 0.01 \text{ cm}^{-1}$

oxide  $j$ . Far from saturation,  $c(\xi)/c_s \ll 1$ , and  $\Delta G_{\text{hydr}}(\xi) \rightarrow \Delta G_{\text{hydr}}$  as calculated before. Taking into account early precipitates as done at the end of Sect. 2.4 is a first simple approach to  $\Delta G_{\text{hydr}}(\xi)$ . Figure 2.15 shows calculated dissolution rates of a high alumina stone wool glass, a MacInnes-Dole glass, and glass 74 SiO<sub>2</sub>, 10 CaO, and 16 Na<sub>2</sub>O (by mol) in comparison to experimental values.

## 2.6 Reaction Path Calculation, Corrosion Layers, Long-Term Behavior

Upon long exposure times, the system approaches saturation. Then  $c(\xi)/c_s$  increases to a value close to 1. In fact, as a glass is always less stable than its isochemical crystalline state, its saturation concentration  $c_s$  is always higher than the saturation concentration  $c_{\text{ppt}}$  imposed by the appearance of solid precipitates in the solution. Therefore, a glass keeps dissolving until complete mineralization, albeit at a reduced rate  $r_\infty$  determined by the ratio  $c_{\text{ppt}}/c_s$ . Under such conditions,  $\Delta G_{\text{hydr}}(\xi)$  can no longer be approached by taking into account some early precipitates known by experience. Rather, a full-fledged reaction path calculation has to be performed allowing the aqueous species to interact and to form precipitates according to their actual concentration. The principle of reaction path calculation is sketched in Fig. 2.16: Amounts of oxides in proportion to the glass composition are transferred to the aqueous system in a sequence of steps  $\Delta\xi$ , where  $\xi$  denotes a reaction path or

**Fig. 2.16** Reaction path calculation scenario



turnover variable. The total amount of Si is preferentially taken as a measure of  $\xi$ . After each step, the aqueous equilibrium is calculated, comprising all aqueous species and precipitates formed. This yields a plot of concentrations (masses per solution volume) of aqueous species and precipitates as a function of  $\xi$ . The relation to the time scale is given by the reaction rate, Eq. (2.17b), as  $d\xi = r \cdot dt$ . Figure 2.17 shows the result of such a calculation for the glass 74 SiO<sub>2</sub>, 10 CaO, and 16 Na<sub>2</sub>O (by mol). In this plot, all aqueous species of the individual elements are summarized by curves Si(aq), Ca(aq), and Na(aq), respectively. The calculation shows that the first solid phase is colloidal (amorphous) silica Si(am). When Si(am) appears, Si(aq) approaches a constant level denoting the silica saturation at this stage. Upon further Si turnover, the level Si(aq) may change; it will adapt to the nature of precipitates formed in the solution. Next, a calcium silicate hydrate (CSH) precipitate is formed, stopping the further increase of Ca(aq) in the solution. Only Na(aq) keeps increasing and, along with this, the pH value. From Fig. 2.10, it is expected to settle at pH = 11.4. For the calculation of Fig. 2.17, a Gibbs energy minimizer software [52] was used.

Figure 2.18 shows SEM images of glass surfaces with precipitates of the kind as predicted in Fig. 2.17 and compiled in Table 2.2. Panel **a** shows a precipitate developing on the surface of glass 72 SiO<sub>2</sub>, 12 CaO, 12 Na<sub>2</sub>O (by mol) corroded at 98 °C,  $s = 0.1 \text{ cm}^{-1}$ . By XRD, the precipitate was identified as a CSH phase. Panel **b** shows a thick crust developing on the surface of a simulated radioactive waste glass hydrothermally corroded in high ionic strength solution at 200 °C for 10 d,  $s = 0.1 \text{ cm}^{-1}$ . The vertical sequence of phases from bottom to top verifies the phases consecutively determined by reaction path calculation from Si(am) at the bottom to analcime (Na<sub>2</sub>O · Al<sub>2</sub>O<sub>3</sub> · 4SiO<sub>2</sub> · 2H<sub>2</sub>O) found as small individual cubes on top of the crust. Panel **c** shows the surface of a similar glass swept by a rubber wiper. As said before, crusts of this kind are easily removed from the residual glass.

Equation (2.17b) clearly predicts a slowdown of corrosion rates during the experiments due to saturation effects. The equation does, however, not take into account any transport processes within and across the layers formed during corrosion. From metal corrosion, it is known that oxide scales firmly adhering to the metal surface inhibits the corrosion process in a most effective way. For example, the base metal alumina oxidizes rapidly, but a firmly adhering alumina layer passivates the metal



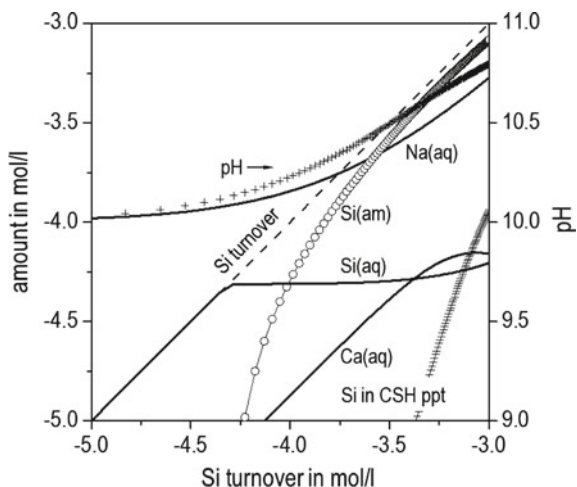


**Fig. 2.17** Reaction path calculation for a glass 74 SiO<sub>2</sub>, 10 CaO, 16 Na<sub>2</sub>O (by mol) as a function of the cumulative turnover of silica

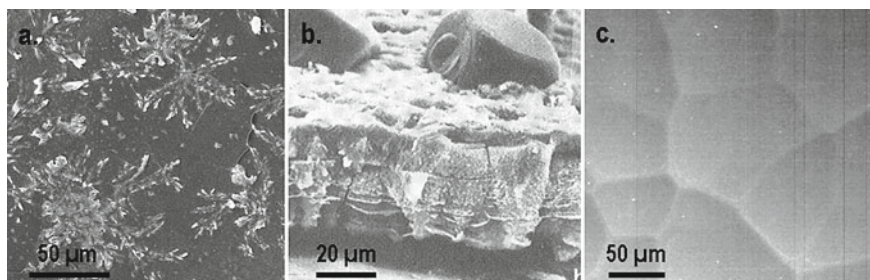


**Fig. 2.18** **a** CSH precipitate on top of a corroded glass 72 SiO<sub>2</sub>, 12 CaO, 12 Na<sub>2</sub>O (by mol). **b** Crust of precipitates on top of a simulated radioactive waste glass hydrothermally corroded in high ionic strength solution; cubes on top: analcime crystals. **c** Surface of a sample similar to the one in panel b; the crust was removed completely by means of a rubber wiper

and forestalls the diffusion of oxygen to the bulk metal, hence any further attack. By contrast, the oxide layer formed on the much nobler iron shows poor adherence only. Thus, iron keeps rusting. The degree of adherence of an oxide layer is estimated from the so-called Pilling-Bedworth ration  $PBR = V_{Ox}/V_{Me}$ ;  $V_{Ox}$  and  $V_{Me}$  are the molar volumes of oxide and metal (per g-atom of metal), respectively. Good adherence requires  $1.3 < PBR < 1.7$ . The formation of well-adhering oxide scales (SiO<sub>2</sub>, Al<sub>2</sub>O<sub>3</sub>, and Cr<sub>2</sub>O<sub>3</sub>) on top of the bulk metal plays a key role in the design of stainless steel. It lies close to explore a similar approach to the corrosion resistance of glasses. In doing this, we have to clearly distinguish the different types of layers by their nature as stated at the beginning of Sect. 2.3 [36]. Figure 2.19 gives a classification of different mechanisms of layer formation.

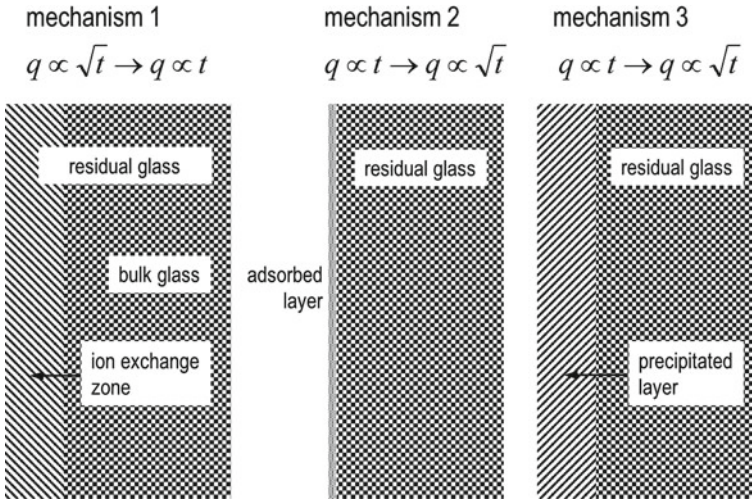


**Fig. 2.19** Illustration of three different corrosion mechanisms simultaneously present at a corroding glass surface in a limited solution volume; mechanism 1 is the ion exchange process as illustrated in detail in Fig. 2.3; the ion exchange zone remains an integral part of the residual glass (see Fig. 2.4) and cannot be separated from the bulk glass; mechanism 2 is the molecular adsorption of ions released from the glass at the surface of the residual glass; mechanism 3 is the formation of a sequence of precipitated phases on top of the residual glass; after long times, an ultimate precipitate is formed at the outermost part (see Fig. 2.18b); in most cases, the layer can be removed from the residual glass by a rubber wiper (see Fig. 2.18c); the evolution of the respective time laws of the mass loss per surface area  $q$  is given above the sketches

The first mechanism refers to the formation of a sub-surface layer, often termed “leached layer”. It rests on the reactions illustrated in Figs. 2.3 and 2.4. The qualitative classification by Hench as shown in Fig. 2.14 refers to the nature of sub-surface layers, too. For sufficiently silica-rich glasses, the sub-surface layer acts as a protective layer. Nobody has ever designed this mechanism on purpose; it is just a most favorable behavior of silica-rich glasses. The effect may be enhanced by the presence of elements known to form stable hydroxides, like Zn, Al, Fe, Ti. The time law of evolution of the sub-surface layer was described by Doremus [53] as

$$L = \left( v_0 \cdot t + \frac{D}{v_0} \right) \cdot \operatorname{erf}(z) + \sqrt{\frac{D \cdot t}{\pi}} \cdot \exp(-z^2) \quad (2.19a)$$

with

$$z = \frac{v_0 \cdot t}{\sqrt{4 \cdot D \cdot t}}; \quad (2.19b)$$

$v_0$  = initial stationary dissolution velocity,  $D$  = effective diffusion coefficient;  $L$  = depth of alteration of the bulk glass comprising both dissolution and sub-surface

layer formation. The matrix dissolution proceeds like  $L_{\text{diss}} = v_0 \cdot t$ . In the short-term limit,  $L = \sqrt{D \cdot t / \pi}$ , in the long-term limit,  $L = v_0 \cdot t + D/v_0$  with a stationary depth  $L_D = D/v_0$  of the sub-surface layer. In all cases, the sub-surface layer remains an integral part of the residual glass and cannot be separated from the bulk glass. At neutral or slightly caustic pH, the stationary state  $L_D = D/v_0$  is typically reached after a few 10 h of exposure only. In certain glasses (see Fig. 2.6b, d) as well as in strong acids, the establishment of stationary conditions may last significantly longer. Then, in any case, the dissolution proceeds at a stationary velocity  $v_0$  as long as there is no substantial accumulation of dissolved matter in the solution.

The second mechanism refers to molecular adsorption at the surface of the residual glass. Oxides known to form stable hydroxides may also form an adsorbed molecular layer on top of the residual glass, covering the surface like  $\theta = k \cdot c / (1 + k \cdot c)$ . The initial stationary dissolution velocity  $v_0$  is slowed down by a factor  $(1 - \theta)$ . The resulting time law reads

$$L = \lambda \cdot \left( \sqrt{1 + 2 \cdot \frac{v_0 \cdot t}{\lambda}} - 1 \right), \quad (2.20)$$

with  $\lambda = 1/(k \cdot s \cdot \rho)$ , a short-term limit  $L = v \cdot t$ , and a long-term limit  $L = \sqrt{2 \cdot \lambda \cdot v_0 \cdot t}$ ;  $k$  = adsorption constant,  $c$  = concentration of the aqueous oxide species,  $s$  = glass surface to solution volume ratio,  $\rho$  = density of the bulk glass. This type of layer exerts a protective effect, especially at elevated pH values.

The third mechanism refers to the formation of precipitates at the surface of the residual glass. This type of layer resembles the formation of oxide scales on metals. Formally, the kinetics of glass dissolution imposed by these layers is identical to Eq. (2.20), however, with

$$\lambda = \frac{D}{v_0} \cdot \frac{c_s}{\rho}, \quad (2.21)$$

where  $c_s$  is the saturation concentration of silica in the presence of the precipitates formed (see Figs. 2.17 and 2.18). Unfortunately, as a general observation, these layers do not adhere well to the residual glass. As stated before, they may be removed by a rubber wiper in most cases (see Fig. 2.18c). The effect of precipitated layers on the mass loss per surface area is shown in Figs. 2.20 and 2.21 [54]. The results refer to a simulated atomic waste glass (SM58) hydrothermally corroded in a saturated salt brine and in 0.01 molar NaOH solution, respectively. Manipulations on the samples were performed to discriminate between saturation effects versus the effect of the precipitated layer as a diffusion barrier. The details are described in the figure legends. In the series of experiments in salt brines, the slowdown of corrosion rate with time is primarily due to saturation effects; the precipitated layer exerts a minor effect only (120 °C) or no effect at all (200 °C). It is in very caustic solution only (Fig. 2.21) that the precipitated layers slow down the—albeit extremely high-dissolutions rates by their action as diffusion barriers.

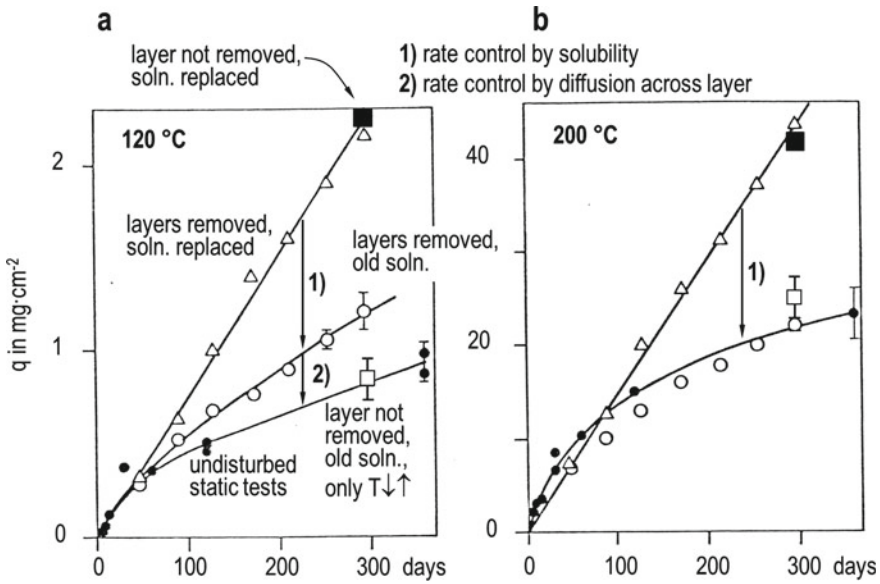


**Fig. 2.20** Mass loss per surface area (residual glass) of a simulated atomic waste glass SM58 hydrothermally corroded in salt brine at  $120\text{ }^{\circ}\text{C}$  (panel a) and  $200\text{ }^{\circ}\text{C}$  (panel b) [xx]; glass surface area to solution volume ratio to solution volume ratio  $s = 0.034\text{ cm}^{-1}$ ; comparison of different manipulations to the results of undisturbed static tests; manipulations refer to the replacement of brine containing dissolved glass by fresh brine or to the removal of the precipitated layer on the residual glass; for tests with manipulated samples retaining their layer, the mass loss of the residual glass could be determined after 300 d only; the tests marked with an open square are control tests probing the effect of cooling down and heating up during the manipulations; the effect is negligible

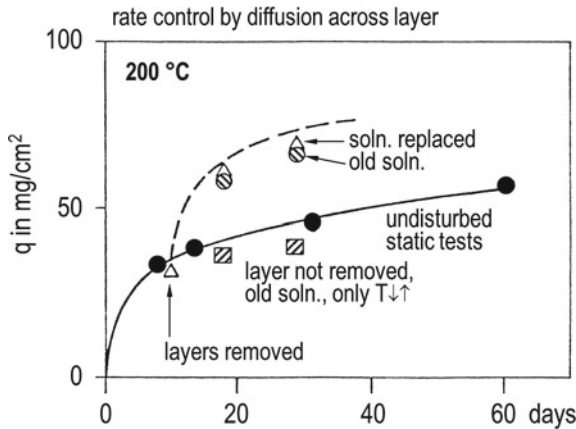


**Fig. 2.21** Mass loss per surface area (residual glass) of a simulated atomic waste glass SM58 hydrothermally corroded in  $\text{NaOH}$  ( $0.01\text{ mol/L}$ ) at  $200\text{ }^{\circ}\text{C}$  [xx]; glass surface area to solution volume ratio to solution volume ratio  $s = 0.034\text{ cm}^{-1}$ ; comparison of different manipulations to the results of undisturbed static tests; manipulations like in Fig. 2.20

In any exposure of glass to a finite volume of solution, all mechanisms mentioned above work together. They yield a temporal sequence of evolution of the actual corrosion rate ranging from an initial stage during which a stationary sub-surface layer is established, a stage of a stationary initial dissolution rate, an intermediate state where diffusion processes may play a role, even an intermediate halt of corrosion brought about by a metastable saturation equilibrium, toward an ultimate long-term rate.

## 2.7 Summary and Outlook

An extended guideline has been presented on how experiments targeting the chemical durability of glasses should be designed and evaluated.

As for the mechanistic understanding of chemical durability, it has been shown that the simple textbook scenario glass “corrosion = network dissolution + leaching” is incomplete. The nature of the proton as an elementary particle, not an ion, has been emphasized. The correct understanding rests, to a large extent, on the theory of the glass electrode [4].

By a thermodynamic approach, the chemical durability could be quantified for glasses with arbitrary composition and for simple as well as very complex aqueous systems. The approach may be extended in a systematic way to solutions containing organic constituents by adding the respective data of oxide speciation to Table 2.2.

The predominant effect governing the reaction rate is the occupation of the glass surface by charges. When combining this approach with the thermodynamic approach, then dissolution rates of glasses are predicted in a reliable way.

In order to complete the picture, the potentially protective role of three different types of layers, i.e., a sub-surface layer as an integral part of the residual glass, an adsorbed molecular layer on the surface of the residual glass, and a layer of precipitates formed on top of the residual glass, was discussed. Here, the sub-surface layer constitutes an initial stationary rate which prevails until substantial amounts of dissolved matter is accumulated in the solution. Adsorbed layers may yield a slowdown of corrosion rates, especially at elevated pH values. Under conditions close to saturation, a layer of precipitates forms on top of the corroding glass. This layer controls the further corrosion attack via the concentration of silica. In most cases, however, it does not act as a transport barrier.

Long-term exposure and conditions close to saturation are a field where many unsolved questions prevail. It still is a matter of debate [22, 23]. The temporal sequence of stages of corrosion: establishment of the surface equilibrium, non-stationary leaching, dissolution at a stationary rate  $r_0$ , formation of precipitates with an ultimate slowdown of rates to a long-term rate  $r_\infty = r_0 \cdot (1 - c_{\text{ppt}}/c_{\text{am}}) \approx 0.01 \cdot r_0$  [43] is generally accepted and well substantiated by experiments. This is shown, again, for a large series of experiments performed on the simulated atomic waste glass SM58 (see Fig. 2.22). The product  $s \cdot t$  is chosen to represent the time scale: At different ratios  $s$  of glass surface to solution volume, the accumulation of dissolved

matter in the solution after time  $t$  increases as  $s \cdot t$ . Initially, the dissolution proceeds at the initial stationary rate  $r_0$ , then decrease, with the onset of this decrease depending on  $s$ . When the saturation limit  $c_S$  with respect to amorphous silica is reached, then the rates approach zero according to the relation  $r = r_0 \cdot (1 - c/c_S)$ . However, since the glass is a non-equilibrium solid, this is an intermediate state only. As soon as more stable precipitates than amorphous silica is formed, the rate resumes momentum again. Let  $c_{\text{ppt}}$  be the concentration of silica with respect to an ultimately formed precipitate. The thermodynamically more stable precipitate yields  $c_{\text{ppt}} < c_S$ . As a result, after sufficiently long times, a final corrosion rate  $r_\infty = r_0 \cdot (1 - c_{\text{ppt}}/c_S) > 0$  is reached, i.e., the glass keeps dissolving until its complete mineralization. For the example chosen,  $r_\infty \approx 0.01 \cdot r_0$ . It has been speculated—and in fact observed in a few cases—that after very long time, the rate accelerates again beyond the level of  $r_\infty$  (see the discussion in [22]). This may occur indeed if the nature of precipitates changes after very long time from a precipitate ppt (considered as “ultimate”) to an even more stable precipitate ppt2 with  $c_{\text{ppt2}} < c_{\text{ppt}}$ . Then, the rate would increase from  $r_{\infty,\text{ppt}} = r_0 \cdot (1 - c_{\text{ppt}}/c_S)$  to  $r_{\infty,\text{ppt2}} = r_0 \cdot (1 - c_{\text{ppt2}}/c_S) > r_{\infty,\text{ppt}}$ . Unfortunately, a direct investigation of the behavior over extremely long times is beyond experimental reach. The longest exposure times reported are in the order of 10 years only. Reaction path calculations may provide a valid answer, though. They would have to be extended over ranges of turnover far beyond what was shown in Fig. 2.17. The crucial issue consists in identifying the nature of precipitates that will ultimately form. This is well-known for systems with compositions resembling basalt or other natural analogs, however, not for the complex artificial compositions of nuclear waste glasses. To date, this remains an unsolved problem.

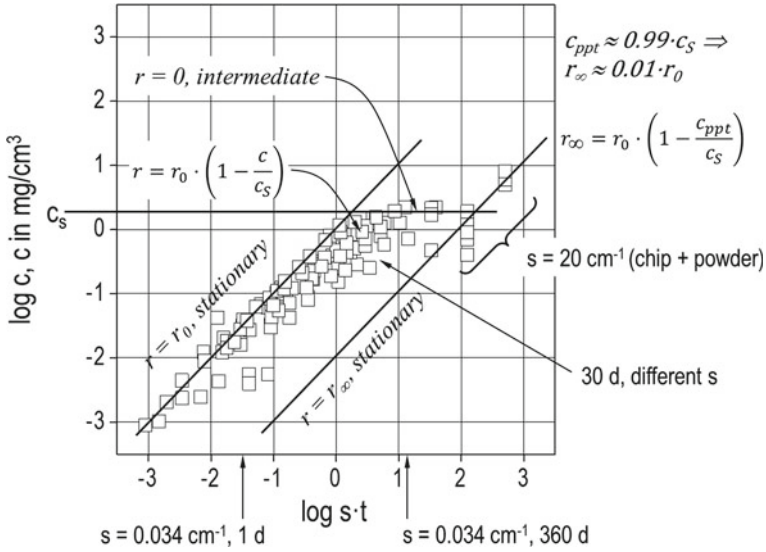


**Fig. 2.22** Corrosion tests on a simulated atomic waste glass SM58 hydrothermally corroded in salt brine at 200 °C; matter release from the residual glass  $c$  is given by  $c = q \cdot s$ ;  $q$  = mass loss per surface area in  $\text{mg}/\text{cm}^2$ ,  $s$  = ratio of glass surface area to solution volume; test at different  $s$  are plotted as a function of the product  $s \cdot t$ ,  $t$  = time in days;  $c_s$  = solubility limit of glassy  $\text{SiO}_2$ ,  $c_{\text{ppt}}$  = solubility limit of  $\text{SiO}_2$  in the presence of an ultimate precipitate;  $r_0$  = initial stationary corrosion rate in  $\text{g}/(\text{cm}^2 \cdot \text{d})$  in the system undersaturated with respect to glassy  $\text{SiO}_2$ ;  $r_\infty$  = long-term stationary rate in the presence of an ultimate precipitate

## References

1. Cremer M (1906) Z Biol 4:562
2. Haber F, Klemensiewicz Z (1909) Z Phys Chem 67:385
3. Baucke FGK (1985) The glass electrode—applied electrochemistry of glass surfaces. J Non-Cryst Solids 73:215–231
4. Baucke FGK (1996) Glass electrodes: why and how they function. Ber Bunsenges Phys Chem 100:1466–1474
5. Belyustin AA (2011) The centenary of glass electrode. From Max Cremer to F.G.K. Baucke. J Solid State Electrochem 15:47–65
6. The Chemical Durability of Glass (1972–1973) A bibliographic review of literature, vols 1–2. International Commission on Glass, Charleroi
7. Scholze H (1991) Glass—nature, structure, and properties. Springer, Berlin
8. Paul A (1982, 1990) Chemistry of glasses. Chapman & Hall, London
9. Doremus RH (1994) Glass science. Wiley, New York
10. Clark DE, Pantano CG, Hench LL (1979) Corrosion of glass. Books for the Glass Industry, New York
11. Clark DE, Zoitos BK (eds) (1992) Corrosion of glass, ceramics, and ceramic superconductors. Noyes Publications, Park Ridge
12. Conradt R (1999) Thermodynamics of glass corrosion. In: Bach H, Krause D (eds) Analysis of the composition and structure of glass and glass ceramics. Springer, Berlin
13. Pourbaix M (1974) Atlas of electrochemical equilibria in aqueous solutions. National Association of Corrosion Engineers, Houston



14. Iler RK (1979) *The chemistry of silica*. Wiley, New York
15. Butler JN (1982) *Carbon dioxide equilibria and their application*. Addison-Wesley Publ., Sydney
16. Bergna HE (1994) *The colloid chemistry of silica*. Am Chem Soc, Washington
17. Sposito G (1996) *The environmental chemistry of alumina*. Florida, Boca Raton
18. Bowers TS, Jackson KJ, Helgeson HC (1984) *Equilibrium activity diagrams for coexisting minerals and aqueous solutions at pressures and temperatures to 5 kb and 600 °C*. Springer, Berlin
19. Baes CF Jr, Mesmer RE (1981) The thermodynamics of cation hydrolysis. *Am J Sci* 281:935–962
20. Aargard P, Helgeson HC (1982) Thermodynamic and kinetic constraints on reaction rates among minerals and aqueous solutions, I. Theoretical considerations. *Am J Sci* 282:237–285 (1982)
21. Conradt R (2008) Chemical durability of oxide glasses in aqueous solutions: a review. *J Am Ceram Soc* 91:728–735
22. Gin S, Abdelouas A, Criscenti LJ et al (2013) An international initiative on long-term behavior of nuclear waste glass. *Mater Today* 16:243–248
23. Gin S, Guo X, Delaye J-M et al (2020) Insights into the mechanisms controlling the residual corrosion rate of borosilicate glasses. *Mater Degrad (Nat Partner J NJP)*
24. Richter T, Frischat GH, Borchardt G (1985) Short time leaching of a soda-lime glass in H<sub>2</sub>O and D<sub>2</sub>O. *Phys Chem Glasses* 26:208–212
25. Scholze H, Helmreich D, Bakardijev I (1975) Investigations on the behavior of soda lime glasses in diluted acids (German). *Glastech Ber* 48:237–247
26. Scholze H (1975) Significance of the leached layer for the chemical durability: investigation with soda-lime-silica glass. *Glastech Ber* 58:116–124
27. Baer DR, Pederson LR, McVay GL (1984) Glass reactivity in aqueous solutions. *J Vac Sci Technol A* 2:738–743
28. March P, Rauch F (1990) Leaching studies of soda-lime-silica glass using deuterium- and <sup>18</sup>O-enriched solutions. *Glastech Ber* 63:154–162
29. Helmich M, Rauch F (1993) On the mechanism of diffusion of water in silica glass. *Glastech Ber* 66:195–200
30. Wang C, Häfner W, Krausch G, Rädlein E (2004) Study of surface changes on industrial glasses with AFM, FE-SEM, EDX, SNMS and LM. Pt. 1: glass skin and corrosion. *Glass Sci Technol* 77:103–101 (2004)
31. Smets BMJ, Lommen TPA (1981) SIMS and XPS investigation of the leaching of glasses. *Verres Réfract.* 35:84–90
32. Lanford WA (1978) <sup>15</sup>N profiling: scientific applications. *Nucl Instr Methods* 149:1–8
33. Schreiner M, Piplits K, March P, Stingeder G, Rauch F, Grassenbauer M (1989) Surface analytical investigation of leached potash-lime-silicate glass. *Fresen J Analyt Chem* 333:386–387
34. Djambazov P, Prange A, Conradt R (2008) Glass surface analysis by an optimized sequential etching technique using the corrosive agent HF/HNO<sub>3</sub>. *Adv Mater Res* 39–40:351–354
35. Hench LL (1975) Characterization of glass corrosion and durability. *J Non-Cryst Solids* 19:27–39
36. Doremus RH, Mehrotra Y, Lanford WA et al (1983) Reaction of water with glass: influence of a transformed surface layer. *J Mater Sci* 18:612–622
37. Bunker BB, Headley TJ, Douglas SC (1984) Gel structure in leached alkali silicate glass. *Mater Res Soc Symp Proc* 32:41–46
38. Casey WH, Westrich HR, Banfield JF, Ferruzzi G, Arnold GW (1993) Leaching and reconstruction at the surfaces of dissolving chain-silicate minerals. *Nature* 366:253–256
39. Portal S, Sempere R (2003) Study of alkali silicate glass corrosion using spectroscopy ellipsometry and secondary ion mass spectroscopy. *Phys Chem Glasses* 44:303–307
40. Pantano CG, Hamilton JP (2000) Characterization and structure of leached surface layers on glass. *Rev Staz Sper Vetro* A6:81–86



41. Tomozawa M, Capella S (1983) Microstructure in hydrated silicate glasses. *J Am Ceram Soc* 66:C24–C25
42. Liesegang RE (1896). *Naturwiss Wochenschr* 11:353; (1897) *Z. Phys. Chem* 23:365.
43. Conradt R, Roggendorf H, Ostertag R (1986) The basic corrosion mechanisms of HLW glasses. Comm. Europ. Union, Luxembourg
44. Conradt R, Roggendorf H, Scholze H (1984) Chemical durability of a multicomponent glass in a simulated carnallite/rock salt environment. *Mater Res Soc Symp Proc* 26:9–15
45. Djambazov P (2014) Theoretical and experimental investigation of the early stages of aqueous corrosion of silicate glasses (German). Thesis, RWTH Aachen
46. Jantzen CM, Plodinec MJ (1984) Thermodynamic model of natural, medieval, and nuclear waste glass durability. *J Non-Cryst Solids* 62:207–223
47. Jantzen CM (1992) Thermodynamic approach to glass corrosion. In: Clark DE, Zaitos BK (eds) *Corrosion of glass, ceramics, and ceramic superconductors*. Noyes Publ., Park Ridge
48. Conradt R, Geasee P (1996) An improved thermodynamic approach to the stability of multi-component silicate glasses in aqueous solutions. *Ber Bunsenges Phys Chem* 100:1408–1410
49. Conradt R (2001) A proposition for an improved theoretical treatment of the corrosion of multi-component glasses. *J Nucl Mater* 298:19–26
50. Grambow B (1992) Geochemical approach to glass dissolution. In: Clark DE, Zaitos BK (eds) *Corrosion of glass, ceramics, and ceramic superconductors*. Noyes Publ., Park Ridge
51. Boksay Z, Bouquet G (1980) The pH dependence and an electrochemical interpretation of the dissolution rate of a silicate glass network. *Phys Chem Glasses* 21:110–113
52. Roine A, Outokumpu HSC chemistry ver. 3.02. Chemical reaction and equilibrium software with extensive database. Pori, Finland
53. Doremus RH (1981) Time dependence of the reaction of water with glass. *Nucl Chem Waste Manage* 2:119–123
54. Conradt R, Roggendorf H, Scholze H (1985) Investigation on the role of surface layers in HLW glass leaching. *Mater Res Soc Symp Proc* 50:203–210

# Chapter 3

## Radiation Heat Transfer in Glass Melts: Key Concepts and Phenomena



Manoj Choudhary

### 3.1 Introduction

This chapter describes key concepts and phenomena involved in heat transfer by thermal radiation in silica-based glass melts during industrial glass melting and melt delivery processes. We emphasize melting and delivery because they share commonalities across different segments of the glass industry (e.g., container, fibers, sheets, tubes, tableware). The forming processes, on the other hand, tend to be segment specific. Nevertheless, some of the topics covered here, particularly, those dealing with the basic concepts, apply to forming processes also. Thermal radiation in glass melts takes place along with the conduction and convection heat transfers, but at the elevated temperatures encountered in melting and delivery processes (1500–1800 K), thermal radiation is usually the dominant mode of heat transfer. We should also note that heat transfer in glass furnaces occurs in combination with and as a part of several chemical and physical processes. These include combustion, batch reactions, evolution of gases, volatilization from glass melt surface, dissolution of silica grains in the glass melt, and glass melt and gas flows [1–3]. The rate of heat transfer impacts all of them because the thermodynamic, kinetic, and transport properties of materials involved are functions of temperature. Thus, heat transfer plays an important role in determining factors of critical importance in glass manufacturing, namely energy efficiency, productivity, environmental emissions, and furnace life. We focus on thermal radiation because of its dominance among the three modes of heat transfer and also because radiative heat transfer in glass furnaces possesses certain special attributes that are not very familiar to glass technologists.

A key aspect of radiation heat transfer in glassmaking processes is the presence of participating media—i.e., media that emit, absorb, and/or scatter radiation passing through them. The various media present in industrial glass furnaces (the mixture

---

M. Choudhary (✉)

Materials Science and Engineering, The Ohio State University, Columbus, USA

e-mail: [mchoudhary61@gmail.com](mailto:mchoudhary61@gmail.com)

of raw materials or the glass batch, combustion gases, foam, and the glass melt) do so. These participating media entail different geometric scales and radiation properties and, as a consequence, have specific features and involve different levels of complexities. However, the mathematical formulations described here apply to all of them.

The chapter builds on earlier publications by the author and his colleagues on heat transfer in glass furnaces [4–6] and includes elements of Refs. [2, 3] cited above. We begin with a review of some basic concepts of thermal radiation in Sect. 3.2. Next we discuss the emission, absorption, and scattering in participating media and derive the radiative transport equation (RTE—the equation that describes the change in the radiative intensity with position along a specific direction due to emission, absorption, and scattering) in Sect. 3.3. This is followed, in Sect. 3.4, by a discussion of the radiative heat flux and its divergence—the entities that are related to the radiative intensity and appear in the energy equation, and are needed to calculate the temperature distribution in the participating medium. In Sect. 3.5, we present the two limiting cases of the RTE—the optically thin and thick cases and discuss the latter in some detail as the optically thick approximation involving the concept of radiation or photon conductivity is widely used in the modeling of thermal radiation in the glass melts. The absorption spectra of commercial glass melts are reviewed in Sect. 3.6. Section 3.7 describes two approaches for the modeling of radiative heat transfer in glass melts—the discrete ordinates method involving numerical solution of the RTE and the optically thick approximation approach (also called the Rosseland approach) involving the radiative conductivity. This section also provides values of the radiation conductivity of a number of commercial glass melts. In Sect. 3.8, we compare modeling results on flow and heat transfer in a float glass furnace melting an ultra-clear glass obtained using the two approaches described in Sect. 3.7. Finally, we present some concluding remarks in Sect. 3.9.

## 3.2 Review of Some Basic Concepts of Thermal Radiation

A detailed discussion of the vast topic of the fundamentals of thermal radiation is well beyond the scope of this chapter. We will limit ourselves to the bare minimum essential to describe the main theme of concern to us, namely thermal radiation in participating media. In describing the theory and basic concepts in this section, we will closely follow the texts of Sparrow and Cess [7] and Modest [8].

### 3.2.1 Planck's Law (Spectral/Monochromatic Blackbody Emissive Power)

A **blackbody** is an idealized body that absorbs all the electromagnetic radiation incident on it. It is a perfect absorber and a perfect emitter of electromagnetic radiation. The **total emissive power** of a black body,  $E_b$ , is the radiative heat flux emitted by it over the entire wavelength spectrum. It is expressed in the units of  $\text{W m}^{-2}$ . The **spectral or monochromatic emissive power** of a black body,  $E_{b\lambda}$ , is its emissive power at a given wavelength per unit wavelength interval and is given by Planck's law. It is specified in units:  $\text{W m}^{-2} \text{ m}^{-1}$  (or  $\text{W m}^{-2} \mu\text{m}^{-1}$  if the wavelength is in  $\mu\text{m}$ ).

$$E_{b\lambda} = \frac{C_1}{n^2 \lambda^5 (e^{C_2/n\lambda T} - 1)} \quad (3.1)$$

where  $n$  is the refractive index of the medium surrounding the black body,  $\lambda$  is the wavelength, and  $T$  is the absolute temperature. The constants  $C_1$  and  $C_2$  are given below.

$$C_1 = 2\pi hc_0^2 = 3.7419 \times 10^{-16} \text{ W m}^2 \quad (3.2a)$$

$$C_2 = hc_0/k = 1.4388 \times 10^{-2} \text{ m K} \quad (3.2b)$$

where  $h$  is the Planck constant ( $=6.626 \times 10^{-34} \text{ J s}$ ),  $c_0$  is the speed of light in vacuum ( $=2.9979 \times 10^8 \text{ m s}^{-1}$ ), and  $k$  is the Boltzmann constant ( $1.3806 \times 10^{-23} \text{ J K}^{-1}$ ).

Equation (3.1), expressed in terms of the wavelength,  $\lambda$ , is the frequently used form of Planck's law. It is valid for a constant or wavelength-independent refractive index,  $n$ . This is the certainly the case for vacuum ( $n = 1$ ) and ordinary gases such as  $\text{CO}_2$ ,  $\text{N}_2$ ,  $\text{O}_2$ , and water vapor present in the combustion chamber of glasses ( $n \approx 1$ ). It is also a good assumption for semitransparent media such as glass in the wavelength range of interest for thermal radiation calculations (e.g., for quartz,  $1.52 < n < 1.68$  in the  $0.2\text{--}2.4 \mu\text{m}$  wavelength range) [8, p. 7].

### 3.2.2 Stefan–Boltzmann Law (Total Blackbody Emissive Power)

From the definitions of the total and the spectral emissive powers, it is clear that

$$E_b = \int_0^\infty E_{b\lambda} d\lambda \quad (3.3)$$

Thus, the total blackbody emissive power  $E_b$  is obtained by integrating the spectral blackbody emissive power  $E_{b\lambda}$  over the entire wavelength spectrum.

$$E_b = \int_0^{\infty} E_{b\lambda} d\lambda = n^2 \sigma T^4 \tag{3.4}$$

where  $\sigma$  is the Stefan–Boltzmann constant.

$$\sigma = 5.670 \times 10^{-8} \text{ W m}^{-2} \text{ K}^{-4} \tag{3.5}$$

Equation (3.4) is the well-known Stefan–Boltzmann law, and its derivation assumes the refractive index,  $n$  to be independent of the wavelength.

### 3.2.3 Intensity of Radiation

The **intensity of radiation** is a measure of the radiative energy passing in any given direction. The concept is similar to the emissive power discussed above, but unlike the emissive power, the intensity is direction specific. We define the relationship between the emissive power and the radiative intensity with reference to Fig. 3.1, which shows a pencil of rays emitted from a surface  $dA$  and forming an infinitesimal solid angle,  $d\Omega$ .

Let  $dE_\lambda$  be the rate of spectral or monochromatic radiant energy emitted by  $dA$  per unit area in the direction  $\theta$  and contained within the solid angle,  $d\Omega$ . The **spectral radiative intensity**,  $I_\lambda$ , is the rate of radiative energy flow per unit area normal to the pencil of rays per unit solid angle per unit wavelength. It is expressed in  $\text{W m}^{-2} \text{ sr}^{-1} \mu\text{m}^{-1}$  (the wavelength unit is  $\mu\text{m}$ ). The steradian (sr) is the unit of solid angle. From this definition given, it is clear that

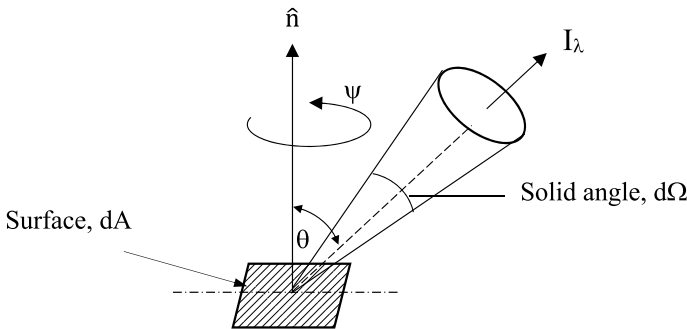
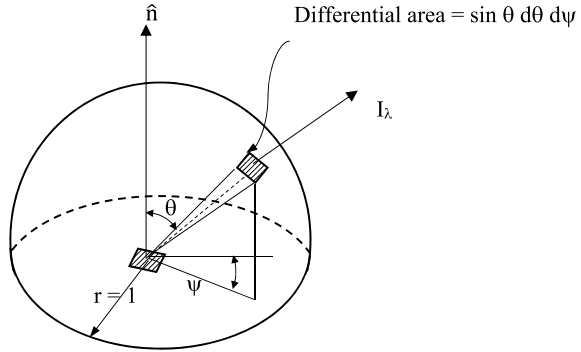


Fig. 3.1 Pencil of rays along direction  $\theta$  and forming the solid angle,  $d\Omega$

**Fig. 3.2** Radiant energy emitted from the surface into a unit hemispherical enclosure



$$I_\lambda = \frac{1}{\cos \theta} \frac{dE_\lambda}{d\Omega} \tag{3.6}$$

The term  $\cos \theta$  comes because the intensity is defined with reference to area normal to the pencil of rays whereas the emissive power is defined with respect to the area of the emitting surface (i.e.,  $dA$ ). With reference to Fig. 3.2, the solid angle is defined as the differential area on the unit hemisphere. As mentioned before, its unit is steradian (sr).

$$d\Omega = \sin \theta \, d\theta \, d\psi \tag{3.7}$$

The spectral energy flux emitted from the surface and passing through the hemisphere,  $E_\lambda$  is obtained by combining Eqs. (3.6) and (3.7) and integrating

$$E_\lambda = \int_0^{2\pi} \int_0^{\pi/2} I_\lambda \cos \theta \sin \theta \, d\theta \, d\psi \tag{3.8}$$

The **total radiative intensity**,  $I$  is the rate of radiative energy flow per unit area normal to the pencil of rays per unit solid angle. It is expressed in  $\text{W m}^{-2} \text{sr}^{-1}$ . It is obtained by integrating  $I_\lambda$  over the entire wavelength domain.

$$I = \int_0^\infty I_\lambda \, d\lambda \tag{3.9}$$

The total emissive power  $E$  and the total radiative intensity are related as

$$E = \int_0^{2\pi} \int_0^{\pi/2} I \cos \theta \sin \theta \, d\theta \, d\psi \tag{3.10}$$

There are many cases in which radiation is (or approximated to be) independent of direction or isotropic. In such situations

$$E_{\text{isotropic}} = \pi I_{\text{isotropic}} \quad (3.11)$$

The blackbody emissive power is isotropic, and (3.8) and (3.10) take the simple forms

$$E_{b\lambda} = \pi I_{b\lambda} \quad (3.12a)$$

$$E_b = \pi I_b \quad (3.12b)$$

The above discussion and the equations were for radiation leaving a surface. The concept of radiative intensity also applies to media that emit, absorb, and scatter radiation. In that case, however, the total intensity,  $I$ , at a given location is the net rate of radiative energy flow (i.e., the balance of emission, absorption, and scattering) per unit area normal to the rays per unit solid angle. For the spectral intensity,  $I_\lambda$ , we add the term per unit wavelength.

### 3.2.4 Radiation Properties of Surfaces

There are 4 radiation properties associated with a surface. Three of them deal with the interaction of the surface with incoming or incident radiation. The incident radiation may be reflected away, absorbed by, or transmitted through the surface. The fraction of the incident radiation that is reflected is called the **reflectivity**,  $\rho$ . The fraction absorbed is called the **absorptivity**,  $\alpha$  and the fraction transmitted is called the **transmissivity**,  $\tau$ . The sum of these three must equal 1.

$$\rho + \alpha + \tau = 1 \quad (3.13)$$

Obviously, these properties have values between 0 and 1. For an opaque material  $\tau = 0$ .

The fourth property deals with the energy emitted from the surface and is called the emissivity, **emissivity**,  $\varepsilon$ . It is the ratio of the energy emitted from the surface and the energy emitted by a black surface at the same temperature.

$$\varepsilon = \frac{E}{E_b} \quad (3.14)$$

Emissivity also varies between 0 and 1. For a black surface  $\alpha = 1$ ,  $\rho = \tau = 0$ , and  $\varepsilon = 1$ .

All the properties mentioned above may depend on temperature and the wavelength. The emissivity may vary with the outgoing directions; absorptivity may depend on the incoming or incident directions, and reflectivity and transmissivity may vary with both incoming and outgoing directions. To account for the wavelength and directional dependence, we use the hemispherical (i.e., directionally averaged) values at specific wavelength. These are called **hemispherical spectral reflectivity** ( $\rho_\lambda$ ), **hemispherical spectral absorptivity** ( $\alpha_\lambda$ ), **hemispherical spectral transmissivity** ( $\tau_\lambda$ ), and **hemispherical spectral emissivity** ( $\varepsilon_\lambda$ ).

The directional spectral absorptivity and emissivity are related by **Kirchhoff's law**. It states that for a system in thermodynamic equilibrium, the directional absorptivity and emissivity are equal. This is stated below.

$$\alpha_\lambda(\theta, \psi) = \varepsilon_\lambda(\theta, \psi) \quad (3.15)$$

If the absorptivity and emissivity do not depend on the direction and/or the irradiation is diffuse (i.e., independent of direction), then the hemispherical absorptivity and emissivity are also equal.

$$\alpha_\lambda = \varepsilon_\lambda \quad (3.16)$$

A surface whose emissivity and absorptivity are independent of wavelength (i.e.,  $\varepsilon_\lambda$  and  $\alpha_\lambda$  do not depend on the wavelength  $\lambda$ ) is called a **gray surface**.

### 3.3 Radiation in Absorbing, Emitting, and Scattering Media

Radiation intensity passing through a participating medium (i.e., a medium that absorbs, emits, and scatter radiation passing through it) in any direction is attenuated, i.e., loses energy, by absorption and scattering. At the same time, however, it is augmented, i.e., gains energy by emission and by a fraction of radiation scattered elsewhere that reaches it. The scattering away from the direction and causing attenuation being considered is called "out-scattering." The scattering being received from elsewhere and causing augmentation is referred to as the "in-scattering."

The major material domains in a glass furnace (combustion gases, glass melt, foam on the melt surface, the melting batch) are participating media. The physics or mechanism of absorption, emission, and scattering in these media are different. In the case of glass melt, minor materials, especially the first row transition metal ions, may cause significant absorption. In case of gases, the absorption or emission is associated with transition between the energy levels of atoms/molecules present in the gas. The basic difference between absorption and scattering is that absorbed energy is converted into the internal energy, while the scattered energy is redirected. Scattering may be caused by gas molecules and due to inhomogeneities present in



the medium (e.g., suspended solid particles or liquid droplets in the gas, bubbles in foam and glass met). Scattering is usually ignored in the analysis and modeling of radiation heat transfer in glass melts.

### 3.3.1 Attenuation of Radiative Intensity by Absorption and Scattering

Figure 3.3 shows a beam of radiation of intensity  $I_\lambda$  traveling within a pencil of rays in a participating medium. It undergoes attenuation by absorption and scattering as it traverses through the distance  $ds$ . The amount of absorption and scattering has each been found to be directly proportional the intensity and the distance.

The amounts absorbed and scattered in the path length  $ds$  are

$$(dI_\lambda)_{\text{abs}} = -\kappa_\lambda I_\lambda ds; \quad (dI_\lambda)_{\text{sca}} = -\gamma_\lambda I_\lambda ds \quad (3.17a, b)$$

where  $\kappa_\lambda$  and  $\gamma_\lambda$  are the spectral absorption and scattering coefficients, respectively. The total attenuation due to both absorption and scattering is called **extinction** and is given by

$$dI_\lambda = -(\kappa_\lambda + \gamma_\lambda) I_\lambda ds \quad (3.18)$$

The sum  $\kappa_\lambda + \gamma_\lambda$  is called the spectral **extinction coefficient**,  $\beta_\lambda$ .

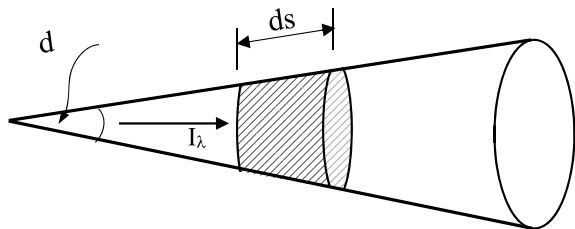
$$\beta_\lambda = \kappa_\lambda + \gamma_\lambda \quad (3.19)$$

Integration of Eq. (3.18) from 0 to  $s$  gives

$$I_\lambda = I_{o\lambda} \exp\left(-\int_0^s \beta_\lambda ds\right) = I_{o\lambda} e^{-\tau_{s\lambda}} \quad (3.20)$$

where  $I_{o\lambda}$  is the radiative intensity at  $s = 0$  and  $\tau_{s\lambda}$  is the optical distance defined as

**Fig. 3.3** Attenuation of radiative intensity by absorption and scattering



$$\tau_{s\lambda} = \int_0^s \beta_\lambda ds \quad (3.21)$$

A medium whose absorption and scattering coefficients are independent of wavelength (i.e.,  $\kappa_\lambda$  and  $\gamma_\lambda$  do not depend on the wavelength  $\lambda$ ) is called a **gray medium**.

### 3.3.2 Augmentation of Radiative Intensity by Emission and Scattering

For a medium in local thermodynamic equilibrium (atomic and molecular states are characterized by their equilibrium distributions), the radiation intensity is isotropic, and from Kirchhoff's law (given earlier by Eq. (3.16) for absorptivity and emissivity of surfaces, here, we are discussing a medium), the emission coefficient equals the absorption coefficient,  $\kappa_\lambda$ . Thus, the emission intensity (rate of energy emitted per unit area) is  $\kappa_\lambda \cdot I_{b\lambda}$ . Thus, the **augmentation due to emission** is

$$(dI_\lambda)_{\text{emi}} = \kappa_\lambda I_{b\lambda} ds = \kappa_\lambda \frac{E_{b\lambda}}{\pi} ds \quad (3.22)$$

We now consider the augmentation of the radiative intensity due to in-scattering (the portion of energy scattered elsewhere and redirected to the location being considered). We follow the approach of Modest [8, pp. 282–283]. Let us consider, as shown in Fig. 3.4, a pencil of rays of radiative intensity  $I_\lambda(s')$  moving in the direction  $s'$  and forming solid angle  $d\omega'$ . The beam impinges on a differential volume  $dV$  of area  $dA$  and thickness  $ds$  of a participating medium. We want to calculate how much of the incident radiant energy is scattered in the direction  $s$ .

Let us recall that the radiative intensity is the energy flux (i.e., rate of energy transfer per unit area normal to the rays) per unit solid angle and per unit wave length interval. So, the energy flux in the pencil of rays of solid angle  $d\omega'$  is

$$I_\lambda(s') d\Omega' d\lambda$$

The amount of energy from within the solid angle  $d\omega'$  impinging on the surface  $dA$  is

$$I_\lambda(s') (dA \cos \theta) d\Omega' d\lambda$$

where, as shown in Fig. 3.4,  $\theta$  is the angle formed by  $s'$  and  $s$ . A portion of the incident energy is scattered as it travels through the distance  $ds/\cos \theta$  of the participating medium. The total amount of energy scattered away from  $s'$  is,

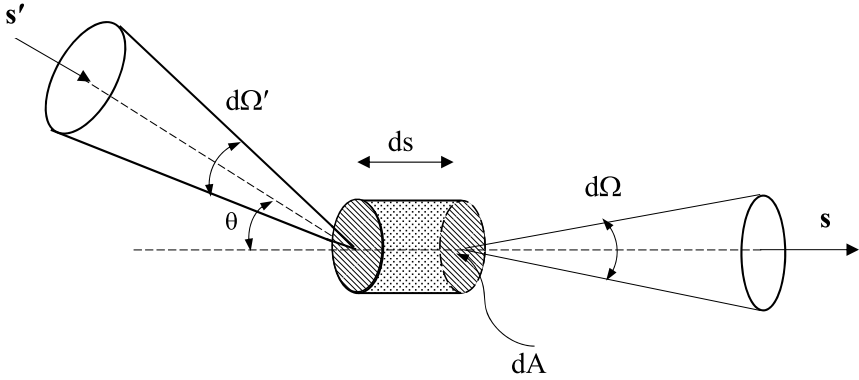


**Fig. 3.4** Scattering of radiation from direction  $s'$  into direction  $s$

$$\gamma_\lambda I_\lambda(s') (dA \cos \theta) d\Omega' d\lambda \left( \frac{ds}{\cos \theta} \right) = \gamma_\lambda I_\lambda(s') dA d\Omega' d\lambda ds$$

Only, a fraction of the above amount is scattered in the direction of interest  $s$ . Let  $\Phi_\lambda(s', s)$  be the probability of a ray in the direction  $s'$  being scattered in the direction  $s$ .  $\Phi_\lambda$  is called the **scattering phase function**. The amount of energy scattered flux from the pencil of rays of solid angle  $d\omega'$  into the pencil of rays of solid angle  $d\omega$  is

$$\gamma_\lambda I_\lambda(s') dA d\Omega' d\lambda \Phi_\lambda(s', s) \frac{d\Omega}{4\pi}$$

The augmentation of the radiative intensity in the direction  $s'$  due to scattering from all directions is obtained by integrating the above over the entire  $4\pi$  steradians solid angle domain.

$$(dI_\lambda)_{\text{isca}}(s) dA d\Omega d\lambda = \frac{\gamma_\lambda}{4\pi} dA d\Omega d\lambda ds \int_{4\pi} I_\lambda(s') \Phi_\lambda(s', s) d\Omega'$$

From the above, we get

$$(dI_\lambda)_{\text{isca}}(s) = ds \frac{\gamma_\lambda}{4\pi} \int_{4\pi} I_\lambda(s') \Phi_\lambda(s', s) d\Omega' \quad (3.23)$$

The phase function satisfies the normalization condition

$$\frac{1}{4\pi} \int_{4\pi} \Phi_\lambda(s', s) d\Omega \equiv 1 \quad (3.24)$$

### 3.3.3 The Radiative Transfer Equation

The radiative transfer equation (RTE) is the radiative energy balance equation. It describes the change in the radiative intensity with time and position due to emission, absorption, and scattering as the radiative energy travels in a given direction in a participating medium. We will not consider the time or the transient effect, which is typically not relevant in heat transfer applications. In the preceding sections, we presented the equations for the attenuation and augmentation of the spectral radiation intensity. The RTE brings them all together as shown below.

$$\frac{dI_\lambda}{ds} = \mathbf{s} \cdot \nabla I_\lambda = \kappa_\lambda \frac{E_{b\lambda}}{\pi} - \beta_\lambda I_\lambda + \frac{\gamma_\lambda}{4\pi} \int_{4\pi} I_\lambda(\mathbf{s}') \Phi_\lambda(\mathbf{s}', \mathbf{s}) d\Omega' \quad (3.25)$$

Equation (3.25) describes the change in the spectral radiative intensity in direction  $\mathbf{s}$  as a result of augmentation due to emission, attenuation due to absorption and out-scattering, and augmentation due to in-scattering. Using the optical coordinate  $\tau_{s\lambda}$  defined in Eq. (3.21), the RTE may be written as

$$\frac{dI_\lambda}{d\tau_{s\lambda}} = -I_\lambda + (1 - \omega_\lambda) \frac{E_{b\lambda}}{\pi} + \frac{\omega_\lambda}{4\pi} \int_{4\pi} I_\lambda(\mathbf{s}') \Phi_\lambda(\mathbf{s}', \mathbf{s}) d\Omega' \quad (3.26)$$

where  $\omega_\lambda$ , called the single scattering albedo, is

$$\omega_\lambda = \frac{\gamma_\lambda}{\kappa_\lambda + \gamma_\lambda} = \frac{\gamma_\lambda}{\beta_\lambda} \quad (3.27)$$

The RTE has two limiting cases, namely optically thin and optically thick cases. Before describing them, it is helpful to review how the radiative intensity is related to the radiative heat flux and its divergence. We do so in the next section.

## 3.4 Radiative Heat Flux and Its Divergence

In glass melting processes, as in any high temperature process involving fluids, heat transfer takes place by all three modes, namely conduction, convection, and radiation. In the special case of a participating medium, such as a glass melt, as we have discussed above, thermal radiation interacts with the medium through emission, absorption, and scattering. The net effect of this interaction is the radiative heat flux in the medium which must be accounted for in the energy conservation equation, written below in its commonly used form (and neglecting effects such as viscous dissipation) for viscous flows of incompressible fluids [9].

$$\rho C_p \frac{\partial T}{\partial t} = -\rho C_p \mathbf{v} \cdot \nabla T + \nabla \cdot k \nabla T - \nabla \cdot \mathbf{q}_R + \dot{Q} \quad (3.28)$$

where  $T$  is the temperature,  $\rho$  the density,  $C_p$  the specific heat at constant pressure,  $\mathbf{v}$  the velocity vector,  $k$  the thermal conductivity,  $\mathbf{q}_R$  the radiative flux, and  $\dot{Q}$  the volumetric rate of heat generation. Equation (3.28) represents the rate of change of enthalpy of a fluid due to the net rates of heat transfer by convection, conduction and radiation, and the rate of heat generation (all on a per unit volume basis). Our interest is in calculating the radiative heat flux,  $\mathbf{q}_R$  and its divergence  $\nabla \cdot \mathbf{q}_R$ . It should be clear from the RTE that the presence of the radiative flux makes Eq. (3.28) an integro-differential equation (unless scattering is ignored, in which case it is the more familiar differential equation). In the following, we simply present equations for the radiative fluxes and their divergences without any mathematical derivations.

The spectral and total heat fluxes,  $\mathbf{q}_{R\lambda}$ , and  $\mathbf{q}_R$  are given by the following equations [8, pp. 292–295].

$$\mathbf{q}_{R\lambda} = \int_{4\pi} I_\lambda(\mathbf{s}) \hat{\mathbf{s}} \, d\Omega \quad (3.29)$$

$$\mathbf{q}_R = \int_0^\infty \mathbf{q}_{R\lambda} \, d\lambda \quad (3.30)$$

where  $\hat{\mathbf{s}}$  in Eq. (3.29) is the unit vector in the  $s$ -direction. For the Cartesian coordinate system, for example, Eq. (3.29) can be separated into the  $x$ ,  $y$ , and  $z$  components of the spectral radiative flux.

$$\nabla \cdot \mathbf{q}_{R\lambda} = \kappa_\lambda \left[ 4E_{b\lambda} - \int_{4\pi} I_\lambda \, d\Omega \right] = \kappa_\lambda [4E_{b\lambda} - G_\lambda] \quad (3.31)$$

$$\nabla \cdot \mathbf{q}_R = \nabla \cdot \int_0^\infty \mathbf{q}_{R\lambda} \, d\lambda \quad (3.32)$$

### 3.5 Approximate and Limiting Cases of RTE

In Sects. 3.3 and 3.4, we discussed three-dimensional radiative heat transfer in emitting, absorbing, and scattering media. Heat transfer in glass melting furnaces is three-dimensional, and later, in Sect. 3.8, we will discuss some calculate results for 3D heat transfer in a glass furnace. But, first, we describe some simpler versions

and limiting cases of the RTE using one-dimensional treatment. This provides useful physical insights in a clear and easier to understand manner.

### 3.5.1 One-Dimensional RTE in a Non-scattering Medium

Let us consider one-dimensional radiative heat transfer in a non-scattering medium confined between two infinite, parallel, opaque, and diffuse surfaces. The system is shown in Fig. 3.5. As noted earlier in connection with Eq. (3.13), an opaque surface does not transmit light through it. A diffuse surface emits and reflects radiation equally in all angular directions. We will use this case with its simple equations as the reference point to subsequently discuss the two limiting cases of the RTE, namely the optically thin and thick cases. The following discussion closely follows the approaches in [4, 7, pp. 207–221].

With reference to Fig. 3.5, the upward and downward monochromatic radiative intensities along an angle  $\theta$  with the  $z$ -direction are denoted by  $I_{+\lambda}$  and  $I_{-\lambda}$  respectively.

For a non-scattering medium, the one-dimensional RTEs for the positive and negative  $y$  directions are

$$\cos \theta \frac{dI_{+\lambda}}{dz} = \kappa_\lambda \left( \frac{E_{b\lambda}}{\pi} - I_{+\lambda} \right) \tag{3.33}$$

$$\cos \theta \frac{dI_{-\lambda}}{dz} = \kappa_\lambda \left( \frac{E_{b\lambda}}{\pi} - I_{-\lambda} \right) \tag{3.34}$$

Let us introduce the following parameters

$$\tau_\lambda = \int_0^z \kappa_\lambda dz; \quad \tau_{L\lambda} = \int_0^L \kappa_\lambda dz; \quad \mu = \cos \theta \tag{3.35}$$

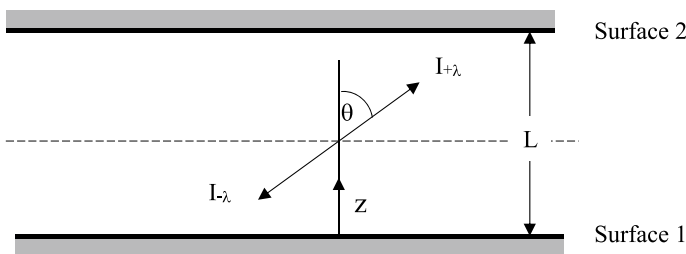


Fig. 3.5 One-dimensional radiative heat transfer in a medium between two plane, parallel surfaces

We had previously, in Eq. (3.21), defined optical coordinate terms of the extinction coefficient,  $\beta$  and the directional coordinate  $s$ . In the present case of no scattering and 1D thermal radian, we are using the absorption coefficient  $\kappa$  and direction  $z$  to define the optical coordinate  $\tau_\lambda$  and the optical thickness  $\tau_{L\lambda}$ . Equations (3.33) and (3.34) may now be written as

$$\mu \frac{dI_{+\lambda}}{d\tau_\lambda} = \frac{E_{b\lambda}}{\pi} - I_{+\lambda} \quad (3.36)$$

$$\mu \frac{dI_{-\lambda}}{d\tau_\lambda} = \frac{E_{b\lambda}}{\pi} - I_{-\lambda} \quad (3.37)$$

The boundary conditions for the above equations may be expressed in terms of the surface radiosities or energy fluxes leaving surfaces 1 and 2,  $R_{1\lambda}$ , and  $R_{2\lambda}$ . For diffuse surfaces assumed here, the radiation intensities are independent of direction and we may write

$$I_{+\lambda}(o) = \frac{R_{1\lambda}}{\pi} \quad (3.38)$$

$$I_{-\lambda}(\tau_{L\lambda}) = \frac{R_{2\lambda}}{\pi} \quad (3.39)$$

Integration of Eqs. (3.36) and (3.37) with the boundary conditions Eqs. (3.38) and (3.39) gives

$$I_{+\lambda} = \frac{R_{1\lambda}}{\pi} e^{-\tau_\lambda/\mu} + \frac{1}{\pi} \int_0^{\tau_\lambda} E_{b\lambda}(t) e^{-(\tau_\lambda-t)/\mu} \frac{dt}{\mu} \quad (3.40)$$

$$I_{-\lambda} = \frac{R_{2\lambda}}{\pi} e^{(\tau_{L\lambda}-\tau_\lambda)/\mu} - \frac{1}{\pi} \int_{\tau_\lambda}^{\tau_{L\lambda}} E_{b\lambda}(t) e^{-(\tau_\lambda-t)/\mu} \frac{dt}{\mu} \quad (3.41)$$

The first terms on the right hand side of Eqs. (3.40) and (3.41) represent attenuation of energy originating at surfaces 1 [in Eq. (3.40)] and 2 [in Eq. (3.41)]. The integral terms represent augmentation due to emission over a finite path length.

Our principal interest is in calculating the radiative flux and its divergence. These are given by the 1D equivalents of Eqs. (3.29)–(3.32).

$$q_{R\lambda}(\tau_\lambda) = \int_{4\pi} I_\lambda(\mathbf{s}) \hat{\mathbf{s}} d\Omega = 2\pi \int_0^\pi I_\lambda \cos \theta \sin \theta d\theta = 2\pi \int_{-1}^1 I_\lambda \mu d\mu \quad (3.42)$$

The integral in Eq. (3.40) may be decomposed into two parts as shown below

$$q_{R\lambda}(\tau_\lambda) = 2\pi \int_0^1 I_{+\lambda}\mu \, d\mu - 2\pi \int_0^{-1} I_{-\lambda}\mu \, d\mu \quad (3.43)$$

On substituting Eqs. (3.38) and (3.39) into Eq. (3.43), we get

$$\begin{aligned} q_{R\lambda}(\tau_\lambda) &= 2R_{1\lambda}E_3(\tau_\lambda) - 2R_{2\lambda}E_3(\tau_{L\lambda} - \tau_\lambda) \\ &+ 2 \int_0^{\tau_\lambda} E_{b\lambda}(t)E_2(\tau_\lambda - t)dt - 2 \int_{\tau_\lambda}^{\tau_{L\lambda}} E_{b\lambda}(t)E_2(t - \tau_\lambda)dt \end{aligned} \quad (3.44)$$

where the functions  $E_n(t)$  are known as exponential integral functions given by

$$E_n(t) = \int_0^1 \mu^{n-2} e^{-t/\mu} \, d\mu \quad (3.45)$$

The integral functions are explained and tabulated in [7, pp. 351–353, 8, pp. 852–854]. We provide below some values and approximations for the integral functions.

$$E_1(0) = \infty; \quad E_2(0) = 1; \quad E_3(0) = \frac{1}{2}; \quad E_4(0) = \frac{1}{3} \quad (3.46)$$

For small values of  $t$

$$E_2(t) \sim 1; \quad E_3(t) \sim \frac{1}{2} - t \quad (3.47)$$

For large values of  $t$

$$E_n(t) \sim \frac{e^{-t}}{t} \left[ 1 - \frac{n}{t} + \frac{n(n+1)}{t^2} - \frac{n(n+1)(n+2)}{t^3} + \dots \right], \quad n = 0, 1, 2, \dots \quad (3.48)$$

Finally,

$$\int E_n(t)dt = -E_{n+1}(t) \quad (3.49)$$

The radiative heat flux from surface 1 is obtained from Eq. (3.44) by letting  $\tau_\lambda = 0$ .

$$q_{R\lambda}(0) = R_{1\lambda} - 2R_{2\lambda}E_3(\tau_{L\lambda}) - 2 \int_0^{\tau_{L\lambda}} E_{b\lambda}(t)E_2(t) \, dt \quad (3.50)$$



The first term on the right hand side of Eq. (3.50) is the radiative flux leaving surface 1; therefore, the other terms represent the incident flux on this surface,  $H_{1\lambda}$ .

$$H_{1\lambda} = 2R_{2\lambda}E_3(\tau_{L\lambda}) + 2 \int_0^{\tau_{L\lambda}} E_{b\lambda}(t)E_2(t) dt \quad (3.51)$$

Recalling the definition of the radiosity as the sum of energy leaving a surface due to emission and reflection, we may write

$$R_{1\lambda} = \varepsilon_{1\lambda}E_{b1\lambda} + (1 - \varepsilon_{1\lambda})H_{1\lambda} \quad (3.52)$$

Using Eqs. (3.51) and (3.52), we get

$$R_{1\lambda} = \varepsilon_{1\lambda}E_{b1\lambda} + 2(1 - \varepsilon_{1\lambda}) \left[ R_{2\lambda}E_3(\tau_{L\lambda}) + \int_0^{\tau_{L\lambda}} E_{b\lambda}(t)E_2(t) dt \right] \quad (3.53)$$

Similarly for surface 2

$$R_{2\lambda} = \varepsilon_{2\lambda}E_{b2\lambda} + 2(1 - \varepsilon_{2\lambda}) \left[ R_{1\lambda}E_3(\tau_{L\lambda}) + \int_0^{\tau_{L\lambda}} E_{b\lambda}(t)E_2(\tau_{L\lambda} - t) dt \right] \quad (3.54)$$

In writing Eqs. (3.53) and (3.54), we have used the assumption stated earlier, namely the surfaces are diffuse and opaque. It is clear that for **black surfaces**

$$R_{1\lambda} = E_{b1\lambda}; \quad R_{2\lambda} = E_{b2\lambda} \quad (3.55)$$

As mentioned earlier, our interest is in calculating the divergence of the radiative flux,  $\nabla \cdot \mathbf{q}_R$ . For the 1-dimensional case considered here, the divergence of the spectral radiative flux  $\nabla \cdot \mathbf{q}_{R\lambda}$  is

$$\nabla \cdot \mathbf{q}_{R\lambda} = \frac{dq_{R\lambda}}{dz} = \kappa_\lambda \frac{dq_{R\lambda}}{d\tau_\lambda} \quad (3.56)$$

We get the following equation by differentiating Eq. (3.44)

$$-\frac{dq_{R\lambda}}{d\tau_\lambda} = 2R_{1\lambda}E_2(\tau_\lambda) + 2R_{2\lambda}E_2(\tau_{L\lambda} - \tau_\lambda) + 2 \int_0^{\tau_{L\lambda}} E_{b\lambda}(t)E_1|\tau_\lambda - t| dt - 4E_{b\lambda}(\tau_\lambda) \quad (3.57)$$

### 3.5.2 *Optically Thin Limit* ( $\tau_{L\lambda} \ll 1$ )

Using the low “ $t$ ” approximations for  $E_2(t)$  and  $E_3(t)$  given in Eq. (3.47) into Eq. (3.44), we get the following expression for the spectral radiative heat flux.  $q_{R\lambda}$ .

$$q_{R\lambda}(\tau_\lambda) = R_{1\lambda}(1 - 2\tau_\lambda) - R_{2\lambda}(1 - 2\tau_{L\lambda} + 2\tau_\lambda) + 2 \int_0^{\tau_\lambda} E_{b\lambda}(t) dt - 2 \int_{\tau_\lambda}^{\tau_{L\lambda}} E_{b\lambda}(t) dt \quad (3.58)$$

For  $\tau_{L\lambda} \ll 1$ , Eq. (3.58) simplifies to

$$q_{R\lambda} = R_{1\lambda} - R_{2\lambda} \quad (3.59)$$

Using the approximations described above, we can get the surface radiosities for the optically thin case.

$$R_{1\lambda} = \varepsilon_{1\lambda} E_{b1\lambda} + (1 - \varepsilon_{1\lambda}) R_{2\lambda} \quad (3.60)$$

$$R_{2\lambda} = \varepsilon_{2\lambda} E_{b2\lambda} + (1 - \varepsilon_{2\lambda}) R_{1\lambda} \quad (3.61)$$

Using Eqs. (3.60) and (3.61), we can express Eq. (3.59) as

$$q_{R\lambda} = R_{1\lambda} - R_{2\lambda} = \frac{E_{b1\lambda} - E_{b2\lambda}}{1/\varepsilon_{1\lambda} + 1/\varepsilon_{2\lambda} - 1} \quad (3.62)$$

The above expression is the same as that for radiation between two surfaces separated by a transparent or nonparticipating medium. The divergence of the radiative flux for the optically thin limit is obtained from Eq. (3.57) by using the same kind of approximations as described above.

$$-\frac{dq_{R\lambda}}{d\tau_\lambda} = 2[R_{1\lambda} + R_{2\lambda} - 2E_{b\lambda}(\tau_\lambda)] \quad (3.63)$$

We may also write Eq. (3.63) as

$$-\frac{dq_{R\lambda}}{dz} = 2\kappa_\lambda[R_{1\lambda} + R_{2\lambda} - 2E_{b\lambda}(\tau_\lambda)] \quad (3.64)$$

**Although we had assumed no scattering, Eq. (3.64) is general and independent of the scattering coefficient.** Scattering does not play a role in the optically thin limit. The gradient of the total radiative flux is obtained by integrating Eqs. (3.63) or (3.64) over all wavelengths.

### 3.5.3 Optically Thick Limit ( $\tau_{L\lambda} \gg 1$ )

The optically thick assumption, also known as the diffusion approximation and the Rosseland approximation, is frequently used in the modeling of radiative heat transfer in glass melts. This assumption simplifies of the radiative flux equation, Eq. (3.44) as shown below. The simplification results from the fact that the integral functions appearing in Eq. (3.44) rapidly decay as the optical thickness increases [see Eq. (3.48)].

Let us start by expanding the blackbody emissive power,  $E_{b\lambda}$  about  $\tau_\lambda$ , using Taylor series. We do so because, as seen in Eq. (3.44),  $E_{b\lambda}$  is multiplied or weighted by the exponential integral  $E_2$ .

$$E_{b\lambda}(t) = E_{b\lambda}(\tau_\lambda) + \frac{dE_{b\lambda}}{d\tau_\lambda}(t - \tau_\lambda) + \frac{1}{2} \frac{d^2 E_{b\lambda}}{d\tau_\lambda^2}(t - \tau_\lambda)^2 + \dots \quad (3.65)$$

Substituting the first two terms on the right hand of Eq. (3.65) into the integral terms in Eq. (3.44), we get

$$\begin{aligned} q_{R\lambda}(\tau_\lambda) &= 2R_{1\lambda}E_3(\tau_\lambda) - 2R_{2\lambda}E_3(\tau_{L\lambda} - \tau_\lambda) \\ &+ 2E_{b\lambda}(\tau_\lambda) \left[ \int_0^{\tau_\lambda} E_2(x) dx - \int_0^{\tau_{L\lambda} - \tau_\lambda} E_2(x') dx' \right] \\ &- 2 \frac{dE_{b\lambda}}{d\tau_\lambda} \left[ \int_0^{\tau_\lambda} x E_2(x) dx + \int_0^{\tau_{L\lambda} - \tau_\lambda} x' E_2(x') dx' \right] + \dots \end{aligned} \quad (3.66)$$

where  $x = \tau_\lambda - t$ , and  $x' = t - \tau_\lambda$ . In writing Eq. (3.66), we have ignored the terms containing the second and higher-order derivatives of  $E_{b\lambda}$ . To apply Eq. (3.66) for the optically thick condition ( $\tau_{L\lambda} \rightarrow \infty$ ), let us first consider regions away from the boundaries, where  $\tau_\lambda \rightarrow \infty$  and  $(\tau_{L\lambda} - \tau_\lambda) \rightarrow \infty$  prevail. Noting that  $E_2(\infty) = E_3(\infty) = 0$ , Eq. (3.66) simplifies to

$$q_{R\lambda} = -4 \frac{dE_{b\lambda}}{d\tau_\lambda} \int_0^\infty x E_2(x) dx \quad (3.67)$$

On using Eq. (3.49), the integral term in Eq. (3.67) may be written as

$$\int_0^\infty x E_2(x) dx = -x E_3(x)|_0^\infty + \int_0^\infty E_3(x) dx = -E_4(x)|_0^\infty = \frac{1}{3} \quad (3.68)$$

Equation (3.67) takes the simple form

$$q_{R\lambda} = -\frac{4}{3} \frac{dE_{b\lambda}}{d\tau_\lambda} \quad (3.69)$$

We had assumed no scattering for the sake of simplification in writing the equations, but Eq. (3.69) is also applicable for an optically thick absorbing and scattering medium. In the presence of scattering, however, we have to use the extinction coefficient  $\beta_\lambda$  introduced in Eq. (3.19) in defining the optical distance  $\tau_\lambda$ . For the one-dimensional case considered here, Eq. (3.69) takes the following form when both absorption and scattering are present.

$$q_{R\lambda} = -\frac{4}{3} \frac{dE_{b\lambda}}{d\tau_\lambda} = -\frac{4}{3\beta_\lambda} \frac{dE_{b\lambda}}{dz} \quad (3.70)$$

Scattering is usually ignored in the modeling of radiative heat transfer in glass melts. We will, however, use Eq. (3.70) in the remainder of this section. As indicated earlier [Eq. (3.30)], the total radiative flux,  $q_R$ , is obtained by integrating Eq. (3.70) over all the wavelengths.

$$q_R = \int_0^\infty q_{R\lambda} d\lambda = -\frac{4}{3} \int_0^\infty \frac{1}{\beta_\lambda} \frac{dE_{b\lambda}}{dz} d\lambda = -\frac{4}{3\beta_R} \frac{dE_b}{dz} \quad (3.71)$$

where  $\beta_R$ , called the **Rosseland mean extinction coefficient**, is defined by

$$\frac{1}{\beta_R} = \int_0^\infty \frac{1}{\beta_\lambda} \frac{dE_{b\lambda}}{dE_b} d\lambda \quad (3.72)$$

As seen earlier in Eq. (3.4), for a constant or wavelength independent refractive index  $n$ , the blackbody emissive power,  $E_b = n^2 \sigma T^4$ . Thus, we may also write Eq. (3.72) as

$$\frac{1}{\beta_R} = \int_0^\infty \frac{1}{\beta_\lambda} \frac{dE_{b\lambda}}{dE_b} d\lambda = \frac{1}{4n^2\sigma T^3} \int_0^\infty \frac{1}{\beta_\lambda} \frac{dE_{b\lambda}}{dT} d\lambda \quad (3.73)$$

Further, we may write the heat flux, Eq. (3.71) as

$$q_R = -\frac{4}{3\beta_R} \frac{dE_b}{dz} = -\left[ \frac{16n^2\sigma T^3}{3\beta_R} \right] \frac{dT}{dz} \quad (3.74)$$

Equation (3.74) has the form of the Fourier equation for heat conduction. The term in the parenthesis may be called the photon or radiative conductivity,  $k_R$ .

$$k_R = \frac{16n^2\sigma T^3}{3\beta_R} \tag{3.75}$$

In the calculation of thermal radiative heat flux in glass melts, scattering phenomena are usually neglected (i.e.,  $\gamma_\lambda = 0$ ) and the extinction coefficient  $\beta_\lambda = \kappa_\lambda$ .

In deriving the optically thick approximation for the radiative heat flux, we had confined ourselves to regions away from the boundary surfaces to meet the requirements  $\tau_\lambda \rightarrow \infty$ , and  $(\tau_{L\lambda} - \tau_\lambda) \rightarrow \infty$ . These conditions imply that we need to be away at least one mean free path distance away from the surfaces. If the optically thick condition prevails, we can use Eq. (3.70) everywhere in the medium including at the boundaries provided we also use this equation in the energy conservation equation, Eq. (3.28). This is necessitated by the conservation of energy. *If radiation is the only mode of heat transfer* in a participating medium, then one may have to allow for a jump or discontinuity in the temperature between the boundary and the adjacent medium. This is referred to as the Deissler’s jump or the radian slip boundary condition. Heat transfer in the glass melting process occurs by all three modes (by conduction, convection, and radiation) and temperature discontinuity or jump at the boundary does not exist. More details on this topic may be found in Refs. [7, pp. 222–225, 8, pp. 484–486].

### 3.5.4 An Approximate Solution for One-Dimensional Gray Medium

We present below an approximate solution for the special case of a gray, non-scattering, one-dimensional medium confined between two black parallel plates at temperatures  $T_1$  and  $T_2$ . We further assume radiative equilibrium ( $dq_R/dz = 0$ ). The derivation of the solution is given in [7, pp. 240–241, 8, pp. 488–490]. The dimensionless temperature  $T_b^*$  and heat flux  $q_b^*$  are given by

$$T_b^* = \frac{T_1^4 - T_2^4}{T_1^4 - T_2^4} = \frac{2 + 3\tau}{4 + 3\tau_L} \tag{3.76}$$

$$q_b^* = \frac{q}{n^2\sigma(T_1^4 - T_2^4)} = \frac{4}{4 + 3\tau_L} \tag{3.77}$$

where with reference to Fig. 3.5,  $\tau = \kappa z$  and  $\tau_L = \kappa L$  with  $\kappa$  being the absorption coefficient of the medium. Further, as explained earlier,  $n$  is the refractive index, and  $\sigma$  is the Stefan–Boltzmann constant. We can see in Eq. (3.77) that at  $z = 0$ ,  $T \neq T_1$  and at  $z = L$ ,  $T \neq T_2$ . The discontinuity in the temperature at the two plates is the Deissler’s jump referred to earlier.

An extension of the above case is to allow the surfaces to be diffuse emitters and reflectors instead of being black. This is what we had assumed in Sect. 2.5.1. The dimensionless temperature and heat flux are now given by

$$T^* = \frac{T_1^4 - T_2^4}{T_1^4 - T_2^4} = \frac{T_b^* + \left(\frac{1}{\varepsilon_2} - 1\right)q_b^*}{1 + \left(\frac{1}{\varepsilon_1} + \frac{1}{\varepsilon_2} - 2\right)q_b^*} \tag{3.78}$$

$$q^* = \frac{q}{n^2\sigma(T_1^4 - T_2^4)} = \frac{q_b^*}{1 + \left(\frac{1}{\varepsilon_1} + \frac{1}{\varepsilon_2} - 2\right)q_b^*} \tag{3.79}$$

### 3.6 Absorption Spectra of Glass Melts

For the calculation thermal radiation flux in glass melts, we need the refractive index,  $n$ , and the absorption coefficient,  $\kappa_\lambda$  values in the wavelength domain of 0.5–4.0  $\mu\text{m}$  and the temperature range of about 1400–2000 K. In the wavelength domain of interest to us, the refractive index depends weakly on the wavelength and is assigned a constant value (assumed independent of both wavelength and temperature). Choudhary and Potter [4] provide an extensive review of the open literature data on absorption spectra of glass melts. The spectra of six commercial glass melts at various temperatures were measured by Prokhorenko [10]. The spectra of these glass melts at 1473 K are shown in Fig. 3.6 [5].

At wavelengths below about 0.5  $\mu\text{m}$  (not shown in Fig. 3.6), there is strong absorption due to electron transfer among atoms. Also, in this range, the temperature gradient of the blackbody emissive power,  $dB_\lambda/dT$  is small [4]. Therefore, as Eqs.

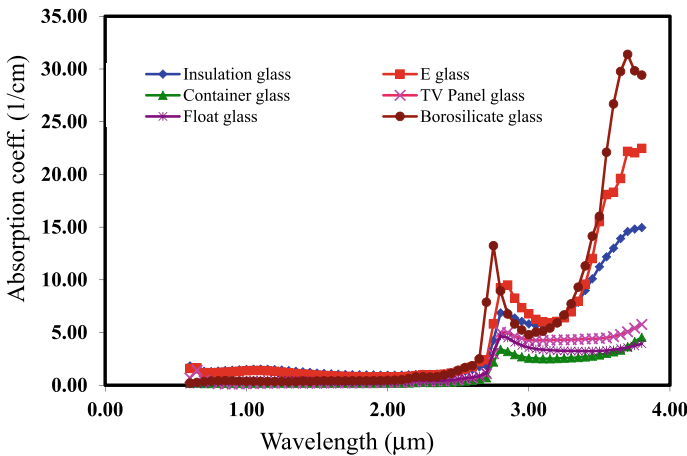


**Fig. 3.6** Absorption spectra of 6 commercial glass melts at 1473 K [5]. Adapted from Choudhary et al. [5] with permission from John Wiley and Sons. Receipt of data from O. A. Prokhorenko of Laboratory of Glass Properties LLC gratefully acknowledged

(3.73) and (3.74) indicate, the radiative flux will be relatively small. Hence, we need not concern ourselves with wavelengths below about  $0.5 \mu\text{m}$ .

In the wavelength range  $0.5\text{--}2.5 \mu\text{m}$ , most major components of silicate glasses do not absorb, but minor or tramp materials, especially first row transition metal ions, may exhibit strong absorption. The intensity and the wavelength domain of absorption of an ion depend strongly on its oxidation state (referred to as the redox state) and coordination. These, in turn, depend on the temperature, the base glass composition, and the operating conditions in the glass furnace. Choudhary and Potter [4] discuss the role of several transition metal ions in influencing absorption spectra of soda-lime-silicate glasses and also describe an approach to calculate the absorption coefficient of glass melts as a function of the type and the amount of transition metal ions present in the composition.

The absorption in the  $2.5\text{--}4 \mu\text{m}$  region is due primarily to the vibration of the hydroxyl ions, which are present to some degree in all silicate glasses. At wavelength greater than about  $4 \mu\text{m}$ , silicate glasses are opaque, and there is no contribution to the radiative heat transfer.

We had noted earlier that the presence of the transition metal ions significantly impacts the absorption spectrum of glass melts, especially in the  $0.5\text{--}2.5 \mu\text{m}$  wavelength region. Figure 3.7 shows the absorption spectra, at  $1473 \text{ K}$ , of two reinforcement fiberglass melts [5]. The glass melts are of similar nominal composition but differ in their iron contents (concentration on mass basis are; Fiberglass 1:  $\text{FeO} = 0.17\%$ ,  $\text{Fe}_2\text{O}_3 = 0.35\%$ ; Fiberglass 2:  $\text{FeO} = 0.07\%$ ,  $\text{Fe}_2\text{O}_3 = 0.22\%$ ).

The effect of the iron oxide content on the absorption coefficient is evident in Fig. 3.7, which shows the melt containing higher amount of iron oxides (Fiberglass 1) is more absorbing than the other melt (Fiberglass 2).

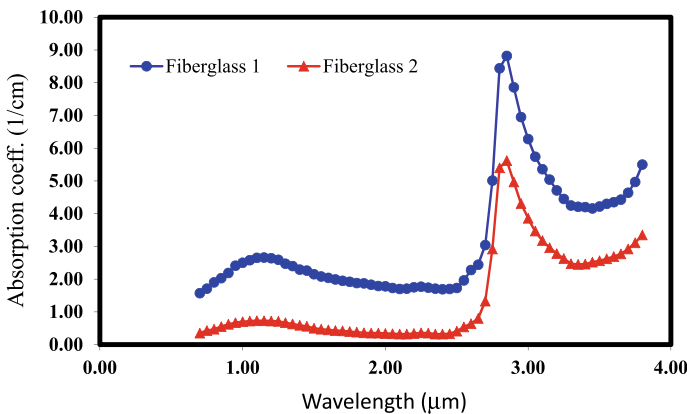


**Fig. 3.7** Absorption spectra for 2 reinforcement fiberglass melts at  $1473 \text{ K}$  [5]. Adapted from Choudhary et al. [5] with permission from John Wiley and Sons

### 3.7 Modeling of Thermal Radiation in Glass Melts

Over the years, the modeling of radiative heat transfer (i.e., the solution of the RTE with the appropriate boundary conditions) in glass furnaces has become progressively more sophisticated. This is especially true for the modeling of thermal radiation in the combustion chamber. The predominant approach used in the combustion chamber is the discrete ordinate method (DOM). While the DOM is also used for modeling of radiative heat transfer in the melt region, the more commonly used approach is the optically thick or diffusion or Rosseland approximation method (RAM). As described in Sect. 3.5.3, the optically thick approximation involves the calculation of a photon or radiative conductivity [Eq. (3.75)], and the radiative heat flux  $q_R$  is calculated using the Fourier conduction equation [Eq. (3.74)]. The optically thick approximation obviates the need for solving the RTE. We will present some radiative conductivity values subsequently. First, we provide a rudimentary description of the DOM. A detailed description is available in Modest [8, pp. 541–576] and Coelho [11].

#### 3.7.1 Discrete Ordinates Method (DOM)

As the name of the approach suggests, DOM involves solving the RTE, Eq. (3.80), along a finite number of discrete directions.

$$\frac{dI_\lambda}{ds} = \mathbf{s} \cdot \nabla I_\lambda = \kappa_\lambda \frac{E_{b\lambda}}{\pi} - \beta_\lambda I_\lambda + \frac{\gamma_\lambda}{4\pi} \int_{4\pi} I_\lambda(\mathbf{s}') \Phi_\lambda(\mathbf{s}', \mathbf{s}) d\Omega' \quad (3.80)$$

As explained earlier, Eq. (3.80) describes the change in the monochromatic or spectral radiative intensity along the direction,  $\mathbf{s}$ . In the DOM, the solid angle domain  $4\pi$  is subdivided into a finite number of discrete directions. The directional variation, i.e., the derivative on the left-hand side of Eq. (3.80), is discretized or converted into its algebraic equivalent, using finite difference-based (or finite volume) techniques. The integral term on the right-hand side of Eq. (3.80) is calculated using numerical quadrature.

In the modeling of radiative heat transfer in glass melts (and also quite often in the combustion gases), scattering is usually ignored. Thus, the integral term in Eq. (3.80) disappears, and the extinction coefficient is simply the absorption coefficient ( $\beta_\lambda = \kappa_\lambda$ ). The simplified RTE for the glass melts is

$$\frac{dI_\lambda}{ds} = \mathbf{s} \cdot \nabla I_\lambda = \kappa_\lambda \frac{E_{b\lambda}}{\pi} - \kappa_\lambda I_\lambda \quad (3.81)$$

The solution RTE [Eq. (3.80) or Eq. (3.81)] requires **boundary conditions**, which depend upon the radiative characteristics of the boundary surfaces. In the case of a



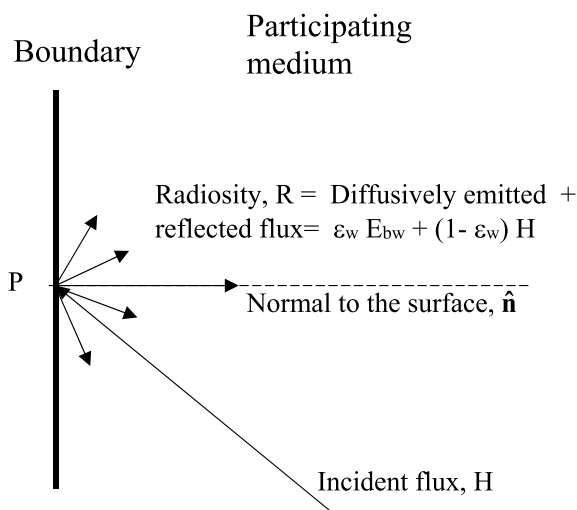
glass melt in a furnace, the boundary surfaces are the refractory walls, the melt-combustion gas interface, the melt-foam interface, and the melt-batch interface. The detailed radiative characteristics and properties of these surfaces are not known. Indeed, even the locations, shapes, and the extent of some of these boundary surfaces, especially the various interfaces mentioned above, are not known accurately. So, simplifications and approximations are inevitable both regarding the geometry, and the radiative characteristics of the surfaces and their radiative properties such as the emissivity have to be guessed. The boundary surfaces may be opaque (e.g., refractory wall) or semitransparent (e.g., combustion gas—melt interface, part of the radiative flux from the combustion chamber enters the glass melt). The surfaces are often idealized as

- Diffusively emitting and reflecting (as was the case in Sect. 3.5.1)
- Diffusively emitting and specularly reflecting (i.e., reflection takes place in preferred directions).

The RTE boundary conditions have been discussed in detail by Modest [8, pp. 288–290]. In the following, we illustrate the setting up of boundary condition for the case of a diffusively emitting and reflecting opaque surface adjacent to a participating medium. We had already described this boundary condition in Sect. 3.5.1 [Eqs. (3.38) and (3.39)] when discussing one-dimensional thermal radiation in a participating medium contained between two parallel plates. We provide additional details now (see Fig. 3.8). For simplicity, we will consider the surface and the participating medium to be gray. The spectral version of the expressions and the equations may be obtained by using the subscript  $\lambda$  with the radiation entities (intensity, flux, and emissivity).

The radiative flux leaving the point  $P$  is the radiosity  $R$  as shown in Fig. 3.8. The radiative intensity leaving this point  $I_{\text{out}}$  is

**Fig. 3.8** Incident, emitted, and reflected radiation fluxes at a diffuse and gray surface adjacent to a gray participating medium



$$I_{\text{out}} = \frac{R}{\pi} = \varepsilon_w \frac{E_{bw}}{\pi} + (1 - \varepsilon_w) \frac{H}{\pi} \quad (3.82)$$

where  $\varepsilon_w$  is the emissivity of the boundary surface and  $E_{bw}$  is the blackbody emissive power of the surface. The hemispherical irradiation (i.e., the incident heat flux,  $H$ ) is the radiative intensity coming from the fluid to the surface at point  $P$  from the solid angle  $2\pi$  and is given by

$$H = \int_{2\pi} I_{\text{in}}(\mathbf{s}) |\mathbf{s} \cdot \hat{\mathbf{n}}| d\Omega \quad (3.83)$$

On combining Eqs. (3.82) and (3.83), we get

$$I_{\text{out}} = \varepsilon_w \frac{E_{bw}}{\pi} + \frac{(1 - \varepsilon_w)}{\pi} \int_{2\pi} I_{\text{in}}(\mathbf{s}) |\mathbf{s} \cdot \hat{\mathbf{n}}| d\Omega \quad (3.84)$$

Equation (3.84) is the boundary condition linking the intensity leaving a surface at a given point on it to the intensity received by the surface at the same point. It should be noted that Eq. (3.84) incorporates the temperature of the surface since  $E_{bw} = n^2 \sigma T_w^4$ . When the medium and the boundary are not gray, we need to write Eq. (3.84) for the spectral entities (i.e., for specific wavelengths).

### 3.7.2 Diffusion Approximation: Radiative Conductivity of Glass Melts

As mentioned above, the optically thick approximation is commonly used in the modeling of the radiative heat transfer in glass melts. This approach requires the calculation of the radiative conductivity,  $k_R$ , by using Eqs. (3.73) and (3.75) given earlier. Since scattering is ignored in modeling of thermal radiation in glass melts, the extinction coefficient  $\beta_\lambda = \kappa_\lambda \cdot k_R$  takes the following form.

$$k_R = \frac{16n^2\sigma T^3}{3\kappa_R} \quad (3.85)$$

$$\frac{1}{\kappa_R} = \int_0^\infty \frac{1}{\kappa_\lambda} \frac{dE_{b\lambda}}{dE_b} d\lambda = \frac{1}{4n^2\sigma T^3} \int_0^\infty \frac{1}{\kappa_\lambda} \frac{dE_{b\lambda}}{dT} d\lambda \quad (3.86)$$

The radiative heat flux  $\mathbf{q}_R$  is given by

$$\mathbf{q}_R = -k_R \nabla T = -\frac{16n^2\sigma T^3}{3\kappa_R} \nabla T \quad (3.87)$$

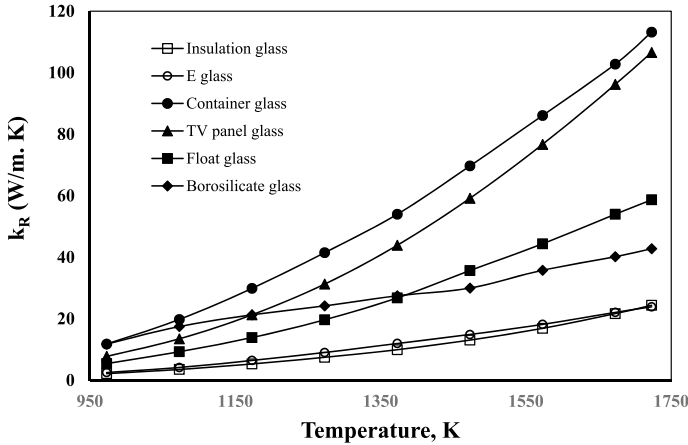


**Fig. 3.9** Radiative conductivity of commercial glasses calculated using the absorption spectra measured by Prokhorenko [10]. Receipt of data from O. A. Prokhorenko of Laboratory of Glass Properties LLC gratefully acknowledged

Equation (3.87) is the three-dimensional form of Eq. (3.74).

The Rosseland mean absorption coefficient,  $\kappa_R$ , may be calculated from the measured spectra (e.g., Fig. 3.6) by numerical integration. Substituting  $\kappa_R$  into Eq. (3.85), one can calculate the radiative conductivity,  $k_R$ . The refractive index of the glass melts of Fig. 3.6 is taken as 1.5 in the wavelength range of interest to us (0.5–4  $\mu\text{m}$ ). Figure 3.9 shows the radiative conductivity versus temperature calculated using the absorption spectra measured by Prokhorenko [10].

Radiative conductivities of the two fiberglass melts with the absorption spectra of Fig. 3.7 are shown in Fig. 3.10 [5]. It is seen in Fig. 3.10 that the radiative conductivity of the more absorbing fiberglass melt (designated fiberglass 1) is only about 1/5 to 1/3 of that of the less absorbing melt (designated fiberglass 2).

### 3.8 Illustrative Thermal Radiation Modeling Results

A critically important question in the modeling of radiative heat transfer in glass melts is how do the results calculated using the diffusion approximation compare versus those obtained using more elaborate methods such as the DOM. Clearly, if the optical thickness is much larger than 1 (i.e., the glass melt depth is much larger than the mean-free path of photons), then we would expect the results from the two methods to be close. But, this statement is too qualitative to be of value in deciding what approach to use. In the following, we attempt to provide a more quantitative guideline by showing results obtained using DOM and the Rosseland approximation method (RAM).

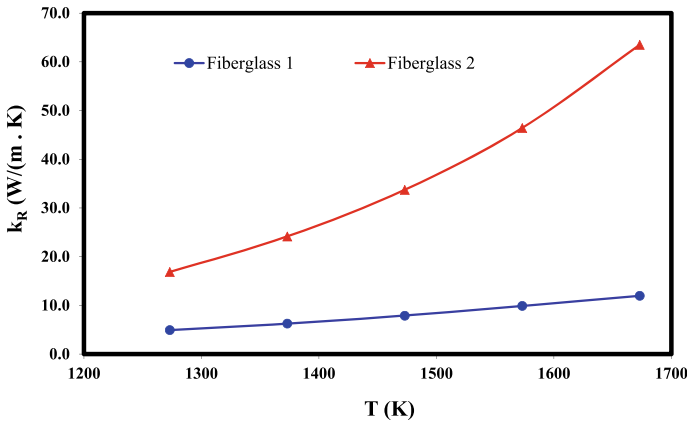


**Fig. 3.10** Radiative conductivity of fiberglass melts of absorption spectra of Fig. 3.7 [5]. Adapted from Choudhary et al. [5] with permission from John Wiley and Sons

As pointed out in Introduction, radiative heat transfer in the glass melt in a furnace occurs simultaneously and in combination with several other physical and chemical phenomena, not only in the melt but also in other domains of a glass furnace, namely the batch (mixture of raw materials), the foam on the batch/melt surface (gas bubbles surrounded by melt lamella), and the combustion chamber. The list of transport phenomena taking place in the furnace is comprehensive and includes laminar, thermal buoyancy driven flow and heat transfer in the melt, turbulent flow and heat transfer in the combustion chamber, flow and heat transfer in the melting batch (a porous mixture of solid and liquid with gas and liquid flowing through it), and heat transfer in the foam (and flow also if one considers the drainage of the melt from the foam). Further, each of the four domains is a participating medium with vastly different radiative properties. Because of these complexities, one does not have the luxury of modeling thermal radiation in the melt separately from other phenomena in the melt and/or other regions of the glass furnace. We discuss below the modeling results for glass melters and channels reported by Choudhary et al. [5].

Choudhary et al. [5] modeled the melting of a very low iron oxide containing ultra-clear glass in a float glass furnace, using oxygen-natural gas combustion. The throughput rate was 150 Metric tons/day. The absorption spectrum was approximated as shown below:

$$\kappa_\lambda = 1000 \text{ m}^{-1} \quad 0 < \lambda \leq 0.7 \mu\text{m}$$

$$\kappa_\lambda = 5 \text{ m}^{-1} \quad 0.7 < \lambda \leq 1.3 \mu\text{m}$$

$$\kappa_\lambda = 20 \text{ m}^{-1} \quad 1.3 < \lambda \leq 1.8 \mu\text{m}$$

$$\kappa_\lambda = 50 \text{ m}^{-1} \quad 1.8 < \lambda \leq 2.7 \mu\text{m}$$

$$\kappa_\lambda = 1000 \text{ m}^{-1} \quad \lambda > 2.7 \mu\text{m}$$

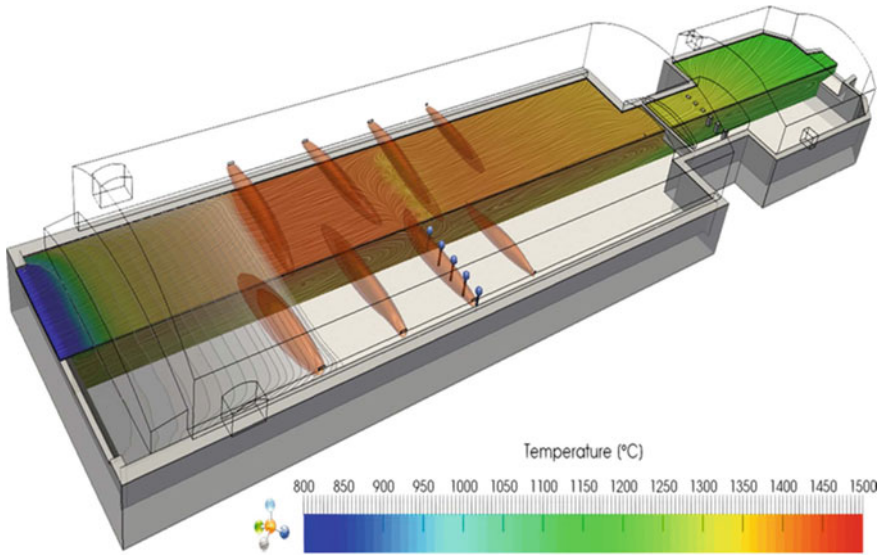


**Fig. 3.11** Schematics of the oxy-fuel float furnace modeled by Choudhary et al. [5]. Adapted from Choudhary et al. [5] with permission from John Wiley and Sons

As indicated above, the melt was assumed opaque ( $\kappa_\lambda = 1000 \text{ m}^{-1}$ ) at wavelengths less than  $0.7 \mu\text{m}$  and also greater than  $2.7 \mu\text{m}$ . The Rosseland averaged absorption coefficient over the entire wavelength domain,  $\kappa_R$ , was calculated to be  $9.35 \text{ m}^{-1}$ . Using this value along with the glass depth of  $1.05 \text{ m}$  gives the optical thickness of about 9.8. The melter length and width were  $23 \text{ m}$  and  $7 \text{ m}$ , respectively. Other details on the dimensions, the operating conditions, and the glass melt properties are provided in [5]. The furnace modeled is shown schematically in Fig. 3.11.

The radiative heat transfer in the melt was modeled in two ways: (1) the Rosseland approximation approach for the entire wavelength domain, and (2) a hybrid approach that used discrete ordinates in the  $0.7 < \lambda \leq 1.3 \mu\text{m}$ ,  $1.3 < \lambda \leq 1.8 \mu\text{m}$  bands and the Rosseland approach elsewhere (i.e., for  $\lambda < 0.7 \mu\text{m}$  and  $\lambda > 1.8 \mu\text{m}$ —the regions where the absorption is strong). Thus, in the hybrid approach, the radiative heat flux was calculated using Eq. (3.87) in the wavelength domains below  $0.7 \mu\text{m}$  and above  $1.8 \mu\text{m}$  and elsewhere (i.e.,  $0.7 < \lambda \leq 1.3 \mu\text{m}$ ,  $1.3 < \lambda \leq 1.8 \mu\text{m}$ ) using Eqs. (3.29) and (3.30).

In the following, we will use the abbreviation RAM and DOM, introduced earlier, to refer to the Rosseland approximation and discrete ordinates methods. We should keep in mind, however, that in the DOM, we used Rosseland approximation in certain wavelength domains where the absorption coefficient was  $\geq 50 \text{ m}^{-1}$  (i.e., the optical thickness was  $\geq 52.5$ ). Figure 3.12 shows isotherms in the central longitudinal section (i.e., the half width symmetry plane) calculated by the RAM and DOM. It is seen in Fig. 3.12 that, in the melting end of the furnace, the DOM allows for more penetration of the heat from the surface into the bulk glass. This results in the DOM giving a

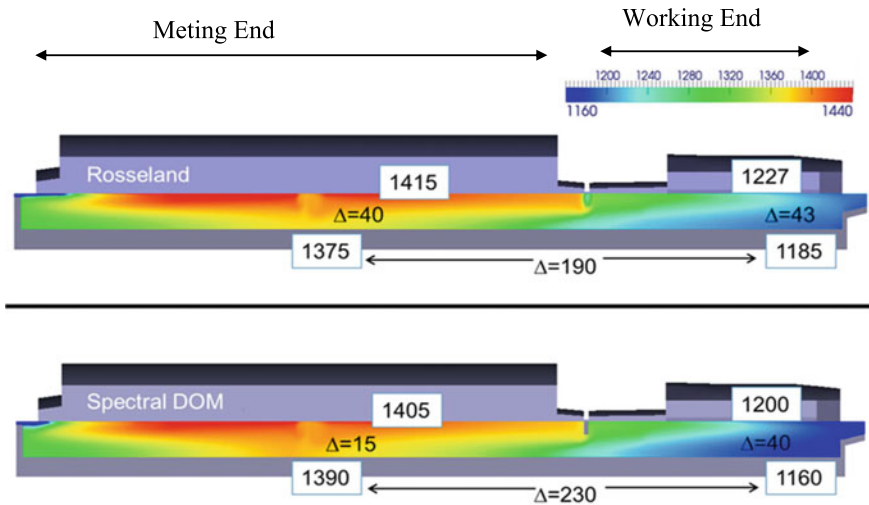


**Fig. 3.12** Isotherms ( $^{\circ}\text{C}$ ) in the central longitudinal section calculated using the Rosseland (top) and the hybrid discrete methods (bottom) [5]. Adapted from Choudhary et al. [5] with permission from John Wiley and Sons

smaller temperature differential (DT) in the vertical direction ( $15\text{ }^{\circ}\text{C}$  vs.  $40\text{ }^{\circ}\text{C}$  for the RAM), higher bottom glass-refractory contact temperature ( $1390\text{ }^{\circ}\text{C}$  vs.  $1375\text{ }^{\circ}\text{C}$  for the RAM), and a lower glass surface hot spot (maximum) temperature ( $1405\text{ }^{\circ}\text{C}$  vs.  $1415\text{ }^{\circ}\text{C}$  in the RAM). Not shown in Fig. 3.12 are the crown (the refractory cover or roof of the furnace) temperatures. DOM also gives a lower crown hot spot temperature than the RAM.

It is interesting to note that while the DOM gives higher bulk glass and refractory temperatures in the melting end, in the working end, the temperatures calculated by the DOM are about  $25\text{ }^{\circ}\text{C}$  lower than that calculated by the RAM. As a consequence, the temperature difference between the melting and the working ends calculated using DOM is about  $40\text{ }^{\circ}\text{C}$  higher. Since the flow of the glass melt is driven by thermal natural convection, the temperature differences calculated by the two approaches also imply differences in the flow distribution. Figure 3.13, for example, shows the residence time distribution calculated using the two approaches [5]. It is seen that the DOM predicts a much shorter minimum dwell time than the RAM.

It follows from the above discussion that the results calculated by the two methods would lead to different predictions about important practical parameters such as the energy efficiency, refractory corrosion, and volatilization from the glass surface and glass quality. Thus, the DOM results would imply higher energy efficiency, greater bottom refractory corrosion, lower volatilization, and perhaps lower glass quality than the RAM results.

The results presented above indicate that, even at an optical thickness of about 10, the flow and temperature distribution in the glass melt, calculated using the

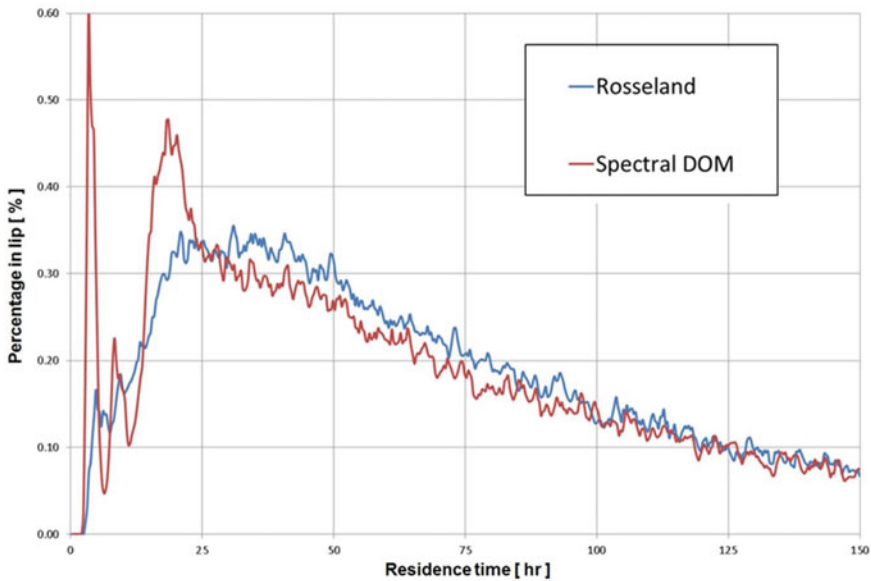


**Fig. 3.13** Residence time distribution calculate using the RAM and DOM approaches [5]. Adapted from Choudhary et al. [5] with permission from John Wiley and Sons

RAM, are significantly different from those calculated using the DOM. This is likely because, as mentioned earlier, in the modeling of glass furnaces we deal with several mutually coupled phenomena not only in the melt but also in the other domains. The radiative heat flux in the melt impacts the temperature, which impacts the flow of the melt, which then impacts the temperature, while at the same time, these phenomena influence batch melting and combustion and are, in turn, impacted by them. The models calculate the net effect of all these phenomena.

Based on additional calculations of flow and heat transfer in the delivery channels of a reinforcement fiberglass furnace, Choudhary et al. [5] suggested that the threshold optical thickness for the use of RAM should be about 20. The mean free path length reported by Prokhorenko [10] is in the range of 0.5–3.5 cm. Many industrial glass melting furnaces have glass melt depth of about 1 m. It seems, therefore, that the optical thickness of 20 should be met in most, if not all, of the commercial glass melting furnaces. The exceptions, as we have seen, would be ultra-clear glasses with very little or trace amounts of the first-row transition metal ions. The melting section of a glass furnace has a more complex set of phenomena than its delivery channels, which do not have processes involved in the batch and foam domains, have lower temperatures (i.e., thermal radiation is relatively less important than in the melter) and are of simpler geometry. In view of all this, even when the optical thickness exceeds 20, it would still be prudent to use the hybrid discrete method, as used in the results discussed above, for modeling the radiative heat transfer in the glass melt.

The hybrid approach, by combining the discrete-order approach in the low absorption wavelength domain (generally 0.5–2.5  $\mu\text{m}$ ) with the Rosseland approximation elsewhere, represents a good balance of accuracy and the computational burden of modeling.

### 3.9 Concluding Remarks

The various heat transfer media present in industrial glass melting furnaces (glass melt, combustion gases, melting batch, and foam) are participating in nature, i.e., they interact with thermal radiation passing through them by emission, absorption, and/or scattering. This chapter described key concepts, phenomena, mathematical formulations, and properties involved in the study and analysis of radiative heat transfer in such media with a focus on glass melts. The chapter began with a review of some of the basic concepts of thermal radiation and then described its main theme, namely the description and the mathematical formulation of the radiative transfer equation (RTE)—the equation that describes the change in the radiative intensity with position along a specific direction due to absorption, emission, and scattering in participating media. For mathematical simplicity and the ease of explanation, the RTE was derived by considering one-dimensional radiative heat transfer and later, its general, three-dimensional form was given. The two limiting cases of the RTE, namely the optically thin and thick approximations, were discussed. The optically thick (also known as diffusion and Rosseland) approximation involving the use of the radiative conductivity is widely used in the modeling of thermal radiation in glass melts and hence was discussed in greater detail. The boundary conditions for the RTE and the discrete ordinates method for numerically solving the RTE were also discussed.

Scattering is typically ignored in the analysis of thermal radiation in glass melts. Therefore, the chapter focused on absorption in silicate melts, which takes place in the wavelength range of about 0.5–4.0  $\mu\text{m}$  and is strongly impacted by the presence of the first-row transition metal ions. Measured absorption spectra of commercial glass melts and their radiative conductivities were reviewed. Results on flow and temperature distributions in an ultra-clear glass in an oxy-fuel furnace, calculated using the discrete ordinates method and the optically thick approximation, were compared. Although the optical thickness (ratio of the characteristic distance for heat flow to the mean free path of photons) for many commercial glass melting processes may be significantly larger than 1 (i.e., they may appear to meet the criterion of the application of optically thick approximation), it is recommended that hybrid modeling approaches be used. These approaches combine the discrete ordinates method in the low-absorption wavelength regions with the optically thick approach in the high-absorption domains of the spectrum and constitute a good balance of accuracy and computational burden.



## References

1. Beerkens RG (2002) Modeling of the melting process in industrial glass furnaces. In: Krause D, Lock H (eds) Section 2.1, Mathematical simulation in glass technology. Springer, Berlin, pp 17–73
2. Choudhary MK, Venuturumilli R, Hyre MR (2010) Mathematical modeling of flow and heat transfer phenomena in glass melting, delivery, and forming processes. *Int J Appl Glass Sci* 1(2):188–214
3. Choudhary MK (2021) Mathematical modeling of rate phenomena in glass melting furnaces. In: Li H (ed) *Fiberglass science and technology*. Springer Nature Switzerland AG (to be published)
4. Choudhary MK, Potter RM (2005) Heat transfer in glass-forming melts. In: Pye LD, Montenero A, Joseph I (eds) *Properties of glass forming melts*. CRC Press, Boca Raton, pp 249–293
5. Choudhary MK, Purnode B, Lankhorst AM, Habraken AFJA (2018) Radiative heat transfer in processing of glass-forming melts. *Int J Appl Glass Sci* 9(2):218–234
6. Choudhary MK (2018) Heat transfer phenomena in industrial glass melting and delivery processes. In: Takada A, Parker J, Duran A, Bange K (eds) *Teaching glass better*. International Commission on Glass, Madrid, pp 287–309
7. Sparrow EM, Cess RD (1978) *Radiation heat transfer*, Augmented edn. Hemisphere Publishing Corporation, Washington, pp 207–221, 222–225, 240–241, 351–353
8. Modest MF (2013) *Radiative heat transfer*, 3rd edn. Academic Press, Elsevier, Oxford, pp 282–283, 288–290, 292–295, 488–490, 541–576, 852–854
9. Bird RB, Stewart WE, Lightfoot EN (2007) *Transport phenomena*, 2nd edn. Wiley, New York, pp 337–341
10. Prokhorenko OA (2005) Radiative thermal conductivity of melts. In: Seward TP, Vascott T (eds) *High temperature glass melt property database for process modeling*. American Ceramic Society, Westerville, pp 95–117
11. Coelho PJ (2011) Discrete ordinates and finite volume methods. *Thermopedia*. <http://www.thermopedia.com>

# Chapter 4

## Thermomechanical Behaviour During Forming of Silicate Glasses—Modelling and Characterization



Dipayan Sanyal and Rahul Kumar

### 4.1 Introduction

Low  $T_g$  mouldable optical glass is being manufactured by several global commercial glass manufacturers, such as Schott AG, Germany, OHARA Inc., Japan, Hoya Corporation, Japan, FISBA AG, Switzerland, CDGM Glass Company Ltd., China and so on. These glasses primarily cater to manufacturing of precision optical components by a process of replicative moulding. Replicative or precision moulding has attracted a lot of attention in the recent times as an alternative and viable process chain for mass manufacturing of a variety of complex shaped optical components, such as aspheric camera lenses, CD/DVD pick up lenses, lens for optical sensors and laser optics, micro lens array, hologram devices, Fresnel lenses and so on [1, 2]. The conventional manufacturing process chain for these optical components which is based on multi-step grinding and polishing of glass preforms in various sizes and shapes, typically of cylindrical, polygonal or spherical geometry is not amenable to mass manufacturing of optics in large numbers due to the rather elaborate and time-consuming process of abrasive machining. In addition, the process of abrasive machining during conventional manufacturing also leads to sub-surface damages and residual stresses in the optics which might lead to catastrophic failure in service [3]. Precision moulding of glass optics obviates the need of abrasive machining of glass blanks, replacing the multi-step process chain with a single step high temperature glass moulding step which reduces the manufacturing time by several orders of magnitude while ensuring high quality and precision of the fabricated optics. The choice of low  $T_g$  optical glass is necessitated for reducing the process cycle, lowering energy cost and increasing the yield for mass manufacturing.

---

D. Sanyal (✉) · R. Kumar

Advanced Ceramics and Composite Division, CSIR-Central Glass and Ceramic Research Institute, Kolkata 700032, India

e-mail: [dsanyal@cgcri.res.in](mailto:dsanyal@cgcri.res.in)

The process of precision forming of glass optics requires preparation of a volume proportioned glass blank or gob having the desired optical surface quality which need to be placed within a pair of moulds. The moulds are made of hard alloy or ceramics—preferably the latter—due to superior hardness and resistance to thermal shock and fatigue of ceramics over metallic alloys. The pair of moulds need to be machined with a great deal of precision to form negative replicas of the surfaces of the two sides of the optical components to be fabricated by the forming process. The glass gob is first flushed with gaseous nitrogen and subsequently heated by IR heaters rapidly to a temperature above the glass transition temperature (for the particular grade of glass). After achieving sufficient homogenization of temperature in the glass gob, the moulds are closed on the heated gob and held for a short duration of time to achieve the desired pressing load. The mould is then opened with simultaneous purging of gaseous nitrogen for dissipating heat. Figure 4.1 is a schematic representation of the entire replicative forming process for precision optics.

Notwithstanding the advantage of the new process chain, the success of this method lies in an accurate understanding of the rheological, viscoelastic and thermophysical behaviour of glass at elevated temperature such that the forming process yields the accurate shape and properties of the moulded optics. In this paper, the

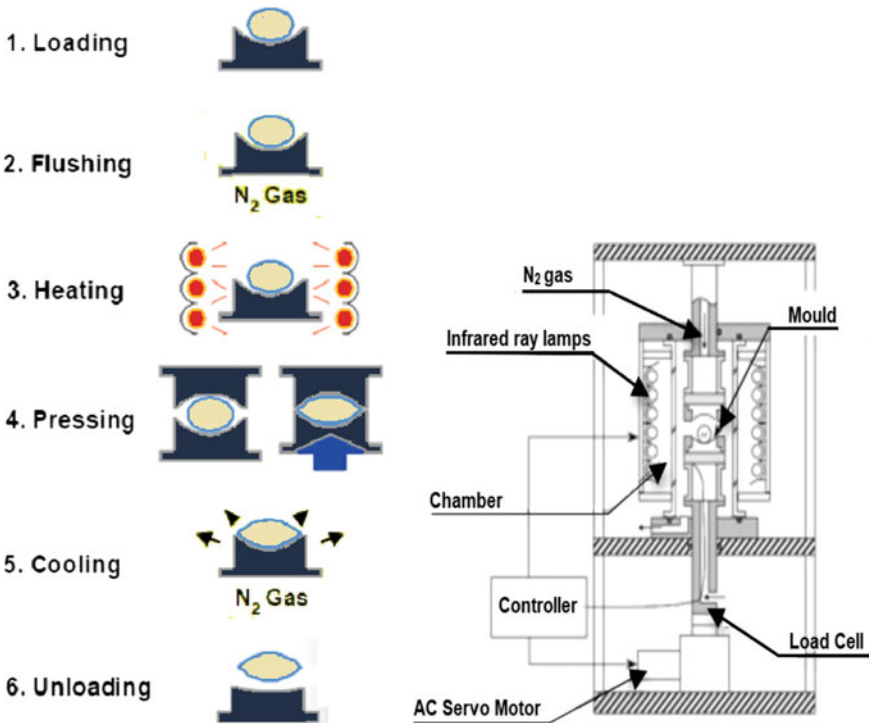


**Fig. 4.1** Schematic depiction of replicative forming machine and process chain for precision optics (adapted from GMP series machine specifications at [www.shibuara-machine.co.jp](http://www.shibuara-machine.co.jp))

fundamental aspects of the thermophysical behaviour of glass at temperatures above the glass transition temperature ( $T_g$ ) will be presented along with brief description of the influencing parameters and experimental characterization techniques.

### 4.2 Rheological Behaviour of Silicate Glasses

Inorganic silicate glasses exhibit a nonlinear variation of dynamic viscosity ( $\eta$  in Pa.s) versus temperature ( $T$  in  $^{\circ}\text{C}$ ), as shown schematically in Fig. 4.2. Table 4.1 enlists the range of working temperatures defined for glass manufacturing industries defined with reference to various ranges of viscosities. Since glassy state of matter is defined as a state of supercooled liquid, it is indeed quite appropriate to study rheology of glass in terms of its viscosity and temperature. The range of viscosity being very large, the ordinate is plotted in log scale.

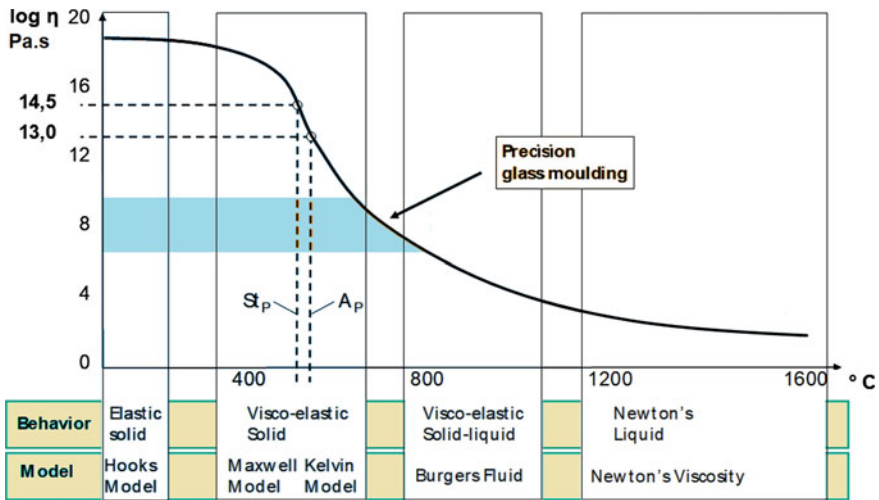


**Fig. 4.2** Schematic depiction of rheological behaviour of inorganic glasses through viscosity vs temperature plot (adapted from [36])

**Table 4.1** Definition of various working temperatures for glass manufacturing based on ranges of viscosity [4]

Reference temperature	Viscosity (Pa.S)
Practical melting temperature	1–10
Working point	$10^3$
Littleton softening point	$10^{6.6}$
Annealing point	$\sim 10^{12}$
Glass transition point	$\sim 10^{12} - 10^{12.5}$
Strain point	$\sim 10^{13.5}$

From Fig. 4.2, it is seen that at a very low temperature (near ambient), the viscosity of glasses is extremely high ( $> 10^{18}$  Pa.s), where it behaves like elastic solid obeying Hooke’s law with a linear variation of shear stress ( $\sigma$ ) with respect to shear strain ( $\varepsilon$ ) with  $G$ , shear modulus, as the proportionality constant.

$$\sigma = 2G\varepsilon \tag{4.1}$$

Unlike metals and alloys, characterized by the presence of a sharp melting point (pure metals) or eutectic temperature (alloys), where the values of various thermodynamic properties (such as the specific heat, heat capacity, coefficient of thermal expansion and compressibility) change quite sharply and abruptly, and glasses are known to exhibit a gradual variation in these properties with temperature as shown in Fig. 4.3. The glass transition temperature can be defined both as a thermodynamic and a kinetic parameter. The estimation of  $T_g$  can be made by several experimental techniques, such as (a) differential scanning calorimetry (b) dilatometry (c) rheometry (d) nanoindentation and so on. All these techniques are available and have been employed at CSIR-CGCRI to estimate  $T_g$  of various grades of glass. Depending on the heating/cooling rate, the plots of thermodynamic properties versus temperature will exhibit changing slopes which contributes to the kinetic aspects of  $T_g$  evaluation (e.g.  $T_{g1}$  and  $T_{g2}$  in Fig. 4.3). The point of intersection of the extended linear portions of the slopes of the solid-like portion (dashed line at low temperature) and the liquid-like portion (dashed line at high temperature) provides estimation of the  $T_g$ .

At a very high temperature (typically  $> 1000$  °C), glasses behave as low viscous liquid (typically  $\eta < 10$  Pa.s) with sufficient fluidity for performing refining and homogenization operations. Majority of the glasses are known to exhibit Newtonian

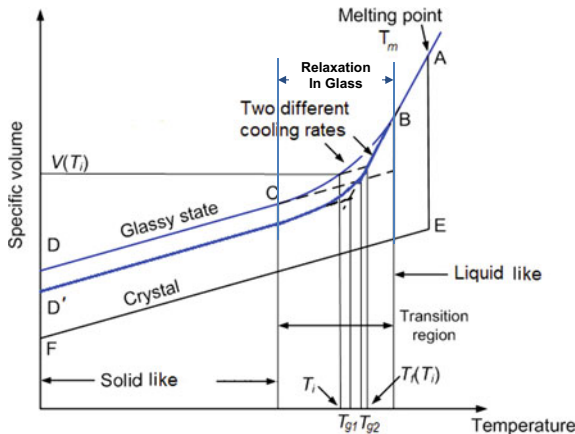


**Fig. 4.3** Schematic depiction of gradual variation of thermodynamic property (e.g. specific volume) with temperature for a glass unlike abrupt and sharp variation for a pure crystalline solid (adapted from [13] and [19])

behaviour where shear stress varies linearly with the velocity gradient ( $du/dy$ ) or the shear strain rate ( $\dot{\epsilon}$ ) with a constant proportionality factor of dynamic viscosity ( $\eta$ ) which is the real part of the complex viscosity under forced harmonic oscillation of shear stress applied at elevated temperature.

$$\sigma = -\eta \frac{du}{dy} = \eta \dot{\epsilon} \quad (4.2)$$

At working point, the viscosity is still low enough ( $\sim 10^3$  Pa.s) to make the glass amenable to shaping by blowing, pressing and other operations with retention of shape upon release of shear force. At the softening point, glass flows under self-weight (typical dimensions are defined for estimation of the softening point). For replicative forming of precision glass optics, annealing point is very important. While annealing is an integral processing step in any glass forming operation for reducing or controlling residual stresses, this assumes additional significance for moulded optics as a means (a) to lower residual stresses by several orders of magnitude than the corresponding levels for ordinary glassware to prevent warping during abrasive polishing, (b) to minimize the spatial variation of refractive index and (c) to stabilize physical properties even at elevated temperatures. The annealing point is defined by a specific viscosity at which the glass will hold its shape while facilitating rapid relieving of internal stresses in several minutes.

### 4.2.1 Viscous Behaviour of Glasses

The viscous behaviour of inorganic silicate glasses has been extensively studied in the literature for various grades of glass. The relaxation behaviour of glass is exhibited during the intermediate zone of temperature sandwiched between the solid-like and liquid-like glass behaviour as shown in Fig. 4.3. The relaxation phenomena are governed by viscous behaviour of glass. As will be shown in the next section (see Eq. 4.12), the relaxation time is a ratio of the dynamic viscosity and the shear modulus. More viscous the glass, the larger is the time to relax to the equilibrium structure. Many different models of viscosity have been proposed for glasses of different chemical compositions. The simplest model of dynamic viscosity assumes a thermally activated phenomenon with exponential variation with inverse temperature as proposed by Frenkel and Andrade [5].

$$\eta(T) = A \exp\left(\frac{Q}{RT}\right) \quad (4.3)$$

The above model is easy to use and can capture the linear variation with inverse temperature in log–log scale for very strong glasses (e.g. bulk metallic glasses). But the Arrhenius type behaviour of the above equation does not match with experimental viscosity variation with temperature for various fragile glasses, such as soda lime

silicate and sodium borosilicate glasses [6]. For supercooled fragile liquids, several correlations for viscosity versus temperature are offered by Adam and Gibbs [7], Avramov and Milchev [8], and Vogel, Fulcher and Tamman [9]. Table 4.2 enlists these correlations, adjustable coefficients and the major assumptions behind the derivation of these correlations [10].

All the above correlations in Table 4.2 work well within the regime, where activation energy changes with temperature. An all-encompassing correlation covering the Arrhenius type viscosity variations at very low and high temperatures and the activation energy dependent viscosity variation at intermediate temperatures has been proposed by Douglas [11] which comprises double exponentials as

$$\eta(T) = AT \exp\left(\frac{B}{RT}\right) \left[1 + C \exp\left(\frac{D}{RT}\right)\right] \quad (4.4)$$

where  $A$ ,  $B$ ,  $C$  and  $D$  adjustable parameters. The equation has been derived under the assumption that the oxygen atoms in silicate glasses can occupy two different positions separated by an energy barrier [10]. The viscosity data of some oxide glasses [12] with the various regimes of applicability of various correlations is shown in Fig. 4.4. It may be mentioned here that the structural relaxation of glass towards its

**Table 4.2** Viscosity vs temperature correlations for fragile glasses

S. No	Name	Correlation	Parameters	Assumptions
1	Adam and Gibbs	$\ln[\eta(T)] = A_{AG} + \frac{B_{AG}}{TS_{conf}(T)}$	$A_{AG}$ and $B_{AG}$ are adjustable parameters and $S_{conf}$ is the configurational entropy	At $T < T_g$ , the molecules are trapped in one configurational state, but for $T > T_g$ , many configurational states are possible
2	Avramov and Milchev	$\ln[\eta(T)] = A_{AM} + 2.3(13.5 - A_{AM})\left(\frac{T_g}{T}\right)^a$	$A_{AM}$ is an adjustable parameter	Viscosity is a function of the total entropy of the system which governs the distribution of activation energy barriers
3	Vogel, Fulcher and Tamman (VFT)	$\ln[\eta(T)] = A_{VFT} + \frac{B_{VFT}}{R(T-T_V)}$	$A_{VFT}$ , $B_{VFT}$ and $T_V$ are adjustable parameters	Viscosity is dependent on the excess or free volume per molecule. Molecular transport is known to occur when the void volume exceeds a critical value

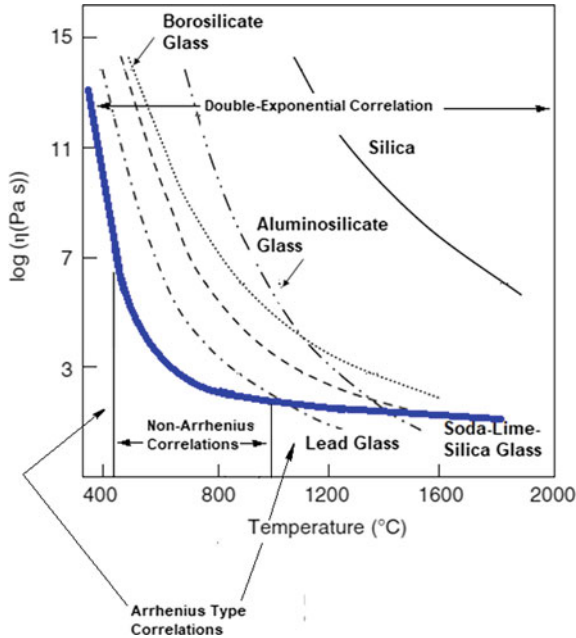


**Fig. 4.4** Viscosity variation with temperature for several oxide glasses [12] and the various regimes of applicability of correlations (blue solid line is a schematic representation of the predicted viscosity from various correlations) (adapted from [4])

equilibrium state is reflected in the nonlinear variation of viscosity with temperature which is briefly discussed under Sect. 4.3.

### 4.2.2 Viscoelastic Behaviour of Glasses

At a moderate range of elevated process temperature above  $T_g$  up to the annealing point, the inorganic glasses exhibit viscosity too high to achieve fluidity as in the case of viscous liquid, but still lower than the frozen state akin to elastic solid. At this intermediate zone, glasses exhibit viscoelastic behaviour in the form of a time-dependent response to mechanical stress or strain. In this window of temperature, the stress varies not only with strain exhibiting solid-like elastic behaviour (Eq. 4.1), but also with strain rate showing liquid-like viscous behaviour (Eq. 4.2). The rheological characteristics exhibited by inorganic glasses constitute various types of deformation and flow such as,

- (a) Creep: increase of strain with time at elevated temperature, if stress is held constant



- (b) Stress relaxation: decrease of stress with time at elevated temperature, if strain is held constant
- (c) Hysteresis: phase lag between applied stress and strain along with dissipation of mechanical energy, when cyclic load is applied.

Under the application of an instantaneous shear load (or stress), viscoelastic glass exhibits three distinctly different deformation behaviours (a) an instantaneous reversible elastic deformation (giving rise to instantaneous elastic strain,  $\epsilon_i$ ) due to bond stretching (b) a time-dependent reversible elastic deformation (resulting in delayed elastic strain,  $\epsilon_d$ ) due to gradual structural expansion caused by molecular rearrangement in the direction of the application of load and (c) a dissipative deformation and strain ( $\epsilon_\eta$ ) caused by viscous or molecular momentum transport under the action of shear force. On removal of the applied load,  $\epsilon_i$  and  $\epsilon_d$  recover completely—the former instantaneously and the latter after a certain passage of time taken for disentanglement of the molecular units to come back to the original positions. However, the viscous deformation is irrecoverable due to absence of requisite thermodynamic driving force [3]. Figure 4.5 illustrates the instantaneous stress–strain behaviour of a typical inorganic glass at the viscoelastic regime of operation.

For analysis of viscoelastic stress–strain behaviour, the stress and strain tensors are often resolved into deviatoric and dilatational components as shown below:

$$\sigma_{ij} = s_{ij} + \frac{1}{3}\delta_{ij}\sigma \tag{4.5}$$

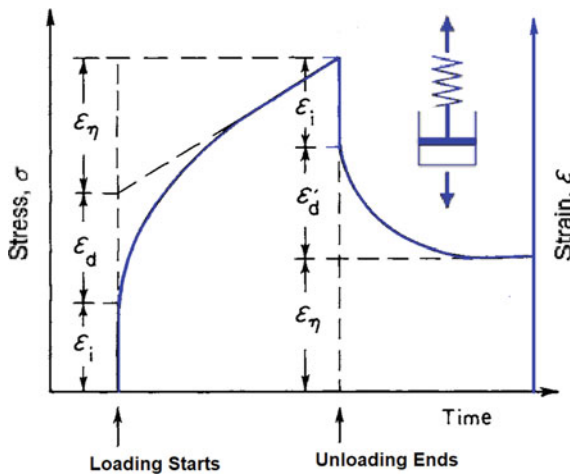


**Fig. 4.5** Stress–strain behaviour under instantaneous loading and unloading of glass under viscoelastic regime of operation (dashed line represents stress, solid coloured line represents strain during the loading and unloading time window, spring and dashpot provides an analogue of the viscoelastic solid) (adapted from [37])

$$\varepsilon_{ij} = e_{ij} + \frac{1}{3}\delta_{ij}\varepsilon \quad (4.6)$$

where  $s_{ij}$ ,  $\sigma$ ,  $e_{ij}$  and  $\varepsilon$  are the deviatoric stress, dilatational stress, deviatoric strain and dilatational strain, respectively.  $\delta_{ij}$  is known as the Kronecker delta defined as

$$\delta_{ij} = \begin{cases} 0 & \text{for } i \neq j \\ 1 & \text{for } i = j \end{cases}$$

The dilatational components of stress and strain are given as

$$\sigma = \sigma_{11} + \sigma_{22} + \sigma_{33} \quad (4.7)$$

$$\varepsilon = \varepsilon_{11} + \varepsilon_{22} + \varepsilon_{33} \quad (4.8)$$

The elastic (Hookean) and viscous (Newtonian) deviatoric stress–strain behaviour can be obtained by rearranging Eqs. (4.1), (4.2), (4.5) to (4.8) as follows:

$$s_{12} = 2Ge_{12}^E \quad (4.9)$$

$$s_{12} = 2G\dot{\eta}_{12}^V \quad (4.10)$$

where superscript  $E$  and  $V$  denote the elastic and viscous components, respectively.

The simplest physical analogues of viscoelastic behaviour of glasses at elevated temperature are given by a spring and a dashpot in series, parallel or in various combinations (Fig. 4.6). The spring represents the elastic solid, and the dashpot represents the viscous liquid. The most common model for a viscoelastic solid is given by the Maxwell model having a spring and a dashpot in series. In this model, the applied deviatoric stress  $s_{12}$  is the same for both spring and dashpot, and the deviatoric total strain  $e_{12}$  is given as

$$e_{12} = e_{12}^E + e_{12}^V \quad (4.11)$$

The elastic and viscous components of the deviatoric strain and strain rate are given by Eqs. (4.9) and (4.10), respectively. The expression for the deviatoric stress in the Maxwell model can be obtained from Eqs. (4.9) to (4.11) as

$$\dot{s}_{12} = 2G\dot{e}_{12} - \frac{s_{12}}{\tau_s} \quad (4.12)$$

where  $\tau_s = \eta/G$  is the shear stress relaxation time. For a constant strain applied instantaneously at time  $t = 0$ , the integral form of Eq. (4.12) is expressed as

$$s_{12}(t) = 2Ge_{12}(0)e^{-\frac{t}{\tau_s}} = s_{12}(0)e^{-\frac{t}{\tau_s}} \quad (4.13)$$

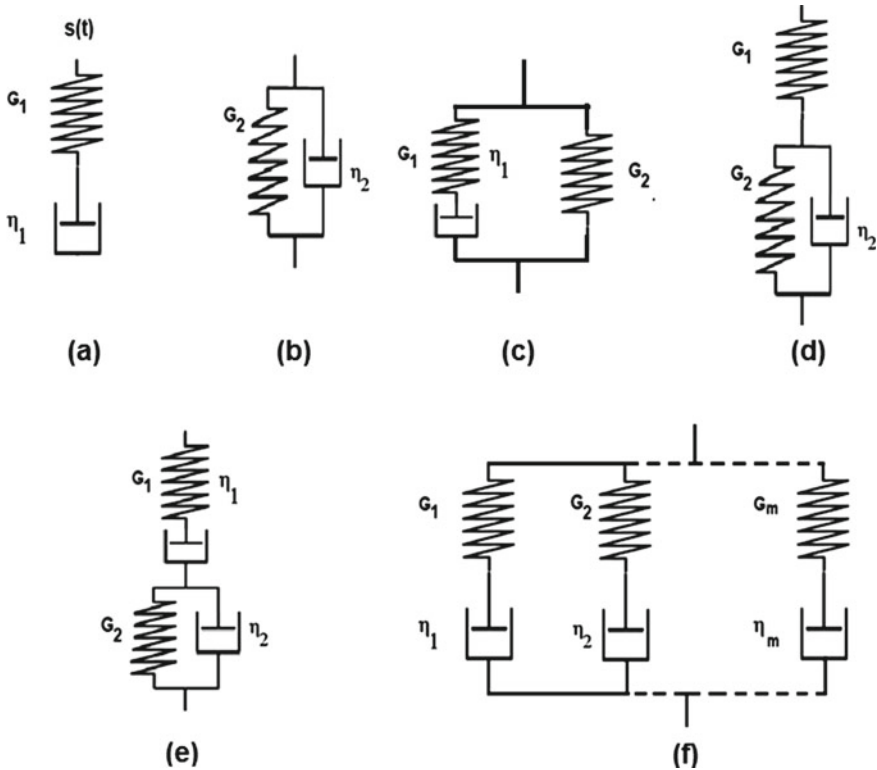


**Fig. 4.6** Physical analogues for various viscoelastic material models **a** Maxwell model **b** Kelvin–Voigt model **c** Zener–Maxwell model **d** Zener–Kelvin model **e** Burger model **f** Generalized Maxwell model

A physical interpretation of the stress relaxation time could be obtained from the above equation. When  $t = \tau_s$ , the stress  $s_{12}(t)$  becomes  $(1/e)$  times the initial stress  $s_{12}(0)$ , or,  $s_{12}(t) = 0.368\{s_{12}(0)\}$ . In other words, stress relaxation time is the time when the stress decays to 36.8% of its initial value.

Since inorganic glasses can have vastly different compositions (e.g. borosilicate, aluminosilicate, phosphate, silicophosphate, chalcogenide and so on), the mechanical behaviour of various glasses differs from one another. The viscoelastic behaviour of glasses can be expressed under the assumption of linear viscoelastic behaviour (that is, stress is linearly proportional to the strain) either (a) by a linear combination of various mechanical analogues or (b) by the Boltzmann superposition principle. In terms of the mechanical analogues, various linear combinations of springs and dashpots have been proposed to yield different viscoelastic models, such as Kelvin–Voigt model, Burger model and generalized Maxwell model to describe the viscoelastic material behaviour of inorganic glasses.

### 4.2.3 Maxwell Model

$$s_{ij}(t) = s_{ij}(t_0)e^{-\frac{(t-t_0)}{\tau_s}} \text{ where } \tau_s = \frac{\eta_1}{G_1} \quad (4.14)$$

Kelvin–Voigt model:

$$s_{ij}(t) = s_{ij}(t_0) \left[ 1 + \frac{\eta_2}{G_2} \delta(t - t_0) \right] \quad (4.15)$$

Burger model:

$$s_{ij}(t) = \frac{s_{ij}(t_0)}{\sqrt{(G_1\eta_1 + G_1\eta_2 + G_2\eta_1)^2 - 4G_1G_2\eta_1\eta_2}} \times \left[ \left( G_2\eta_1 - \frac{\eta_1\eta_2}{\tau_{s1}} \right) e^{-\frac{(t-t_0)}{\tau_{s1}}} - \left( G_2\eta_1 - \frac{\eta_1\eta_2}{\tau_{s2}} \right) e^{-\frac{(t-t_0)}{\tau_{s2}}} \right] \quad (4.16)$$

where  $G_1$ ,  $G_2$ ,  $\eta_1$ ,  $\eta_2$  are the shear moduli and dynamic viscosities for the spring-dashpot combinations in series and parallel, respectively, for the Burger model as shown in Fig. 4.6. The relaxation times  $\tau_{s1}$  and  $\tau_{s2}$  for the series and parallel parts of the spring-dashpot combinations are defined as follows:

$$\tau_{s1} = \frac{2\eta_1\eta_2}{(G_1\eta_1 + G_1\eta_2 + G_2\eta_1) - \sqrt{(G_1\eta_1 + G_1\eta_2 + G_2\eta_1)^2 - 4G_1G_2\eta_1\eta_2}}$$

$$\tau_{s2} = \frac{2\eta_1\eta_2}{(G_1\eta_1 + G_1\eta_2 + G_2\eta_1) + \sqrt{(G_1\eta_1 + G_1\eta_2 + G_2\eta_1)^2 - 4G_1G_2\eta_1\eta_2}} \quad (4.17)$$

Often, a generalized Maxwell equation can be employed to represent a complex stress versus strain behaviour of the unknown viscoelastic behaviour of a glass. From Fig. 4.6, it is seen that the total stress on the material is the sum of the partial stresses on each of the  $m$  numbers spring-dashpot segments which are connected in parallel with the same strain  $e_{12}$  acting on each segment. The viscoelastic mechanical behaviour for the generalized Maxwell model is given as follows:

$$s_{ij}(t) = 2Ge_{ij} \sum_{i=1}^m w_i e^{-\frac{t}{\tau_i}} \quad (4.18)$$

It may be pointed out here that the simple Maxwell model and the Kelvin–Voigt model comprise one Hookean and one Newtonian element, that is, the spring and dashpot, in series and in parallel, respectively. These offer simple expressions, but are constrained in representing the physics of the viscoelastic behaviour. The Kelvin–Voigt model can represent the delayed elastic deformation, but not the other

components. In comparison, the Burger model can represent all three deformations, namely the elastic recoverable deformation, the delayed elastic deformation and the viscous irrecoverable deformation. Depending on the high temperature rheological behaviour of the glass, more complex models can be constituted, such as the generalized Burger's model, where several Burger's elements (spring and dashpot connected in parallel) are connected in series. The more complex the physical analogue is, and the model can capture the complex viscoelastic rheology of the glass. But the expression becomes more and more complex to handle mathematically.

## 4.3 Relaxation Phenomena in Silicate Glasses

### 4.3.1 Structural Relaxation

Inorganic glasses are known to exhibit a state of supercooled liquid during cooling from high temperature to ambient temperature without crystallization. These glasses undergo two kinds of relaxation phenomena—stress relaxation and structural relaxation. Structural relaxation arises out of the propensity of the glass to lower its Gibbs free energy further from its unstable state at room temperature to thermodynamically favourable liquid state with time overcoming kinetic constraints. The structural relaxation has been defined by Scherrer [13] and Doss et al. [14] as “the response of a material subjected to an isothermal hold measured through observable changes in the material's properties (volume in this case) due to structural rearrangements over time”. Structural relaxation expresses itself through slow change in volume with time which is characteristic of  $\alpha$ -relaxation. Experimental observations of structural relaxation have been reported by several researchers [15–17]. Following Scherer [13], it can be shown that structural relaxation behaviour in a glass subjected to an instantaneous dip in its temperature from the equilibrated temperature near its glass transition is expressed as a gradual change in its property  $p_S$  towards the equilibrium value at the new temperature (Fig. 4.7) as a result of slow molecular rearrangement which is distinct from the instantaneous vibrational contribution  $p_V$ .  $p$  designates any measurable property, e.g. refractive index, density, enthalpy, volumetric thermal expansion, etc.  $t$  represents time and  $T$  represents temperature. It may be mentioned here that the schematic diagram (Fig. 4.7) exhibits that glass stabilized at higher temperature than that imposed at  $t = t_0$  possesses more open structure and larger volumes such that it relaxes at a faster rate than if it were to be heated from a lower stabilized temperature ( $T_1 < T_2$  hypothetically). Structural relaxation therefore depends on the thermal history experienced by the glass.

Attempts have been made to capture the physics of structural relaxation using models analogous to stress relaxation by Tool [18], Narayanaswamy [19], Moynihan et al. [20]. The Tool's model of structural relaxation is based on a structural order parameter defined by him as the fictive temperature ( $T_f$ ). Originally, the fictive temperature has been defined by Tool [18] as a measure of the structural state of

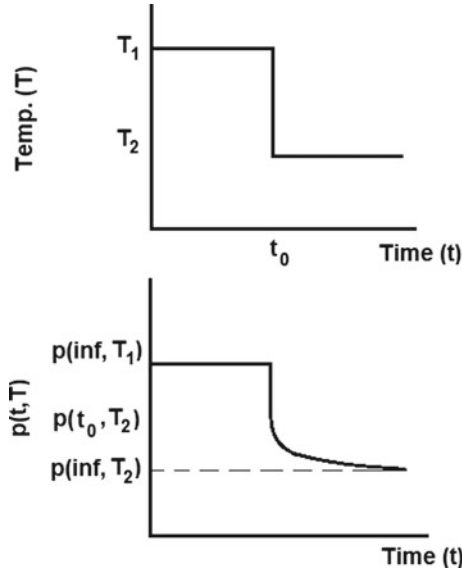


**Fig. 4.7** Change in property  $p(t, T)$  of glass equilibrated around  $T_g$  with instantaneous change in temperature from  $T_1$  to  $T_2$  at time  $t = t_0$  with asymptotic approach towards equilibrated value at  $T_2$  as a result of structural relaxation (adapted from [13])

the glass whose time rate of change is inversely proportional to the viscosity as follows:

$$\frac{dT_f}{dt} = \left[ K \exp\left(\frac{T}{p}\right) \exp\left(\frac{T_f}{q}\right) \right] (T - T_f) \tag{4.19}$$

where  $K$ ,  $p$  and  $q$  are arbitrary constants. The first expression on the right hand side within parenthesis is inversely proportional to the viscosity of glass.

Fictive temperature can be defined in the most general sense as a structural order parameter  $\xi(S, V)$  with respect to thermodynamic parameters total entropy  $S$  and total volume  $V$  as follows [21]:

$$T_f = \left( \frac{\partial U}{\partial S} \right)_V = T - A \left( \frac{\partial \xi}{\partial S} \right)_V \tag{4.20}$$

For quantitative estimation of  $\xi$ , the Kohlrausch stretched exponent formula can be used as given below [22]:

$$\frac{\xi}{\xi(0)} = \exp \left[ - \left( \frac{t}{\tau_\kappa} \right)^\beta \right] \tag{4.21}$$

Where  $\beta = 1 - n$  and  $\tau_\kappa = \tau_0(1 - n)^{-1/(1-n)}$  where  $n$  is the Kohlrausch exponent with values less than 1 which needs to be experimentally determined. The experimentally estimated values of exponent  $\beta$  typically lies  $0.3 \leq \beta \leq 0.75$ .

The original Naryanaswamy model for structural relaxation based on the generalized Arrhenius equation was modified by Moynihan to yield a relaxation time

$$\tau = \tau_0 \exp \left[ X \frac{\Delta H}{RT} + (1 - X) \frac{\Delta H}{RT} \right] \quad (4.22)$$

where  $0 < X < 1$  is the parameter which partitions the activation energy into a temperature dependent part and a structure dependent part [23]. For estimating the non-Arrhenius structural relaxation times, several phenomenological models have been proposed, such as the free volume model [24], the entropy model [8], the instantaneous shear modulus model [25] and so on. More recently, more sophisticated models of structural relaxation have been proposed based on equilibrium and non-equilibrium shear viscosity [26, 27], extended de Donder non-equilibrium thermodynamic model [28] and so on.

### 4.3.2 Stress Relaxation

The stress relaxation phenomena in glasses can be defined as “the time-dependent response of the stress developed within a material subjected to a mechanical strain” [13, 14]. Creep and stress relaxation are two opposite phenomena which capture the essence of mechanical relaxation behaviour in glass. Creep is defined as time-dependent escalation in strain in an isothermally held glass sample when the initially applied stress is held constant. Stress relaxation on the other hand is defined as the time-dependent decrement in stress in an isothermally held glass sample when the initially applied strain is held constant. Figure 4.8 depicts schematically the creep and stress relaxation behaviour in glass as defined above. Creep occurs when deformation is time dependent at constant stress. Under uniaxial loading, the time-dependent variation of stress as a result of instantaneous stress applied at time  $t_0$  is given by the Heaviside step function  $H$

$$s(t) = s_0 H(t - t_j) \quad (4.23)$$

where  $s_0$  is the stress applied at  $t_j$  and the Heaviside step function  $H$  is defined as

$$H = \begin{cases} 0 & \text{for } t - t_j < 0 \\ 1 & \text{for } t - t_j \geq 0 \end{cases} \quad (4.24)$$

At any time instant  $t$ , the time-dependent deformation (strain) behaviour will be expressed as

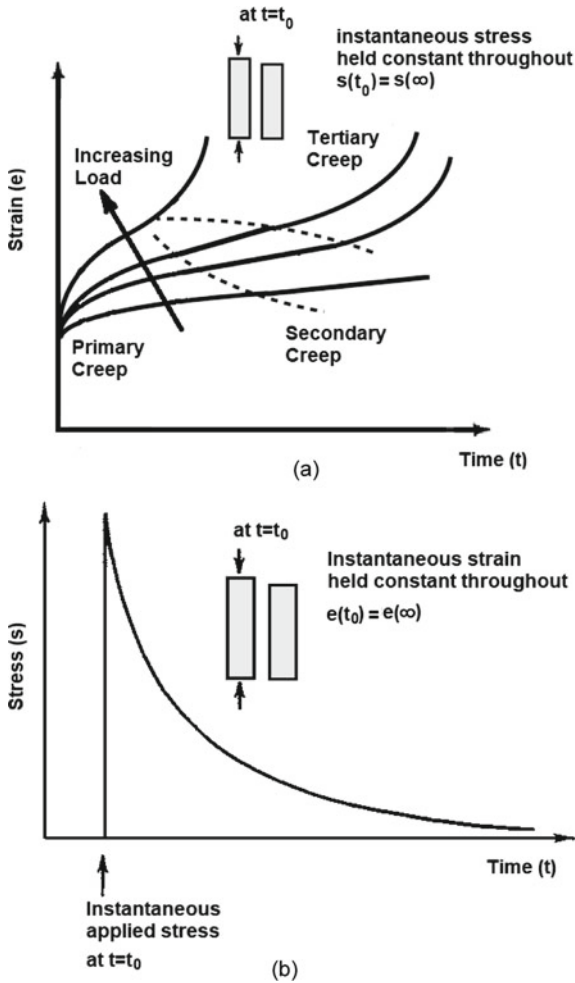


**Fig. 4.8** Schematic diagram representing mechanical relaxation behaviour during **a** creep **b** stress relaxation for isothermally held glass samples (adapted from [13] & [29])

$$e(t) = J(t - t_j)s_0 \tag{4.25}$$

where  $J = e(t)/s_0$  is the creep compliance of the material [29]. For a glass sample undergoing creep, the response function for creep compliance is given as

$$J(t) = J_0 \left\{ 1 - \exp\left(-\frac{t}{\tau_c}\right) \right\} \tag{4.26}$$

where  $\tau_c$  is known as the creep or retardation time. For a Maxwellian viscoelastic behaviour (Eq. 4.15), the creep compliance can be expressed as



$$J(t) = \frac{1}{G} + \frac{t}{\eta} \quad (4.27)$$

The Maxwell model does not capture the linear primary creep behaviour well. The Kelvin–Voigt model yields a response

$$J(t) = \frac{1}{G} \left\{ 1 - \exp\left(-\frac{t}{\tau_c}\right) \right\} \quad (4.28)$$

where the retardation time  $\tau_c = \eta/G$  is the ratio of the dynamic viscosity to the shear modulus. The Zener–Maxwell model (also called the standard linear solid model) containing three mechanical elements—a spring in parallel with a spring–dashpot in a series—exhibits a more complex creep response as given below

$$J(t) = \frac{1}{G_2} - \frac{G_1}{G_2(G_1 + G_2)} \exp\left(\frac{-t}{\tau_c}\right) \quad (4.29)$$

where the retardation time  $\tau_c$  is given in terms of the relaxation time  $\tau_R$  as

$$\tau_c = \tau_R \left( \frac{G_1 + G_2}{G_2} \right) \quad (4.30)$$

Equation (4.27) clearly shows that retardation time is not identical with the relaxation time. More fundamentally, the relationship between them can be defined through a parameter known as relaxation strength which is defined as a ratio of change in material modulus during relaxation to the modulus at very long time as [29]

$$\Delta = \left| \frac{(G_0 - G_\infty)}{G_\infty} \right| \text{ and } t_c = t_R(1 + D) \quad (4.31)$$

For low magnitudes of relaxation strength  $G_0/G_\infty \ll 1$ , the retardation time equals the relaxation time.

Transient stress relaxation of glass which have been described by various mechanical analogues in the previous section on viscoelastic behaviour of glasses can be experimentally evaluated under quasi-static loading (compressive or flexural). The stress–strain constitutive behaviour derived in the previous section is based on the viscoelastic response to a unit step function in stress or strain under isothermal conditions. For a more general situation where an arbitrary history of stress and strain is involved, the constitutive relation may be derived for linear viscoelastic materials using the Boltzmann superposition principle [13] which states that the effect of any compound cause can be expressed as the sum of the individual effects of component causes. The derived stress–strain relation is expressed in terms of a Boltzmann hereditary integral as follows:

$$s(t) = \int_0^t G(t - \tau) \frac{de(\tau)}{d\tau} d\tau \quad (4.32)$$

and

$$e(t) = \int_0^t J(t - \tau) \frac{ds(\tau)}{d\tau} d\tau \quad (4.33)$$

Often, stress relaxation behaviour is experimentally determined by dynamic mechanical analysis (DMA), where glass at isothermal, high temperature is subjected to periodically oscillating load which leads to a complex shear stress as follows:

$$s^* = s_0 \cos \omega t + i s_0 \sin \omega t = s_0 \exp i \omega t \quad (4.34)$$

The dynamic stress–strain behaviour is expressed as

$$s^* = G^* e^* \quad (4.35)$$

where  $G^*$  is the complex shear modulus comprising a real part  $G'$  called the storage modulus and an imaginary part  $G''$  called the loss modulus as follows

$$G^* = G' + i G'' \quad (4.36)$$

The storage modulus represents the recoverable stored energy due to elastic deformation and the loss modulus represents the energy dissipated due to viscous flow. These moduli are dependent on the frequency of oscillation  $\omega$ . The dynamic stress and strain are out of phase with the phase shift  $\Delta t$  and the phase angle  $\delta$  as shown in Fig. 4.9. The ratio of the storage and the loss modulus is a measure of the phase angle  $\delta$  as follows:

$$\tan \delta = \frac{G''}{G'} \quad (4.37)$$

where  $\tan \delta$  is the loss factor and a measure of the dissipate mechanical energy for the viscoelastic glass due to cyclic loading. Under forced harmonic oscillation, the viscosity is also defined as a frequency dependent complex quantity  $\eta^* = \eta' + i\eta''$ , where  $\eta'$  is the real part of the complex viscosity.  $\eta'$  is known as the dynamic viscosity and is defined as the ratio of the loss modulus to the angular frequency,  $\eta' = G''/\omega$ . Both the moduli ( $G'$  and  $G''$ ) are frequency dependent. For a Maxwell solid, they are given as [4]:

$$G' = \frac{\omega^2 \tau^2}{1 + \omega^2 \tau^2} G \quad (4.38)$$

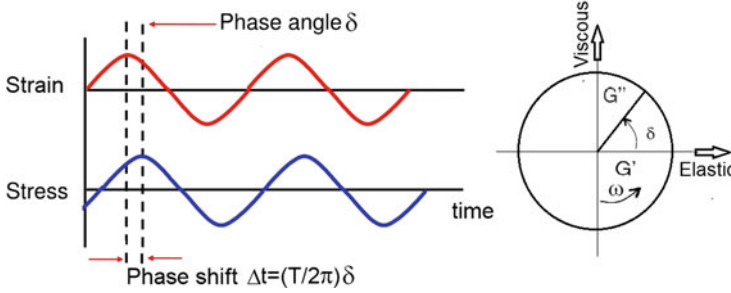


**Fig. 4.9** Schematic representation of the dynamic stress–strain behaviour of viscoelastic glass, where stress and strain are out of phase with phase shift  $\Delta t$  and phase angle  $\delta$  (adapted from [4])

$$G'' = \frac{\omega\tau}{1 + \omega\tau} G \quad (4.39)$$

At very high frequency ( $\omega \rightarrow \infty$ ), the storage modulus equals the value for the purely elastic regime, and at very small frequencies ( $\omega \rightarrow 0$ ), the phase angle equals  $90^\circ$  implying purely viscous regime.

## 4.4 Modelling and Characterizations

The deformation behaviour of inorganic glass at temperatures above  $T_g$  is of relevance to several glass moulding processes. In the preceding sections, the viscous and viscoelastic rheological behaviour of inorganic glasses have been discussed in some detail. In this section, the characterization of such glasses for property estimation and modelling of the deformation behaviour along with numerical simulation using finite element method (FEM) will be briefly presented.

### 4.4.1 Fictive Temperature and Glass Transition Temperature

Since the glass transition temperature  $T_g$  is the temperature for transition from solid-like elastic behaviour to liquid-like viscous behaviour, its estimation is of primary importance for high temperature forming of any inorganic glass. Unlike the melting point of a crystalline material, the  $T_g$  for a glassy material is not a sharp and unique point in the property temperature space and can be determined as the point of intersection between the extrapolated glass and the liquid equilibrium lines [30] by a number of techniques, such as differential scanning calorimetry (DSC), dilatometry and rheometry. For quantitative estimation of structural relaxation in glass, a parameter called the fictive temperature ( $T_f$ ) has been defined by Tool [18] as a measure of deviation from the equilibrium state. The fictive temperature was originally defined

by Tool as “the temperature at which the glass would be in equilibrium, if heated or cooled very rapidly to it”. In case of glass formation by the melt-quench route, if a melt (that is, an equilibrium liquid glass) is quenched instantaneously to form glass, the fictive temperature is the temperature of the melt immediately before the quench. The fictive temperature can be experimentally estimated from the viscosity versus temperature plot as the point of intersection of the isostructural viscosity line and the equilibrium line [31]. The isostructural viscosity line is traced when the experimental timespan of measurement of viscosity versus temperature does not alter the glass structure appreciably. The magnitudes of  $T_f$  and  $T_g$  are dependent on the technique and heating (or cooling) rate. In the present chapter, we present the estimation of  $T_f$  and  $T_g$  for different grades of silicate glass by rheometry, DSC and dilatometry studies performed at CSIR-CGCRI using Anton Paar MCR 502 rheometer and Netzsch STA449 F3 simultaneous thermal analyser, respectively. Figure 4.10 provides a plot of  $\log(\text{viscosity})$  versus inverse temperature, where the point of inflection (change in slope of the curve) signifies the fictive temperature ( $T_f$ ) for a particular grade of silicate glass LB2000. Figure 4.11 is the trace of a temperature modulated DSC study for LB2000 glass. From the TMDSC trace, the  $T_g$  of LB2000 glass is estimated as 510.7 °C.

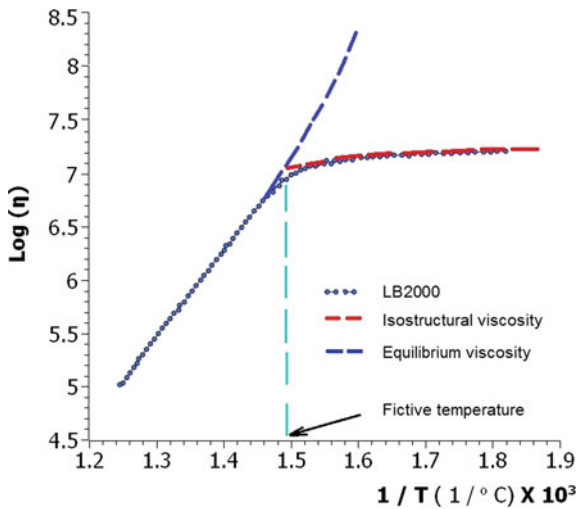


**Fig. 4.10** Log viscosity versus inverse temperature plot for silicate glass LB2000 (blue-filled circles are the experimentally observed behaviour at CSIR-CGCRI, blue dashed line is the equilibrium shear viscosity, the red dashed line is the isostructural viscosity and the point of inflection is the fictive temperature)

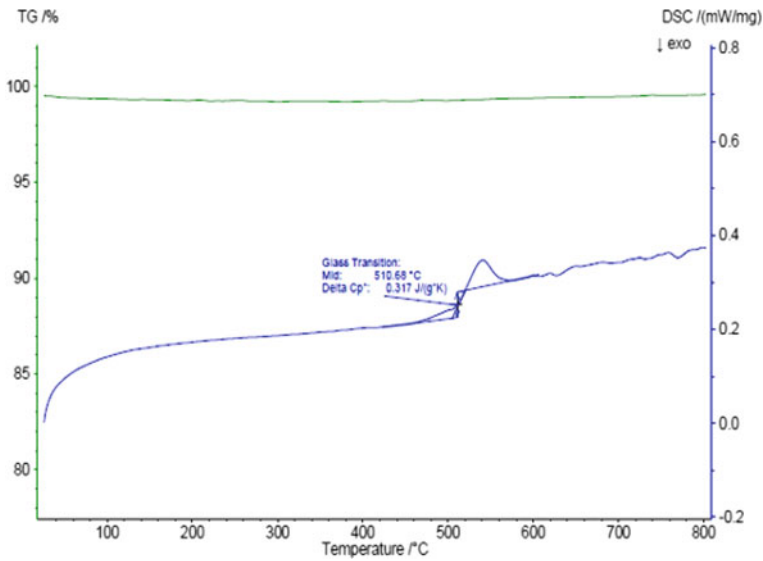


**Fig. 4.11** Temperature modulated DSC trace for silicate glass LB2000 experimentally obtained at CSIR-CGCRI

#### 4.4.2 Stress Relaxation Behaviour

Studies on high temperature creep cum stress relaxation behaviour of LB2000 silicate glass were carried out under quasi-static condition with rectangular prismatic samples with 20 mm × 20 mm square cross-section and 30 mm height. The samples were raised to temperature near the  $T_g$  (500–550 °C) in a resistive heating furnace attached to ITW BISS stress relaxation testing machine and isothermally held at the respective temperature under a small compressive pre-load for a sufficient time till the actuator position recorded negligible thermal drift. The compressive load was then increased abruptly to a pre-designated limit (typically in the range of 200–400 N) and held constant thereafter for a pre-designated duration of time for studying creep behaviour, where the deformation in glass sample continuously increased. The load was subsequently raised in a single step to 800 N and the resulting deformation was held constant under the isothermal high temperature near  $T_g$  for a pre-designated duration of time whereby the relaxation of stress with time was recorded. A typical creep-relaxation data recorded for the optical silicate glass LB2000 for experiment conducted at CSIR-CGCRI at 500 °C is plotted in Fig. 4.12. The solid red line has been used to join the experimental points for tracing the loading cycle and impart clarity. Similar plots were recorded for the same glass at various temperatures near  $T_g$  up to 550 °C to characterize the viscoelastic behaviour of the glass and ascertain the deformation behaviour during precision forming at high temperature.

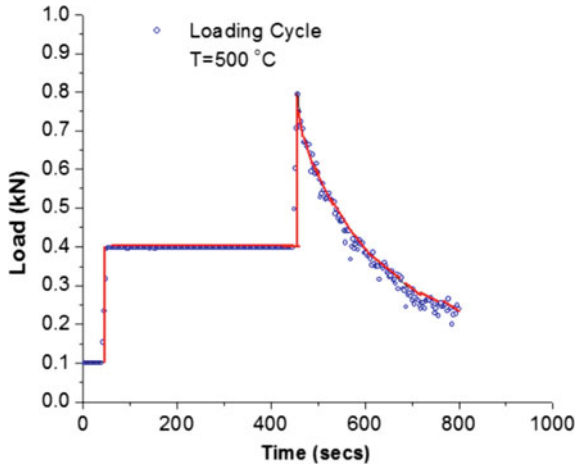


**Fig. 4.12** Creep-relaxation loading cycle for test performed on LB2000 glass at CSIR-CGCRI

### 4.4.3 Material Modelling

Several studies on viscoelastic stress relaxation behaviour in silicate glasses at elevated temperature have been reported [32–35] with or without material model. No material model is universally accepted for accurate prediction of relaxation in silicate glasses. The Kohlrausch-Williams-Watt (KWW) function used by various researchers for representing stress relaxation behaviour does not account correctly for the relaxation mechanism of glass in short time scales and leads to infinite relaxation at zero time [34]. It was also shown that for shear and uniaxial responses, KWW function cannot give a correct representation of the experimental viscoelastic functions and constants [35]. On the basis of these observations, it was deemed necessary to model stress relaxation behaviour with the help of a generalized framework of viscoelasticity which proposes various combination of springs and dashpots as mechanical analogues of elastic and viscous components to constitute various models, such as the Maxwell model (Eq. 4.14), the Kelvin–Voigt model (Eq. 4.15), the Burger model (Eq. 4.16) and so on. The efficacy of the various models to describe the viscoelastic behaviour adequately varies from glass to glass. For the LB2000 glass, the experimental viscoelastic stress relaxation behaviour at 535 °C carried out at CSIR-CGCRI has been modelled accurately by the Burger model in comparison with the Maxwell model which either overestimates or underestimates the stress state at small time (< 180 s) and large times (> 180 s), respectively, as shown in the stress versus time plot in Fig. 4.13. The superior match of the Burger model with the experimental stress relaxation data can be explained on the basis of the inherent strength of the model to capture the physics of the instantaneous elastic deformation, delayed elastic deformation and the irrecoverable viscous deformation in comparison with the Maxwell model which has limitations.

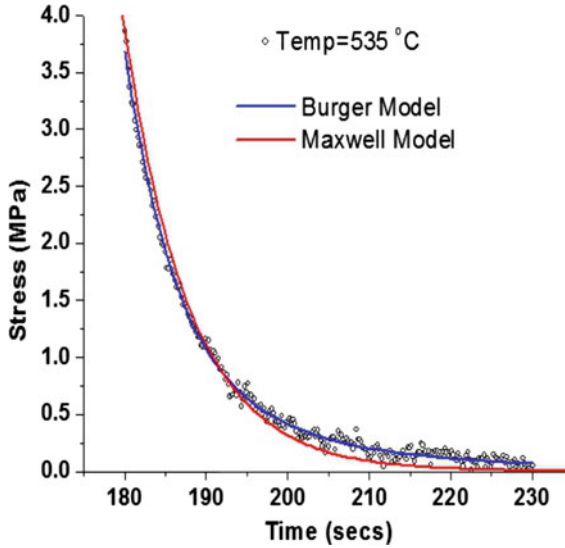


**Fig. 4.13** Stress relaxation behaviour of LB2000 glass at 535 °C—comparison of the material model with experimental data obtained at CSIR-CGCRI

#### 4.4.4 Benchmark Simulation

High temperature forming of inorganic silicate glasses has been studied for various applications including fabrication of precision optical components. Accurate prediction of the shape of the components after hot forming requires numerical simulation of the thermomechanical deformation behaviour using finite element (FE) framework. FE simulation of the glass forming process chain not only requires accurate estimation of the thermophysical properties, but also depends on the correct choice of the viscoelastic material model for the optical glass. In addition, the accuracy and efficacy of simulation depend on the choice of elements and the numerical solution framework of the finite element software. While some FE software are based on Arbitrary Lagrangian Eulerian (ALE) framework (e.g. POLYFLOW) and treats the deformation in viscoelastic solid using a continuum fluid dynamic formulation, several other software (e.g. ANSYS, ABAQUS, MSC.MARC, etc.) adopt a small deformation-based continuum solid mechanics approach representing the linear viscoelastic behaviour using a Prony series. For example, the ABAQUS implementation of time domain viscoelasticity utilizes a linear elastic traction-separator behaviour under the assumption that the deviatoric (shear) and volumetric behaviours are independent in multiaxial stress states and the dissipative losses are primarily caused by viscous effects. The Prony series representation of the dimensionless relaxation modulus in ABAQUS is as follows:

$$g_R(t) = 1 - \sum_{i=1}^N \bar{g}_i^P \left( 1 - e^{-\frac{t}{\tau_i^{\bar{g}}}} \right)$$

where  $\bar{g}_i^P$ ,  $\tau_i^G$ ,  $N$ , etc. are material constants with  $i = 1, 2, \dots, N_0$ . For linear isotropic elasticity, substitution in the small-strain expression for the shear stress yields

$$\tau(t) = G_0 \left( \varepsilon - \sum_{i=1}^N \varepsilon_i \right)$$

where

$$\varepsilon_i = \frac{\bar{g}_i^P}{\tau_i^G} \int_0^t e^{-\frac{s}{\tau_i^G}} \varepsilon(t-s) ds$$

The  $\varepsilon_i$  is interpreted as state variables that control the stress relaxation, and  $\varepsilon_{cr} = \sum_{i=1}^N \varepsilon_i$  is the “creep” strain. The Prony series implementations in ANSYS and MSC.MARC software are having specific details which can be obtained from the respective software manuals.

Before using the computational FE tools, it is imperative to perform a simulation of a benchmark case whereby the computational results from various software packages would be compared with the experimental data to test the efficacy and accuracy of the results from each package. The benchmark case has been reported in Jain [3]. A cylindrical glass sample (BK7) of diameter 6.35 mm and height 6.35 mm is compressed by two flat platens under a constant strain rate at 671 °C. Due to small deformations applied, the above boundary condition can be interpreted as compressive deformation under constant mould velocity of 0.01 mm/sec. The above geometry was created and meshed with 1000 4-noded quadrilateral axisymmetric elements with 50 nodes along x and 20 nodes along y direction, respectively. The viscoelastic material behaviour was modelled using a Zener-Maxwell model where the constitutive equation is given as follows:

$$s(t) = \varepsilon \eta \left[ 1 - \exp\left(-\frac{E_M}{\eta} t\right) \right] + E_H \dot{\varepsilon} t$$

where  $s(t)$  is the stress,  $E_M$  and  $E_H$  are the elastic parameters and is the  $\dot{\varepsilon}$  constant strain rate. The problem was solved using all the above mentioned software packages. The results of computation using MSC.MARC and POLYFLOW are given in Fig. 4.14 which shows the von Mises stress distribution in the BK7 glass cylinder at 671 °C. The glass in contact with the moulds experiences friction and due to unconstrained deformation towards the periphery of the cylinder, barrelling of the glass cylinder is observed. The highest stress states are observed at the glass edges in contact with the mould and towards the centre of the cylinder due to constraints on the material flow in these region leading to stress build up. Figure 4.15 depicts the computed stress build up at the edge of the glass near the mould using MSC.MARC, POLYFLOW and ABAQUS. While computing in ABAQUS, elements C3D8 and C3D20H were used in ABAQUS internal solver and in UMAT for nonlinear Hex elements, respectively. The computed results were compared with the experimental data reported by Jain [3]. It is seen from Fig. 4.15a that POLYFLOW provides the best match for the early part of the stress build up (up to 10 s), while MSC.MARC gives



good match for larger time ( $> 10$  s). Figure 4.15b shows that ABAQUS internal solver is able to predict the stress build up fairly accurately at larger time ( $> 10$  s), while the ABAQUS UMAT implementation of nonlinear Hex elements provides a more accurate match at smaller time ( $< 10$  s). Overall, the simulations run using ABAQUS internal solver could capture the dynamics of stress build up with an excellent match with the experimental data.

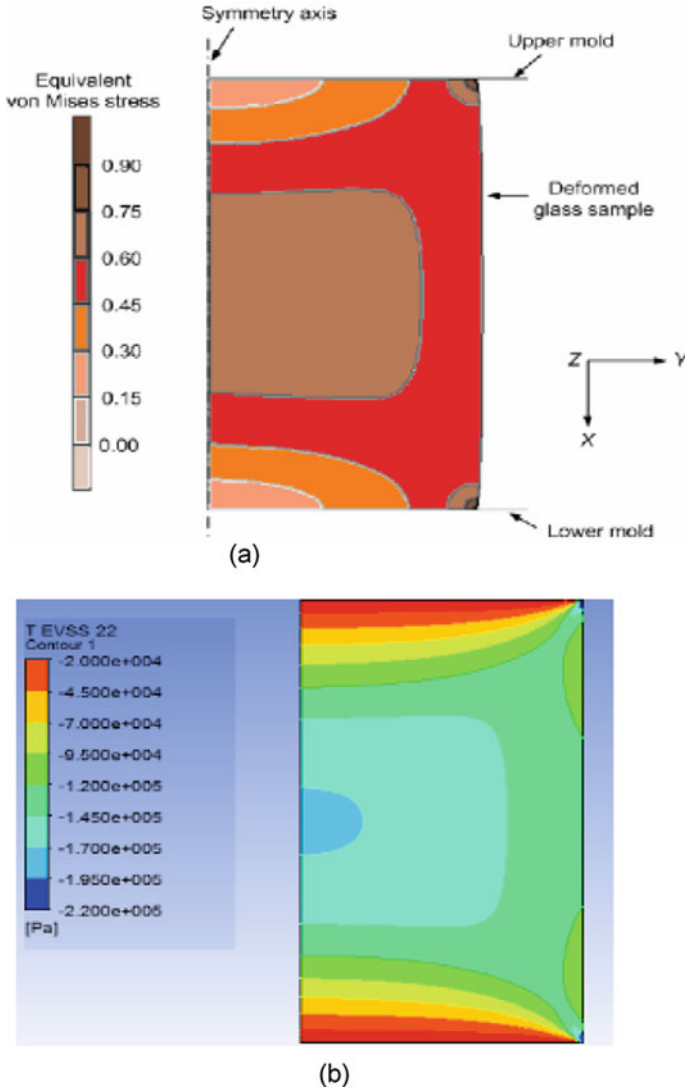


**Fig. 4.14** Von Mises stress distribution for the BK7 glass cylinder obtained by finite element computation at CSIR-CGCRI using **a** MSC.MARC and **b** POLYFLOW

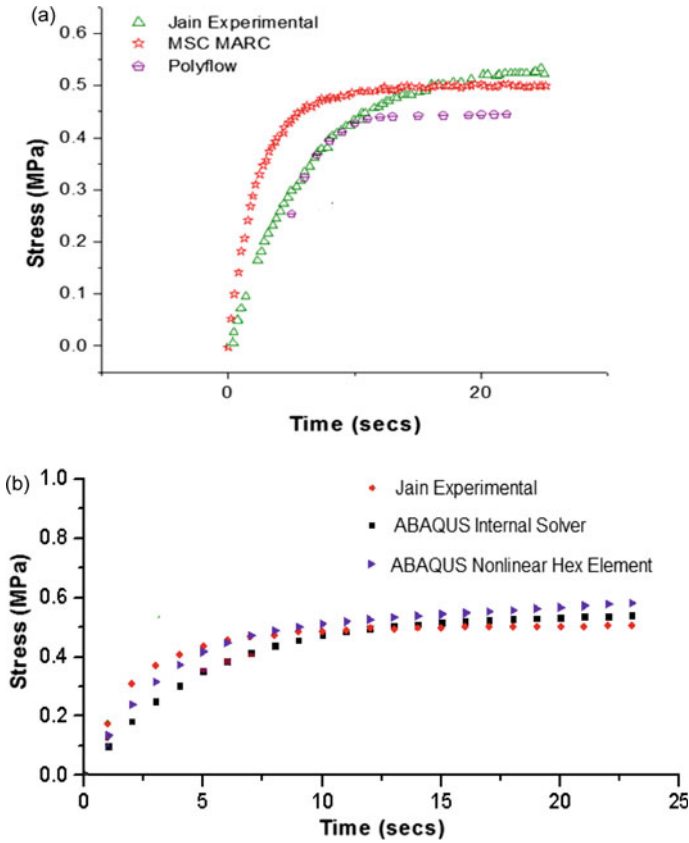


**Fig. 4.15** Comparison of simulation runs carried out at CSIR-CGCRl versus experiment for the glass cylinder compression benchmark case [3] **a** Simulation by FE software MSC.MARC and POLYFLOW **b** Simulation by ABAQUS

### 4.5 Conclusion

Viscous and viscoelastic behaviour of silicate glasses have a great bearing on analysis of the high temperature deformation behaviour during the forming process chain for making precision glass optics and other components of emerging technological importance. The models for estimation of viscosity of glasses with Arrhenius and non-Arrhenius type variations are applicable in specific thermal regimes, while a new class of models with double exponentials offers estimation of viscosity for a wide spectrum of temperatures. Relaxation phenomena in silicate glass—both structural and stress relaxation—are intimately linked with the viscoelastic behaviour at temperatures above the glass transition. Structural relaxation models are based on Arrhenius type variations of a structural order parameter known as the fictive temperature. For non-Arrhenius type variations, phenomenological models of structural relaxation

are based on thermodynamic parameters, such as free volume and entropy. Stress relaxation in silicate glass can be ascertained experimentally either by quasi-static creep-relaxation studies or by applying dynamic oscillatory loading at high temperature. Estimation of the viscoelastic behaviour of glasses is complex where various combinations of spring and dashpot elements yield different models with different capabilities to capture the instantaneous elastic strain, delayed elastic strain and irrecoverable viscous strain under an applied deviatoric stress. The experimental determination of the glass transition temperature, viscosity, fictive temperature and relaxation times carried out at CSIR-CGCRI have been briefly outlined. Material modelling of viscoelastic deformation behaviour in silicate glass (e.g. LB2000) based on creep-relaxation data obtained at CSIR-CGCRI has been reported. The implementation of material model in a finite element framework and the resulting efficacy and accuracy of computed transient stress build up for a benchmark glass pressing problem reported in literature has been presented for three FE software, MSC.MARC, POLYFLOW and ABAQUS. The ABAQUS computations provide a reasonably good match with the experimental data for a large span of time and is recommended for simulating viscoelastic deformation behaviour in silicate glasses.

**Acknowledgements** The authors would like to acknowledge the financial support from the Department of Science & Technology (DST), India, under the Advanced Manufacturing Technology (AMT) programme and Council of Scientific & Industrial Research.

## References

1. Franse J (1990) *Rep Prog Phy* 53:1049–1094
2. Garg S, Sanyal D, Mahajan P (2011) In: Proceedings of 3rd glass forming simulation workshop, Glass Service Ltd., Vsetin, Czech Republic, pp 194–203
3. Jain A (2006) Experimental study and numerical analysis of compression molding process for manufacturing precision aspherical glass lenses. Ph. D thesis, the Ohio State University
4. Le Bourhis E (2014) *Glass: mechanics and technology*, 2nd edn. Wiley-VCH, Weinheim, Germany
5. Frenkel YI (1946) *Kinetic theory of liquids*. Oxford University Press, Oxford, UK
6. Callister WD Jr (2001) *Fundamentals of material science and engineering*. Wiley, New York, USA
7. Kurkjian CR, Prindle WR (1998) *J Am Ceram Soc* 81:795
8. Adam G, Gibbs JH (1965) *J Chem Phys* 43:139–146
9. Avramov I (2000) *J Non-Crystalline Solids* 262:258–263
10. Ojovan MI (2008) *Adv Cond Matter Phys* 1–23. <https://doi.org/10.1155/2008/817829>
11. Douglas RW (1949) *J Soc Glas Technol* 33:138–162
12. Zarzycki J (1991) *Glasses and the Vitreous State*, Cambridge University Press, Cambridge, UK (1991)
13. Scherer GW (1986) *Relaxation in glass and composites*. Wiley, New York
14. Doss K, Wilkinson CJ, Yang Y, Lee K-H, Huang L, Mauro JC (2020) *J Am Ceram Soc* 103:3590–3599
15. Ritland HN (1954) *J Am Ceram Soc* 37:370–377
16. Goldstein M, Nakonecznyj M (1965) *Phys Chem Glas* 6:126–133
17. Mauro JC, Uzun SS, Bras W, Sen S (2009) *Phy Rev Lett* 102:155506–1:4

18. Tool AQ (1946) *J Am Ceram Soc* 29:240–253
19. Naraynaswamy OS (1971) *J Am Ceram Soc* 54:491–498
20. Moynihan CT, Eastal AJ, DeBolt MA, Tucker J (1976) *J Am Ceram Soc* 59:12–16
21. Smelzer JWP, Gutzow IS, Glasses and the glass transition, pp 91–164
22. Gutzow I, Grigorova T, Avramov I, Schmelzer JWP (2001) *Phys Chem Glasses* 43C:477
23. Mijovic J, Nicolais L, Damore A, Kenny JM (1994) *Polymer Eng Sci* 34:381–389
24. Turnbull D, Cohen MH (1961) *J Chem Phys* 34:120
25. Dyre JC, Olsen NB, Christensen T (1996) *Phys Rev B* 53:2171
26. Welch RC, Smith JR, Potuzak M, Guo X, Bowden BF, Kiczanski TJ et al (2013) *Phys Rev Lett* 110:265901
27. Gulbiten O, Mauro JC, Guo X, Boratav ON (2018) *J Am Ceram Soc* 101:5–11
28. Gujrati PD (2010) *Phys Rev E* 81:051130–1:13
29. Lakes R (2009) *Viscoelastic materials*. Cambridge University Press, New York
30. Badrinarayanan P, Zheng W, Li Q, Simon SL (2007) *J Non Cryst Solids* 353:2603–2612
31. Mauro JC, Allan DC, Potuzak M (2009) *Phys Rev B* 80:94204
32. Shen J, Green DJ, Tressler RE, Shelleman DL, Non-Cryst J (2003) *Solids* 324:277–278
33. Shang H, Rouxel T, Buckley M, Bernard C (2006) *J Mater Res* 21:632–638
34. De Bast J, Gilard P (1963) *Phys Chem Glasses* 4:117–128
35. Duffrene L, Gy R, Burlet H, Piques R, Non-Cryst J (1997) *Solids* 215:208–217
36. SIMUGLASS India EU FP7 project report. <https://cordis.europa.eu>
37. Rekshon SM (1986) In: Uhlmaun DR, Kreidl NJ (eds) *Glass science and technology*, vol 3. Academic Press Inc., Orlando, Florida

# Chapter 5

## Coloured Glass



J. M. Parker

### 5.1 Summary

Glass makers have for millennia been able to make a wide variety of coloured glasses but reproducing and controlling the shade has proved more difficult. A useful tool now available to technologists is optical absorption spectroscopy. This has proved useful for understanding sources of variation such as redox phenomena in glass and for measuring the concentrations of minor elements; it underpins many applications of glasses in art and science.

Here, we will examine the relationship of optical spectra to composition, coordination number, oxidation state and redox interactions. The observed absorption peaks display systematic, predictable shifts with composition but significant deviations from average behaviour are also observed and can be important in designing optical applications. Other factors affecting absorption include the creation of nanocrystalline environments for the absorbing ions; producing strong local electric fields associated with plasmon resonances in metallic nanoparticles and using diffraction.

### 5.2 Introduction and History

Iron is a persistent impurity in most naturally occurring minerals used to make glass, particularly in sand. It typically introduces a greenish hue to glass products but can also give a blueish or yellowish cast. Figure 5.1 shows a cheap glass paperweight made 150 years ago; its colour, due to iron, is clearly green. In thin sections, such as the walls of wine glasses, the colour is less obvious but shows up where light has had a longer pathlength, for example in the rim or the circumference of the foot. Even

---

J. M. Parker (✉)

Department of Materials Science and Engineering, The University of Sheffield, Sheffield, UK  
e-mail: [j.m.parker@sheffield.ac.uk](mailto:j.m.parker@sheffield.ac.uk)



**Fig. 5.1** Victorian dump (paperweight) made from glass left over in the crucible at the end of the working day (left). The green tint arises from iron present as an impurity. The paperweight on the right is a modern copy coloured using chromium

the Romans were aware that this ‘discoloration’ arose from impurities and that purer (whiter) raw materials reduced discoloration. They also learned that adding certain minerals improved the colour of the glass; such additions have been termed glass maker’s soap.

Of course, we now know that the most abundant impurity is often iron and the reason for variability is that iron exists in two oxidation states: ferrous ( $\text{Fe}^{2+}$ ) absorbing principally at the red end of the absorption spectrum and ferric ( $\text{Fe}^{3+}$ ) absorbing mostly blue. For millennia, elimination of colour was the glass makers’ dream—they strived to use the purest materials and develop strategies for decontamination, without fully understanding the problem. Their success in decontamination is illustrated by the following figures for typical iron levels (wt%  $\text{Fe}_2\text{O}_3$ ): Roman glass > 2000 ppm  $\text{Fe}_2\text{O}_3$ , float glass 1000 ppm, good quality container glass 300 ppm, photovoltaic glass panels 80 ppm, low grade optical fibres for lighting 1 ppm and telecoms grade optical fibres 0.1 ppb. The role of glass makers soap and the range of colours that could be generated when things went wrong remained something of a mystery until the start of the twentieth century.

For millennia, other elements have also been deliberately dissolved in glasses to create colour. These effects often go back to the early Egyptian and Phoenician glass makers whose goals were to produce decorative beads and expensive perfume bottles. They learned which coloured rocks to add and perhaps the effect of impurities left over from making metals such as bronze. The creators of stained glass windows in the cathedrals built from 1000AD onwards took this art to new heights. They knew that many different minerals could be added to glass melts to produce a rich palette of colours and understood the tricks necessary to produce a desired artistic effect.

**Table 5.1** Common TM cation colourants

$\text{Ti}^{4+}/\text{Ti}^{3+}$	Clear/purple
$\text{V}^{5+}/\text{V}^{4+}/\text{V}^{3+}$	Colourless/blue/green
$\text{Cr}^{6+}/\text{Cr}^{3+}$	Yellow/green
$\text{Mn}^{3+}/\text{Mn}^{2+}$	Purple/clear
$\text{Fe}^{3+}/\text{Fe}^{2+}$	Yellow/blue
$\text{Co}^{2+}$	Blue or pink
$\text{Ni}^{2+}$	Purple or yellow
$\text{Cu}^{2+}/\text{Cu}^{1+}$	Blue-green/clear

We know now that these colourants were often based on the transition metals (TMs and  $3d$  elements). Table 5.1 lists many of the ions that are used now for colouring glass. Like iron, most have at least two oxidation states, each state giving a different colour.

This article explores why glassmakers have found it difficult to predict and control the colour of their glasses and comments on modern applications of colourants to produce not only exciting artistic effects but also useful optical devices. Many authors have reviewed this subject before and in more depth than can be accomplished here [1–5].

### 5.3 Light Absorption

Transition metal ions colour glasses because they absorb certain photons in the incident light spectrum. Because the electrons only exist in defined energy levels, specific photons, with energies ( $h\nu$ ,  $\nu$  = frequency) corresponding to the differences between these energy levels, are lost from the incident beam. The transmitted photons, therefore, have a specific energy or ‘colour’ spectrum.  $4f$  rare earth ions (REs) such as neodymium and erbium behave similarly.

Our colourant TM and RE ion dopants have empty  $d$  and  $f$  orbital electronic levels, respectively, whose energies compared with the ground state of the atom correspond to visible and IR photons. Strictly though transitions between these levels stimulated by photons are not allowed, according to quantum mechanical selection rules because the photon carries not only energy but also spin; whereas there is no change of spin for transitions between  $d$  orbitals. We see them because thermal and structural disorder allows the rules to be broken but the consequence is that (1) they occur with low probability, i.e. they give weak absorptions and (2) the strength of the absorption can vary with factors such as local atomic environment—it is not solely a property of the atom itself.

Figure A



A cobalt blue glass cased with a beautifully carved white glass, containing many small crystalline particles (size approx. wavelength/2) that are transparent but with a different refractive index to the glass. They scatter visible light efficiently making the glass opaque. The blue glass surface has also been roughened to make it translucent. Photo by S Bruntnell of a cameo vase made by Wedgwood in the Turner Museum of Glass

As well as the empty energy levels associated with the dopant ions, there are electronic energy levels associated with the bonding and antibonding electronic levels. The energy gaps between occupied bonding and empty antibonding levels correspond to UV photons. So UV absorption is linked to the excitation of electrons to antibonding levels.  $\text{SiO}_2$  and tailored phosphate glasses are exceptionally UV transparent because of a lack of non-bridging oxygens with their less tightly bonded electrons and smaller energy gaps. These intense (allowed) absorptions underpin the phenomenon of refractive index. So point defects, for example an  $-\text{Si}-\text{O}-\text{O}-\text{Si}-$  bond, will introduce extra empty levels at lower energies in the near UV or visible; consequently radiation damage in a glass often discolours it brown. It will also change refractive index; the diffraction pattern created using a split beam from a high energy laser can, therefore, create periodic refractive index modulations in the glass, useful for example in multiplexing of communications signals.

### ***5.3.1 Measuring Absorption***

In optical absorption spectroscopy, ions are excited from their ground states. Even the lowest available empty energy states for electrons in TM ions have energies



much greater than the corresponding ground state, i.e.  $\gg kT$ , a measure of the thermal energy in the lattice per atom. The consequence is 100% occupancy of the ground state electronic energy levels at room temperature. The absorption spectrum can be measured using a two-beam spectrophotometer which scans through the wavelength range being studied. The two beams are produced by splitting a beam from a single source; each travels to the detector, one directly there and the other through the sample; finally, the ratio of their intensities is measured. Such a comparison automatically takes account of variations of detector sensitivity and source intensity with wavelength although a correction for losses caused by reflection (at two surfaces) is needed. An alternative mode of operation is to place a thin sample into one beam and a thicker one in the second. This allows reflection losses to be compensated automatically whilst still eliminating the effects of sensor and source variations. Whichever mode is used the data are normally also corrected for sample thickness to allow comparisons of the absorption peak intensities.

A second class of instruments for making these measurements, particularly in the infrared, uses Fourier transformation methods. The sample is illuminated with many light wavelengths simultaneously. So the instrument does not have to scan, reducing operational times.

In emission spectroscopy, ions are first excited into a higher level using a tuneable, high energy laser beam and then the emission spectrum, as they return to their ground state directly or via intermediate levels, is probed. A range of excitation wavelengths can be scanned to examine emissions from individual excited states.

Whatever method is used the glass samples must be homogeneous, bubble free and well-polished, with flat, parallel surfaces to give accurate results. Shape defects refract the incident beam, changing the way it falls on the detector. In two-beam instruments such errors are manifested as a step in the measured spectrum at a specific wavelength. These instruments use more than one detector to extend the range of sensitivity to different wavelengths and the step in the recorded data (e.g. at 860 nm) corresponds to a wavelength where there is a changeover from one detector to another.

Absorption is measured as  $-\log_{10}(I_t/I_o)$ ,  $I_o$  being the incident intensity and  $I_t$  the intensity transmitted through the sample; the absorption is proportional to sample thickness. It is corrected for pathlength to give absorbance, which is in turn proportional to ion concentration. Concentration is in units of mass per unit volume because the beam being absorbed sweeps out a certain volume of glass, not mass per unit mass. So, the glass density matters. Another way to express absorption is as an absorption cross section per atom ( $\text{cm}^2/\text{ion}$ ).

The peaks seen on an absorption spectrum for a glass are typically broad, never the sharp line spectra seen in astronomical textbooks. The two main reasons for this are

- (a) Thermal disorder—the vibrations of surrounding ligands (also seen in crystalline hosts),

- (b) Structural disorder in glassy materials—in crystals, this contribution is effectively zero; it is also much reduced for RE elements because their relatively tightly confined 4f electronic orbitals are much less influenced by their surroundings than for TM ions.

Like the intense UV absorption peaks mentioned earlier, these peaks will contribute to the glass refractive index. The effect though is extremely small because the absorption peaks are so weak; their large breadth also reduces the significance of their contribution. In designing optical devices such as switches, intense and sharp absorption peaks are needed to create large nonlinear effects.

### 5.3.2 *De-Excitation Processes*

What happens after absorption? Do the number of excited atoms increase indefinitely with light exposure? At any one time, what proportion of ions are in an excited state and how does that influence the absorption spectrum?

What happens to an excited ion next is a competition between:

- (a) Transfer of the excess energy to the lattice as phonons/heat (usually fast, can be used to measure the absorption coefficient of a glass by observing the associated temperature rise)
- (b) Transfer of energy to the electrons of a similar, unexcited ion nearby, and then to the lattice (this process has a significant concentration dependence)
- (c) Emission of a photon, usually with a Stokes shift to a longer wavelength than the original absorption wavelength (such luminescence is characterised by a time constant which measures the decay process after the exciting light source is switched off).

In most TM = doped silicate glasses, these decay processes are very fast and exposure to the light intensities found in a spectrometer make little difference to the population of the energy levels. A few TMs and most REs are a little different though either because of the quantum mechanical rules governing the transitions (for TM ions) or because the electrons in the 4f levels of REs scarcely interact with their surroundings. Looking for such exceptional behaviour is often the aim of optical designers. Fluorescence is often the dominant process when dealing with REs, i.e. (c) rather than (a). This is particularly the case if the glassy host has low phonon energy vibrations (fluoride, tellurite and chalcogenide glasses) because many different vibrational modes must be excited simultaneously to transfer sufficient energy to the lattice for process (a). Glasses displaying strong fluorescence at certain critical wavelengths (silica transmission windows, or emissions matched to important physical and biological processes) are needed to create fibre laser amplifiers.

### 5.3.3 Interpreting Absorption Spectra—Peak Positions

As explained the wavelengths corresponding to the peak positions on a TM absorption spectrum correspond to the energy levels of the orbitals of its  $3d$  electrons. Schrödinger's wave equation describes the orbitals available for a single electron in a hydrogen atom; it identifies five different  $3d$  orbitals all with the same energy and none of which are occupied in the ground state for hydrogen. In  $3d$  TM atoms, the available orbitals are filled progressively by electrons; the more stable (lower energy) orbitals corresponding to  $n = 1$  ( $s$  only),  $n = 2$  ( $s$  and  $p$ ),  $n = 3$  ( $s$  and  $p$ ) and  $n = 4$  ( $s$ ) are filled first. In many electron atoms, the energy levels that were degenerate in hydrogen split into multiple levels because of electrostatic and magnetic interactions. Bates [2], based on the work of Tanabe and Sugano [6], has described ligand field theory starting from the  $3d$  energy levels in free ions ( $d^n$ ) to the further splitting that occurs when these ions are placed in tetrahedral and octahedral electrostatic fields of varying strengths (denoted in the literature by the quantity  $10Dq$ ). These levels are separated by energies that are typically in the near UV, visible and near IR. The corresponding absorption spectra contain multiple, overlapping peaks which makes analysis difficult. Peak positions/heights/widths are all host and coordination number dependent.

Nevertheless, good fits to observe spectra can be obtained by assuming that each optical transition gives rise to a Gaussian peak profile in the absorption spectrum. Allowing the positions, heights and widths of the peaks to vary until the best fit is obtained will usually give a good reproduction of the measured spectrum.

$Fe^{3+}$  ions have five  $3d$  electrons, while  $Fe^{2+}$  ions have six. In crystalline minerals containing either of these ions, the surrounding oxygen ligands often form tetrahedral or octahedral sites. The  $3d$  energy levels of these ions are further split according to the influence of the electrostatic field generated by the ligands on the central ion. Such models have often been used to interpret the spectra of iron containing glasses. More recent evidence from neutron diffraction, EXAFS and molecular dynamic studies suggest that in glassy structures the octahedral and tetrahedral  $Fe^{2+}$  and  $Fe^{3+}$  sites may in reality be distorted and often tend to [5] coordination: this will affect the observed peak splitting but the energy level diagrams developed by Tanabe and Sugano do not have equivalent forms for this coordination. Crystal field stabilisation energies for these ions in different coordination sites are likely to be small compared with the thermal energy available per atom at  $T_g$  ( $3kT_g$ ); the origin of such preferred coordination states may, therefore, involve longer range interactions and larger groups.

### 5.3.4 *Interpreting Absorption Spectra—The Effect of Host Composition*

Often the glass technologist is interested in the influence of the host glass on dopant energy levels; perhaps because a particular colour is required by an artist or certain optical properties are needed for an optical device. Differences arise from:

- (a) Glass structure (e.g. the  $\text{Fe}^{2+}$  absorption peak near 800 nm shifts significantly further into the IR in a fluoride glass host compared with a common silicate glass),
- (b) The coordination can shift dramatically from octahedral/to fivefold/to tetrahedral; for Co, the corresponding colour changes dramatically is from blue to pink,
- (c) The colours generated may also depend on the  $T_g$  for the glass because higher temperatures favour lower coordination numbers; the absorption spectrum is fixed by the structural state quenched into the glass on cooling,
- (d) The redox states, e.g. the balance between  $\text{Ti}^{4+}$  and  $\text{Ti}^{3+}$ ,  $\text{Mn}^{3+}$  and  $\text{Mn}^{2+}$  or  $\text{Cu}^{2+}$  and  $\text{Cu}^{1+}$  may change with host composition as well as melting conditions (see later).

Duffy [7] developed the concept of ‘Optical’ basicity to express systematically the effect of composition on glass chemistry and specifically absorption peak positions. This quantity is a ‘composite’ parameter. It takes into account an independent measure of the contribution of each glass component based on their effect on the position of the  $\text{Pb}^{2+} 6s \rightarrow 6p$  transition in the near UV.

An *acidic environment* is present in glasses rich in small, highly charged cations, e.g. Si. Acidic glasses in general cause transition metal ions to favour lower oxidation states, e.g.  $\text{Fe}^{2+}$  and higher coordination numbers (e.g.  $\text{Ni}^{2+}$  in octahedral sites). The ligand field splitting energy usually denoted as  $10Dq$  is also lower (but note that individual absorption peaks can shift to lower or higher energies). The reason for these trends is that small highly charged cations strongly attract the available electrons on the oxygen ligands, taking them away from the larger and less highly charged TM dopant ions.

*Basic environments* are rich in large, low charge cations, e.g. Cs. Higher oxidation states are favoured for dopant ions favoured, e.g.  $\text{Fe}^{3+}$ , while lower coordination numbers are preferred (e.g.  $\text{Ni}^{2+}$  goes to tetrahedral sites). The effective values of  $10Dq$  are larger.

Such models can help to explain (semi) quantitatively the differences between Cs and Li silicate glasses, the trends in behaviour for borosilicate, phosphate, and borate glasses and even the effect of different anions such as fluorides.

Extended studies of a wide range of glasses show that optical basicity is a useful ‘composition’ parameter to discriminate between the optical absorption behaviour of different glasses. Often the behaviour observed is an ‘average’ of that for all the many components taken independently. It seems that in such cases the random network model is appropriate. Sometimes, however, significant deviations in behaviour occur,

for example Mg does not always fit exactly with the results for the whole series of divalent cations from Mg to Ba, i.e. behaviour is selective. Such deviations are useful when trying to make glasses with ‘exceptional’ properties for particular applications.

Historically an important application for absorption spectroscopy was to measure the concentrations of ionic species in a glass based on the heights of the absorption peaks. Because the absorption spectrum is host dependent this has most value where the glass compositions being melted do not vary significantly. Bamford [3] has written a textbook on the method and gives calibration data for common colourant ions.

### 5.3.5 *Consequences of Different Iron Oxidation States for Applications*

As the introduction explained both  $\text{Fe}^{2+}$  and  $\text{Fe}^{3+}$  ions absorb light, influencing the transparency of an artefact and its colour, the precise shade observed being influenced by the  $\text{Fe}^{2+}:\text{Fe}^{3+}$  ratio. Various applications either require transparency or opacity in different parts of the spectrum. The list below has been split into applications linked to UV transmission and ones linked to the near IR part of the spectrum:

1. UV/blue transparency (low  $\text{Fe}^{3+}$ ) important for:
  - Food protection, off-flavours in beer (UV opacity needed; UV can affect flavour)
  - Sunburn, Vitamin D generation (opacity for protection or transparency for health)
  - High resolution photolithography, requiring shortest wavelength UV radiation
  - Sterilisation (transparency needed)
2. IR transparency (low  $\text{Fe}^{2+}$ ) particularly important for:
  - Solar cells (avoid  $\text{Fe}^{2+}$  to improve efficiency)
  - Radiation conductivity and heat transport in furnace (fix  $\text{Fe}^{2+}$ )

## 5.4 Perceived Colour—Colour Coordinates

Colour, like beauty, is in the eye of the beholder! Colour coordinates offer a systematic way of ascribing numbers to colours. The factors that we need to consider are

- (a) The light source intensity as a function of wavelength. Incandescent, LED and fluorescent lamps give different spectra.
- (b) The sample absorption as a function of wavelength. The sample modifies the light spectrum from the lamp.
- (c) Finally, the standard response of the human eye as a  $f(\lambda)$ .

The response of the eye has been carefully measured by CIE, and the results have been widely published [3]. Multiplying these three factors together for ‘each’ wavelength in the visible range means that we can determine the response of each of the three main sensors in the eye (cones). CIE has also produced a colour plot to relate these colour coordinates to different the various colours experienced. On this plot, the results for each of the three colour responses are combined to give a 2D map of different colours, with the Z-axis expressing intensity/brightness.

Figure B



This vase (in the Turner Museum of Glass) is coloured using the rare earth, neodymium. Its absorption spectrum has sharper absorption lines than for transition metals, giving rise to dichroism—the colour observed varies according to the light source and the glass thickness. Here we see blues and pinks

#### 5.4.1 *Optimising Iron Colour*

Such colour calculations illustrate the colour variation caused by the redox state of a commercial glass containing low levels of iron. In Fig. 5.2, CIELAB coordinates have been calculated for a fixed concentration of iron (0.1 wt %) but different redox ratios ( $\text{Fe}^{2+}/\text{Fe}^{3+}$ ) caused by varying conditions such as melting temperature or batch chemistry [8]. These coordinates have then been plotted graphically. This shows that highly oxidised glasses are yellow in hue, highly reduced glasses blue and



**Fig. 5.2** CIELAB colour coordinates for different iron redox states. The coordinates are for glasses of total fixed iron (0.1 wt%) but varying Fe<sup>2+</sup>:Fe<sup>3+</sup> ratios; Fe<sup>3+</sup> concentrations are increasing in 0.01 wt % steps from left to right. The y-axis measures the blue (–): yellow (+), while the x-axis measures the green (–) to red (+) ratio. The z-axis out of the page represents intensity. Very oxidised glasses are yellow, very reduced glasses are blue; most commercial glasses green

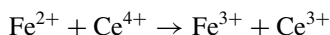
intermediate ratios are green. The redox ratio which gives a glass closest to being colourless is where the curve is closest to the origin (almost 100% Fe<sup>3+</sup>).

### 5.5 Kinetics and Cooling

Experimentally, it takes around 100 h at 1450 °C for a glass melt in a crucible  $2 \times 10^{-2}$  m deep to reach equilibrium with the oxygen concentration in air that is to achieve a state where the redox ion ratio remains constant. This suggests that oxygen can diffuse at most  $2 \times 10^{-2}$  m under these conditions. Now, oxygen diffusion is needed to change redox. If the same glass melt is quenched in 1 min, the diffusion distance for oxygen is reduced by a factor  $\sqrt{(t_1/t_2)} = (100 \times 60/1)^{1/2} = 70$ , i.e. from 20 to 0.3 mm. This distance although small is still an overestimate because it ignores the effect of temperature on D; the redox ratio for a single ion will, therefore, alter little during cooling, even if the casting atmosphere differs from that over the melt and even though the room temperature equilibrium differs from that at melting temperatures. If the glass is poorly refined and has numerous small oxygen rich bubbles, then they may influence the conclusion because diffusion distances will be much less.

### 5.5.1 Redox Reactions with Two or More Redox Ions

As mentioned in the introduction, historically, one way to reduce the green tint caused by iron impurities was to add manganese to the melt. It became known as glassmakers' soap because appeared to wash away the colour. It did this by a redox reaction:  $\text{Mn}^{3+}$  presents in the high temperature melt oxidises any  $\text{Fe}^{2+}$  to the  $\text{Fe}^{3+}$  state on cooling; ferric ions have a smaller effect on glass colour. This is apparent from the colour coordinate plots in Fig. 5.2. More recently technologists have experimented with the addition of cerium ions which have a similar effect



How do we know which redox ion pairs will act as oxidising agents? A simple but qualitative way to express the reaction direction is given in Table 5.2 produced by Barton [9]. The oxidised state of an element higher up the list (such as Mn) will tend to oxidise one below; for a mixture of Ce and Fe, Ce will tend to be reduced and Fe oxidised.

Fundamentally, this list is based on equilibrium thermodynamics. The order can be determined knowing the Gibb's free energies for different states. Voltametry is a measurement technique which allows us to determine the relative positions of different ions [10]. Such data are useful to rank different oxidising agents but should always be confirmed by experiment.

Here, we report the results of an undergraduate experiment on the cerium/iron pair. The  $\text{Fe}^{2+}$  concentrations have been measured using UV/vis absorption spectroscopy based on the  $\text{Fe}^{2+}$  peak height at a defined  $\lambda$  and the reported extinction coefficients for  $\text{Fe}^{2+}$  at this wavelength for glass samples of a similar composition. The resulting graph has a gradient of  $-0.05/0.4 = -0.12$  (Fig. 5.3). If the above equation is correct, we might expect a gradient of one. The explanation of the apparent discrepancy is that not all added Ce is present in the melt as  $\text{Ce}^{4+}$ .

**Table 5.2** Oxidised species near the top of the table will tend to oxidise the reduced states of species lower down, while themselves being reduced, e.g.  $\text{Mn}^{3+} + \text{Fe}^{2+} \rightarrow \text{Mn}^{2+} + \text{Fe}^{3+}$

Chromium, $\text{Cr}^{6+}/\text{Cr}^{3+}$
Manganese, $\text{Mn}^{3+}/\text{Mn}^{2+}$
Cerium, $\text{Ce}^{4+}/\text{Ce}^{3+}$
Vanadium, $\text{V}^{5+}$ , $\text{V}^{4+}$ , $\text{V}^{3+}$
Copper, $\text{Cu}^{2+}$ , $\text{Cu}^{1+}$
Arsenic, $\text{As}^{5+}$ , $\text{As}^{3+}$
Antimony, $\text{Sb}^{5+}$ , $\text{Sb}^{3+}$
Iron, $\text{Fe}^{3+}$ , $\text{Fe}^{2+}$
Tin, $\text{Sn}^{4+}$ , $\text{Sn}^{2+}$



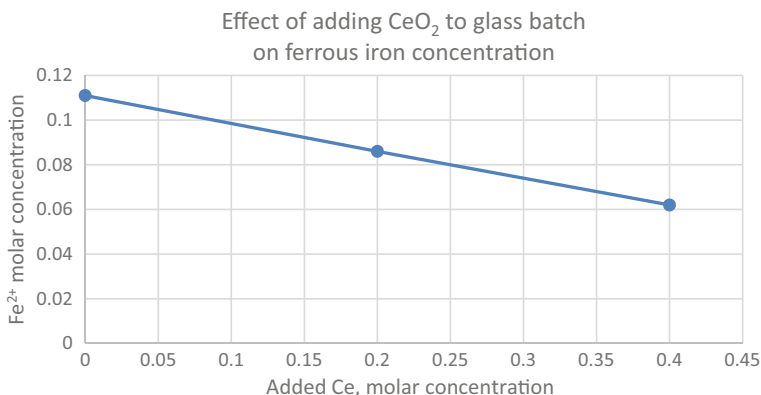


**Fig. 5.3** Molar concentrations of Fe<sup>2+</sup> in three glasses with increasing amounts of CeO<sub>2</sub> added to the batch

Consider a glass melted with 1wt % iron and zero Ce for long enough to be unaffected by the artificial atmosphere created initially by batch decomposition. At equilibrium with the laboratory ‘atmosphere’, the proportion of iron ions present will be approximately 20% Fe<sup>2+</sup> and 80% Fe<sup>3+</sup>. Consider a second glass melted with 1% Ce and zero Fe, this will contain 88% Ce<sup>3+</sup> and 12% Ce<sup>4+</sup> at equilibrium with the same atmosphere based on the observed results. Now, these two glasses must also be at equilibrium with each other. If they are mixed together at high temperature, the redox ratios will not change.

When does the redox reaction take place then? Clearly not at the melting temperature. We must conclude that the observed redox reaction occurs during cooling but how far do they go? Down to what temperature? A simple model is to assume that reactions go to completion (stoichiometric calculation). The data in Table 5.3 is taken from Schreiber et al. [11] for three melts at equilibrium in air at 1400 °C but then cooled to room temperature for measurement. One contains Fe alone, a second Cr alone, and the third has both at the same concentrations. The analysis of the mixed glass confirms that in this case, the reaction proceeds to completion.

Schreiber et al. [11] also analysed samples from melts initially equilibrated at 1100 °C, and the results are presented in Table 5.4. The reactions appear to go to completion again on cooling; the results for glasses melted with a single dopant also demonstrate graphically how lower temperatures favour oxidised states for both Fe and Cr.

The final concentrations for Fe/Cr also suggest that in the Fe/Ce system the reaction probably proceeds to completion. We can, however, re-write the equation to acknowledge that it is an equilibrium reaction with a temperature dependence

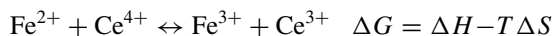


**Table 5.3** Measured redox ion concentrations for Fe and Cr ions in glasses melted at 1400 °C, both singly and together. Calculated values deduced from the melts made singly show that redox reactions proceed to completion in doubly doped glass

Fe alone	0.13 Fe <sup>2+</sup>	0.85 Fe <sup>3+</sup>
Cr alone	0.049 Cr <sup>3+</sup>	0.006 Cr <sup>6+</sup>
Melt containing both: (3Fe <sup>2+</sup> + Cr <sup>6+</sup> → 3Fe <sup>3+</sup> + Cr <sup>3+</sup> )		
Fe (calculated)	0.13–3 × 0.006	0.85 + 3 × 0.006
Fe (calculated)	0.112	0.868
Fe (observed)	0.112 Fe <sup>2+</sup>	0.868 Fe <sup>3+</sup>
Cr (calculated)	0.049 + 0.006 =	0.000
Cr (observed)	0.055 Cr <sup>3+</sup>	0.000 Cr <sup>6+</sup>

**Table 5.4** Measured redox ion concentrations for Fe and Cr ions in glasses melted at 1100 °C, both singly and together

Fe alone	0.025Fe <sup>2+</sup>	0.955Fe <sup>3+</sup>
Cr alone	0.039Cr <sup>3+</sup>	0.016Cr <sup>6+</sup>
With both		
Fe at RT	0.000 Fe <sup>2+</sup>	0.980 Fe <sup>3+</sup>
Cr at RT	0.047 Cr <sup>3+</sup>	0.008 Cr <sup>6+</sup>
Actual Fe	Fe <sup>2+</sup> Absent	
Actual Cr	0.008 Cr <sup>6+</sup>	

Calculated values deduced from the melts made singly show that redox reactions also proceed to completion in a doubly doped glass. In the singly doped glasses, the redox equilibrium shifts towards a more oxidised state

We can write:  $RT \ln K = -\Delta G$  where  $K$ , the equilibrium constant =  $a(\text{Fe}^{3+}) \times a(\text{Ce}^{4+}) / (a(\text{Fe}^{2+}) \times (\text{Ce}^{4+}))$ , where  $a(\text{Fe}^{3+})$ , etc., is the activity of the Fe<sup>3+</sup> ion, often assumed to be proportional to concentration, etc.

This format makes no assumption about the direction of this reaction, which will be defined by the sign of the Gibbs free energy,  $\Delta G$ . Both Fe and Ce would tend towards a more oxidised state on cooling if they could, but which wins out depends on  $\Delta G$ . The answer in this case is evidently iron.

The Fe<sup>2+</sup> versus Ce line drawn is apparently straight. Note though that it is only based on three measurements and no error bars are given. More results are needed for a proper analysis. A larger driving force for a redox reaction means that the reaction goes effectively to completion and the above plot would be linear whereas a small driving force means it would not go to completion and a curved relationship would be expected.

### 5.5.2 Kinetics of Redox Reactions

The active ions (Fe and Ce in the above case) are close together—long diffusion distances are not needed for mutual redox reactions. Even at 0.1% concentrations their separation may be only 2 nm. Assuming oxygen diffusion is the rate controlling step, the time needed for the redox reaction based on the earlier results for diffusion in glass melts is just  $100 \text{ h} \times (10^{-7})^2$  or  $4 \times 10^{-9} \text{ s}$  at the melting temperature (using  $Dt \sim d^2$ ). Mutual redox reactions clearly happen extremely quickly at high temperatures. A key question though is what is the lowest temperature at which these reactions proceed? If  $D$  changes in proportion to the melt viscosity, then times will increase by  $10^{11}$  from  $1400 \text{ }^\circ\text{C}$  to  $T_g$ . This corresponds to  $4 \times 10^2 \text{ s}$  (7 min) at  $T_g$ , i.e. kinetic effects become important at around the glass transformation temperature during quenching. You the reader can now probably appreciate why the colour variations seen by early glass makers were perceived as such a mystery.

### 5.5.3 Redox Reactions as a Function of Temperature

Figure 5.4 shows the effect of equilibrating glasses containing two redox species (Fe and Cu) at different temperatures near  $T_g$ , followed by a rapid quench, i.e. we are observing the effect of fictive temperature. Significant differences are seen. This has implications for the effect of different heat treatment schedules on glass colour, the simplest being variations between bottles that have travelled down the centre of an annealinglehr compared with those that have travelled down the outside edge. A more extreme effect is likely to be seen in a process such as thermal toughening.

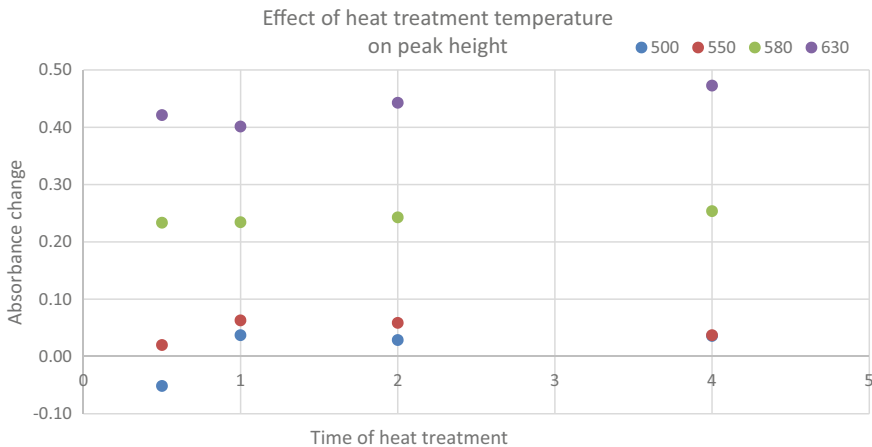


**Fig. 5.4** Shows the effect on absorbance peak height of annealing a glass containing two redox species (Fe, Cu) at different temperatures near  $T_g$ , followed by a rapid quench to room temperature

Conversely solarisation is the result of energetic UV photons reversing a redox reaction that has occurred during glass making. Removing solarisation defects requires sample annealing near  $T_g$ .

## 5.6 Rare Earth Elements and Optical Properties

Rare earths were not available to early glass makers and even now are costly. Their use as colourants has, therefore, been limited. Because the 4f electrons are buried deep within the atom the energy levels are only slightly affected by their environment. Consequently, the absorption peaks are much sharper than for transition metals. This lack of interaction also means that the excited states have longer lifetimes and sometimes much longer. The decay mechanism from their excited state is much more likely to involve photon emission rather than phonon excitation (heat). This gives the ions a role in any application involving fluorescence such as laser manufacture; recently they have been discovered by the community of artists.

One goal for the technologist has been to develop low phonon energy glasses such as fluorides and tellurite. Energy transfer from an excited atom to its host requires the excitation of phonons in the glass matrix. If these phonons are of very low energies (i.e. involved heavy and weakly bonded atoms) this reduces the probability of the event (see earlier). A related aim is to minimise concentration effects. At higher dopant concentrations photon exchange between neighbouring ions increases in probability which then in turn leads to more rapid transfer of energy to the matrix.

A second goal has been to optimise the emission spectrum of certain key ions so that they can be used as fibre amplifiers for multiplexed signals with a broad wavelength spread. Experimentation has shown that a little Al in place of Si in a silica glass fibre broadens and flattens the Er emission at the critical telecommunication wavelength of 1.55  $\mu\text{m}$ , allowing more wavelengths to be used.

## 5.7 Defects

High energy photons can cause significant damage to the structure of a glass often introducing defect sites that persist for long periods; indeed, the high temperatures needed to make and pull silica preforms can also generate defects. Common defects include  $E'$  ( $\equiv\text{Si}\bullet$ ),  $-\text{Si}-\text{O}-\text{O}-\text{Si}$  bonds, non-bridging oxygen hole centres, NBOHCs ( $\equiv\text{Si}-\text{O}\bullet$ ) or germanium lone pair centres, GLPCs (Ge is a common dopant used to control refractive index and create a core-clad structure). Now, the optical transitions linked to these defects are often centred in the near UV so they can discolour the glass by absorbing blue light. Importantly, their optical transitions are allowed and so, being strong, they can have an easily measurable influence on refractive index. Such effects are used to create a periodic refractive grating along the length of an optical fibre core by, for example using the interference between two high energy

beams from a laser source. Such gratings can be highly reflective for transmitted light of wavelength  $\lambda$ , when their spacing is  $\lambda/2n$ ,  $n$  being the core refractive index. By analogy with X-ray diffraction, such gratings are sometimes called Bragg gratings. They can be very valuable in creating optical measurement devices, e.g. strain will change the wavelength for maximum reflectivity. They are also invaluable as a way of separating optical components in multiplexed systems.

Another optical application of defects can be in information storage. The chalcogenide elements S, Se, and Te (often with Ge, As, Sb...) have bonding electrons which are much less strongly bonded to their atoms than in silicates. Consequently, chalcogenide glasses are more easily modified by light which has given the possibility of an enormous range of optical applications, e.g. xerography.

## 5.8 Colouring Glasses by Nanoparticles

So far only the absorption spectra associated with colourant ions have been considered. Another way to produce coloured glasses is via the precipitation of nanoparticles of metals such as gold or silver, or of semiconductors such as Cd(S, Se). Photons can excite oscillations of the free electrons in metals. This results in a strong absorption of energy at the resonant frequency. For copper and gold, the absorption is strongest in the blue/green part of the spectrum and so the resulting glasses are coloured red. For silver, the absorption occurs principally near the UV edge removing blue and the glasses are coloured the complementary colour yellow. If the absorbing nanoparticles grow too large (compared with the wavelength of light), then they can also scatter light strongly. Since scattering is greater at short wavelengths, the colour seen in reflected light can be very different to that in transmission as seen in the famous Lycurgus cup, created in Roman times.

In the case of semiconductor particles, energy absorption involves excitation of electrons from the valence band to the conduction band and is, therefore, defined by the band-gap. Among the best known examples, the Cd(S, Se) solid solution series has band-gaps corresponding to light from the blue to the red end of the spectrum and glass colours can range from yellow to deep red. Only a very small % of crystalline material is needed to give a strong colour. The optical absorption spectrum also shows interesting features defined by the electronic energy level structure; the band edge shows a strong peak associated with the formation of an electron-hole pair in the semiconductor particle (exciton). The wave function for this pair extends over significant distances and so is influenced by particle size.

These glasses coloured by precipitates require careful control of the nucleation and growth process. Many nuclei are needed with limited growth to give nanoparticles that have the requisite absorption characteristics for the required intensity of colour without unwanted light scattering. Usually, this requires a separate controlled heat treatment close to the glass transition temperature although precipitation on first cooling the product is also possible. In the case of metal precipitates, a redox process is usually involved [1]. Initially, the metal ions are in solution (e.g. as  $\text{Ag}^+$  or  $\text{Au}^+$  ions)

but then are reduced to the metallic state by a redox ion such as  $\text{Sn}^{2+}$  at temperatures near  $T_g$ . The low solubility of metal atoms and relatively high diffusion rates are ideal for high nucleation rates. They grow to spherical particles that are usually less than 10 nm in size.

Formulae are available [12, 13] for calculating the absorption and the scattering of such nanoparticles. Many studies have demonstrated shifts in absorption peaks linked to particle size; some of these effects are linked to quantum confinement (e.g. for Cd(S, Se) dopants). There is a strong dependence on the particle shape, and this effect was used by Corning to develop a range of polychromatic glasses. Initially, dendritic silver halide glasses are precipitated in the glass, and then, light is used to reduce the tips of the dendrites to silver needles. The aspect ratio of the nanoparticles defines the colour seen [14].

Focussed high powered lasers are also able to initiate such behaviour allowing complex, coloured images to be created inside a glass article. A similar approach uses light to initiate the reduction process by for example by electron transfer from a redox ion ( $\text{Ce}^{3+}$ ) to a metal ion ( $\text{Ag}^+$ ). The small silver nanoparticles created can then nucleate growth of silicate particles [15].

## 5.9 Glass Ceramics for Optical Devices

Earlier we considered how composition changes offered a way of systematically modifying optical properties, e.g. the energy levels of TM dopants. A relatively recent way to take this further has been to find glass compositions that easily form glass ceramics where the crystalline phase sequesters most of the active dopant ions. A key criterion as in the last section is that absorption processes dominate over scattering and that requires a nanocrystalline material.

Many of these precipitates are based on fluorides and indeed the hosts too may be fluoride or oxyfluoride rather than oxide glasses. This gives the advantage that the host is a low phonon energy material and so excited state lifetimes are significantly greater.

## 5.10 Periodic Structures

In the section on defects, we mentioned the creating of Bragg gratings by introducing defects along the core of an optical fibre. Another way of creating such periodic structures is by building many layers of alternating refractive index. Coating methods such as sol gel or deposition techniques described elsewhere in this book are now available to build up such structures with thicknesses, for example  $\lambda/4$  and the capacity to modify light beams in complex but very precise ways, e.g. for use as band pass filters.

**Acknowledgements** I wish to thank my many co-workers: including Dr P France, Prof A Seddon, Prof A Jha, Dr P Bingham, Dr T Volotinnen, whose interest in the subject over the years has stimulated and helped to form my own perspectives.

This chapter is based heavily on one published in the ICG volume 'Teaching Glass better' with some updating for clarification [16].

## References

1. Weyl WA (1951) Coloured glasses. Society of Glass Technology, Sheffield
2. Bates T (1962) In: Mackenzie JD (ed) Modern aspects of the vitreous state, vol 2. Butterworths, London
3. Bamford CR (1976) Colour generation and control in glass. Elsevier, Amsterdam
4. Wong J, Angell CA (1976) Glass: structure by spectroscopy. Marcel Dekker, New York
5. Parker JM (2004) Rev Prog Color 34:26
6. Sugano S, Tanabe Y, Kamimura H (1970) Multiplets of transition-metal ions in crystals. Academic Press, New York
7. Duffy JA (1993) Geochim Cosmochim Acta 57(16):3961
8. Simpson & Myers (1978) Glass Tech 19:82
9. Barton J (2000) Verre 6:33
10. Schreiber HD, Wilk NR Jr, Schreiber CW (1999) J Non-Cryst Solids 253:68
11. Schreiber HD, Peters LJ, Beckman JW, Schreiber CW (1996) Glastech Ber 69:1
12. Rawson H (1965) Phys Chem Glasses 6:81
13. France PW, Drexhage MG, Parker JM, Moore MW, Carter SF, Wright JV (1990) Fluoride glass optical fibres. Blackie, Glasgow, p 186
14. Beall GH (1978) Glass Tech 19:109
15. Rawson H (1991) Glasses and their applications. The Institute of Metals, London
16. Parker JM (2018) Teaching glass better, 43. The International Commission on Glass, Spain

# Chapter 6

## Computer Modeling of Glass Structures and Properties



Akira Takada

### 6.1 Introduction

Computer modeling is now ubiquitous in industry. It can be categorized into two areas; one is macroscopic or continuum and another is microscopic or atomistic modeling. Macroscopic or continuum modeling is chiefly used for product design and process optimization. On the other hand, microscopic or atomistic modeling is primarily used for materials design. Both approaches have their own strong points. Hence, it is more and more important to use both of them in a complementary way or to switch from one method to the other one depending on emerged problems on site. Typical macroscopic and its corresponding microscopic approaches are compared in Fig. 6.1 for each glass manufacturing stage. Both of the two are important in glass industry, however, in this paper the microscopic modeling usually called atomistic modeling is focused on to contribute to advanced glass materials design.

In the long history of modeling technique of glass structure, the first realistic modeling was not made by computer, but by hand. The hand-made model was constructed for SiO<sub>2</sub> glass by Bell and Dean [2] who patiently assembled manually rods and balls to compose 188 tetracoordinated units with a total of 614 atoms. The disordered linkage of the SiO<sub>4</sub> groups, which were assumed to be rigid, did satisfy Zachariasen's structural rules which are constituents of famous continuous random network (CRN) model [3].

From the angles and distances, they measured, Bell and Dean also determined the pair distribution functions for Si–Si, Si–O, and O–O, from which they derived a radial distribution function that was in good agreement with the experimentally data over their full range of definition, i.e., out to a distance of about five times the Si–O bond length. Yielding in particular an average O–Si–O bridging angle of 153°, this model

---

A. Takada (✉)

University College London, Gower Street, London W1E6BT, UK

e-mail: [akira.takada@ucl.ac.uk](mailto:akira.takada@ucl.ac.uk)

Ehime University, 10-13 Dogo-Himata, Matsuyama 790-8577, Ehime, Japan



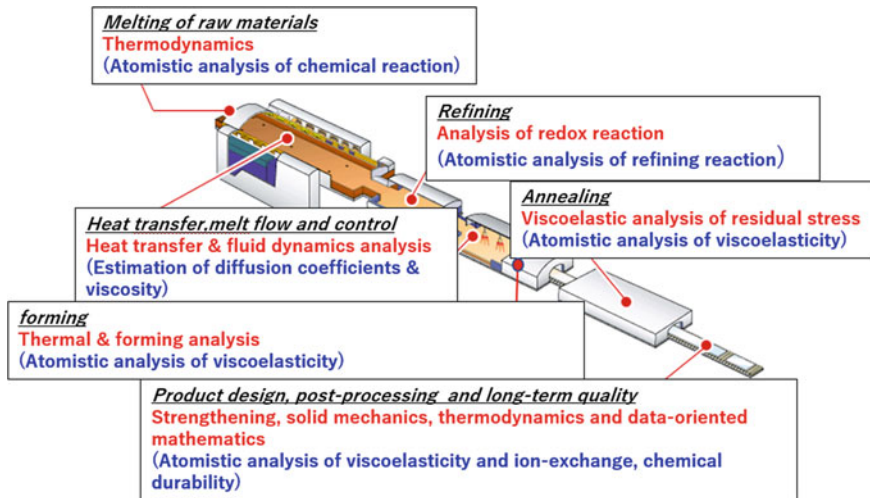


**Fig. 6.1** Macroscopic and microscopic simulations in glass manufacturing stage. Words in parentheses are categorized as microscopic simulation. Modified from Ref. [1]

enabled the three-dimensional atomic configuration of  $\text{SiO}_2$  glass to be visualized, but it suffered from an obviously large arbitrariness in its hand-made combination of building blocks. In addition, the model did not lend itself to estimations of physical properties. An exception was the density, which was calculated for an internal portion of the model system consisting of 72  $\text{SiO}_2$  units, to yield a value of  $1.99 \text{ g/cm}^3$  that proved to be much lower than the actual  $2.20 \text{ g/cm}^3$ .

Atomistic simulations have rendered such toy block models obsolete as they readily provide not only atomic coordinates but also predict physical properties for glass and melts of any composition under a variety of temperature, pressure or energy conditions. Besides, the accuracy and versatility of these calculations has been improving steadily thanks to faster computing processors, more efficient algorithms and bigger systems investigated. Originally, these simulations were mainly developed to give exact solutions to problems in statistical mechanics which would otherwise have been intractable for complex states of matter such as liquids, glasses or aggregates.

The first computer simulations were made with the Monte-Carlo (MC) method (e.g., [4]), which had been devised in the 1930s to solve general mathematical and statistical problems. It took advantage of the first electronic computers to sample the configurations of the system according to Boltzmann statistics, and weight them evenly when calculating the associated properties of interest. Because of this reliance on Boltzmann statistics, however, only equilibrium states can be investigated in MC simulations. At the cost of much computational complexity, the advantage of Molecular Dynamics (MD) simulations (e.g., [5]) is to characterize at every moment the state of the system by the positions and momenta of its constituting atoms and, thus, to account for the dynamics of the system whether in equilibrium or not. For

SiO<sub>2</sub>, the first MD simulation performed by Woodcock et al. [6] for instance dealt with the anomalous properties of the melt and assigned increases in diffusion coefficients to pressure-induced structural changes. Following this pioneering study on a real material, a great many MD simulations have been carried out on glass/melt systems since that time.

Interatomic potentials are critical ingredients in both MC and MD simulations (e.g., [5]). As a preamble, it is thus appropriate to begin with a brief review of the manner in which they are determined within the general framework of computer simulations. The principles of MC and MD simulations will then be presented. Finally, simulations made on amorphous oxide glasses will illustrate the interest and diversity of results that can be obtained with MD simulations and their complementarity with those of experimental studies. Amorphous SiO<sub>2</sub>, silicates will be mentioned but special interest will be paid to the structure of B<sub>2</sub>O<sub>3</sub> glass that actually represents stringent tests of simulations as it requires accurate descriptions of both short- and medium-range order to be understood.

## 6.2 Basics of Numerical Simulations

### 6.2.1 General Features

Atomistic simulations rely on statistical mechanical models. As such they may be performed within three main kinds of statistical ensembles. The canonical *NPT* ensemble (constant number of atoms, pressure, and temperature) is chiefly used in heating or quenching cycles. In contrast, the micro-canonical *NVE* ensemble (constant number of atoms, volume, and energy) is primarily used when properties are calculated within the precise framework of statistical mechanics. As for the grand canonical ensemble  $\mu VT$  ensemble (constant chemical potential, volume, and temperature), it is typically used to investigate chemical equilibrium in systems that can exchange energy and matter with a reservoir.

For an isolated macroscopic system made up of a very large number  $N$  of atoms, each having three degrees of freedom, the microscopic state at a given instant is completely specified by the values of  $3N$  coordinates  $r(i)$ , collectively denoted by  $r^N$ , and  $3N$  momenta  $p(i)$ , denoted similarly by  $p^N$ . The values of the variables  $r^N$  and  $p^N$  define a point in a  $6N$ -dimensional space, called the phase space, symbolized by  $\Gamma_N$ . If  $H(r^N, p^N)$  is the Hamiltonian of the system, the path followed by this point in the phase space is determined by Hamilton's equations:

$$\dot{r} = \partial H / \partial p(i) \quad (6.1)$$

$$\dot{p} = -\partial H / \partial r(i) \quad (6.2)$$

where  $i = 1, \dots, N$ . In principle,  $6N$  coupled equations subjected to  $6N$  initial conditions should be solved to specify the values of all  $r(i)$  and  $p(i)$  at a given time.

The first difficulty encountered is that the timescale of microscopic processes is ultimately controlled by the  $10^{-14}$ – $10^{-15}$  s period of atomic vibrations. In atomistic simulation, a time integration with similar discrete steps thus is required to describe accurately the time evolution of a system. Even with today's most powerful computers, this constraint restricts simulations to low-viscosity conditions at which relaxation times are lower than about  $10^{-6}$  s to be consistent with the calculational time steps.

It follows that the glass transition cannot be investigated as a number of calculations steps of the order  $10^{18}$  would be required to deal with a relaxation time of  $\sim 10^3$  s. Likewise, crystal nucleation and growth or liquid–liquid phase separation take place too slowly to be subjected to atomistic simulations. Besides, simulated melts are quenched at cooling rates at least six orders of magnitude faster than the highest rates of  $\sim 10^6$  K/s achievable practically. The fictive temperatures of the simulated glasses that then be up to 1000 K higher than those of real glasses, which one should keep in mind when making any kind of comparison between both kinds of materials.

Besides, a second difficulty stems from the fact that  $N$  is of the order of the Avogadro number ( $6.02 \times 10^{23}$ ) for any macroscopic system. Experience shows, however, that accurate results can be obtained for systems of only a few hundred or thousand atoms as long as structural units bigger than the system itself are not involved in the processes investigated. To avoid either creating surface or setting up a wall, periodic boundary conditions are usually imposed in numerical simulations. The cubic box is replicated throughout space to form an infinite lattice. As an atom moves in the original box, its periodic image in each of the neighboring boxes moves in exactly the same way. As an atom leaves the central box, one of its images will enter through the opposite face.

To simulate accurately a non-crystalline configuration in the cell, a larger number of atoms are nonetheless preferable. When a small cell of around several hundred atoms is studied, periodic boundary conditions for instance prevent structural units larger than the cell from forming. As already alluded to, any structural unit or spatial fluctuation larger than the wavelength which is greater than half of the cell size cannot be calculated appropriately because the repeatedly arranged fragments would be involved in the results. On the other hand, the maximum number of atoms which can be currently processed is of the order of  $10^5$ – $10^6$ . To check whether the number of atoms or the size of simulation cell is sufficient or not, the best way is to double the number of atoms and to maintain the same density through an adjustment of the cell size and then to make sure that there is little change in the calculated structural data.

## 6.2.2 The Importance of Interatomic Potentials

Strictly speaking, in numerical simulations the Hamiltonian  $H$  should be calculated from the quantum wave-function equation,  $H\psi = E\psi$ , where  $\psi$  and  $E$  are the wave-function and energy of the system, respectively. However, such calculations require so much computing work that they are currently restricted to smaller systems typically made up of a few tens of atoms. In the present paper, simulations made within a classical framework will thus be considered instead. They rely on the fact that the differences between vibrational and electronic energies and frequencies are so large that atomic vibrations may be considered to take place within a fixed electronic configuration. This is the celebrated Born–Oppenheimer approximation whereby the Hamiltonian of a system is expressed as the sum of kinetic and potential energies, which are functions of the selected set of coordinates  $q(i)$  and momenta  $p(i)$ :

$$H(p, q) = K(p) + U_p(q) \quad (6.3)$$

In Eq. (6.3) the kinetic energy,  $K(p)$ , is simply expressed as a function of the mass and of the velocity calculated for each atom. The potential energy,  $U_p(q)$ , is much less readily determined because it strongly depends on the specific interactions between the various kinds of atoms present in the system. Quite generally, however, interaction potentials are markedly asymmetrical in terms of interatomic distances because they rise extremely steeply when atoms get mutually very close whereas they reach a constant value—the dissociation energy—when atoms become so distant that they can be considered as no longer bonded. As introduced in 1929 to represent isolated diatomic molecules, the Morse potential accounts well for this asymmetry:

$$U_p(r_{ij}) = E_0\{[1 - \exp(-k(r_{ij} - r_0))]^2 - 1\}, \quad (6.4)$$

where  $E_0$ ,  $k$ , and  $r_0$  are the dissociation energy, a measure of the bond strength, and the equilibrium interatomic distance of the molecule, respectively, three parameters that are determined from vibrational spectroscopy data.

In a condensed phase, potentials are much more complicated since a given atom interacts with a great many others over distances that can be large. To keep the number of parameters as small as possible in the expression of potential energies, one thus groups into the same term all interactions between given pairs of like or unlike atoms regardless of their mutual distances. Although the Morse potential remains a good starting point for systems where bonding is covalent, other kinds of analytical expressions are generally used for potential energies in the MC and MD simulations dealt with in this chapter. As borne out by the variations with composition of macroscopic properties, atomic interactions have the simplifying feature that they are primarily pairwise in oxide or salt systems. This feature is embodied in the most popular potentials used for these systems, namely, the Buckingham,

$$U_p(r_{ij}) = A \exp(-r_{ij}/\rho) - C/r_{ij}^6, \quad (6.5)$$

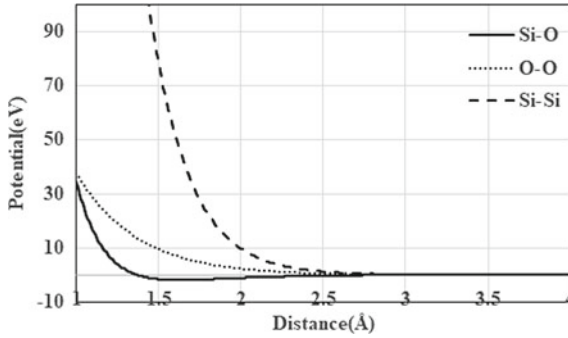


**Fig. 6.2** Examples of potential energy models: Morse and Buckingham potentials used in SiO<sub>2</sub> simulations for Si–O and for O–O and Si–Si, respectively [7]

and the Born-Mayer-Huggins potentials,

$$U_p(r_{ij}) = A \exp[B(\rho - r_{ij})] - C/r_{ij}^6 - D/r_{ij}^8, \quad (6.6)$$

where  $r_{ij}$  is the distance between two atoms, and  $A$ ,  $\rho$ ,  $C$ ,  $D$  are parameters inherent to each interaction (Fig. 6.2).

In both potentials, the first, second, and third terms represent repulsive interaction, dipole–dipole dispersion, and dipole–quadrupole dispersion, respectively. In more precise formulations, ternary and higher-order effects must be accounted for so that the potential energy is made up of terms depending on the coordinates of individual atoms, pairs, triplets, etc.,

$$U_p = \sum_i u_1(r(i)) + \sum_i \sum_{j>i} u_2[r(i), r(j)] \\ + \sum_i \sum_{j>i} \sum_{k>j} u_3[r(i), r(j), r(k)] + \dots \quad (6.7)$$

The first term  $u_1$  is discarded in standard simulations because it accounts for external fields (i.e., wall, electrical field, gravity, etc.). The second term  $u_2$  is the most important since it represents the relevant pair potentials. When determined empirically, it actually includes three-body and many-body effects, which is why models relying on simple pair potential model reproduce reasonably well liquid or glass structures, and why it is better in this case to denote it by the term of ‘effective’ pair potential.

As illustrated by Eq. (6.7), empirical potentials have a great flexibility since specific terms may be added if needed. When electrostatic interactions are important, a Coulomb charge–charge interaction may for instance be included in the form,

$$U_{zz}(r_{ij}) = z_i z_j / (4\pi \epsilon_0 r_{ij}), \quad (6.8)$$

where  $z_i$ ,  $z_j$ , and  $\epsilon_0$  are the charge on atom  $i$  and  $j$  and the permittivity of free space. Because the Coulombic series converges very slowly, the Ewald, particle-mesh or multi-pole techniques are used in periodic systems. Likewise, more complex

models implement three- and four-body terms to reproduce bond-bending and torsional forces, respectively. Alternatively, polarizable or shell models are employed to consider ions as non-rigid entities and, thus, to account for the effects of the deformation of electron clouds with suitable additional parameters.

From a practical standpoint, the parameters of equations such as (6.4)–(6.7) can be estimated in two different ways depending on the nature of the data to which they are fitted [5]. In the most rigorous way, one relies on energy profiles determined in first-principles calculations or quantum mechanical simulations of appropriate reference systems. Alternatively, potential energy parameters are fitted through MD or lattice dynamics calculations to some selected physical properties. Structural and elastic data are generally chosen because they are most directly related to interatomic potentials. Thermal properties may also be used, but they are sensitive to second-order effects such as anharmonicity and are in turn generally predicted less accurately.

### 6.2.3 Scheme of Molecular Dynamics Simulation

The main advantage of MD simulation is to provide important structural information that complements conclusions drawn from experimental studies. One such important result was the demonstration that the structure of alkaline silicate glasses is composed of glass-former-rich and modifier-rich regions at the atomistic level [8]. The computer modeling supported the structure model, so-called the *modified random network* (MRN) model proposed by Greaves for oxide glasses like alkaline silicates. Not only diffraction but also atomistic simulation studies confirm a degree of micro-heterogeneity in glass.

For such reasons, molecular dynamics simulations have become the most popular method to study theoretically glass and liquid structures (e.g., [7, 9]). Their main advantage is to yield from the three-dimensional coordinates calculated for all atoms a variety of structural information that can often be checked against experimental data. In addition, they also provide information that escape experimental determinations and may thus point to the existence of unknown structural features.

Since they deal with the instantaneous state of a system, MD simulations rest on the Lagrangian function  $L(r, \dot{r})$  of coordinates  $r$  and their time derivatives  $\dot{r}$  as defined in terms of kinetic ( $K$ ) and potential ( $U_p$ ) energies

$$L = K - U_p \quad (6.9)$$

and on the Lagrangian equations of motion

$$d(\partial L / \partial \dot{r}) / dt - (\partial L / \partial r) = 0. \quad (6.10)$$

This leads to

$$m(i)\ddot{r} = f(i) \quad (6.11)$$

where  $m(i)$  is the mass of atom  $i$  and

$$f(i) = \nabla_{r(i)} L = \nabla_{r(i)} U_p \quad (6.12)$$

where  $f(i)$  is the force exerted on atom  $i$ .

If the coordinates of all atoms are known at time  $t_0$ , all the exerted forces and the resulting velocities are calculated with Eq. (6.12) and then Eq. (6.11). All the velocities and coordinates after time step of  $\Delta t$  are updated by the time integration of the equations of motion (6.11).

When MD methods are applied to glass or disordered systems, several important points should be noted:

- (1) As the proper choice of the interaction potential model is extremely important, a model with complex interaction potentials may be required if any dynamic structure or property is to be calculated after along with the static structure.
- (2) The particular starting configuration is not important as long as equilibration time steps are numerous enough at high temperature. Almost the same structural information should be obtained from different initial configurations. If not, the calculated results are unreliable.

Advanced techniques may be used to calculate structure and properties more efficiently. To omit unimportant contributions to the dynamics, one can for example keep constant bond lengths such as O–H during the MD calculation. As an alternative to this dynamic constraint method [5], one can use non-equilibrium MD [5], which is especially efficient to calculate transport properties such as viscosity. Unlike with conventional MD, a continual friction force can be imposed on the system and its response be monitored.

#### ***6.2.4 Practical Recipe for Numerical Simulation***

Many software codes are available to start numerical simulation these days. Among them, the frequently used codes are DLPOLY, GULP, LAMMPS, and NAMD for the classical MD simulation, and ABINIT, CASTEP, CPMD, CRYSTAL, GAUSSIAN, SHIESTA, and VASP for quantum mechanical simulation.

In the classical or quantum simulation, three common limitations have to be borne in mind. The first limitation originates from system size. Since a simulation box with periodic boundary is normally used, a small size of system is subject to the constraint so that all the atoms in the box should be arranged in a periodic manner with the outer replica cells. A system size of more than 10,000 atoms (i.e., more than several tens of angstrom) is advisable. In the case of quantum mechanical simulation, a calculation with only a hundred or at most a few hundred is feasible. It is, therefore, important to check whether there exists a questionable local distortion or not when the calculated results are analyzed.

The second arises from the real time span, i.e., how long the phenomenon is simulated. The time step is typically 1–2 fs for the classical MD and 0.1–0.2 fs for the ab initio MD calculation, respectively. When the simulation is concerned with the estimation of diffusion coefficients in liquid states, at least several nanoseconds (ns) of calculation are required. On the other hand, when it is concerned with a relaxation phenomenon, it is advisable to take at least ten times as long a time span as the relaxation time constant in question.

The third is the accuracy of calculations. This problem differs depending on which simulation model is used. When the classical MD or MC method is used, the most crucial issue is which potential model is employed. The potential model is intrinsically empirical. After the form of potential function is chosen, its parameters are fitted so that an objective function is minimized. Two different procedures are mainly taken to fit the parameters. The first is to collect coordinates and bulk modulus of known crystal from experimental data. Then the parameters are fitted so that the weighted sum of deviations between experimental and the corresponding calculated data is minimized. The second is to collect energy data in liquid states by using the ab initio MD simulation. In either case, the MD or MC results using the fitted potential have to be carefully checked in terms of structure and properties. In contrast, quantum mechanical simulation needs no potential model. In other words, scientists need not worry about the construction of a potential model. However, either a small cell size or a short time span may cause an insufficiently relaxed structure. Careful examination of the calculated results is required also in the case of quantum mechanical simulation.

## 6.3 Modeling of Glass Structures

### 6.3.1 Overall Structure and Short-Range Order

In atomistic simulations the positional correlation of atoms is easily investigated within a radius of half of simulation cell size ( $\sim 25 \text{ \AA}$ ). The most widely derived results are the pair distribution function (PDF), the radial distribution function (RDF) or total correlation function,  $T(r)$ , which can be readily compared with those obtained in diffraction studies.

In simulations, the PDF and the RDF are derived as follows. The single and pair (2-body) probability density  $P_N^{(1)}$ ,  $P_N^{(2)}$  are defined as

$$P_N^{(1)}(r) = \langle \sum_i \delta(r - r_i) \rangle \quad (6.13)$$

$$P_N^{(2)}(r, r') = \langle \sum_i \sum_{j(j \neq i)} \delta(r - r_i) \delta(r' - r_j) \rangle \quad (6.14)$$

where  $N$  is again the number of atoms and  $r_i$  is the coordinate of atom  $i$ .



The value of  $P_N^{(1)}(r)$  in homogeneous system turns out to be the number density  $(\rho) N/V$  where  $V$  is the volume.

Moreover,  $P_N^{(2)}(r, r')$  is expressed in terms of the PDF,  $g(r, r')$ , and density  $(\rho)$  as:

$$P_N^{(2)}(r, r') = \rho^2 g(r, r'). \quad (6.15)$$

As to the RDF,  $J(r)$ , it is defined as the number of atoms between  $r$  and  $r + dr$  from the center of an arbitrary origin atom:

$$J(r) = 4\pi r^2 g(r, r'). \quad (6.16)$$

An alternative function called total distribution function,  $T(r)$ , is calculated as:

$$T(r) = 4\pi \rho r g(r, r'). \quad (6.17)$$

The information directly obtained from diffraction experiments is the intensity  $I(q)$ , which is related with  $J(r)$  by

$$J(r) = 1 + \{1/(2\pi 2\rho)\} \int q I(q) \sin(qr) dQ. \quad (6.18)$$

Finally, the frequently used structure factor,  $S(q)$ , is the Fourier transform of the number density  $\rho_q$  first calculated in atomistic simulation.

$$\rho_q = \sum_i \exp(-qr_j). \quad (6.19)$$

Then  $S(q)$  is calculated from  $\rho_q$ .

$$S(q) = \langle \rho_q \rho_q^- \rangle. \quad (6.20)$$

It is quite important to reproduce the experimental  $J(r)$  in the real space domain or  $I(q)$  in the wave-number domain to validate the calculated three-dimensional structure.

Depending on the atoms considered, X-ray and neutron diffraction experiments can yield different profiles so that both kinds of profiles should be calculated and compared with the relevant data as done in Figs. 6.3 and 6.4 for MD simulated  $B_2O_3$  glass [10]. Once the total correlation and interference functions have been validated, more detailed analysis based on PDF functions can be performed and important insight into structural order be obtained. Although the experimental peak positions are reproduced reasonably well by the calculated  $T(r)$  and  $I(q)$ , there are some discrepancies for the peak values. The position and width of the first peak represent the average length and the length distribution of B–O bonds, respectively. In addition, the area of the first peak region can provide information on coordination number (CN). The information on CN is important to investigate coordinate states

for Si, B, Ge, and Al atoms. The second peak position and peak curve are mostly affected bond angles of O–B–O and B–O–B as shown in Fig. 6.5. As indicated by a detailed analysis of the data, most of the discrepancy is due to a simulated fraction of only 30–50% for the so-called boroxol  $B_3O_6$  rings compared to the 60–80% range of the experimental values [11, 12].

In silicate glasses another fundamental feature to describe variations of structure and properties is the ‘ $Q_n$  distribution’, where the subscript  $n$  indicates the number of bridging oxygen (BO) in an  $SiO_4$  tetrahedra. In MD simulations it is easy to identify nonbridging oxygens (NBO) on the basis of the cut-off radius. The calculated  $Q_n$  distributions for sodium-silicate glasses have been compared with that determined by MAS-NMR experiments as shown in Fig. 6.6 [13]. The MD calculations reproduce the experiments reasonably, although the extremely rapid quenching rates prevailing in the MD simulation may broaden the distribution, which does depend on actual  $T, P$  conditions. The analysis of  $Q_n$  is also important for phosphate glasses, because  $Q_n$  distribution reflects their polymer-like structure that results from the existence of

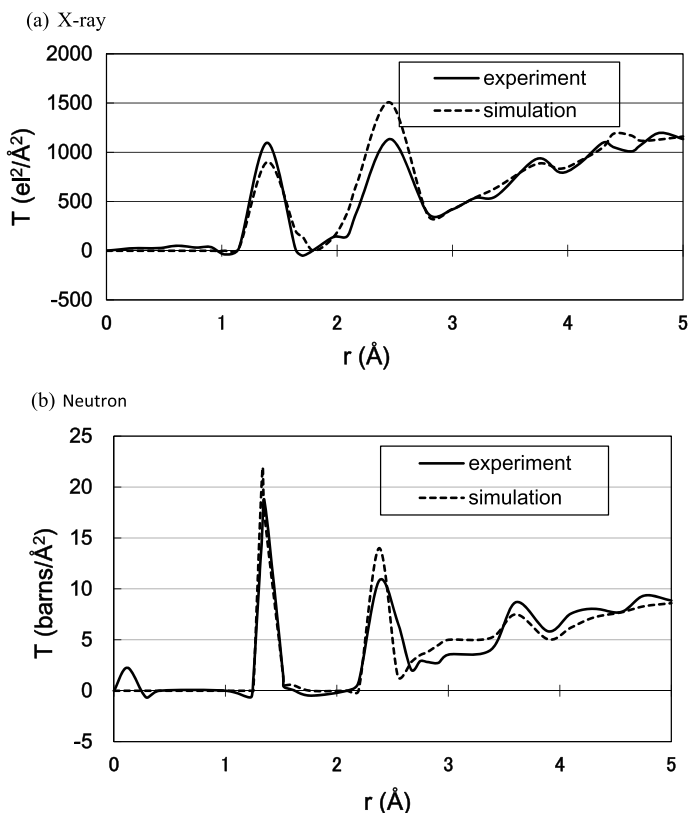


**Fig. 6.3** Comparisons between the experimental [11] and simulated [10] X-ray (a) and neutron (b) total correlation functions of  $B_2O_3$  glass

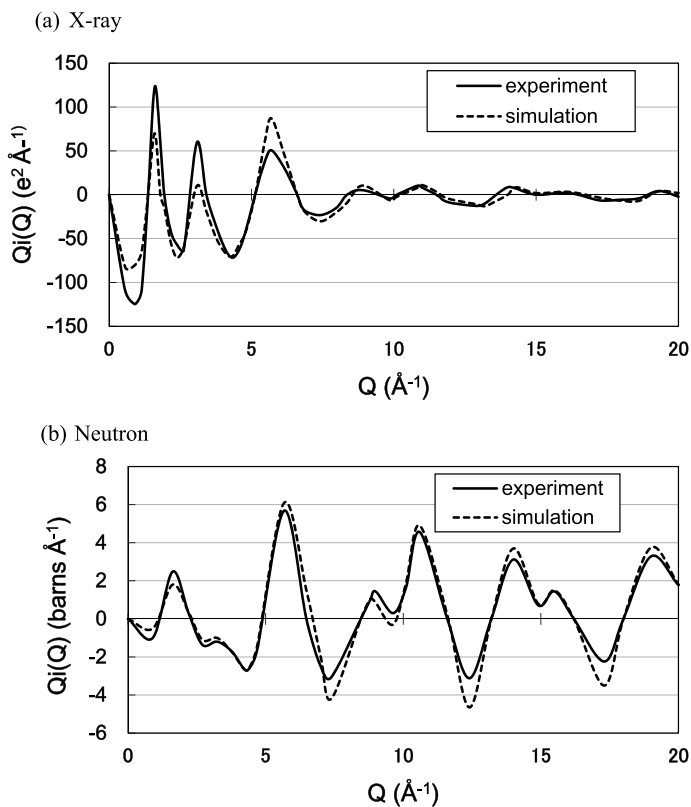


**Fig. 6.4** Comparisons between the experimental [11] and simulated [10] X-ray (a) and neutron (b) interference functions of  $B_2O_3$  glass

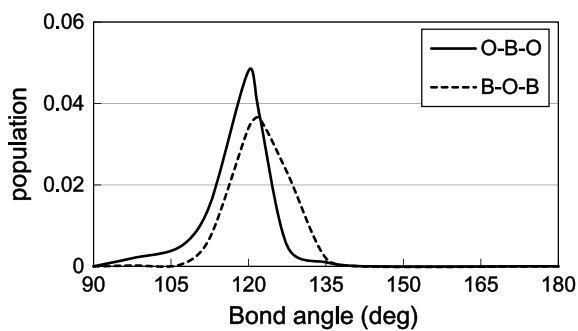


**Fig. 6.5** Bond angle distribution in simulated  $B_2O_3$  glass [11]

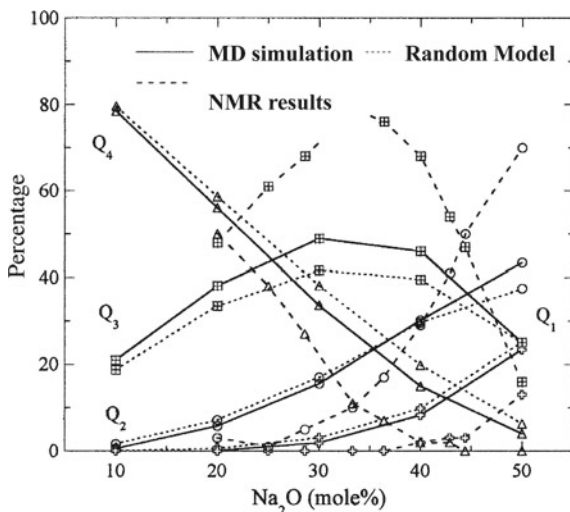


**Fig. 6.6** Calculated  $Q_n$  distribution of  $x\text{Na}_2\text{O}-\text{SiO}_2$  glasses. Modified from Ref. [13]

doubly-bonded oxygen atoms. In the case of phosphate glass not many MD studies have been published and more validated potential models need to be developed.

### 6.3.2 Ring Size Distribution and Geometrical Modeling for Medium-Range Order

Medium-range order is difficult to study either experimentally or through atomistic simulations. The size distribution of rings made up of cations and oxygen atoms is in particular an important parameter when investigating geometrical features in the 5–15 Å range. A ring is usually characterized by the number of its network-forming cations, which can be derived from the calculated atomic coordinates as shown in Fig. 6.7 for simulated  $\text{B}_2\text{O}_3$  and  $\text{SiO}_2$  glasses. Compared with cristobalite, tridymite, and quartz, whose ring sizes are 6, 6, and both 6 and 8, respectively, simulated  $\text{SiO}_2$  glass shows a broad distribution around 6. It has been speculated that the existence of sizes of odd-numbered rings are characteristic of disordered structures and might impede glass crystallization, because five-fold rotational symmetry does not exist in crystals where 4-, 6-, and 8-membered rings are primarily observed. In  $\text{B}_2\text{O}_3$  glass, which is extremely reluctant to crystallize, the existence of  $\text{B}_3\text{O}_6$  units indeed causes the presence of a peak at 3 in the ring statistics.

Different from the analytic methods discussed so far, there is a geometrical method relying on the so-called ‘Voronoi diagram’ [14]. It is largely employed for monatomic system for which partitioning three-dimensional space is simple and easy when the

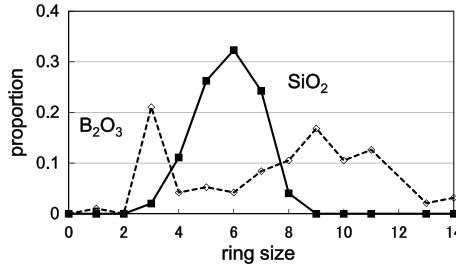


**Fig. 6.7** Ring size distribution in simulated B<sub>2</sub>O<sub>3</sub> and SiO<sub>2</sub> glasses [7, 11]. Data sampled at 0 K

calculated atomic coordinates obtained by atomistic simulations are used to delineate the portion of space assigned to every atom. These Voronoi polyhedra are then characterized by their numbers of faces and corners whose distributions change as positional relationships vary in the glass structure. Typical Voronoi polyhedra calculated only from the coordinated of oxygen atoms are shown in Fig. 6.8. Based on the information on Voronoi index vector, degree of geometrical similarity between silica polymorphs and glass can be discussed as shown in Tables 6.1 and 6.2.

## 6.4 Modeling of Glass Properties

Fundamental thermodynamic properties can be calculated once numerical simulations have yielded atomic configurations and velocities. The pressure is for example calculated from

$$P = (N/V)kT - 1/(3V) \langle \sum_i \sum_{j(j \neq i)} \partial U_{pij} / \partial r_{ij} r_{ij} \rangle \quad (6.21)$$

where the bracket indicates an equilibrium time average and  $N$ ,  $V$ ,  $T$ ,  $U_{ij}$ , and  $r_{ij}$  are as usual the number of atoms, cell volume, temperature, pair potential and distance between atoms  $i$  and  $j$ .

The internal energy ( $E_{\text{int}}$ ) is:

$$E_{\text{int}} = (3/2)kT + \langle \sum_i \sum_{j(j \neq i)} U_{pij}(r_{ij}) \rangle, \quad (6.22)$$

and the molar heat capacity at constant volume ( $C_v$ ):

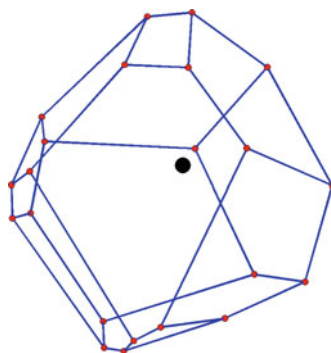
$$C_v = (\partial E_{\text{int}} / \partial T)_V. \quad (6.23)$$

Alternatively, one can derive  $C_v$  from the potential energy fluctuations through,

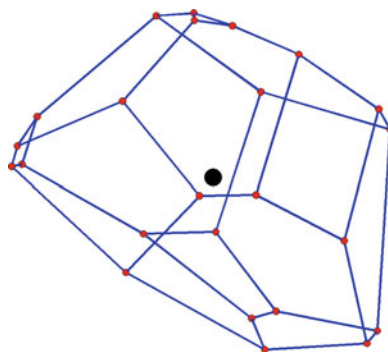
$$\langle U^2 \rangle - \langle U \rangle^2 = (2/3)Nk^2T^2(1 - (3/2)k/C_v). \quad (6.24)$$

**Fig. 6.8** Representative Voronoi polyhedra of simulated glass. For the definition of vector  $(n_3, n_4, n_5, n_6, n_7)$ , refer to Table 6.1 [14]

**Polyhedron of type  $(0, 3, 6, 4, 0)$  in glass**



**Polyhedron of type  $(1, 3, 4, 5, 1)$  in glass**



**Polyhedron of type  $(0, 3, 6, 3, 0)$  in glass**

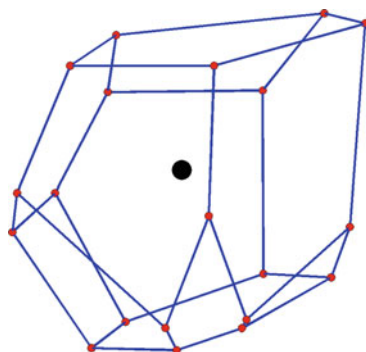


**Table 6.1** Voronoi index vectors in monatomic crystals and silica structures

HCP	(0, 6, 0, 8, 0)		
FCC	(0, 12, 0, 0, 0)		
HCP	(0, 12, 0, 0, 0)		
Icosahedron	(0, 0, 12, 0, 0)		
Quartz	(0, 6, 2, 6, 0)	(0, 5, 3, 5, 1)	(1, 4, 3, 5, 2)
Cristobalite	(0, 3, 6, 5, 0)	(0, 4, 4, 6, 0)	(0, 4, 4, 7, 0)
Coesite	(0, 2, 8, 4, 0)	(2, 2, 4, 6, 2)	(1, 2, 6, 3, 1)
Stishovite	(0, 3, 6, 5, 0)	(0, 2, 8, 3, 0)	(0, 4, 4, 7, 0)
Glass	(0, 3, 6, 4, 0)	(1, 3, 4, 5, 1)	(0, 3, 6, 3, 0)

The formulation of vector is  $(n_3, n_4, n_5, n_6, n_7)$ , where  $n_3, n_4, n_5, n_6$  or  $n_7$  indicates the number of triangles, quadrangles, pentagons, hexagons, and heptagons on the surface of each polyhedron [14]

**Table 6.2** Degree of geometrical similarity between silica polymorphs and glass

	Quartz (%)	Cristbalite (%)	Coesite (%)	Stishovite (%)	Total (%)
At 200 K	36	27	34	6	103
At 2000 K	32	25	28	4	89
At 4000 K	22	17	17	4	60
At 20 GPa	37	39	41	11	128
Decompressed	33	30	32	5	100

The first, second, third, fourth, and fifth row indicate ratios for as-annealed glass at 200 K and at 0 GPa, heated at 2000 K and at 0 GPa, heated at 4000 K and at 0 GPa, compressed under 20 Pa and at 200 K, and decompressed from 20 GPa and at 200 K, respectively [14]

And two other interesting properties are the thermal expansion coefficient ( $\alpha_p$ )

$$\alpha_p = (1/V)(\partial V/\partial T)_p = (1/T)\{1 - (1/V)(\partial H/\partial p)_T\}, \quad (6.25)$$

where  $H$  is enthalpy, and the thermal pressure coefficient ( $\beta_V$ ):

$$\beta_V = (\partial p/\partial T)V = (1/T)\{(\partial E_{\text{int}}/\partial V)_T + P\}. \quad (6.26)$$

After a model of atomistic simulation is validated so that it can reproduce static structure of glass, it can be applied to investigate a variety of properties such as thermal, mechanical, transport, optical properties and phase stability. The author refers the interested reader to Ref. [1] for the examples of property analysis by computer simulation. In addition, recent review papers are reported in Ref. [9].

## 6.5 Experimental and Computational Complementarity

The statically arrangement of structural units for  $B_2O_3$  glass and the dynamically arrangement of structural units for  $SiO_2$  glass represent new insights on glass structure provided by MD simulations, in these cases, by the torsion angle distributions, which escape any experimental determinations. These two examples thus illustrate the complementary nature of numerical simulations and experimental studies of glass structure. When the history of structural studies on glass is looked back on, it is clear that both diffraction and spectroscopic studies have made fundamental contributions to the construction of structural models. The radial distribution function (RDF) or the pair distribution function (PDF) can indeed be readily calculated from the Fourier transform of experimental X-ray, neutron or electron diffraction data. Because this type of information represents averaged one-dimensional structural data, however, there is always some arbitrariness when reconstructing the actual three-dimensional configuration in which one is interested.

Other probes such as IR, Raman, or NMR spectroscopies can provide information only on short-range order in glass structure. In contrast, atomistic simulations do provide realistic three-dimensional configuration directly as long as an appropriate atomistic model is employed. One could confidently argue that a structural model of glass is reliable when the model matches the results of both experiments and atomistic simulations. In summary, the relation between atomistic simulation and experiment is complementary because both methodologies provide insights on different aspects of glass structure. Atomistic simulations nonetheless possess two other advantages over experimental methods. The first is that they can determine three-dimensional configurations from short-to medium-range order extending up to the size of cell length (10–100 nm). The second is that a very broad range of atomistic simulations becomes possible as soon as an appropriate simulation model is established. For example, it is easy to change external conditions such as temperature, pressure or other external forces to investigate their effects on structure. And physical and chemical properties can be readily derived from the potential energy and structural models with standard statistical mechanical methods. In addition, atomistic simulation is quite useful to investigate glass properties under high temperature and high pressure in which experiments are difficult to conduct.

## 6.6 Perspectives

Development of both faster computing processors and efficient simulation algorithms have expanded the range of atomistic simulation and narrowed down their discrepancies with experiments. Simulations would nonetheless benefit from improved accuracy. As becoming more common, the best way to achieve this goal is to perform first-principles MD calculation from beginning to end. Although such calculations made with standard quantum mechanical codes remain difficult when dealing with a



large number of atoms, progress should result from the use of the so-called order- $N$  and linear scaling methods, which have developed vigorously during the past decade. For oxide glasses, recent codes such as SIESTA or CONQUEST now have the potential ability to handle systems of around one thousand atoms with a supercomputer whereas calculations for systems ten times bigger should become feasible in the next decade. Alternatively, better classical potentials can be derived from the energy data yielded by first-principles methods. Machine learning is more and more popular to fit classical potentials by using the energy data.

There exist several challenging glass research areas to which it is not easy to apply atomistic simulation. The first is the essence of glass transition and slow relaxation phenomena. The dynamical change of structure rapidly slows down. Atomic simulation can only trace an event occurring within a time span of  $\mu\text{s}$ . The second challenge is to reproduce crystallization and phase separation. To do this, much longer time span of simulation and a large size of simulation box are required. The third is to calculate entropic properties in non-equilibrium. Once entropic properties are estimated, many properties can be derived from them. A new theory of non-equilibrium statistical thermodynamics is desired. The fourth challenge is to develop the algorithm of calculating the excited electronic states more accurately. Such algorithm will facilitate the advanced design of optical and optoelectronic materials. Simulation scientists discuss the present problem and the future directions on atomistic simulation in the TC27 Technical Committee of the International Commission on Glass (ICG). Young scientists are encouraged to make contact with TC27 members.

Finally, the author refers the interested reader to Ref. [15] for investigating into glass science and technology in general.

In a near future, the author strongly expects that any macroscopic property will be explained in terms of microscopic structure by atomistic and first-principles simulations, and multi-scale simulation will be ubiquitous as shown in Fig. 6.9. In addition, next-generation technology in computer modeling will be developed as shown in Fig. 6.10. Computational design of glass materials will advance rapidly in good harmony with experimental studies.

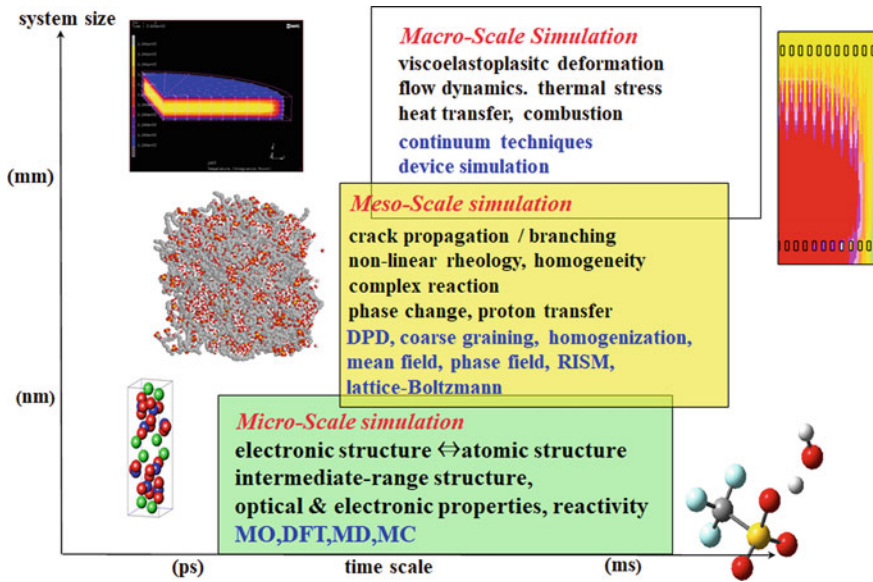


Fig. 6.9 Multi-scale simulation [1]

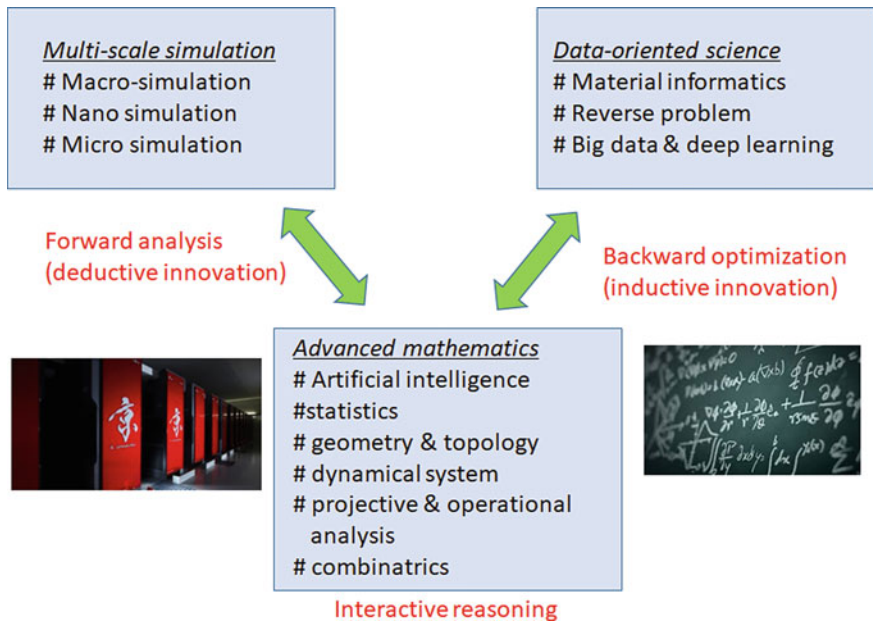


Fig. 6.10 Overview of next-generation technology in numerical modeling [1]

## References

1. Takada A, Parker J, Durán A, Bange K (2018) Teaching glass better. Cyan, Madrid
2. Bell RJ, Dean P (1971) The structure of vitreous silica: validity of the random network theory. *Philos Mag* 25:1381–1398
3. Zachariasen WH (1932) The atomic arrangement in glass. *J Amer Chem Soc* 54:3841–3851
4. Landau DP, Binder K (2000) A guide to Monte-Carlo simulations in statistical physics. Cambridge University Press, Cambridge
5. Allen MP, Tildesley DJ (2017) Computer simulation of liquids, 2nd edn. Oxford University Press, Oxford
6. Woodcock LV, Angell CA, Cheeseman P (1976) Molecular dynamics studies of the vitreous state: simple ionic systems and silica. *J Chem Phys* 65:1565–1577
7. Takada A, Cormack AN (2008) Computer simulation models of glass structure. *Phys Chem Glasses: Eur J Glass Sci Technol B* 49:127–135
8. Vessal B, Greaves GN, Marten PT, Chadwick AV, Mole R, Houde-Walter S (1992) Cation microsegregation and ionic mobility in mixed alkaline glasses. *Nature* 356:504–506
9. Massobrio C, Du J, Bernasconi M, Salmon PS (2015) Molecular dynamics simulations of disordered materials. Springer, Heidelberg
10. Takada A, Catlow CRA, Price GD (1995) Computer modeling of B<sub>2</sub>O<sub>3</sub>: Part II. Molecular dynamics simulation of vitreous structures. *J Phys Condens Matter* 7:8693–8722
11. Johnson PAV, Wright AC (1982) A neutron diffraction investigation of the structure of vitreous boron trioxide. *J Non-Cryst Solids* 50:281–311
12. Hannon AC, Wright AC, Blackman JA, Sinclair RN (1995) The vibrational modes of B<sub>2</sub>O<sub>3</sub>: inelastic neutral scattering and modelling studies. *J Non-Cryst Solids* 182:78–89
13. Olivier L, Yuan X, Cormack AN, Jäger C (2001) Combined <sup>29</sup>Si double quantum NMR and MD simulation studies of network connectivities of binary Na<sub>2</sub>O-SiO<sub>2</sub> glasses: new prospects and problems. *J Non-Cryst Solids* 293–295:53–66
14. Takada A (2018) Voronoi tessellation analysis of SiO<sub>2</sub> systems based on oxygen packing. *J Non-Cryst Solids* 499:309–327
15. Richet P (ed) (2021) Encyclopedia of glass science, technology, history, and culture. Wiley, New York

# Chapter 7

## Atomic Structure of Glasses Investigated by Diffraction and Scattering of Radiations



Bernard Hehlen and René Vacher

### 7.1 Diffraction—Elastic Scattering

#### 7.1.1 X-Ray and Neutron Diffraction Method

In an X-ray diffraction experiment, the sample receives a parallel beam of monochromatic X-rays. This incident beam is a plane wave; the electric field  $E$  received by an atom at  $r$  from the origin is given by:  $E_i = E_i^0 \exp i(\mathbf{k}_i \cdot \mathbf{r} - \omega t)$ , where  $\mathbf{k}_i$  is the wave vector, parallel to the propagation direction,  $|\mathbf{k}| = 2\pi/\lambda$ ,  $\lambda$  is the wavelength,  $\nu$  is the frequency,  $\omega = 2\pi\nu$  is the angular frequency. In this chapter, bold characters indicate vectors. Each atom emits a spherical wave at the frequency of the incident radiation (Fig. 7.1). All atoms in a plane normal to the propagation direction  $\mathbf{k}_i$  vibrate in phase, as  $\mathbf{k}_i \cdot \mathbf{r}$  is constant for such planes. The propagation velocity is  $c = \omega/|\mathbf{k}|$ . The scattered field, detected in the direction  $\mathbf{k}_s$  at a distance  $R$  much larger than the size of the sample, is the sum of the electric field scattered by all atoms. Let us define the scattering angle  $2\theta = \widehat{\mathbf{k}_i, \mathbf{k}_s}$ . Figure 7.2 is a picture of the experimental arrangement for X-ray or neutron diffraction studies.

A necessary condition for obtaining a diffraction signal is that the electric fields received from all atoms are in phase. This may be the case in particular when the atoms are located in planes:

- (i) All atoms in a plane parallel to the bisector of the angle  $2\theta$  between incident and scattered directions scatter in phase; as shown in Fig. 7.3, all paths such as  $AB + BC$  and  $A'B' + B'C'$  are equal. As incident and scattered X-rays have the same frequency  $\omega$  and wavelength  $\lambda$ , then  $|\mathbf{k}_i| = |\mathbf{k}_s| = k$ . We define the scattering vector

---

B. Hehlen · R. Vacher (✉)

Université Montpellier and CNRS, UMR 5221, Laboratoire Charles Coulomb, 34095 Montpellier, France

e-mail: [rene.vacher@umontpellier.fr](mailto:rene.vacher@umontpellier.fr)

**Fig. 7.1** Radiation by a single atom

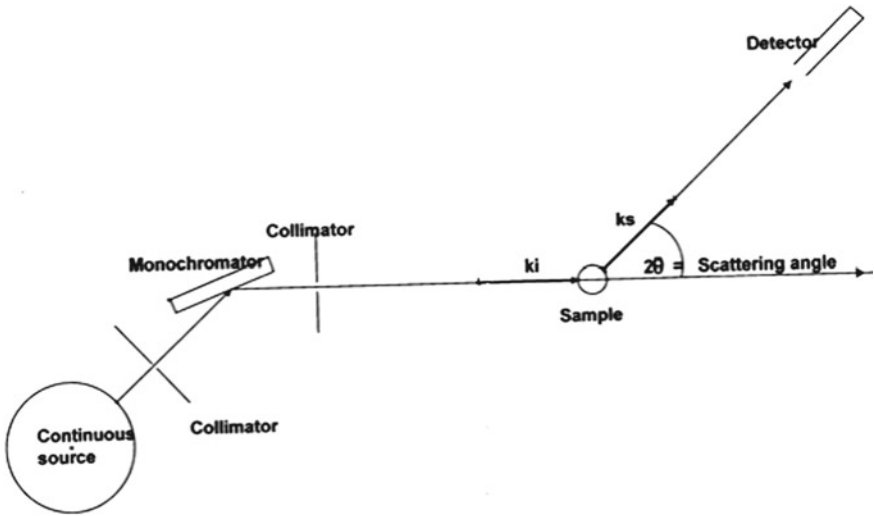
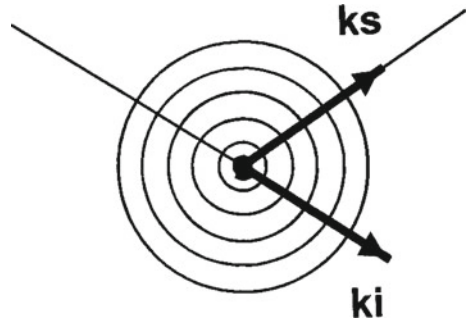


**Fig. 7.2** Schematic picture of an X-ray or neutron diffraction experiment

$$\mathbf{Q} = \pm(\mathbf{k}_i - \mathbf{k}_s) \quad |\mathbf{Q}| = 2k \sin \theta = \frac{4\pi}{\lambda} \sin \theta$$

- (ii) Keeping the orientations of the plane and of the incident and scattered beams identical to those in Fig. 7.3, let us now consider a second plane at a distance  $d$  and parallel to the previous one. B and B'' are two points on the same normal to the planes, B on the first plane, B'' on the second. The path difference between the two rays scattered by B and B'', (AB + BC) and (A''B'' + B''C''), respectively, is  $\delta = 2d \sin \theta$ . The corresponding phase difference is  $\varphi = \frac{2\pi\delta}{\lambda} = \frac{4\pi}{\lambda} d \sin \theta = |\mathbf{Q}|d$ . But in fact, as all the points of the same plane perpendicular to  $|\mathbf{Q}|$  scatter in phase, this result is true for the phase shift between any two points belonging one to the first, the other to the second plane. If these points are separated by  $\mathbf{r}$ , one has:  $\varphi = \mathbf{Q} \cdot \mathbf{r}$ . The two planes scatter in phase if  $2d \sin \theta = n\lambda$ , where  $n$  is an integer.

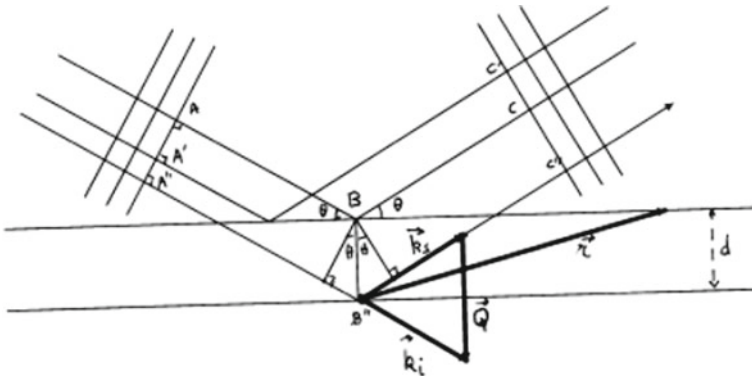


Fig. 7.3 Diffraction by atomic planes

With the same geometrical considerations, if  $r$  is the distance between the origin and a point, the field emitted by an atom at this point is written:  $E_s = E_s^0 \exp i(\mathbf{Q} \cdot \mathbf{r} - \omega t)$ . In this Part I devoted to elastic scattering, the oscillatory term  $-i\omega t$  is always implied: it is not shown in the equations.

We can thus easily state the conditions for Bragg diffraction in crystals: a family of reticular planes scatters X-rays and neutrons if:

- (i) The normal to these planes is parallel to  $\mathbf{Q}$ , and
- (ii) The distance  $d$  between two adjacent planes is:  $d = \frac{n}{2 \sin \theta} = \frac{2n\pi}{|\mathbf{Q}|}$ .

### 7.1.2 Description of Glass Structure

The main difference between crystal and glass is structural. To understand it, we must refer to the liquid state. Liquids are obtained from solids by heating them above a certain temperature, termed melting temperature. For instance, the melting temperature of quartz is 1650 °C. In the crystal, molecules form an ordered, rigid lattice, the chemical bonds holding adjacent molecules close to each other. When the melting temperature is reached, the thermal agitation breaks this perfect organization: the chemical bonds between molecules are continuously broken and rebuilt at high rate (at the picosecond scale), and molecules take distance from each other in a random way, leading to a dynamic structure which is neither fixed nor ordered as it was in the crystal phase. To obtain a glass from the liquid, we must perform a fast cooling. Then, the viscosity of the liquid increases rapidly, and the molecules do not have time to reach an equilibrium position as they had in the crystal: a solid is obtained, the disordered structure is frozen in and the material cannot flow any more. A metastable state is obtained: the glassy state.

Significant advances in understanding the atomic structure of glasses were made in the 1930s. Figure 7.4 (left) shows the image obtained by Bragg diffraction of X-rays on a crystal of  $\alpha$ -cristobalite, one of the crystalline forms of silicon dioxide

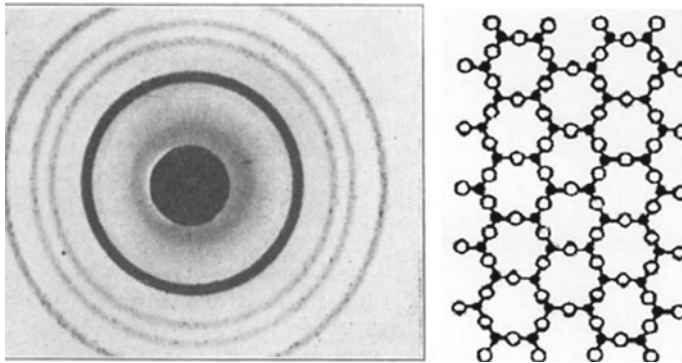


**Fig. 7.4** Left: X-ray diffraction pattern from cristobalite (from [34]), right: hypothetic crystalline structure of an oxide  $A_2O_3$

[34]. The diagram is a series of narrow circular rings of different radius. Each ring in this diagram corresponds to one family of reticular planes. From the radius of those rings, it is possible to deduce the position of all atoms in the unit cell. One finds that the elementary unit of the structure is a  $SiO_4$  tetrahedron. Those elements connect regularly to form the crystal. A 2-dimensional picture of the crystalline structure of an oxide  $A_2O_3$  is shown in Fig. 7.4 (right). Here, the elementary unit is a triangle  $AO_3$ . When a similar diffraction measurement is done on a sample of vitreous silica, the glassy state of silicon dioxide, the main feature of the diagram is a diffuse ring, shown in Fig. 7.5 (left). It should be noted that this picture is very similar to that which is obtained from a sample of liquid. What information about the structure of the glass can we get from such a result?

At the same period, Zachariassen [41] proposed, based on chemical and thermodynamic arguments, that the atomic structure of glass is what he called a “continuous random network” (CRN). A two-dimensional schematic representation of this network for a glass of composition  $A_2O_3$  is shown in Fig. 7.5 (right). According to Zachariassen’s analysis, the structure in three dimensions of an oxide glass must obey the following rules:

- (i) An oxygen atom is linked to not more than two cations;
- (ii) The number of oxygen atoms surrounding cations must be small (3 or 4);
- (iii) Oxygen polyhedra ( $SiO_4$  tetrahedra in vitreous silica, as in silicon dioxide crystals) share corners with each other, not edges or faces;
- (iv) at least, three corners in each oxygen polyhedron must be shared.

In the analysis of his diffraction results, Warren [34] supported the CRN assumption.

Following [38], we can distinguish four levels in the glass structure:

- (I) The structural unit;
- (II) The interconnection of adjacent structural units;
- (III) The network topology;

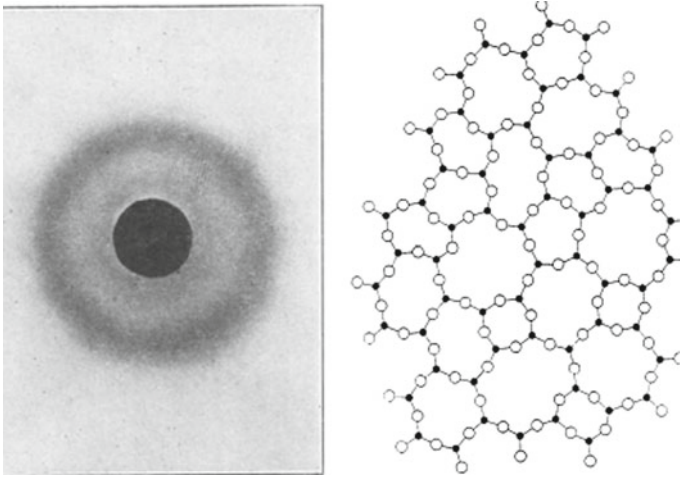


**Fig. 7.5** Left: X-ray diffraction pattern from vitreous silica (from [34]), right: schematic picture of a continuous random network for an  $A_2O_3$  oxide (from [41])

#### (IV) Longer range density fluctuations.

In a disordered structure, determining the exact position  $\mathbf{r}$  of each atom is obviously impossible: the structure must be represented by statistical quantities. The basis of the description is to choose an atom as the origin  $O$  of the coordinates and to locate the atoms which form a pair with it. Let us first consider a glass made up of only one type of atoms (*homoatomic* glass). We define the *radial density*  $\rho(r)$  as the number of atoms per unit volume at a distance  $r$  of  $O$ , and the *radial distribution function*  $4\pi r^2 \rho(r) dr$  (RDF) as the number of atomic centres in a shell between spheres of radius  $r$  and  $r + dr$  centred on  $O$  (see illustration in Fig. 7.6). Those quantities fluctuate strongly at short distances. At long distances, the volume of the shell increases and  $\rho(r)$  tends to the average density  $\rho_0 = N/V$ , where  $N$  is the number of atoms in the volume  $V$ . One also defines the *pair distribution function*:  $g(r) = \rho(r)/\rho_0$  (Fig. 7.7a) which is the probability of presence of a pair of atoms at distance  $r$ , and the *pair correlation function*  $G(r) = \frac{\rho(r) - \rho_0}{\rho_0} = g(r) - 1$  (Fig. 7.7b). An example of RDF is given in Fig. 7.7c. It should be noted that, because of the disorder of the structure, the same result for the above quantities will be found whatever the atom chosen for origin, and also, they do not depend of the orientation, but only of the scalar value of  $r$ : glass is isotropic. For *heteroatomic* structures, the same quantities can be defined for each different pair  $(\alpha, \beta)$  of atoms, for example  $g_{11}$ ,  $g_{12}$ ,  $g_{22}$ , and so on.



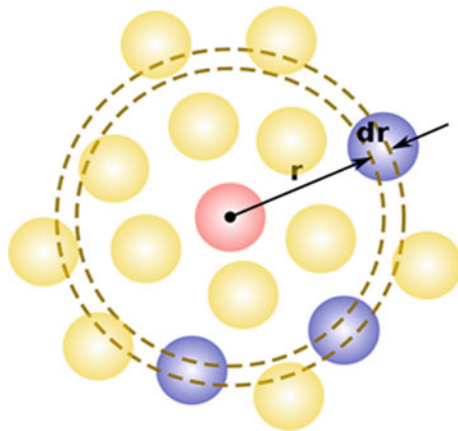


**Fig. 7.6** Illustration of the definition of the radial distribution function

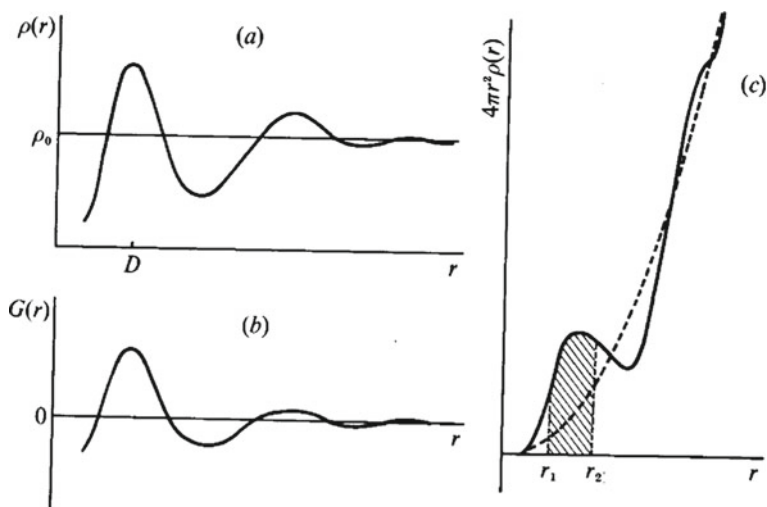


**Fig. 7.7** Schematic representation of **a** the radial density  $\rho(r)$ , **b** the pair correlation function  $G(r)$  and **c** the radial distribution function RDF (from [42])

### 7.1.3 Amplitude of the Scattered Field: The Form Factor

As shown above (Sect. 7.1.1), if the origin of phases is taken at O, the origin of coordinates, the field scattered by a single atom at  $r$  is:

$$E_S(r) = E_S^0 e^{i(k_s \cdot r - k_i \cdot r)} = E_S^0 e^{iQ \cdot r} \quad (7.1)$$

Here,  $E_S^0$  is the amplitude scattered by the atom, called the form factor  $f$  for X-rays and the neutron scattering length for neutrons.

For X-rays, scattering comes from the vibration of electrons. The first consequence is that the greater the atomic number  $Z$  of the nucleus, the higher the scattering of the atom. Then, X-rays are more sensitive to heavy atoms than to light ones (hydrogen, lithium, etc.). On the other hand, the form factor differs little between neighbouring atoms in the periodic table. More precisely, when we observe the diffraction of an atom in the direction defined by the scattering vector  $\mathbf{Q}$ , the form factor is the  $\mathbf{Q}$ -component of the Fourier transform of the spatial electron charge density  $\rho_e(\mathbf{r})$ :  $f(\mathbf{Q}) = \int \rho_e(\mathbf{r}) e^{i\mathbf{Q}\cdot\mathbf{r}} d^3\mathbf{r}$ . Examples are presented in Fig. 7.8.

For neutrons, we only consider here nuclear scattering for the sake of simplicity: for a magnetic material, we should also consider magnetic scattering. The atomic nucleus is smaller by several orders of magnitude than the wavelength associated with the incident neutrons, so that the nucleus can be considered as a point. Then,  $\rho_e(\mathbf{r})$  is a Dirac function and the scattering length, its Fourier transform, is independent of  $\mathbf{Q}$ . Unlike X-rays, the neutron scattering length can vary considerably from one element to another and also between isotopes of the same element. An experimental determination of the scattering length  $b$  as a function of  $Z$  is shown in Fig. 7.9.

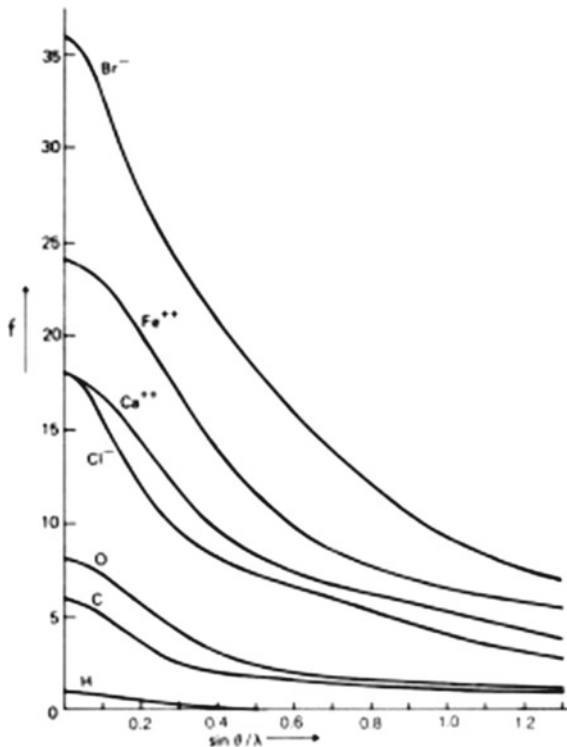
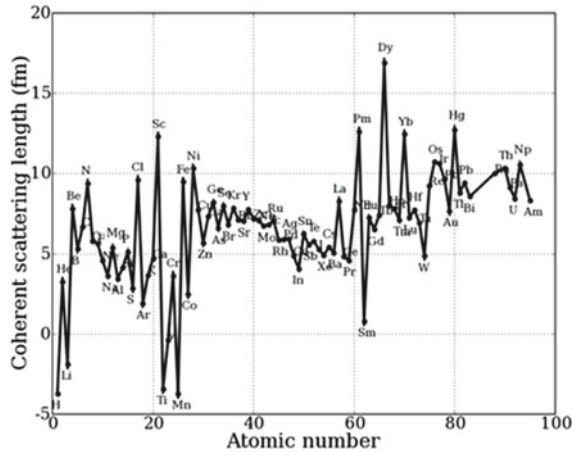


Fig. 7.8  $Q$ -dependence of the form factor for several atoms (from <https://mini.physics.sunysb.edu>)

**Fig. 7.9** Neutron scattering length of atoms



### 7.1.4 Diffracted Intensity

The intensity scattered by one atom is the square of the field  $E_s(\mathbf{r})$  calculated in Eq. (7.1):

$$I(\mathbf{Q}) = E_s(\mathbf{Q})E_s^*(\mathbf{Q}) \quad (7.2)$$

For a real sample, we have to sum the intensities scattered by all the atoms. Consider first the X-ray diffraction of a *homoatomic sample* whose atomic form factor is  $f$ :

$$I(\mathbf{Q}) = \sum_i f e^{i\mathbf{Q}\cdot\mathbf{r}_i} \sum_j f e^{-i\mathbf{Q}\cdot\mathbf{r}_j} = \sum_i \sum_j f^2 e^{i\mathbf{Q}\cdot\mathbf{r}_{ij}}, \quad (7.3)$$

where  $\mathbf{r}_{ij} = \mathbf{r}_i - \mathbf{r}_j$  is the distance of the two atoms in the pair  $(i, j)$ . From Eq. (7.3), we see that the scattered intensity is a sum over pairs of atoms. Taking into account the isotropy of the glass, we first calculate the average value of  $e^{i\mathbf{Q}\cdot\mathbf{r}_{ij}}$  in all directions for a given  $\mathbf{r}_{ij}$ , i.e. when atom  $i$ , origin of  $\mathbf{r}_{ij}$ , is at the centre of a sphere of radius  $r_{ij}$  and its end runs over the sphere in all directions with the same probability. One gets:

$$e^{i\mathbf{Q}\cdot\mathbf{r}_{ij}} = \frac{1}{4\pi r_{ij}^2} \int_0^\pi e^{iQr_{ij}\cos\varphi} 2\pi r_{ij} \sin\varphi \, d\varphi = -\frac{1}{2} \left[ \frac{e^{iQr_{ij}\cos\varphi}}{iQr_{ij}} \right]_0^\pi = \frac{\sin(Qr_{ij})}{Qr_{ij}}, \quad (7.4)$$

where  $\varphi$  is the angle  $(\widehat{\mathbf{Q}, \mathbf{r}_{ij}})$ . Only the real part is conserved in the last equality of Eq. (7.4). Then, Eq. (7.3) becomes:

$$I(Q) = f^2 \sum_i \sum_j \frac{\sin Qr_{ij}}{Qr_{ij}}. \quad (7.5)$$

This formula due to Debye is the basis for experimental studies of the structure of glasses. To calculate  $I(Q)$ , we must now make the sums. It should be noted that fixing a value for the index  $i$  amounts to choosing one given atom as the centre of the coordinates, and then the sum over  $j$  corresponds to summing the intensities over all the pairs around this atom. As a result of the structural disorder, the same result will be found for each summation on  $j$  whatever the index  $i$ . The summation on  $i$  is therefore simply a multiplication by the number  $N$  of atoms.

Separating terms with  $i = j$  from those with  $i \neq j$ , Eq. (7.5) becomes:

$$I(Q) = f^2 \sum_i \frac{\sin Qr_{ii}}{Qr_{ii}} + f^2 \sum_i \sum_{j \neq i} \frac{\sin Qr_{ij}}{Qr_{ij}}. \quad (7.6)$$

The quotient in the first term of the right-hand side of this equation is equal to 1, so the sum over  $i$  of this term is equal to  $N$ . Replacing the sum over  $i$  by a multiplication by  $N$  as explained above, one gets

$$I(Q) = Nf^2 \left( 1 + \sum_{j \neq i} \frac{\sin Qr_{ij}}{Qr_{ij}} \right). \quad (7.7)$$

The sum over atoms in this equation can be replaced by an integral over all spherical shells centred on atom  $i$ . Introducing the RDF of the atoms,  $4\pi r^2 \rho(r)$ , and replacing  $r_{ij}$  by  $r$ , the radius of the spherical shell,  $I(Q)$  becomes:

$$I(Q) = Nf^2 \left[ 1 + 4\pi \int_0^\infty r^2 \rho(r) \frac{\sin Qr}{Qr} dr \right] \equiv Nf^2 S(Q). \quad (7.8)$$

For neutron scattering, the same equation gives the value of  $I(Q)$ , replacing the atomic form factor  $f$  by the neutron scattering length  $b$ .

The above relation defines the *structure factor*  $S(Q)$ :

$$S(Q) = 1 + 4\pi \int_0^\infty r^2 \rho(r) \frac{\sin Qr}{Qr} dr \quad (7.9)$$

In the above equation, let us separate the average value  $\rho_0$  of the atomic density from its fluctuations  $\rho(r) - \rho_0$ . Then:

$$S(Q) = 1 + 4\pi \int_0^{\infty} r^2 (\rho(r) - \rho_0) \frac{\sin Qr}{Qr} dr + 4\pi \int_0^{\infty} r^2 \rho_0 \frac{\sin Qr}{Qr} dr. \quad (7.10)$$

Except for very small values of  $Q$  which are not relevant for diffraction,  $\sin Qr$  is strongly oscillating with  $r$ , and the last term in the above expression is negligible. Thus, introducing  $g(r) = \rho(r)/\rho_0$ , one finds:

$$S(Q) - 1 = \rho_0 \int_0^{\infty} 4\pi r^2 (g(r) - 1) \frac{\sin Qr}{Qr} dr, \quad (7.11)$$

and by Fourier transform, the pair distribution function  $g(r)$  is obtained:

$$g(r) = 1 + \frac{1}{(2\pi)^3 \rho_0} \int_0^{\infty} 4\pi Q^2 (S(Q) - 1) \frac{\sin Qr}{Qr} dQ. \quad (7.12)$$

For *polyatomic glasses*, the above calculation has to be done separately for each pair  $(\alpha, \beta)$  of atoms. Following [9], the structure factor for this pair is:

$$S_{\alpha\beta}(Q) = 1 + 4\pi \rho \int_0^{\infty} r^2 (g_{\alpha\beta}(r) - 1) \frac{\sin Qr}{Qr} dr, \quad (7.13)$$

where the partial pair distribution function  $g_{\alpha\beta}(r)$ , i.e. the probability to find an atom  $\beta$  at a distance  $r$  from an atom  $\alpha$  is, by Fourier transform of Eq. (7.13):

$$g_{\alpha\beta}(r) = 1 + \frac{1}{(2\pi)^3 \rho_0} \int_0^{\infty} 4\pi Q^2 (S_{\alpha\beta}(Q) - 1) \frac{\sin Qr}{Qr} dQ \quad (7.14)$$

The total intensity diffracted is then:

$$I(Q) = \sum_{\alpha, \beta} c_{\alpha} f_{\alpha}(Q) c_{\beta} f_{\beta}(Q) S_{\alpha\beta}(Q) \quad (7.15)$$

where  $c_{\alpha}$  and  $c_{\beta}$  are the atomic concentrations of atoms  $\alpha$  and  $\beta$ , respectively. The pair distribution function is:

$$g(r) = 1 + \sum_{\alpha, \beta} c_{\alpha} c_{\beta} f_{\alpha}(Q) f_{\beta}(Q) [g_{\alpha\beta}(r) - 1] \quad (7.16)$$

Equations (7.15) and (7.16) are valid for neutrons, replacing  $f$  by  $b$ .

### 7.1.5 Structure of Vitreous Silica and Some Silicate and Borate Glasses

In Fig. 7.10, we have grouped together several plots extracted from Henninger et al. [25]. They show the intensities scattered by a sample of vitreous silica irradiated by X-rays and by neutrons. The corresponding RDFs are also shown. X-ray and neutron curves are rather different: this is due to the fact that, while  $f(Q)$  is larger than  $b$  for silicon, the reverse is true for oxygen. However, the position of the peaks in the RDF is very similar. The experimental values of the position of the peaks taken from Henninger et al. [25] are given in Table 7.1. The maximum of the first peak is located at  $\sim 0.159$  nm, which correspond to the distance between silicon and oxygen in crystalline silicon oxides. One observes a second peak around 0.26 nm, which is the distance between neighbouring oxygen–oxygen pairs in the crystalline phases of  $\text{SiO}_2$ . From these two results, the conclusion is that the structural unit of vitreous silica is a regular tetrahedron  $\text{SiO}_4$  with one Si atom in the centre and one O atom on each of its corners, as it is in the  $\text{SiO}_2$  crystals. The next peak is observed around 0.32 nm: Fig. 7.5b suggests that it corresponds to the pair of silicon atoms at the centre of two neighbouring tetrahedra.

More recent diffraction experiments and data analysis in vitreous silica have been presented by [39]. The main results are  $0.1608 \pm 0.0004$  nm for the distance Si–O,  $0.2626 \pm 0.0006$  nm for O–O, and  $\sim 0.31$  for Si–Si. For the latter, it should be noted that, because of the disorder in the relative orientation of neighbouring tetrahedra, the diffraction is averaged over the sample, producing a broadening of the line. From the above results, one finds a Si–O–Si angle of  $\sim 150^\circ$ . A picture of two elementary tetrahedra and of their interconnection is shown in Fig. 7.11.

Figure 7.12 shows the RDF of silica compared to those of two silicate glasses [40]. The sharp peak around 1.6 Å (Si–O distance) observed in silica glass is also present in the two silicates. The peak around 2.6 Å in silica glass, assigned to the pair O–O, is also present on the tail of a higher peak in  $\text{MgSiO}_3$ . For  $\text{CaSiO}_3$ , the second peak is higher and broader, suggesting a superposition of peaks. Since the O–O distance for a regular  $\text{SiO}_4$  tetrahedron with Si–O equal to 1.64 Å should be 2.67 Å, the second peak was assigned to the Ca–O and O–O pairs [40]. This shows that the  $\text{SiO}_4$  tetrahedron is the fundamental unit of those silicates. In the case of  $\text{CaSiO}_3$ , by adding a study by Raman scattering to the X-ray diffraction experiments, Yin et al. were able to propose a model of the structure of this glass compatible with the experimental results.

Concerning boron oxide  $\text{B}_2\text{O}_3$ , Zachariassen [41] noticed that the conditions to form a glass are met if the elementary unit is a triangle with one atom of boron at the centre and three atoms of oxygen at its corners. This structure was confirmed in an X-ray diffraction study [35]. As far as the interconnection of those triangles is concerned, Raman scattering [13] and precise neutron scattering [14] have shown that most of these elementary units form planar  $\text{B}_3\text{O}_6$  “boroxol” units, shown in Fig. 7.13a. The RDF extracted from neutron diffraction results have been successfully fitted to

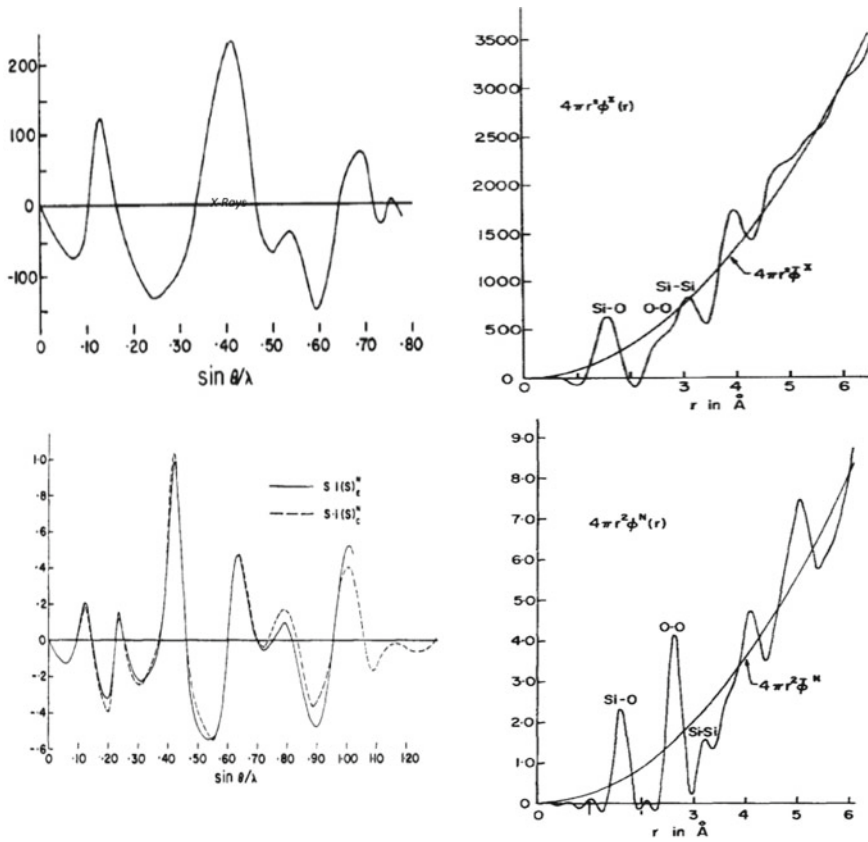


**Fig. 7.10** Left plots: the intensities diffracted by a sample of vitreous silica in X-ray (up) and neutron (down) diffraction. The curves on the right-hand side of the figures are the corresponding radial distribution functions extracted by Fourier transform (from [25])

**Table 7.1** Interatomic distances in silica glass (from [25])

	Si-O	O-O	Si-Si
Neutron, $\lambda = 0.797 \text{ \AA}$	1.59 $\text{\AA}$	2.62 $\text{\AA}$	3.22 $\text{\AA}$
Neutron, $\lambda = 1.094 \text{ \AA}$	1.63	2.62	No peak
X-rays, $\lambda = 0.71 \text{ \AA}$	1.55	2.55	3.07

a model in which 80% of the boron atoms are included in boroxol rings, the 20% remaining forming independent  $\text{BO}_3$  triangles (Fig. 7.13b).

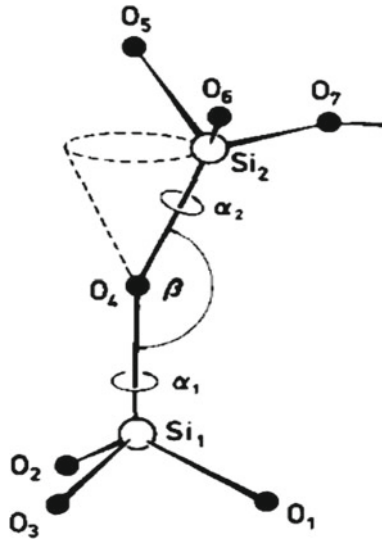


Fig. 7.11 Two elementary units in vitreous silica and their interconnection (from [39])

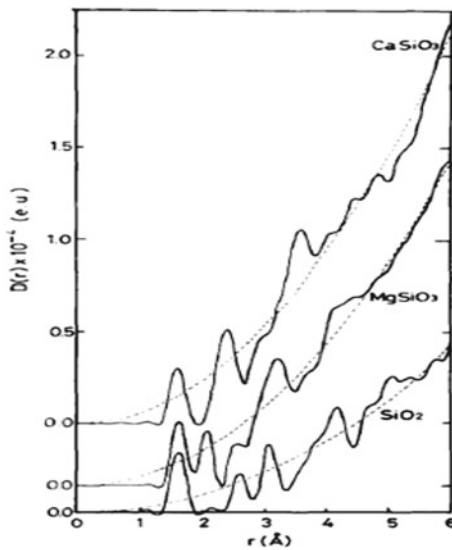
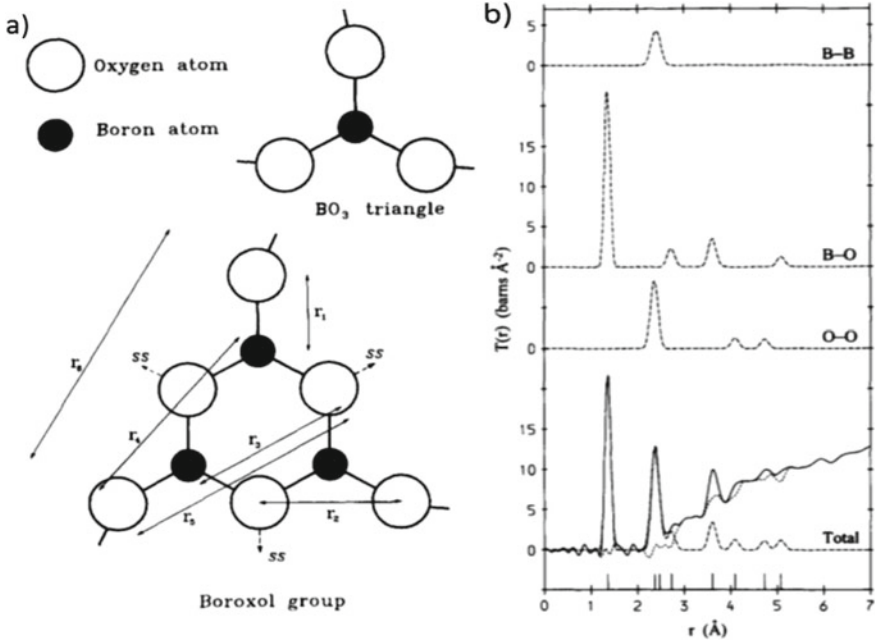


Fig. 7.12 RDF of some silicate glasses (from [40])

### 7.1.6 Neutron Diffraction: Isotopic Substitution

When one of the elements constituting the glass has two isotopes whose neutron scattering length is appreciably different, one can use a method of subtraction [8] to





**Fig. 7.13** **a** Boron oxide glass: the elementary unit and the boroxol triangle; **b** the RDF calculated (dashed lines) and experimental (solid line) for boron oxide glass (from [14])

obtain the RDF around one atom of this element, or the RDF of this element alone. As shown above (Sect. 7.1.4), the neutron diffraction intensity for a polyatomic glass is:

$$I^N(Q) = \sum_{\alpha, \beta} c_{\alpha} c_{\beta} b_{\alpha} b_{\beta} S_{\alpha\beta}(Q). \tag{7.17}$$

If the element M has two isotopes, with scattering lengths  $b_{M1}$  and  $b_{M2}$ , two samples are prepared, one with isotope  $M_1$ , the other with isotope  $M_2$ . One gets for the sample (7.1) with  $M_1$ :

$$I_1(Q) = \sum_{\alpha, \beta \neq M} c_{\alpha} c_{\beta} b_{\alpha} b_{\beta} S_{\alpha\beta}(Q) + \sum_{\substack{\alpha, M \\ \alpha \neq M}} c_{\alpha} c_M b_{\alpha} b_{M1} S_{\alpha M}(Q) + c_M^2 b_{M1}^2 S_{MM}(Q), \tag{7.18}$$

and for the sample (7.2) with  $M_2$ :

$$I_2(Q) = \sum_{\alpha, \beta \neq M} c_\alpha c_\beta b_\alpha b_\beta S_{\alpha\beta}(Q) + \sum_{\substack{\alpha, M \\ \alpha \neq M}} c_\alpha c_M b_\alpha b_{M2} S_{\alpha M}(Q) + c_M^2 b_{M2}^2 S_{MM}(Q). \tag{7.19}$$

Subtracting  $I_2$  from  $I_1$ , one obtains  $\Delta_1 M$ , which contains only the partial structure factors centred on one atom M:

$$\Delta_1 M(Q) = \sum_{\substack{\alpha, M \\ \alpha \neq M}} c_\alpha c_M b_\alpha (b_{M1} - b_{M2}) S_{\alpha M}(Q) + c_M^2 (b_{M1}^2 - b_{M2}^2) S_{MM}(Q). \tag{7.20}$$

By Fourier transform, one obtains from the above equation the pair correlation function centred on element M:

$$g_{M\alpha}(r) = \frac{2}{\pi} \int \Delta_1 M(Q) \sin QrdQ = 2 \sum_{\alpha \neq M} c_\alpha c_M b_\alpha (b_{M1} - b_{M2}) (g_{\alpha M}(r - 1)) + c_M^2 (b_{M1}^2 - b_{M2}^2) (g_{MM}(r) - 1). \tag{7.20}$$

In Sect. 7.1.5, we have shown that, in  $\text{CaSiO}_3$  glass, the basic structural unit is the  $\text{SiO}_4$  tetrahedron. What about the calcium atoms? Eckersley et al. [8] applied the isotopic substitution method to this glass, one sample being prepared with natural Ca, the other with essentially pure  $^{44}\text{Ca}$ . The difference spectrum is shown in Fig. 7.14. The main feature in this spectrum is a sharp peak near 2.4 Å which coincides with the same peak observed in crystalline  $\text{CaSiO}_3$  also shown in Fig. 7.14 [5]. This peak was assigned to the pair C–O. A careful analysis of this strongly suggests that the Ca atoms are at the centre of a coordination polyhedron mainly ordered, probably octahedral as in the crystal.

The above subtraction procedure is called “first difference”. We can go further and obtain the RDF for one given atom in using the “second difference”. For that,

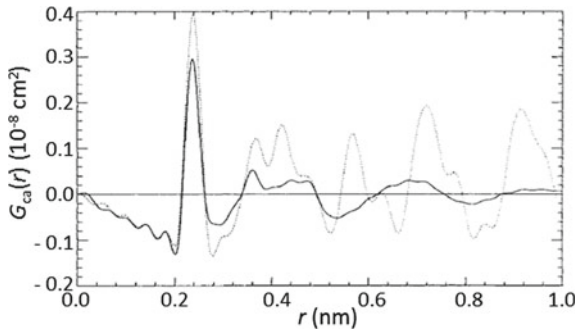


Fig. 7.14 RDF around Ca in glassy (solid line) and crystalline (dashed line)  $\text{CaSiO}_3$  (from [5])

we need to prepare a sample with a mixture of isotopes  $M_1$  and  $M_2$  in concentrations such that the neutron scattering length  $b_{M_3}$  of that mixture fulfils the relation  $b_{M_1} - b_{M_2} = b_{M_2} - b_{M_3}$ . The intensity  $I_3(Q)$  of neutrons diffracted for that mixture is:

$$I_3(Q) = \sum_{\alpha, \beta \neq M} c_\alpha c_\beta b_\alpha b_\beta S_{\alpha\beta}(Q) + \sum_{\substack{\alpha, M \\ \alpha \neq M}} c_\alpha c_M b_\alpha b_{M_3} S_{\alpha M}(Q) + c_M^2 b_{M_3}^2 S_{MM}(Q), \quad (7.21)$$

and the difference  $\Delta_2 M(Q) = I_2(Q) - I_3(Q)$  is:

$$\Delta_2 M(Q) = \sum_{\substack{\alpha, M \\ \alpha \neq M}} c_\alpha c_M b_\alpha (b_{M_2} - b_{M_3}) S_{\alpha M}(Q) + c_M^2 (b_{M_2}^2 - b_{M_3}^2) S_{MM}(Q). \quad (7.22)$$

By subtracting  $\Delta_2$  from  $\Delta_1$ , one obtains the second difference:

$$\Delta_1 M(Q) - \Delta_2 M(Q) = \frac{1}{2} c_M^2 (b_{M_3} - b_{M_1})^2 S_{MM}(Q). \quad (7.23)$$

Then, the pair distribution function  $g_{MM}(r)$  can be calculated. Figure 7.15 shows the RDF for various cations [5]. The best way to comment on this figure is to use some of the authors' sentences. "Between 3 and 5 Å, all the  $G_{MM}(r)$  functions exhibit a split second peak related to the second neighbours. These peaks appear for distances close to those of compositionally equivalents crystals, which indicate that some structural crystalline arrangements are maintained in the glass structure. However, the simulation on  $\text{CaSiO}_3$  shows the presence of additional peaks in the crystal beyond 5 Å, which contradicts the possibility of microcrystallite models".

## 7.2 Inelastic Scattering

Atoms submitted to a thermal energy  $k_B T$  vibrate, and for a given molecule or crystalline structure, the symmetry of the atomic displacements reflects the atomic symmetry. Within the framework of the group theory developed for liquids and crystals, the vibrational motions are linear combination of normal modes and hence vibrational spectroscopies provide an indirect way to probe the structure. In disordered materials, for example, such as crystalline-like materials or glasses, it can provide information hardly accessible otherwise. However, the atomic disorder lifts the selection rules and eventually produces strong line broadening of the vibrational responses. This departure from the theoretical framework combined with the overlapping of the responses often limits quantitative data treatments. For the present case of glasses, the elementary structural units constituting the materials ( $\text{SiO}_4$  tetrahedra,  $\text{BO}_3$  triangles, etc.) are often well defined and their inelastic scattering may therefore

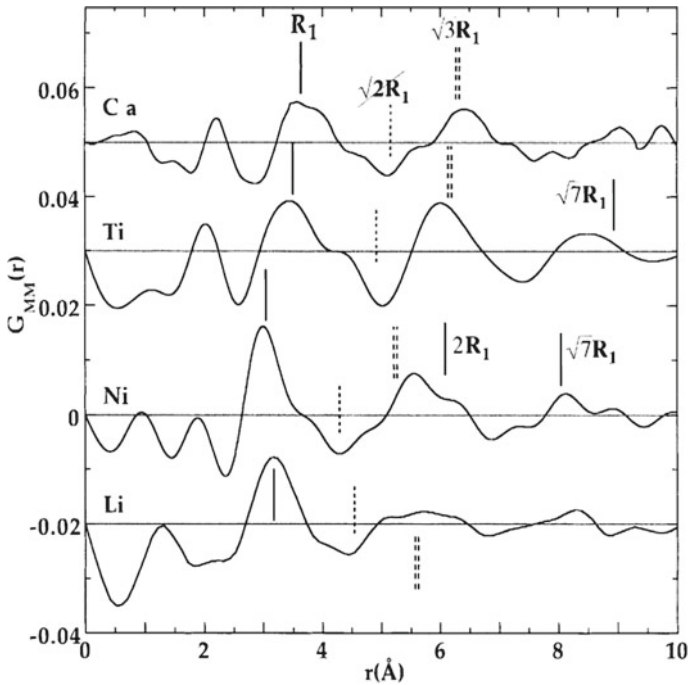


**Fig. 7.15** Second difference correlation function in various glasses: Ca in CaO-SiO<sub>2</sub> [11], Ti in K<sub>2</sub>O-TiO<sub>2</sub>-2SiO<sub>2</sub> [4], Ni in 2CaO-NiO-3SiO<sub>2</sub> [12] and Li in LiSi<sub>2</sub>O<sub>5</sub> [43].  $R_1$  is the first M-M distance (from [5])

fulfil, at least partially, the molecular selection rules. Despite, this departure from the theoretical framework considerably limits the breadth of the vibrational analysis. Nowadays, one way to get around this issue is to confront spectroscopic data with numerical simulations.

In this section, we will briefly describe the origin of inelastic scattering and give the selection rules for the case of Raman spectroscopy. The reader will find the details of the calculation in the book “Teaching Glass Better” where the treatment has been done in full [22]. Examples of the description of glassy structures from their Raman spectra will be given at the end of the chapter.

### 7.2.1 Inelastic Scattering Spectroscopy

Within the set of available vibrational spectroscopies, it is worth separating scattering techniques from “resonant” (non-scattering) in-lab experiments as for example infrared absorption and microwave techniques. In infrared spectroscopy, the medium is excited by a polychromatic beam in the wavelength region  $\sim 0.5$  mm to  $1 \mu\text{m}$ . These

IR-wavelengths exactly overlap those of the vibrations and the response results from a resonant process between the incoming beam and the vibrations. Only modes which modulate the dipole moment  $\mu$  of the molecule, i.e. polar modes, are involved in the interaction process. Microwave acoustics may be defined as the subject embodying the propagation of acoustic waves in solid-state materials at-micron-order wavelength. Here, a transducer is used for the emission (and possibly the reception) of the microwave signal. When its frequency matches that of the sound velocities in the media the microwave acoustic modes propagate and their velocity and attenuation are measured.

By contrast, an inelastic scattering experiment is a non-resonant process where the media is irradiated by a monochromatic beam, and the frequency dependence of the radiation scattered under the angle  $\theta$  is analysed (Fig. 7.16b). The interaction can be viewed as a two photon process where an incident photon  $\omega_I$  scatters a photon at  $\omega_S$  after interaction with an excitation  $\Omega$  in the medium (Fig. 7.16a). The latter can be either an optic vibration (Raman) an acoustic mode (Brillouin) or a relaxation (Brillouin and Raman), as shown in Fig. 7.16c.

The scattering wave vector  $q$  of the experiment and the running frequency  $\omega$  are defined by the conservation of momentum and energy (kinematic conditions). A peak develops in the vibrational spectral when  $\omega$  and  $q$  equal that of the excitation,  $\Omega$  and  $Q$ , respectively, and then:

$$Q = q = \pm(k_S - k_I) \quad (24a)$$

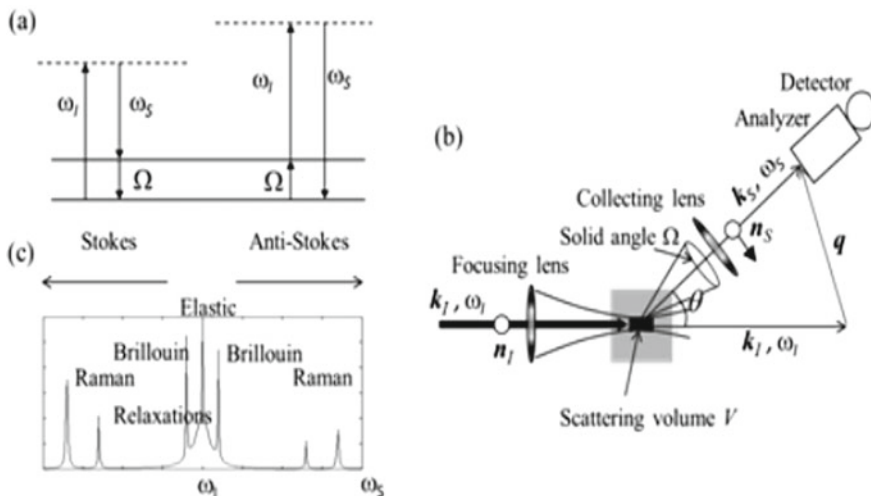


**Fig. 7.16** **a** Inelastic scattering diagram, **b** schematic view of a scattering experiment and **c** typical inelastic spectrum comprising optic vibrations (Raman), acoustic modes (Brillouin) and relaxational motions (Brillouin and Raman). The elastic peak at  $\omega = \omega_I$  is also shown (from [22])

$$\Omega = \omega = \pm(\omega_S - \omega_I) \quad (24b)$$

During the scattering process, a phonon is created (Stokes process) or annihilated (anti-Stokes process). The signs – and + in Eq. 7.24 define Stokes ( $\omega_S = \omega_I - \Omega_{\text{Stokes}}$ ) and anti-Stokes ( $\omega_S = \omega_I + \Omega_{\text{anti-Stokes}}$ ) processes, respectively. The efficiency of the two processes is controlled by the Bose–Einstein population factor

$$n(\omega) = \frac{1}{\exp\left(\frac{\hbar\Omega}{k_B T}\right) - 1}, \quad (7.25)$$

where  $k_B$  is the Boltzmann's constant and  $T$  the sample temperature. Stokes and anti-Stokes responses can be related as follow

$$\frac{I_{\text{Stokes}}}{[n(\omega) + 1]} = \frac{I_{\text{Anti-Stokes}}}{n(\omega)} \quad (7.26)$$

where  $I_{\text{Stokes}}$  and  $I_{\text{Anti-Stokes}}$  are the intensities measured in the Stokes and anti-Stokes side, respectively. In practice, a correction by Eq. 7.26 is necessary to normalize spectra obtained at different temperatures. Equation 7.26 can also be used to extract an unknown background from a given spectrum. This deserves, however, to measure both Stokes and anti-Stokes responses.

## 7.2.2 Origin of the Scattering

According to the linear response theory, the intensity  $I(\mathbf{q}, \omega)$  scattered by an elementary volume  $V$  in the material is proportional to the space and time Fourier transform of the correlation function of the physical quantity  $A$  which couples with the incoming radiation [1]:

$$I(\mathbf{q}, \omega) \propto \text{FT} \left\{ \int_V \int_t A(\mathbf{r}, t) A(\mathbf{r} + \mathbf{r}', t + \tau) dt d\mathbf{r} \right\} \quad (7.27)$$

In Eq. (7.27)  $A(\mathbf{r}, t)$  represents the space and time fluctuations of  $A$  (noise signal) and the integral

$$G(\mathbf{r}', \tau) = \langle A(\mathbf{r}, t) A(\mathbf{r} + \mathbf{r}', t + \tau) \rangle = \int_V \int_t A(\mathbf{r}, t) A(\mathbf{r} + \mathbf{r}', t + \tau) dt d\mathbf{r} \quad (7.28)$$

is the space and time correlation function of  $A(\mathbf{r}, t)$ .

**Table 7.2** Physical quantity at the origin of the scattering depending on the incident radiation

Radiation (perturbation)	Variable that couples with the incident radiation	Scattered intensity
X-rays	Electronic density of charges	$\text{FT}\{\langle \rho_e(0, 0) \rho_e(\mathbf{r}, t) \rangle\}$
Light	Electrical polarization	$\text{FT}\{\langle \mathbf{p}(0, 0) \mathbf{p}(\mathbf{r}, t) \rangle\}$
Raman	Dynamical polarizability	$\text{FT}\{\langle \alpha'(0, 0) \alpha'(\mathbf{r}, t) \rangle\}$
Hyper-Raman	Dynamical hyperpolarizability	$\text{FT}\{\langle \beta'(0, 0) \beta'(\mathbf{r}, t) \rangle\}$
Brillouin	Polarizability via photoelastic tensor	$\text{FT}\{\langle p'(0, 0) p'(\mathbf{r}, t) \rangle\}$
Neutrons	Neutron scattering length	$\text{FT}\{\langle b(0, 0) b(\mathbf{r}, t) \rangle\}$

It is worth noting that the integration in space gives rise to the elastic response described in Sect. 7.1 and in case of a scattering by the electrons, the result corresponds to the sum in given by Eq. (7.3). For inelastic scattering, time correlation function adds to the spatial one treated above. If there exist spatial correlations between  $A(\mathbf{r}, t)$  at different points, one must take the phase into account and the intensity will depend on the scattering vector  $\mathbf{q}$ . This is the case for example for acoustic modes which are plane waves, but not for optic modes in liquids which are fully localized vibrations, i.e. without phase relationship between vibrating units.

Expression (7.28) applies whatever the nature of the incident radiation, as summarized in Table 7.2: for X-rays and neutron scattering,  $A$  stands for the electronic density  $\rho_e$  and the neutron scattering length  $b$ , respectively. For light scattering,  $A$  associates with the induced dipole  $\mathbf{p}$  which can be expanded in terms of the incident electric field  $\mathbf{E}_I$ . Up to the second order, it reads:

$$\mathbf{p} = \alpha \mathbf{E}_I + \frac{1}{2} \beta \mathbf{E}_I \mathbf{E}_I + \dots \quad (7.29)$$

where  $\alpha$  is the polarizability tensor responsible for Raman scattering, and  $\beta$  the hyperpolarizability tensor responsible for hyper-Raman scattering. It is the modulation of  $\delta \mathbf{p}$  with respect to the normal coordinate  $X$  of the mode which leads to the scattering, i.e.  $\alpha' = \partial \alpha / \partial X$  and  $\beta' = \partial \beta / \partial X$ . The induced dipole  $\mathbf{p}$  also modulates the photoelastic (Pockel's) tensor  $p$  giving rise to the Brillouin scattering from acoustic modes. It is worth noting that all of these physical quantities are modulated simultaneously by the incident radiation  $\mathbf{E}_I$ . It is the spectrometer which will select which one will be probed: the high resolution of a Fabry–Perot interferometer is used to probe low frequency vibrations and hence Brillouin scattering by sound waves. A grating diffractometer will detect optic vibrations at higher frequencies. To measure Raman modes, the central wavelength of the diffractometer must be set close to that of the incoming laser source, and for hyper-Raman scattering, close to half the latter (double frequency).

A treatment of the oscillating dipole shows that the scattered field  $\mathbf{E}_S$  is proportional to the induced dipole  $\mathbf{p}$ , and it is possible to calculate the exact expression of the intensity scattered in a light scattering experiment, known as the Wiener–Khinchine

theorem:

$$I(\mathbf{q}, \omega) = \text{FT} \left\{ \int_V \int_t E_S^*(\mathbf{r}, t) E_S(\mathbf{r} + \mathbf{r}', t + \tau) dt d\mathbf{r} \right\} \quad (7.30)$$

Regarding the experimental scheme shown in Fig. 7.16b, the time-dependent (inelastic) term of the above expression can be understood as follow:

1. A photon is scattered under the angle  $\theta$  at time  $t$  and another at time  $t' = t + \tau$ , leading to the scattered fields  $E_S(t)$  and  $E_S(t + \tau)$ , respectively.
2. The detector measures the intensity of the scattered field. However, the photons emitted at  $t$  and  $t'$  may have a different optical path in the spectrometer, and both possibly reach the detector at the same time. Therefore the product  $E_S^* \cdot E_S$  should be averaged over all photons emitted at  $t$  and  $t + \tau$ , that is  $\langle E_S^*(t) \cdot E_S(t + \tau) \rangle$ . This strictly corresponds to the temporal correlation function of  $E_S$ .
3. The spectrometer (“analyser” in Fig. 7.16b) makes the Fourier transform of the scattered fields,  $\text{TF}\{E_S(t)\} = \int E_S(t) e^{-i\omega t} dt$  and  $\text{TF}\{E_S(t')\} = \int E_S(t') e^{-i\omega t'} dt'$ . Therefore, the detector exactly measures the spectral component of Eq. (7.30):

$$I(\omega) = \text{FT}\{\langle E_S^*(t) E_S'(t + \tau) \rangle\} \quad (7.31)$$

### 7.2.3 Raman Selection Rules

The calculation of Eq. (7.31) is performed in many textbooks [3, 16] as well as in *Teaching Glass Better* [22]. The Raman intensity for Stokes scattering reads:

$$I(\omega) = \frac{\hbar n_S N \omega_I \omega_S^3}{2 n_I (\epsilon_0 c^2)^2} \left( \hat{\mathbf{n}}_S \cdot \overline{\overline{\alpha'}} \cdot \hat{\mathbf{n}}_I \right)^2 \frac{n(\omega) + 1}{\omega} S_{\text{norm}}(\omega). \quad (7.32)$$

The term  $\omega_S^3$  tells that the inelastic intensity measured by CCD camera is proportional to  $1/\lambda_S^3$  and not  $1/\lambda_S^4$  as for photomultipliers (as expressed by [29]). The double tensor product in Eq. (7.32):

$$R = \left( \hat{\mathbf{n}}_S \cdot \overline{\overline{\alpha'}} \cdot \hat{\mathbf{n}}_I \right)^2 \quad (7.33)$$

accounts for the *fluctuations of the dynamical polarizability*  $\overline{\overline{\alpha'}}$  *along the incident* ( $\hat{\mathbf{n}}_I$ ) *and scattered* ( $\hat{\mathbf{n}}_S$ ) *polarization direction of the beam*. It is this term which is at the origin of the Raman selection. The symmetry of the tensor  $\overline{\overline{\alpha'}}$  for every Raman active vibrations and every crystalline space group is summarized in crystallographic



books [26, 30]. Finally,  $S_{\text{norm}}(\omega)$  is the normalized spectral response function. It is defined so that its integral over  $\omega$  is equal to one for any couple  $(\omega_0, \Gamma)$  of the mode.

### Crystals

In crystals, the intensity of Raman active modes ( $\alpha' \neq 0$ ) is modulated by the product

$$R = \sum_{\delta} \sum_{i,j} |n_i^I n_j^S \alpha_{ij}^{\delta}|^2 \quad (7.34)$$

where  $\delta$  denotes the degeneracy of the mode, and the indices  $i$  and  $j$  refer to the laboratory frame. It is worth noting that the direction of  $\mathbf{q}$  does not play a role in the Raman selection rules.

### Gases and liquids

Molecular selection rules account for systems with very weak intermolecular interactions defining perfectly incoherent scattering. The vibrations are perfectly localized and the motions of the molecules are independent to each other. This usually concerns gases and liquids. For such disordered media, Eq. (7.33) has to be averaged over all accessible orientations of the molecules:

$$\langle R \rangle = \left\langle \sum_{\delta} \sum_{i,j} |n_i^I n_j^S \alpha_{ij}^{\delta}|^2 \right\rangle \quad (7.35)$$

For a collection of randomly orientated molecules, the calculation shows that there remain only two independent quantities: the polarized ( $\langle R_{\parallel} \rangle$ ) and depolarized ( $\langle R_{\perp} \rangle$ ) Raman intensities. If the indices  $i, j$  refer to indexes in the molecular frame, one obtains [6]:

$$\langle R_{\perp} \rangle = \frac{1}{15} \sum_i \alpha_{ii}^2 - \frac{1}{15} \sum_{i<j} \alpha'_{ii} \alpha'_{jj} + \frac{1}{5} \sum_{i<j} \alpha_{ij}^2 \quad (36a)$$

and

$$\langle R_{\parallel} \rangle = \frac{1}{5} \sum_i \alpha_{ii}^2 + \frac{2}{15} \sum_{i<j} \uparrow \alpha'_{ii} \alpha'_{jj} + \frac{4}{15} \sum_{i<j} \alpha_{ij}^2. \quad (36b)$$

It can be shown that the Raman depolarization ratio defined as  $\rho = \langle R_{\perp} \rangle / \langle R_{\parallel} \rangle = I_{\perp}^{RS} / I_{\parallel}^{RS}$  lies between 3/4 and 0 for depolarized and fully polarized vibrations, respectively.

Finally, for the crystalline and liquid cases, according to the *fluctuation-dissipation* theorem, the dissipative part of the dynamical susceptibility  $\chi_M(\omega)$ , namely  $\text{Im}[\chi_M(\omega)]$ , is proportional to the response function  $S_{\text{norm}}(\omega)$ . For an oscillator and a relaxator, the latter reads:

$$\text{Im}[\chi_M(\omega)] = \frac{\Gamma\omega}{(\omega_0^2 - \omega^2)^2 + \Gamma^2\omega^2} \propto S_{\text{osc}}(\omega) \quad (37a)$$

and

$$\text{Im}[\chi_M(\omega)] = \frac{\omega/\tau_0}{\omega^2 + 1/\tau_0^2} \propto S_{\text{rel}}(\omega), \quad (37b)$$

respectively. For weakly damped vibrations, namely  $\Gamma \ll \omega$ ,  $S_{\text{osc}}(\omega)$  can be approximated to a Lorentzian.

### Glasses

In glasses, the elementary units constituting the network are distorted and the molecular selection rules are often lifted, excepted in simple glasses where they partially apply [19, 32]. In most cases, the coupling term  $R$  is not known and it is replaced by a frequency-dependent coefficient  $C(\omega)$ . Similarly, the vibrational response function of a mode  $\sigma$  transforms into a distribution of oscillators of slightly different frequencies leading to a ‘‘Raman vibrational’’ density of states’’  $g_\sigma(\omega)$ . Accordingly, Eq. (7.28) reads:

$$I_\sigma \propto I_L \frac{n_S}{n_I} N \omega_S^3 \frac{[n(\omega) + 1]}{\omega} C_\sigma(\omega) \cdot g_\sigma(\omega) \quad (7.38)$$

where  $N$  is the number of scatterers and can be replaced by the sample density  $\rho$ . The quantity to be conserved in a Raman experiment is, therefore,  $I_{\sigma,N} = C_\sigma(\omega) \cdot g_\sigma(\omega)$ .

Another effect that distorts the response function in glasses arises from the spatial localization of extended waves due to the random medium- and long-range interatomic connectivity. This induces a loss of coherence of the scattering process due to the partial or total meaningless of the wave vector  $\mathbf{Q}$  of the vibration [24]. In crystals, modes are extended, i.e., their spatial coherence length is larger than the probed wavelength, and hence, they propagate as plane waves with atomic displacements  $X(\mathbf{r}, t) = X_0 e^{\pm i(\mathbf{Q}\mathbf{r} - \Omega t)}$ . Conversely in liquids, there is no phase relationship between vibrations at  $\mathbf{r}$  and  $\mathbf{r}'$ . In that case,  $\mathbf{Q}$  is meaningless and the atomic displacements read  $X(t) = X_0 e^{\pm i\Omega t}$ . Glasses provide a more complex situation where a mode  $\sigma$  can involve one elementary unit (‘‘liquid-like’’ vibrations such as the ring modes in  $\text{SiO}_2$  and  $\text{B}_2\text{O}_3$ , several elementary units as for the Si–O–Si bending modes constituting the R-band in  $\text{SiO}_2$  [10], and possibly a large number of elementary units (‘‘crystal-like’’ vibrations such as the rocking of Si–O–Si structures responsible for the polar mode  $\text{TO}_4$  in  $\text{SiO}_2$  [19, 37]. This obviously affects both the selection rules and the response function  $S_\sigma(\omega)$  in a non-trivial way.

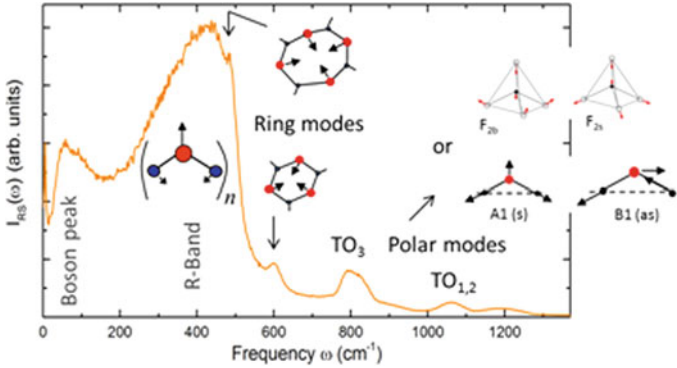


Fig. 7.17 Atomic displacements of the Raman modes of  $\nu$ -SiO<sub>2</sub>

## 7.2.4 Raman Spectroscopy in Silicate Glasses

### Vibrations in vitreous silica

The vibrational spectra of simple oxide glasses are fairly well known. We refer the reader to [17, 17], and references therein, for a complete description of the Raman, infrared and hyper-Raman modes in the glass formers  $\nu$ -SiO<sub>2</sub> and  $\nu$ -B<sub>2</sub>O<sub>3</sub>. In  $\nu$ -SiO<sub>2</sub>, the broad R-band in the Raman spectrum corresponds to bending motions of (Si–O–Si)<sub>n</sub> bonds with  $n \geq 5$  (Fig. 7.17). The atomic structures with  $n = 3$  and  $n = 4$  construct rings whose bending, also called “breathing modes”, lead to the narrow D1 and D2 peaks at 490 cm<sup>-1</sup> and 605 cm<sup>-1</sup>, respectively.

The three peaks at higher frequency, TO<sub>1,3</sub>, are infrared active vibrations and hence correspond to motions which carry a dipole moment [28]. The underlying atomic displacements can be interpreted by considering either the SiO<sub>4</sub> tetrahedron (T<sub>d</sub> point group) or the Si–O–Si (C<sub>2v</sub> point group) unit structures [19, 33]. In the latter case, TO<sub>1</sub> and TO<sub>2</sub> modes combine symmetric (s) and antisymmetric (as) stretching. Finally, the boson peak at low frequency is associated to coupled translation and libration motions of rigid SiO<sub>4</sub> tetrahedra. The librational component is active in hyper-Raman scattering [17] and has a major weight in the density of vibrational states [2], while Raman is likely more sensitive to the translational component [19].

### Si–O–Si angle in sodosilicate glasses

It has been shown that the frequency of the R, D1 and D2 bands can be related the Si–O–Si angle [18]: the higher the frequency, the weaker the angle. This provides a way to quantitatively estimate the angle reduction in permanently densified silica [18] and in compressed silica [36]. Interestingly, the conversion also works in sodosilicate glasses [21]. Here, the R-band splits into two components when increasing the sodium concentration (Fig. 7.18). The broad component decreases with sodium content and was interpreted as Si–O–Si bending in the connected network (R-like band). Conversely, the narrow one increases with sodium content and is assumed to

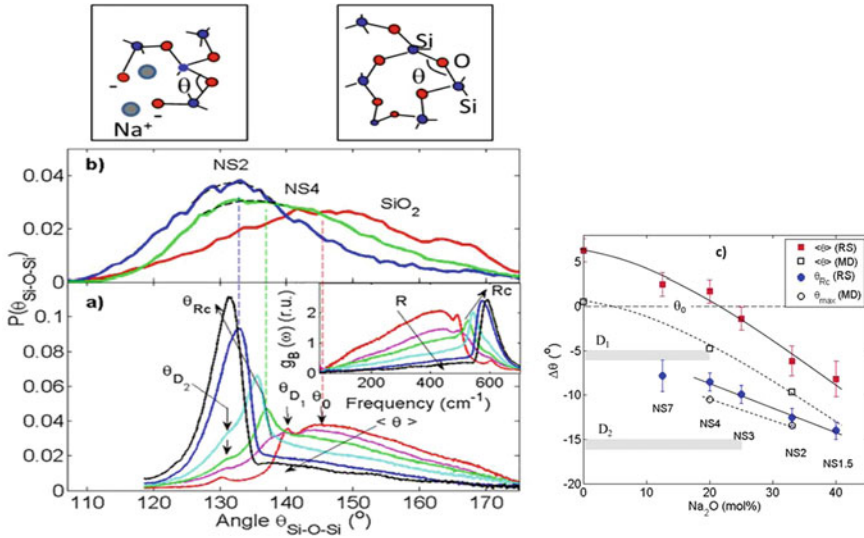


**Fig. 7.18** Si–O–Si angular distribution  $P(\theta)$  in the series of sodosilicate glasses, from  $\text{SiO}_2$  to NS1.5 (from [21]). **a**  $P(\theta)$  extracted from the polarized (VV) Raman spectra: from red to black curve:  $\text{SiO}_2$ , NS7, NS4, NS3, NS2, NS1.5. The inset shows  $g_B(\omega)$  after subtraction of the boson peak. **b**  $P(\theta)$  obtained from atomistic simulations in  $\text{SiO}_2$ , NS4 and NS2 [31]. Top of panel b: schematic view of sodosilicate-like regions (left) and silica-like regions (right). **c** Variation of the Si–O–Si angle  $\theta$  as a function of the sodium content in regions close to sodium atoms ( $\theta_{\text{Rc}}$ ) and in silica-like regions ( $\langle \theta \rangle$ ) obtained from Raman data (RS) and ab initio molecular dynamic simulations (MD)

arise from Si–O–Si bending close to sodium atoms (Rc band). Cations depolymerize the silica network and hence release the constraints. One therefore naturally expects smaller Si–O–Si angles, with weaker angular spread, giving the relatively narrow Rc component at higher frequency than the R-like one.

*Cation modes in ternary aluminosilicates*

The depolarized Raman spectra (VH) in binary- and ternary aluminosilicate glasses present two modes, hereafter called  $\omega_1$  and  $\omega_2$ , which are associated to vibrations of the cations [20]. In binary compounds, both modes originate from vibration of the cation relative to its non-bridging oxygen (Fig. 7.19a). In ternary glasses (Fig. 7.19b), the two modes are still present, and similarly to the binary situation, the intensity of  $\omega_1$  decreases to zero as the cation content [20, 23]. This shows that network modifier and charge compensator cations participate to this mode. The intensity of  $\omega_2$  behaves a very different way. It decreases to zero when the glass reaches the peraluminate join  $R = 1$ , where  $R$  is the ratio between cation oxide and alumina content. This observation holds for any alkaline and alkaline earth cations (except Mg), highlighting that in ternary aluminosilicate glasses, the Raman mode  $\omega_2$  solely arises from cations at modifier place [23]. Accordingly, the VH Raman spectrum provides a way to detect non-network former cations in the glass.

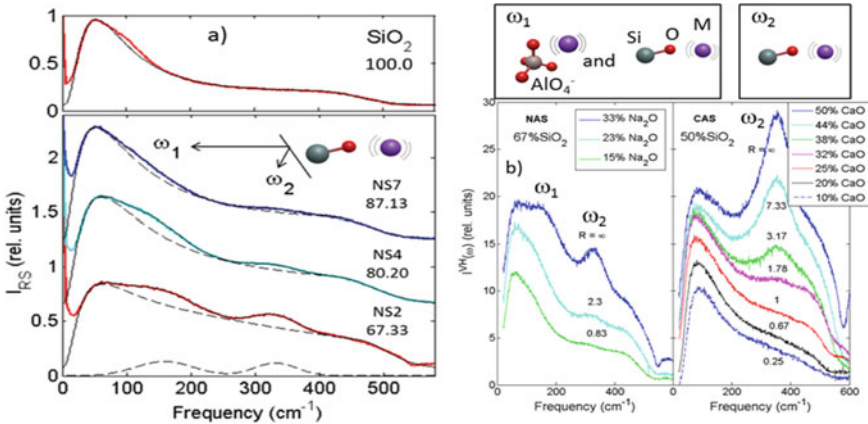


**Fig. 7.19** **a** Depolarized Raman spectra (VH) of sodosilicate glasses NS2, NS4 and NS7 and pure silica in the region of the cations modes  $\omega_1$  and  $\omega_2$  (from [23]). The solid lines result from a fit using a modified lognormal function for the boson peak and its tail and Gaussians for the cation modes  $\omega_1$  and  $\omega_2$  (dashed lines). **b** VH spectra in sodo-aluminate silica (NAS) and calcium-alumino silica (CAS), showing that the cation mode  $\omega_2$  decreases to zero at  $R \cong 1$  [20]. On top: schematic view of the cation (M) vibrations  $\omega_1$  and  $\omega_2$  in ternary glasses. Note that alkali-earth cations vibrate around two non-bridging oxygens or two  $\text{AlO}_4^-$  tetrahedra

### 7.3 Conclusion

We have seen that X-ray and neutron diffraction techniques, often associated with numerical simulation, allow a better understanding of the organization of the disordered atomic structure of a glass. The main limitation of these techniques is the number of different chemical elements in the material. As far as inelastic scattering is concerned, the lifting of the Raman selection rules often limits the analysis of the vibrations to simple materials, except may be for modes which are well defined and decoupled from the rest of the network. Despite, it is worth to correlate the Raman data to other light spectroscopies experiments such as IR-absorption or hyper-Raman scattering, and to compare the vibrational spectroscopy of the glass to that of the corresponding crystal, if exists. The support of classical or ab-initio numerical simulation methods is also a real asset. Quantum-based techniques are currently mature for calculating IR spectra and Raman spectra [27], but still, they are limited to a relatively weak number of atoms, and therefore mostly apply to simple glasses. However, new methods allowing to model amorphous materials with a large number of atoms are emerging [7, 15] and open a way for calculating multicomponent glasses.

## References

1. Berne BJ, Pecora R (1976) *Dynamic light scattering*. Wiley, New York
2. Buchenau U, Prager M, Nücker N et al (1986) Low frequency modes in vitreous silica. *Phys Rev B* 34:5665–5673
3. Chu B (1974) *Laser light scattering*. Academic, New York
4. Cormier L, Gaskell PH, Calas G, Soper AK (1998) Medium range order around titanium in a silicate glass studied by neutron diffraction with isotopic substitution. *Phys Rev B* 58:11322–11330
5. Cormier L, Calas G, Gaskell PH (2001) Cationic environment in silicate glasses studied by neutron diffraction with isotopic substitution. *Chem Geol* 174:349–363
6. Cyvin SJ, Rauch JE, Decius JC (1965) Theory of hyper-Raman effects (nonlinear inelastic scattering): selection rules and depolarization ratios of the second-order polarizability. *J Chem Phys* 43:4083
7. Deringer VL, Bernstein N, Csanyi G et al (2021) Origins of structural and electronic transitions in disordered silicon. *Nature* 589:59–64
8. Eckersley MC, Gaskell PH, Barnes AC, Chieux P (1988) Structural ordering in a calcium silicate glass. *Nature* 335:525–527
9. Faber TE, Ziman JM (1965) A theory of the electrical properties of liquid metals: III. The resistivity of binary alloys. *Philos Mag* 11:153–173
10. Galeener FL, Leadbetter AJ, Stringfellow MW (1983) Comparison of the neutron, Raman, and infrared spectra of vitreous SiO<sub>2</sub>, GeO<sub>2</sub>, and BeF<sub>2</sub>. *Phys Rev B* 27:1052–1078
11. Gaskell PH, Eckersley MC, Barnes AC, Chieux P (1991) Medium range order in the cation distribution of a calcium silicate glass. *Nature* 350:675–677
12. Gaskell PH, Zhao Z, Calas G, Galoisy L (1992) In: Pye LD, LaCourse WC, Stevens HJ (eds) *The physics of non-crystalline solids*. Taylor and Francis, London, pp 53–58
13. Goubeau J, Keller H (1953) Raman-Spektren und Structure von Boroxol Verbindungen. *Z Anorg Allg Chem* 272:303–312
14. Hannon AC, Grimley DI, Hulme RA, Wright AC, Sinclair RN (1994) Boroxol groups in vitreous boron oxide: new evidence from neutron diffraction and inelastic neutron studies. *J Non-Cryst Solids* 177:299–316
15. Hasmy A, Ispas S, Hehlen B (2021) Percolation transitions in compressed SiO<sub>2</sub> glasses. *Nature* (in press)
16. Hayes W, Loudon R (2004) *Scattering of light by crystals*. Dover, Mineola, NY
17. Hehlen B, Courtens E, Vacher R, Yamanaka A, Kataoka M, Inoue K (2000) Hyper-Raman scattering observation of the boson peak in vitreous silica. *Phys Rev Lett* 84:5355–5358
18. Hehlen B (2009) Inter-tetrahedra bond angle of permanently densified silicas extracted from their Raman spectra. *J Phys Condens Matter* 22:025401
19. Hehlen B, Simon G (2012) The vibrations of vitreous silica observed in hyper-Raman scattering. *J Raman Spectrosc* 43:1941–1950
20. Hehlen B, Neuville DR (2015) Raman response of network modifier cations in alumino-silicate glasses. *J Phys Chem B* 119:4093–4098
21. Hehlen B, Neuville DR, Kilymis D, Ispas S (2017) Bimodal distribution of Si–O–Si angles in sodo-silicate glasses. *J Non-Cryst Solids* 469:39–44
22. Hehlen B, Vacher R (2018) Light scattering by atomic vibrations. In: Takada A, Parker J, Duran A, Bange K (eds) *Teaching glass better*. International Commission on Glass, Madrid
23. Hehlen B, Neuville DR (2020) Non network-former cations in oxide glasses spotted by Raman scattering. *Phys Chem Chem Phys* 22:12724–12731
24. Hehlen B, Rufflé B (2021) Atomic vibrations in glasses. In: Richet P (ed) *Encyclopedia of glass science, technology, history, and culture*, section III.4. Wiley, New York
25. Henninger EH, Buschert RC, Heaton LeRoy (1967) Atomic structure and correlation in vitreous silica by X-ray and neutron diffraction. *J Phys Chem Solids* 28:423–432
26. Herzberg G (1945) *Molecular spectra and molecular structure*, vol II. Infrared and Raman spectra of polyatomic molecules. Van Nostrand, New York

27. Kilymis D, Ispas S, Hehlen B, Peugnet S, Delaye JM (2019) Vibrational properties of sodosilicate glasses from first-principles calculation. *Phys Rev B* 99:054209
28. Kirk CT (1988) Quantitative analysis of the effect of disorder-induced mode coupling on infrared absorption in silica. *Phys Rev B* 38:1255–1273
29. Long DA (1977) Raman spectroscopy. McGraw Hill, New York
30. Poulet H, Mathieu JP (1970) Spectres de vibrations et symétrie des cristaux. Gordon & Breach, Paris
31. Rahmani A, Benoit M, Benoit C (2003) Signature of small rings in the Raman spectra of normal and compressed amorphous silica: a combined classical and ab initio study. *Phys Rev B* 68:184202
32. Simon G, Hehlen B, Vacher R, Courtens E (2007) Hyper-Raman scattering analysis of the vibrations in vitreous boron oxide. *Phys Rev B* 76:054210
33. Taraskin SN, Elliott SR (1997) Nature of vibrational excitations in vitreous silica. *Phys Rev B* 56:8605–8622
34. Warren BE (1934) X-ray determination of the structure of glass. *J Am Ceram Soc* 17:249–254; The diffraction of X-rays in glass. *Phys Rev* 45:657–661
35. Warren BE, Krutter H, Morningstar O (1936) Fourier analysis of X-ray patterns of vitreous SiO<sub>2</sub> and B<sub>2</sub>O<sub>3</sub>. *J Am Ceram Soc* 19:202–205
36. Weigel C, Foret M, Hehlen B, Kint M, Clément S, Polian A, Vacher R, Rufflé B (2016) Polarized Raman spectroscopy of v-SiO<sub>2</sub> under rare-gas compression. *Phys Rev B* 93:224303
37. Wilson M, Madden PA, Hemmati M, Angell CA (1996) Polarization effects, network dynamics, and the infrared spectrum of amorphous SiO<sub>2</sub>. *Phys Rev Lett* 77:4023–4026
38. Wright AC, Clare AG, Grimley DI, Sinclair RN (1989) Neutron-scattering studies of network glasses. *J Non-Cryst Solids* 112:33–47
39. Wright AC (1990) Diffraction studies of glass structure. *J Non-Cryst Solids* 123:129–148
40. Yin CD, Okuno M, Morikawa H, Marumo F, Yamanaka T (1986) Structural analysis of CaSiO<sub>3</sub> glass by X-ray diffraction and Raman spectroscopy. *J Non-Cryst Solids* 80:167–174
41. Zachariasen WH (1932) The atomic arrangement in glasses. *J Am Chem Soc* 54:3841–3851
42. Zarzycki J (1991) Glasses and the vitreous state. Cambridge University Press, Cambridge
43. Zhao J, Gaskell PH, Cluckie MM, Soper AK (1998) A neutron diffraction, isotopic substitution study of the structure of a Li<sub>2</sub>O.2SiO<sub>2</sub> glass. *J Non-Cryst Solids* 232:721–727

# Chapter 8

## Melt-Derived Bioactive Glasses: Approaches to Improve Thermal Stability and Antibacterial Property by Structure–Property Correlation



Sakthi Prasad, Anustup Chakraborty, and Kaushik Biswas

### 8.1 Introduction

Bioactive glasses fall under a class of synthetic biomaterials which exhibits natural bonding with tissues as well as possess the ability to repair, regenerate, and induce growth of tissue at the damaged site through interfacial reactions [1, 2]. Presently, 45S5 glass (Bioglass<sup>®</sup>) has completed 50 years since its discovery and its products have been in clinical usage for the past 35 years [2–4]. A 45S5 is a silicate-based bioactive glass that was first discovered by Prof. Larry Hench at the University of Florida in 1969 and exhibited bone bonding in rats [1, 2, 4]. Prof. Larry Hench had developed bioactive glasses with the idea of finding a material that would integrate with the host tissue inside the human body [2, 4]. Later on, many interesting features were revealed in 45S5 glass which makes it an extraordinary biomaterial. Despite the assumption that 45S5 glass would bond only with the calcified tissues, Wilson et al. have demonstrated the ability of 45S5 glass to bond with soft connective tissues when the interface is immobile [2]. Furthermore, it was discovered that 45S5 glass can interact genetically and stimulate the process of bone formation (osteostimulation) through the process of ion release during its dissolution in the physiological medium [2].

The discovery of 45S5 glass introduced a new class of biomaterials called “Bioactive materials” which exhibit the ability to bond with the host tissue. In bioactive glasses, this natural bonding occurs due to the interfacial layer made of hydroxy-carbonated apatite (HCA) resulting from a series of reactions with the surrounding environment at the host tissue site [1, 5]. This HCA layer is chemically identical to the mineral part of the bone tissue and supports the cells to attach from the host tissue

---

S. Prasad · A. Chakraborty · K. Biswas (✉)  
Specialty Glass Division, CSIR-Central Glass and Ceramic Research Institute, Kolkata 700032,  
India  
e-mail: [kbiswas@cgeri.res.in](mailto:kbiswas@cgeri.res.in)

Academy of Scientific and Innovative Research (AcSIR), Ghaziabad 201002, India



site and proliferate leading to natural bonding. Therefore, bioactive glasses are being widely used for the repair and regeneration of bone and treatments related to bone diseases.

Bioactivity could be categorized into two sub-categories called Class-A bioactivity and Class-B bioactivity based on the interaction of the bioactive material with the host tissue. Class-A biomaterial like 45S5 glass exhibits intracellular and extracellular responses such as osteostimulation, osteoinduction, and osteoproduction [2, 4–6]. Class-A bioactive materials can upregulate cellular activity, activate genetic responses in cells, and help in the differentiation of cells from progenitor cells along with cellular attachment and proliferation [2, 4–6]. Class-B bioactive materials exhibit only extracellular responses such as osteoconduction and help in the attachment and proliferation of cells [2, 4–6].

The bioactive glasses undergo a series of reactions with the physiological medium at the interface of host tissue and bioactive glass leading to a biological bond [4, 5, 7]. It is well established that bioactive glasses convert to bone through 12 steps in which the chemical processes for HCA layer formation and the biological processes for the reconstruction of the HCA layer into the bone matrix are involved [4, 5, 7]. The chemical processes in silicate-based bioactive glasses leading to the formation of the HCA layer have been experimentally determined using Fourier-transform infrared (FTIR) spectroscopy, X-ray diffraction (XRD), scanning electron microscopy (SEM), and energy-dispersive X-ray spectroscopy (EDS) techniques [8]. The first five reaction steps leading to the formation of the HCA layer can occur in any aqueous environment similar to the physiological medium while subsequent reaction steps occur only under *in vivo* conditions. The *in vitro* studies on bioactive glasses is carried out commonly using simulated body fluid (SBF) and TRIS buffer solutions both of which are adjusted to a pH 7.4 at the beginning of the study to match the pH of the physiological medium. In this regard, the work done by Kokubo et al. needs to be highlighted, since the SBF prepared according to their method has significantly improved the reproducibility and reliability of predicting the *in vitro* bioactive behavior of the bioactive glasses [9].

Commercial melt-derived silicate bioactive glasses include 45S5 glass (Bioglass®), S53P4 glass (Bonalive®), and 13-93 glass [10–12]. The 45S5 glass received its United States food and drug administration (FDA) approval and European Conformité Européenne (CE) mark in 1985 and 1995, respectively [4, 13, 14]. While S53P4 glass received a CE mark in 2006 and was approved for FDA 510k in 2008 [14, 15], 13-93 glass also obtained clinical approval for *in vivo* usage in Europe and the USA [16–18].

The bioactive glass products based on 45S5, 13-93, and S53P4 glass compositions are used commercially for the treatments of periodontal, orthopedic, maxillofacial, and dental defects [13, 14, 19–22]. Although the monolithic devices made of Bioglass® such as middle ear prosthesis (MEP) or endosseous ridge maintenance implant (ERMI) showed significant improvement over conventional hydroxyapatite (HA) implants, MEPs, and ERMIs were discontinued due to their availability in fixed shapes and sizes [13, 23]. Afterwards, bioactive glass particulates and putty with different particle size ranges were clinically well accepted for the repair of

bone defects. Furthermore, NovaMin<sup>®</sup> (NovaMin Technology, FL, owned by GlaxoSmithKline, UK), particulates of 45S5 glass was developed in 2004 and are used in toothpaste for treating dentine hypersensitivity [13, 19]. NovaMin<sup>®</sup> particles tend to attach to the exposed dentinal tubules under the oral environment leading to the remineralization of the eroded tooth surface. Furthermore, bioactive glasses have been successfully coated over the metallic implants to provide osseointegration with host tissues. Additionally, Vitryxx<sup>®</sup> (Schott, Germany), particulates of 45S5 glass are commercially used in skincare-and nailcare-based cosmetics. Moreover, strontium containing silicate-based bioactive glass called Stronbone<sup>™</sup> developed by Hill and Stevens has received European CE approval for clinical usage in bone remodeling and osteoporosis treatments [22].

Commercial melt-derived silicate-based bioactive glasses have been clinically used for treatments in more than millions of patients until now [11, 13, 14, 19]. However, a major challenge associated with these glasses is their tendency to crystallize uncontrollably during thermal treatments due to low thermal stability [24–26]. Therefore, these glasses could not be subjected to scaffold synthesis through thermal treatments and fiber drawing at high temperatures [24–26].

Scaffolds and fibers are advantageous in providing biological support to cells for attachment and adequate mechanical performance at the bone defect [27, 28]. Development of scaffolds requires the sintering of green bodies prepared from the bioactive glass powders using foam replication, freeze-drying, extrusion, porogen inclusion techniques, and additive manufacturing techniques such as 3D printing [27, 28]. The sintering process of consolidating the glass powders is driven by the viscous flow mechanism which occurs at temperatures above the glass transition temperature ( $T_g$ ) [29, 30]. The viscous flow-assisted sintering process which is required to develop scaffolds with adequate mechanical strength and toughness could get hindered due to the uncontrolled crystallization in bioactive glasses [29–31]. Similarly, crystallization during the fiber drawing process can lead to difficulty in obtaining uniform amorphous fibers [32, 33]. Moreover, uncontrolled crystallization during sintering can result in uneven dissolution rates from the crystalline and residual glassy phases further leading to irregular/delayed formation of apatite. Therefore, there has been a need to formulate bioactive glasses possessing superior thermal stability which support thermal processing and sintering above  $T_g$  without devitrification.

Bacterial infections in the human body are prone to occur either during the exposure of the inner tissue during trauma, via the bloodstream or during surgeries (nosocomial origin) [34]. Antibacterial properties in bioactive glasses are beneficial to prevent implant-related infections post-surgery of nosocomial origin and also for the treatment of osteomyelitis, caries, and periodontal diseases caused by bacterial infections [21, 35–40]. Conventional treatment for chronic osteomyelitis involves multiple surgical procedures and prolonged hospitalization for the removal of the infected part, antibiotic treatment, and tissue regeneration at the defect site [20–22, 34, 37, 41–43]. Moreover, the widespread usage of antibiotic drugs has resulted in the emergence of multidrug-resistant bacteria which makes it difficult to cure the disease with conventional treatment [44, 45]. In recent years, bioactive glasses are being explored as an alternative to conventional antibiotic treatments after the

evidence of bactericidal action along with bone regeneration [20–22, 34, 37, 41–45]. Furthermore, it has been shown that repetitive usage of bioactive glasses for the treatment of bacterial infections has not reduced their efficacy [44]. In 45S5 and S53P4 bioactive glasses, the rise in pH and the increase in osmotic pressure during dissolution were attributed to their antibacterial properties [39]. However, bioactive glasses can be designed to impart antibacterial action involving mechanisms other than the mechanisms involved with the increase in pH and osmotic pressure against a wide spectrum of disease-causing bacteria. Another major concern arises due to the involvement of biofilm-forming bacteria leading to an increased risk of implant failures. Additionally, long term and controlled release of ions is required for improving the antibacterial properties of glasses which can be achieved by structural modification of bioactive glasses.

## 8.2 General Composition of Melt-Derived Bioactive Glasses

The bioactive glasses are generally prepared through conventional melt-quenching and sol–gel techniques [46, 47]. The preparation of glasses through the conventional melt-quenching technique involves lesser handling steps compared to the sol–gel technique [46, 47]. In the conventional melt quenching technique, steps such as batch preparation, batch charging and melting, melt refining and homogenization, and quenching/cooling of melts are carried out. However, in the sol–gel technique, processes involving solvent selection, precursor selection and addition, catalyst and surfactant addition, control of pH and temperature, gelation steps, removal of solvents and other organic additives through heat treatments are performed. Though the sol–gel glass synthesis technique offers an advantage of forming nanoporous and textured nano-sized glass powders, the melt-quenching technique offers large scale, homogenous, and faster production of glass powders [46, 47].

During the bioactive glass preparation through the conventional melt-quenching route, the batches are prepared with appropriately weighed raw materials in the form of oxides, carbonates, nitrates, sulfates, and halides followed by homogenous mixing [46–48]. The batches are charged in platinum or refractory pots for placing inside the furnace and heated to melting temperatures. An additional batch calcination step may be carried out to remove the gases evolved from the batches before the charging step. The melt is then refined to remove the bubbles and homogenized through mechanical stirring and viscosity-temperature adjustments. The refined and homogenized melts can be either cast into a stainless steel or graphite molds to obtain glass blocks or quenched into the water to obtain glass frits [46–48]. An additional process of annealing is carried out for the melt-casted glass blocks to remove the residual stresses formed during the cooling process [46–48]. The melt-derived bioactive glass particulates are prepared by crushing and grinding the glass blocks and frits [46–48].

Most of the silicate-based melt-derived bioactive glasses like 45S5 and S53P4 glasses are primarily based on the  $\text{SiO}_2\text{--Na}_2\text{O--CaO--P}_2\text{O}_5$  glass system. Each of

the oxides in the glass system has a structural role in the glass as well as possesses biological importance contributing to the dissolution behavior and apatite forming ability of the glasses.

Silica ( $\text{SiO}_2$ ) is a well-known network former according to glass structural theories (Zachariasen random network model) and acts as a backbone for the glass network [49]. It is also reported that the silicate content plays an important role in controlling the glass formability and apatite forming ability of bioactive glass. It is worth mentioning that around 40–60 wt% of  $\text{SiO}_2$  is present in bioactive glasses synthesized through the conventional melt-quenching technique [2].

Silicate glasses have short-range order originating from the tetrahedral units with Si as the central cation surrounded by four oxygen anions [50]. In the absence of any network modifiers, each oxygen is shared with two Si cations called bridging oxygen (BO) resulting in the formation of Si–O–Si linkages [51]. In the present chapter, any tetrahedral structural unit would be represented as  $Q^n_M$ , where  $n$  represents the number of BO and M represents the central cation forming the tetrahedral units. The structural unit in network modifier free silicate glasses can be denoted as  $Q^4_{\text{Si}}$  where four represents the number of BO present in each silicate structural unit. With the addition of network modifiers like  $\text{Na}_2\text{O}$  or  $\text{CaO}$  in silicate glass, the bridging oxygen converts to non-bridging oxygen (NBO) and results in the formation of Si–O–Na or Si–O–Ca bonds [51]. An increase in the content of network modifiers in the glass leads to the formation of silicate tetrahedral units with decreased BO and are denoted as  $Q^3_{\text{Si}}$ ,  $Q^2_{\text{Si}}$ ,  $Q^1_{\text{Si}}$ ,  $Q^0_{\text{Si}}$  units depending on the number of NBOs formed as shown in Fig. 8.1a.

Since the ion dissolution from silicate bioactive glasses depends on the network modifier contents/number of NBO present in the glass, a parameter called network connectivity ( $\text{NC}_{\text{Si}}$ ) has been used to theoretically obtain the degree of network connectivity for silicate-based bioactive glasses [52].  $\text{NC}_{\text{Si}}$  denotes the average bridging oxygen per silicate tetrahedral unit and can be theoretically calculated based on Eq. (8.1) from the composition of bioactive glasses (in mol%). However, the equation considers that all the phosphate species remain in the form of orthophosphate ( $Q^0_{\text{P}}$ ) units, and therefore some amount of network modifiers are utilized to charge compensate NBOs of  $Q^0_{\text{P}}$  units and remain unavailable to silicate units [52]. This modified equation is based on the findings from structural investigations of bioactive glasses using magic angle spinning nuclear magnetic resonance (MAS-NMR) spectroscopy [53]. The ionic dissolution is faster in glasses with lower  $\text{NC}_{\text{Si}}$  while an increase in the  $\text{NC}_{\text{Si}}$  value denotes a slower ionic dissolution.

$$\text{NC}_{\text{Si}} = \frac{[(4 * \text{SiO}_2) - (2 * \text{Na}_2\text{O}) - (2 * \text{CaO}) + (6 * \text{P}_2\text{O}_5)]}{\text{SiO}_2} \quad (8.1)$$

Structural studies based on MAS-NMR spectroscopy and molecular dynamics simulation have revealed that the silicate units in 45S5 glass are distributed as  $Q^1_{\text{Si}}$ ,  $Q^2_{\text{Si}}$ , and  $Q^3_{\text{Si}}$  units in which  $Q^2_{\text{Si}}$  units are found in higher proportions [54, 55]. Therefore, well-known 45S5 glass can be expected to primarily contain a network of linearly connected  $Q^2_{\text{Si}}$  units along with some  $Q^1_{\text{Si}}$  and  $Q^3_{\text{Si}}$  units. The in vitro tests

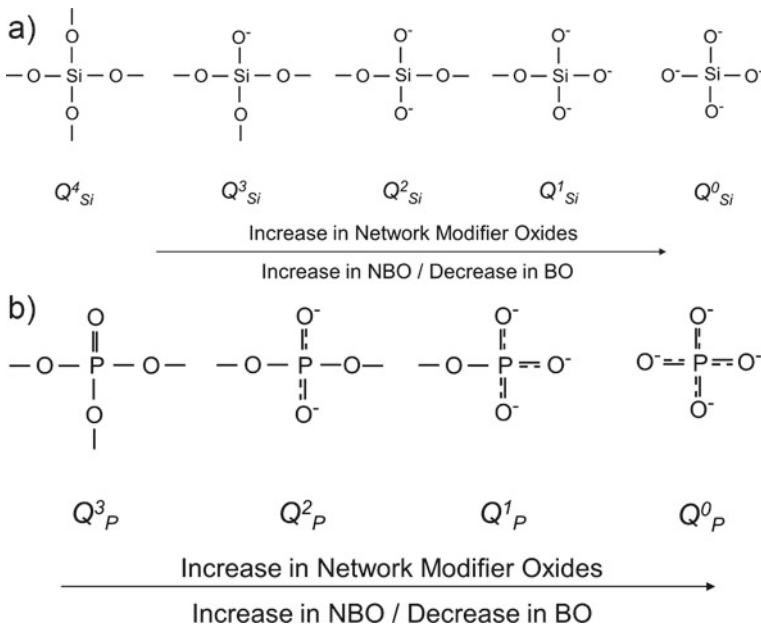


**Fig. 8.1** Tetrahedral units of **a** silicate and **b** phosphate showing the changes in the bridging oxygen (BO) and non-bridging oxygen (NBO) with the increase in the network modifier oxides

on 45S5 bioactive glasses have shown that the silicates are released as soluble silica into the physiological environment during the breakage of Si–O–Si bonds [56]. This soluble silica along with calcium ions actively takes part in bone metabolism and has shown activation and upregulation of several genetic and cellular activities leading to Class-A bioactivity in 45S5 glass [57, 58].

Sodium oxide ( $Na_2O$ ) is a network modifier (according to Zachariasen random network model) and its presence leads to the formation of non-bridging oxygen (NBO) in silicate tetrahedral units [49]. The  $Na_2O$  in the glass system gives rise to  $Na^+$  ions to be associated with the NBOs. These sites are important to initiate the first reaction step at the bioactive glass surface during interaction with the surrounding physiological medium. The  $Na^+$  ions in the bioactive glass are exchanged with the  $H^+$  ions in the surrounding medium leading to the release of  $Na^+$  ions and an increase in the pH of the surrounding medium locally [4, 5, 7, 8]. The release of  $Na^+$  ions (increase in osmotic pressure) and its associated pH increase have also been attributed to impart antibacterial effects in bioactive glasses [39]. Meanwhile, the presence of  $Na_2O$ /alkali oxide in the bioactive glass composition causes a high dissolution rate and may impart cytotoxic effects from the released sodium ions as pointed out by Ferreira and Rebelo [26].

Calcium oxide ( $CaO$ ) is also a network modifier (according to Zachariasen random network model) and its presence also leads to the formation of NBO in the silicate glass similar to the effect of  $Na_2O$  [49]. The presence of  $CaO$  in a bioactive glass

system results in the existence of  $\text{Ca}^{2+}$  ions near NBO sites. The  $\text{Ca}^{2+}$  ions are primary components of calcium phosphates formed during the reaction between bioactive glass with the host tissue under the physiological environment [2, 5, 7, 8, 59]. The  $\text{Ca}^{2+}$  ions can be released in exchange with the  $\text{H}^+$  ions leading to supersaturation of  $\text{Ca}^{2+}$  ions in the surrounding medium [2, 5, 7, 8, 59]. This reaction leads to the formation of the ACP layer through precipitation which further transforms into the HCA layer [2, 5, 7, 8, 59]. The released  $\text{Ca}^{2+}$  ions also exhibit intracellular responses which are important in Class-A bioactive materials [57].

Phosphorus pentoxide ( $\text{P}_2\text{O}_5$ ) is another glass network former (according to Zachariasen random network model) similar to  $\text{SiO}_2$  [49, 60].  $\text{P}_2\text{O}_5$  is present in smaller proportions compared to the other oxides in commercial bioactive glasses like 45S5 (2.6 mol%) and S53P4 (1.7 mol%) [61]. Generally, phosphate glasses without any network modifiers have  $Q^3_{\text{P}}$  units with three numbers of BO (P–O–P linkages) and one oxygen attached with  $\text{P}^{5+}$  cation through a double bond (P=O) as represented in Fig. 8.1b [60, 62]. The BO decreases in the phosphate tetrahedral units with an increase in the network modifier contents leading to the formation of  $Q^2_{\text{P}}$ ,  $Q^1_{\text{P}}$ , and  $Q^0_{\text{P}}$  units as shown in Fig. 8.1b [60]. The  $\pi$  bond associated with P=O in the phosphate units becomes delocalized in the presence of NBO and the degree of delocalization increases with the increase in the NBO bonded to the phosphate units. As mentioned earlier, the orthophosphate units have been associated with a distribution of  $\text{Ca}^{2+}$  and  $\text{Na}^+$  ions based on the proportion of CaO and  $\text{Na}_2\text{O}$  contents in the glass compositions [53, 54, 63]. Bioactive glasses having phosphate content higher than that of 45S5 (2.6 mol%) and S53P4 (1.7 mol%) glasses have been found to have a minor proportion of  $Q^1_{\text{P}}$  units (<10%) along with a major proportion of  $Q^0_{\text{P}}$  units (>90%) [53, 54, 64]. Structural investigations revealed that the  $Q^1_{\text{P}}$  units are connected to the silicates resulting in the formation of Si–O–P bonds [54, 64]. Such Si–O–P bonds are absent in the 45S5 glass while the phosphates in the orthophosphate structure lead to possible phase separation with silicate-rich and phosphate-rich regions within the glasses [65, 66]. The phosphate ions along with the calcium ions are beneficial for the formation of ACP and HCA layers [2, 5, 7, 8, 59]. Therefore, the apatite formation is reported to depend on both  $\text{NC}_{\text{Si}}$  value as well as the phosphate content in the glasses [64].

### 8.3 Glass Thermal Stability

Glass thermal stability can be defined as the stability of glass against crystallization during heat treatments [67, 68]. This property of glass is useful in subjecting the glass blocks and powder compacts to thermal treatments, sintering, and fiber drawing. Since bioactive glasses are used for various hard tissue and soft tissue applications, the development of a bioactive glass product in various shapes and forms through sintering and thermal processing is advantageous. The thermal stability of glass is predicted using specific temperature values obtained from differential scanning calorimetry (DSC) or differential thermal analysis (DTA) technique.

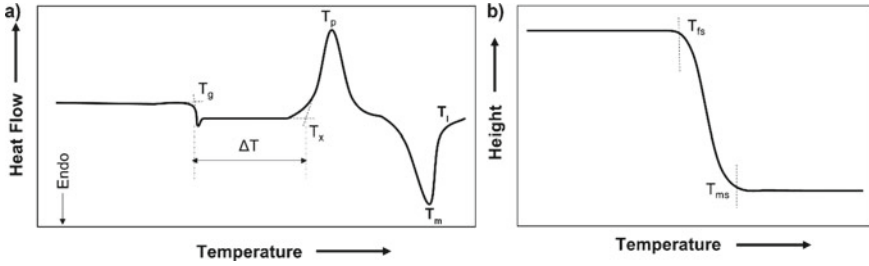


**Fig. 8.2** a DSC thermograms showing glass transition ( $T_g$ ), crystallization onset ( $T_x$ ), crystallization peak ( $T_p$ ), melting ( $T_m$ ), and liquidus ( $T_l$ ) temperatures; b height versus temperature plot from HSM marked with first shrinkage ( $T_{fs}$ ) and maximum shrinkage ( $T_{ms}$ ) temperatures

The temperature values obtained from DSC or DTA include glass transition temperature ( $T_g$ ), crystallization onset temperature ( $T_x$ ), crystallization peak temperature ( $T_p$ ), melting temperature ( $T_m$ ), and liquidus temperature ( $T_l$ ) (Fig. 8.2a). Additionally, the temperature values obtained from DSC or DTA techniques are dependent on the heating rate used during the DSC or DTA measurements. The glass thermal stability is commonly reported in the form of the thermal stability factor ( $\Delta T$ ) as proposed by Angell given in Eq. (8.2) [68]. Hrubý proposed a parameter called the Hrubý parameter ( $K_H$ ) to quantify the glass thermal stability against crystallization during heating given by Eq. (8.3) [67, 69].

$$\Delta T = T_x - T_g \quad (8.2)$$

$$K_H = (T_x - T_g)/(T_l - T_x) \quad (8.3)$$

The glasses having higher values of the above-mentioned parameters are expected to have better thermal stability against crystallization during heating. However, the parameters are expected to change with the heating rates due to the variations in the values of  $T_g$ ,  $T_x$ ,  $T_p$ ,  $T_m$ , and  $T_l$ .

The interference of crystallization on sintering can be obtained from the sinterability parameter ( $S_c$ ) [70]. It is calculated from the difference between the maximum shrinkage temperature ( $T_{ms}$ ) corresponding to the completion of densification obtained from the hot stage microscope and the onset of crystallization temperature obtained from either DTA/DSC technique [70]. The maximum shrinkage temperature ( $T_{ms}$ ) value is obtained for the glass powder compacts from the height/area/relative density versus the temperature plot obtained from the hot stage microscope (Fig. 8.2b). The sinterability parameter ( $S_c$ ) is calculated as per Eq. (8.4) and this parameter indicates the dominance of sintering over the crystallization in glass powders.

$$S_c = T_x - T_{ms} \quad (8.4)$$



## 8.4 Improving the Thermal Stability and Bioactivity Using Compositional Modifications

Brink worked on compositional modifications in bioactive glasses toward improving the hot working/thermal processing properties by incorporating alkali oxide ( $K_2O$ ), alkaline earth oxide ( $MgO$ ), and  $B_2O_3$  into bioactive glasses [12, 71]. Such an attempt has been reported to be successful in formulating bioactive glass compositions with bone-bonding behavior as well as a wider hot working/thermal processing range [12, 71]. From 13 to 93 bioactive glass possesses higher thermal stability against crystallization and is extensively used for scaffold developments and fiber manufacturing [16, 18, 32, 72]. Andersson et al. reported the changes in the in vitro and in vivo performance of bioactive glasses subjected to compositional modifications [10].

Nonetheless, there exists a need to understand the structural changes within the glass owing to the compositional modifications to control the desired properties of the bioactive glasses. Additionally, several researchers have adopted various compositional modifications including the incorporation of  $B_2O_3$ ,  $K_2O$ ,  $Li_2O$ ,  $MgO$ ,  $SrO$ ,  $ZnO$ , and fluorides or by incrementing  $CaO$  or  $P_2O_5$  to obtain bioactive glasses with improved thermal stability, faster dissolution behavior, and apatite forming ability. Furthermore, recent studies have been performed to elucidate the structural modifications in the bioactive glass using Raman spectroscopy, MAS-NMR spectroscopy, and molecular dynamics simulation. Hence, the structure–property correlation based on the effect of compositional modifications in bioactive glasses toward thermal stability, dissolution behavior, and apatite forming ability is discussed further. Some of the silicate-based bioactive glass compositions which were subjected to the above-mentioned compositional modifications are reported in Table 8.1.

**Table 8.1** Bioactive glass compositions (in mol%) subjected to compositional modifications in the literature

Glass name	$SiO_2$	$Na_2O$	$CaO$	$P_2O_5$	$K_2O$	$MgO$	$SrO$	$CaF_2$
45S5 [2]	46.1	24.4	26.9	2.6	–	–	–	–
S53P4 [10]	54.86	22.65	21.77	1.72	–	–	–	–
13-93 [12]	54.6	6	22.1	1.7	7.9	7.7	–	–
ICIE1 [53]	49.46	26.38	23.08	1.07	–	–	–	–
ICIE16 [53]	49.46	6.6	36.27	1.07	6.6	–	–	–
Stronbone [73]	44.5	4	17.8	4.5	4	7.5	17.8	–
FastOS <sup>®</sup> BG [74]	38.49	–	36.07	5.61	–	19.24	–	0.59



### 8.4.1 Incorporation of $B_2O_3$

Boron plays an important role in the formation of bone and trace levels of boron are present in healthy bones through dietary intake [75]. The presence of boron in bones is associated with a reduced risk of osteoarthritis in bones [75, 76]. Boron is additionally found to possess osteogenic and angiogenic properties which are beneficial in the repair and regeneration of hard and soft tissues [77–82].

$B_2O_3$  is a network forming oxide and vitreous  $B_2O_3$  glass consisting of triangular borate units ( $BO_3$ ) which are arranged in the form of six membered boroxol rings [83, 84]. Upon introduction of modifier oxides, the  $BO_3$  units convert to tetragonal while the modifier cations take part as charge compensators for the  $BO_4$  units [83, 84]. This transformation of  $BO_3$  units into  $BO_4$  units continues only up to a certain modifier oxide content beyond which it results in the formation of  $BO_3$  units with NBO. Moreover, structural entities such as metaborate, pyroborate, and orthoborate units are formed with the increasing number of NBO [83, 84]. During incorporation of  $B_2O_3$  into a silicate glass in the presence of network modifying oxides, the network modifying cations can either associate as modifiers with  $SiO_4$  or  $BO_3$  units or as charge compensators with  $BO_4$  units [85]. Yun, Bray, and Dell have developed a model which can predict the role of the network modifying cations in the alkali borosilicate glass system based on  $K = [SiO_2]/[B_2O_3]$  and  $R = [Na_2O]/[B_2O_3]$  ratio [85–87].

The incorporation of  $B_2O_3$  replacing  $SiO_2$  (in wt%) in 45S5 glasses led to the faster dissolution of the bioactive glasses, while such glasses could not be easily processed into scaffolds [88]. On the contrary, Jung was able to successfully incorporate  $B_2O_3$  in 13-93 glass composition by completely replacing  $SiO_2$  (in wt%) called 13-93B3 glass which could be shaped into scaffolds and drawn into fibers [88]. Additionally, Fu et al. successfully prepared borosilicate and borate scaffolds by modifying 13-93 glass composition through gradual replacement of  $SiO_2$  with  $B_2O_3$  (in mol%) [89]. However, the thermal behavior of the above-mentioned glasses obtained through DSC/DTA as well as thermal stability factor and Hruby parameter values have not been reported anywhere. Gradual replacement of  $SiO_2$  with  $B_2O_3$  (in mol%) in S53P4 glass composition led to a gradual decrease in the  $T_g$  value [90, 91]. However,  $T_x$  and  $\Delta T$  values of the glasses initially increased up to 50% replacement of  $SiO_2$  with  $B_2O_3$  followed by a gradual decrease in both  $T_x$  and  $\Delta T$  values [90, 91]. Brandt-Slowik gradually replaced up to 25% of total  $SiO_2$  with  $B_2O_3$  in 45S5 glass composition and reported a gradual reduction in  $T_g$  with a simultaneous increase in  $K_H$  values, respectively [92]. Though a gradual increase in the  $\Delta T$  value of the glass powders (<38  $\mu m$ ) was reported with the incorporation of  $B_2O_3$ , the  $\Delta T$  value of coarse powders (500–1000  $\mu m$ ) was increased with the incorporation of  $B_2O_3$  [92]. Both the  $B_2O_3$ -free 45S5 and  $B_2O_3$  incorporated 45S5 glasses were crystallized into sodium-calcium-silicate based (combeite) crystalline phase while the crystallization kinetics study on the glasses revealed a dominance of surface crystallization for fine powders and complex volume crystallization for coarse powders, respectively [92]. Hmood et al. and Arango-Ospina et al. incorporated up to 3 mol% and 8 mol%

$B_2O_3$  by replacing  $SiO_2$  in ICIE16 glass, respectively [93, 94]. While Hmood et al. reported increased  $\Delta T$  values on glass powders ( $<160 \mu\text{m}$ ), Arango-Ospina observed decreased  $\Delta T$  values on glass powders ( $<45 \mu\text{m}$ ) with the incorporation of  $B_2O_3$  in ICIE16 glass, respectively [93, 94]. Therefore, the variation in the  $\Delta T$  values corresponding to the particle size of the analyzed glass powders suggests a possible change in the mechanism of crystallization in glass powders with different particle size ranges. The changes in the crystallization behavior due to the particle size distribution of the glass powders have been reported by Massera et al. and Brandt-Slowik [92, 95].

The incorporation of  $B_2O_3$  into the bioactive silicate glass composition has resulted in the formation of  $BO_3$  units with NBOs and  $BO_4$  units as shown in Fig. 8.3a, while the average coordination of boron increases with increasing  $B_2O_3$  content [96]. An increase in the chemical shift value (deshielding) of  $^{29}\text{Si}$  MAS-NMR spectra (Fig. 8.3b, c) with a simultaneous decrease in the chemical shift value (shielding) of  $^{31}\text{P}$  MAS-NMR spectra (Fig. 8.3d, e) of glasses, respectively were reported with the gradual replacement of  $SiO_2$  with  $B_2O_3$  in bioactive glasses [97, 98]. The changes in the chemical shift values of  $^{29}\text{Si}$  MAS-NMR spectra of glasses were associated with both the increased network connectivity of silicate units as well as the formation of  $SiO_4-BO_4$  bridges in the glass structure with the incorporation of  $B_2O_3$  [97, 98].

The majority of phosphate species were reported to exist as orthophosphate ( $Q^0_P$ ) units after  $B_2O_3$  incorporation, and the changes in the chemical shift values of  $^{31}\text{P}$  MAS-NMR spectra of glasses were assigned to a slightly increased association of Ca species around the  $Q^0_P$  units [97, 98]. A gradual decrease in the  $BO_3$  units with a simultaneous increase in the  $BO_4$  units has been observed as a result of  $B_2O_3$  incorporation in 45S5 glass [92, 97]. Additionally, Yu and Eden stated that the formation of  $SiO_4-BO_4$  and  $SiO_4-BO_2O^-$  ( $BO_3$  unit with an NBO) linkages are favored during the incorporation of  $B_2O_3$  with a higher Si/B ratio [97]. Therefore, such intermixing of silicate and borate units owing to the incorporation of  $B_2O_3$  is expected to reduce the tendency to crystallize into the combeite crystalline phase during heat treatment [91]. The incorporation of  $B_2O_3$  in silicate bioactive glasses (45S5, S53P4, 13-93, and ICIE16) has resulted in faster dissolution, ion release, and apatite formation as widely evidenced under in vitro static and dynamic conditions [79, 88, 89, 91–94, 99–103]. This is due to the faster hydrolysis rate of B–O–B bonds and B–O–Si compared to Si–O–Si bonds [104, 105].

#### 8.4.2 Increment of CaO

The conventional silicate-based bioactive glass compositions generally contain a high amount of CaO and  $Na_2O$  as network modifying oxides to aid the dissolution and apatite formation under the physiological environment [14, 19]. Though both CaO and  $Na_2O$  in bioactive glasses disrupt the silicate network by converting BO to NBO,  $Ca^{2+}$  ions maintain the rigidity of the silicate glass network due to the higher field strength compared to  $Na^+$  ions [106, 107]. Upon substitution of  $Na_2O$

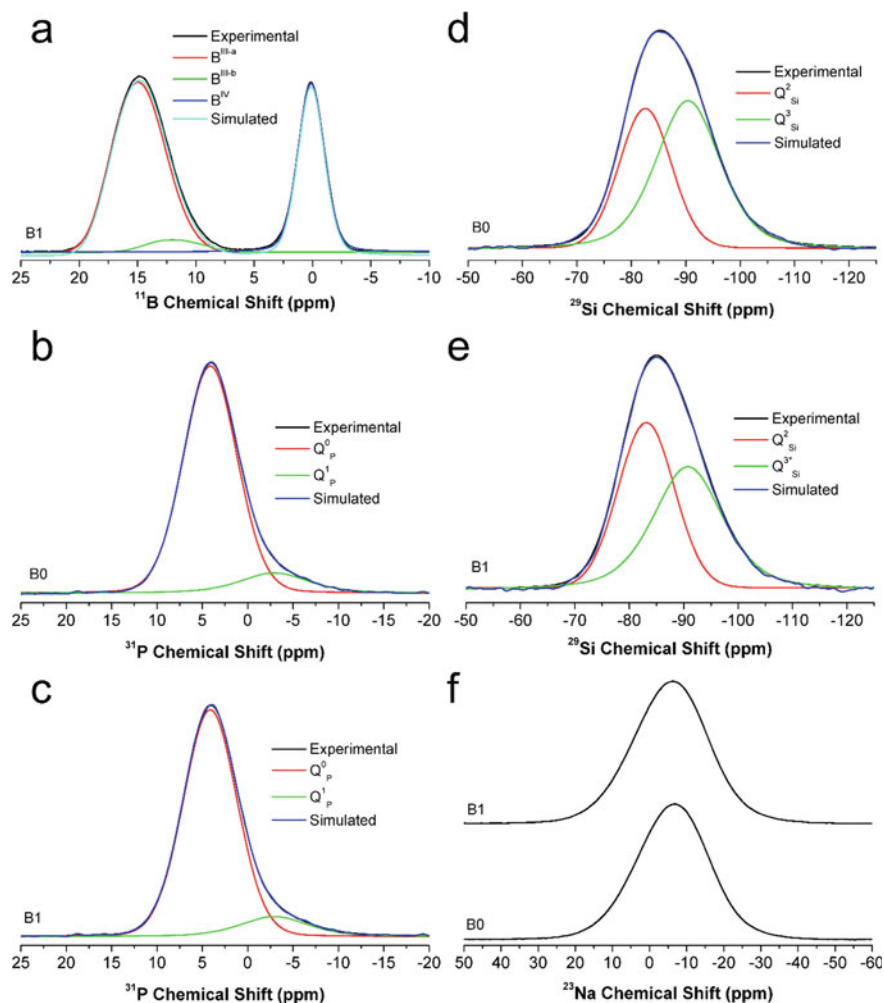


**Fig. 8.3**  $^{11}\text{B}$  MAS-NMR spectra of borosilicate glass,  $^{31}\text{P}$  and  $^{29}\text{Si}$  MAS-NMR spectra of silicate (b, d) and borosilicate (c, e) glasses, respectively, and a  $^{23}\text{Na}$  MAS-NMR spectra of silicate and borosilicate glasses. Reprinted with permission from [98]. Copyright © 2019 American Chemical Society

with CaO in silicate-based bioactive glasses, the higher field strength of the  $\text{Ca}^{2+}$  ions increases the rigidity of the silicate network without decreasing the network connectivity. Although most bioactive glass compositions are rich in  $\text{Na}_2\text{O}$  content, it has been reported that CaO-rich ( $\text{Na}_2\text{O}$ -free) bioactive glass composition could be developed without affecting the bioactivity [74, 108, 109].

Arstila et al. reported that the glasses like 45S5 (consisting of an equivalent amount of CaO and  $\text{Na}_2\text{O}$ ) tend to crystallize in the sodium-calcium-silicate based (combeite-type) phase during thermal treatments [110, 111]. Meanwhile, CaO-rich

silicate bioactive glasses crystallized into calcium silicate (wollastonite) crystalline phases [110, 111]. The crystallization temperature for combeite-type crystalline phases was reported to be around 600–770 °C while the crystallization temperature for wollastonite-type crystalline phases was reported at around 830–930 °C [110, 111]. Though the glass transition temperature ( $T_g$ ) of CaO-rich bioactive glasses is higher than glasses like 45S5, the CaO-rich glasses exhibited higher  $T_x - T_g$  and  $K_H$  values [26, 74, 110–112]. A CaO-rich silicate-based bioactive glass modified from 45S5 glass composition was developed by Bellucci et al. which was reported to possess improved thermal processing properties [113, 114]. ICIE16 glass with higher CaO:Na<sub>2</sub>O content than 45S5 glass exhibited improved thermal processing behavior than 45S5 glass [115]. Groh et al. developed a CaO-rich silicate-based bioactive glass with a  $\Delta T$  value larger than that of 45S5 and ICIE16 glasses [116]. Additionally, an alkali-free CaO-rich FastOS<sup>®</sup>BG glass has been successfully developed into scaffolds and fibers through thermal processing [26, 117].

Elgayar et al. observed a gradual change in the chemical shift values toward lower frequencies in the <sup>29</sup>Si and <sup>31</sup>P MAS-NMR spectra of soda-lime-phosphosilicate bioactive glasses with the gradual replacement of Na<sub>2</sub>O with CaO (without changing total CaO + Na<sub>2</sub>O) [53]. Such changes in the chemical shift values have been reported due to the differences in the electronegativity and field strength of the cations. Moreover, the phosphate species were observed to exist in the form of orthophosphate ( $Q^0_P$ ) units, while the distribution of Na<sup>+</sup> and Ca<sup>2+</sup> cations around the orthophosphate units were directly proportional to the Na<sub>2</sub>O and CaO contents in the glass composition [53]. Mathew et al. reported a random distribution of Na and Ca species around  $Q^0_P$ ,  $Q^1_{Si}$ , and  $Q^2_{Si}$  units, while a slightly lesser random distribution of Na and Ca species was reported around  $Q^1_P$ ,  $Q^3_{Si}$ , and  $Q^4_{Si}$  units [118]. Though the high field strength of Ca<sup>2+</sup> cations could decrease the overall dissolution rate of bioactive glass, the release of Ca<sup>2+</sup> ions into the surrounding physiological medium enables faster apatite formation in combination with the released phosphate ions [116]. However, an increased amount of Ca<sup>2+</sup> ions in the solution beyond the saturation level could lead to precipitation of calcium carbonate crystalline phase with/without an apatite crystalline phase [119]. Interestingly, the formation of the calcium carbonate crystalline phase can be beneficial due to its high biocompatibility with cells for attachment and proliferation [119].

### 8.4.3 Incorporation of K<sub>2</sub>O

Potassium is naturally present in human body fluids and enters the body through dietary intake [120]. Potassium plays an important role in maintaining bone health and preserving calcium content within bones as well as in preventing osteoporosis [120]. A potassium cation has a higher ionic radius and lower field strength compared to that of a sodium cation [121]. Moreover, K<sub>2</sub>O is an alkali oxide and plays the role of a network modifier in silicate glasses similar to Na<sub>2</sub>O [121]. Tylkowski et al. and Crovace et al. studied the effect of incorporation of K<sub>2</sub>O replacing Na<sub>2</sub>O (in

mol equivalent) in 45S5 glass composition [121, 122]. Similarly, Hupa et al. developed  $K_2O$  incorporated S53P4 glasses by gradually replacing  $Na_2O$  with  $K_2O$  [123]. Tylkowski et al. and Crovace et al. observed an initial decrease in  $T_g$  up to 50% replacement of  $Na_2O$  with  $K_2O$  followed by an increase in  $T_g$  confirming the mixed alkali effect between  $K_2O$  and  $Na_2O$  in the glass as shown in Fig. 8.4a [121, 122]. However, the  $T_x$  values were found to change non-linearly with the gradual incorporation of  $K_2O$  replacing  $Na_2O$ . Crystallization studies on the glasses confirmed the formation of the sodium-calcium-silicate crystalline phase and potassium-calcium-silicate crystalline phase in  $Na_2O$ -rich and  $K_2O$ -rich glasses, respectively [122]. The glass with equal amounts of  $Na_2O$  and  $K_2O$  was crystallized into both sodium-calcium-silicate and potassium-calcium-silicate crystalline phases during heat treatment [122]. The  $\Delta T$  values were reported to be maximum for the glass in which 50% and 75% of  $Na_2O$  were replaced with  $K_2O$  for fine powders (25–75  $\mu m$ ) and coarse powders (<250  $\mu m$ ), respectively [121, 122]. Additionally, Crovace et al. reported a maximum  $K_H$  value for the glass in which 50% of  $Na_2O$  was replaced with  $K_2O$  [122]. Both the density and oxygen density of the glasses reduced gradually with the incorporation of  $K_2O$  replacing  $Na_2O$  in 45S5 glass [121, 122]. This corresponds to an increasing molar volume of the glass with the incorporation of  $K_2O$  as well as a gradual reduction in the compactness of the glass. Analysis of the viscosity-temperature dependence behavior of the glasses as displayed in Fig. 8.4b confirmed a comparatively lower viscosity for the glass in which  $Na_2O$  was partially replaced with  $K_2O$  [122]. The highest viscosity at a given temperature was observed on the glass in which  $Na_2O$  was completely replaced with  $K_2O$  [122]. The observed viscosity-temperature behavior of the glasses corroborated the lower viscosity of glasses to the mixed-alkali effect in the presence of  $K_2O$  and  $Na_2O$  which additionally improved the densification behavior during the viscous flow sintering [122].

The *in vitro* behavior of the bioactive glasses studied under TRIS solution confirmed the formation of apatite within 6 h for  $K_2O$ -free 45S5 glass and within 12 h for  $K_2O$  incorporated 45S5 glasses, respectively [124]. However, the decrease

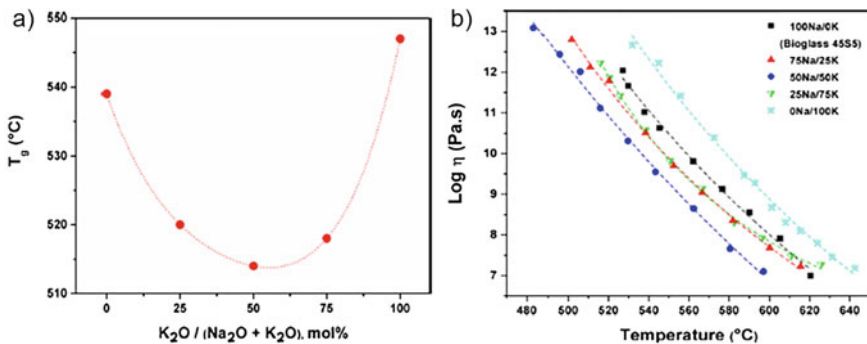


**Fig. 8.4** The nonlinear variation of **a**  $T_g$  and **b** viscosity-temperature dependence behavior of bioactive glasses due to the mixed-alkali effects with the incorporation of  $K_2O$  replacing  $Na_2O$  in 45S5 glass. Reprinted from [122]. Copyright © 2013 with permission from Elsevier

in the compactness of the  $K_2O$  incorporated glass structure led to faster dissolution and ion release from the glasses [124]. Hupa et al. also reported faster dissolution and ion release from S53P4 glasses when  $Na_2O$  was gradually replaced with  $K_2O$  [123]. Elgayar et al. observed a decrease in the chemical shift values from  $^{29}Si$  and  $^{31}P$  MAS-NMR spectra of glasses incorporated with  $K_2O$  replacing  $Na_2O$  corresponding to the shielding effect due to lower field strength of  $K^+$  ions compared to  $Na^+$  ions [53]. Therefore, the replacement of  $Na_2O$  with  $K_2O$  does not lead to any change in the NBO associated with silicate and phosphate tetrahedral units while phosphate species existed as orthophosphate units irrespective of the presence of  $Na_2O$  or  $K_2O$  in the glass.

#### 8.4.4 Incorporation of $Li_2O$

Lithium is present as a trace element in the human body and possesses osteoprotective properties [125, 126].  $Li_2O$  is an alkali oxide and plays the role of a network modifier in silicate glasses similar to  $Na_2O$  [121]. Therefore,  $Li_2O$  is incorporated into silicate bioactive glasses by gradually replacing  $Na_2O$  content [121].  $Li^+$  cation has a lower atomic radius and higher field strength than that of  $Na^+$  cation [121]. Tylkowski and Brauer studied the effect of incorporation of  $Li_2O$  for  $Na_2O$  in 45S5 glass and observed the mixed alkali effect on  $T_g$  values of the glasses [121]. The  $T_g$  values decreased initially (replacement of  $Na_2O$  with  $Li_2O$  up to 50%) followed by a gradual increase. Moreover, the  $T_x - T_g$  ( $\Delta T$ ) values of the glasses increased gradually with the replacement of  $Na_2O$  with  $Li_2O$  [121]. The oxygen density of the glasses was gradually increased with the replacement of  $Na_2O$  with  $Li_2O$  leading to the formation of a compact glass structure [121]. The ion release and dissolution behavior of the glasses in TRIS solution was marginally slower with  $Li_2O$  incorporation but did not show any evidence of a mixed alkali effect [124]. Similarly, the apatite formation on the glasses was evidenced within 6 h for  $Li_2O$ -free 45S5 glass and within 24 h for  $Li_2O$  incorporated 45S5 glasses in TRIS solution [124]. It was additionally mentioned that the ion release and dissolution behavior of the glasses depend on the compactness of the glass structure rather than the mixed alkali effect [124].

#### 8.4.5 Incorporation of $MgO$

Magnesium is naturally present in the human blood plasma and bones while taking an active role in controlling the cellular activity and metabolism of bones [127–129].  $MgO$  is an alkaline earth oxide like  $CaO$  and has been reported to behave as an intermediate like  $Al_2O_3$  or as a network modifier like  $CaO$  [130, 131]. Generally,  $MgO$  has been incorporated into bioactive glasses by gradually replacing  $CaO$  from bioactive glass compositions [127–132]. Watts et al. and Souza et al. reported a reduction in the  $T_g$  value on gradual replacement of  $CaO$  with  $MgO$  in 45S5 and

ICIE1 glass compositions, respectively [128, 131]. Furthermore, an increase in the crystallization onset temperature ( $T_x$ ) was reported by both Souza et al. and Watts et al. during the replacement of CaO with MgO [128, 131]. Thus, a steady increase in the  $\Delta T$  value was reported with the gradual replacement of CaO with MgO by Watts et al. and Souza et al. [128, 131].

$^{29}\text{Si}$  MAS-NMR studies on MgO incorporated glasses as shown in Fig. 8.5a revealed a decrease in the chemical shift values (shielding effect) denoting an increase in the network connectivity of silicate units [131]. Therefore, MgO primarily plays the role of network former in the silicate glass, i.e., the presence of a tetrahedral unit with a central  $\text{Mg}^{2+}$  cation coordinated by four  $\text{O}^{2-}$  anions. Additionally, the reduction in the  $T_g$  values in the glasses has been attributed to the formation of Si–O–Mg bonds with lower bond strength instead of Si–O–Si bonds in MgO incorporated silicate glasses [131]. The increase in  $T_x$  value was attributed to the inhibition of the sodium-calcium-silicate crystalline phase during heat treatment due to the reduction in NBO associated with the silicate network, the lower field strength of  $\text{Mg}^{2+}$  cations, decrease in the CaO content and the formation of Si–O–Mg bonds instead of Si–O–Si bonds [127, 128, 131, 132]. The  $^{31}\text{P}$  MAS-NMR studies on MgO incorporated glasses confirmed the existence of phosphate species as orthophosphate ( $Q^0_p$ ) units [131]. Moreover, the increase in the chemical shift values from  $^{31}\text{P}$  MAS-NMR spectra as shown in Fig. 8.5b was reported to be due to the formation of a sodium-rich environment around the orthophosphate units on the replacement of CaO with MgO [131]. Therefore, it was confirmed that with the replacement of CaO (network modifying oxide) with MgO (network forming oxide), the NBOs of  $Q^0_p$  units were charge-balanced by the  $\text{Na}^+$  cations as  $\text{Na}_2\text{O}$  is a network modifying oxide [131]. Furthermore, partial replacement of CaO with MgO did not lead to any mixed ion effects as the structural role of MgO is different compared to CaO in the phosphosilicate bioactive glass.

Though incorporation of MgO replacing CaO has improved the thermal stability of silicate bioactive glass,  $\text{Mg}^{2+}$  ions act as inhibitors to the formation of crystalline

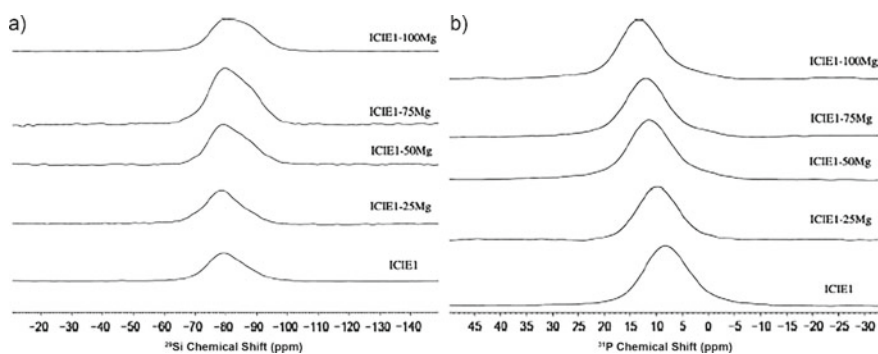


**Fig. 8.5** a  $^{29}\text{Si}$  and b  $^{31}\text{P}$  MAS-NMR spectra of ICIE1 bioactive glass gradually incorporated with MgO replacing CaO (from bottom to top). Reprinted from [131]. Copyright © 2010 with permission from Elsevier



apatite from ACP [123, 128, 129, 133, 134]. However, the effect of MgO incorporation on the rate of ion dissolution from bioactive glasses is ambiguous and the dissolution rate has either decreased or remained unaffected [123, 129, 131]. Moreover, the replacement of CaO with MgO would lead to an overall increase in the silicate network connectivity as well as a decrease in the release of  $\text{Ca}^{2+}$  cations leading to a reduction in apatite formation.

#### 8.4.6 Incorporation of SrO

Strontium plays important role in osteogenesis and is commonly used for the treatment of osteoporosis by promoting osteoblast activity and simultaneously inhibiting osteoclast activity [135]. SrO is an alkaline earth oxide like CaO and plays the role of network modifier in the glass structure while the field strength of  $\text{Sr}^{2+}$  ion is lower compared to  $\text{Ca}^{2+}$  ion [135–138]. Therefore, SrO is incorporated into bioactive glass compositions by replacing CaO in mol equivalent. Fredholm et al. and O'Donnell et al. incorporated SrO in ICIE1 and 45S5 glass compositions, respectively by gradually replacing CaO [136, 139]. Such compositional modification was found to result in a gradual reduction in the  $T_g$  value [136, 139]. This effect was associated with the expansion of the glass network and the lowering of glass rigidity based on the decrease in oxygen density [136, 139]. A reduction in the  $T_p$  value was observed with the gradual increase in the incorporation of SrO replacing CaO. Bellucci et al. reported an increase in the  $T_x - T_g$  ( $\Delta T$ ),  $K_H$ , and  $S_c$  values with the replacement of 10 mol% CaO with SrO in the silicate-based bioactive glass composition [127]. However, O'Donnell et al. reported a reduction in both  $T_x$  and  $T_x - T_g$  values up to 50% substitution of CaO with SrO and an increase in both  $T_x$  and  $T_x - T_g$  values during the substitution of CaO with SrO beyond 50% [139]. This was due to the inhibition of the combeite crystalline phase in the presence of the incorporated SrO up to 50% replacement of CaO [139]. Lotfibakhshaiesh et al. studied the thermal properties of silicate-based bioactive glasses in which CaO was gradually replaced with SrO resulting in the reduction in  $T_g$  and  $T_x$  values and an increase in the thermal stability factor ( $\Delta T$ ) [140]. The analysis of the crystalline phase in the heat-treated glasses using XRD revealed the formation of the strontium silicate crystalline phase instead of the calcium silicate crystalline phase [140].

The replacement of CaO with SrO in bioactive glasses did not lead to any changes in the network connectivity of the silicate units as confirmed by the  $^{29}\text{Si}$  MAS-NMR studies [140]. Fredholm et al. observed identical chemical shift values from the  $^{29}\text{Si}$  and  $^{31}\text{P}$  MAS-NMR spectra of the glasses (Fig. 8.6a, b) after the replacement of CaO with SrO [136]. Du and Xiang analyzed SrO incorporated 45S5 glass using molecular dynamics simulation and reported the absence of mixed ion effects in the properties during the gradual substitution of CaO with SrO [138]. Sriranganathan et al. studied the effect of SrO/CaO content in Stronbone™ glass composition and observed a reduction in the  $T_g$  and  $T_p$  values [73]. Additionally,  $T_x - T_g$  ( $\Delta T$ ) values were found to initially decrease on partial replacement of CaO with SrO while an



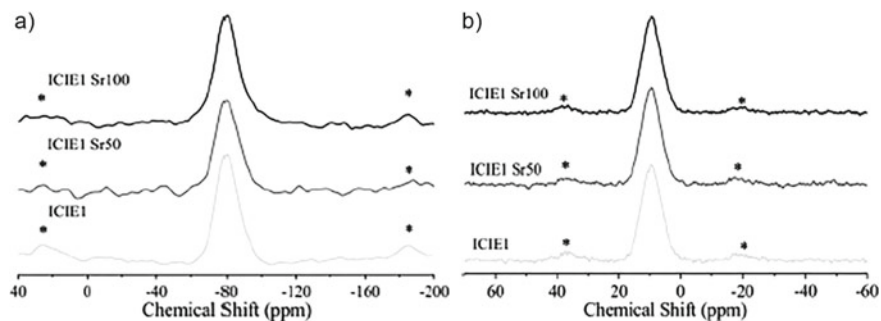


**Fig. 8.6** a  $^{29}\text{Si}$  and b  $^{31}\text{P}$  MAS-NMR spectra of ICIE1 bioactive glass gradually incorporated with SrO replacing CaO (from bottom to top). Spinning sidebands are represented by \*. Reprinted from [137]. Copyright © 2010 with permission from Elsevier

increase in the  $T_x - T_g$  ( $\Delta T$ ) value was evidenced after full replacement of CaO with SrO corroborating the results reported by O'Donnell et al. [139].

Sriranganathan et al. observed delayed apatite formation in glasses in which CaO was partially replaced with SrO compared to SrO free glasses [73]. However, the glasses with CaO fully replaced with SrO did not exhibit any strontium apatite formation during SBF and TRIS immersion and rather exhibited the formation of strontium orthophosphate crystals [73]. Therefore, it was reported that the presence of SrO without CaO in the glass did not favor either octa-calcium phosphate (OCP) or apatite crystalline phase under SBF and TRIS immersion [73]. Goel et al. have also reported delayed apatite formation in SrO incorporated bioactive glasses compared to SrO-free parent glass [141]. Hupa et al. reported faster dissolution of S53P4 glass on gradual replacement of CaO with SrO [123]. Therefore, the faster dissolution of silicate bioactive glasses with the replacement of CaO with SrO has been attributed to the expansion of the glass network without any changes in the silicate network connectivity. On the contrary, delayed apatite formation has been associated with the inhibitory effects of Sr during the formation of crystalline apatite. Strontium incorporated bioactive glasses have been commonly used for osteoporosis and dentine hypersensitivity applications [142, 143]. The strontium ions released from the glasses replace the calcium ions in the crystalline apatite aiding in the remineralization process [142, 143].

#### 8.4.7 Incorporation of ZnO

Zinc plays an important role in the skeletal system by controlling the DNA synthesis and alkaline phosphatase activity in osteoblast cells and actively taking part in bone metabolism [147]. ZnO falls under the category of intermediate network modifiers as per the Dietzel field strength criteria [147]. ZnO has been incorporated into bioactive glasses either by replacing either CaO or MgO or Na<sub>2</sub>O or SiO<sub>2</sub>. Lusvardi et al.

incorporated ZnO by replacing mol equivalents of the 45S5 glass composition itself [148]. Kamitakahara et al. replaced CaO with ZnO partially in apatite-wollastonite (A-W) glass composition and reported a gradual reduction in the  $T_g$  and  $T_{p1}$  values of the glass [149]. Kapoor et al. observed a gradual reduction in the  $T_g$  value with the partial replacement of MgO with ZnO in phosphosilicate-based glass composition [150]. Chen et al. were able to incorporate up to 19 mol% ZnO replacing SiO<sub>2</sub> in a glass beyond which crystallization of sodium zinc silicate crystallization phase occurred [151]. The dissolution behaviour of ZnO incorporated silicate glasses was used to confirm the role of ZnO as the network former [151]. Lusvardi et al. and Linati et al. confirmed the existence of ZnO<sub>4</sub> tetrahedral units and Si–O–Zn bonds based on Raman spectroscopy and <sup>29</sup>Si MAS-NMR spectroscopy, respectively, in ZnO incorporated silicate bioactive glasses [152, 153]. Since the behaviour of ZnO in silicate bioactive glasses is similar to that of MgO, the replacement of MgO with ZnO led to the preservation of the silicate network connectivity. Accordingly, Sergi et al., Goel et al., and Kapoor et al. developed ZnO incorporated bioactive glasses in which MgO was gradually replaced with ZnO in phosphosilicate-based bioactive glasses [150, 154, 155]. Such compositional modifications led to a reduction in both  $T_g$  and  $T_x$  values and an overall increase in the  $\Delta T$  value [150, 155]. The reduction in the  $T_g$  value was assigned to the lower field strength of Zn<sup>2+</sup> ions compared to Mg<sup>2+</sup> ions though the difference in the ionic radius is small [150, 154, 155]. The sinterability parameter ( $S_c$ ) was reported to increase up to 4 mol% incorporation of ZnO [150]. The reduction in the  $T_x$  value was due to the formation of calcium zinc silicate crystalline phase (evident during the incorporation of ZnO above 4 mol%) instead of diopside and fluorapatite crystalline phases [150]. The chemical shift values obtained from <sup>29</sup>Si to <sup>31</sup>P MAS-NMR spectra of the glasses exhibited minor changes with the partial replacement of MgO with ZnO, therefore confirming the similar structural role of ZnO compared to MgO in silicate-based bioactive glasses [150]. Moreover, the phosphate species were distributed in the form of orthophosphate ( $Q^0_p$ ) units [150].

Wetzel et al. reported that the replacement of CaO with ZnO up to 4 mol% caused a decrease in  $T_g$  value and increase in  $T_x$  value, while  $\Delta T$  and  $K_H$  values started to gradually increase with ZnO incorporation [156]. Chen et al. reported that the glasses incorporated with ZnO replacing SiO<sub>2</sub> were stable in neutral pH buffers and therefore concluded that the incorporated ZnO plays the role of network former rather than network modifier [151].

Blochberger et al. reported a reduction in the apatite formation on the incorporation of ZnO replacing CaO under TRIS solution [129]. Moreover, a gradual reduction in the dissolution rate of ions from the glasses with the incorporation of ZnO replacing CaO was reported under TRIS immersion [129]. The reduction in the dissolution of glass and apatite formation has been attributed to the network forming role of ZnO contrary to the network modifier role of CaO leading to an increased silicate network polymerization. Goel et al. observed a delay in the apatite formation on glasses incorporated with ZnO replacing MgO under TRIS immersion confirming the inhibitory effects of Zn on apatite formation [154]. Similarly, Sergi et al. reported slower dissolution as well as slower apatite formation on glasses with

ZnO replacing MgO which has been attributed to the association of  $\text{Ca}^{2+}$  ions with the  $\text{ZnO}_4$  tetrahedral units instead of  $\text{SiO}_4$  tetrahedral units [155].

#### 8.4.8 Increment of $\text{P}_2\text{O}_5$

O'Donnell investigated the effect of  $\text{P}_2\text{O}_5$  incorporation in bioactive glasses based on the  $\text{SiO}_2$ – $\text{Na}_2\text{O}$ – $\text{CaO}$ – $\text{P}_2\text{O}_5$  system [157, 158]. Since the phosphate species in bioactive glasses exist in the form of  $Q^0_{\text{P}}$  units, a gradual increase in the replacement of  $\text{SiO}_2$  with  $\text{P}_2\text{O}_5$  led to an increase in the  $\text{NC}_{\text{Si}}$  value. However, the incorporation of  $\text{P}_2\text{O}_5$  along with modifier oxides (three times  $\text{P}_2\text{O}_5$ ) for charge balancing led to the retainment of the  $\text{NC}_{\text{Si}}$  value. The incorporation of  $\text{P}_2\text{O}_5$  up to ~4 mol% in bioactive glasses has resulted in a reduction in  $T_{\text{g}}$  and an increase in  $T_{\text{x}}$  (in both methods) leading to an increase in the thermal stability factor ( $\Delta T$ ) [157]. Moreover, the increase in the  $\Delta T$  values was significant in the glasses in which the  $\text{NC}_{\text{Si}}$  value is increased during the incorporation of  $\text{P}_2\text{O}_5$ . This was assigned to the reduction in the number of modifier cations associated with the silicate units undergoing diffusion and leading to nucleation and growth of sodium-calcium-silicate crystals. However, a decreasing trend in the  $T_{\text{x}}$  and  $\Delta T$  values was reported with the incorporation of  $\text{P}_2\text{O}_5$  above ~4 mol%. Further, the decrease in the  $T_{\text{x}}$  value was reported to be based on the crystallization of either orthophosphate or pyrophosphate units [157]. Tilocca and Cormack, Lusvardi et al., and Linati et al. reported phase separation of orthophosphate clusters within the sodium-calcium-phosphosilicate-based bioactive glasses having  $\text{P}_2\text{O}_5$  content in the range of 6–12 mol% [153, 159, 160]. Molecular dynamics simulated structure of 45S5 glass with 2.57 mol%  $\text{P}_2\text{O}_5$  and glass with 12.17 mol%  $\text{P}_2\text{O}_5$  is displayed in Fig. 8.7 in which the phosphate units are distributed uniformly and clustered, respectively, differentiating the extent of phosphate phase separation in the glasses [159]. Such phase-separated orthophosphate clusters could give rise to the crystallization of phosphate crystalline phase during thermal treatments thus leading to a reduction in the  $T_{\text{x}}$  value.

The MAS-NMR studies have revealed a non-preferential association of  $\text{Na}^+$  and  $\text{Ca}^{2+}$  cations around the orthophosphate ( $Q^0_{\text{P}}$ ) units [53]. Mathew et al. reported the existence of pyrophosphate ( $Q^1_{\text{P}}$ ) units in addition to the  $Q^0_{\text{P}}$  units in bioactive glasses with  $\text{P}_2\text{O}_5$  above 4 mol% [161]. Additionally, an increase in the amount of  $Q^1_{\text{P}}$  units was reported with an increase in the  $\text{NC}_{\text{Si}}$  value without altering the  $\text{P}_2\text{O}_5$  content in the glass composition [161]. Prasad et al. developed bioactive glass with high  $\text{CaO}$  and  $\text{P}_2\text{O}_5$  (3.7 mol%) content and reported an increase in the  $\Delta T$  value [98]. Moreover, the phosphate units within the glass were distributed in the form of  $Q^0_{\text{P}}$  units (~90%) and  $Q^1_{\text{P}}$  units (~10%) as confirmed by  $^{31}\text{P}$  MAS-NMR spectra analysis (Fig. 8.3b), while the phosphate units did not contribute to any crystallization of the phosphate phase during heat treatment [98]. The orthophosphate ( $Q^0_{\text{P}}$ ) units are isolated and distributed across the silicate network structure while the pyrophosphate ( $Q^1_{\text{P}}$ ) units are connected to the silicate network structure leading to the formation of  $\text{Si-O-P}$  bonds [159]. Moreover, the orthophosphate ( $Q^0_{\text{P}}$ ) units contribute to the

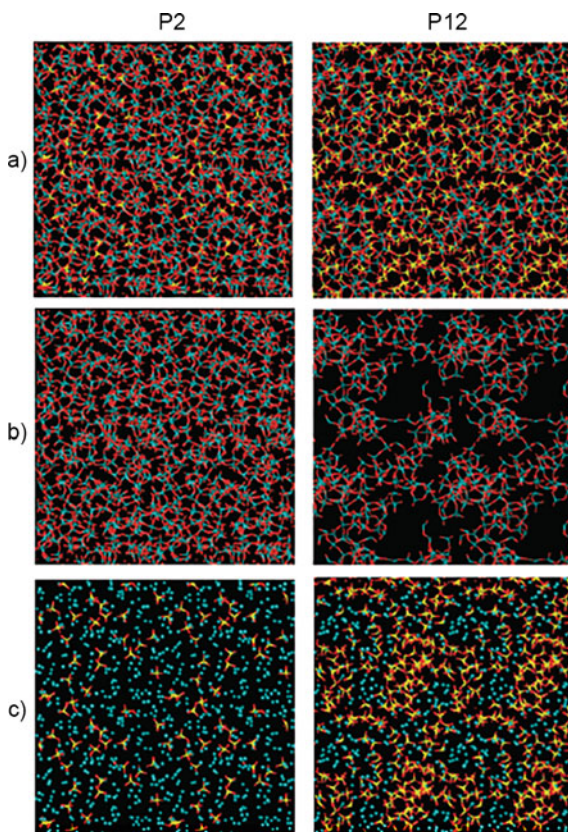


**Fig. 8.7** **a** Simulated structure of P2 glass with 2.57 mol%  $P_2O_5$  in the left column and P12 glass with 12.17 mol%  $P_2O_5$  in the right column showing both silicate network structure and phosphate units [Si (turquoise), P (yellow), and O (red)]; **b** silicate network structure; and **c** distribution of phosphate units along with Si atoms. Reprinted with permission from [159]. Copyright © 2007 American Chemical Society

release of phosphate ions as well as the formation of ACP and apatite layers [98]. Therefore, the thermal stability of silicate bioactive glasses could be improved with the incorporation of  $P_2O_5$ , provided the orthophosphate clusters present in the glass do not promote the formation of phosphate-based crystalline phase during the thermal processing of glass. Additionally, the increase in the silicate network polymerization (increase in  $NC_{Si}$  value) and the formation of  $Q^1_P$  units (presence of Si–O–P bonds) owing to the incorporation of  $P_2O_5$  may contribute to the improved thermal stability of the glass.

### 8.4.9 Incorporation of Fluoride

Fluorides have been found to promote osteoblast proliferation, alkaline phosphatase activity, remineralization of fluorapatite (FAp), and antibacterial properties [40, 162–165]. Moreover, FAp has better acid resistance than hydroxyapatite (HAp) aiding in dentine and enamel repair as well as for caries treatments [165, 166]. The fluorides have been incorporated in silicate bioactive glasses in the form of either  $\text{CaF}_2$  or NaF [165, 167]. The incorporation of  $\text{CaF}_2$  replacing  $\text{CaO}/\text{Na}_2\text{O}$  leads to an increase in silicate network connectivity ( $\text{NC}_{\text{Si}}$ ) [165, 167]. An alternative approach to fluoride incorporation in the bioactive glass composition is by adding  $\text{CaF}_2$  without changing the proportion of network formers to network modifiers which does not alter the  $\text{NC}_{\text{Si}}$  value [165, 166, 168].

Brauer et al. incorporated  $\text{CaF}_2$  replacing CaO in ICIE1 silicate bioactive glass composition and reported a gradual decrease in  $T_g$  and  $T_x$  values and an increase in  $T_x - T_g$  value in both glass powder and glass frit up to 17 mol%  $\text{CaF}_2$  incorporation [169]. Crystallization of glasses followed by XRD analysis revealed the presence of combeite crystalline phase in low  $\text{CaF}_2$  incorporated glasses. However, crystallization of the calcium fluorosilicate (cuspidine) phase and calcium fluoride (fluorite) phases were observed in the glass with further incorporation of  $\text{CaF}_2$ . A consistent decrease in  $T_g$  and  $T_x$  values has been reported up to the incorporation of 6 mol%  $\text{CaF}_2$  in high  $\text{P}_2\text{O}_5$  (6.33 mol%) containing silicate-based bioactive glasses while the  $\Delta T$  value was increased [170]. The high  $\text{P}_2\text{O}_5$  containing  $\text{CaF}_2$  incorporated silicate bioactive glasses showed a tendency to crystallize into sodium-calcium-fluorophosphate crystalline phases during the heat treatment [170]. A similar reduction in  $T_g$  was observed with the replacement of CaO with  $\text{CaF}_2$  in 45S5 and S53P4 glass composition [171, 172]. Though a gradual increase in the  $\Delta T$  value was reported with the replacement of CaO with  $\text{CaF}_2$ , glasses with  $\text{CaF}_2$  above 10.88 mol% were reported to have the sodium fluoride (villiumite) crystalline phase [172].

Molecular dynamics simulation of  $\text{CaF}_2$  incorporated glasses has revealed the presence of a silica-rich network region and inter-network region with modifier cations and fluoride along with a phosphate-rich interfacial region within the glasses without any presence of Si–F and P–F bonds [167, 172–174]. However,  $^{19}\text{F}$  MAS-NMR studies and computational studies have revealed that the fluorides are coordinated with either Na–Ca equally [167] or Na-rich (–200 ppm) in addition to Na–Ca combined environments (–114 and –152 ppm) as shown in Figs. 8.8a and 8.9a [166, 168, 172, 174]. Such fluoride environments have given rise to the crystallization of  $\text{CaF}_2$  or NaF phases during heat treatment of fluorinated bioactive glasses. Similarly, the energetically weak interactions between the silicate network and fluorides in fluorinated bioactive glasses have led to a gradual reduction in the  $T_g$  value with  $\text{CaF}_2$  incorporation [171]. Incorporation of  $\text{CaF}_2$  up to 8 mol% in CaO-rich silicate bioactive glasses maintaining constant  $\text{NC}_{\text{Si}}$  value has been reported to result in a reduction in  $T_g$ ,  $T_x$ , and  $\Delta T$  values [116, 175]. However, the presence of  $\text{CaF}_2$

resulted in a reduction of the sintering temperature thereby aiding the viscous flow behavior during sintering.

The chemical shift values from  $^{29}\text{Si}$  MAS-NMR spectra of glasses were decreased with the gradual incorporation of  $\text{CaF}_2$  replacing  $\text{CaO}$  as shown in Fig. 8.8b [172, 174]. Such changes were associated with the increase in  $Q^3_{\text{Si}}$  units with a simultaneous decrease in the  $Q^2_{\text{Si}}$  units confirming an increase in the silicate network polymerization with  $\text{CaF}_2$  incorporation. The changes in the chemical shift values from  $^{31}\text{P}$  MAS-NMR spectra of bioactive glasses were small during the incorporation of  $\text{CaF}_2$  replacing  $\text{CaO}$  as shown in Fig. 8.8c [172, 174]. Since the proportion of Na to Ca is similar in glasses subjected to the replacement of  $\text{CaO}$  with  $\text{CaF}_2$ , the minor changes in the chemical shift values from  $^{31}\text{P}$  MAS-NMR spectra were associated

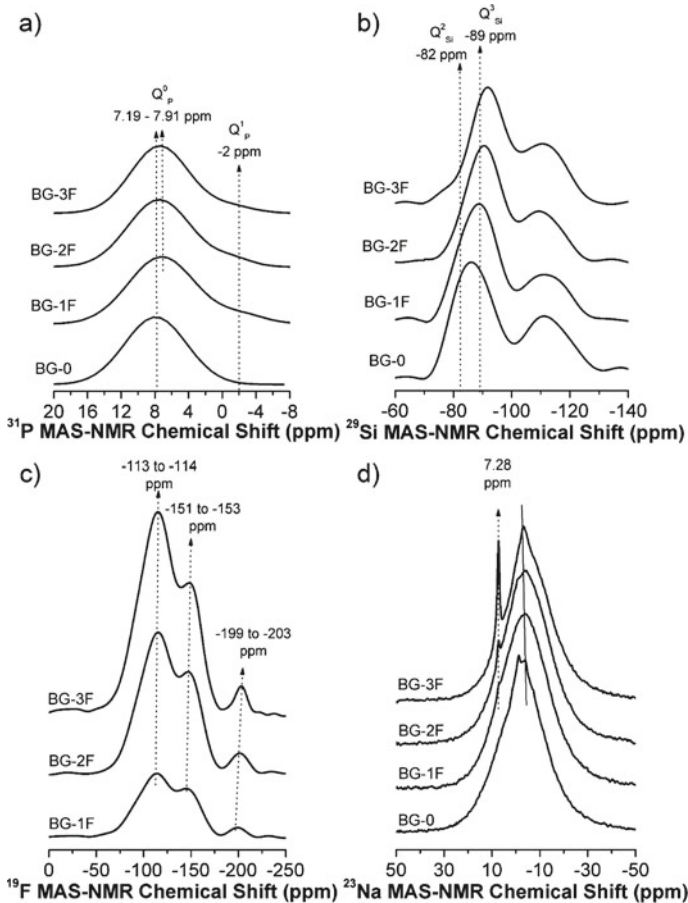


**Fig. 8.8** a  $^{31}\text{P}$ , b  $^{29}\text{Si}$ , c  $^{19}\text{F}$ , and d  $^{23}\text{Na}$  MAS-NMR of silicate bioactive glasses with  $\text{CaF}_2$  incorporation replacing  $\text{CaO}$  (from bottom to top). Reprinted from [172]. Copyright © 2020 with permission from Elsevier



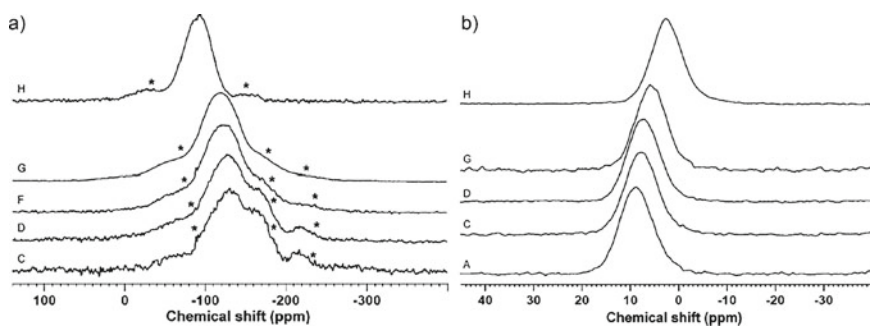


**Fig. 8.9** a  $^{19}\text{F}$  and b  $^{31}\text{P}$  MAS-NMR of silicate bioactive glasses with  $\text{CaF}_2$  incorporation (from bottom to top) in which A represents  $\text{CaF}_2$ -free glass and H represents  $\text{Na}_2\text{O}$ -free glass. Spinning sidebands are represented as \*. Reprinted from [166]. Copyright © 2010 with permission from Elsevier

with the variations in the Na-Ca environment around fluoride species. Moreover, the majority of the phosphate species exist as orthophosphate ( $Q^0_{\text{P}}$ ) units with either minor formation or absence of  $Q^1_{\text{P}}$  units/Si-O-P bonds [172, 174].

Contrastingly, there is no change in the chemical shift values from  $^{29}\text{Si}$  MAS-NMR spectra of glasses in which  $\text{CaF}_2$  is incorporated without changing the ratio of network former to network modifiers confirming that there is no change in the silicate network polymerization [166, 168]. A gradual decrease in the chemical shift values from  $^{31}\text{P}$  MAS-NMR spectra of silicate bioactive glasses during the incorporation of  $\text{CaF}_2$  (without changing the proportion of network formers to network modifiers) was reported [166, 168]. Since there is an increase in the proportion of Ca compared to Na, the changes in the chemical shift values from  $^{31}\text{P}$  MAS-NMR spectra confirm an increase in the proportion of Ca in the environment of the phosphate units as shown in Fig. 8.9b. Moreover, the phosphate species exist in the form of  $Q^0_{\text{P}}$  units irrespective of the  $\text{CaF}_2$  incorporation.

The bioactive behavior of  $\text{CaF}_2$  incorporated bioactive glasses depends primarily on the proportion of network former to network modifier and the content of  $\text{P}_2\text{O}_5$  in the glass composition [40, 165, 176]. Additionally, the fluoride ions from the bioactive glasses are released in exchange with the  $\text{OH}^-$  ions from the surrounding medium. Moreover, the formation of fluorapatite (FAp) is dominated compared to hydroxyapatite (HAp) on the bioactive glasses incorporated with  $\text{CaF}_2$  due to the release of fluoride ions and their availability in the surrounding medium. However, in low  $\text{P}_2\text{O}_5$  containing high  $\text{CaF}_2$  incorporated bioactive glasses, faster release of  $\text{Ca}^{2+}$  and  $\text{F}^-$  ions compared to  $\text{P}^{5+}$  ions has been reported to result in the formation of fluorite ( $\text{CaF}_2$ ) crystals or calcite ( $\text{CaCO}_3$ ) instead of FAp [162, 166, 174]. On the other hand, high  $\text{P}_2\text{O}_5$  containing high  $\text{CaF}_2$  incorporated bioactive glasses have been reported to result in the formation of FAp as well as fluorite [165, 176]. The delay in the formation of apatite in  $\text{CaF}_2$  incorporated bioactive glasses has been reported to occur due to various factors such as (i) an increase in the network connectivity, (ii) the formation of silica-rich and fluoride-modifier cations-rich regions, and (iii)

the inhibitory action of  $F^-$  ions in the conversion of amorphous calcium phosphate (ACP) into apatite [172, 177–180]. The formation of silica-rich and fluoride-modifier cations-rich regions has been reported to provide an uneven/non-uniform surface for the precipitation and formation of apatite crystals.

## 8.5 Antibacterial Properties

The antibacterial action of soda-lime-phosphosilicate bioactive glasses originates from its dissolution process under the physiological environment which in turn causes an increase in pH and osmotic pressure [38, 44, 45, 181]. An increase in both pH and osmotic pressure of the physiological environment affects the functions within the bacterial cells leading to damage of the cell membrane and inhibitory effects on DNA synthesis. Another proposed mechanism for the antibacterial properties of bioactive glasses is based on the rupture of the bacterial cell membrane by the sharp needle-like apatite crystals which form on the surface of bioactive glasses [182]. Using these mechanisms, bioactive glasses like 45S5, S53P4, and 13-93 have shown inhibitory effects on the growth of several Gram-positive and Gram-negative bacterial species [183–188]. The antibacterial properties of bioactive glasses could be further enhanced either by the incorporation of ions such as Ag, Cu, Ce, and Ga exhibiting antibacterial action or by the loading of antibiotic drugs which are released under the physiological environment [38, 44, 45, 181, 189–191]. However, the following section will discuss the mechanism of antibacterial action in bioactive silicate glasses incorporated with  $B_2O_3$ ,  $K_2O$ ,  $Li_2O$ ,  $MgO$ ,  $SrO$ ,  $ZnO$ , and fluorides.

Ottomeyer et al. observed inhibitory effects of 13-93B3 ( $B_2O_3$  incorporated 13-93) bioactive glass powder on several Gram-positive and Gram-negative bacteria along with methicillin-resistant *S. aureus* (MRSA) bacteria [36]. However, the lower antibacterial efficacy against Gram-negative *E. coli* bacteria compared to Gram-positive (*S. epidermidis*) and MRSA bacteria evidenced from live-dead cell assay was attributed to the mechanism of cell membrane disruption exhibited by 13-93B3 bioactive glass powders. A 13-93B3 bioactive (borate) glass fibers were reported to exhibit antibacterial properties against Gram-negative (*P. aeruginosa* and *A. baumannii*) and Gram-positive (*S. aureus*) bacterial biofilms [192]. Moreover, the evidenced antibacterial properties were attributed to the released borate ions rather than the released alkali ions and pH increase. However, Rau et al. did not evidence of any antibacterial effects from 13-93B3 glass-coated Ti implants against *E. faecalis*, *E. coli*, *P. aeruginosa*, and *S. aureus* [193]. The antibacterial effects from bioactive glasses primarily depend on the concentration of the released ions and pH increase against the bacterial cultures. Therefore, further investigation of antibacterial properties is necessary to understand the antibacterial effects of bioactive glass coatings. Prasad et al. evidenced bactericidal effects against *E. coli* from S53P4 glass powders incorporated with  $B_2O_3$  at a concentration of  $100 \text{ mg mL}^{-1}$  compared to S53P4 glass powders [91]. The observed antibacterial effects from  $B_2O_3$  incorporated S53P4



glasses were attributed to the faster dissolution and pH increase with the incorporation of  $B_2O_3$  as well as to the release of boron as evidenced under in vitro conditions. The pH increase in borate bioactive glasses was associated with the faster exchange of  $Na^+/Ca^{2+}$  ions from the glass with the  $H^+$  ions from the surrounding environment [104, 105, 194].

There is no literature available on the effect of antibacterial properties with the systematic incorporation of  $K_2O$ ,  $Li_2O$ , and  $MgO$  in silicate bioactive glasses. However, the faster dissolution of  $K_2O$  incorporated bioactive glasses is expected to favor antibacterial effects from the bioactive glasses [124]. F18, a silicate-based bioactive glass containing  $K_2O$  and  $MgO$  has been reported to exhibit bactericidal and anti-biofilm properties against *S. aureus* and MRSA [195].

Liu et al. reported a steady increase in the antibacterial effects against subgingival *A. actinomycetemcomitans* and *P. gingivalis* bacteria with the gradual incorporation of SrO in silicate-based bioactive glasses [196]. Moreover, the antibacterial efficacy of the SrO incorporated glasses was reported to increase with the increment in the concentration of the glass powders. Brauer et al. reported that the incorporation of Strontium ( $SrO + SrF_2$ ) up to 0.5 mol% in bioactive glass-based bone cement resulted in improved antibacterial effects against *S. faecalis* and *S. aureus* [197]. However, the incorporation of ( $SrO + SrF_2$ ) above 0.5 mol% up to 10 mol% did not significantly improve the antibacterial properties of the bioactive glass-based bone cement. Additionally, the antibacterial effects against *S. faecalis* and *S. aureus* have been correlated with the concentration of  $Sr^{2+}$  ions in the bacterial inoculum. Strontium has been reported to exhibit antibacterial effects by inhibiting the accumulation of intracellular polysaccharides in *S. mutans* bacteria by Wegman et al. [198].

Popa et al. observed a gradual reduction in the colony forming units (CFU) of *E. coli* and *S. aureus* with the incorporation of ZnO/SrO up to 6 mol% in a silicate-based bioactive glass confirming the bactericidal effects of Zn/Sr [196]. Additionally, the incorporation of ZnO/SrO was reported to promote the formation of a zone of inhibition around the glass powder compacts on *S. aureus* and *E. coli* cultured agar plates. Therefore, the antibacterial effects from the ZnO/SrO incorporated bioactive glasses were reported to be identical against Gram-negative (*E. coli*) and Gram-positive (*S. aureus*) bacteria. Moreover, glasses incorporated with both ZnO and SrO exhibited better antibacterial properties against *E. coli* and *S. aureus* compared to individual incorporation of ZnO/SrO and were correlated with synergistic effects from Zn and Sr. While, the presence of Zn in the bacterial environment leads to an increase in the reactive oxygen species (ROS) causing intracellular oxidative stress resulting in membrane damage, the presence of Sr inhibits the maturation of RNA required for protein synthesis [196].

Prasad et al. analyzed the antibacterial properties of fluoride incorporated S53P4 glass against *E. coli* bacteria and observed bactericidal action at 20 mg mL<sup>-1</sup> concentration of glass powders in the inoculum [172]. The antibacterial properties were reported to be originating from the changes in pH and the released  $F^-$  ions from the glasses. Liu et al. reported a gradual increase in the inhibition of Gram-negative (*P. gingivalis* and *A. actinomycetemcomitans*) bacteria with an increase in the incorporation of  $CaF_2$  in high  $P_2O_5$  containing silicate bioactive glasses [40]. Additionally,

a gradual increase in the concentration of the glass powders was reported to further inhibit the growth of bacteria. At each concentration of glass powders, maximum bacterial inhibition was evidenced for glass powders incorporated with 5 mol% of  $\text{CaF}_2$ , whereas further incorporation of  $\text{CaF}_2$  did not significantly increase the bacterial inhibition [40]. The antibacterial mechanism of fluorides in caries prevention has been reported based on the diffusion of fluoride in the form of HF into the cell membrane of bacteria affecting the intracellular pH leading to the inhibition of metabolism [199–201].

## 8.6 Conclusions and Future Trends

Several compositional modifications in bioactive glasses have led to improvements in thermal stability favoring thermal processing, sintering, and fiber drawing of bioactive glasses. Such improvements have been attributed to structural changes in bioactive glasses involving increased silicate network polymerization, mixed-alkali effects, and the formation of mixed network-former bonds. Moreover, the structural changes in bioactive glasses due to compositional modifications have been well understood using molecular dynamics simulation and MAS-NMR spectroscopy techniques. The knowledge of composition-structure-properties correlation has further encouraged researchers in designing novel bioactive glass compositions as an alternative to commercial glasses. The overall dissolution behavior and apatite formation on bioactive glasses have been associated with the silicate network connectivity, field strength of ions, and oxygen density. Additionally, the evidence of a wide range of mechanisms of antibacterial action from bioactive glasses assures the huge potential of modified bioactive glasses for treatments against bacterial infections.

The persistent efforts by several groups of researchers to improve the thermal stability of bioactive glasses and the existing knowledge base of composition-structure-property correlation in bioactive glasses propel the need for the design of materials by machine learning approaches to predict novel bioactive glass compositions with improved thermal stability. Such efforts are essential in the future to overcome the limitations of the laborious endeavor of compositional modifications involving various approaches.

**Acknowledgements** The authors are thankful to Dr. Suman K. Mishra, Director of CSIR-CGCRI, Dr. Saurindra Mahanty, AcSIR Coordinator of CSIR-CGCRI, Mr. Sitendu Mandal, Head of Specialty Glass Division, Dr. Annapurna Kalyandurg, Dr. Vamsi K. Balla and Dr. Amarnath R. Allu for their support, motivation and encouragement.

## References

1. Hench LL, Splinter RJ, Allen WC, Greenlee TK (1971) Bonding mechanisms at the interface of ceramic prosthetic materials. *J Biomed Mater Res* 5:117–141. <https://doi.org/10.1002/jbm.820050611>
2. Hench LL (2006) The story of Bioglass®. *J Mater Sci Mater Med* 17:967–978. <https://doi.org/10.1007/s10856-006-0432-z>
3. Greenspan D (2019) Bioglass at 50-A look at Larry Hench's legacy and bioactive materials. *Biomed Glas* 5:178–184. <https://doi.org/10.1515/bglass-2019-0014>
4. Hench LL (2013) Chronology of bioactive glass development and clinical applications. *New J Glas Ceram* 03:67–73. <https://doi.org/10.4236/njgc.2013.32011>
5. Hench LL (1991) Bioceramics: from concept to clinic. *J Am Ceram Soc* 74:1487–1510. <https://doi.org/10.1111/j.1151-2916.1991.tb07132.x>
6. Hench LL (1994) Bioactive ceramics: theory and clinical applications. *Bioceramics* 7:3–14. <https://doi.org/10.1016/B978-0-08-042144-5.50005-4>
7. Hench LL, LaTorre GP, Andersson ÖH (1991) The kinetics of bioactive ceramics part III: surface reactions for bioactive glasses compared with an inactive glass. In: Bonfield W, Hastings GW, Tanner KEBT-B (eds) *Bioceramics*. Butterworth-Heinemann, pp 155–162
8. Kim CY, Clark AE, Hench LL (1989) Early stages of calcium-phosphate layer formation in bioglasses. *J Non Cryst Solids* 113:195–202. [https://doi.org/10.1016/0022-3093\(89\)90011-2](https://doi.org/10.1016/0022-3093(89)90011-2)
9. Kokubo T, Kushitani H, Sakka S et al (1990) Solutions able to reproduce in vivo surface-structure changes in bioactive glass-ceramic A-W3. *J Biomed Mater Res* 24:721–734. <https://doi.org/10.1002/jbm.820240607>
10. Andersson OH, Liu G, Karlsson KH et al (1990) In vivo behaviour of glasses in the SiO<sub>2</sub>-Na<sub>2</sub>O-CaO-P<sub>2</sub>O<sub>5</sub>-Al<sub>2</sub>O<sub>3</sub>-B<sub>2</sub>O<sub>3</sub> system. *J Mater Sci Mater Med* 1:219–227. <https://doi.org/10.1007/BF00701080>
11. Jones JR (2015) Reprint of: review of bioactive glass: from Hench to hybrids. *Acta Biomater* 23:S53–S82. <https://doi.org/10.1016/j.actbio.2015.07.019>
12. Brink M (1997) The influence of alkali and alkaline earths on the working range for bioactive glasses. *J Biomed Mater Res* 36:109–117. [https://doi.org/10.1002/\(SICI\)1097-4636\(199707\)36:1%3c109::AID-JBM13%3e3.0.CO;2-D](https://doi.org/10.1002/(SICI)1097-4636(199707)36:1%3c109::AID-JBM13%3e3.0.CO;2-D)
13. Baino F, Hamzehlou S, Kargozar S (2018) Bioactive glasses: where are we and where are we going? *J Funct Biomater* 9
14. Hench LL, Jones JR (2015) Bioactive glasses: frontiers and challenges. *Front Bioeng Biotechnol* 3:1–12. <https://doi.org/10.3389/fbioe.2015.00194>
15. Hupa L, Hupa M (2010) Recent research on composition dependence of the properties of bioactive glasses. *Ceram Trans* 218:145–156
16. Huang TS, Rahaman MN, Doiphode ND et al (2011) Freeze extrusion fabrication of 13–93 bioactive glass scaffolds for repair and regeneration of load-bearing bones. *Ceram Trans* 228:45–55
17. Ylänen H (2017) *Bioactive glasses: materials, properties and applications*. Woodhead Publishing
18. Fu Q, Rahaman MN, Sonny Bal B et al (2008) Mechanical and in vitro performance of 13–93 bioactive glass scaffolds prepared by a polymer foam replication technique. *Acta Biomater* 4:1854–1864. <https://doi.org/10.1016/j.actbio.2008.04.019>
19. Jones JR, Brauer DS, Hupa L, Greenspan DC (2016) Bioglass and bioactive glasses and their impact on healthcare. *Int J Appl Glas Sci* 7:423–434. <https://doi.org/10.1111/ijag.12252>
20. Lindfors N, Geurts J, Drago L et al (2017) Antibacterial bioactive glass S53P4 for chronic bone infections—a multinational study. In: Drago L (ed) *Advances in experimental medicine and biology*. Springer International Publishing, Cham, pp 81–92
21. Lindfors NC, Hyvönen P, Nyyssönen M et al (2010) Bioactive glass S53P4 as bone graft substitute in treatment of osteomyelitis. *Bone* 47:212–218. <https://doi.org/10.1016/j.bone.2010.05.030>

22. Van Gestel NAP, Geurts J, Hulsen DJW et al (2015) Clinical applications of S53P4 bioactive glass in bone healing and osteomyelitic treatment: a literature review. *Biomed Res Int*. <http://doi.org/10.1155/2015/684826>
23. Jones JR, Brauer DS, Greenspan DC et al (2016) Bioglass and bioactive glasses and their impact on healthcare 434:423–434. <https://doi.org/10.1111/ijag.12252>
24. Bellucci D, Cannillo V, Sola A (2010) An overview of the effects of thermal processing on bioactive glasses. *Sci Sinter* 42:307–320. <https://doi.org/10.2298/SOS1003307B>
25. Fernandes HR, Gaddam A, Rebelo A et al (2018) Bioactive glasses and glass-ceramics for healthcare applications in bone regeneration and tissue engineering. *Materials (Basel)* 11:2530. <https://doi.org/10.3390/ma11122530>
26. Ferreira JMF, Rebelo A (2017) The key features expected from a perfect bioactive glass—how far we still are from an ideal composition? *Biomed J Sci Tech Res* 1:4–7. <http://doi.org/10.26717/bjstr.2017.01.000335>
27. Baino F, Novajra G, Vitale-Brovarone C (2015) Bioceramics and scaffolds: a winning combination for tissue engineering. *Front Bioeng Biotechnol* 3:202. <https://doi.org/10.3389/fbioe.2015.00202>
28. Fu Q, Mauro JC, Rahaman MN (2016) Bioactive glass innovations through academia-industry collaboration. *Int J Appl Glas Sci* 7:139–146. <https://doi.org/10.1111/ijag.12202>
29. Kingery WD, Berg M (1955) Study of the initial stages of sintering solids by viscous flow, evaporation-condensation, and self-diffusion. *J Appl Phys* 26:1205–1212. <https://doi.org/10.1063/1.1721874>
30. Prado MO, Zanotto ED (2002) Glass sintering with concurrent crystallization. *Comptes Rendus Chim* 5:773–786. [https://doi.org/10.1016/S1631-0748\(02\)01447-9](https://doi.org/10.1016/S1631-0748(02)01447-9)
31. Lefebvre L, Gremillard L, Chevalier J et al (2008) Sintering behaviour of 45S5 bioactive glass. *Acta Biomater* 4:1894–1903. <https://doi.org/10.1016/j.actbio.2008.05.019>
32. Eichhorn J, Elschner C, Groß M et al (2021) Spinning of endless bioactive silicate glass fibres for fibre reinforcement applications. *Appl Sci* 11:7927
33. Arstila H, Tukiainen M, Hupa L et al (2006) In vitro reactivity of bioactive glass fibers. In: *Advances in science and technology*, pp 246–251
34. Lindfors N, Romano C, Scarponi S et al (2017) Chapter 14: bioactive glasses in infection treatment. In: *RSC smart materials*. The Royal Society of Chemistry, pp 316–335
35. Ribeiro M, Monteiro FJ, Ferraz MP (2012) Infection of orthopedic implants with emphasis on bacterial adhesion process and techniques used in studying bacterial-material interactions. *Biomater* 2:176–194. <https://doi.org/10.4161/biom.22905>
36. Ottomeyer M, Mohammadkahn A, Day D, Westenberg D (2016) Broad-spectrum antibacterial characteristics of four novel borate-based bioactive glasses. *Adv Microbiol* 06:776–787. [https://doi.org/10.1016/0304-3940\(77\)90092-1](https://doi.org/10.1016/0304-3940(77)90092-1)
37. Fernandes JS, Martins M, Neves NM et al (2016) Intrinsic antibacterial borosilicate glasses for bone tissue engineering applications. *ACS Biomater Sci Eng* 2:1143–1150. <https://doi.org/10.1021/acsbiomaterials.6b00162>
38. Fernandes JS, Gentile P, Pires RA et al (2017) Multifunctional bioactive glass and glass-ceramic biomaterials with antibacterial properties for repair and regeneration of bone tissue. *Acta Biomater* 59:2–11. <https://doi.org/10.1016/j.actbio.2017.06.046>
39. Stoor P, Soderling E, Salonen JI (1998) Antibacterial effects of a bioactive glass paste on oral microorganisms. *Acta Odontol Scand* 56:161–165. <https://doi.org/10.1080/000163598422901>
40. Liu J, Rawlinson SCF, Hill RG, Fortune F (2016) Fluoride incorporation in high phosphate containing bioactive glasses and in vitro osteogenic, angiogenic and antibacterial effects. *Dent Mater* 32:e221–e237. <https://doi.org/10.1016/j.dental.2016.07.003>
41. Jia WT, Fu Q, Huang WH et al (2015) Comparison of borate bioactive glass and calcium sulfate as implants for the local delivery of teicoplanin in the treatment of methicillin-resistant *Staphylococcus aureus*-induced osteomyelitis in a rabbit model. *Antimicrob Agents Chemother* 59:7571–7580. <https://doi.org/10.1128/AAC.00196-15>

42. Inzana JA, Schwarz EM, Kates SL, Awad HA (2016) Biomaterials approaches to treating implant-associated osteomyelitis. *Biomaterials* 81:58–71. <https://doi.org/10.1016/j.biomaterials.2015.12.012>
43. Rahaman MN, Bal BS, Huang W (2014) Review: emerging developments in the use of bioactive glasses for treating infected prosthetic joints. *Mater Sci Eng C* 41:224–231. <https://doi.org/10.1016/j.msec.2014.04.055>
44. Drago L, Toscano M, Bottagisio M (2018) Recent evidence on bioactive glass antimicrobial and antibiofilm activity: a mini-review. *Materials (Basel)* 11:1–11. <https://doi.org/10.3390/ma11020326>
45. Rivadeneira J, Gorustovich A (2017) Bioactive glasses as delivery systems for antimicrobial agents. *J Appl Microbiol* 122:1424–1437. <https://doi.org/10.1111/jam.13393>
46. Kaur G, Pickrell G, Srianganathan N et al (2016) Review and the state of the art: sol–gel and melt quenched bioactive glasses for tissue engineering. *J Biomed Mater Res Part B Appl Biomater* 104:1248–1275. <https://doi.org/10.1002/jbm.b.33443>
47. Lombardi M, Gremillard L, Chevalier J et al (2013) A comparative study between melt-derived and sol-gel synthesized 45S5 bioactive glasses. *Key Eng Mater* 541:15–30. <https://doi.org/10.4028/www.scientific.net/KEM.541.15>
48. Hupa L (2011) Melt-derived bioactive glasses. In: Ylänen HOBT-BG (ed) *Bioactive glasses: materials, properties and applications*. Woodhead Publishing, UK, pp 3–28
49. Zachariasen WH (1932) The atomic arrangement in glass. *J Am Chem Soc* 54:3841–3851. <https://doi.org/10.1021/ja01349a006>
50. Doweidar H (1996) The density of alkali silicate glasses in relation to the microstructure. *J Non Cryst Solids* 194:155–162. [https://doi.org/10.1016/0022-3093\(95\)00489-0](https://doi.org/10.1016/0022-3093(95)00489-0)
51. Brauer DS (2015) Bioactive glasses—structure and properties. *Angewandte* 2–24. <http://doi.org/10.1002/anie.201405310>
52. Hill RG, Brauer DS (2011) Predicting the bioactivity of glasses using the network connectivity or split network models. *J Non Cryst Solids* 357:3884–3887. <https://doi.org/10.1016/j.jnoncrystalsol.2011.07.025>
53. Elgayar I, Aliev AE, Boccaccini AR, Hill RG (2005) Structural analysis of bioactive glasses. *J Non Cryst Solids* 351:173–183. <https://doi.org/10.1016/j.jnoncrystalsol.2004.07.067>
54. Pedone A, Charpentier T, Malavasi G, Menziani MC (2010) New insights into the atomic structure of 45S5 bioglass by means of solid-state NMR spectroscopy and accurate first-principles simulations. *Chem Mater* 22:5644–5652. <https://doi.org/10.1021/cm102089c>
55. Mathew R, Stevansson B, Tilocca A, Edén M (2014) Toward a rational design of bioactive glasses with optimal structural features: composition-structure correlations unveiled by solid-state NMR and MD simulations. *J Phys Chem B* 118:833–844. <https://doi.org/10.1021/jp409652k>
56. Lebecq I, Désanglois F, Leriche A, Follet-Houttemane C (2007) Compositional dependence on the in vitro bioactivity of invert or conventional bioglasses in the Si-Ca-Na-P system. *J Biomed Mater Res Part A* 83:156–168. <https://doi.org/10.1002/jbm.a.31228>
57. Hench LL (2009) Genetic design of bioactive glass. *J Eur Ceram Soc* 29:1257–1265. <https://doi.org/10.1016/j.jeurceramsoc.2008.08.002>
58. Hoppe A, Güldal NS, Boccaccini AR (2011) A review of the biological response to ionic dissolution products from bioactive glasses and glass-ceramics. *Biomaterials* 32:2757–2774. <https://doi.org/10.1016/j.biomaterials.2011.01.004>
59. Ohtsuki C, Kokubo T, Yamamuro T (1992) Mechanism of apatite formation on CaO-SiO<sub>2</sub>-P<sub>2</sub>O<sub>5</sub> glasses in a simulated body fluid. *J Non Cryst Solids* 143:84–92. [https://doi.org/10.1016/S0022-3093\(05\)80556-3](https://doi.org/10.1016/S0022-3093(05)80556-3)
60. Brow RK (2000) Review: the structure of simple phosphate glasses. *J Non Cryst Solids* 263:1–28. [https://doi.org/10.1016/S0022-3093\(99\)00620-1](https://doi.org/10.1016/S0022-3093(99)00620-1)
61. Boccaccini AR, Brauer DS, Hupa L (2017) *Bioactive glasses*. The Royal Society of Chemistry
62. Abou Neel EA, Pickup DM, Valappil SP et al (2009) Bioactive functional materials: a perspective on phosphate-based glasses. *J Mater Chem* 19:690–701. <https://doi.org/10.1039/b810675d>

63. Ahmed I, Lewis M, Olsen I, Knowles JC (2004) Phosphate glasses for tissue engineering: part 1. Processing and characterisation of a ternary-based  $P_2O_5$ -CaO- $Na_2O$  glass system. *Biomaterials* 25:491–499. [https://doi.org/10.1016/S0142-9612\(03\)00546-5](https://doi.org/10.1016/S0142-9612(03)00546-5)
64. Yu Y, Mathew R, Edén M (2018) Quantitative composition–bioactivity relationships of phosphosilicate glasses: bearings from the phosphorus content and network polymerization. *J Non Cryst Solids* 502:106–117. <https://doi.org/10.1016/j.jnoncrysol.2018.07.060>
65. Golovchak R, Thapar P, Ingram A et al (2014) Influence of phase separation on the devitrification of 45S5 bioglass. *Acta Biomater* 10:4878–4886. <https://doi.org/10.1016/j.actbio.2014.07.024>
66. Kowal TJ, Golovchak R, Chokshi T et al (2017) Role of phase separation on the biological performance of 45S5 Bioglass®. *J Mater Sci Mater Med* 28:161. <https://doi.org/10.1007/s10856-017-5976-6>
67. Jiusti J, Zanotto ED, Feller SA et al (2020) Effect of network formers and modifiers on the crystallization resistance of oxide glasses. *J Non Cryst Solids* 550:120359. <https://doi.org/10.1016/j.jnoncrysol.2020.120359>
68. Nascimento MLF, Souza LA, Ferreira EB, Zanotto ED (2005) Can glass stability parameters infer glass forming ability? *J Non Cryst Solids* 351:3296–3308. <https://doi.org/10.1016/j.jnoncrysol.2005.08.013>
69. Hrubý A (1972) Evaluation of glass-forming tendency by means of DTA. *Czechoslov J Phys* 22:1187–1193. <https://doi.org/10.1007/BF01690134>
70. Lara C, Pascual MJ, Durán A (2004) Glass-forming ability, sinterability and thermal properties in the systems RO-BaO-SiO<sub>2</sub> (R = Mg, Zn). *J Non Cryst Solids* 348:149–155. <https://doi.org/10.1016/j.jnoncrysol.2004.08.140>
71. Brink M, Turunen T, Happonen RP, Yli-Urpo A (1997) Compositional dependence of bioactivity of glasses in the system  $Na_2O$ - $K_2O$ -MgO-Cao- $B_2O_3$ - $P_2O_5$ -SiO<sub>2</sub>. *J Biomed Mater Res* 37:114–121. [https://doi.org/10.1002/\(SICI\)1097-4636\(199710\)37:1%3c114::AID-JBM14%3e3.0.CO;2-G](https://doi.org/10.1002/(SICI)1097-4636(199710)37:1%3c114::AID-JBM14%3e3.0.CO;2-G)
72. Coon E, Whittier AM, Abel BM et al (2021) Viscosity and crystallization of bioactive glasses from 45S5 to 13-93. *Int J Appl Glas Sci* 12:65–77. <https://doi.org/10.1111/ijag.15837>
73. Sriranganathan D, Kanwal N, Hing KA, Hill RG (2016) Strontium substituted bioactive glasses for tissue engineered scaffolds: the importance of octacalcium phosphate. *J Mater Sci Mater Med* 27:1–10. <https://doi.org/10.1007/s10856-015-5653-6>
74. Goel A, Kapoor S, Rajagopal RR et al (2012) Alkali-free bioactive glasses for bone tissue engineering: a preliminary investigation. *Acta Biomater* 8:361–372. <https://doi.org/10.1016/j.actbio.2011.08.026>
75. Chapin RE, Ku WW, Kenney MA et al (1997) The effects of dietary boron on bone strength in rats. *Toxicol Sci* 35:205–215. <https://doi.org/10.1093/toxsci/35.2.205>
76. Newnham RE (1991) Agricultural practices affect arthritis. *Nutr Health* 7:89–100. <https://doi.org/10.1177/026010609100700204>
77. Balasubramanian P, Hupa L, Jokic B et al (2017) Angiogenic potential of boron-containing bioactive glasses: in vitro study. *J Mater Sci* 52:8785–8792. <https://doi.org/10.1007/s10853-016-0563-7>
78. Haro Durand LA, Vargas GE, Romero NM et al (2015) Angiogenic effects of ionic dissolution products released from a boron-doped 45S5 bioactive glass. *J Mater Chem B* 3:1142–1148. <https://doi.org/10.1039/c4tb01840k>
79. Balasubramanian P, Büttner T, Míguez Pacheco V, Boccaccini AR (2018) Boron-containing bioactive glasses in bone and soft tissue engineering. *J Eur Ceram Soc* 38:855–869. <https://doi.org/10.1016/j.jeurceramsoc.2017.11.001>
80. Fernandes JS, Gentile P, Crawford A et al (2017) Substituted borosilicate glasses with improved osteogenic capacity for bone tissue engineering. *Tissue Eng Part A* 23:1331–1342. <https://doi.org/10.1089/ten.tea.2016.0386>
81. Ojansivu M, Mishra A, Vanhatupa S et al (2018) The effect of S53P4-based borosilicate glasses and glass dissolution products on the osteogenic commitment of human adipose stem cells. *PLoS ONE* 13:e0202740. <https://doi.org/10.1371/journal.pone.0202740>



82. Xia L, Ma W, Zhou Y et al (2019) Stimulatory effects of boron containing bioactive glass on osteogenesis and angiogenesis of polycaprolactone: in vitro study. *Biomed Res Int*. <http://doi.org/10.1155/2019/8961409>
83. Wright AC (2015) My borate life: an enigmatic journey. *Int J Appl Glas Sci* 6:45–63. <http://doi.org/10.1111/ijag.12113>
84. Wright AC, Dalba G, Rocca F, Vedishcheva NM (2010) Borate versus silicate glasses: why are they so different? *Phys Chem Glas Eur J Glas Sci Technol Part B* 51:233–265
85. Yun YH, Bray PJ (1978) Nuclear magnetic resonance studies of the glasses in the system  $\text{Na}_2\text{OB}_2\text{O}_3\text{SiO}_2$ . *J Non Cryst Solids* 27:363–380. [https://doi.org/10.1016/0022-3093\(78\)90020-0](https://doi.org/10.1016/0022-3093(78)90020-0)
86. Dell WJ, Bray PJ, Xiao SZ (1983)  $^{11}\text{B}$  NMR studies and structural modeling of  $\text{Na}_2\text{OB}_2\text{O}_3\text{SiO}_2$  glasses of high soda content. *J Non Cryst Solids* 58:1–16. [https://doi.org/10.1016/0022-3093\(83\)90097-2](https://doi.org/10.1016/0022-3093(83)90097-2)
87. Manara D, Grandjean A, Neuville DR (2009) Structure of borosilicate glasses and melts: a revision of the Yun, Bray and Dell model. *J Non Cryst Solids* 355:2528–2531. <https://doi.org/10.1016/j.jnoncrysol.2009.08.033>
88. Jung S (2010) Borate based bioactive glass scaffolds for hard and soft tissue engineering. Missouri University of Science and Technology
89. Fu Q, Rahaman MN, Bal BS et al (2010) Silicate, borosilicate, and borate bioactive glass scaffolds with controllable degradation rate for bone tissue engineering applications. II. In vitro and in vivo biological evaluation. *J Biomed Mater Res Part A* 95:172–179. <https://doi.org/10.1002/jbm.a.32823>
90. Fabert M, Ojha N, Erasmus E et al (2017) Crystallization and sintering of borosilicate bioactive glasses for application in tissue engineering. *J Mater Chem B* 5:4514–4525. <https://doi.org/10.1039/c7tb00106a>
91. Prasad SS, Datta S, Adarsh T et al (2018) Effect of boron oxide addition on structural, thermal, in vitro bioactivity and antibacterial properties of bioactive glasses in the base S53P4 composition. *J Non Cryst Solids* 498:204–215. <https://doi.org/10.1016/j.jnoncrysol.2018.06.027>
92. Brandt-Slowik J (2020) Structure, solubility and crystallisation behaviour of bioactive borosilicate glasses
93. Hmood F, Goerke O, Schmidt F (2018) Chemical composition refining of bioactive glass for better processing features, part I. *Biomed Glas* 4:82–94. <https://doi.org/10.1515/bglass-2018-0008>
94. Arango-Ospina M, Hupa L, Boccaccini AR (2019) Bioactivity and dissolution behavior of boron-containing bioactive glasses under static and dynamic conditions in different media. *Biomed Glas* 5:124–139. <https://doi.org/10.1515/bglass-2019-0011>
95. Massera J, Fagerlund S, Hupa L, Hupa M (2012) Crystallization mechanism of the bioactive glasses, 45S5 and S53P4. *J Am Ceram Soc* 95:607–613. <https://doi.org/10.1111/j.1551-2916.2011.05012.x>
96. Lu X, Deng L, Huntley C et al (2018) Mixed network former effect on structure, physical properties, and bioactivity of 45S5 bioactive glasses: an integrated experimental and molecular dynamics simulation study. *J Phys Chem B* 122:2564–2577. <https://doi.org/10.1021/acs.jpcc.7b12127>
97. Yu Y, Edén M (2016) Structure-composition relationships of bioactive borophosphosilicate glasses probed by multinuclear  $^{11}\text{B}$ ,  $^{29}\text{Si}$ , and  $^{31}\text{P}$  solid state NMR. *RSC Adv* 6:101288–101303. <https://doi.org/10.1039/c6ra15275a>
98. Prasad S, Gaddam A, Jana A et al (2019) Structure and stability of high CaO- and  $\text{P}_2\text{O}_5$ -containing silicate and borosilicate bioactive glasses. *J Phys Chem B* 123:7558–7569. <https://doi.org/10.1021/acs.jpcc.9b02455>
99. Jung SB, Day DE (2009) Conversion kinetics of silicate, borosilicate, and borate bioactive glasses to hydroxyapatite. *Phys Chem Glas Eur J Glas Sci Technol Part B* 50:85–88
100. Balasubramanian P, Grünewald A, Detsch R et al (2016) Ion release, hydroxyapatite conversion, and cytotoxicity of boron-containing bioactive glass scaffolds. *Int J Appl Glas Sci* 7:206–215. <https://doi.org/10.1111/ijag.12206>

101. Brown RF, Rahaman MN, Dwilewicz AB et al (2009) Effect of borate glass composition on its conversion to hydroxyapatite and on the proliferation of MC3T3-E1 cells. *J Biomed Mater Res Part A* 88A:392–400. <http://doi.org/10.1002/jbm.a.31679>
102. Yao A, Wang D, Huang W et al (2007) In vitro bioactive characteristics of borate-based glasses with controllable degradation behavior. *J Am Ceram Soc* 90:303–306. <https://doi.org/10.1111/j.1551-2916.2006.01358.x>
103. Huang W, Day DE, Kittiratanapiboon K, Rahaman MN (2006) Kinetics and mechanisms of the conversion of silicate (45S5), borate, and borosilicate glasses to hydroxyapatite in dilute phosphate solutions. *J Mater Sci Mater Med* 17:583–596. <https://doi.org/10.1007/s10856-006-9220-z>
104. Bunker BC (1986) Solution chemistry of silicate and borate materials. *MRS Proc* 73:49. <http://doi.org/10.1557/PROC-73-49>
105. Bunker BC, Arnold GW, Day DE, Bray PJ (1986) The effect of molecular structure on borosilicate glass leaching. *J Non Cryst Solids* 87:226–253. [http://doi.org/10.1016/S0022-3093\(86\)80080-1](http://doi.org/10.1016/S0022-3093(86)80080-1)
106. Brauer DS (2015) Bioactive glasses—structure and properties. *Angew Chemie Int Ed* 54:4160–4181. <https://doi.org/10.1002/anie.201405310>
107. Döhler F, Groh D, Chiba S et al (2016) Bioactive glasses with improved processing. Part 2. Viscosity and fibre drawing. *J Non Cryst Solids* 432:130–136. <https://doi.org/10.1016/j.jnoncrysol.2015.03.009>
108. Chen X, Chen X, Brauer DS et al (2017) Sodium is not essential for high bioactivity of glasses. *Int J Appl Glas Sci* 8:428–437. <https://doi.org/10.1111/ijag.12323>
109. Kapoor S, Semitela Â, Goel A et al (2015) Understanding the composition-structure-bioactivity relationships in diopside (CaO·MgO·2SiO<sub>2</sub>)-tricalcium phosphate (3CaO·P<sub>2</sub>O<sub>5</sub>) glass system. *Acta Biomater* 15:210–226. <https://doi.org/10.1016/j.actbio.2015.01.001>
110. Arstila H, Vedel E, Hupa L, Hupa M (2007) Factors affecting crystallization of bioactive glasses. *J Eur Ceram Soc* 27:1543–1546. <https://doi.org/10.1016/j.jeurceramsoc.2006.04.017>
111. Arstila H, Zhang D, Vedel E et al (2005) Bioactive glass compositions suitable for repeated heat-treatments. In: *Key engineering materials*, pp 925–928
112. Kapoor S, Goel A, Pascual MJ, Ferreira JMF (2016) Alkali-free bioactive diopside-tricalcium phosphate glass-ceramics for scaffold fabrication: sintering and crystallization behaviours. *J Non Cryst Solids* 432:81–89. <https://doi.org/10.1016/j.jnoncrysol.2015.05.033>
113. Bellucci D, Cannillo V, Sola A (2011) A new highly bioactive composite for scaffold applications: a feasibility study. *Materials (Basel)* 4:339–354
114. Bellucci D, Sola A, Cannillo V (2012) Low temperature sintering of innovative bioactive glasses. *J Am Ceram Soc* 95:1313–1319. <https://doi.org/10.1111/j.1551-2916.2012.05100.x>
115. Wu ZY, Hill RG, Yue S et al (2011) Melt-derived bioactive glass scaffolds produced by a gel-cast foaming technique. *Acta Biomater* 7:1807–1816. <https://doi.org/10.1016/j.actbio.2010.11.041>
116. Groh D, Döhler F, Brauer DS (2014) Bioactive glasses with improved processing. Part 1. Thermal properties, ion release and apatite formation. *Acta Biomater* 10:4465–4473. <https://doi.org/10.1016/j.actbio.2014.05.019>
117. Gaddam A, Gołębiewski P, Fernandes HR et al (2021) Development of microfibers for bone regeneration based on alkali-free bioactive glasses doped with boron oxide. *J Am Ceram Soc* 104:4492–4504. <https://doi.org/10.1111/jace.17853>
118. Mathew R, Stevansson B, Edén M (2015) Na/Ca intermixing around silicate and phosphate groups in bioactive phosphosilicate glasses revealed by heteronuclear solid-state NMR and molecular dynamics simulations. *J Phys Chem B* 119:5701–5715. <https://doi.org/10.1021/acs.jpcc.5b01130>
119. Mozafari M, Banijamali S, Baino F et al (2019) Calcium carbonate: adored and ignored in bioactivity assessment. *Acta Biomater* 91:35–47. <https://doi.org/10.1016/j.actbio.2019.04.039>
120. Lambert H, Frassetto L, Moore JB et al (2015) The effect of supplementation with alkaline potassium salts on bone metabolism: a meta-analysis. *Osteoporos Int* 26:1311–1318. <https://doi.org/10.1007/s00198-014-3006-9>



121. Tylkowski M, Brauer DS (2013) Mixed alkali effects in Bioglass® 45S5. *J Non Cryst Solids* 376:175–181. <https://doi.org/10.1016/j.jnoncrysol.2013.05.039>
122. Crovace MC, Soares VO, Rodrigues ACM et al (2021) Understanding the mixed alkali effect on the sinterability and in vitro performance of bioactive glasses. *J Eur Ceram Soc* 41:4391–4405. <https://doi.org/10.1016/j.jeurceramsoc.2020.11.020>
123. Hupa L, Fagerlund S, Massera J, Björkvik L (2016) Dissolution behavior of the bioactive glass S53P4 when sodium is replaced by potassium, and calcium with magnesium or strontium. *J Non Cryst Solids* 432:41–46. <https://doi.org/10.1016/j.jnoncrysol.2015.03.026>
124. Brückner R, Tylkowski M, Hupa L, Brauer DS (2016) Controlling the ion release from mixed alkali bioactive glasses by varying modifier ionic radii and molar volume. *J Mater Chem B* 4:3121–3134. <https://doi.org/10.1039/c5tb02426a>
125. Khorami M, Hesarak S, Behnamghader A et al (2011) In vitro bioactivity and biocompatibility of lithium substituted 45S5 bioglass. *Mater Sci Eng C* 31:1584–1592. <https://doi.org/10.1016/j.msec.2011.07.011>
126. Miguez-Pacheco V, Büttner T, Maçon ALB et al (2016) Development and characterization of lithium-releasing silicate bioactive glasses and their scaffolds for bone repair. *J Non Cryst Solids* 432:65–72. <https://doi.org/10.1016/j.jnoncrysol.2015.03.027>
127. Bellucci D, Sola A, Salvatori R et al (2017) Role of magnesium oxide and strontium oxide as modifiers in silicate-based bioactive glasses: effects on thermal behaviour, mechanical properties and in-vitro bioactivity. *Mater Sci Eng C* 72:566–575. <https://doi.org/10.1016/j.msec.2016.11.110>
128. Souza MT, Crovace MC, Schröder C et al (2013) Effect of magnesium ion incorporation on the thermal stability, dissolution behavior and bioactivity in Bioglass-derived glasses. *J Non Cryst Solids* 382:57–65. <https://doi.org/10.1016/j.jnoncrysol.2013.10.001>
129. Blochberger M, Hupa L, Brauer DS (2015) Influence of zinc and magnesium substitution on ion release from Bioglass 45S5 at physiological and acidic pH. *Biomed Glas* 1:93–107. <https://doi.org/10.1515/bglass-2015-0009>
130. Oliveira JM, Correia RN, Fernandes MH, Rocha J (2000) Influence of the CaO/MgO ratio on the structure of phase-separated glasses: a solid state <sup>29</sup>Si and <sup>31</sup>P MAS NMR study. *J Non Cryst Solids* 265:221–229. [https://doi.org/10.1016/S0022-3093\(99\)00957-6](https://doi.org/10.1016/S0022-3093(99)00957-6)
131. Watts SJ, Hill RG, O'Donnell MD, Law RV (2010) Influence of magnesia on the structure and properties of bioactive glasses. *J Non Cryst Solids* 356:517–524. <https://doi.org/10.1016/j.jnoncrysol.2009.04.074>
132. Wetzel R, Bartzok O, Hupa L, Brauer DS (2019) Low Mg or Zn substitution for improved thermal properties of Bioglass 45S5. *Mater Lett* 256:126599. <https://doi.org/10.1016/j.matlet.2019.126599>
133. Ma J, Chen CZ, Wang DG et al (2010) Effect of magnesia on the degradability and bioactivity of sol-gel derived SiO<sub>2</sub>-CaO-MgO-P<sub>2</sub>O<sub>5</sub> system glasses. *Colloids Surf B Biointerfaces* 81:87–95. <https://doi.org/10.1016/j.colsurfb.2010.06.022>
134. Ma J, Chen CZ, Wang DG et al (2010) In vitro degradability and bioactivity of mesoporous CaO-MgO-P<sub>2</sub>O<sub>5</sub>-SiO<sub>2</sub> glasses synthesized by sol-gel method. *J Sol-Gel Sci Technol* 54:69–76. <https://doi.org/10.1007/s10971-010-2159-z>
135. Kargozar S, Montazerian M, Fiume E, Baino F (2019) Multiple and promising applications of strontium (Sr)-containing bioactive glasses in bone tissue engineering. *Front Bioeng Biotechnol* 7:161
136. Fredholm YC, Karpukhina N, Law RV, Hill RG (2010) Strontium containing bioactive glasses: glass structure and physical properties. *J Non Cryst Solids* 356:2546–2551. <https://doi.org/10.1016/j.jnoncrysol.2010.06.078>
137. O'Donnell MD, Hill RG (2010) Influence of strontium and the importance of glass chemistry and structure when designing bioactive glasses for bone regeneration. *Acta Biomater* 6:2382–2385. <https://doi.org/10.1016/j.actbio.2010.01.006>
138. Du J, Xiang Y (2012) Effect of strontium substitution on the structure, ionic diffusion and dynamic properties of 45S5 bioactive glasses. *J Non Cryst Solids* 358:1059–1071. <https://doi.org/10.1016/j.jnoncrysol.2011.12.114>

139. O'Donnell MD, Candarlioglu PL, Miller CA et al (2010) Materials characterisation and cytotoxic assessment of strontium-substituted bioactive glasses for bone regeneration. *J Mater Chem* 20:8934–8941. <https://doi.org/10.1039/c0jm01139h>
140. Lotfibakhshaiesh N, Brauer DS, Hill RG (2010) Bioactive glass engineered coatings for Ti6Al4V alloys: influence of strontium substitution for calcium on sintering behaviour. *J Non Cryst Solids* 356:2583–2590. <https://doi.org/10.1016/j.jnoncrysol.2010.05.017>
141. Goel A, Rajagopal RR, Ferreira JMF (2011) Influence of strontium on structure, sintering and biodegradation behaviour of CaO-MgO-SrO-SiO<sub>2</sub>-P<sub>2</sub>O<sub>5</sub>-CaF<sub>2</sub> glasses. *Acta Biomater* 7:4071–4080. <https://doi.org/10.1016/j.actbio.2011.06.047>
142. Fredholm YC, Karpukhina N, Brauer DS et al (2012) Influence of strontium for calcium substitution in bioactive glasses on degradation, ion release and apatite formation. *J R Soc Interface* 9:880–889. <https://doi.org/10.1098/rsif.2011.0387>
143. Dai LL, Mei ML, Chu CH, Lo ECM (2021) Remineralizing effect of a new strontium-doped bioactive glass and fluoride on demineralized enamel and dentine. *J Dent* 108:103633. <https://doi.org/10.1016/j.jdent.2021.103633>
144. Gentleman E, Fredholm YC, Jell G et al (2010) The effects of strontium-substituted bioactive glasses on osteoblasts and osteoclasts in vitro. *Biomaterials* 31:3949–3956. <https://doi.org/10.1016/j.biomaterials.2010.01.121>
145. Boyd D, Carroll G, Towler MR et al (2009) Preliminary investigation of novel bone graft substitutes based on strontium–calcium–zinc–silicate glasses. *J Mater Sci Mater Med* 20:413–420. <https://doi.org/10.1007/s10856-008-3569-0>
146. Zhang Y, Wei L, Chang J et al (2013) Strontium-incorporated mesoporous bioactive glass scaffolds stimulating in vitro proliferation and differentiation of bone marrow stromal cells and in vivo regeneration of osteoporotic bone defects. *J Mater Chem B* 1:5711–5722. <https://doi.org/10.1039/c3tb21047b>
147. Balasubramanian P, Strobel LA, Kneser U, Boccaccini AR (2015) Zinc-containing bioactive glasses for bone regeneration, dental and orthopedic applications. *Biomed Glas* 1:51–69. <https://doi.org/10.1515/bglass-2015-0006>
148. Lusvardi G, Zaffe D, Menabue L et al (2009) In vitro and in vivo behaviour of zinc-doped phosphosilicate glasses. *Acta Biomater* 5:419–428. <https://doi.org/10.1016/j.actbio.2008.07.007>
149. Kamitakahara M, Ohtsuki C, Inada H et al (2006) Effect of ZnO addition on bioactive CaO-SiO<sub>2</sub>-P<sub>2</sub>O<sub>5</sub>-CaF<sub>2</sub> glass-ceramics containing apatite and wollastonite. *Acta Biomater* 2:467–471. <https://doi.org/10.1016/j.actbio.2006.03.001>
150. Kapoor S, Goel A, Correia AF et al (2015) Influence of ZnO/MgO substitution on sintering, crystallisation, and bio-activity of alkali-free glass-ceramics. *Mater Sci Eng C* 53:252–261. <https://doi.org/10.1016/j.msec.2015.04.023>
151. Chen X, Brauer DS, Karpukhina N et al (2014) “Smart” acid-degradable zinc-releasing silicate glasses. *Mater Lett* 126:278–280. <https://doi.org/10.1016/j.matlet.2014.04.009>
152. Lusvardi G, Malavasi G, Menabue L et al (2004) A combined experimental and computational approach to (Na<sub>2</sub>O)<sub>1-x</sub>CaO(ZnO)<sub>x</sub>·2SiO<sub>2</sub> glasses characterization. *J Non Cryst Solids* 345–346:710–714. <https://doi.org/10.1016/j.jnoncrysol.2004.08.153>
153. Linati L, Lusvardi G, Malavasi G et al (2005) Qualitative and quantitative structure-property relationships analysis of multicomponent potential bioglasses. *J Phys Chem B* 109:4989–4998. <https://doi.org/10.1021/jp046631n>
154. Goel A, Kapoor S, Tilocca A et al (2013) Structural role of zinc in biodegradation of alkali-free bioactive glasses. *J Mater Chem B* 1:3073–3082. <https://doi.org/10.1039/c3tb20163e>
155. Sergi R, Bellucci D, Salvatori R et al (2019) Zinc containing bioactive glasses with ultra-high crystallization temperature, good biological performance and antibacterial effects. *Mater Sci Eng C* 104:109910. <https://doi.org/10.1016/j.msec.2019.109910>
156. Wetzel R, Blochberger M, Scheffler F et al (2020) Mg or Zn for Ca substitution improves the sintering of bioglass 45S5. *Sci Rep* 10:15964. <https://doi.org/10.1038/s41598-020-72091-7>
157. O'Donnell MD, Watts SJ, Law RV, Hill RG (2008) Effect of P<sub>2</sub>O<sub>5</sub> content in two series of soda lime phosphosilicate glasses on structure and properties—part II: physical properties. *J Non Cryst Solids* 354:3561–3566. <https://doi.org/10.1016/j.jnoncrysol.2008.03.035>

158. O'Donnell MD, Watts SJ, Law RV, Hill RG (2008) Effect of P<sub>2</sub>O<sub>5</sub> content in two series of soda lime phosphosilicate glasses on structure and properties—part I: NMR. *J Non Cryst Solids* 354:3554–3560. <https://doi.org/10.1016/j.jnoncrysol.2008.03.034>
159. Tilocca A, Cormack AN (2007) Structural effects of phosphorus inclusion in bioactive silicate glasses. *J Phys Chem B* 111:14256–14264. <https://doi.org/10.1021/jp075677o>
160. Lusvardi G, Malavasi G, Menabue L et al (2005) A computational tool for the prediction of crystalline phases obtained from controlled crystallization of glasses. *J Phys Chem B* 109:21586–21592. <https://doi.org/10.1021/jp0546857>
161. Mathew R, Turdean-Ionescu C, Stevansson B et al (2013) Direct probing of the phosphate-ion distribution in bioactive silicate glasses by solid-state NMR: evidence for transitions between random/clustered scenarios. *Chem Mater* 25:1877–1885. <https://doi.org/10.1021/cm400487a>
162. Gentleman E, Stevens MM, Hill RG, Brauer DS (2013) Surface properties and ion release from fluoride-containing bioactive glasses promote osteoblast differentiation and mineralization in vitro. *Acta Biomater* 9:5771–5779. <https://doi.org/10.1016/j.actbio.2012.10.043>
163. Farley JR, Wergedal JE, Baylink DJ (1983) Fluoride directly stimulates proliferation and alkaline phosphatase activity of bone-forming cells. *Science* 80(222):330–332. <http://doi.org/10.1126/science.6623079>
164. Wiegand A, Buchalla W, Attin T (2007) Review on fluoride-releasing restorative materials—fluoride release and uptake characteristics, antibacterial activity and influence on caries formation. *Dent Mater* 23:343–362. <https://doi.org/10.1016/j.dental.2006.01.022>
165. Shah FA (2016) Fluoride-containing bioactive glasses: glass design, structure, bioactivity, cellular interactions, and recent developments. *Mater Sci Eng C* 58:1279–1289. <https://doi.org/10.1016/j.msec.2015.08.064>
166. Brauer DS, Karpukhina N, O'Donnell MD et al (2010) Fluoride-containing bioactive glasses: effect of glass design and structure on degradation, pH and apatite formation in simulated body fluid. *Acta Biomater* 6:3275–3282. <https://doi.org/10.1016/j.actbio.2010.01.043>
167. Lusvardi G, Malavasi G, Cortada M et al (2008) Elucidation of the structural role of fluorine in potentially bioactive glasses by experimental and computational investigation. *J Phys Chem B* 112:12730–12739. <https://doi.org/10.1021/jp803031z>
168. Brauer DS, Karpukhina N, Law RV, Hill RG (2009) Structure of fluoride-containing bioactive glasses. *J Mater Chem* 19:5629–5636. <https://doi.org/10.1039/b900956f>
169. Brauer DS, Hill RG, O'Donnell MD (2012) Crystallisation of fluoride-containing bioactive glasses. *Phys Chem Glas Eur J Glas Sci Technol Part B* 53:27–30
170. Brauer DS, Anjum MN, Mneimne M et al (2012) Fluoride-containing bioactive glass-ceramics. *J Non Cryst Solids* 358:1438–1442. <https://doi.org/10.1016/j.jnoncrysol.2012.03.014>
171. Lusvardi G, Malavasi G, Tarsitano F et al (2009) Quantitative structure-property relationships of potentially bioactive fluoro phospho-silicate glasses. *J Phys Chem B* 113:10331–10338. <https://doi.org/10.1021/jp809805z>
172. Prasad S, Ganisetti S, Jana A et al (2020) Elucidating the effect of CaF<sub>2</sub> on structure, biocompatibility and antibacterial properties of S53P4 glass. *J Alloys Compd* 831:154704. <https://doi.org/10.1016/j.jallcom.2020.154704>
173. Christie JK, Pedone A, Menziani MC, Tilocca A (2011) Fluorine environment in bioactive glasses: Ab initio molecular dynamics simulations. *J Phys Chem B* 115:2038–2045. <https://doi.org/10.1021/jp110788h>
174. Pedone A, Charpentier T, Menziani MC (2012) The structure of fluoride-containing bioactive glasses: new insights from first-principles calculations and solid state NMR spectroscopy. *J Mater Chem* 22:12599–12608. <https://doi.org/10.1039/c2jm30890h>
175. Blaeß C, Müller R, Poologasundarampillai G, Brauer DS (2019) Sintering and concomitant crystallization of bioactive glasses. *Int J Appl Glas Sci* 10:449–462. <https://doi.org/10.1111/ijag.13477>
176. Mneimne M, Hill RG, Bushby AJ, Brauer DS (2011) High phosphate content significantly increases apatite formation of fluoride-containing bioactive glasses. *Acta Biomater* 7:1827–1834. <https://doi.org/10.1016/j.actbio.2010.11.037>

177. Cocchi M, Durante C, Lusvardi G et al (2012) Evaluation of the behaviour of fluorine-containing bioactive glasses: reactivity in a simulated body fluid solution assisted by multivariate data analysis. *J Mater Sci Mater Med* 23:639–648. <https://doi.org/10.1007/s10856-011-4543-9>
178. Lusvardi G, Malavasi G, Menabue L et al (2009) Fluoride-containing bioactive glasses: surface reactivity in simulated body fluids solutions. *Acta Biomater* 5:3548–3562. <https://doi.org/10.1016/j.actbio.2009.06.009>
179. Christie JK, Brauer DS (2017) The role of fluoride in the nanoheterogeneity of bioactive glasses
180. Blumenthal NC, Posner AS, Holmes JM (1972) Effect of preparation conditions on the properties and transformation of amorphous calcium phosphate. *Mater Res Bull* 7:1181–1189. [https://doi.org/10.1016/0025-5408\(72\)90097-9](https://doi.org/10.1016/0025-5408(72)90097-9)
181. Echezarreta-López MM, Landin M (2013) Using machine learning for improving knowledge on antibacterial effect of bioactive glass. *Int J Pharm* 453:641–647. <https://doi.org/10.1016/j.ijpharm.2013.06.036>
182. Echezarreta-López MM, De Miguel T, Quintero F et al (2014) Antibacterial properties of laser spinning glass nanofibers. *Int J Pharm* 477:113–121. <https://doi.org/10.1016/j.ijpharm.2014.09.050>
183. Leppäranta O, Vahtio M, Peltola T et al (2008) Antibacterial effect of bioactive glasses on clinically important anaerobic bacteria in vitro. *J Mater Sci Mater Med* 19:547–551. <https://doi.org/10.1007/s10856-007-3018-5>
184. Munukka E, Leppäranta O, Korkeamäki M et al (2008) Bactericidal effects of bioactive glasses on clinically important aerobic bacteria. *J Mater Sci Mater Med* 19:27–32. <https://doi.org/10.1007/s10856-007-3143-1>
185. Allan I, Newman H, Wilson M (2001) Antibacterial activity of particulate Bioglass® against supra- and subgingival bacteria. *Biomaterials* 22:1683–1687. [https://doi.org/10.1016/S0142-9612\(00\)00330-6](https://doi.org/10.1016/S0142-9612(00)00330-6)
186. Zhang D, Munukka E, Leppäranta O et al (2006) Comparison of antibacterial effect of three bioactive glasses. In: *Key engineering materials*, pp 345–348
187. Zhang D, Munukka E, Hupa L et al (2007) Factors controlling antibacterial properties of bioactive glasses. In: *Key engineering materials*, pp 173–176
188. Zhang D, Leppäranta O, Munukka E et al (2010) Antibacterial effects and dissolution behavior of six bioactive glasses. *J Biomed Mater Res Part A* 93:475–483. <https://doi.org/10.1002/jbm.a.32564>
189. Ranga N, Poonia E, Jakhar S et al (2019) Enhanced antimicrobial properties of bioactive glass using strontium and silver oxide nanocomposites. *J Asian Ceram Soc* 7:75–81. <https://doi.org/10.1080/21870764.2018.1564477>
190. Qin X, Cao R, Zheng J et al (2020) A new strategy for synthesizing silver doped mesoporous bioactive glass fibers and their bioactivity, antibacterial activity and drug loading performance. *RSC Adv* 10:44835–44840. <https://doi.org/10.1039/d0ra08656h>
191. Shahrbabak MSN, Sharifianjazi F, Rahban D, Salimi A (2019) A comparative investigation on bioactivity and antibacterial properties of sol-gel derived 58S bioactive glass substituted by Ag and Zn. *Silicon* 11:2741–2751. <https://doi.org/10.1007/s12633-018-0063-2>
192. Jung S, Day T, Boone T et al (2019) Anti-biofilm activity of two novel, borate based, bioactive glass wound dressings. *Biomed Glas* 5:67–75. <https://doi.org/10.1515/bglass-2019-0006>
193. Rau JV, De Bonis A, Curcio M et al (2020) Borate and silicate bioactive glass coatings prepared by nanosecond pulsed laser deposition. *Coatings* 10:1–13
194. Stone-Weiss N, Pierce EM, Youngman RE et al (2018) Understanding the structural drivers governing glass–water interactions in borosilicate based model bioactive glasses. *Acta Biomater* 65:436–449. <https://doi.org/10.1016/j.actbio.2017.11.006>
195. Passos TF, Souza MT, Zanotto ED, de Souza CWO (2021) Bactericidal activity and biofilm inhibition of F18 bioactive glass against *Staphylococcus aureus*. *Mater Sci Eng C* 118:111475. <https://doi.org/10.1016/j.msec.2020.111475>

196. Popa AC, Fernandes HR, Neculescu M et al (2019) Antibacterial efficiency of alkali-free bio-glasses incorporating ZnO and/or SrO as therapeutic agents. *Ceram Int* 45:4368–4380. <https://doi.org/10.1016/j.ceramint.2018.11.112>
197. Brauer DS, Karpukhina N, Kedia G et al (2013) Bactericidal strontium-releasing injectable bone cements based on bioactive glasses. *J R Soc Interface* 10:20120647. <https://doi.org/10.1098/rsif.2012.0647>
198. Wegman MR, Eisenberg AD, Curzon MEJ, Handelman SL (1984) Effects of fluoride, lithium, and strontium on intracellular polysaccharide accumulation in *S. mutans* and *A. viscosus*. *J Dent Res* 63:1126–1129. <https://doi.org/10.1177/00220345840630090601>
199. Van Loveren C (1990) The antimicrobial action of fluoride and its role in caries inhibition. *J Dent Res* 69:676–681. <https://doi.org/10.1177/00220345900690s131>
200. Marquis RE (1995) Antimicrobial actions of fluoride for oral bacteria. *Can J Microbiol* 41:955–964. <https://doi.org/10.1139/m95-133>
201. Featherstone JDB (1999) Prevention and reversal of dental caries: role of low level fluoride. *Community Dent Oral Epidemiol* 27:31–40. <https://doi.org/10.1111/j.1600-0528.1999.tb01989.x>

# Chapter 9

## Nuclear Waste Vitrification and Chemical Durability



Russell J. Hand

### 9.1 Introduction

All human activities produce wastes, whether these are waste products arising from something as basic as eating or drinking, or from more complex activities such as the production of materials and products or from power generation. What we do with the wastes that we produce depends both on the type of waste and the type and level of hazard involved. For example, does the waste pose a biological, chemical, physical or radiological hazard; or possibly a combination of two or more of these hazards? Legislation, commonly at the national level, then determines how particular wastes are to be treated.

Traditional electricity generation has involved the large scale burning of fossil fuels producing CO<sub>2</sub> and, depending on the fuel used, ashes as wastes. Green electricity generating options, such wind turbines and solar energy avoid CO<sub>2</sub> generation during use, but wastes are still produced both during the manufacturing stage and at end of life. Electricity generation using nuclear power also avoids the large scale generation of CO<sub>2</sub> but produces a range of radioactive wastes that need to be appropriately treated. The potential of nuclear power to provide large scale low carbon electricity generation means that there are currently a significant number of new nuclear reactors being constructed globally [1]. These will add to the nuclear wastes that have been produced by existing nuclear power programmes. In addition, there are wastes from weapons programmes, which differ in detail from power programme wastes, but nonetheless need to be treated.

Radioactive wastes can be divided into the following major categories (see, for example, [2]): very low level waste (VLLW), low level waste (LLW), intermediate level waste (ILW) and high level waste (HLW), with activity levels and the degree

---

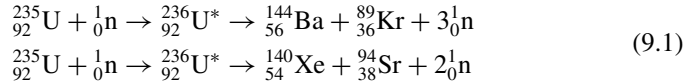
R. J. Hand (✉)

Department of Materials Science and Engineering, University of Sheffield, Sir Robert Hadfield Building, Mappin Street, Sheffield S1 3JD, UK

e-mail: [r.hand@sheffield.ac.uk](mailto:r.hand@sheffield.ac.uk)

of hazard increasing going from VLLW to HLW. High level wastes are also usually heat generating. The precise definitions of these waste categories vary from country to country as do the waste treatment routes.

The wastes produced by nuclear power depend on whether an open or closed nuclear cycle is being used.<sup>1</sup> In either case, nuclear fuel can only be “burnt” in a reactor for a finite time; although the nuclear industry talks about fuel burn-up the process involved is not combustion. Instead a fissile nucleus, e.g.  $^{235}\text{U}$ , interacts with a thermal neutron to produce an excited state, which then breaks into two lighter fission products releasing both energy and more neutrons, e.g.



A wide range of fission products are produced by fission reactions, such as those shown in Eq. (9.1). While the energy and the neutrons are important from the point of view of generating electricity, it is the fission products that limit the period of time the fuel can spend in the reactor. As shown in Fig. 9.1, the fission products mainly come from the centre of the periodic table. Many of these fission products contain excess neutrons and thus are radioactive in their own right, with half-lives varying from the very short (< 1 s) to the very long (>  $10^6$  y). Some of the fission products are neutron poisons that accumulate during use; these species gradually limit the potential for further fission reactions. Other fission products negatively impact the fuel structure, while others that are gaseous can pressurise the fuel. Eventually, accumulation of such fission products will make continued use of the fuel uneconomic, even though it still contains usable fissile material. At this stage, the fuel will be removed the reactor and placed in cooling ponds or possibly dry storage. For an open cycle system, this spent nuclear fuel (SNF) will eventually be disposed in a suitable repository. With a closed fuel cycle, the SNF is reprocessed so that the remaining fissile material can be made into a new mixed oxide fuel. During reprocessing, the fuel is dissolved in nitric acid and, once the reusable U and Pu has been extracted, a highly radioactive, acidic liquor that is both physically and radiogenically hot remains. This high level liquid waste (HLLW) contains both the fission products and contaminated metals from the fuel rods [4].

As shown in Fig. 9.2a, although HLLW is highly radioactive and it is present in the smallest volumes. Larger volumes of ILWs are produced, and these cover a wide variety of materials; for UK data see [5] and Fig. 9.2b. Still larger volumes of LLWs are generated and these again include a wide range of materials.

---

<sup>1</sup> For simplicity, a U-based fuel cycle is assumed in the following description as this is the cycle that has been most widely used to date. It is worthy of note that India is developing a Th-based cycle.

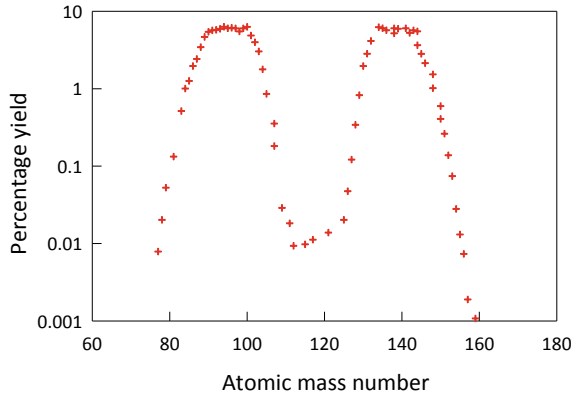


**Fig. 9.1** Distribution of fission products produced from  $^{235}\text{U}$  (redrawn from [3])

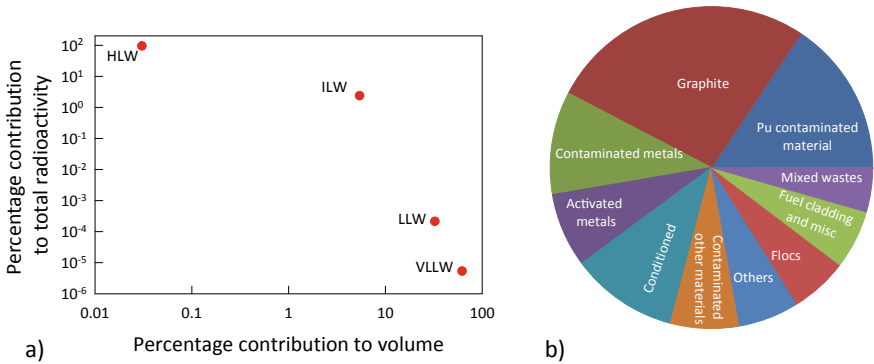


**Fig. 9.2** Percentage contribution to total activity versus waste volume **a** and **b** materials making up UK ILW by volume (2019 data [5])

## 9.2 Waste Vitrification

A range of process routes are used for processing and immobilising radioactive wastes into waste forms that are suitable for disposal. These process routes can be sub-divided into encapsulation routes and routes that involve waste incorporation at the atomic scale. In encapsulation routes, the waste is surrounded by a packaging material but its physical form is not fundamentally changed. Bitumenization and cementation are examples of such encapsulation processes which tend to be used for lower level wastes. Routes involving incorporation of the waste at the atomic scale by either incorporation of the waste are ceramisation (e.g. Synroc) or, the topic of this chapter, vitrification.

Vitrified waste forms typically result in significant volume reduction of the waste (typically by a factor of  $\sim 5$  [6]), whereas encapsulation necessarily leads to a volume



increase. Hence, although a vitrification process may be more costly to initially implement, the long-term storage and disposal costs associated with the immobilised waste are significantly reduced [7, 8]. Vitrification is particularly suitable for wastes that contain a wide range of fission products as glasses are a good solvent for wider range of elements although some species can pose challenges (see Sect. 9.2.2).

### 9.2.1 Glasses for Waste Vitrification

Glass compositions for waste vitrification should have good solubility for the elements present in the waste coupled with relatively low processing temperatures. Lower process temperatures will minimise the volatilisation of radioisotopes, such as  $^{137}\text{Cs}$  during processing; such volatilisation means that not all of the waste is incorporated into the waste form leading to secondary waste streams that require further processing. The vitrified product should also be chemically durable.

The need for both relatively low processing temperatures and good chemical durability (in general these two features tend to be inversely correlated) has resulted in the widespread adoption of borosilicate glasses for waste vitrification. This is because borosilicates represent a good compromise between the conflicting requirements of process temperature and durability. In addition, as boron is a good thermal neutron absorber, its presence is beneficial if there are any criticality concerns with the waste.

For waste vitrification, you can either consider the composition of the final glass into which the waste has been incorporated or the base composition to which the waste will be added. This does lead to confusion in the literature with different compositions being referred to by the same name. For example, the French SON-68 is variously used to refer to a base glass or a waste loaded glass; for example, compare [9] and [10]. Waste additions are usually made on a weight percentage basis (especially as the wastes may not be chemically homogeneous), and thus, compositions are often reported on a weight per cent basis. However, from a chemical perspective, where possible, reporting mole percentage compositions are to be preferred. For example, Table 9.1 shows that the UK MW base glass contains the same amounts of  $\text{Li}^+$  and  $\text{Na}^+$  ions; this is not obvious from the weight per cent figures. The presence of mixed alkalis offers benefits in terms of chemical durability while keeping the required processing temperatures relatively low. Often the base glass is less durable than the waste loaded glass.

**Table 9.1** Composition of UK MW base glass in wt% and mol%

Oxide	Wt%	Mol%
$\text{Li}_2\text{O}$	5.3	10.5
$\text{Na}_2\text{O}$	11.1	10.5
$\text{B}_2\text{O}_3$	21.9	18.5
$\text{SiO}_2$	61.7	60.5

While borosilicate glasses have been most widely used a range of other glass compositions have also been considered for waste vitrification applications. These include high silica glasses and aluminosilicates, both of which have melting temperatures meaning that sintering routes are required. The latter are closer to natural glasses. Lanthanum borosilicates, referred to as LaBS glasses, have been considered for Pu containing wastes [11]; such glasses can accommodate > 10 wt% PuO<sub>2</sub>. Phosphate glasses have been looked at for wastes high in Al and Na and have been used in Russia [12] with iron phosphate glasses also receiving attention [13].

## 9.2.2 *Problem Species and Waste Loading*

Waste loading is limited by a number of factors. While glasses are good solvents for many elements, there are a number of species that can be challenging to incorporate into a melt and thus a vitrified product, especially when relatively low processing temperatures are used. In addition, highly active wastes will undergo significant self-heating and the allowable waste loading will be related both to the glass transition temperature and the maximum thermal loading allowed in the storage facility. For wastes, that contain fissile materials avoidance of criticality is obviously an essential consideration.

Ru is a particular challenge, and some RuO<sub>2</sub> crystals are expected in vitrified HLW. The formation of spinel species may also occur. As long as these crystals are completely encapsulated by the glass and do not compromise the durability of the waste form they may be accepted. In some cases, glass composites wherein specific crystals are designed into the final waste form may be adopted as a way of increasing the waste incorporation level in the waste form.

In a number of cases, problematic species are incorporated anionically. Three examples of these are Mo, S and Cl, which are considered in more detail in the following sections.

### 9.2.2.1 **Molybdenum**

MoO<sub>3</sub> is typically present in as Mo<sup>6+</sup> cations that form tetrahedral MoO<sub>4</sub><sup>2-</sup> anions with oxygen. These anionic units are then associated with alkali and alkaline earth modifier species in the glass [14]. As a result, Mo is not well bonded into the glass and it can be readily removed from the melt to form crystalline species; it is also relatively mobile in the final glass. Although Mo itself in HLW solutions is not radioactive, it can readily associate with other radioactive species, such as Cs, forming poorly durable “yellow phase” (a complex mixture of alkali molybdates, chromates and sulphates) in the melt and the final product [15]. CaMoO<sub>4</sub> is significantly less water soluble than other alkali molybdates, and as a result, the French programme has developed a glass composite wherein CaMoO<sub>4</sub> crystals are deliberately precipitated

in, and encapsulated by, a borosilicate glass matrix [16]. Such glass composites (also referred to as glass ceramics) are being looked for other wastes as well [8].

### 9.2.2.2 Sulphur

S may be incorporated as  $\text{SO}_4^{2-}$  although other states such as  $\text{S}^{2-}$  are possible depending on the overall redox state of the melt. Typical sulphate solubility in most oxide glasses is  $< 1$  wt%  $\text{SO}_3$  with sulphates being used for fining purposes in commercial glass melting, although excess sulphur can lead to the formation of a low thermal conductivity foam on the melt surface [17] or more typically in waste vitrification a molten salt layer [18]. Sulphur solubility in the melt has been found to increase with decreasing network polymerisation [19] and decreasing cation field strength [20], with barium containing glasses such as the Indian SB-44 glass being an example of this approach [21].

### 9.2.2.3 Halides

Halides can arise in nuclear wastes both as fission products (e.g. isotopes of iodine) and from pyrochemical reprocessing using molten salt technologies (e.g. chlorides). Halides are generally challenging to incorporate into oxide glasses with incorporation rates decreasing with increasing atomic number; they are expected to incorporate as halide anions substituting for oxygen. Calcium aluminosilicates have been shown to be capable of reasonable chloride loadings. For example, in a glass based on  $51.4\text{CaO}$   $7.17\text{Al}_2\text{O}_3$   $41.43\text{SiO}_2$  (mol%) up to  $7.8 \pm 0.1$  atomic % Cl could be incorporated representing a  $71 \pm 1\%$  retention of the added chloride [22]. More generally Cl solubility in aluminosilicates being found to depend both on the basic capacity of the glass melt to incorporate Cl and on the stability of the network after Cl incorporation [23].

## 9.2.3 Vitrification Technologies

A range of vitrification technologies have been developed, of which three main ones are currently in use. These are hot wall induction heated melters, Joule heated ceramic melters and cold crucible induction heated melters. These technologies are considered in more detail below. Further, details of other melter technologies that have been considered can be found in Ojovan and Lee [6].

### 9.2.3.1 Hot Wall Induction Heated Melters

The Atelier de Vitrification de Marcoule (AVM) process is a two stage process. In the first stage, the liquid waste initially passes through a rotary calciner, which is on a shallow (2% or 1.73°) slope [24], to drive off most of the nitrates. In the second stage, the calcined waste passes into an induction heated metallic melter along with a base glass frit. As the melt relies on heat transfer from the melting vessel into the calcined waste plus glass frit, its scaleability is limited. An increase in throughput was achieved by moving from a cylindrical melting vessel at Marcoule, France to an elliptical one at Cap La Hague, France, where a total of six lines were installed in the R7 and T7 plants [25]. In the latter case, the process is known as the AVH process. A version of the AVH process has also been implemented at Sellafield, UK on three separate lines.

In the AVM/AVH process, the melting temperature is limited to ~ 1050 °C by the thermomechanical properties of the melter. The melters are nickel-based alloys (melting T ~ 1350 °C), either an Inconel alloy or more recently in the UK a Nicrofer alloy. Although other refractory metals are used elsewhere in commercial glass production they have not been adopted in waste vitrification technologies [26].

Frit and calcined waste are progressively batched into the melter with a full melting cycle taking 8 h. A sparge (which may be an inert gas or air) is used to help with homogenisation in the melt. At the end of the melting cycle, the melt is poured into stainless steel canister, with two pours being required to fill a canister. After filling a lid is automatically welded onto canister and it is then decontaminated using high pressure water jets before being transferred to an above ground store, which is cooled by passive convection, for interim storage.

### 9.2.3.2 Joule Heated Ceramic Melters (JHCMS)

As implied by their name in a Joule heated ceramic melter (JHCM), the melt is directly heated by Joule heating arising from current passing between electrodes. This technology is scalable which enables greater throughput. JHCMS require the melt to be conducting, and thus, additional heating is required to initially produce a melt. With this technology, the base glass composition could be added as a frit or as a glass forming raw materials along with the waste; in practice the feed is usually in the form of an aqueous slurry [27]. Adding glass forming materials rather than a frit allows the base glass composition to be adjusted based on the actual waste composition.

The waste and glass frit or batch forms a cold cap covering the melt, and this material is gradually incorporated by melting from the bottom of the cold cap. A foam forms between the melt pool and the upper parts of the cold cap where dehydration and other reactions occur; the foam limits heat transfer to the reaction zone [28]. The cold cap may also limit the volatilisation of problematic radioisotopes.

Ru, Rh and Pd can segregate and tend to sink to the bottom of the melt where they can give rise to a low resistance pathway through the melt, which means increased

power is needed to achieve the same degree of heating. One approach to circumvent this problem is to use a melter with a steeply sloped base [29].

Joule heated ceramic melters (JHCMS) have been implemented in the USA at several sites including the Defence Waste Processing Facility (DWPF) at Savannah River, where over 7000 t of vitrified product in over 4200 canisters had been produced by 2019 [30]. JHCMS have also been implemented in Belgium, Germany, India, Japan and Russia [12].

### 9.2.3.3 Cold Crucible Melters (CCMs)

In a cold crucible melter (CCM), a conducting melt is again required as high frequency induction is used to induce currents in the melt and thereby directly heat the melt. The melter walls are water cooled, and as a result, a layer of solidified melt forms between the melter walls and the melt. This skull layer avoids the need for refractory liner. As a result, higher melting temperatures can be used than would, otherwise, be possible. Of course, higher temperatures will lead to increase volatilisation of potentially problematic species.

CCMs have been implemented in Russia as well as on an existing vitrification line in the R7 plant at Cap La Hague in France [25] and in South Korea.

## 9.3 Durability

After interim storage, it is expected that the vitrified waste forms will be emplaced in an underground repository at depths of 500 m or greater. Although such repository designs are based on a multi-barrier approach (waste form, canister, backfill and rock), it has to be assumed that at some point water will reach the waste form. While the return of any such water to the surface is expected to be very slow due to the burial depth it is, nonetheless, important to ensure that the vitrified waste form is resistant to chemical attack by water. In addition to chemical durability, thermal, mechanical and radiation durability should also be taken into consideration.

### 9.3.1 Thermal Durability

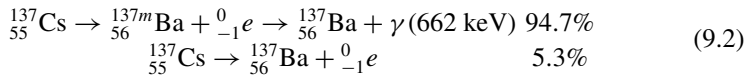
Vitrified waste forms are typically a few tens of centimetres in diameter, and thus, the effective cooling rates will be low especially on the centreline (which will cool most slowly) due to the lower thermal conductivity of oxide glasses. In addition with heat generating HLW, the centreline temperature of the waste form will remain significantly elevated for decades due to radiogenic heating. Therefore, vitrified products, especially for HLW, need to have a high resistance to crystallisation. In practice, limited amounts of crystalline  $\text{RuO}_2$  and spinel phases may be tolerated in the glass.

### 9.3.2 Mechanical Durability

Although the mechanical properties of vitrified waste forms are usually considered as being of secondary concern they will impact the amount of cracking seen in the waste form. The presence of cracks increases the amount of surface that is potentially available for chemical attack when water does reach the glass, although archaeological evidence indicates that the constrained nature of such cracks might well limit the extent of corrosion that will occur in them [31]. While it is not possible to directly assess the extent of cracking in active waste forms attempts have been to quantify the extent of cracking in inactive ones, although due to differences in thermal gradients over time it has to be recognised that there may be differences between the two [32]. The reported data for the mechanical properties of nuclear waste glasses fall in a relatively narrow range reflecting the predominance of borosilicate glasses in waste vitrification. Typical reported Young’s moduli are ~ 80–90 GPa, fracture toughness values ~ 0.7–1.0 MPa m<sup>1/2</sup> and hardness ~ 5.5–7.5 GPa [33].

### 9.3.3 Radiation Durability

Damage can arise from the radiogenic decay of elements in the waste form. This damage includes direct displacement cascades arising from  $\alpha$  decays in particular and, to a much lesser extent,  $\beta$  decays.  $\alpha$  decays arise from long lived transuranics in the waste, whereas many fission products undergo  $\beta$  decays. Both  $\alpha$  and  $\beta$  decays involve transmutations which may involve a change of elemental valence which could impact on the glass structure. For example, the  $\beta^-$  decay of <sup>137</sup>Cs (whether it goes via an excited state or not [34]):



results in the presence of a 2 + Ba ion rather than a 1 + ion in the glass structure. These decays and the associated displacement cascades are believed to result in a lower density glass with a higher fictive temperature although there is good evidence that the overall effects are limited and saturate after a certain dose. Thus, for example, density and thus volume changes up to ~ 1% have been observed in glasses doped with <sup>244</sup>Cm by Ewing et al. [35] with the fractional change in volume,  $\Delta V/V$ , being fitted by

$$\frac{\Delta V}{V} = A[1 - \exp(-BD)] \tag{9.3}$$

where  $D$  is dose and  $A$  and  $B$  are constants. It has been found that the volume changes tend to saturate for doses  $\geq 10^{25}$   $\alpha/m^3$  (see Fig. 9.3a).

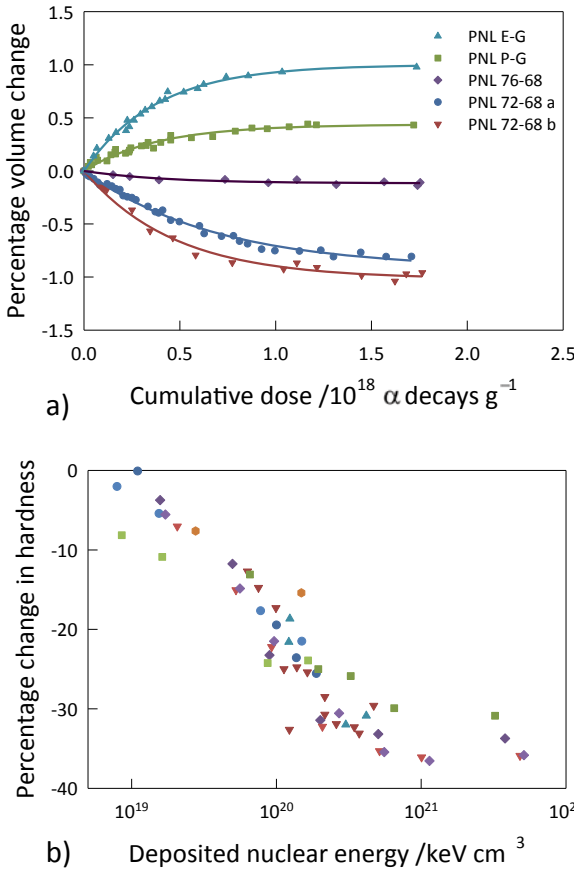


**Fig. 9.3** Impact of radiation on nuclear waste glasses: **a** change of volume with dose for various US trial glasses (modified from [35]) and **b** change of hardness with dose for French R7T7 and SON-68 glasses, a US glass and the international simple glass (data taken from [36–38])

As shown in Fig. 9.3b, a number of studies involving self-irradiation by alpha particles and heavy ion irradiation have all indicated that the hardness of the vitrified waste forms decrease with increasing dose; with a maximum drop in hardness of ~ 35% [36–38]. The less dense, higher fictive temperature, irradiated glass structure means that greater compaction under indentation is possible. Corresponding reductions in modulus and an increase in (indentation) fracture toughness under irradiation have also been reported [39]. These effects have recently been reviewed by Malkovsky et al. [40].

### 9.3.4 Chemical Durability Testing

A number of tests for assessing chemical durability, usually in an aqueous environment, have been developed. The tests have been developed for a variety of different purposes and consequently offer different insights into glass durability. Durability testing is necessarily conducted on a relatively short timescales compared to the required life time for the waste forms. As a result, various methods have been used to accelerate the corrosion reactions with the primary approaches being increased temperature ( $\leq 90^\circ\text{C}$ , unless pressure is also used) and increased sample surface area (powder samples). Nevertheless, the studied timescales remain short compared to disposal requirements, even for so-called “long-term” tests lasting a number of years [41]. Thus, while the results of durability testing can be used to inform modelling of long-term performance and the development of disposal safety cases, such models necessarily have to extrapolate from the available data.

#### 9.3.4.1 Product Consistency Test

The product consistency test (PCT) [42] was originally developed to ensure that different batches of the radioactive glass being produced at the DWPF exhibited consistent behaviour. The test was developed as a short term, 7 d, quality test but has been used to examine a much wider range of conditions. The test utilises a sieved powdered specimen submerged in a small volume of fluid at an elevated temperature. Hence, the surface area of glass ( $S_g$ ) to volume of solution ( $V_s$ ) is high, and as a result, the solution chemistry will change quite quickly as species leach out of the glass. Surface area is commonly based on a geometric calculation assuming spherical particles and the known sieve sizes using

$$S_g = \frac{3m_g}{\rho_g \bar{r}_g} \quad (9.4)$$

where  $m_g$ ,  $\rho_g$  and  $\bar{r}_g$  are the mass, density and average particle size of the glass, respectively. Although direct Brunauer, Emmet, Teller (B.E.T.) surface area measurements give  $S_g$  values  $\sim 3 \times$  that of the geometric calculation Icenhower and Steefel concluded that the calculated geometric surface area is to be preferred to avoid over-weighting the effect of small particles [43]. Typically, for PCT  $S_g/V_s \sim 2000 \text{ m}^{-1}$ , although tests utilising both lower and higher values have been reported (see, for example [44, 45] respectively). For higher  $S_g/V_s$  values, in particular alteration, products may cause the powder to adhere together thereby reducing the effective  $S_g/V_s$  value during the test. This change is difficult to quantify. If significant dissolution without agglomeration occurs, then the surface area reduces with time. In this case, the surface area  $S_t$ , at time  $t$  can be quantified using



$$S_t = \frac{3}{\rho \bar{r}_g} m_g^{1/3} m_t^{2/3} \quad (9.5)$$

where  $m_t$  is the mass of glass at time  $t$  [46].

Analysis of the solution chemistry after leaching allows the normalised loss of specific elements to be followed as a function of time. Normalised loss of element  $i$ ,  $NL_i$ , from the sample is given by

$$NL_i = \frac{C_i}{f_i(S_g/V_s)} \quad (9.6)$$

where  $C_i$  is the element concentration in solution (corrected by the amount found in the blanks). A normalised loss rate,  $NR_i$ , may be calculated using

$$NR_i = \frac{C_i}{f_i(S_g/V_s)t} \quad (9.7)$$

where  $t$  is time, usually measured in days. Given the discrete nature of the time intervals used, if possible, an equation should be fitted to the  $NL_i$  data and differentiated to give a rate. However, this may not be possible and such fitted equations are necessarily empirical and only reliably apply within the range of the fitted data; for an example, see [47].

### 9.3.4.2 MCC-1 Test

The materials characterisation centre originally developed several tests to assess the durability of nuclear waste glasses, with PCT being a modification of one of these tests (MCC-5). MCC-1 is a 28 d monolith test with  $S_g/V_s \sim 10 \text{ m}^{-1}$  [48]. As well as solution analyses, it is possible to mount and section the monoliths from the MCC-1 test so that the surface alteration layers can be characterised.

### 9.3.4.3 Single Pass Flow Through Test

The single pass flow through (SPFT) test [49] is designed to minimise solution feedback effects. While either crushed glass or a monolith can be used, the latter is easier.  $NR_i$  is plotted as a function of the flow rate ( $q$ ) over surface area with forward rate conditions corresponding to the region where the steady state loss rates become constant (see Fig. 9.4).

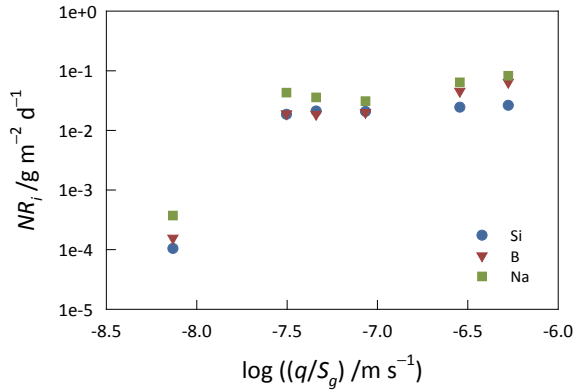


Fig. 9.4 Example NR<sub>i</sub> versus log(q/S<sub>g</sub>) data for Si, B and Na measured in an SPFT test

### 9.3.4.4 Vapour Hydration Test (VHT)

The vapour hydration test is a highly accelerated test that utilises both elevated temperatures and pressures [50]. A monolith specimen is suspended in a pressure bomb at a temperature typically in excess of 100 °C, although temperatures between 70 and 250 °C can be used. If the relative humidity is > 80% (usually it is 100%), then a thin film of water forms on the monolith and the sample dissolves in this condensed film; the thickness of the film does initially increase with time leading to a variable S<sub>g</sub>/V<sub>s</sub> value. While this is a good test for observing the formation of alteration products on the sample surface high variability has been reported between both operators and different laboratories. In addition, test conditions are clearly very different to any plausible disposal environment.

### 9.3.4.5 The International Simple Glass (ISG)

In addition to the development of standard test protocols in recent years, a standard glass has also been developed and studied to gain greater insight into the durability of nuclear waste glasses. This international simple glass is essentially a simplified version of the French R7T7 glass with the composition 12.2Na<sub>2</sub>O 5.7CaO 1.7ZrO<sub>3</sub> 3.8Al<sub>2</sub>O<sub>3</sub> 16.0B<sub>2</sub>O<sub>3</sub> 60.1SiO<sub>2</sub> (mol%) [51]. The original ISG was manufactured by Mo-Sci Corporation in the US and distributed to interested laboratories on request. Recently, a new batch has been produced by Corning (ISG-1) as well as a second composition in which half of the CaO has been replaced by MgO (ISG-2).

### 9.3.5 Durability Behaviour Under Low Flow Conditions

As water flow through a repository should be very low significant solution feedback effects are expected to occur as species from the glass are released into solution. This leads to a characteristic dissolution behaviour with time which is summarised in Fig. 9.5. It can be seen that the initial or forward rate of dissolution is relatively high (region I) and that it reduces due to combination of surface changes in the glass and solution saturation until a residual or final rate is reached (region II). Precipitation of phases that remove Si from solution may then lead to a resumption in alteration (region III). It should be noted that in earlier literature, the curve shown in Fig. 9.5 is broken into five stages rather than three kinetic stages shown here (compare [52] and [53]).

Affinity/transition state theory has been used to model the data shown in Fig. 9.5. Using this approach, the dissolution rate of element  $i$ ,  $r_i$ , is given by

$$r_i = k_0 v_i \exp\left(\frac{-E_a}{RT}\right) \left[1 - \left(\frac{Q}{K_g}\right)^\sigma\right] \prod_j a_j^{n_j}, \tag{9.8}$$

where  $k_0$  is the forward rate constant,  $v_i$  is the concentration of species  $i$  in the glass,  $E_a$  is the activation energy,  $R$  is the gas constant and  $T$  is absolute temperature,  $a_i$  is the activity of species  $i$ ,  $Q$  is the ion activity product,  $K_g$  is the solubility constant for the rate controlling reaction and  $\sigma$  the Temkin coefficient, which is related to the rate of decomposition of the activated complex [54].

Assuming the formation of orthosilicic acid ( $H_4SiO_4$ ) is the rate-limiting reaction for dissolution [55], and taking  $\sigma = 1$  for borosilicate glass, then the normalised release rate can be obtained from Eq. (9.8)

$$NR_i = k_0 \times 10^{npH} \exp\left(\frac{-E_a}{RT}\right) \left[1 - \frac{Q}{K}\right] \tag{9.9}$$

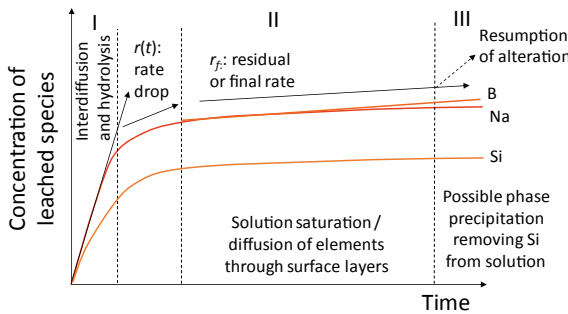


**Fig. 9.5** Schematic diagram showing the concentration of dissolved species in solution as a function of time for borosilicate glass leached under low flow conditions

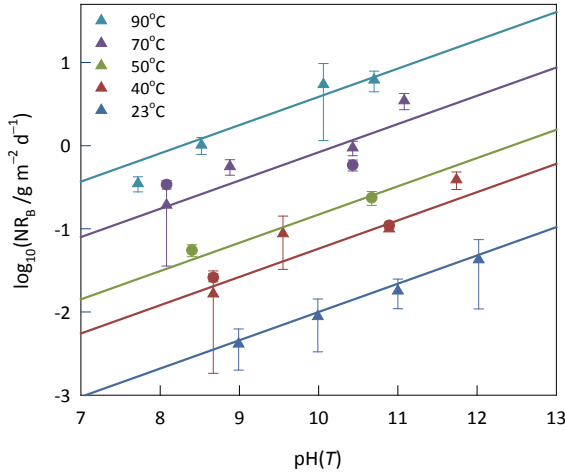


**Fig. 9.6** Example multiple linear regression fit for the forward rate of ISG in the alkaline regime (modified from [56])

Under forward rate conditions the term in square brackets in Eq. (9.9) equals 1 and thus taking logs on both sides gives

$$\log_{10} \text{NR}_i = \log_{10} k_0 + \eta \text{pH} - \frac{E_a}{2.303RT}. \tag{9.10}$$

Using multiple linear regression Eq. (9.10) can be fitted to SPFT data. An example fit for ISG in the alkaline regime is shown in Fig. 9.6 where  $\log_{10}(k_0/\text{g m}^{-2} \text{d}^{-1}) = 8.62 \pm 0.54$ ,  $\eta = 0.34 \pm 0.03$  and  $E_a = 79.5 \pm 3.5 \text{ kJ mol}^{-1}$  [56]. By looking at such fits for a range of glasses Neeway et al. have concluded that the parameters are correlated, which will impact models developed from such fits [57].

Equation (9.8) implies that changes in the solution chemistry due to the species being released from the glass are solely responsible for the rate drop shown in Fig. 9.5, with silica saturation, usually assumed to be limiting dissolution. However, others have explained the rate drop via the formation of a protective gel layer, arising from the condensation of silica from solution, on the glass surface. In some instances, this layer is considered as being divided into a porous gel and a passivating reactive interphase (PRI), which has been modelled using the GRAAL model [52, 58]. More recently Geisler et al. have considered the effects of changes in the local solution chemistry between the glass surface and the gel layer [59].

The residual rate seen in region II in Fig. 9.5 is significantly lower than the forward rate given by Eq. (9.10). The residual rate is, however, always nonzero. It is also possible for a resumption of alteration to occur as shown in region III of Fig. 9.5. The resumption of alteration is associated with the precipitation of secondary phases, specifically zeolites, and in some cases calcium silicate hydrate (CSH) phases [60].

### **9.3.6 Durability of Natural and Anthropogenic Analogue Glasses**

Insight into the long-term behaviour of glasses can also be obtained by consideration of the behaviour of archaeological glasses or, over longer timescales natural glasses such as basalts in the natural environment. Even though the environment experienced by such samples is not usually well constrained, compared to laboratory experiments, the features seen on such glasses can be used to support or otherwise the understanding gained from our relatively short term laboratory experiments.

#### **9.3.6.1 Archaeological Glasses**

Archaeological sites can provide examples of manmade glasses that have survived in the natural environment for extended periods. As well as the environment not being well constrained the original glass may not be compositionally uniform, and there can be difficulties in knowing whether the original surface (albeit in altered form) is still present. In cases of extreme alteration, it may not always be possible to determine the original chemical composition of the glass. Despite these difficulties, such glasses still provide insight into the long-term behaviour of glass in the natural environment.

Complex sequences of layers have been observed on many archaeological samples [61]. The number of these can vary from point to point due to localised attack; despite this complication, it has been suggested that the number of layers might be correlated with age. It should be noted, however, that apparently cyclical layers have also been observed in laboratory experiments (see, for example, [56, 62]). Glass blocks recovered from a Roman era wreck in the Mediterranean show evidence of the formation of complex sequences of alteration layers in crack, consisting of smectites and carbonates, that completely fill those cracks [63, 64]. The behaviour of glasses recovered from vitrified hillforts is also receiving significant attention within the nuclear glass community [65].

#### **9.3.6.2 Performance of Replica Glasses**

As well as studying the performance of archaeological glasses that have been exposed to the natural environment for extended periods there is interest in studying modern replica versions of these glasses either in laboratory or the natural environment, with the former being more controlled but latter being more amenable to longer term testing. For example, synthetic basaltic glasses have been shown to exhibit similar leaching kinetic glasses to nuclear waste glasses [66].

The Ballidon experiment is an example of where modern versions of historic and ancient glasses have been buried. This experiment started as a purely archaeological experiment; however, inactive samples of nuclear waste glasses have been buried at this site since 1986. Studies of replica Roman, mediaeval and seventeenth

century glasses extracted from Ballidon have all shown the development of a series of layers on the sample surface [67], with the details depending on the underlying glass composition.

### 9.3.6.3 Natural Glasses

Natural glasses include obsidians and basalts. Both are aluminosilicates with obsidians having the higher silica contents. Neither contain boron unlike the majority of nuclear waste glasses. Although glasses are not the thermodynamically stable state the rate of crystallisation of obsidians is very slow at low temperatures ( $\sim 20^\circ\text{C}$ ) [68] and, although higher rates have been observed for the alteration (or palagonisation) of the lower silica content basalts, the long-term rates are still very low [69]. Palagonites are earthy or clay-like materials found on natural basalts with composition being dependent on the parent basalt, temperature and the rate of flow of the attacking fluid; the process of palagonisation is believed to involve hydration of the basalt [70]. In the natural environment, microbes and other micro-organisms may also have an impact on the corrosion process [71]. While the impact of microbial interactions with glass have been recognised for significant time the potential for microbially mediated corrosion of vitrified nuclear waste has only recently started to attract attention [72].

## 9.4 Summary

The use of nuclear fission to generate electricity leads to spent nuclear fuel. For a U-based fuel, this still contains reusable U and Pu along with a wide range of fission products. In a closed fuel cycle, the separation of the reusable materials leads to a range of nuclear wastes. Vitrification has been applied to the immobilisation of these wastes, most notably the heat generating HLW as well as a range of ILWs. Glasses are flexible solvents for a wide range of elements and are thus very suitable for chemically complex waste streams arising from reprocessing. While glass production involves high temperatures, the process results in notable waste volume reduction and thus, significant cost savings associated with storage and disposal. Borosilicate glasses are the most widely favoured compositions for waste vitrification as they provide a good compromise between processing temperature and long-term chemical durability. Other silicate glasses have also been considered and Russia has utilised some phosphate glasses.

Understanding the long-term chemical durability of vitrified waste forms is crucial to developing a safety case for their disposal. A range of laboratory-based dissolution experiments have shown that in general dissolution is initially rapid, but then slows down due to changes in solution chemistry arising from the species removed from the glass during dissolution, and/or the development of a protective surface layer. More rapid alteration may restart due to the precipitation of secondary phases

from solution. There is evidence of some cyclical processes occurring during dissolution leading to the formation of multiple layers on the glass surface. Natural and anthropogenic analogues are being used to validate the outcomes of the laboratory durability experiments.

## References

1. International Atomic Energy Agency (2021) Nuclear power reactors in the world. Reference data series no 2, IAEA, Vienna. <https://www.iaea.org/publications/14989/nuclear-power-reactors-in-the-world>
2. International Atomic Energy Agency (2009) Classification of radioactive waste. IAEA Safety Standards, series no GSG-1, IAEA, Vienna. <https://www.iaea.org/publications/8154/classification-of-radioactive-waste>
3. Young HD, Freedman RA (2004) Sears & Zemansky's university physics 11th edn. Addison Wesley, p 1464
4. Denniss IS, Jeapes AP (1996) Reprocessing irradiated fuel. In: Wilson PD (ed) The nuclear fuel cycle: from ore to waste. Oxford University Press, pp 116–137
5. Nuclear Decommissioning Authority (2019) 2019 UK radioactive waste inventory. NDA, Moor Row, Cumbria. <https://ukinventory.nda.gov.uk/wp-content/uploads/2020/01/2019-Waste-Report-Final.pdf>
6. Ojovan MI, Lee WE (2005) An introduction to nuclear waste immobilisation. Elsevier, Amsterdam, pp 232–241. <https://doi.org/10.1016/B978-008044462-8/50019-3>
7. Hyatt NC, Schwarz RR, Bingham PA, Stennett MC, Corkhill CL, Heath PG, Hand RJ, James M, Pearson A, Morgan S (2014) Thermal treatment of simulant plutonium contaminated materials from the Sellafield site by vitrification in a blast-furnace slag. *J Nucl Mater* 444:186–199. <https://doi.org/10.1016/j.jnucmat.2013.08.019>
8. Donald IW (2010) Waste immobilization in glass and ceramic based hosts: radioactive, toxic and hazardous wastes. Wiley-Blackwell, Oxford. <https://doi.org/10.1002/9781444319354>
9. Donald IW, Metcalfe BL, Taylor RNJ (1997) The immobilization of high level radioactive wastes using ceramics and glasses. *J Mater Sci* 32:5851–5887. <https://doi.org/10.1023/A:1018646507438>
10. Guittonneau C, Gin S, Godon N, Mestre JP, Dugne O, Allegri P (2011) A 25-year laboratory experiment on French SON68 nuclear glass leached in a granitic environment—first investigations. *J Nucl Mater* 408:73–89. <https://doi.org/10.1016/j.jnucmat.2010.10.075>
11. Pierce EM, McGrail BP, Martin PF, Marra J, Arey BW, Geiszler KN (2007) Accelerated weathering of high-level and plutonium-bearing lanthanide borosilicate waste glasses under hydraulically unsaturated conditions. *Appl Geochem* 22:1841–1859. <https://doi.org/10.1016/j.apgeochem.2007.03.056>
12. Ojovan MI, Lee WE (2011) Glassy wasteforms for nuclear waste immobilization. *Metal Mater Trans A* 42:837–851. <https://doi.org/10.1007/s11661-010-0525-7>
13. Brow RK, Kim CW, Reis ST (2020) Iron polyphosphate glasses for waste immobilization. *Int J Appl Glass Sci* 11:4–14. <https://doi.org/10.1111/ijag.13565>
14. Calas G, Le Grand M, Galois L, Ghaleb D (2003) Structural role of molybdenum in nuclear glasses: an EXAFS study. *J Nucl Mater* 322:15–20. [https://doi.org/10.1016/S0022-3115\(03\)00277-0](https://doi.org/10.1016/S0022-3115(03)00277-0)
15. Caurant D, Majérous O, Fadel E, Quintas A, Gervais C, Charpentier T, Neuville D (2010) Structural investigations of borosilicate glasses containing MoO<sub>3</sub> by MAS NMR and Raman spectroscopies. *J Nucl Mater* 396:94–101. <https://doi.org/10.1016/j.jnucmat.2009.10.059>
16. Henry N, Deniard P, Jobic S, Brec R, Fillet C, Bart F, Grandjean A, Pinet O (2004) Heat treatments versus microstructure in a molybdenum-rich borosilicate. *J Non-Cryst Solids* 333:199–205. <https://doi.org/10.1016/j.jnocrsol.2003.09.055>

17. Beerkens R (2007) Sulphur chemistry and sulphate fining and foaming of glass melts. *Glass Technol Eur J Glass Sci Technol A* 48:41–52
18. Vienna JD, Kim D-S, Muller IS, Piepel GF, Kruger AA (2014) Toward understanding the effect of low-activity waste glass composition on sulfur solubility. *J Am Ceram Soc* 97:3135–3142. <https://doi.org/10.1111/jace.13125>
19. Xu X, Youngman RE, Kapoor S, Goel A (2021) Structural drivers controlling sulfur solubility in alkali aluminoborosilicate glasses. *J Am Ceram Soc* 104:5030–5049. <https://doi.org/10.1111/jace.17778>
20. Bingham PA, Hand RJ (2008) Sulphate solubility and glass formation in phosphate systems for nuclear and toxic waste immobilization. *Mater Res Bull* 43:1679–1693. <https://doi.org/10.1016/j.materresbull.2007.07.024>
21. Kaushik CP, Mishra RK, Sengupta P, Kumar A, Das D, Kale GB, Raj K (2006) Barium borosilicate glass—a potential matrix for immobilization of sulfate bearing high-level radioactive waste. *J Nucl Mater* 358:129–138. <https://doi.org/10.1016/j.jnucmat.2006.07.004>
22. Schofield JM, Bingham PA, Hand RJ (2009) The immobilisation of a chloride containing actinide waste surrogate in calcium aluminosilicate glasses. *Ceram Trans* 207:69–80
23. Tan S, Hand RJ (2018) Incorporation and phase separation of Cl in alkaline earth aluminosilicate glasses. *J Nucl Mater* 507:135–144. <https://doi.org/10.1016/j.jnucmat.2018.04.044>
24. Harrison MT (2014) Vitrification of high level waste in the UK. *Proc Mater Sci* 7:10–15. <https://doi.org/10.1016/j.mspro.2014.10.003>
25. Vernaz E, Bruezière J (2014) History of nuclear waste glass in France. *Proc Mater Sci* 7:3–9. <https://doi.org/10.1016/j.mspro.2014.10.002>
26. Bingham PA, Connelly AJ, Hyatt NC, Hand RJ (2011) Corrosion of glass contact refractories for the vitrification of radioactive wastes: a review. *Int Mater Rev* 56:226–242. <https://doi.org/10.1179/1743280410Y.0000000005>
27. Hrma P, Klouzek J, Pokorny R, Lee SM, Kruger AA (2019) Heat transfer from glass melt to cold cap: gas evolution and foaming. *J Am Ceram Soc* 102:5853–5865. <https://doi.org/10.1111/jace.16484>
28. Lee S-M, Hrma P, Pokorny R, Klouzek J, VanderVeer BJ, Dixon DR, Luksic SA, Rodriguez CP, Chun J, Schweiger MJ, Kruger AA (2017) Effect of melter feed foaming on heat flux to the cold cap. *J Nucl Mater* 496:54–65. <https://doi.org/10.1016/j.jnucmat.2017.09.016>
29. Grünwald W, Roth G, Tobie W, Weiß K, Weisenberger S (2008) The role of the platinum group elements ruthenium, rhodium and palladium in the vitrification of radioactive high level liquid waste using joule heated ceramic lined waste melters. *Glass Technol Eur J Glass Sci Technol* 49:266–278  
<https://www.energy.gov/em/articles/dwpf-powers-progress-savannah-river-site> (2019)
30. Verney-Carron A, Gin S, Libourel G (2004) A fractured roman glass block altered for 1800 years in seawater: analogy with nuclear waste glass in a deep geological repository. *Geochim Cosmochim Acta* 72:5372–5385. <https://doi.org/10.1016/j.gca.2008.08.018>
31. Repina M, Renard D, Bouyer F, Lagneau V (2019) Coupling image analysis and thermomechanical simulation results to produce a model of the fracture network in a nuclear glass canister. *J Nucl Mater* 522:265–285. <https://doi.org/10.1016/j.jnucmat.2019.05.013>
32. Connelly AJ, Hand RJ, Bingham PA, Hyatt NC (2011) Mechanical properties of nuclear waste glasses. *J Nucl Mater* 408:188–193. <https://doi.org/10.1016/j.jnucmat.2010.11.034>
33. NuDat 3.0. <https://www.nndc.bnl.gov/nudat3/>
34. Ewing RC, Weber WJ, Clinard FW (1995) Radiation effects in nuclear waste forms for high-level radioactive waste. *Prog Nucl Energy* 29:63–127. [https://doi.org/10.1016/0149-1970\(94\)00016-Y](https://doi.org/10.1016/0149-1970(94)00016-Y)
35. Peuket S, Noël P-Y, Loubet J-L, Pavan S, Nivet P, Chenet A (2006) Effects of deposited nuclear and electronic energy on the hardness of R7T7-type containment glass. *Nucl Instrum Methods Phys Res B* 246(2006):379–386. <https://doi.org/10.1016/j.nimb.2005.12.053>
36. de Bonfils S, Peuket S, Panczer G, de Ligny D, Henry S, Noël P-Y, Chenet A, Champagnon B (2010) Effect of chemical composition on borosilicate glass behavior under irradiation. *J Non-Cryst Solids* 356:388–393. <https://doi.org/10.1016/j.jnoncrsol.2009.11.030>



38. Karakurt G, Abdelouas A, Guin J-P, Nivard M, Sauvage T, Paris M, Bardeau J-F (2016) Understanding of the mechanical and structural changes induced by alpha particles and heavy ions in the French simulated nuclear waste glass. *J Nucl Mater* 475:243–254. <https://doi.org/10.1016/j.jnucmat.2016.04.022>
39. Inagaki Y, Furuya H, Ono Y, Idemitsu K, Banba T, Matsumoto S, Muraoka S (1993) Effects of  $\alpha$ -decay on mechanical properties of simulated nuclear waste glass. *Mater Res Soc Symp Proc* 294:191–198. <https://doi.org/10.1557/PROC-294-191>
40. Malkovsky VI, Yudintsev SV, Ojovan MI, Petrov VA (2020) The influence of radiation on confinement properties of nuclear waste glasses. *Sci Technol Nucl Installations* 2020:88875723. <https://doi.org/10.1155/2020/8875723>
41. Curti E, Crovisier JL, Morvan G, Karpoff AM (2006) Long-term corrosion of two nuclear waste reference glasses (MW and SON68): a kinetic and mineral alteration study. *Appl Geochem* 21:1152–1168. <https://doi.org/10.1016/j.apgeochem.2006.03.010>
42. ASTM C1285-21 (2021) Standard test methods for determining chemical durability of nuclear, hazardous, and mixed waste glasses and multiphase glass ceramics: the product consistency test (PCT). ASTM International, West Conshohocken, PA. <https://doi.org/10.1520/C1285-21>
43. Icenhower JP, Steefel CI (2013) Experimentally determined dissolution kinetics of SON68 glass at 90 °C over a silica saturation interval: evidence against a linear rate law. *J Nucl Mater* 439:137–147. <https://doi.org/10.1916/j.jnucmat.2013.04.008>
44. Utton CA, Hand RJ, Bingham PA, Hyatt NC, Swanton SW, Williams SJ (2013) Dissolution of vitrified wastes in a high-pH calcium-rich solution. *J Nucl Mater* 435:112–122. <https://doi.org/10.1016/j.jnucmat.2012.12.032>
45. Fournier M, Ducasse T, Pérez A, Barchouchi A, Daval D, Gin S (2019) Effect of pH on the stability of passivating gel layers formed on International Simple Glass. *J Nucl Mater* 524:21–38. <https://doi.org/10.1016/j.jnucmat.2019.06.029>
46. McGrail BP, Ebert WL, Bakel AJ, Peeler DK (1997) Measurement of kinetic rate law parameters on a Na-Ca-Al borosilicate glass for low-activity waste. *J Nucl Mater* 249:175–189. [https://doi.org/10.1016/S0022-3115\(97\)00213-4](https://doi.org/10.1016/S0022-3115(97)00213-4)
47. Backhouse DJ, Corkhill CL, Hyatt NC, Hand RJ (2019) Investigation into the role of Mg and Ca in the structure and durability of aluminoborosilicate glass. *J Non-Cryst Solids* 512:41–52. <https://doi.org/10.1016/j.jnoncrysol.2019.03.003>
48. ASTM C-1220-17 (2017) Standard test method for static leaching of monolithic waste forms for disposal of radioactive waste. ASTM International, West Conshohocken, PA. <https://doi.org/10.1520/C1220-17>
49. ASTM C1662-18 (2018) Standard practice for measurement of the glass dissolution rate using the single-pass flow-through test method. ASTM International, West Conshohocken, PA. <https://doi.org/10.1520/C1662-18>
50. ASTM C1663-18 (2018) Standard test method for measuring waste glass or glass ceramic durability by vapor hydration test. ASTM International, West Conshohocken, PA. <https://doi.org/10.1520/C1663-18>
51. Ryan JV, Kaspar T, Pantano CG, Rice J, Trivelpiece C, Hyatt NC, Corkhill CL, Mann C, Hand RJ, Kirkham MA, Crawford CL, Jantzen CM, Du J, Lu X, Harrison MT, Cushman C, Linford MR, Smith NJ (2019) Physical and optical properties of the international simple glass. *npj Mater Degrad* 3:15. <https://doi.org/10.1038/s41529-019-0069-2>
52. Frugier P, Gin S, Minet Y, Chave T, Bonin B, Godon N, Lartigue J-E, Jollivet P, Ayrat A, de Windt L, Santarini G (2008) SON68 nuclear glass dissolution kinetics: current state of knowledge and basis of the new GRAAL model. *J Nucl Mater* 380:8–21. <https://doi.org/10.1016/j.jnucmat.2008.06.044>
53. Gin S, Jollivet P, Fournier M, Berthon C, Wang Z, Mitroshkov A, Zhu Z, Ryan JV (2015) The fate of silicon during glass corrosion under alkaline conditions: a mechanistic and kinetic study with the international simple glass. *Geochim Cosmochim Acta* 151:68–85. <https://doi.org/10.1016/j.gca.2014.12.009>
54. Aagaard P, Hegleson HC (1982) Thermodynamic and kinetic constraints on reaction rates among minerals and aqueous solutions. I Theor Considerations *Amer J Sci* 282:237–285. <https://doi.org/10.2475/ajs.282.3.237>

55. Grambow B (1985) A general rate equation for nuclear waste glass corrosion. *Proc MRS* 44:15–27. <https://doi.org/10.1557/PROC-44-15>
56. Backhouse DJ, Fisher AJ, Neeway JJ, Corkhill CL, Hyatt NC, Hand RJ Corrosion of the international simple glass under acidic to hyperalkaline conditions. *npj Mater Degrad* 2:29. <https://doi.org/10.1038/s41529-018-00050-5>
57. Neeway JJ, Rieke PC, Parrauzot BP, Ryan JV, Asmussen RM (2018) The dissolution behaviour of borosilicate glasses in far-from equilibrium conditions. *Geochim Cosmochim Acta* 226:132–148. <https://doi.org/10.1016/j.gca.2018.02.001>
58. Gin S, Frugier P, Jollivet P, Bruguier F (2013) New insight into the residual rate of borosilicate glasses: effect of S/V and glass composition. *Int J Appl Glass Sci* 4:371–382. <https://doi.org/10.1111/ijag.12048>
59. Geisler T, Nagel T, Kilburn MR, Janssen A, Icenhower JP, Fonseca POC, Grange M, Nemchin AA (2015) The mechanism of borosilicate glass corrosion revisited. *Geochim Cosmochim Acta* 158:112–129. <https://doi.org/10.1016/j.gca.2015.02.039>
60. Fournier M, Gin S, Frugier P (2014) Resumption of nuclear glass alteration: state of the art. *J Nucl Mater* 448:348–363. <https://doi.org/10.1016/j.jnucmat.2014.02.022>
61. Newton RG (1966) Some problems in the dating of ancient glass by counting the layers in the weathering crust. *Glass Technol* 7:22–25
62. Geisler T, Janssen A, Scheiter D, Stephan T, Berndt J, Putnis A (2010) Aqueous corrosion of borosilicate glass under acidic conditions: a new corrosion mechanism. *J Non-Cryst Solids* 356:1458–1465. <https://doi.org/10.1016/j.jnoncrysol.2010.04.033>
63. Verney-Carron A, Gin S, Libourel G (2008) A fractured roman glass block altered for 1800 years in seawater: analogy with nuclear waste glass in a deep geological repository. *Geochim Cosmochim Acta* 72:5372–5385. <https://doi.org/10.1016/j.gca.2008.08.018>
64. Verney-Carron A, Gin S, Libourel G (2010) Archaeological analogs and the future of nuclear waste glass. *J Nucl Mater* 406:365–370. <https://doi.org/10.1016/j.jnucmat.2010.09.028>
65. McCloy JS, Marcial J, Clarke JS, Ahmadzadeh M, Wolff JA, Vicenzi EP, Bollinger DL, Ogenhall E, Englund M, Pearce CI, Sjöblom R, Kruger AA (2021) Reproduction of melting behaviour for vitrified hillforts based on amphibolite, granite, and basalt lithologies. *Sci Rep* 11:1272. <https://doi.org/10.1038/s41598-020-80485-w>
66. Techer I, Advocat T, Lancelot J, Liotard J-M (2000) Basaltic glass: alteration mechanisms and analogy with nuclear waste glasses. *J Nucl Mater* 282:40–46. [https://doi.org/10.1016/S0022-3115\(00\)00399-8](https://doi.org/10.1016/S0022-3115(00)00399-8)
67. McLoughlin SD, Hand RJ, Hyatt NC, Lee WE, Notingher I, McPhail DS, Henderson J (2005) The long term corrosion of glasses: analytical results after 32 years of burial at Ballidon. *Glass Technol Eur J Glass Sci Technol A* 47:59–67
68. Marshall RR (1961) Devitrification of natural glass. *GSA Bull* 72:1493–1520. [https://doi.org/10.1130/0016-7606\(1961\)72\[1493:DONG\]2.0.CO;2](https://doi.org/10.1130/0016-7606(1961)72[1493:DONG]2.0.CO;2)
69. Crovisier J-L, Advocat T, Dussossoy J-L (2003) Nature and role of natural alteration gels formed on the surface of ancient volcanic glasses (natural analogs of waste containment glasses). *J Nucl Mater* 321:91–109. [https://doi.org/10.1016/S0022-3115\(03\)99206-X](https://doi.org/10.1016/S0022-3115(03)99206-X)
70. Stroncik NA, Schmincke H-U (2001) Palagonite—a review. *Int J Earth Sci (Geol Rundsch)* 91:680–697. <https://doi.org/10.1007/s00531-001-0238-7>
71. Dultz S, Boy J, Dupont C, Halisch M, Behrens H, Welsch A-M, Erdmann M, Crumm S, Helsch G, Deubener J (2014) Alteration of a submarine basaltic glass under environmental conditions conducive for microorganisms: growth patterns of the microbial community and mechanism of palagonite formation. *Geomicrobiol J* 31:813–834. <https://doi.org/10.1080/01490451.2014.897774>
72. Weaver JL, DePriest PT, Plymale AE, Pearce CI, Arey B, Koestler RJ (2021) Microbial interactions with silicate glasses. *npj Mater Degrad* 5:11. <https://doi.org/10.1038/s41529-021-00153-w>

# Chapter 10

## Glass–ceramics: A Potential Material for Energy Storage and Photonic Applications



Anirban Chakrabarti, Sreedevi Menon, Anal Tarafder,  
and Atiar Rahaman Molla

### 10.1 Introduction

#### 10.1.1 History

Glass is a fascinating material that has drawn the curiosity of mankind since the Stone/Bronze Ages (3300 BC) due to astounding properties such as its transparency, luster, and chemical durability. Applications from glassware to window panes, insulators, and many others have made it an essential part of everyday life. Glass is an amorphous (non-crystalline) material, lacking long-range atomic order while exhibiting short-range order. Developing crystal phases within the glass can drastically alter its properties and has always been an interesting area in which scientists have been keen to work [1].

In 1739, French chemist, René-Antoine Ferchault de Réaumur attempted to partially crystallize glass by heat-treating soda-lime-silica glass bottles in a bed of gypsum and sand for several days; the glass became a porcelain-like opaque material. Even though he was able to crystallize glass, the prepared solid deformed and had low strength due to uncontrolled surface crystallization [2, 3].

200 years later, in 1953, a serendipitous event was observed by the American inventor Stanley Donald Stookey of Corning Glass Works, USA, and paved the way for the discovery of modern glass–ceramics. During his research on photo-etchable material to be used in televisions, he accidentally overheated an experimental glass. To his surprise, instead of melting, the glass turned into an opaque polycrystalline ceramic material with improved mechanical strength and insulating

---

A. Chakrabarti · S. Menon · A. Tarafder (✉) · A. R. Molla  
CSIR-Central Glass and Ceramic Research Institute, Kolkata 700032, India  
e-mail: [anal@cgcric.res.in](mailto:anal@cgcric.res.in); [analtarafder@gmail.com](mailto:analtarafder@gmail.com)

A. R. Molla  
e-mail: [atiar@cgcric.res.in](mailto:atiar@cgcric.res.in); [atiariitk@gmail.com](mailto:atiariitk@gmail.com)

properties compared with the parent glass. The new material had lithium disilicate ( $\text{Li}_2\text{Si}_2\text{O}_5$ ) and quartz ( $\text{SiO}_2$ ) as the main crystalline phases; he named it Fotoceram [4–6].

### ***10.1.2 Definition of Glass–ceramics***

By definition, Glass–Ceramics (GCs) are prepared by controlled crystallization of glasses via different processing methods. GCs contain at least one type of functional crystalline phase and a residual glass. The volume fraction crystallized may vary from ppm to almost 100% [7]. It is a combination of glass and ceramics and thus inherits properties from both parents; in most cases superior to them. Small crystals are developed in the base glass by controlled nucleation and subsequently, grow while altering the composition of the base glass. Hence, the selection of a suitable glass composition that has the potential to undergo controlled crystal nucleation and growth by heat treatment is the sole requirement for the fabrication of glass–ceramics. Such glass–ceramics may have improved thermal, mechanical, electrical, chemical, biological, and optical properties compared with their parent glasses and ceramics and they have found wide-ranging applications in the domestic, space, defense, electronics, health, architecture, chemical, energy, and waste management fields [2]. According to Stookey, the definition of glass–ceramics stands as “Glass–ceramics are made by first melting and forming special glasses containing nucleating agents and then controlling the crystallization of the glass” [2]. A group of experts proposed a modern definition “Glass–ceramics are inorganic, non-metallic materials prepared by controlled crystallization of glasses via different processing methods. They contain at least one type of functional crystalline phase and a residual glass. The volume fraction crystallized may vary from ppm to almost 100%” [2, 7].

### ***10.1.3 Importance of Glass–ceramics***

Glass–ceramics are a class of material that show immense potency in properties and applications. The properties of glass–ceramics can be tailored for particular applications by choosing specific chemical compositions of the base glass and by controlling nucleation and crystallization. Glass–ceramics can have a variety of compositions and the possibility of developing special microstructures. The microstructure developed in a glass–ceramic plays a very important role in achieving the desired properties which in turn makes them suitable for various domestic and advanced applications. The morphology of the crystals can be tailored by changing the compositions and processing parameters. Their improved properties include low or zero porosity, high mechanical strength, low or even negative thermal expansion, high-temperature stability, fluorescence, machinability, and chemical durability, to name a

few, and their transparency can be controlled from completely transparent to opaque, depending on the size of the crystals generated and their volume fraction [2, 8].

### 10.1.4 Crystallization of Glass

Crystallization of glass is the crucial step in the development of glass–ceramics and includes two stages: *nucleation* and *crystal growth*. Nucleation is initiated by the appearance of small areas of longer-range atomic order than the parent glass, called embryos. If these embryos attain a critical minimal size they lead to the formation of “nuclei”, which are capable of developing spontaneously into larger particles of the new phase [2].

The process of nucleation can be distinguished as homogeneous or heterogeneous. In homogeneous nucleation, the crystal phase is developed within the glass matrix without the presence of any foreign particle, and the nuclei formed and the crystals grown from them have the same chemical composition, whereas heterogeneous nucleation is aided by the presence of foreign particles and the constitution of nuclei and crystals developed will be different [2].

Homogeneous nucleation results in the same probability of critical nucleus formation in any volume or surface region of the system under study. In classical studies on crystallization in supercooled liquids, including inorganic glass formers, Tamman [9] proposed that below the equilibrium melting temperature there is a metastable zone of supercooling where nuclei do not form at an appreciable rate, but if the melt is provided with nuclei by seeding, crystals can grow. Below this temperature region, crystallization is controlled by two factors: the rate of formation of nuclei and crystal growth rate. At lower temperatures, the melts exhibit increased viscosity which inhibits the atomic rearrangements and diffusion processes necessary for nucleation and crystal growth. Hence, melts that facilitate this condition, such as those which can form glasses, show a peak in nucleation and crystal growth rates when they are cooled. A plot of nucleation and growth rates versus temperature for viscous melts is shown in Fig. 10.1 [2, 10].

To produce a large number of small crystals, Fig. 10.1 shows that nucleation should occur at or near the temperature of the maximum nucleation rate. Also below the temperature  $T_3$ , homogeneous nucleation is zero because the melt viscosity is too high [2, 11, 12].

Homogeneous nucleation is restricted to a few glass systems. The development of heterogeneous nucleation paved the way for the fabrication of useful glass–ceramics where crystallization is aided by the presence of impurities or foreign particles. These impurities that promote crystallization are called nucleating agents or catalyzers. Heterogeneous nucleation dominates over homogeneous nucleation because it requires a lower driving force than homogeneous nucleation. The prominent feature of heterogeneous nucleation is that the interfacial tension between heterogeneity and nucleated phase must be low. Therefore, the contact angle  $\theta$  at the substrate-melt-precipitate junction is an important parameter to be considered.

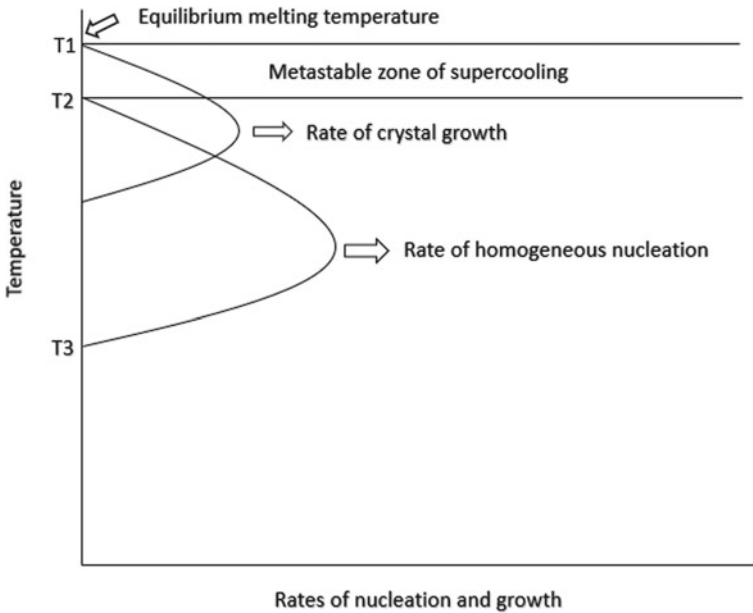


**Fig. 10.1** Rates of homogeneous nucleation and crystal growth in a viscous liquid

The activation energy for heterogeneous nucleation is given by, [2]

$$\Delta G_h^* = \Delta G^* f(\theta) \text{ where } f(\theta) = \frac{(2 + \cos \theta)(1 - \cos \theta)^2}{4} \tag{10.1.1}$$

where  $\Delta G^*$  is the free energy of homogeneous nucleation.

The rate of heterogeneous nucleation is given by [13]

$$I_C = A' \exp \left[ -\frac{\Delta G^* f(\theta)}{kT} \right] \tag{10.1.2}$$

Once a stable nucleus is formed, the next step is the growth of the crystal. This step is crucial as it determines the morphology of the glass–ceramic as well as the production of microcrystals within the glass matrix. The two factors on which crystal growth depends are: [2]

- (i) the rate of rearrangement of the irregular glass structure into the periodic lattice of a growing crystal,
- (ii) the elimination of the rate of release of energy in the phase transformation.

### 10.1.5 Fabrication Techniques

The conventional procedure for glass–ceramics manufacturing has three steps: (i) preparation of a homogeneous glass by melting, homogenizing, and refining a mixture of raw materials (batch) usually containing one or more nucleating agents, (ii) shaping of the glass to produce the required article by various methods like molding, pressing, blowing, rolling, etc. and (iii) controlled heat treatment to convert the glass into a glass–ceramic [7]. Several methods are employed including traditional melt-quenching to sol–gel and vapor deposition techniques. As mentioned earlier, in each case, two factors are important selection of a suitable glass composition and a proper heat-treatment protocol. Some glasses are difficult to devitrify whereas others undergo uncontrolled crystallization resulting in unsuitable microstructures. Also, heat treatment must be carefully controlled: errors can result in either a smaller number of larger crystals or deformation of the glass–ceramics. So, the fabrication process for glass–ceramics is highly sophisticated [7] and is discussed below in detail.

#### (i) Conventional method (Two-stage)

In this approach, once the glass is formed from the melt, its crystallization requires two stages: (i) treatment at a lower temperature (around  $T_N$ ) to give a high nucleation rate and many nuclei throughout the glass interior and (ii) a higher temperature heat treatment, around  $T_g$ , so the nuclei grow quickly into fully formed crystals. Here, the very limited overlap between nucleation and growth curves is noteworthy [14]. (Fig. 10.2).

#### (ii) Modified conventional method (Single stage)

Often the nucleation and growth rate curves hardly overlap and a two-stage treatment is necessary. If they effectively merge, however, nucleation and crystal growth can take place together in a single-stage heat treatment at  $T_{NG}$ . Optimizing the glass

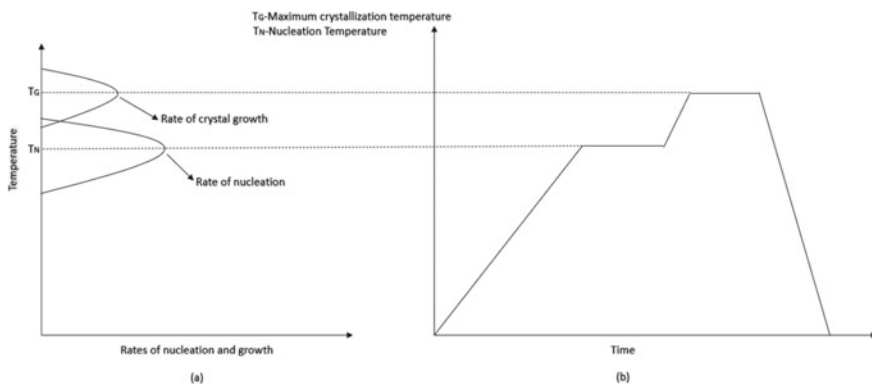


**Fig. 10.2** Crystallization of glass to form glass–ceramic: **a** insignificant overlap between nucleation and growth rates, **b** two-stage heat treatment

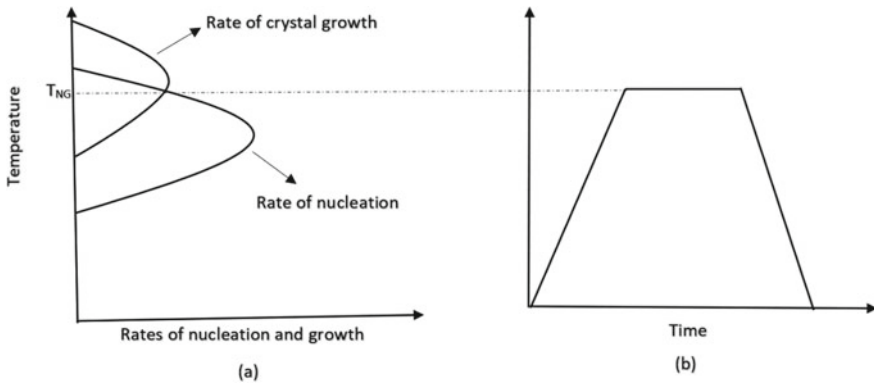


**Fig. 10.3** One step glass–ceramic formation: **a** nucleation and growth rate overlap significantly **b** single-stage heat-treatment suffices

composition and incorporating nucleating agents favors overlap of these curves. “Silceram” was the first glass-ceramic to be synthesized by this method [14, 15]. (Fig. 10.3)

### (iii) Petrurgic method

A very old method allowed both nucleation and crystal growth to take place during the cooling of the melt. The parent melt was carefully cooled without a hold at an intermediate temperature. Close observation of the production of “Silceram” showed that whether the glass was heated up to  $T_{NG}$  or cooled down to  $T_{NG}$  made little difference. This led to the development of the petrurgic method which along with the modified conventional method is much more cost-effective than the conventional approach [14, 16].

### (iv) Powder method—sintering with simultaneous crystallization

A common method used for the synthesis of ceramics is cold compacting a powder followed by heat treatment at an elevated temperature. The same route can be used for the fabrication of glass–ceramics. Compaction and sintering with simultaneous crystallization of glass powders requires heat and the glass–ceramics produced by this method have inferior properties to those manufactured by other techniques. It is always advantageous to sinter a parent glass by viscous flow at a lower temperature. The rates of viscous flow sintering and crystallization and their interaction have to be noted. Rapid crystallization can lead to a high degree of crystallinity which may restrict sintering and cause unwanted porosity. At the same time, if the sintering is fully completed before crystallization, then the final product resembles that produced by other fabrication methods. With careful control of rates, dense glass–ceramics can be created by a method where both crystallization and sintering take place at the same time and temperature. This method allows the properties of glass–ceramics to be altered by optimizing the composition and sintering temperature to change the microstructure and crystalline phases [17–20].



(v) **Sol–gel precursor glass**

In the last decades, a new technology called the sol–gel method has been developed for glass fabrication. Here, bulk solid materials are produced from a solution of small particles. The process involves the conversion of monomers into a colloidal solution called a sol by crosslinking them to form an integrated network (gel). Glass–ceramics can be produced from precursor glass of high purity manufactured by a sol–gel method. But the drawback of this method is its high cost of fabrication. So, this method is used primarily for specialized glass that cannot be produced by conventional melting techniques [21].

### 10.1.6 *Properties*

(i) **Thermal properties**

Glass-ceramics can have expansion coefficients similar to those of ordinary glasses or ceramics but can also display an astounding range of values from negative, zero to highly positive. The crystal phases formed, their volume fraction, morphology, etc. and the residual glass determine the coefficient, which can differ widely from that of the parent glass [2].

(ii) **Optical properties**

Light transmission and absorption are important properties for glass-ceramics defining their color and opalescence. Depending on the type and size of the crystals and their microstructure, glass-ceramics can vary from opaque to translucent to highly transparent [2, 22]. Fluorescence can also be important.

(iii) **Chemical properties**

Glass-ceramics can exhibit remarkable chemical stability compared to the parent glass. The bulk chemistry, the durability of each of the crystalline phases, and the microstructure influence the chemical stability. The glassy phase in the glass-ceramic is usually attacked first by an exchange of its mobile cations (usually alkali metal ions) with hydrogen ions. This results in hydration which ruptures the silica network. So, glass-ceramics with a lower volume of residual glass phase are advisable for high chemical durability. Selection of a chemical composition with lower concentrations of alkali metal oxides can also improve chemical durability [2].

(iv) **Biological properties**

Glass-ceramics with biomedical applications are an expanding field of study and have noteworthy clinical applications; they paved the way for a new class of materials called bioglass-ceramics. Implanting these glass-ceramics into the human body showed no local or systematic toxicity, no inflammation, and no foreign body response; they also bonded to soft and hard tissues. Their enhanced

mechanical and biocompatibility properties has promoted their application in orthopedic and dental surgery [2].

(v) **Mechanical properties**

Generally, glass-ceramics have higher mechanical strength compared to ordinary glasses and other types of ceramics. It is mainly attributed to the crystal phase dispersed homogeneously in the glass matrix and the unique microstructure. The main advantages of glass-ceramics are that they show high toughness, high hardness, and strength along with other properties like translucency and the ability to be pressed or cast, without shrinking or developing pores [2].

(vi) **Electrical properties**

Glass-ceramics are usually electrical insulators with high resistivity; however, exceptions exist. Their ability to withstand high temperatures makes them applicable in devices that require insulators that operate at elevated temperatures. Ferroelectric glass-ceramics are an upcoming field that contributes immensely to the area of energy storage. This will be discussed in detail in the latter part of this chapter [2].

### 10.1.7 Applications

Their extraordinary blend of properties makes glass-ceramics amazing materials with wide-ranging applications. They have become an interdisciplinary field offering potential usage in many fields including energy, display, healthcare, defense, space, etc. A few of the major applications of glass-ceramics are dealt with in the following section.

(i) **Technical applications**

- Machinable glass-ceramic

This is a combination of fluorophlogopite mica and borosilicate glass which can be machined into complex shapes with precise dimensions by conventional metal-working tools. Corning Inc. developed a commercial material under the trademark MACOR<sup>®</sup> with a unique combination of properties. It is a white, non-wetting, odorless, and non-outgassing material with zero porosity, composed of 55% fluorophlogopite mica and 45% borosilicate. It is widely used in the aerospace industry and for medical equipment, vacuum technology, welding, and nuclear studies [23].

(ii) **Consumer applications**

- $\beta$ -Spodumene Solid-Solution Glass-ceramics

$\beta$ -Spodumene solid-solution glass-ceramics have a low thermal expansion coefficient, good mechanical strength, and high resistance to thermal shock. These properties along with transparency find wide applications in low-cost

kitchen utensils and cookware. Pyroceram<sup>®</sup> 9608 developed by Stookey was the first commercial glass-ceramic used in household crockery. It had a low thermal expansion coefficient of  $0.7 \times 10^{-6}/\text{K}$ . Its major crystal phase was  $\beta$ -spodumene solid solution ( $\text{LiAlSi}_2\text{O}_6\text{-SiO}_2$ ) with minor amounts of rutile ( $\text{TiO}_2$ ). Several other  $\beta$ -spodumene solid-solution glass-ceramics ruled the market under the trademarks Cer-Vit<sup>™</sup> (Owens-Illinois), Herculit<sup>™</sup> (PPG), and Neoceram<sup>™</sup> N-11 (Nippon Electric Glass) [8, 24, 25].

### (iii) **Glass-ceramics for biomedical applications**

A material for biomedical application must be inert, non-toxic and biocompatible, and in some cases, bioactive too. According to Hench, a bioactive material has the property of bonding with living tissues. It forms a biologically active hydroxycarbonate apatite layer that can bond with bone and soft tissues [26–28].

For years, bioactive ceramics and glasses were used but had their drawbacks. So bioceramics were complex and expensive to produce whereas bioactive glasses had low mechanical strength and hardness. The development of bio glass-ceramics was a boon to overcoming these issues [29, 30]. The ease of synthesis by glass-making techniques and their high mechanical strength made them superior.

Bio glass-ceramics are used for two main purposes: implantology and restorative dentistry. For the former application glass-ceramics require biocompatibility, bioactive properties, high bending strength, toughness, and appropriate Young's modulus. Translucency or color is not a necessity. Restorative dental application, on the other hand, should not be bioactive. These materials are not embedded or implanted into the body. They are used to replace natural teeth. So, the shade, translucency, toughness, and wear must be similar to that of natural teeth.

Examples of glass-ceramics used in the clinical application include Cerabone<sup>®</sup>, Ceravital<sup>®</sup>, Bioverit<sup>®</sup>, etc. [8].

Glass–ceramics are also potential candidates for many futuristic areas, such as energy storage and photonic applications but few manuscripts encompass these subjects in depth. So this chapter mainly focuses on the suitability of novel glass–ceramics for these applications.

## 10.2 Glass–ceramics for Energy Storage

### 10.2.1 Introduction

The last decade has witnessed an over-dependence on fossil fuel reserves to meet our daily energy requirements, leading to global warming and environmental pollution. With the high energy demand, depletion of non-renewable energy sources (crude oil, coal, gas) in the near future is inevitable. So, the research and development of clean and green energy sources have become vital with the focus on energy storage and conversion, and less energy consumption [31]. The clean and renewable energy resources presently available include batteries, electrochemical supercapacitors, and dielectric capacitors. Compared to dielectric capacitors, batteries and fuel cells usually possess high energy storage density but lack high-power output. Supercapacitors can satisfy the requirement of high energy and power densities but their performance is sometimes hampered by the slow charge–discharge process. However, dielectric capacitors have the advantages of high-power density, faster charge–discharge rates, and high efficiency which extends their application in electronic devices, pulsed power supplies, and power systems, e.g., electromagnetic guns, inverter equipment, hybrid electric vehicles, military launch platforms, etc. [32, 33]. The currently used commercial capacitors like dielectric polymers and ceramics possess low energy density, small discharge currents, and a short lifetime which limits their applications. These materials fail to achieve the high dielectric breakdown strength (BDS) and low dielectric losses which are necessary for a high energy storage density. For example, ferroelectric ceramics have large dielectric constants but possess a low BDS. Similarly, dielectric polymers exhibit high BDSs but a low dielectric constant which limits their application in the relevant fields [34]. Presently, the need for modernization of electronic and electrical equipment calls for miniaturized, lightweight, cost-effective, and high-energy storage capacities. Therefore, material composition, dielectric behavior (linear/ferroelectric/antiferroelectric), synthesis and fabrication techniques are the key to developing dielectric materials with a high energy storage density [35].

### 10.2.2 Key Parameters for Evaluating Energy Storage Density and Efficiency

Considering a parallel plate conductor capacitor with a dielectric material having plate area “ $A$ ” placed at a distance “ $d$ ” and connected to an external electric field ( $E$ ) of a particular voltage ( $V$ ), its capacitance ( $C$ ) can be evaluated from Eq. (10.2.1) as follows:

$$C = \epsilon_0 \epsilon_r \frac{A}{d} \quad (10.2.1)$$

For linear dielectric materials like glass, the maximum theoretical energy storage density ( $U$ ) is linearly dependent on the dielectric constant and the BDS, as depicted in Eq. (10.2.2)

$$U = \frac{1}{2} \varepsilon_0 \varepsilon_r E_b^2 \quad (10.2.2)$$

where  $E_b$  is the BDS,  $\varepsilon_r$  is the dielectric permittivity and  $\varepsilon_0$  is the free space permittivity ( $8.85 \times 10^{-12}$  F/m).

During the charging process, charges of opposite polarity ( $\pm Q$ ) present in the dielectric material accumulate on the conductor plates with equal probability. Hence, work is done ( $W$ ) to store the energy in a capacitor during each charging cycle which can be calculated from Eq. (10.2.3) [34, 36]

$$W = \int_0^Q V dq = \int_0^Q \frac{Q}{C} dq = 1/2 \frac{Q^2}{C} = 1/2 CV^2 \quad (10.2.3)$$

where  $W$  is the work done to store the amount of energy in one charging cycle,  $V$  is the voltage of the external electric field and  $Q$  is the total charge accumulated on the dielectric material.

The energy density stored in the dielectric capacitor after one charging cycle can be expressed by the following equation [37]:

$$J_s = \frac{W}{Ad} = \frac{\int_0^Q V dq}{Ad} = \int_0^{E_{\max}} D dE \quad (10.2.4)$$

where  $J_s$  is the charged energy density ( $\text{J}/\text{cm}^3$ ),  $D$  corresponds to the dielectric displacement or the charge density at low voltages and  $E_{\max}$  is the maximum strength of the applied electric field.

In dielectric materials like ferroelectrics, relaxor ferroelectrics, or anti-ferroelectrics, the dielectric permittivity is very high and the dielectric polarization is non-linearly dependent on the applied electric field, such that, “ $D$ ” is very close to polarization “ $P$ ”. Therefore, for these materials, Eq. (10.2.4) can be re-arranged as [33, 34]:

$$J_s = \int_0^{E_{\max}} P dE = \int_0^{P_{\max}} E dP \quad (10.2.5)$$

where  $P_{\max}$  is the maximum polarization at the applied electric field strength  $E$ .

Most of the dielectric materials used for fabrication of electrical capacitors consist of linear dielectrics with constant permittivity (e.g.,  $\text{Al}_2\text{O}_3$ , glass), ferroelectrics with spontaneous polarization [e.g.,  $\text{Pb}(\text{Zr}_x\text{Ti}_{1-x})\text{O}_3$  (PZT),  $\text{BaTiO}_3$ ,  $\text{PbTiO}_3$ ,  $(\text{K},\text{Li})\text{NbO}_3$ ,

(Sr,Ba)Nb<sub>2</sub>O<sub>6</sub>, etc.], relaxor ferroelectrics with nanosized domains (e.g., (Pb, La) (Zr,Ti)O<sub>3</sub>) and anti-ferroelectrics with zero net remanent polarization (e.g., AgNbO<sub>3</sub>, PbZrO<sub>3</sub>) [38]. The increase in polarization domain size from a linear dielectric to anti-ferroelectric leads to enhancement in the degree of dielectric nonlinearity which gives rise to the variable nature of the polarization (*P*) versus electric field (*E*) response known as the hysteresis loop as shown in Fig. 10.4.

The area inside the loops of each curve represents the amount of lost energy density (*J<sub>L</sub>*) due to hysteresis behavior, while the red shaded area represents the recoverable energy storage density (*J<sub>r</sub>*) after one charging cycle, i.e., the released energy density in the discharging process. The recoverable energy density (*J<sub>r</sub>*) can be theoretically calculated by numerical integration of the area between the polarization and the *P-E* hysteresis curve as follows:

$$J_r = \int_{P_r}^{P_{max}} E dP \tag{10.2.6}$$

where *P<sub>r</sub>* is the remanent polarization.

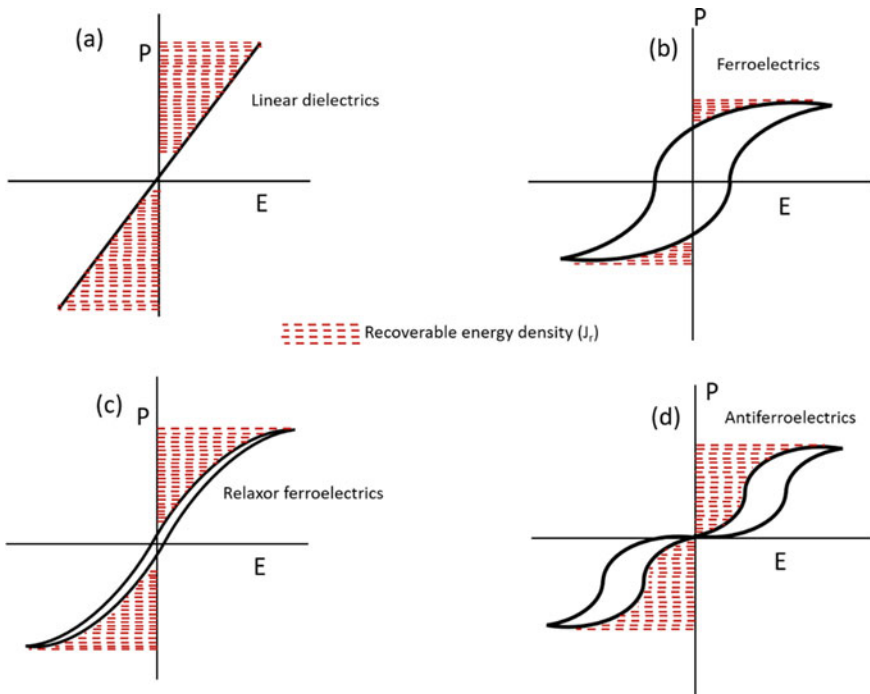


**Fig. 10.4** Polarization versus electric field (*P-E*) hysteresis loops and energy storage density of four classes of dielectric materials: **a** linear; **b** ferroelectrics; **c** relaxor ferroelectrics and **d** anti-ferroelectrics

Hence increased hysteresis behavior shall lead to a higher value of  $P_r$  which will reduce the released energy density.

The total energy storage density is equal to the sum of the stored energy density ( $J_s$ ) and the recoverable energy density ( $J_r$ ) and the energy storage efficiency is represented as:

$$\eta = \frac{J_r}{J_r + J_L} \quad (10.2.7)$$

Linear dielectrics like glasses exhibit a low dielectric constant and a higher BDS which leads to low energy storage density as represented in Eq. (10.2.2) and Fig. 10.5a. In ferroelectrics, a large value of maximum polarization ( $P_{\max}$ ) with high dielectric constant and moderate electric-field endurance can be observed which can give higher stored energy density ( $J_s$ ) compared to linear dielectrics. However, due to remanent polarization effects, the materials have reduced  $J_r$  as shown in Fig. 10.5b, which decreases their efficiency. On the other hand, relaxor-type ferroelectrics possess very low values of remanent polarization along with reduced hysteresis losses due to which their  $J_r$  and energy efficiency is improved compared to normal ferroelectrics. This type of material lacks the desired long-range order with respect to the ferroelectric domains and behaves like a dipolar glass due to which slimmer hysteresis loops are obtained as displayed in Fig. 10.5c. The anti-parallel dipolar arrangements in antiferroelectric materials lead to a lack of ferroelectric domains at low electric fields and have a negligible dielectric loss, hysteresis loss, and remanent polarization effects. An antiferroelectric-ferroelectric phase transition is observed at a threshold electric field intensity which generates double hysteresis loops and high  $J_r$  as shown in Fig. 10.5d. Therefore, for suitability for capacitive energy storage applications, a dielectric material having a high dielectric constant with low dielectric losses at various frequencies, low hysteresis energy loss, high thermal stability, and high BDS is desirable [39, 40].

### 10.2.3 Value of Glass–ceramics for Energy Storage

Traditionally used dielectric ceramics or polymer materials have the disadvantages of particle coarsening and aggregation which sometimes lead to an inferior microstructure and defects that interfere with their poling process. High dielectric losses are incurred with degradation in BDS, causing a significant drop in the energy storage density, thus limiting their applications [42]. For example, antiferroelectric ceramics are reported to possess a theoretical energy storage density as high as 50 J/cm<sup>3</sup> but a considerably lower BDS (10 kV/mm). Also, strain effects are encountered in sintered ferroelectric and antiferroelectric ceramics which lead to cracks and pores in their microstructure, thus dramatically reducing their BDS [38]. Most ferroelectric or antiferroelectric ceramic materials contain lead (Pb) in their composition, a major threat

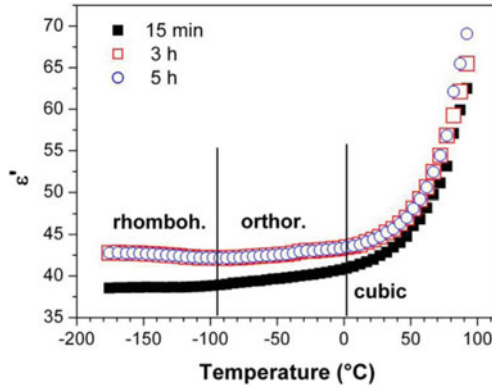


**Fig. 10.5** Real part of the dielectric constant of the glass–ceramic samples crystallized at 550 °C for 15 min, 3 h, and 5 h, respectively. Reproduced with permission from Ref. [41], Copyright © Elsevier

to the environment during processing and disposal. Legislation passed by the European Union in 2003 restricted the use of hazardous metals such as Pb, Cd, and Hg in electronic devices. Increased environmental awareness among research and development groups globally has encouraged the development of lead-free alternatives [43], to replace materials like the PZTs used currently [44].

Compared to sintered ceramics, polymers, or single-crystals, the preparation of glass–ceramics is a simple, low-cost technique. Generally, glass–ceramics are prepared by mixing the raw materials of the glassy phase and the corresponding ceramic crystalline phase uniformly and in appropriate proportions. The mixed raw materials are melted at a high temperature, poured into a pre-heated mold (kept at a comparatively low temperature) (melt-quenching), and annealed to obtain a glass block. A glass–ceramic is usually created by heat-treating the quenched glass block, firstly at the nucleation temperature then at higher temperatures to crystallize it and create the target ceramic phase [42].

Most ferroelectric ceramic compositions have a low glass-forming ability, so increased proportions of glass formers and modifiers are added to the glass composition to stabilize it. With proper optimization of composition and heat treatment, the required primary ferroelectric/antiferroelectric phase can be generated in the glass matrix with an average crystallite size in the nanometer range [45]. This minimizes Rayleigh scattering in the glass–ceramic and transparent ferroelectric glass–ceramics are obtained, potentially useful for nonlinear optical (second harmonic generation) and photonic applications. However, for a superior ferroelectric response for energy storage applications, the ferroelectric crystals must be larger than the domain size for notable polarization switching. Glass–ceramics with a small refractive index difference between the glassy phase and the active ferroelectric phase has optical transparency independent of crystal size. Such glass–ceramics are potential materials for optoelectronic (LED, laser diodes) and energy storage applications [46, 47]. Ferroelectric glass–ceramics are listed as important materials for use in high-temperature



three-phase inverters in automotive technology programs by the U.S. Department of Energy [43].

### 10.2.4 *Categorization of Glass–ceramics for Energy Storage Applications*

Based on in the literature, the various glass–ceramic compositions for energy storage can be categorized into two main classes: titanate and niobate based.

#### (i) **Titanate based glass–ceramics**

The crystal phase in titanate glass–ceramic is perovskite in nature with the general formula  $ABO_3$ , where “A” is a divalent alkaline earth metal cation ( $Ca^{2+}$ ,  $Sr^{2+}$ ,  $Ba^{2+}$ ,  $Pb^{2+}$ ) with a coordination number of 12, while the “B” site cation is a smaller transition metal ion ( $Ti^{4+}/Zr^{4+}$ ) with a coordination number 6. Barium titanate ( $BaTiO_3$ ) and barium strontium titanate ( $Ba_xSr_{1-x}TiO_3$ ) (BST) are two ferroelectric phases with the advantages of high dielectric constant, low dielectric loss, and high breakdown voltage, useful for energy storage applications [48]. Table 10.1 summarizes the key properties of  $BaTiO_3$  and BST-based glass–ceramics.

In 2003, Pennsylvania State University and the Naval Research Laboratory (NRL) investigated the crystallization and dielectric behavior of the  $BaO-TiO_2-Al_2O_3-SiO_2$  glass system [49].  $BaTiO_3$  was the major crystalline phase in glass–ceramics made conventionally. A high room temperature dielectric constant of 350 was obtained with a BDS in the range of 600–800 kV/cm. However, the energy storage density obtained was low ( $< 1 J/cm^3$ ), at high electric fields because the inhomogeneous microstructure created high electric field concentrations, degrading dielectric properties and causing inconsistent values of energy storage density. So, the crystal structure of  $BaTiO_3$  was modified by adding SrO to form BST ( $Ba_xSr_{1-x}TiO_3$ ). Such modifications allowed the Curie temperature of the ferroelectric phase present to be tailored with the possibility of maintaining consistent dielectric properties. Gorzkowski et al. [50] investigated the dielectric properties and energy storage density of BST-based glass–ceramics with the addition of  $Al_2O_3$ ,  $BaF_2$  to the glass composition. Dielectric properties were studied with the glass–ceramics heat-treated at 1200 °C for 2 and 10 h. Table 10.1 shows that the 50/50 BST composition exhibited a peak dielectric constant of 250 at  $-90$  °C, while the highest peak dielectric constant of 1000 was obtained for the 80/20 composition at 80 °C. The BST 50/50 glass–ceramic had a BDS of 800 kV/cm, which decreased from 500 to 300 kV/cm with an increase in barium content for BST 70/30 and BST 80/20 samples, respectively. The energy storage density followed a similar trend, ranging from 0.9  $J/cm^3$  for BST 50/50 to 0.28  $J/cm^3$  for BST80/20 glass–ceramic samples. Such low energy density values were attributed to the dendritic microstructure which created a high field concentration at the dendrite tips causing early breakdown. The microstructures were improved with the addition of refining agents like  $BaF_2$  and the dendrites were converted into a leaf-like structure. The BST 80/20 sample heat-treated at 1200 °C for 2 h exhibited an energy storage density of

**Table 10.1** Key findings of BaTiO<sub>3</sub> and BST-based glass-ceramics

Glass system/Glass composition (mol%)	Crystal phase(s)	Dielectric constant	Dielectric breakdown strength (kV/cm)	Energy storage density (J/cm <sup>3</sup> )	References
36.7BaO-32.4TiO <sub>2</sub> -14.8Al <sub>2</sub> O <sub>3</sub> -14.2SiO <sub>2</sub> -0.6BaF <sub>2</sub> -1.3MgO	BaTiO <sub>3</sub>	350 (25 °C)	600–800		[49]
19.34BaO-19.4SrO-31.32TiO <sub>2</sub> -12.86Al <sub>2</sub> O <sub>3</sub> -17.14SiO <sub>2</sub> (BST 50/50)	Ba <sub>0.5</sub> Sr <sub>0.5</sub> TiO <sub>3</sub> , Ba <sub>2</sub> TiSi <sub>2</sub> O <sub>8</sub>	ε <sub>max</sub> : 250 (-90 °C)	800	0.9	[50]
28.62BaO-12.27SrO-33.11TiO <sub>2</sub> -10.72Al <sub>2</sub> O <sub>3</sub> -14.28SiO <sub>2</sub> -1BaF <sub>2</sub> (BST 70/30)	Ba <sub>0.7</sub> Sr <sub>0.3</sub> TiO <sub>3</sub> , Ba <sub>2</sub> TiSi <sub>2</sub> O <sub>8</sub>	ε <sub>max</sub> : 600 (50 °C)	500		
35.01BaO-8.75SrO-35.43TiO <sub>2</sub> -8.48Al <sub>2</sub> O <sub>3</sub> -11.32SiO <sub>2</sub> -1BaF <sub>2</sub> (BST 80/20)	Ba <sub>0.8</sub> Sr <sub>0.2</sub> TiO <sub>3</sub> , Ba <sub>2</sub> TiSi <sub>2</sub> O <sub>8</sub> , SiO <sub>2</sub>	ε <sub>max</sub> : 1000 (80 °C)	300–550	0.28–0.5	
29.36BaO-7.34SrO-31.50TiO <sub>2</sub> -8.6Al <sub>2</sub> O <sub>3</sub> -21.25SiO <sub>2</sub> -4AlF <sub>3</sub>	Ba <sub>x</sub> Sr <sub>1-x</sub> TiO <sub>3</sub> , BaAl <sub>2</sub> Si <sub>2</sub> O <sub>8</sub>	270 (25 °C)	402		[51]
29.36BaO-7.34SrO-30.5TiO <sub>2</sub> -8.6Al <sub>2</sub> O <sub>3</sub> -21.25SiO <sub>2</sub> -4AlF <sub>3</sub> -1MnO <sub>2</sub>	Ba <sub>x</sub> Sr <sub>1-x</sub> TiO <sub>3</sub> , BaAl <sub>2</sub> Si <sub>2</sub> O <sub>8</sub>	345 (25 °C)	621		
25.95BaCO <sub>3</sub> -8.65SrCO <sub>3</sub> -22SiO <sub>2</sub> -(29.4-x)TiO <sub>2</sub> -12Al <sub>2</sub> O <sub>3</sub> -2BaF <sub>2</sub> -xMnO <sub>2</sub> (x = 0.1, 0.2, 0.3, 0.4, 05)	BaTiO <sub>3</sub> , BaAl <sub>2</sub> Si <sub>2</sub> O <sub>8</sub>	300–380 (25 °C)			[52]
20.1Na <sub>2</sub> O-3Al <sub>2</sub> O <sub>3</sub> -23.1BaO-23TiO <sub>2</sub> -7.6B <sub>2</sub> O <sub>3</sub> -17.4SiO <sub>2</sub> -5.8Fe <sub>2</sub> O <sub>3</sub>	BaTiO <sub>3</sub> , BaTi <sub>0.75</sub> Fe <sub>0.25</sub> O <sub>2.888</sub>	40 (25 °C), 100 kHz)			[41]
(29.6-x)BaO-(7.4-y)SrO-29TiO <sub>2</sub> -12Al <sub>2</sub> O <sub>3</sub> -22SiO <sub>2</sub> -(x + y)CeO <sub>2</sub> ; x = 0, 0.8, 1.6, 2.4; y = 0, 0.2, 0.4, 0.6)	(Ba, Sr)TiO <sub>3</sub> , BaAl <sub>2</sub> Si <sub>2</sub> O <sub>8</sub>	ε <sub>max</sub> : 120-151 (-100–300 °C)	100	0.107–0.088 (J <sub>r</sub> )	[53]
(1-x)(BaO-TiO <sub>2</sub> -SiO <sub>2</sub> -Al <sub>2</sub> O <sub>3</sub> -B <sub>2</sub> O <sub>3</sub> )-xHfO <sub>2</sub> (x = 0–0.7)	BaTiO <sub>3</sub> , BaAl <sub>2</sub> Si <sub>2</sub> O <sub>8</sub>	150–193	673–1054	7.07	[54]

\*ε<sub>max</sub>—peak dielectric constant

0.28 J/cm<sup>3</sup> prior to BaF<sub>2</sub> addition, which rose to 0.5 J/cm<sup>3</sup> with an increase in the BDS from 300 to 550 kV/cm, attributed to the reduction in pores and dendrites in the microstructure which lowered the high field concentrations. However, considerable ferroelectric hysteresis was observed in the 70/30 and 80/20 samples giving low energy densities.

To solve the problem of inhomogeneous microstructure, Wang et al. [55] synthesized BST-based glass–ceramics using conventional and microwave heat-treatment methods. Microwave heat treatment facilitated the transformation of the dendritic morphology into spherical ones, which significantly increased the BDS from 561.3 (conventional crystallization) to 791.4 kV/cm (microwave crystallization). The highest BDS of 900 kV/cm was achieved by combining conventional crystallization and microwave heat treatment. The energy storage density of the sample obtained via conventional crystallization was 0.47 J/cm<sup>3</sup>, which increased to 1.05 (microwave) and 1.13 J/cm<sup>3</sup> (conventional-microwave).

Chen et al. [51] reported improved microstructures and dielectric properties of BST-based glass–ceramics by adding AlF<sub>3</sub> and MnO<sub>2</sub> to the base glass composition. The glass–ceramics heat-treated at 1000 °C for 2 h exhibited controlled crystallization with low dielectric losses (0.02–0.03). The undoped BST-based glass–ceramic exhibited a BDS of 270.1 kV/cm, which increased to 402 kV/cm with the addition of 4 mol% AlF<sub>3</sub>. The highest BDS of 621 kV/cm was obtained with 4 mol% AlF<sub>3</sub> + 1 mol% MnO<sub>2</sub>, due to the refinement of the glass–ceramic microstructure following inhibition of dendritic growth. So, with multiple dopant modifications, BST-based glass–ceramics can be used for high energy density capacitor applications. Wang et al. [52] reported higher room temperature dielectric constants and lower dielectric losses by adding small amounts of MnO<sub>2</sub> to BST-based glass–ceramics. The glass–ceramics heat-treated at 1000 °C for 2 h exhibited dielectric losses between 0.005 and 0.02. A 0.2 mol% MnO<sub>2</sub> addition gave the highest dielectric constant of 380 at room temperature. Recently, Harizanova et al. [41] prepared BaTiO<sub>3</sub>-based glass–ceramics using an alkali-rich aluminoborosilicate glass composition given in Table 10.1. Heat treatment of the base glass at 550 °C for various times led to controlled precipitation of BaTiO<sub>3</sub> crystals of cubic symmetry, concentrated in spherical grains. The electrical conductivity and dielectric properties of the glass–ceramics were determined over the range –170 °C to 97 °C at frequencies from 0.1 to 100 kHz. The room temperature dielectric constant was around 40 at 100 kHz. The variation of dielectric constant with temperature exhibited two diffuse relaxor-type phase transitions which were attributed to rhombohedral-orthorhombic (–123 to –73 °C) and orthorhombic-cubic (–33 to 0 °C) BaTiO<sub>3</sub>, as displayed in Fig. 10.5 of BST-based glass–ceramics [41].

Similarly, Zhao et al. [53] studied the effects of CeO<sub>2</sub> doping on the dielectric properties of (Ba, Sr)TiO<sub>3</sub> glass–ceramics. The glass–ceramics with 2 mol% CeO<sub>2</sub> addition witnessed the highest dielectric constant of 151 around 0 °C along with the highest recoverable energy storage density of 0.107 J/cm<sup>3</sup>. Very recently Wei et al. [54] reported a high energy storage density of Hafnium doped BaTiO<sub>3</sub> glass–ceramics. With 0.3 mol% HfO<sub>2</sub> addition, the average dielectric constant improved up to 193 and the maximum BDS obtained was 1054 kV/cm, which gave a maximum

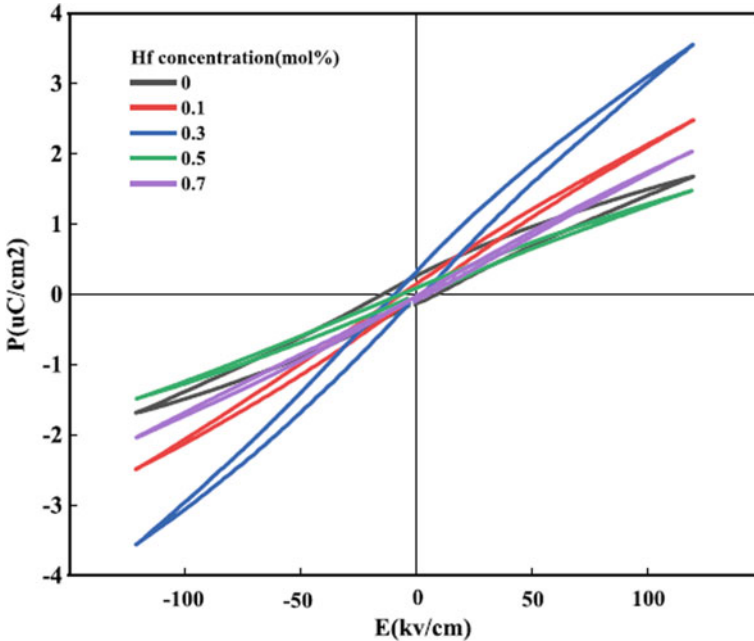


**Fig. 10.6** P-E loops of HfO<sub>2</sub> added BaTiO<sub>3</sub>-based glass-ceramics crystallized at 975 °C for 2 h. Reproduced with permission from Ref. [54], Copyright © Elsevier

theoretical energy storage density of 7.07 J/cm<sup>3</sup> and a discharge density of 0.73 J/cm<sup>3</sup> at room temperature. A high degree of nonlinearity was observed in the P-E loop curve with 0.3 mol% HfO<sub>2</sub> addition, as depicted in Fig. 10.6.

#### (ii) Niobate-based glass-ceramics

Niobate-based glass-ceramics which show high dielectric constant and structural modifications useful for energy storage applications are commonly observed in two crystal structure types—based on perovskite (KNbO<sub>3</sub>, NaNbO<sub>3</sub>, LiNbO<sub>3</sub>) and tungsten bronzes. The latter structures have stoichiometries such as sodium barium niobate (Ba<sub>2</sub>NaNb<sub>5</sub>O<sub>15</sub>), lead niobate (PbNb<sub>2</sub>O<sub>6</sub>), potassium strontium niobate (KSr<sub>2</sub>Nb<sub>5</sub>O<sub>15</sub>), and barium strontium niobate (Sr<sub>x</sub>Ba<sub>1-x</sub>Nb<sub>2</sub>O<sub>6</sub>). The general formula of these phases is (A<sub>1</sub>)<sub>2</sub>(A<sub>2</sub>)<sub>4</sub>(B<sub>1</sub>)<sub>2</sub>(B<sub>2</sub>)<sub>8</sub>O<sub>30</sub>. Alkali and alkaline earth metal ions like Pb<sup>2+</sup>, Ca<sup>2+</sup>, Ba<sup>2+</sup>, Sr<sup>2+</sup>, Na<sup>+</sup>, and K<sup>+</sup> occupy the A<sub>1</sub> and A<sub>2</sub> sites, while higher valent ions such as Nb<sup>5+</sup>, Ta<sup>5+</sup>, Ti<sup>4+</sup>, Zr<sup>4+</sup>, Fe<sup>3+</sup> have an affinity for the B<sub>1</sub> and B<sub>2</sub> sites. Table 10.2 summarizes the important properties of such niobate glass-ceramics.

Zeng et al. [56] investigated the dielectric properties of strontium barium niobate (SBN) based glass-ceramics in a borate glass matrix. BaF<sub>2</sub> was added as a nucleating agent which improved the crystallization and microstructure of the glass-ceramics. The highest room temperature relative dielectric constant of 337 and a BDS of 527 kV/cm were obtained with 5% BaF<sub>2</sub> addition. Similarly, Kamonlert et al. [57]

**Table 10.2** Key findings of niobate-based glass–ceramics

Glass system/Glass composition (mol%)	Crystal phase(s)	Dielectric constant	Dielectric breakdown strength (kV/cm)	Energy storage density (J/cm <sup>3</sup> )	References
BaO-B <sub>2</sub> O <sub>3</sub> -Nb <sub>2</sub> O <sub>5</sub> -SrO-BaF <sub>2</sub>	(Sr <sub>0.63</sub> Ba <sub>0.37</sub> )Nb <sub>2</sub> O <sub>6</sub>	337	527		[56]
25Na <sub>2</sub> O-25Nb <sub>2</sub> O <sub>5</sub> -50SiO <sub>2</sub> +xZrO <sub>2</sub> (x = 0, 1, 3, 5)	NaNbO <sub>3</sub>	153, 669(400 °C)			[57]
(K <sub>0.5</sub> Na <sub>0.5</sub> )NbO <sub>3</sub> -SiO <sub>2</sub> -Al <sub>2</sub> O <sub>3</sub>	(K <sub>0.5</sub> Na <sub>0.5</sub> )NbO <sub>3</sub>	260			[58]
5Na <sub>2</sub> O-20.8BaO-20.8SrO-18.4Nb <sub>2</sub> O <sub>5</sub> -30SiO <sub>2</sub> -5B <sub>2</sub> O <sub>3</sub>	Sr <sub>0.75</sub> Ba <sub>0.25</sub> Nb <sub>2</sub> O <sub>6</sub> , NaSr <sub>1.2</sub> Ba <sub>0.8</sub> Nb <sub>5</sub> O <sub>15</sub>		1400	4.0	[59]
BaO-Na <sub>2</sub> O-Nb <sub>2</sub> O <sub>5</sub> -SiO <sub>2</sub> -Gd <sub>2</sub> O <sub>3</sub>	Ba <sub>2</sub> NaNb <sub>5</sub> O <sub>15</sub> , NaNbO <sub>3</sub>	312-349	323.9-561.6		[60]
21BaO-21SrO-18Nb <sub>2</sub> O <sub>5</sub> -10B <sub>2</sub> O <sub>3</sub> -30SiO <sub>2</sub> + xCeO <sub>2</sub>	Sr <sub>0.75</sub> Ba <sub>0.25</sub> Nb <sub>2</sub> O <sub>6</sub>	49	1250	3.39	[61]
17Na <sub>2</sub> O-17BaO-34Nb <sub>2</sub> O <sub>5</sub> -31SiO <sub>2</sub> -xLa <sub>2</sub> O <sub>3</sub> (x = 0-3)	Ba <sub>2</sub> NaNb <sub>5</sub> O <sub>15</sub> , NaNbO <sub>3</sub>		280	1.2 (J <sub>r</sub> )	[62]
16Na <sub>2</sub> O-8BaO-26Nb <sub>2</sub> O <sub>5</sub> -50SiO <sub>2</sub> +xZrO <sub>2</sub>	Ba <sub>2</sub> NaNb <sub>5</sub> O <sub>15</sub> , NaNbO <sub>3</sub>	293.8			[63]
xSrO-(32-x)BaO32Nb <sub>2</sub> O <sub>5</sub> :36B <sub>2</sub> O <sub>3</sub> (x = 8, 11.2, 14.4, 17.6, 20.8, 24)	(Sr <sub>0.5</sub> Ba <sub>0.5</sub> )Nb <sub>2</sub> O <sub>6</sub> , SrNb <sub>2</sub> O <sub>6</sub>	120	951-1248	1.93-4.88, 0.29-1.01 (J <sub>r</sub> )	[64]
25Na <sub>2</sub> O-10BaO-25Nb <sub>2</sub> O <sub>5</sub> -40SiO <sub>2</sub> +2ZrO <sub>2</sub>	NaNbO <sub>3</sub> , Ba <sub>3</sub> Nb <sub>6</sub> Si <sub>14</sub> O <sub>26</sub>	49.5-116.4			[65]
14.4SrO-17.6BaO-32Nb <sub>2</sub> O <sub>5</sub> -36B <sub>2</sub> O <sub>3</sub>	(Sr <sub>0.5</sub> Ba <sub>0.5</sub> )Nb <sub>2</sub> O <sub>6</sub> , SrNb <sub>2</sub> O <sub>6</sub>	45-117	944-1220	2.97-5.71	[66]
14.3SrO-17.5BaO-31.9Nb <sub>2</sub> O <sub>5</sub> -35.8B <sub>2</sub> O <sub>3</sub> -0.5ZnO-xLa <sub>2</sub> O <sub>3</sub> (x = 0-1.5)	Sr <sub>0.5</sub> Ba <sub>0.5</sub> Nb <sub>2</sub> O <sub>6</sub>	105-160	608-1127	2.6-7.1	[67]

(continued)

Table 10.2 (continued)

Glass system/Glass composition (mol%)	Crystal phase(s)	Dielectric constant	Dielectric breakdown strength (kV/cm)	Energy storage density ( $J/cm^3$ )	References
14.4SrO-17.6BaO-32Nb <sub>2</sub> O <sub>5</sub> -(36-x)B <sub>2</sub> O <sub>3</sub> -xP <sub>2</sub> O <sub>5</sub> (x = 0.3, 5, 10)	Sr <sub>0.5</sub> Ba <sub>0.5</sub> Nb <sub>2</sub> O <sub>6</sub> , Ba <sub>2</sub> P <sub>6</sub> O <sub>17</sub>	55–90	944–1650	3.89–9.1	[68]
15Na <sub>2</sub> O-15K <sub>2</sub> O-30Nb <sub>2</sub> O <sub>5</sub> -27SiO <sub>2</sub> -10B <sub>2</sub> O <sub>3</sub> -3BaF <sub>2</sub> /ZrO <sub>2</sub> /CeO <sub>2</sub>	Na <sub>0.9</sub> K <sub>0.1</sub> NbO <sub>3</sub> , KNbO <sub>3</sub> , NaNbO <sub>3</sub>	107–291	329–523	1.29–1.94	[69]
15Na <sub>2</sub> O-15K <sub>2</sub> O-30Nb <sub>2</sub> O <sub>5</sub> -27SiO <sub>2</sub> -10B <sub>2</sub> O <sub>3</sub> -3CeO <sub>2</sub>	Na <sub>0.9</sub> K <sub>0.1</sub> NbO <sub>3</sub> , KNbO <sub>3</sub> , NaNbO <sub>3</sub>	121–270	380–540	1.55–1.899	[70]
15K <sub>2</sub> CO <sub>3</sub> -15SrCO <sub>3</sub> -30Nb <sub>2</sub> O <sub>5</sub> -32SiO <sub>2</sub> -4Al <sub>2</sub> O <sub>3</sub> -4B <sub>2</sub> O <sub>3</sub>	KSr <sub>2</sub> Nb <sub>5</sub> O <sub>15</sub> , AlNbO <sub>4</sub>	88.8–103	1069.71–1287.15	4.24–8.99	[71]
25.6BaCO <sub>3</sub> -6.4K <sub>2</sub> CO <sub>3</sub> -32Nb <sub>2</sub> O <sub>5</sub> -36SiO <sub>2</sub>	Ba <sub>2</sub> KNb <sub>5</sub> O <sub>15</sub> , BaNb <sub>2</sub> O <sub>6</sub> , K <sub>3</sub> NbO <sub>4</sub>	46–69	1896.9–2418.7	8.60–14.58	[72]
BaO-Na <sub>2</sub> O-Nb <sub>2</sub> O <sub>5</sub> -SiO <sub>2</sub> -B <sub>2</sub> O <sub>3</sub>	Ba <sub>2</sub> NaNbO <sub>15</sub> , NaNbO <sub>3</sub> , BaNb <sub>2</sub> O <sub>6</sub>	100–900	397.6	0.13 ( $J_r$ )	[73]
17Na <sub>2</sub> O-17BaO-34Nb <sub>2</sub> O <sub>5</sub> -31SiO <sub>2</sub> -xSm <sub>2</sub> O <sub>3</sub> (0.5 ≤ x ≤ 3)	Ba <sub>2</sub> NaNb <sub>5</sub> O <sub>15</sub> , NaNbO <sub>3</sub>	399–531	159–212	0.74 ( $J_s$ ), 0.45 ( $J_r$ )	[74]
6.4K <sub>2</sub> O-25.6BaO-32Nb <sub>2</sub> O <sub>5</sub> -36SiO <sub>2</sub> -xGd <sub>2</sub> O <sub>3</sub> (x = 0–3.0)	Ba <sub>2</sub> KNb <sub>5</sub> O <sub>15</sub> , BaNb <sub>2</sub> O <sub>6</sub> , K <sub>3</sub> NbO <sub>4</sub>	62–104	1818	7–12.14	[75]
20BaO-20SrO-20Nb <sub>2</sub> O <sub>5</sub> -5Al <sub>2</sub> O <sub>3</sub> -1.5B <sub>2</sub> O <sub>3</sub> -33.5SiO <sub>2</sub> -xMnO <sub>2</sub> (x = 0.05–0.5)	Sr <sub>0.75</sub> Ba <sub>0.27</sub> Nb <sub>2</sub> O <sub>5.78</sub> , BaAl <sub>2</sub> Si <sub>2</sub> O <sub>8</sub>	80–110	1152–1470.6	9.2	[76]
6.4K <sub>2</sub> O-25.6SrO-32Nb <sub>2</sub> O <sub>5</sub> -36SiO <sub>2</sub> +3ZrO <sub>2</sub> /CeO <sub>2</sub> /CaF <sub>2</sub>	KSr <sub>2</sub> Nb <sub>5</sub> O <sub>15</sub> , Sr <sub>2</sub> Nb <sub>10</sub> O <sub>27</sub>	64–114	1539–1919	4.8–13.5	[77]
24BaO-6Na <sub>2</sub> O-30Nb <sub>2</sub> O <sub>5</sub> -10Al <sub>2</sub> O <sub>3</sub> -30SiO <sub>2</sub>	Ba <sub>2</sub> NaNb <sub>5</sub> O <sub>15</sub>		2322	16.6	[78]
(1-x)[(SrO-K <sub>2</sub> O)-Nb <sub>2</sub> O <sub>5</sub> ]-x[SiO <sub>2</sub> -Al <sub>2</sub> O <sub>3</sub> ]	KSr <sub>2</sub> Nb <sub>5</sub> O <sub>15</sub> , AlNbO <sub>4</sub>	86–140	865–1257	4.5–6.7	[79]
20BaO-20SrO-20Nb <sub>2</sub> O <sub>5</sub> -5Al <sub>2</sub> O <sub>3</sub> -(35-x)SiO <sub>2</sub> -xZrO <sub>2</sub> (x = 0–3)	Sr <sub>0.75</sub> Ba <sub>0.27</sub> Nb <sub>2</sub> O <sub>5.78</sub>	108.9–135.9	1111.2–1377.7	6.7–8.9	[80]

(continued)

**Table 10.2** (continued)

Glass system/Glass composition (mol%)	Crystal phase(s)	Dielectric constant	Dielectric breakdown strength (kV/cm)	Energy storage density ( $J/cm^3$ )	References
$15Bi_2O_3-15Nb_2O_5-40SiO_2-30Al_2O_3$	$\beta$ -BiNbO <sub>4</sub> , Bi <sub>1.3</sub> AlNbO <sub>6</sub>	51–100	1861	15.3	[81]
$6.8Na_2O-27.2BaO-34Nb_2O_5-32SiO_2-xCaF_2$ ( $x = 0-4$ )	$Ba_2NaNb_5O_{15}$ , NaNbO <sub>3</sub> , BaNb <sub>2</sub> O <sub>6</sub> , BaAl <sub>2</sub> Si <sub>2</sub> O <sub>8</sub>	100–141	1320.10–1551.04	8.99–14.3	[82]
BaO-Na <sub>2</sub> O-Nb <sub>2</sub> O <sub>5</sub> -W <sub>2</sub> O <sub>3</sub> -P <sub>2</sub> O <sub>5</sub>	$Ba_2Na_4W_2Nb_8O_3O_3O_3$ , NaNbO <sub>3</sub> ,			0.0112–0.0258 ( $J_r$ )	[83]
$10K_2O-20BaO-10SrO-30Nb_2O_5-25B_2O_3-5P_2O_5$	$Ba_{0.5}Sr_{0.5}Nb_2O_6$ , KSr <sub>2</sub> Nb <sub>5</sub> O <sub>15</sub>	98	1487	9.6 0.48 ( $J_r$ )	[84]
$6Na_2O-21.6BaO-2.4Bi_2O_3-30Nb_2O_5-10Al_2O_3-30SiO_2$	$Ba_2NaNb_5O_{15}$ , NaNbO <sub>3</sub> , BaAl <sub>2</sub> Si <sub>2</sub> O <sub>8</sub>	102–123	1875.75 ± 63.2	18.4 ± 1.3 0.48 ( $J_r$ )	[85]
$6Na_2O-21.6BaO-2.4Bi_2O_3-30Nb_2O_5-10Al_2O_3-30SiO_2-0.2R_2O_3$ (R = La, Gd, Yb)	$Ba_2NaNb_5O_{15}$ , NaNbO <sub>3</sub> , BaAl <sub>2</sub> Si <sub>2</sub> O <sub>8</sub>	121.23	2046.49	22.48	[86]
$40[(1-x)K_2O-xNa_2O]-40Nb_2O_5-20SiO_2$ ( $x = 0-0.50$ )	$Na_{0.35}K_{0.65}NbO_3$ , K <sub>3</sub> Nb <sub>8</sub> O <sub>21</sub>	80–104	550–750	2.44 0.156 ( $J_r$ )	[87]
$6.4Na_2O-25.6SrO-32[(1-x)Nb_2O_5-xTa_2O_5]-36SiO_2$ ( $x = 0, 1, 2, 5, 10$ )	NaNbO <sub>3</sub> , Sr <sub>6</sub> Nb <sub>10</sub> O <sub>30</sub> , NaSr <sub>2</sub> Nb <sub>5</sub> O <sub>15</sub>	57.95–94.5	1385.68–1984.75	4.93–15.22	[88]

studied the effects of  $\text{ZrO}_2$  as a nucleating agent on the crystallization and dielectric properties of  $\text{NaNbO}_3$ -based glass-ceramics. With 1 mol%  $\text{ZrO}_2$ , the sample heat-treated at 900 °C for 1 h exhibited a room temperature dielectric constant of 153, while the undoped sample treated at 750 °C for 1 h showed a permittivity value of 669 at 400 °C. Potassium sodium niobate (KNN) based glass-ceramics with aluminum oxide added were synthesized by heat treatment between temperatures 600–675 °C [58]. The sample with 5 mol%  $\text{Al}_2\text{O}_3$  and heat-treated at 700 °C for 4 h gave the optimum dielectric constant (260) and dielectric loss (0.02) at room temperature. Several thorough investigations of the dielectric and energy storage properties of SBN-based glass-ceramics have been conducted by modifying composition and processing parameters, see Table 10.2 [59, 61, 64, 66–68, 76, 80].  $\text{Sr}_{0.75}\text{Ba}_{0.25}\text{B}_2\text{O}_6$ -based glass-ceramics were synthesized following single-stage and double-stage heat treatments in the temperature range of 800 to 950 °C for 3 h. The glass-ceramics, however, displayed no notable ferroelectric behavior at room temperature. The BDS was found to increase at higher crystallization temperatures. The highest BDS of 1400 kV/cm was obtained for the sample heat-treated at 800 °C for 3 h for nucleation followed by a 3 h heat treatment at 950 °C to crystallize the SBN phase. The maximum theoretical energy storage density ( $U$ ) obtained for the sample was 4 J/cm<sup>3</sup> [59]. Compositional modifications of the base glass composition by increasing the amount of  $\text{B}_2\text{O}_3$  and  $\text{CeO}_2$  (0–8 mol%) decreased the activation energy for crystallization and gave low dielectric losses. At 6.2 mol%  $\text{CeO}_2$ , the sample heat-treated at 800 °C for 2 h exhibited the highest room temperature dielectric constant of 49, a BDS of 1250 kV/cm, a low dielectric loss of 0.01, and a  $U$  value of 3.39 J/cm<sup>3</sup> [61]. Song et al. [64] reported that with an increase in Sr/Ba atomic ratio, the crystallization of the SBN phase was suppressed due to the formation of secondary  $\text{SrNb}_2\text{O}_6$  but uniform, dense and fine-grained microstructures were obtained in the glass-ceramics with a decrease in average grain size from 200 to 30 nm. At the optimum Sr/Ba ratio = 0.82, the GC heat-treated at 800 °C for 3 h exhibited a high dielectric constant of 120, a dielectric loss of 0.06, and a high BDS of 1050 kV/cm. Notable ferroelectric hysteresis behavior was observed in the glass-ceramics up to Sr/Ba = 0.82 and the recoverable/discharged energy density of 1.01 J/cm<sup>3</sup> was obtained. Yang et al. [66] investigated the dependence of the BDS on interfacial polarization for SBN glass-ceramics. The crystallization temperature dependence of the BDS was attributed to the change of interfacial polarization in the glass-ceramics with an increase in the degree of crystallization. The sample crystallized at 800 °C for 3 h was reported to have a BDS of 1050 kV/cm, a dielectric constant of 117 and the highest theoretical energy storage density of 5.71 J/cm<sup>3</sup>. As seen in Table 10.2, similar SBN glass-ceramics doped by replacing  $\text{ZnO}$  with  $\text{La}_2\text{O}_3$  were synthesized with  $\text{La}_2\text{O}_3$  concentrations from 0 to 1.5 mol%. Increasing the  $\text{La}_2\text{O}_3$  concentration raised the BDS of the glass-ceramics from 608 to 1127 kV/cm. An improvement in the  $U$  value by 2.7 times was observed in the sample (7.1 J/cm<sup>3</sup>) doped with 0.5 mol%  $\text{La}_2\text{O}_3$  compared to the undoped sample [67]. Similarly, Chen et al. [68] synthesized SBN glass-ceramics with a modified base glass composition and doped with  $\text{P}_2\text{O}_5$ . The BDS increased with  $\text{P}_2\text{O}_5$  content and the maximum theoretical energy storage density of 9.1 J/cm<sup>3</sup> and a BDS of 1650 kV/cm were obtained in the sample with



5 mol%  $P_2O_5$ . Xiu et al. [76] synthesized SBN-based glass–ceramics doped with different  $MnO_2$  concentrations. Adding  $MnO_2$  in lower amounts led to densification and homogenization of the microstructures of SBN-based glass–ceramics, causing a decrease in dielectric loss from 0.012 to 0.004 with an increase in BDS from 1152.0 to 1470.6 kV/cm. With a 0.05 mol%  $MnO_2$  addition, the BDS reached 1470.6 kV/cm and the  $U$  value of 9.2 J/cm<sup>3</sup> was obtained. Recently, Liu et al. [80] synthesized SBN-based glass–ceramics with zirconium oxide ( $ZrO_2$ ) added. The dielectric constant increased from 108.9 to 135.9 and the BDS increased from 1111.2 to 1129.4 kV/cm with < 0.5 mol%  $ZrO_2$ . The BDS further increased from 1291.6 to 1377.4 kV/cm when the  $ZrO_2$  concentration exceeded 1 mol%. The  $U$  value of 8.9 J/cm<sup>3</sup> was obtained for the glass–ceramic sample with 1 mol%  $ZrO_2$  content. The variation of dielectric constant and loss factor of the SBN glass–ceramics with temperature and the variation of room temperature dielectric constant with  $ZrO_2$  content are displayed in Fig. 10.7.

The dielectric and energy storage properties of sodium/potassium niobate and barium sodium niobate-based glass–ceramics have been investigated by several researchers Table 10.2. The dielectric constant and breakdown strength of the BNN ( $Ba_2NaNb_5O_{15}$ ,  $NaNbO_3$ ) based glass–ceramics were observed to increase with rising  $Gd_2O_3$  content [60]. The glass–ceramic sample with 1 mol%  $Gd_2O_3$  annealed at 900 °C exhibited an optimum dielectric constant of 349 and an average BDS of 561.6 kV/cm. Zhou et al. [62] observed an improved discharged energy density on adding  $La_2O_3$  to BNN-based glass–ceramics. Doping the A sites of the crystal phase with  $La^{3+}$  increased the dielectric constant and improved the microstructure, which

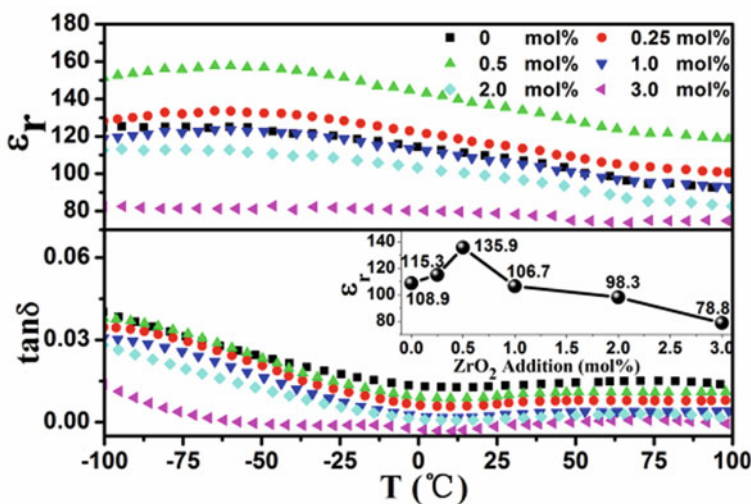


**Fig. 10.7** Dielectric temperature spectra of SBN-based glass–ceramics with  $ZrO_2$  content. Reproduced with permission from Ref. [80], © Elsevier

raised the BDS. A discharged energy density of  $1.2 \text{ J/cm}^3$  was achieved in the glass–ceramic sample containing 2 mol%  $\text{La}_2\text{O}_3$ . The influence of crystallization temperature and nucleating agents on the ferroelectric and energy storage performance in potassium sodium niobate (KNN) ( $\text{Na}_{0.9}\text{K}_{0.1}\text{NbO}_3$ ,  $\text{KNbO}_3$ ,  $\text{NaNbO}_3$ ) based glass–ceramics were investigated. The glass–ceramics heat-treated at the first crystallization peak temperature exhibited a high energy storage density of  $1.94 \text{ J/cm}^3$  [69]. The KNN-based glass–ceramics were also studied [70] with 3 mol%  $\text{CeO}_2$  added and after fabrication using different soaking times at the crystallization peak temperature. The sample crystallized at  $707^\circ\text{C}$  for 2 h plus  $900^\circ\text{C}$  for 3 h had a uniform dispersion of grains and exhibited an energy storage density of  $1.899 \text{ J/cm}^3$ . Figure 10.8 shows the variation in energy storage density and the BDS of KNN glass–ceramics with different soaking times at the second crystallization peak temperature ( $T_{p2}$ ).

Xiao et al. reported the energy storage properties of potassium strontium niobate boroaluminosilicate (KSN-BAS) glass–ceramics synthesized by microwave crystallization [71]. After 10 min of crystallization, the optimum dielectric constant of 102, a BDS of  $1410.81 \text{ kV/cm}$ , and maximum theoretical energy storage density of  $8.99 \text{ J/cm}^3$  were obtained.

The effect of nucleating agents/dopants, crystallization temperature, and technique on the dielectric and energy storage properties of BNN and BKN (barium potassium niobate) based glass–ceramics have been studied. Wang et al. [72] synthesized barium potassium niobate-based glass–ceramics and reported the maximum theoretical energy storage density ( $U$ ) of  $14.58 \pm 1.4 \text{ J/cm}^3$  and BDS of  $2382 \pm 92 \text{ kV/cm}$  for the glass–ceramic heat-treated at  $800^\circ\text{C}$ .  $\text{Gd}_2\text{O}_3$  additions have improved the energy storage properties of BKN-based glass–ceramics [75]. Glass–ceramics with 1 mol%

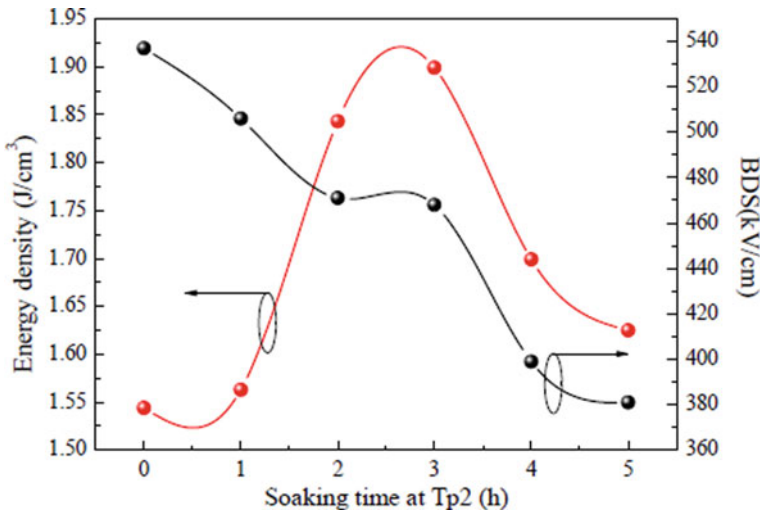


**Fig. 10.8** Variation of energy density and breakdown strength of KNN-based glass–ceramics with different crystallization treatments. Reproduced with permission from Ref. [70], © Elsevier

Gd<sub>2</sub>O<sub>3</sub> exhibited a high energy storage density of 12.14 J/cm<sup>3</sup>, a BDS of 1818 kV/cm with a discharge efficiency of 80%, and a discharge time of 25 ns. The BNN glass–ceramics were synthesized by combining conventional and microwave heating. The highest energy storage was found for glass–ceramics crystallized conventionally at 1000 °C; they had a discharge energy density of 0.13 J/cm<sup>3</sup> at a maximum field of 100 kV/cm [73]. Zhou et al. [74] investigated the microstructure, dielectric performance, and energy storage behavior with Sm<sub>2</sub>O<sub>3</sub> additions. The dielectric constant, BDS, and polarization improved in the glass–ceramic sample with Sm<sub>2</sub>O<sub>3</sub> contents up to 2 mol% leading to a maximum BDS of 212 kV/cm, a highest charge of 0.74 J/cm<sup>3</sup>, and a discharged energy density (0.45 J/cm<sup>3</sup>). The BNN-based glass–ceramics crystallized at 800 °C exhibited the  $U$  value of 16.6 J/cm<sup>3</sup> and a high BDS of 2322 kV/cm [78]. Jiang et al. reported enhanced energy storage density of BNN glass–ceramics by adding CaF<sub>2</sub> as a nucleating agent. With 3 mol% CaF<sub>2</sub>, a high theoretical energy storage density of 14.3 J/cm<sup>3</sup> was obtained having a discharge time of 50 ns and discharge power density of 75.6 MW/cm<sup>3</sup> [82]. Chen et al. [85] reported the synthesis of Bi<sub>2</sub>O<sub>3</sub> modified BNN-based glass–ceramics at four different crystallizing temperatures. The highest relative permittivity of 123 was obtained in the sample heat-treated at 1000 °C, while an optimum BDS of 1878.75 ± 63.2 kV/cm was obtained after heat treatment at 950 °C for 3 h. At 950 °C, the  $U$  value of 18.4 ± 1.3 J/cm<sup>3</sup> was obtained with a discharged energy density of 0.48 J/cm<sup>3</sup>. La, Gd, and Yb doped Bi<sub>2</sub>O<sub>3</sub> added BNN-based glass–ceramics were synthesized recently achieving a superior energy storage density and ultrafast discharge speeds. The Yb<sub>2</sub>O<sub>3</sub> doped BNN-based sample heat-treated at 950 °C for 3 h exhibited the highest BDS of 2046.49 kV/cm, with a low dissipation factor of 0.008 and  $U$  value of 22.48 J/cm<sup>3</sup> [86].

Recently, Du et al. [87] reported optimized energy storage performance for potassium sodium niobate (KNN) based glass–ceramics. A high discharged energy density of 2.44 J/cm<sup>3</sup> and energy storage efficiency of 93% was obtained with an increase in Na<sub>2</sub>O content; at a low field strength, an actual discharge energy density of 0.156 J/cm<sup>3</sup>, a high-power density (19.6 MW/cm<sup>3</sup>), a fast discharge rate (14 ns) and an excellent wide temperature stability range (20–120 °C) were observed. Recently, Ta<sub>2</sub>O<sub>5</sub> doped strontium sodium niobate-based glass–ceramics have been reported to display ultra-low dielectric loss with rapid discharge time [88]. Precipitation of NaNbO<sub>3</sub> increased with Ta<sup>5+</sup> concentration, which improved the dielectric constant and BDS. With 2 mol% Ta<sub>2</sub>O<sub>5</sub>, a maximum theoretical energy storage density of 15.22 J/cm<sup>3</sup> was achieved at 0.41% of dielectric loss. Also, an instantaneous power density of 125 MW/cm<sup>3</sup> was achieved at 400 kV/cm with a discharge time of 10 ns.

## ***10.2.5 Factors Affecting Energy Storage Properties of Glass–ceramics***

### **10.2.5.1 Effect of the Glass Matrix**

The composition and content of a glass matrix influence the crystallization kinetics and microstructure in a glass–ceramic. The nature of crystallization of a glass matrix to form the respective glass–ceramic directly affects its mechanical, thermal, optical, dielectric, and ferroelectric properties. Controlled homogenous nucleation and volume crystallization can generate uniform microstructures in ferroelectric glass–ceramics and improve their mechanical, dielectric, and energy storage properties. With increased glass phase content (silica > 20 wt%) in a ferroelectric glass–ceramic, the BDS and charge–discharge efficiency will increase. In a silica glass composition, additives like  $\text{Al}_2\text{O}_3$ ,  $\text{ZrO}_2$ , and  $\text{B}_2\text{O}_3$  reduce the melting temperature of the glass melt. Network intermediates like  $\text{Al}_2\text{O}_3$  can effectively reduce the number of non-bridging oxygens (NBOs) and improve the BDS. A nucleating agent like  $\text{ZrO}_2$  promotes glass crystallization and enhances the glass network structure.  $\text{ZrO}_2$  facilitates controlled bulk crystallization of the glass which can improve the microstructure and dielectric properties.

### **10.2.5.2 Effect of Microstructure**

The energy storage properties of a ferroelectric glass–ceramic are significantly affected by the size, grain morphology, and the number of defects of the ferroelectric ceramic phase present in the glass matrix. A crystal phase with large grains can lead to cracks, pores, and other defects in the microstructure which will degrade the BDS. Grain boundaries with a low dielectric constant and good insulation performance can endure the majority of the applied electric field and improve the BDS. Glass–ceramics having spherical crystal morphology exhibit a higher BDS compared to glass–ceramics with dendritic morphology. This is because dendritic morphology presents a non-uniform microstructure which leads to an uneven distribution of the applied electric field during polarization. Such an uneven distribution of the field degrades the breakdown strength and energy storage properties of the glass–ceramics.

### **10.2.5.3 Effect of Sample Thickness**

The number of defect centers in glass–ceramics increases with an increase in the sample thickness, which thereby decreases the BDS. The BDS is inverse exponentially related to the thickness of a sample. Literature reports discussed previously suggest that the BDS is greatly reduced if the thickness of samples exceeds 50  $\mu\text{m}$  due to defects and charge trapping on the sample surface. Also, surface roughness in samples leads to an uneven distribution of the electric field. Therefore, for a uniform

distribution of electric field and charge injection at the interface between the metal electrode and glass–ceramic sample, a polished sample surface is necessary.

### **10.2.6 Future Aspects**

The demand for next-generation energy storage systems in modern miniaturized electronic components will require glass–ceramic materials that can provide high power, higher energy density, ultrafast discharge speeds, high-temperature stability, stable frequency, and environmental friendliness. The main obstacle in obtaining high energy density in ferroelectric glass–ceramics is their large interface area, which leads to loss of the applied electric field and degrades the polarization properties and breakdown field strength. Hence a thorough study of the polarization mechanism at the interface, optimization of the fabrication process to modify the interface in the glass–ceramics, and improvement of the dielectric properties are needed. Advanced fabrication methods (e.g., hot pressing, microwave techniques) may be adopted which can give a dense microstructure through adjustment of the grain morphology, size, and defect centers. The dependence of grain morphology and size on energy storage performance should be clarified for the development of glass–ceramic systems with high energy storage performances.

## **10.3 Glass–ceramics for Photonic Applications**

### **10.3.1 Introduction**

Photonics is the physical science of light and technology for the generation, control, and detection of photons. In the twenty-first century, photonics has become a ubiquitous part of our daily life, with a wide range of applications including fiber optics in telecommunications, powerful LEDs, solid-state lasers, compact sensors, photonic computing, and many more. Due to the wide range of applications, progressive research has been carried out in this area over recent decades.

Because glass–ceramics can be uniquely tailored to their application, they are potent candidates for photonics. Transparency is important, at least for the chosen wavelength band, and requires that the crystallites present must be smaller than the wavelength of visible light or the difference in refractive index between the crystal and glass must be small. Another important point is that when they are doped with luminescent materials like rare-earth [89, 90] or transition metal ions [91, 92], the size of nanocrystals within glass–ceramics can have a noticeable effect on spectroscopic properties. Such systems have higher absorption and emission cross-sections, a lower phonon cut-off energy, and better control of the rare-earth ion-ion interaction compared to glass [93, 94]. The first transparent glass–ceramic, called Zerodur was

developed by Schott AG in 1968 and was used in large telescope mirrors and as a sample reference to test the validity of innovative glass structural models [95]. In 1995, Tick et al. generated transparent glass–ceramics for optical amplifiers operating at 1300 nm which turned out to be the first glass–ceramics used in the field of photonics [96, 97].

The major application of glass–ceramic in the photonic field is as waveguides. Rare-earth ion-doped glass–ceramic waveguides with luminescent properties are used as an optical medium for light propagation and luminescent enhancement. However, this imposes stringent requirements on the transparency of the glass–ceramics. Tick in 1998 was able to achieve this and the minimum transmission loss limit of the glass–ceramic investigated was in the order of tens of decibels per kilometer (dB/km) [98]. Glass–ceramic waveguides find applications as optical amplifiers and lasers, linear and nonlinear frequency converters, etc. In comparison with other rare-earth ion-doped waveguides, glass–ceramic waveguides have several advantages. Due to their biphasic nature, they combine the mechanical and optical properties of the glass with a crystal-like environment for rare-earth ions. Also, chemical clustering and luminescence quenching can be reduced by controlling the chemical nature of the rare-earth ions [99, 100].

Currently, research is focused on creating energy-transfer-based systems for photoluminescence applications. Up and down converters for planar waveguides for integrated optics, visible laser light sources, solar cell efficiency enhancement, and specific nanostructured systems used as sensitizers of rare-earth luminescence are some of the major advances in this area [101–104]. In this chapter, a brief review of the recent developments in this important scientific and technological area is presented and some future aspects are outlined.

### ***10.3.2 Classification of Glass–ceramics for Photonic Applications***

Based on the research work carried out in the last decade, glass–ceramics for photonic applications can be categorized mainly into oxide, oxyfluoride, and chalcogenide glass–ceramic. This chapter highlights and describes some of the recent important findings on the photonic application of glass–ceramics.

#### **10.3.2.1 Oxide Glass–ceramics**

Enhanced light energy storage of Eu, Dy doped  $\text{SrAl}_2\text{O}_4$  glass-ceramics was reported by Nakanishi et al. [105]. Intense luminescence from the glass–ceramics was observed in the dark and also luminescence at various wavelengths in the visible region. An increase in luminescence intensity by 101% in the visible and 70% in

the infrared region was observed in erbium-doped bismuth germanate-based glass–ceramics, useful as a host material for waveguiding structures operating in the near-infrared [106]. Lukowiak et al. [107] reported the photorefractive properties of sol–gel derived  $\text{SnO}_2$ – $\text{SiO}_2$  glass–ceramic waveguides activated by  $\text{Eu}^{3+}$  ions. The main findings included high photosensitivity and low propagation losses that make this glass–ceramic an interesting photonic material for smart optical applications. Molla et al. [108] reported the optical properties of hard transparent gahnite glass–ceramics of composition  $\text{SiO}_2$ – $\text{K}_2\text{O}$ – $\text{ZnO}$ – $\text{Al}_2\text{O}_3$ – $\text{TiO}_2$  with low transmission losses, which are potential candidates for application in display panels.  $\text{Er}^{3+}$  activated  $\text{SiO}_2$ – $\text{SnO}_2$  glass–ceramic monoliths and planar waveguides have been obtained by sol–gel techniques.  $\text{SnO}_2$ –based glass–ceramics activated by rare-earth ions have been extensively investigated for several years [109]. This research is still actively developing reliable fabrication protocols and clarifying interesting optical, structural, and spectroscopic features as well as related physical mechanisms [110, 111].

An intense absorption cross-section in the UV range of  $\text{SiO}_2$ – $\text{SnO}_2$  glass–ceramics can be witnessed due to  $\text{SnO}_2$  nanocrystals. These are also effective rare-earth ions sensitizers [17, 112, 113]. The high photorefractivity of sol–gel derived  $\text{SnO}_2$ – $\text{SiO}_2$  glass–ceramic waveguides has often been demonstrated [114, 115]. UV irradiation induces refractive index changes that allow the direct writing of both channel waveguides and Bragg gratings. Manzani et al. [116] reported optical properties of phosphotellurite glass–ceramics with high  $\text{TeO}_2$  content. Glass–ceramics transparent in the visible range were obtained for phosphotellurite samples with large nonlinear absorption coefficients. Recently,  $\text{SiO}_2$ – $\text{SnO}_2$ : $\text{Er}^{3+}$  planar waveguides containing 30 mol%  $\text{SnO}_2$  nanocrystals were fabricated by a sol–gel method and dip-coating techniques. The  $\text{SiO}_2$ – $\text{SnO}_2$ : $\text{Er}^{3+}$  glass–ceramic planar waveguides were reported to have confined propagation modes, a step-index profile with a high confinement of 82% at 1542 nm, and low losses of  $0.6 \pm 0.2$  dB/cm at 1542 nm [117].  $\text{Eu}^{3+}$ -doped  $\text{Na}_2\text{Ta}_8\text{O}_{21}$ -based transparent tantalum phosphate glass and GC nanocomposites were considered promising for nonlinear optical applications. A rich tantalum content precursor glass exhibited high photoluminescence quantum efficiency due to its low phonon energy and high refractive index (1.9461 at 633 nm) [118]. Glass–ceramics produced by the spark plasma sintering method offers the advantage useful for optical applications of creating simple to complex nanostructured transparent glass–ceramics with increased densification and homogenization in a short time. The introduction of a rare-earth dopant ion into these host matrices can provide enhanced luminescence intensity through reduction of the multiphonon and cross relaxations, thus providing longer lifetimes [119]. NIR emitting  $\text{Yb}^{3+}$  doped silica-zirconia-soda glass–ceramic thin films were prepared by Enrichi et al. [120] using sol–gel and dip-coating techniques. Ag was introduced by ion exchange as dimers, multimers, and aggregates in the films to act as sensitizers for the  $\text{Yb}^{3+}$  ions. As a consequence, the emission around 950–1100 nm was significantly enhanced, which could have applications as a spectral downshifter for photovoltaic solar cells and NIR light-emitting sources.

### 10.3.2.2 Oxyfluoride Glass–ceramics

Transparent oxyfluoride glass–ceramics have received considerable attention over the years because of the low phonon energies of the matrix, high chemical durability, and their mechanical stability ascribed to oxides. In these systems, the optical properties of active ions are usually controlled by the fluoride crystal host and the nanocrystals are stabilized by the oxide matrix. By tuning composition and optimizing the preparation process, highly transparent glass–ceramics can be made by matching the matrix refractive index to that of the various crystalline fluoride nanocrystals or by limiting the crystal size to nanometers.  $\text{Yb}^{3+}/\text{Er}^{3+}$  co-doped  $\text{CaF}_2$ -based transparent oxyfluoride glass–ceramics exhibited intense red, green, and blue upconversion emission using 980 nm laser pumping. With a relative temperature sensitivity of  $1.4\% \text{ K}^{-1}$  at 300 K, these glass–ceramics could be used in optical fiber temperature sensing [121]. Cao et al. [122] reported  $\text{BaLuF}_5:\text{Tb}^{3+}$  glass–ceramics as scintillators for X-ray imaging. The photoluminescence and X-ray excited luminescence were significantly enhanced in the glass–ceramics after thermal treatment due to the preferential solution of  $\text{Tb}^{3+}$  in the crystallized low phonon  $\text{BaLuF}_5$  phase.  $\text{SiO}_2\text{--Al}_2\text{O}_3\text{--CdF}_2\text{--}22\text{PbF}_2\text{--}4\text{YF}_3\text{--YbF}_3$ -based glass–ceramics were reported to have a high photoluminescence quantum yield and low background absorption for laser cooling applications [123]. Krishnaiah et al. [124] reported  $\text{Yb}^{3+}$ -doped  $\text{CaF}_2$  nanocrystals in transparent  $\text{SiO}_2\text{--Al}_2\text{O}_3\text{--CaO--CaF}_2$  glass–ceramics with a low  $\text{OH}^-$  content; their potential advantages for optical refrigeration (laser cooling) were studied.  $\text{Ni}^{2+}$  doped transparent bulk glass–ceramics containing  $\text{K}_2\text{SiF}_6$ ,  $\text{ZnF}_2$ , and  $\text{KZnF}_3$  nanocrystals were reported to exhibit broadband luminescence from 1200–2400 nm and were considered to offer the prospect of transition metal ion-based photonics [125]. Rare-earth doped ( $\text{Er}/\text{Yb}$ ,  $\text{Tm}/\text{Yb}$ ,  $\text{Tb}/\text{Yb}$ ) oxyfluoride glasses containing  $\text{Ba}_2\text{LaF}_7$  nanocrystals are reported to have efficient upconversion luminescence along with thermal and mechanical toughness, high optical transmission from the UV to the IR and a low nonlinear refractive index compared to the other commercial laser glasses [126]. Ali et al. [127] reported a large enhancement in upconversion luminescence in  $\text{Er}^{3+}/\text{Yb}^{3+}$  co-doped transparent aluminosilicate glass–ceramics containing  $\text{CaF}_2$  nanocrystals, ascribed to a more ordered crystal structure around the rare-earth ion. Chen et al. reported upconversion temperature sensing in  $\text{SiO}_2\text{--Al}_2\text{O}_3\text{--AlF}_3\text{--Na}_2\text{O--NaF--Gd}_2\text{O}_3/\text{GdF}_3\text{--YbF}_3\text{--ErF}_3$  based glass–ceramics. Enhanced upconversion emission was achieved for  $\text{Yb}/\text{Er}$  co-doped glass–ceramic containing hexagonal  $\text{NaGdF}_4$  nanocrystals and a significant, temperature-sensitive, upconversion fluorescence intensity ratio between the  $\text{Er}^{3+}:^2\text{H}_{11/2} \rightarrow ^4\text{I}_{15/2}$  (520 nm) and  $^4\text{S}_{3/2} \rightarrow ^4\text{I}_{15/2}$  transition (540 nm) was detected, caused by competitive radiative transitions from these two thermally coupled emitting states [128]. Liu et al. reported enhanced upconversion and 2.7  $\mu\text{m}$  emissions in  $\text{Er}^{3+}$  doped silicate glass–ceramics containing lutetium oxyfluoride  $\text{Lu}_n\text{O}_{n-1}\text{F}_{n+2}$  ( $n = 5\text{--}10$ ) nanocrystals [129].  $\text{K}^+$  ion doping of  $\beta\text{-PbF}_2:\text{Er}^{3+}$  based oxyfluoride glass–ceramics was reported to enhance the upconversion luminescence efficiency and temperature sensitivity, making them suitable for optical thermometry [130].  $\text{Yb}^{3+}/\text{Er}^{3+}$  co-doped tellurite-based oxyfluoride transparent glass–ceramics ( $\text{TeO}_2\text{--BaF}_2\text{--YF}_3$ ) were reported to exhibit bright



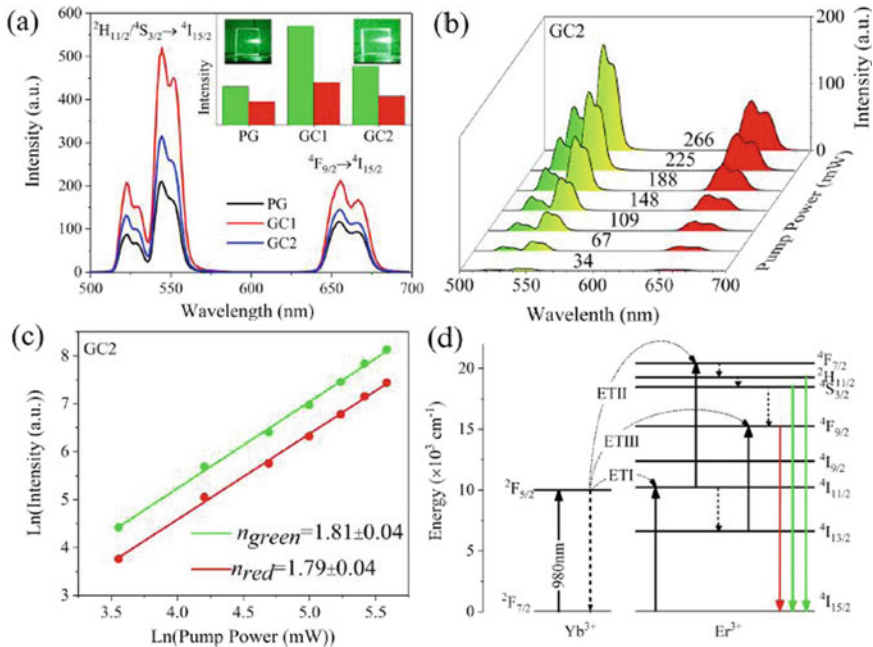


**Fig. 10.9** **a** Upconversion spectra of the PG (precursor glass) and GC2 under 980 nm excitation (0.266 W) with the inset bar graph displaying the integrated intensities for upconverted green and red emissions, **b** upconversion spectra of GC2 depending on pump powers (34–266 mW), **c** double logarithmic plots of upconverted emission intensities versus pump powers for the green (in green color) and red (in red color) emissions of GC2, **d** schematic representation of energy transfer (ET) processes responsible for the upconversion luminescence. Reproduced with permission from Ref. [131], © Elsevier

upconversion luminescence with an enhancement of 40% compared to the base glass. The luminescence intensity was recorded under 980 nm excitation as shown in Fig. 10.9. The results suggest that glass–ceramics can be used as solar cell luminescent concentrators [131].

### 10.3.2.3 Chalcogenide Glass–ceramics

Chalcogenide glasses and chalcogenide glass–ceramics have the advantages of high refractive index ( $\approx 2.2$ ), low cut-off phonon energy ( $\approx 400 \text{ cm}^{-1}$ ), extremely wide IR transmission window ( $\approx 22 \mu\text{m}$ ), and low acoustic velocity that make them attractive for lasers, optical fibers and many other photonic applications [132, 133]. They also have a large nonlinear refractive index and response times that make them suitable for ultrafast all-optical switches. In addition, near and mid-IR (MIR) fluorescence can be generated by pumping rare-earth ions in the glass by a laser diode, useful for IR optical amplification [134, 135].

Lin et al. reported a five-fold increase in the MIR fluorescence at 3.8  $\mu\text{m}$  from  $\text{Tm}^{3+}$  in  $80\text{GeS}_2\text{-}20\text{Ga}_2\text{S}_3\text{:}0.5\text{Tm}_2\text{S}_3$  transparent glass–ceramics at room temperature. The enhanced mechanism of MIR fluorescence in chalcogenide glass–ceramics was evidenced by the phase separation of Ge-rich regions in the glass matrix during crystallization [136]. IR to visible frequency upconversion luminescence was investigated in  $\text{Er}^{3+}$  doped  $\text{Ga}_{10}\text{Ge}_{25}\text{S}_{65}$  based glass and glass–ceramics. The green and red photoluminescence bands of  $\text{Er}^{3+}$  were observed and the upconversion mechanism was investigated [137]. Li et al. investigated the crystallization mechanism in highly transparent  $45\text{GeS}_2\text{:}30\text{Ga}_2\text{S}_3\text{:}25\text{Sb}_2\text{S}_3$  glass–ceramics containing  $\text{Ga}_2\text{S}_3$  nanocrystals. A transmission window from 2 - 10  $\mu\text{m}$  was observed in the MIR region with improved thermal and mechanical stability which makes this material a potential candidate for an IR transmitting fiber [138]. Recently, Zhang et al. [139] investigated the third-order nonlinear optical properties of the chalcogenide glass–ceramic in the  $\text{GeS}_2\text{-Sb}_2\text{S}_3\text{-CsCl}$  system and reported that nano-crystallization of the CsCl phase in the glass matrix could enhance the nonlinear optical properties significantly. The maximum nonlinear refractive index of glass–ceramics was nearly tripled compared to the base glass, while the maximum nonlinear absorption coefficient was also increased by 62%. The acousto-optic properties of  $80\text{GeS}_2\text{-}20\text{Ga}_2\text{S}_3$  base glass and glass–ceramics were studied by Cao et al. [140]. Structural analysis revealed that the generated  $\text{Ga}_2\text{S}_3$  crystal grains and stable tetrahedral network in the residual glass together improved the acoustic and thermomechanical performance of the GC samples at 10.6  $\mu\text{m}$  after heat treatment for 15 h at 380  $^\circ\text{C}$ . Recently, Cui et al. [141] investigated the MIR luminescence properties of  $\text{Ni}^{2+}$  dopants in  $\text{GeS}_2\text{-Sb}_2\text{S}_3\text{-CsI-PbI}_2$  chalcogenide glass–ceramics. Ultrabroad-band emission was observed from 2.5–5.5  $\mu\text{m}$  for the first time in such  $\text{CsPbI}_3$  perovskite nanocrystal containing glass–ceramics, promising application in MIR broadband tunable lasers. A variety of  $\text{Co}^{2+}$ -doped binary ( $\text{ZnS}$ ,  $\text{CdS}$ ,  $\text{ZnSe}$ ) and ternary ( $\text{ZnCdS}$ ,  $\text{ZnSSe}$ ) chalcogenide glass nanocomposites were thermally grown in the parent chalcogenide glasses. Lu et al. [142] reported that the glass nanocomposites exhibited good optical transparency and MIR emissions of  $\text{Co}^{2+}$  in the 3–4  $\mu\text{m}$  spectral range. Through crystal field engineering, the emission properties of  $\text{Co}^{2+}$  including its emission peak wavelength and bandwidth could be tailored over a broad spectral range (2.5–4.5  $\mu\text{m}$ ) as shown in Fig. 10.10, allowing the possibility of MIR photonic applications such as gas sensing.

### 10.3.3 Future Aspects

The prospects of transparent glass–ceramics for photonic applications are very good, with continuously growing applications in the area of integrated optics, lasing, lighting, frequency converters, and sensing. Transparent glass–ceramic nanocomposites offer the advantages of better luminescence efficiency and low attenuation losses, which are important for photonic applications. The performance of such devices can be improved by optimizing the synthesis processes and fabrication technologies for each application. With respect to the development of photonic glass–ceramics, areas

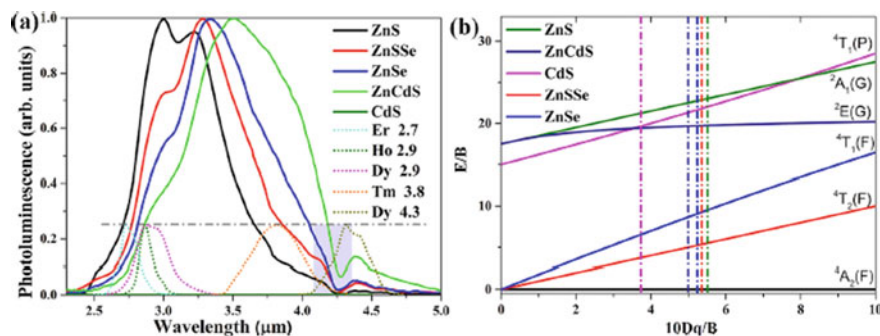


**Fig. 10.10** **a** MIR emission spectra of the ZnS, ZnSSe, ZnSe, ZnCdS, and CdS samples excited by a 1570 nm  $\text{Er}^{3+}$ -doped fiber laser (0.6 W). The characteristic emission spectra of some selected rare-earth ions are also included. The shaded area corresponds to the absorption band of carbon dioxide. **b** Tanabe-Sugano (TS) diagram for the tetrahedrally coordinated  $\text{Co}^{2+}$  in the investigated samples. Reproduced with permission from Ref. [142], © Elsevier

that can be addressed in the near future include: (i) reproducible fabrication protocols; (ii) modeling of transparency constraints including disorder; (iii) enhancing the solubility of the rare-earth ions in the host matrix.

**Acknowledgements** Anirban thanks University Grants Commission, India for his Junior Research Fellowship (JRF) grant. Ms. Sreedevi Menon is thankful to Board of Research in Nuclear Sciences (BRNS), DAE, India for her fellowship through the project sanction no. 58/14/03/2020-BRNS/37055. The authors are thankful to Shri Sitendu Mandal, Head, Specialty Glass Division, and Dr. Suman Kumari Mishra, Director CSIR-CGCRI for their constant support and encouragement. We are grateful to Prof. E. D. Zanotto, Federal University of Sao Carlos, Brazil, and Prof. J. M. Parker, The University of Sheffield, UK for their kind review and critical comments on the manuscript.

## References

- Zanotto ED, Mauro JC (2017) The glassy state of matter: its definition and ultimate fate. *J Non-Cryst Solids* 471:490–495
- McMillan PW (1979) *Glass-ceramics*, 2nd edn. Academic Press, London
- Réaumur RAM (1739) The art of matching a new grid of porcelain. *Memories Acad Sci Paris* 377–88
- Stookey SD (1954) Photosensitively opacifiable glass. U.S. Pat. No. 2 684 911
- Stookey SD (1953) Chemical machining of photosensitive glass. *Ind Eng Chem* 45:115–118
- Stookey SD (1959) Catalyzed crystallization of glasses in theory and practice. *Ind Eng Chem* 51:805
- Deubener J, Allix M, Davis MJ, Duran A, Höche T, Honma T, Komatsu T, Krüger S, Mitra I, Müller R, Nakane S, Pascual MJ, Schmelzer JWP, Zanotto ED, Zhou S (2018) Updated definition of glass-ceramics. *J Non-Cryst Solids* 501:3–10
- Holand W, Beall GH (2012) *Glass-Ceramic technology*, 2nd edn. Wiley, New Jersey
- Weinberg MC (1994) Glass-forming ability and glass stability in simple systems. *J Non Cryst Solids* 167:81–88

10. Marghussian V (2015) *Nano-Glass ceramics: processing, properties and applications*, 1st edn. Elsevier, New York
11. Ray CS, Day DE (1990) Determining the nucleation rate curve for lithium disilicate glass by differential thermal analysis. *J Am Ceram Soc* 73:439–442
12. Xu XJ, Ray CS, Day DE (1991) Nucleation and crystallization of  $\text{Na}_2\text{O} \cdot 2\text{CaO} \cdot 3\text{SiO}_2$  glass by differential thermal analysis. *J Am Ceram Soc* 74:909–914
13. Abyzov AS, Fokin VM, Zanotto ED (2018) Predicting homogenous nucleation rates in silicate glass formers. *J Non Cryst Solids* 500:231–234
14. Khater GA, Safwat EM, Kang J, Yue Y, Khater AGA (2020) Some types of glass-ceramic materials and their applications. *Int J Res* 7:1–16
15. Rawlings R (1997) *Production and properties of Silceram glass ceramics, glass-ceramic materials fundamentals and applications*. 115–133
16. Francis RR, Boccaccini A (2002) Glassceramics from mixtures of coal ash and soda-lime glass by the peturgic method. *J Mater Sci Lett* 21:975–980
17. Hing P, Sinha V, Ling PB (1997) The effects of some processing parameters on the sinterability, microstructures properties of sintered cordierite glass ceramics. *J Mater Process Technol* 63:604–609
18. Lambrinou K, Van der Biest O, Boccaccini A, Taplin D (1996) Densification and crystallization behaviour of barium magnesium aluminosilicate glass powder compacts. *J Eur Ceram Soc* 16:1237–1244
19. Scherer GW (1977) Sintering of low-density glasses: Part I. Theory *J Am Ceram Soc* 60:239–243
20. Zanotto E, Prado M (2001) Isothermal sintering with concurrent crystallization of monodispersed and polydispersed glass particles. Part I. *Phys Chem Glasses* 42:191–198
21. Brinker CJ, Scherer GW (1989) *Sol-gel science*. Academic press, New York
22. Davis MJ, Zanotto ED (2017) Glass-ceramics and realization of the unobtainable: property combinations that push the envelope. *MRS Bull* 42(3):195–199
23. Beall GH (1971) Structure, properties and nucleation of glass-ceramics. In: Hench LL, Freiman SW (eds) *Advances in nucleation and crystallization in glasses*, special publ. No.5. The American Ceramic Society, Columbus, OH pp 251–261
24. Pincus AG (1971) Application of glass-ceramics. In: *Advances in nucleation and crystallization in glasses*. The American Ceramic Society, OH Spec Publ No. 5
25. Tashiro T, Wada M (1963) Glass-ceramics crystallized with zirconia. In: *Advances in glass technology*. Plenum Press, New York
26. Hench LL, Splinter RJ, Allen WC, Greenlee TK (1971) *J Biomed Mater Res* 5:117
27. Ducheyne P, Qiu Q (1999) *Biomaterials* 20:2287
28. Sanz-Herrera JA, Boccaccini AR (2011) *Int J Solids Struct* 48:257
29. Gerhardt LC, Boccaccini AR (2010) *Materials* 3:3867
30. Bains F, Novajra G, Vitale-Brovarone C (2015) *Front. Bioeng Biotechnol* 3:202
31. Martins F, Felgueiras C, Smilkova M, Caetano N (2019) Analysis of fossil fuel energy consumption and environmental impacts in European countries. *Energies* 12:964
32. Arico AS, Bruce P, Scrosati B, Tarascon JM, Schalkwijk WV (2005) Nanostructured materials for advanced energy conversion and storage devices. *Nat Mater* 4:366–377
33. Thomas LA (1972) Applications of ferroelectrics and related materials: a review of developments in Europe. *Ferroelectrics* 3:231–238
34. Hao X (2013) A review on dielectric materials for energy storage applications. *J Adv Dielectr* 3:1330001
35. Yang L, Kong X, Li F, Hao H, Cheng Z, Liu H, Li JF, Zhang S (2019) Perovskite Lead-free dielectrics for energy storage applications. *Prog Mater Sci* 102:72–108
36. Yao ZH, Song Z, Hao H, Yu ZY, Cao MH, Zhang SJ, Lanagan MT, Liu HX (2017) Homogeneous/inhomogeneous-structured dielectrics and their energy-storage performances. *Adv Mater* 29:1601727
37. Damjanovic D (1998) Ferroelectric, dielectric and piezoelectric properties of ferroelectric thin films and ceramics. *Rep Prog Phys* 61:1267–1324

38. Chauhan A, Patel S, Vaish R, Bowen CR (2015) Anti-ferroelectric ceramics for high energy density capacitors. *Materials* 8:8009–8031
39. Dang ZM, Yuan JK, Yao SH, Liao RJ (2013) Flexible nanodielectric materials with high permittivity for power energy storage. *Adv Mater* 25:6334–6365
40. Zou K, Dan Y, Xu H, Zhang Q, Lu Y, Huang H, He Y (2019) Recent advances in lead-free dielectric materials for energy storage. *MRS Bull* 113:190–201
41. Harizanova R, Slavov S, Vladislavova L, Costa LC, Avdeev G, Bocker C, Russel C (2020) Barium titanate containing glass-ceramics - The effect of phase composition and microstructure on dielectric properties. *Ceram Int* 15:24585–24591
42. Karmakar B (2017) *Functional glasses and glass-ceramics: processing properties and applications*. Elsevier, Oxford
43. Kumari P, Rai R, Sharma S, Shandilya M, Tiwari A (2015) State-of-the-art of lead free ferroelectrics: a critical review. *Adv Mater Lett* 6:453–484
44. Sepúlveda A, Schluep M, Renaud FG, Streitcher M, Kuehr R, Hagelüken C, Gereke AC (2010) A review of the environmental fate and effects of hazardous substances released from electrical and electronic equipments during recycling: examples from China and India. *Environ Impact Assess Rev* 30:28–41
45. Jain H (2004) Transparent ferroelectric glass-ceramics. *Ferroelectrics* 306:111–127
46. Chakrabarti A, Biswas K, Molla AR (2018) Eu<sup>3+</sup>-doped ferroelectric BaBi<sub>2</sub>Ta<sub>2</sub>O<sub>9</sub> based glass-ceramic nanocomposites: crystallization kinetics and energy storage properties. *J Alloys Compd* 740:237–249
47. Chakrabarti A, Molla AR (2020) Zirconia assisted crystallization of ferroelectric BaBi<sub>2</sub>Nb<sub>2</sub>O<sub>9</sub> based glass-ceramics: Kinetics, optical and dielectrical properties. *J Alloys Compd* 844:156181
48. Cross LE, Newnham RE (1987) High technology ceramics: past, present and future. In: Kingery WD, Lense E (eds) *History of ferroelectrics*, vol 3. The American Ceramic Society, Inc., Westerville, OH
49. Pan MJ, Bender BA, Lanagan MT, Cheng CT (2005) High energy density ferroelectric glass-ceramics. *Ceram Trans* 169:187–193
50. Gorzkowski EP, PanMJ BenderBA, Wu CCCM (2007) Glass-ceramics of barium strontium titanate for high energy density capacitors. *J Electroceram* 18:269–276
51. ChenJ ZhangY, DengC DaiX (2009) Improvement in the microstructures and dielectric properties of barium strontium titanate glass-ceramics by AlF<sub>3</sub>/MnO<sub>2</sub> addition. *J Am Ceram Soc* 92:1863–1866
52. WangXR ZhangY, Ma T, DengCS DXM (2012) Effects of MnO<sub>2</sub> concentration on dielectric properties of barium strontium titanate glass ceramics. *Ceram Int* 38S:S57–S60
53. Zhao Z, Liang X, Zhang T, Hu K, Li S, Zhang Y (2020) Effects of cerium doping on dielectric properties and defect mechanism of barium strontium titanate glass-ceramics. *J Eur Ceram Soc* 40:712–719
54. Wei J, Jiang D, Yu W, Shang F, Chen G (2021) The effect of Hf doping on the dielectric and energy storage performance of barium titanate based glass ceramics. *Ceram Int* 47:11581–11586
55. Wang J, Tang L, Shen B, Zhai J (2014) Effect of microwave processes on the energy-storage properties of barium strontium titanate glass ceramics. *J Mater Res* 29:288–293
56. Zeng Y, Qin X, Jiang S, Zhang G, Zhang L (2011) Effect of BaF<sub>2</sub> Addition on crystallization kinetics and dielectric properties of B<sub>2</sub>O<sub>3</sub>–Nb<sub>2</sub>O<sub>5</sub>–SrO–BaO glass-ceramics. *J Am Ceram Soc* 94:469–473
57. Kamonlert A, Niyompan A, Tipakontitukul R (2011) Effect of ZrO<sub>2</sub> addition on crystallization and properties of the glass-ceramics contained NaNbO<sub>3</sub> crystals. *Curr Appl Phys* 11:S100–S105
58. Yongsiri P, Eitssayeam S, Inthata U, Rujjanagul G, Sirisoonthorn S, Tunkasiri T, Pengpat K (2011) Fabrication of ferroelectric glass ceramics from (K<sub>0.5</sub>Na<sub>0.5</sub>)NbO<sub>3</sub>–SiO<sub>2</sub>–Al<sub>2</sub>O<sub>3</sub> glass system. *Ferroelectrics* 416:144–150

59. Chen GH, Zhang WJ, Liu XY, Zhou CR (2011) Preparation and properties of strontium barium niobate based glass-ceramics for energy storage capacitors. *J Electroceram* 27:78–82
60. Zhou Y, Zhang Q, Luo J, Tang Q, Du J (2011) Structural and dielectric characterization of  $Gd_2O_3$ -added  $BaO-Na_2O-Nb_2O_5-SiO_2$  glass-ceramic composites. *Acta Mater* 65:296–299
61. Liu T, Chen GH, Song J, Yuan CL (2013) Crystallization kinetics and dielectric characterization of  $CeO_2$ -added  $BaO-SrO-Nb_2O_5-B_2O_3-SiO_2$  glass-ceramics. *Ceram Int* 39:5553–5559
62. Zhou Y, Zhang Q, Luo J, Tang Q, Du J (2013) Structural optimization and improved discharged energy density for niobate glass-ceramics by  $La_2O_3$  addition. *J Am Ceram Soc* 96:372–375
63. Niyompan A, Srisurat K, Tipakontitkul R (2014) Crystallization behavior and dielectric properties of ferroelectric glass-ceramics containing BNN and NN crystals. *Ferroelectrics* 459:172–187
64. Song J, Chen GH, Yuan CL, Yang Y (2014) Effect of the Sr/Ba ratio on the microstructures and dielectric properties of  $SrO-BaO-Nb_2O_5-B_2O_3$  glass-ceramics. *Mater Lett* 117:9.
65. Niyompan A, Tipakontitkul R, Wanram S (2015) Dielectric investigation of ferroelectric glass-ceramics containing sodium niobate and barium niobium silicate crystals. *Ferroelectrics* 488:32–44
66. Yang Y, Song J, Chen GH, Yuan CL, Li X, Zhou CR (2015) Effect of crystallization temperature on the dielectric property and energy density of  $SrO-BaO-Nb_2O_6-B_2O_3$  glass-ceramics. *J Non-Cryst Solids* 410:96–99
67. Zheng J, Chen GH, Yuan CL, Zhou CR, Chen X, Feng Q, Li M (2016) Dielectric characterization and energy-storage performance of lead-free niobate glass-ceramics added with  $La_2O_3$ . *Ceram Int* 42:1827–1832
68. Chen GH, Zheng J, Yuan CL, Zhou C, Kang XL, Xu JW, Yang Y (2016) Enhanced energy storage properties of  $P_2O_5$  modified niobate-based  $B_2O_3$  system glass ceramic composites. *Mater Lett* 176:46–48
69. Pu Y, Liu X, Dong Z, Wang P, Hu Y, Sun Z (2015) Influence of crystallization temperature on ferroelectric properties of  $Na_{0.9}K_{0.1}NbO_3$  glass-ceramics. *J Am Ceram Soc* 98:2789–2795
70. Zheng H, Pu Y, Liu X, Wan J (2016) Correlation between dielectric properties and crystallization treatment in potassium sodium niobate glass-ceramics for energy storage application. *J Alloys Compd* 674:272–276
71. Xiao S, Xiu S, Shen B, Zhai J (2016) Microstructure evolution and energy storage properties of potassium strontium niobate boroaluminosilicate glass-ceramics by microwave crystallization. *J Eur Ceram Soc* 36:4071–4076
72. Wang H, Liu J, Zhai J, Shen B (2016) Ultra high energy-storage density in the barium potassium niobate-based glass-ceramics for energy-storage applications. *J Am Ceram Soc* 99:2909–2912
73. Davis C III, Pertuit AL, Nino JC (2017) Effect of microwave processing on the crystallization and energy density of  $BaO-Na_2O-Nb_2O_5-SiO_2-B_2O_3$  glass-ceramics. *J Am Ceram Soc* 100:65–73
74. Zhou Y, Qiao Y, Tian Y, Wang K, Li G, Chai Y (2017) Improvement in structural, dielectric and energy-storage properties of lead-free niobate glass-ceramic with  $Sm_2O_3$ . *J Eur Ceram Soc* 37:995–999
75. Yang K, Liu J, Shen B, Zhai J, Wang H (2017) Large improvement on energy storage and charge-discharge properties of  $Gd_2O_3$ -doped  $BaO-K_2O-Nb_2O_5-SiO_2$  glass-ceramic dielectrics. *Mater Sci Eng B* 223:178–184
76. Xiu S, Shen B, Zhai J (2017) The effects of  $MnO_2$  addition on the structure and dielectric properties of the strontium barium niobate glass-ceramics. *MRS Bull* 95:349–353
77. Wang S, Tian J, Yang K, Liu J, Zhai J, Shen B (2018) Crystallization kinetics behavior and dielectric energy storage properties of strontium potassium niobate glass-ceramics with different nucleating agents. *Ceram Int* 44:8528–8533
78. Liu J, Yang K, Zhai J, Shen B (2018) Effects of crystallization temperature on phase evolution and energy storage properties of  $BaO-Na_2O-Nb_2O_5-SiO_2-Al_2O_3$  glass-ceramics. *J Eur Ceram Soc* 38(2312):2317

79. Xiu S, Xiao S, Zhai J (2018) Improvement of energy storage properties in niobate glass–ceramics via the adjustment of glass/ceramic ratios. *J Mater Sci: Mater Electron* 29:16758–16764
80. Liu S, Wang J, Ding J, Hao H, Zhao L, Xia S (2019) Crystallization, microstructure and dielectric properties of the SrO–BaO–Nb<sub>2</sub>O<sub>5</sub>–Al<sub>2</sub>O<sub>3</sub>–SiO<sub>2</sub> based glass ceramics added with ZrO<sub>2</sub>. *Ceram Int* 45:4003–4008
81. Tian J, Wang S, Jiang T, Chen K, Zhai J, Shen B (2019) Dielectric characterization of a novel Bi<sub>2</sub>O<sub>3</sub>–Nb<sub>2</sub>O<sub>5</sub>–SiO<sub>2</sub>–Al<sub>2</sub>O<sub>3</sub> glass-ceramic with excellent charge-discharge properties. *J Eur Ceram Soc* 39:1164–1169
82. Jiang T, Chen K, Shen B, Zhai J (2019) Enhanced energy-storage density in sodium-barium-niobate based glass-ceramics realized by doping CaF<sub>2</sub> nucleating agent. *J Mater Sci Mater Electron* 30:15277–15284
83. Ihyadn A, Lahmar A, Mezzane D, Bih L, Alimoussa A, Amjoud M, Marssi MEL, Luk'yanchuk IA (2019) Structural, electrical and energy storage properties of BaO–Na<sub>2</sub>O–Nb<sub>2</sub>O<sub>5</sub>–WO<sub>3</sub>–P<sub>2</sub>O<sub>5</sub> glass–ceramics system. *Mater Res Express* 6:115203
84. Jiang D, Zhong Y, Shang F, Chen G (2020) Crystallization, microstructure and energy storage behavior of borate glass–ceramics. *J Mater Sci: Mater Electron* 31:12074–12082
85. Chen K, Jiang T, Shen B, Zhai J (2021) Effects of crystalline temperature on microstructures and dielectric properties in BaO–Na<sub>2</sub>O–Bi<sub>2</sub>O<sub>3</sub>–Nb<sub>2</sub>O<sub>5</sub>–Al<sub>2</sub>O<sub>3</sub>–SiO<sub>2</sub> glass-ceramics. *Mater Sci Eng B* 263:114885
86. Chen K, Bai H, Yan F, He X, Liu X, Xie S, Shen B, Zhai J (2021) Achieving superior energy storage properties and ultrafast discharge speed in environment-friendly niobate-based glass ceramics. *ACS Appl Mater Interfaces* 13:4236–4243
87. Du X, Pu Y, Li X, Peng X, Sun Z, Zhang J, Ji J, Li R, Zhang Q, Chen M (2021) Optimizing the energy storage performance of K<sub>2</sub>O–Nb<sub>2</sub>O<sub>5</sub>–SiO<sub>2</sub> based glass-ceramics with excellent temperature stability. *Ceram Int* 47(8987):8995
88. Xie S, Liu C, Bai H, Chen K, Shen B, Zhai J (2021) Simultaneously ultra-low dielectric loss and rapid discharge time in Ta<sub>2</sub>O<sub>5</sub> doped niobate based glass-ceramics. *J Mater Sci* 56(16278):16289
89. Tarafder A, Annapurna K, Chaliha RS, Tiwari VS, Gupta PK, Karmakar B (2009) Nanostructuring and fluorescence properties of Eu<sup>3+</sup>: LiTaO<sub>3</sub> in Li<sub>2</sub>O–Ta<sub>2</sub>O<sub>5</sub>–SiO<sub>2</sub>–Al<sub>2</sub>O<sub>3</sub> glass-ceramics. *J Mater Sci* 44(4495):4498
90. Tarafder A, Annapurna K, Chaliha RS, Tiwari VS, Gupta PK (1939) Karmakar B (2009) Processing and properties of Eu<sup>3+</sup>: LiTaO<sub>3</sub> transparent glass-ceramic nanocomposites. *J Am Ceram Soc* 92:1934
91. Dymshits O, Vitkin V, Alekseeva I, Khubetsov A, Tsenter M, Polishchuk A, Volokitina A, Serres JM, Mateos X, Zhilin A, Loiko P (2021) Transparent glass-ceramics based on Co<sup>2+</sup>-doped γ-Ga<sub>x</sub>Al<sub>2–x</sub>O<sub>3</sub> spinel nanocrystals for passive Q-switching of Er lasers. *J Lumin* 234:117993
92. Glazunov IV, Malyarevich AM, Yumashev KV, Dymshits OS, Alekseeva IP, Tsenter MY, Bogdanov KV, Zapalova SS, Zhilin AA (2021) Linear and non-linear optical properties of transparent glass-ceramics based on Co<sup>2+</sup>-doped Zn(Al, Ga)<sub>2</sub>O<sub>4</sub> spinel nanocrystals. *J Non-Cryst Solids* 557:120627
93. Ferrari M, Righini GC (2015) Glass-ceramic materials for guided-wave optics. *Int J Appl Glass Sci* 6(240):248
94. Gangadharini U, Molla AR, Tarafder A, Karmakar B (2013) Synthesis and characterization of Eu<sup>3+</sup>-doped transparent glass-ceramics containing nanocrystalline Sr<sup>II</sup>Nb<sup>IV</sup>O<sub>3</sub>. *J Am Ceram Soc* 96(2155):2162
95. Champagnon B, Boukenter A, Duval E (1987) Early stages of nucleation of Zerodur glass: very low frequency Raman scattering and small angle X-ray scattering investigations. *J Non-Cryst Solids* (94)216:221
96. Łukowiak A et al (1995) Glass-ceramics for photonics: advances and perspectives. In: 2014 16th International conference on transparent optical networks (ICTON), 2014, pp 1–4. <https://doi.org/10.1109/ICTON.2014.6876584>

97. Tick PA, Borrelli NF, Cornelius LK, Newhouse MA (1995) Transparent glass ceramics for 1300 nm amplifier applications. *J Appl Phys* 78:6367–6374
98. Tick PA (1998) Are low-loss glass-ceramic optical waveguides possible? *Opt Lett* (23)1904:1905
99. Bhattacharya S, Acharya A (2020) Photonics. In: Bhattacharya S (ed) *Metal Oxides*. Elsevier, *Metal Oxide Glass Nanocomposites*, pp 259–263
100. Mortier M, Monteville A, Patriarche G, Maze G, Auzel F (2001) New progresses in transparent rare-earth doped glass-ceramics. *Opt Mater* 16:255–267
101. Chiasera A, Alombert-Goget G, Ferrari M, Berneschi S, Pelli S, Boulard B, Duverger-Arfulo C (2011) Rare earth-activated glass-ceramic in planar format. *Opt Eng* 50:071105
102. Dieudonn B, Boulard B, Alombert-Goget G, Chiasera A, Gao Y, Kodjikian S, Ferrari M (2013) Up- and down-conversion in  $\text{Yb}^{3+}$ - $\text{Pr}^{3+}$  co-doped fluoride glasses and glass ceramics. *J Non-Cryst Solids* 377:105–109
103. Kukkonen LL, Reaney IM, Furniss D, Seddon AB (2001) Nucleation and crystallization behaviour of transparent, erbium III doped, oxyfluoride glass ceramics for active photonic devices. *Phys Chem Glasses-Eur J Glass Sci Technol B* 42:265–273
104. Goyes C, Ferrari M, Armellini C, Chiasera A, Jestin Y, Righini GC, Fonthal F, Solarte E (2009)  $\text{CO}_2$  laser annealing on erbium-activated glass-ceramic waveguides for photonics. *Opt Mater* 31:1310–1314
105. Nakanishi T, Watanabe K, Ueda J, Fushimi K, Tanabe S, Hasegawa Y (2015) Enhanced light storage of  $\text{SrAl}_2\text{O}_4$  glass-ceramics controlled by selective europium reduction. *J Am Ceram Soc* 98:423–429
106. Ragin T, Zmojda J, Kochanowicz M, Miluski P, Jelen P, Sitarz M, Dorosz D (2015) Thermal, structural and spectroscopic properties of heavy metal oxide glass and glass-ceramics doped with  $\text{Er}^{3+}$  ions. In: *Proceeding of SPIE 9662:96620N-1-96620N-7*
107. Lukowiak A, Zur L, Tran TNL, Meneghetti M, Berneschi S, Conti GN, Pelli S, Trono C, Bhaktha B N S, Zonta D, Taccheo S, Righini GC, Ferrari M (2017) Sol-Gel-derived glass-ceramic photorefractive films for photonic structures. *Crystals* 7:61–1/7
108. Molla AR, Rodrigues AM, Singh SP, Lancelotti RF, Zanutto ED, Rodrigues ACM, Dousti MR, de Camargo ASS, Magon CJ, Silva IDAA (2017) Crystallization, mechanical, and optical properties of transparent, nanocrystalline gahnite glass-ceramics. *J Am Ceram Soc* 100:1963–1975
109. Tran LTN, Zur L, Massella D, Derkowska-Zielinska B, Chiasera A, Varas S, Armellini C, Martucci A, Zonta D, Tran TTV, Lukowiak A, Taccheo S, Dorosz D, Righini GC, Boucher Y G, Ferrari M (2018)  $\text{SiO}_2$ - $\text{SnO}_2$ : $\text{Er}^{3+}$  transparent glass-ceramics: fabrication and photonic assessment. In: *Proceeding of SPIE 10683:106832C-1/9*
110. Cascales C, Balda R, Lezama L, Fernández J (2018) Site symmetry and host sensitization-dependence of  $\text{Eu}^{3+}$  real time luminescence in tin dioxide nanoparticles. *Opt Express* 26:16155–16170
111. Zur L, Tran TNL, Meneghetti M, Ferrari M (2017) Sol-gel derived  $\text{SnO}_2$ -based photonic systems. In: Klein L, Aparicio M, Jitianu A (eds) *Handbook of Sol-Gel Science and Technology*, 2nd edn. Springer International Publishing AG, Basel, Switzerland, pp 1–19
112. Tran TNL, Massella D, Zur L, Chiasera A, Varas S, Armellini C, Righini G C, Lukowiak A, Zonta D, Ferrari M (2018)  $\text{SiO}_2$ - $\text{SnO}_2$ : $\text{Er}^{3+}$  glass-ceramic monoliths. *Appl Sci* 8:1335–1/8
113. Tran TNL (2019) Tin dioxide based photonic glass-ceramics. Ph.D. thesis, University of Trento
114. Berneschi S, Bhaktha SNB, Chiappini A, Chiasera A, Ferrari M, Kinowski C, Turrell S, Trono C, Brenci M, Cacciari I, Conti NG, Pelli S, Righini GC (2010) Highly photorefractive  $\text{Eu}^{3+}$  activated sol-gel  $\text{SiO}_2$ - $\text{SnO}_2$  thin film waveguides. In: *Proceeding of SPIE 7604:76040Z-1/6*
115. Bhaktha SNB, Berneschi S, Conti NG, Righini G C, Chiappini A, Chiasera A, Ferrari M, Turrell S (2010) Spatially localized UV-induced crystallization of  $\text{SnO}_2$  in photorefractive  $\text{SiO}_2$ - $\text{SnO}_2$  thin film. In: *Proceeding of SPIE 7719:77191B-1/5*
116. Manzani D, Junior JBS, Reyna AS, Neto MLS, Bautista JEQ, Ribeiro SJL, de Araujo CB (2019) Phosphotellurite glass and glass-ceramics with high  $\text{TeO}_2$  contents: thermal, structural and optical properties. *Dalton Trans* 48:6261–6272



117. Tran TNL, Armellini C, Varas S, Carpentiero A, Chiappini A, Gluchowski P, Iacob E, Ischia G, Scotognella F, Bollani M, Lukowiak A, Righini GC, Ferrari M, Chiasera A (2021) Assessment of SnO<sub>2</sub>-nanocrystal-based luminescent glass-ceramic waveguides for integrated photonics. *Ceram Int* 47:5534–5541
118. Marcondes LM, Santagneli SH, Manzani D, Cassanjes FC, Batista G, Mendoza VG, da Cunha CR, Poirier GY, Nalin M (2020) High tantalum oxide content in Eu<sup>3+</sup>-doped phosphate glass and glass-ceramics for photonic applications. *J Alloys Compd* 842:155853
119. Singarapu B, Galusek D, Duran A, Pascual MJ (2020) Glass-ceramics processed by spark plasma sintering (SPS) for optical applications. *Appl Sci* 10:2791
120. Enrichi F, Cattaruzza E, Finotto T, Riello P, Righini GC, Trave E, Vomiero A (2020) Ag-sensitized NIR-emitting Yb<sup>3+</sup>-doped glass-ceramics. *Appl Sci* 10:2184
121. Cai J, Wei X, Hu F, Cao Z, Zhao L, Chen Y, Duan C, Yin M (2016) Up-conversion luminescence and optical thermometry properties of transparent glass ceramics containing CaF<sub>2</sub>:Yb<sup>3+</sup>/Er<sup>3+</sup> nanocrystals. *Ceram Int* 42:13990–13995
122. Cao JK, Chen W, Chen L, Sun XY, Guo H (2016) Synthesis and characterization of BaLuF<sub>5</sub>:Tb<sup>3+</sup> oxyfluoride glass ceramics as nanocomposite scintillator for X-ray imaging. *Ceram Int* 42:17834–17838
123. Krishnaiah KV, Filho ESL, Ledemi Y, Nemova G, Messaddeq Y, Kashyap R (2016) Development of ytterbium-doped oxyfluoride glasses for laser cooling applications. *Sci Rep* 6:21905
124. Kummara VK, Ledemi Y, Filho ESL, Nemova G, Messaddeq Y, Kashyap R (2016) Development of Yb<sup>3+</sup>-doped oxyfluoride glass-ceramics with low OH<sup>−</sup> content containing CaF<sub>2</sub> nanocrystals for optical refrigeration. *Opt Eng* 56:011103
125. Lin C, Li L, Dai S, Liu C, Zhao Z, Bocker C, Russel C (2016) Oxyfluoride glass-ceramics for transition metal ion-based photonics: broadband near-IR luminescence of nickel ion dopant and nanocrystallization mechanism. *J Phys Chem C* 120:4556–4563
126. Qiu J, Jiao Q, Zhou D, Yang Z (2016) Recent progress on upconversion luminescence enhancement in rare-earth doped transparent glass-ceramics. *J Rare Earths* 34:341–367
127. Ali MA, Ren J, Liu X, Qiao X, Qiu J (2017) Understanding enhanced upconversion luminescence in oxyfluoride glass-ceramics based on local structure characterizations and molecular dynamics simulations. *J Phys Chem C* 121:15384–15391
128. Chen D, Liu S, Li X, Wan Z, Li S (2017) Gd-based oxyfluoride glass ceramics: Phase transformation, optical spectroscopy and upconverting temperature sensing. *J Eur Ceram Soc* 37:4083–4094
129. Liu Y, Liu XY, Wang WC, Zhou B, Zhang QY (2017) Phase evolution and photoluminescence in Er<sup>3+</sup> doped glass ceramics containing lutetium oxyfluoride nanocrystals. *Ceram Int* 43:13199–13205
130. Guo Y, Zhao L, Fu Y, Dong H, Yu H (2019) Tailoring up-conversion luminescence for optical thermometry in K<sup>+</sup>/Er<sup>3+</sup> co-doped oxyfluoride glass ceramics. *J Lumin* 210:247–254
131. Zhang Y, Lei H, Li G, Zeng L, Tang J (2020) Yb<sup>3+</sup>/Er<sup>3+</sup> co-doped transparent tellurite glass-ceramic for enhanced upconversion luminescence. *Opt Mat* 99:109552
132. Troles J, Niu Y, Duverger-Arfuso C, Smektala F, Brilland L, Nazabal V, Moizan V, Desevedavy F, Houizot P (2008) Synthesis and characterization of chalcogenide glasses from the system Ga–Ge–Sb–S and preparation of a single-mode fiber at 1.55 μm. *Mater Res Bull* 43:976–982
133. Zakery A, Elliott SR (2003) Optical properties and applications of chalcogenide glasses: a review. *J Non-Cryst Solids* 330:1–12
134. Smektala F, Quemard C, Couderc V, Barthélémy A (2000) Non-linear optical properties of chalcogenide glasses measured by Z-scan. *J Non-Cryst Solids* 274:232–237
135. Shaw LB, Cole B, Thielen PA, Sanghera JS, Aggarwal ID (2001) Mid-wave IR and long-wave IR laser potential of rare-earth doped chalcogenide glass fiber. *J Quantum Electron* 48(1127):1137
136. Lin C, Dai S, Liu C, Song B, Xu Y, Chen F, Heo J (2012) Mechanism of the enhancement of mid-infrared emission from GeS<sub>2</sub>-Ga<sub>2</sub>S<sub>3</sub> chalcogenide glass-ceramics doped with Tm<sup>3+</sup>. *Appl Phys Lett* 100:231910

137. Lozano BW, de Araujo CB, Ledemi Y, Messaddeq Y (2013) Upconversion luminescence in  $\text{Er}^{3+}$  doped  $\text{Ga}_{10}\text{Ge}_{25}\text{S}_{65}$  glass and glass-ceramic excited in the near-infrared. *J Appl Phys* 113:083520
138. Li Z, Li C, Qu G, Nie Q, Dai S (2014) Optical properties and crystallization behavior of  $45\text{GeS}_2\cdot 30\text{Ga}_2\text{S}_3\cdot 25\text{Sb}_2\text{S}_3$  chalcogenide glass. *J Non-Cryst Solids* 383:112–115
139. Zhang C, Zhang J, Lin C, Dai S, Chen F (2020) Improvement of third-order nonlinear properties in  $\text{GeS}_2\text{-Sb}_2\text{S}_3\text{-CsCl}$  chalcogenide glass ceramics embedded with CsCl nano-crystals. *Ceram Int* 46:27990–27995
140. Cao Z, Dai S, Ding S, Wang M, Xu L, Liu C, Lin C (2021) Chalcogenide glass ceramics: a high-performing innovative infrared acousto-optic material. *J Eur Ceram Soc* (in press). <https://doi.org/10.1016/j.jeurceramsoc.2021.07.022>
141. Cui M, Yang A, Sun M, Lin H, Lin H, Ren J, Yang Z (2021) 2.5–5.5  $\mu\text{m}$  mid-infrared emission from  $\text{Ni}^{2+}$ -doped chalcogenide glass ceramics containing  $\text{CsPbI}_3$  perovskite nanocrystals. *J Am Ceram Soc* 00:1–6 (in press). <https://doi.org/10.1111/jace.17941>
142. Lu X, Zhang R, Zhang Y, Zhang S, Ren J, Strizik L, Wagner T, Farrell G, Wang P (2020) Crystal-field engineering of ultrabroadband mid-infrared emission in  $\text{Co}^{2+}$ -doped nano-chalcogenide glass composites. *J Eur Ceram Soc* 40:103–107